frontiers | Research Topics

Developmental and acquired mechanisms of calcific aortic valve disease

Edited by
Joy Lincoln, Lakshmi Prasad Dasi and Katherine Yutzey

Published in
Frontiers in Cardiovascular Medicine

ISSN 1664-8714
ISBN 978-2-83251-582-2
DOI 10.3389/978-2-83251-582-2

About Frontiers

Frontiers is more than just an open access publisher of scholarly articles: it is a pioneering approach to the world of academia, radically improving the way scholarly research is managed. The grand vision of Frontiers is a world where all people have an equal opportunity to seek, share and generate knowledge. Frontiers provides immediate and permanent online open access to all its publications, but this alone is not enough to realize our grand goals.

Frontiers journal series

The Frontiers journal series is a multi-tier and interdisciplinary set of open-access, online journals, promising a paradigm shift from the current review, selection and dissemination processes in academic publishing. All Frontiers journals are driven by researchers for researchers; therefore, they constitute a service to the scholarly community. At the same time, the *Frontiers journal series* operates on a revolutionary invention, the tiered publishing system, initially addressing specific communities of scholars, and gradually climbing up to broader public understanding, thus serving the interests of the lay society, too.

Dedication to quality

Each Frontiers article is a landmark of the highest quality, thanks to genuinely collaborative interactions between authors and review editors, who include some of the world's best academicians. Research must be certified by peers before entering a stream of knowledge that may eventually reach the public - and shape society; therefore, Frontiers only applies the most rigorous and unbiased reviews. Frontiers revolutionizes research publishing by freely delivering the most outstanding research, evaluated with no bias from both the academic and social point of view. By applying the most advanced information technologies, Frontiers is catapulting scholarly publishing into a new generation.

What are Frontiers Research Topics?

Frontiers Research Topics are very popular trademarks of the *Frontiers journals series*: they are collections of at least ten articles, all centered on a particular subject. With their unique mix of varied contributions from Original Research to Review Articles, Frontiers Research Topics unify the most influential researchers, the latest key findings and historical advances in a hot research area.

Find out more on how to host your own Frontiers Research Topic or contribute to one as an author by contacting the Frontiers editorial office: frontiersin.org/about/contact

Developmental and acquired mechanisms of calcific aortic valve disease

Topic editors

Joy Lincoln — Medical College of Wisconsin, United States

Lakshmi Prasad Dasi — Georgia Institute of Technology, United States

Katherine Yutzey — Cincinnati Children's Hospital Medical Center, United States

Citation

Lincoln, J., Dasi, L. P., Yutzey, K., eds. (2023). *Developmental and acquired mechanisms of calcific aortic valve disease*. Lausanne: Frontiers Media SA.

doi: 10.3389/978-2-83251-582-2

Table of contents

frontiers in Cardiovascular Medicine

ORIGINAL RESEARCH
published: 17 May 2021
doi: 10.3389/fcvm.2021.673519

Diagnostic and Prognostic Accuracy of Aortic Valve Calcium Scoring in Patients With Moderate-to-Severe Aortic Stenosis

Jamila Boulif[1,2†], Alisson Slimani[1,2†], Siham Lazam[1,2], Christophe de Meester[1,2], Sophie Piérard[1,2], Agnès Pasquet[1,2], Anne-Catherine Pouleur[1,2], David Vancraeynest[1,2], Gébrine El Khoury[1,2], Laurent de Kerchove[1,2], Bernhard L. Gerber[1,2] and Jean-Louis Vanoverschelde[1,2]*

[1] Pôle de Recherche Cardiovasculaire, Institut de Recherche Expérimentale et Clinique, Université Catholique de Louvain, Brussels, Belgium, [2] Divisions of Cardiology and Cardiothoracic Surgery, Cliniques Universitaires Saint-Luc, Brussels, Belgium

OPEN ACCESS

Edited by:
Joy Lincoln,
Medical College of Wisconsin,
United States

Reviewed by:
Antonino S. Rubino,
University of Campania Luigi Vanvitelli, Italy
Francesco Pollari,
Nürnberg Hospital, Germany

***Correspondence:**
Jean-Louis Vanoverschelde
jean-louis.vanoverschelde@uclouvain.be

[†]These authors have contributed equally to this work

Specialty section:
This article was submitted to Heart Valve Disease, a section of the journal Frontiers in Cardiovascular Medicine

Received: 27 February 2021
Accepted: 06 April 2021
Published: 17 May 2021

Citation:
Boulif J, Slimani A, Lazam S, de Meester C, Piérard S, Pasquet A, Pouleur A-C, Vancraeynest D, El Khoury G, de Kerchove L, Gerber BL and Vanoverschelde J-L (2021) Diagnostic and Prognostic Accuracy of Aortic Valve Calcium Scoring in Patients With Moderate-to-Severe Aortic Stenosis. Front. Cardiovasc. Med. 8:673519. doi: 10.3389/fcvm.2021.673519

Background: Assessing the true severity of aortic stenosis (AS) remains a challenge, particularly when echocardiography yields discordant results. Recent European and American guidelines recommend measuring aortic valve calcium (AVC) by multidetector row computed tomography (MDCT) to improve this assessment.

Aim: To define, using a standardized MDCT scanning protocol, the optimal AVC load criteria for truly severe AS in patients with concordant echocardiographic findings, to establish the ability of these criteria to predict clinical outcomes, and to investigate their ability to delineate truly severe AS in patients with discordant echocardiographic AS grading.

Methods and Results: Two hundred and sixty-six patients with moderate-to-severe AS and normal LVEF prospectively underwent MDCT and Doppler-echocardiography to assess AS severity. In patients with concordant AS grading, ROC analysis identified optimal cut-off values for diagnosing severe AS using different AVC load criteria. In these patients, 4-year event-free survival was better with low AVC load (60–63%) by these criteria than with high AVC load (23–26%, log rank $p < 0.001$). Patients with discordant AS grading had higher AVC load than those with moderate AS but lower AVC load than those with severe high-gradient AS. Between 36 and 55% of patients with severe LG-AS met AVC load criteria for severe AS. Although AVC load predicted outcome in these patients as well, its prognostic impact was less than in patients with concordant AS grading.

Conclusions: Assessment of AVC load accurately identifies truly severe AS and provides powerful prognostic information. Our data further indicate that patients with discordant AS grading consist in a heterogenous group, as evidenced by their large range of AVC load. MDCT allows to differentiate between truly severe and pseudo-severe AS in this population as well, although the prognostic implications thereof are less pronounced than in patients with concordant AS grading.

Keywords: aortic stenosis, low gradient, aortic valve calcium, computed tomgraphy, outcome

INTRODUCTION

Several recent retrospective studies have indicated that, in elderly patients and particularly in elderly women with severe aortic stenosis (AS), physicians are frequently confronted with lower than expected mean transvalvular gradients, even in the presence of a preserved left ventricular ejection fraction (LVEF) (1–5). To differentiate this new form of severe AS from the classical "low flow (LF)—low gradient" (LG) form seen in patients with LV dysfunction (1), the term "paradoxical LG-AS" was recently proposed (2, 3).

There is considerable debate as to the clinical significance of severe paradoxical LG-AS. Because it is frequently associated with concentric LV remodeling (5), low transvalvular flow rates (2), increased interstitial fibrosis (6), reduced LV long-axis function (5, 7), and guarded prognosis (2, 4, 8–10), several authors have hypothesized it could represent a more advanced form of severe AS. On the other hand, the results of recent natural history studies have indicated that severe paradoxical LG-AS usually evolves into severe high gradient (HG)-AS overtime (11–13) and that its clinical outcome resembles that of moderate AS (12, 14), thus challenging the former hypothesis. It was further suggested that severe paradoxical LG-AS could be an intermediary stage between moderate AS and severe HG-AS (11).

To get further insight into the pathophysiology of this challenging condition, an alternate method for assessing AS severity is highly desirable. We and others have previously shown that aortic valve calcification (AVC) load is a fundamental marker of the severity of the aortic valve (AV) lesions seen in "degenerative" AS and that it can be accurately quantified by use of X-Ray computed tomography modalities, such as Electron Beam Computed Tomography (EBCT) and Multidetector Computed Tomography (MDCT) (15, 16). Based on these observations, the most recent European Society of Cardiology (ESC) guidelines have recommended to use this approach to delineate the severity of AS in patients with discordant grading by echocardiography (17), and proposed specific AVC load thresholds to be used for diagnosing truly severe AS in this setting. Unfortunately, the proposed thresholds were derived from a single multicenter study, which used a wide variety of scanning protocols (18–20), some of which have been shown to significantly affect the resulting AVC load values. Accordingly, the aims of the present study were to define, using a standardized MDCT scanning protocol, the optimal AVC load criteria for truly severe AS in patients with concordant echocardiographic findings, to establish the potential of these criteria to predict clinical outcomes and to investigate their ability to delineate truly severe AS in patients with discordant echocardiographic AS grading.

METHODS

Patients' Population

Between February 1st, 2013 and August 31th, 2015, 584 consecutive patients with LVEF $>$ 50% and at least moderate native AS, defined as an effective orifice area (EOA) $<$ 1.5 cm^2 and an indexed EOA (EOAi) $<$ 0.9 cm^2/m^2 by transthoracic echocardiography were prospectively identified in the valvular Clinic of the Cliniques Universitaires St-Luc and approached for inclusion in the IRB approved study (2014/29Nov/560). Patients were included into the study after giving written informed consent. Patients with rheumatic AS, LV dysfunction, more than mild aortic regurgitation or mitral valve disease, poor quality of echocardiographic images or a life expectancy $<$ 1 year in the absence of severe AS were not considered for inclusion. The final study population consisted of 266 patients (**Figure 1**). After consenting to participate into the study, all patients underwent a comprehensive echocardiographic assessment of their AS and an MDCT examination within 10 $\pm$ 19 days of their echocardiographic examination.

Doppler Echocardiography Measurements

Echocardiographic data were obtained with commercially available ultrasound systems (IE33 or EPIC, Philps Medical System Andover, MA) conducted by experienced sonographers. All patients underwent a comprehensive examination, including M-mode, 2-dimensional and Doppler examinations according to ASE/EACVI recommendations.

For assessment of AS, multiple transducer positions were systematically used to record peak aortic jet velocities. The left ventricular outflow tract (LVOT) diameter was obtained from the parasternal long-axis view in mid-systole, parallel to the valve plane and immediately adjacent to the aortic leaflet insertion into the annulus. The LVOT velocity was recorded from the apical window by placing the pulsed-wave-Doppler sample volume in the LVOT, proximal to the aortic valve. Proper positioning of the sample volume was ensured by verifying the presence of smooth spectral velocity curves associated with an aortic valve closing click. Care was taken to optimize the ultrasound beam—blood flow alignment and to avoid sampling in the transvalvular jet or the proximal flow convergence region by excluding velocity curves with spectral broadening at peak ejection. The maximal velocity across the aortic valve was measured with continuous-wave Doppler from multiple positions (apical, right parasternal, suprasternal, and subxyphoidal). The highest velocity signal was used to calculate peak and mean gradients. The EOA was calculated by use of the continuity equation, assuming that the LVOT area had a circular shape. LV volumes and LVEF were calculated by use of the biplane Simpson method and left atrial volume using biplane area-length method. In case of atrial fibrillation, 5–10 consecutive beats were systematically averaged.

Severe AS was defined as an indexed EOAi $<$ 0.6 cm^2/m^2 and was further stratified into subgroups with high and paradoxically low transvalvular gradients, respectively, in the presence of a mean transvalvular gradient (MPG) $\geq$ and $<$ 40 mmHg. On the basis of EOAi and MPG, patients were categorized in 3 groups: 2 groups with concordant AS grading (moderate AS with an EOAi $>$ 0.6 cm^2/m^2 and a MPG $<$ 40 mm Hg and severe high gradient AS with EOAi $\leq$ 0.6 cm^2/m^2 and a MPG $\geq$ 40 mm Hg) and 1 group with discordant AS grading (severe paradoxical LG-AS with an EOAi $<$ 0.6 cm^2/m^2 and MPG $<$ 40 mmHg). Patients with severe paradoxical LG-AS were further stratified into subgroups with low flow (LF) and normal flow (NF), respectively, in the presence of an indexed stroke volume $<$ 35 or $\geq$ 35 mL/m^2.

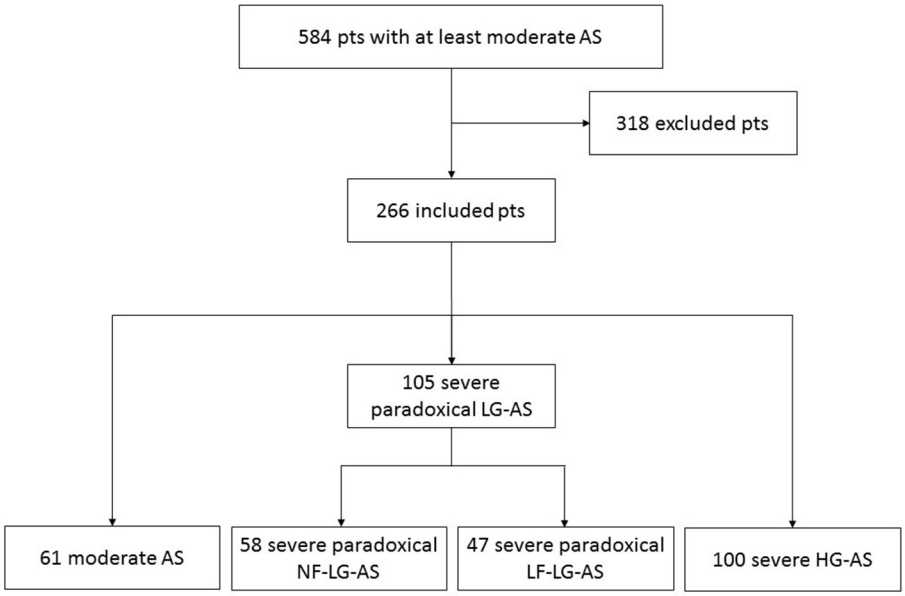

FIGURE 1 | Flow chart of the study population. Pts, patients; AS, aortic stenosis; NF, normal flow; LF, low flow; LG, low gradient; HG, high gradient.

Multidetector Computed Tomography Measurements

All MDCT examinations were performed by use of a helical 256-slice CT scanner (Brillance ICT, Philips Healthcare, Cleveland, Ohio, USA). Acquisition parameters were set as follows: tube potential of 120 kV, tube current of 250 mA, gantry rotation time of 330 ms, detector configuration of 32 × 0.625 mm, and pitch of 0.14–0.18. Contiguous non-overlapping slices of 2.5 mm were acquired in a craniocaudal direction during inspiratory breathhold and using prospective ECG-triggering at 75% of R-R interval and a CB filter. No contrast enhancement was needed and no beta-blocker was administered for the purpose of the examination. The average of the total estimated effective radiation dose per CT scan was 0.89 ± 0.08 mGy and the average dose-length product was 64 ± 6 mGy.cm.

All measurements of AVC were performed on dedicated workstations using a validated commercially available software (heartbeat calcium scoring; Philips Medical Systems). Calcifications were identified by using a threshold of CT attenuation of 130 Hounsfield Units (HU), based on Agatston scoring method (21). Measurements were made in the axial view by a single investigator who identified the calcifications corresponding to the aortic valve leaflets. For this purpose, the aortic valve was visualized in multiple planes, including cross-sectional valve plane, to accurately exclude contiguous calcium in the mitral valve annulus, the aortic wall and the coronary arteries. The Agatston score was reported as Agatston units (AU). AVC index was computed as the Agatston score divided by BSA and AVC density as Agatston score indexed to the LVOT cross sectional area (measured from echocardiographic data). The accuracy of our measurements was demonstrated in a previous study by anatomical validation, using *in vivo* ($r = 0.86$, $p < 0.001$) and *ex vivo* ($r = 0.93$, $p < 0.001$) AVC measurements (16).

Outcome

Follow-up events were obtained for all patients between September and December 2018 by recalling physicians, cardiologists or patients themselves. Causes of death were established by autopsy records if the patient died in hospital, and otherwise by the referring physician. The primary outcome was the time to first event of death or aortic valve replacement, including both open surgical and transcatheter procedures. Decisions to proceed to aortic valve replacement were made according to international clinical guidelines and independently of MDCT calcium scoring, the results of which were not made available to the multidisciplinary discussion team. Patients in whom a decision to refer to aortic valve replacement had been made prior to the CT calcium scoring were excluded from the outcome analyses ($n = 78$).

Statistical Methods

All analyses were performed using the SPSS v19.0 (SPSS Inc., IBM, Chicago, IL) software. Normality was assessed by use of the Kolmogorov Smirnov-test. Continuous variables were expressed as mean ± 1 SD and were compared among groups using ANOVA when normally distributed or else using the Kruskall-Wallis-test. Individual differences among groups were compared *post-hoc* using Tukey-Kramers-test for normally distributed data with equal variances, the Games–Howell-test for normally distributed data with unequal variances and the Mann-Whitney *U*-tests (with Bonferroni correction for multiple comparisons) for non-normally distributed data. Categorical

TABLE 1 | Baseline demographic and clinical characteristics.

	MAS ($n = 61$)	Severe paradoxical NF-LG-AS ($n = 58$)	Severe paradoxical LF-LG-AS ($n = 47$)	Severe HG-AS ($n = 100$)	*P*-value
Age, y	79 ± 10	76 ± 10	77 ± 10	76 ± 10	0.52
Male sex, *n* (%)	31 (51)	35 (60)	30 (64)	55 (55)	0.519
Body surface area, kg/m²	1.77 ± 0.21	1.84 ± 0.20	1.83 ± 0.17	1.84 ± 0.23	0.191
Heart rate, beat/min	69 ± 12	68 ± 13	73 ± 18	67 ± 12	0.173
Systemic hypertension, *n* (%)	56 (92)†§	40 (69)*	38 (81)	72 (72)*	0.009
Dyslipidemia, *n* (%)	37 (61)	42 (72)	35 (74)	67 (67)	0.394
Diabetes, *n* (%)	11 (18)	12 (21)	13 (28)	18 (18)	0.552
Smoking, *n* (%)	24 (39)	24 (41)	22 (47)	39 (39)	0.827
Family history, *n* (%)	9 (15)	11 (19)	10 (22)	15 (15)	0.736
Coronary artery disease, *n* (%)	25 (41)	25 (43)	28 (60)	41 (41)	0.169
Atrial fibrillation, %	13 (21)	13 (22)	18 (38)§	17 (17)‡	0.039
GFR, mL/min	75 ± 32†	61 ± 27*	64 ± 20	63 ± 28	0.034
NYHA class III to IV, *n* (%)	15 (25)	14 (24)	14 (30)	28 (28)	0.646
Angina, *n* (%)	17 (28)	18 (31)	15 (32)	28 (28)	0.944
Syncope, *n* (%)	3 (5)	3 (5)	7 (15)	9 (9)	0.219

*AS, aortic stenosis; GFR, glomerular filtration rate; MAS, moderate AS; HG, high gradient; LF, low flow; LG, low gradient; NF, normal flow; NYHA, New York Heart Association. *$p < 0.05$ vs. MAS; †$p < 0.05$ vs. severe paradoxical NF-LG-AS; ‡$p < 0.05$ vs. severe paradoxical LF-LG-AS; §$p < 0.05$ vs. severe HG-AS.*

TABLE 2 | Baseline echocardiographic characteristics.

	MAS ($n = 61$)	Severe paradoxical NF-LG-AS ($n = 58$)	Severe paradoxical LF-LG-AS ($n = 47$)	Severe HG-AS ($n = 100$)	*P*-value
Mean transvalvular flow rate, mL/s	244 ± 44‡	240 ± 41‡	167 ± 36*†§	233 ± 57‡	<0.001
Peak velocity, cm/s	270 ± 45†‡§	360 ± 29*‡§	325 ± 51*†§	460 ± 52*†‡	<0.001
Mean gradient, mmHg	18 ± 6†‡§	31 ± 4*‡§	25 ± 8*†§	53 ± 13*†‡	<0.001
EOA, cm²	1.28 ± 0.16†‡§	0.91 ± 0.15*‡§	0.74 ± 0.19*†	0.68 ± 0.16*†	<0.001
Indexed EOA, cm²/m²	0.73 ± 0.10†‡§	0.50 ± 0.02*‡§	0.40 ± 0.09*†	0.37 ± 0.08*†	<0.001
Indexed LVEDV, mL/m²	60 ± 15‡	56 ± 15	50 ± 14*§	61 ± 15‡	0.974
LV ejection fraction, %	61 ± 7	60 ± 7	58 ± 6	59 ± 6	0.152
Indexed LV stroke volume, mL/m²	45 ± 10‡	43 ± 6‡	28 ± 5*†§	42 ± 9‡	<0.001
Indexed LA volume, mL/m²	72 ± 34	61 ± 28§	72 ± 40	76 ± 31†	0.064
LVOT diameter, cm	2.1 ± 0.2§	2.1 ± 0.2§	2.0 ± 0.2*†	2.0 ± 0.2	<0.001
A. Fib., *n* (%)	7 (11)‡	3 (5)‡	13 (28)*†§	6 (6)‡	<0.001

*AS, aortic stenosis; EOA, effective orifice area; LA, left atrium; LV, left ventricle; LVEDV, left ventricular end-diastolic volume; LVOT, left ventricle outflow tract; MAS, moderate AS; HG, high gradient; LF, low flow, LG, low gradient; NF, normal flow, TR, tricuspid regurgitation. *$p < 0.05$ vs. MAS; †$p < 0.05$ vs. severe paradoxical NF-LG-AS; ‡$p < 0.05$ vs. severe paradoxical LF-LG-AS; §$p < 0.05$ vs. severe HG-AS.*

variables were expressed as counts and percentages and were compared among groups using χ^2 or the Fisher exact-test. In patients with concordant echocardiographic data, receiver operator curves were used to assess AVC load thresholds and to identify the optimum thresholds for severe AS. Their predictive value was evaluated by computing the area under the ROC curves. Kaplan–Meier curves and Cox proportional hazards regression analyses were used to determine the ability of these AVC load thresholds to predict adverse clinical events. Where appropriate, collinearity of variables was assessed before inclusion in the multivariable model. All tests were two-sided and a *p*-value of < 0.05 was considered indicative of a statistically significant difference.

RESULTS

Baseline Clinical, Hemodynamic, and Echocardiographic Characteristics

The final study population consisted of 266 patients [151 men (57%), mean age: 77 ± 10 years] of which, 61 (22.9%) presented with moderate AS, 58 (22%) with severe paradoxical NF-LG-AS, 47 (18%) with severe paradoxical LF-LG-AS and 100 (38%) with severe HG-AS (**Figure 1**). The clinical and demographic characteristics of these 4 groups are shown in **Table 1** and their echocardiographic parameters in **Table 2**. Overall, the clinical, demographic and echocardiographic characteristics were similar between groups, except for the glomerular filtration rate,

TABLE 3 | AVC load in patients with moderate AS, severe paradoxical LG-AS and severe HG-AS.

	MAS ($n = 61$)	Severe paradoxical NF-LG-AS ($n = 58$)	Severe paradoxical LF-LG-AS ($n = 47$)	Severe HG-AS ($n = 100$)	*P*-value
AVC, AU	1,185 ± 674†‡§	1,891 ± 951*§	1,842 ± 888*§	3,339 ± 1,710*†‡	<0.001
Men	1,462 ± 685§	2,190 ± 969§	2,027 ± 741§	3,975 ± 1,941*†‡	<0.001
Women	900 ± 537§	1,435 ± 730§	1,516 ± 1,046§	2,563 ± 913*†‡	<0.001
AVC density, AU/cm²	332 ± 192†‡§	543± 278*§	620 ± 334*§	1,005 ± 443 *†‡	<0.001
Men	401 ± 206‡§	601 ± 304§	659 ± 299*§	1,115 ± 500*†‡	<0.001
Women	206 ± 148‡§	454 ± 212§	551 ± 389*§	871 ± 319*†‡	<0.001
AVC index, AU/m²	666 ± 373†‡§	1,021 ± 493*§	1,004 ± 487*§	1,815 ± 858*†‡	<0.001
Men	785 ± 389§	1,139 ± 518§	1,084 ± 413§	2,040 ± 975*†‡	<0.001
Women	543 ± 316§	845 ± 393§	865 ± 585§	1,540 ± 593*†‡	<0.001

*Values are mean ± SD. AVC, aortic valve calcium. *p < 0.05 vs. MAS; †p < 0.05 vs. severe paradoxical NF-LG-AS; ‡p < 0.05 vs. severe paradoxical LF-LG-AS; §p < 0.05 vs. severe HG-AS.*

which was significantly higher in patients with moderate AS than in those with severe paradoxical NF-LG-AS and atrial fibrillation, which was more prevalent in patients with severe paradoxical LF-LG-AS than in those with severe HG-AS. In addition, patients with moderate AS had higher prevalence of hypertension. Patients with severe paradoxical NF-LG-AS also exhibited larger EOAis than the other severe AS groups whereas severe paradoxical LF-LG-AS displayed lower LV volume indexes than the other groups.

AVC Load in the Different AS Groups

As shown in **Table 3** and **Figure 2**, patients with moderate AS displayed significantly lower Agatston score, AVC density and AVC index than patients with severe HG-AS. Agastson score, AVC density and AVC index of patients with severe paradoxical LG-AS was intermediate between MAS and severe AS. Among patients with severe paradoxical LG-AS, no differences in Agatston score, AVC density or AVC index were found between those with NF and those with LF (**Table 3**). These observations were made in both men and women, while Agastson score AVC density and AVC index were systematically higher in men than in women.

MDCT Diagnostic Thresholds in Patients With Concordant AS Grading

As shown in **Table 4**, using ROC analysis, the best cutoff values to identify severe AS were an Agatston score ≥ 1,577 AU for women and ≥ 2,238 AU for men, an AVC density ≥ 495 AU/cm² for women and ≥ 581 AU/cm² for men and an AVC index ≥ 891 AU/m² for women and ≥ 1,130 AU/m² for men. AVC density was associated with the highest area under the curve (AUC) both for women and men (AUC: 0.98 and 0.96, respectively), followed by the Agatston score (AUC: 0.94 each) and the AVC index (AUC: 0.96 and 0.93, respectivly).

Prediction of Adverse Events by AVC Load Indices

Event-free survival was assessed in the 188 patients in whom the decision to proceed to surgery had not yet been made at the time of the MDCT investigation. Over a mean follow-up of 31 months (range 1–48 months), 50 died and 94 underwent aortic valve replacement. The overall event-free survival of this cohort was 72 ± 3%, 63 ± 4%, and 46 ± 4% at, respectively, 1, 2, and 4 years. As shown in **Figure 3**, event-free survival was better in patients with moderate AS or severe paradoxical LG-AS than in those with severe HG-AS.

The impact of the different AVC load indices on event-free survival was tested in the entire population (**Figure 4**) as well as in the subgroups of patients with concordant and discordant echocardiographic AS grading (**Figure 5**). To delineate the factors independently associated with the combined end-point of death and aortic valve replacement, different Cox's proportional hazards regression models were generated. Using AVC load indices as continuous variables (**Table 5**, model 1), Cox's analysis identified the AVC index as the sole independent predictor of outcome. Using the best AVC load indices cut-off values, as determined by the ROC curve analyses (**Table 5**, model 2), Cox's analysis identified the AVC Agatston score, age and the effective orifice area as independent predictors of outcome.

Comparison With Previously Published AVC Load Thresholds

Table 5 compares the sensitivity, specificity and overall accuracy of different AVC load thresholds published in the literature to those found in our study. Overall, the sensitivity of these tresholds was similar (from 91 to 93% in women and from 87 to 89% in men). Differences in specificity were nonetheless observed, the thresholds recommended by the ESC guidelines and those proposed by Clavel et al. being less specific than those proposed by Pawade et al. or those found in the present study.

Using univariate Cox's proportional hazard analyses, we also compared the ability of the different AVC load thresholds to predict outcome. As shown in **Tables 6** and **7**, all AVC load thresholds were highly predictive of the combined end-point of death and need for aortic valve replamcement. Yet, the model based on the thresholds found in the present study was the most powerful, as shown by its higher χ^2 and its lower AIC and SBC.

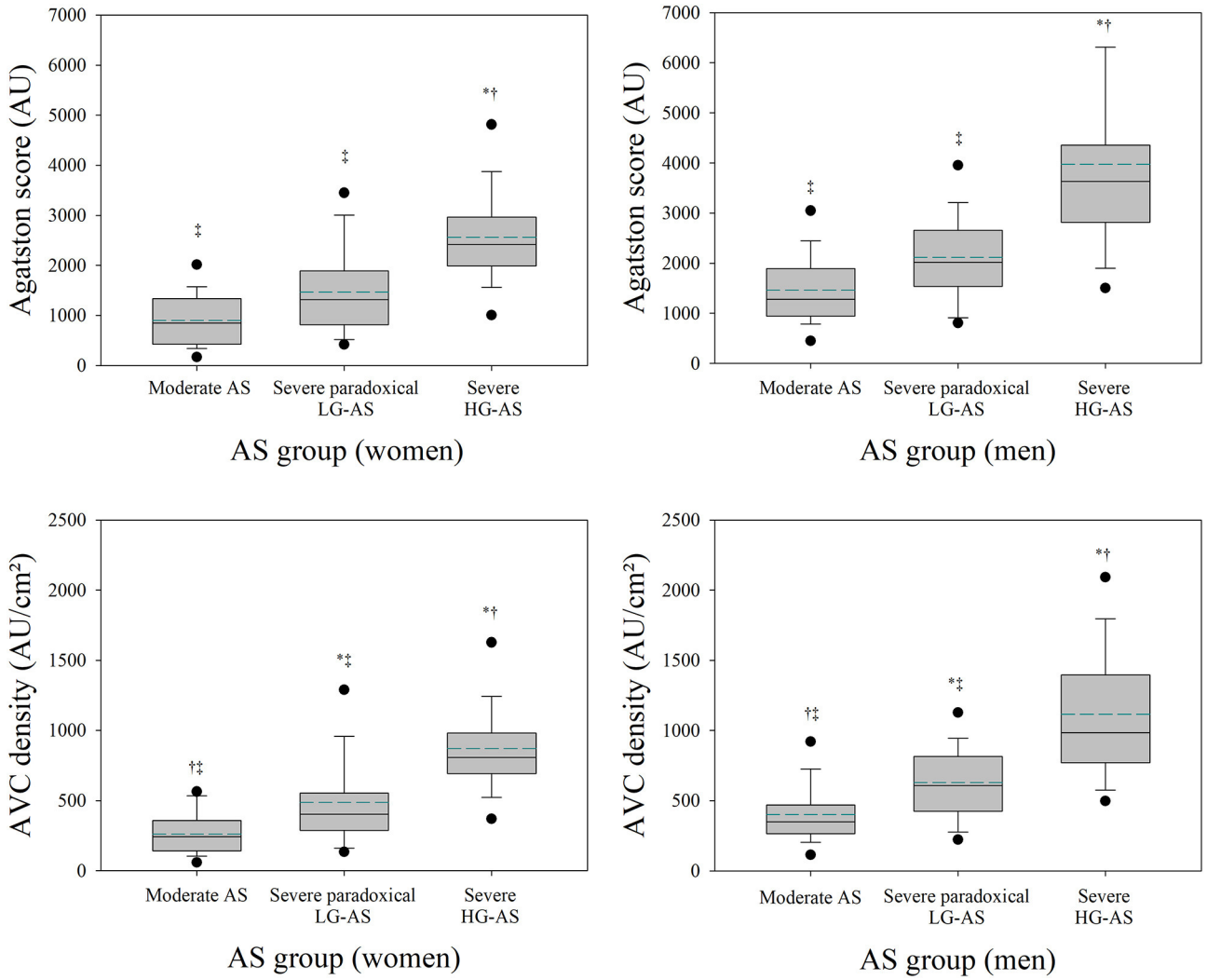

FIGURE 2 | AVC load indices in patients with moderate-to-severe aortic stenosis. Box plots of aortic valve Agatston score (AVC) and AVC density in women (left upper panel) and men (right upper panel) with moderate-to-severe aortic stenosis. The upper and lower edges of the boxes represent the 25th and 75th percentiles. The horizontal line within the boxes represents the median value and the dashed line the mean value. Error bars represent the 95% confidence interval. Pts, patients; AS, aortic stenosis; NF, normal flow; LF, low flow; LG, low gradient; HG, high gradient. $^{*}p < 0.05$ vs. MAS; $^{\dagger}p < 0.05$ vs. severe paradoxical LG-AS; $^{\ddagger}p < 0.05$ vs. severe HG-AS.

Proportion of Truly Severe AS in the Different AS Severity Groups

Figure 6 shows the proportion of patients with truly severe AS based on the AVC load thresholds found in our study. As shown, the different AVC load indices correctly identified > 90% of patients with severe HG-AS and > 85% of patients with moderate AS. Depending on the parameter used, 36–55% of patients with severe paradoxical LG-AS also met AVC load criteria for severe AS. **Figure 7** shows the same analysis according to the AVC load thresholds proposed in the literature. These thresholds identified a similar proportion of severe calcifications in patients with severe HG-AS. By contrast, all 3 literature thresholds identified a larger proportion of patients with moderate AS displaying severe calcifications. Similar observations were made in patients with severe paradoxical LG-AS.

DISCUSSION

The aims of the present study were to define, using a standardized MDCT scanning protocol, the optimal AVC load criteria for truly severe AS in patients with concordant echocardiographic AS grading, to establish the potential of these criteria to predict clinical outcomes and to investigate their ability to delineate truly severe AS in patients with discordant echocardiographic AS grading. Our results can be summarized as follows:

- AVC load increases from moderate AS, over severe paradoxical LG-AS to severe HG-AS.
- In patients with concordant echocardiographic AS grading, all different AVC load indices permit to distinguish between moderate AS and severe HG-AS with a similar overall accuracy of 87–91%.

TABLE 4 | Diagnostic accuracy of severe calcification in patients with concordant echocardiographic grading.

		Cutoff	Sensitivity (%)	Specificity (%)	Accuracy (%)	AUC
AVC (AU)						
Women	ESC guidelines (17)	1,200	93	66	69	–
	Clavel et al. (18)	1,274	93	73	85	–
	Pawade et al. (22)	1,377	93	83	89	–
	Boulif et al.	1,569	91	90	90	0.94
Men	ESC guidelines (17)	2,000	89	84	87	–
	Clavel et al. (18)	2,065	89	84	87	–
	Pawade et al. (22)	2,062	89	84	87	–
	Boulif et al.	2,238	87	87	87	0.94
AVC density (AU/cm²)						
Women	ESC guidelines (17)	-	-	-	-	–
	Clavel et al. (18)	292	98	60	83	–
	Pawade et al. (22)	420	93	83	89	–
	Boulif et al.	495	91	90	91	0.98
Men	ESC guidelines (17)	-	-	-	-	–
	Clavel et al. (18)	476	100	77	92	–
	Pawade et al. (22)	527	94	81	89	–
	Boulif et al.	581	87	87	87	0.96
AVC index (AU/m²)						
Women	ESC guidelines (17)	-	-	-	-	–
	Clavel et al. (18)	637	96	56	80	–
	Pawade et al. (22)	784	91	83	85	–
	Boulif et al.	891	91	90	91	0.96
Men	ESC guidelines (17)	-	-	-	-	–
	Clavel et al. (18)	1,067	89	83	87	–
	Pawade et al. (22)	1,058	89	84	87	–
	Boulif et al.	1,130	87	87	87	0.93

AUC, area under the curve; AVC, aortic valve calcium.

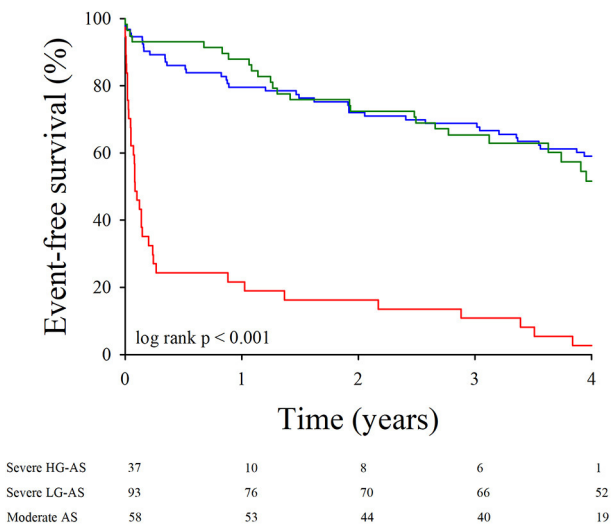

FIGURE 3 | Event-free survival according to baseline AS severity. Kaplan-Meier survival curves for the combined end-point of death and need for aortic valve replacement in patients with severe HG-AS in red, severe paradoxical LG-AS in dark green and moderate AS in dark blue.

- The observed AVC load thresholds also allow predicting which patient will die or require aortic valve replacement.
- Depending on the criteria used, between 36 and 55% of patients with severe paradoxical LG-AS meet AVC load criteria for severe AS, the lowest proportion being found using our own thresholds, and the highest proportion being obtained using the 2017 ESC guidelines thresholds or those proposed by Clavel et al. and Pawade et al.
- The prognostic impact of AVC load thresholds is less in patients with discordant AS grading than in those with concordant AS grading.

Patients with severe paradoxical LG-AS despite normal LVEF pose diagnostic and management challenges that are distinctly different from the majority of patients with severe HG-AS. Both the European and American guidelines recognize the complexity of reaching a final decision in these patients and consider reasonable to propose AVR in symptomatic patients, provided that clinical, hemodynamic, and anatomic data support valve obstruction as the most likely cause of symptoms (17, 23). According to the most recent ESC guidelines, this can be best achieved by measuring AVC load using MDCT (17).

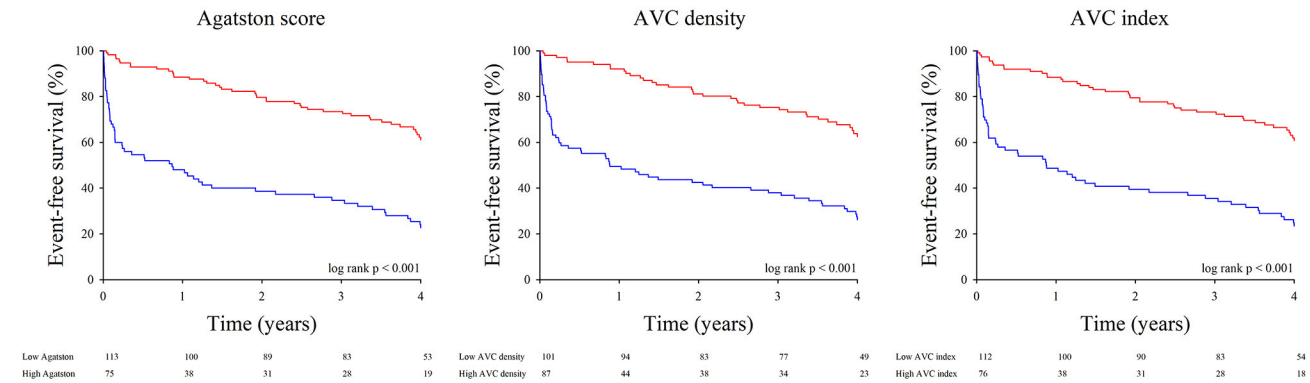

FIGURE 4 | Event-free survival according to AVC load. Kaplan-Meier survival curves for the combined end-point of death and need for aortic valve replacement in patients with low (red line) and high (blue line) AVC load. Left panel: Agatston score; middle panel: AVC density; right panel: AVC index.

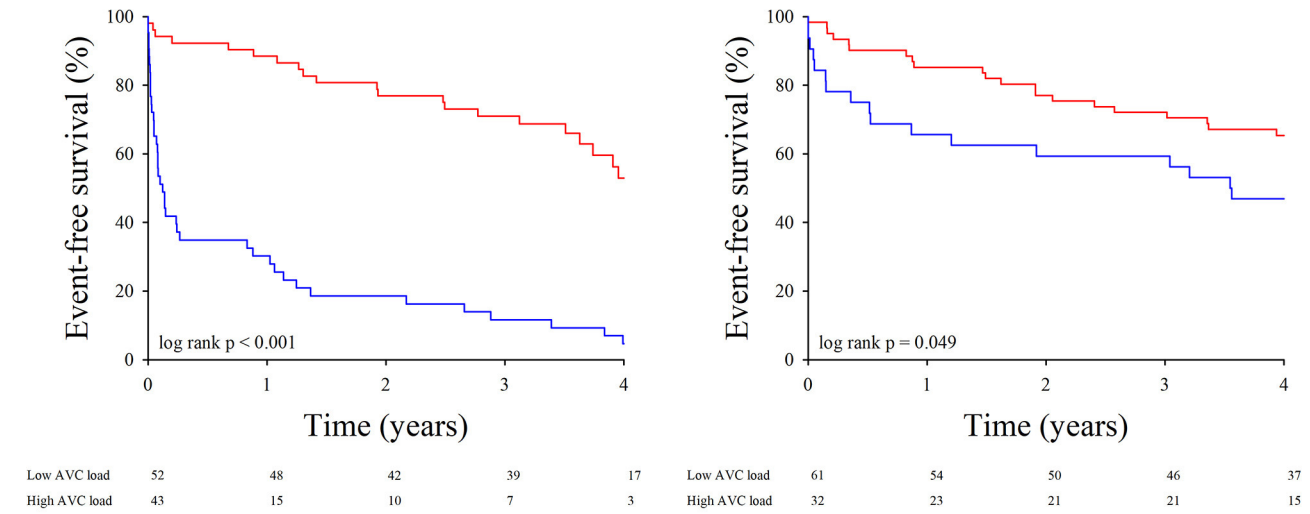

FIGURE 5 | Event-free survival according to AVC load and concordance in AS grading. Kaplan-Meier survival curves for the combined end-point of death and need for aortic valve replacement in patients with in patients with low (red line) and high (blue line) Agatston score. Left panel: patients with concordant AS grading; right panel: patients with discordant AS grading.

AVC Load to Assess the Severity of AS

Earlier studies have shown a definite association between AVC load by EBCT and hemodynamic indices of AS severity (15). More recently, AVC load has also been evaluated with non-ECG gated MDCT (24–26), using a slightly modified Agatston scoring system in order to provide comparable values to the original EBCT quantification. With the introduction of ECG-gating, the quality of cardiac MDCT imaging has improved even further, so that today, MDCT has become the preferred method for assessing AVC load. Its accuracy has been validated in several anatomical studies (16, 26). In the present study, we used this approach to calculate AVC load thresholds that best discriminate between moderate AS and severe HG-AS. Depending on the parameter used (Agatston score, AVC density and AVC index), severe AS was identified with a sensitivity of 87–91%, a specificity of 87–90% and an overall accuracy of 87–91%. Similar results were reported by Clavel et al. (sensitivity of 86–89%, specificity of 80–89%) (18) and Pawade et al. (sensitivity of 80–87%, specificity of 82–84%) (22). Although these last authors found somewhat lower threshold values than in our study, a recent study of Clavel at al. demonstrated that the thresholds of AVC load that best identify adverse outcomes are higher than those proposed in the guidelines and quite similar to those found in the present study (around 1,500 AU in women and 2,250 AU in men) (27).

Which AVC Load Criteria Should We Use to Assess the Severity of AS?

Since absolute AVC load differs between bicuspid and tricuspid valves, but AVC density does not (16), this latter should probably be preferred to avoid misinterpretations of AVC load in patients in whom the underlying valve morphology is uncertain. The use of AVC density could also avoid underestimation or

TABLE 5 | Cox's proportional hazard analysis for the combined end-point of overall mortality and need for aortic valve replacement in the subgroup of 188 patients without a straightaway indication for AVR.

	Univariate analysis			Multivariate analysis		
Variable	**HR**	**95% CI**	***p*-value**	**HR**	**95% CI**	***p*-value**
Model 1						
AVC index (/100 AU/m²)	1.10	1.08–1.13	<0.001	1.10	1.08–1.13	<0.001
AVC (/100 AU)	1.05	1.04–1.07	<0.001			
AVC density (/100 AU/cm²)	1.15	1.10–1.21	<0.001			
Mean gradient (/mmHg)	1.04	1.02–1.05	<0.001			
Peak velocity (/m/s)	2.13	1.65–2.74	<0.001			
Effective orifice area (/cm²)	0.16	0.00–0.37	<0.001			
Age (/year)	1.03	1.01–1.05	0.009			
LA dimension (/10 mm)	1.07	1.02–1.14	0.012			
TR < 2/4	0.25	0.00–0.87	0.029			
Model 2						
High AVC	3.51	2.36–5.24	<0.001	2.82	1.85–4.31	<0.001
High AVC density	3.31	2.20–4.99	<0.001			
High AVC index	3.13	2.10–4.66	<0.001			
Mean gradient (/mmHg)	1.04	1.02–1.05	<0.001			
Peak velocity (/m/s)	2.13	1.65–2.74	<0.001			
Effective orifice area (/cm²)	0.16	0.00–0.37	<0.001	0.31	0.00–0.69	0.004
Age (/year)	1.03	1.01–1.05	0.009	1.03	1.01–1.05	0.024
LA dimension (/10 mm)	1.07	1.02–1.14	0.012			
TR < 2/4	0.25	0.00–0.87	0.029			

LA, left atrium; TR, Tricuspid regurgitation severity.

TABLE 6 | Prognostic accuracy of severe calcification in patients with concordant echocardiographic grading.

AVC thresholds	**HR**	**95%CI**	χ^2	***p*-value**	**AIC**	**SBC**
Clavel et al. (18)	2.27	1.49–3.54	12.82	<0.001	964	967
Guidelines (17)	2.79	1.84–4.25	23.22	<0.0001	953	956
Pawade et al. (22)	2.79	1.86–4.19	24.67	<0.0001	953	956
Boulif et al.	3.51	2.36–5.24	37.99	<0.0001	940	943

AIC, Aikake Information Criterion; SBC, Schwarz Bayesian Criterion.

TABLE 7 | Prognostic accuracy of severe calcification in patients with concordant echocardiographic grading.

		Cutoff	**Sensitivity (%)**	**Specificity (%)**	**Accuracy (%)**	**AUC**
AVC (AU)						
Women	ESC guidelines (17)	1,200	65	60	63	-
	Clavel et al. (18)	1,274	61	62	61	-
	Pawade et al. (22)	1,377	56	68	61	-
	Boulif et al.	1,569	54	82	68	0.68
Men	ESC guidelines (17)	2,000	67	69	68	-
	Clavel et al. (18)	2,065	65	73	69	-
	Pawade et al. (22)	2,062	65	73	69	-
	Boulif et al.	2,238	60	80	69	0.70

AUC, area under the curve; AVC, aortic valve calcium.

overestimation of AS severity in patients with small or large annuli, as highlighted by several authors (16, 18, 27). However, current guidelines do not provide any recommendation in this regard. The present study shows that AVC density has the highest accuracy in identifying truly severe AS in patients with concordant AS grading. The thresholds found in our

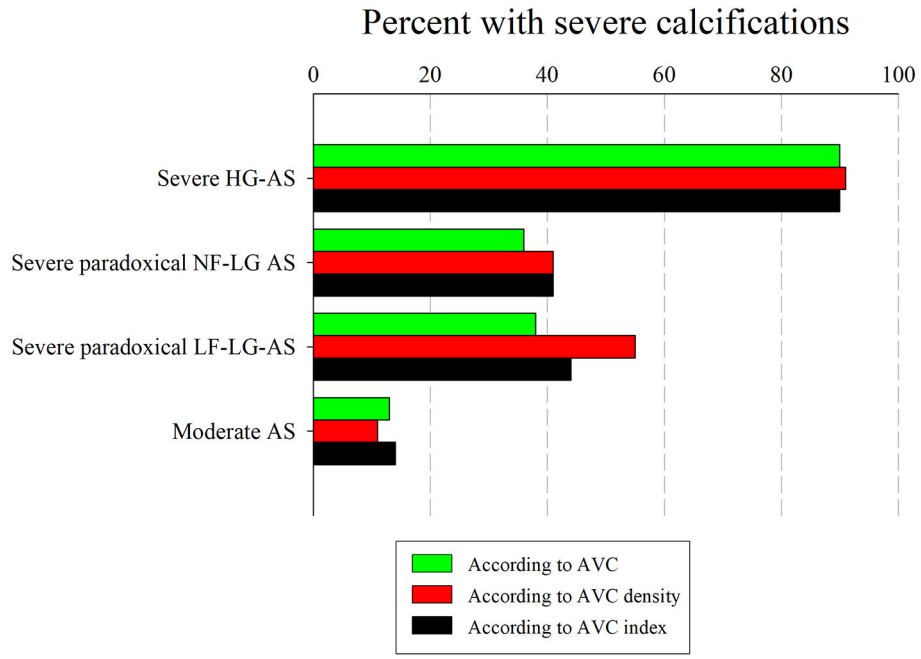

FIGURE 6 | Percent of patients with high AVC load in the different AS severity groups. Percent patients with high Agatston score (in green), high AVC density (in red) and high AVC index (in black) in subgroups with severe HG-AS, severe paradoxical normal flow (NF) or low flow (LF) LG-AS and moderate AS.

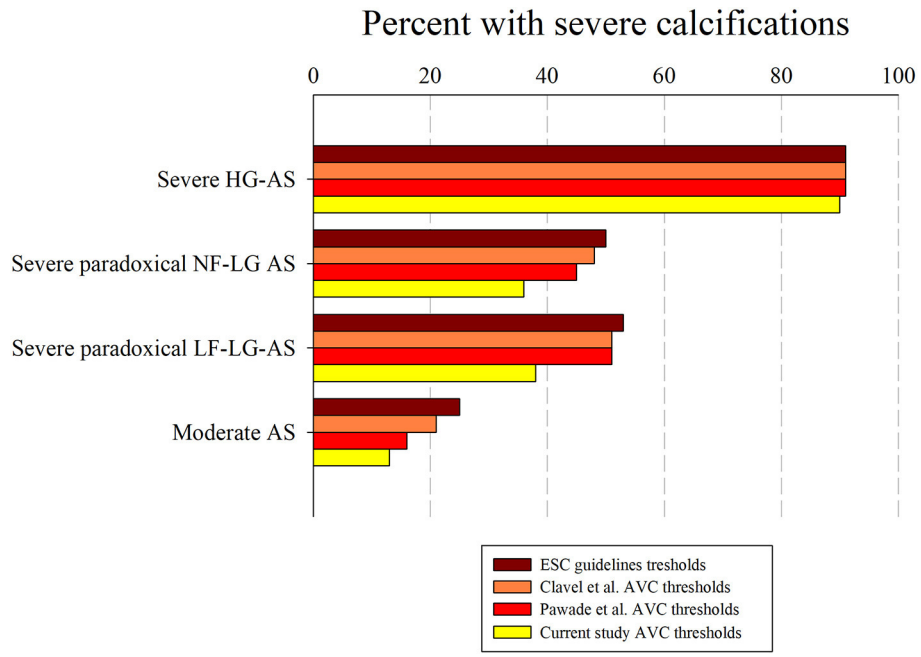

FIGURE 7 | Percent of patients with high AVC load in the different AS severity groups. Percent of patients with high Agatston score according to current thresholds, guidelines thresholds, Clavel's thresholds and Pawade's in subgroups with severe HG-AS, severe paradoxical normal flow (NF) or low flow (LF) LG-AS and moderate AS.

study are also similar to those that were recently found by Clavel et al. as being associated with poor outcomes (430 AU/cm² in women and 560 AU/cm² in men) (27). Further studies are needed to confirm the potential interest in using this parameter instead of the more commonly used Agatston score. Our survival analyses nonetheless suggest that

it does allow better prediction of clinical outcomes than the Agatston score.

AVC Load in Patients With Severe Paradoxical LG-AS

An important finding of this study is that AVC load is significantly lower in patients with severe paradoxical LG-AS than in those with severe HG-AS, irrespective of the flow pattern. It is also higher than in patients with moderate AS. Similar results were reported by Clavel et al. (18) and more recently by Kamperidis et al. (28).

In an earlier analysis of the same cohort, we had already observed that a higher AVC load was needed to define severe AS on the basis of a MPG $\geq$ 40 mmHg or a Vmax $>$ 4 m/s than on the basis of an EOAi $<$ 0.6 cm²/m². We then hypothesized that use of the continuity equation to assess AS severity was responsible for these observations, as the EOAi derived from Doppler echocardiography is usually smaller than the anatomic valve area measured by planimetry, autopsy, or cardiac catheterization. Although the differences between the anatomic and effective valve areas are commonly explained by the continuing convergence of streamlines beyond the anatomical orifice, we have recently shown that in reality, it was largely due to the underestimation of subvalvular flow when inputting a circular LVOT area into the continuity equation (29). Since guidelines for grading AS severity were initially derived from invasive measurements reflecting anatomic valve area, inconsistent grading of AS severity on the basis of mean pressure gradients (or Vmax) and EOAi were to be expected. The present data indicate that use of AVC load might be helpful to better define AS severity, particularly when Doppler echocardiographic data are the most discordant, i.e., in patients with severe paradoxical LG-AS. Indeed, when using the above described AVC load thresholds to define severe AS, 36–55% of patients with severe paradoxical LG-AS meet AVC load criteria for severe AS. These findings are in line with those of Clavel et al. who also found that a substantial proportion (45–53%) of patients with severe paradoxical LG-AS meet AVC load criteria for severe AS (18). This confirms that patients with severe paradoxical LG-AS consist in an heterogenous population, and that use of MDCT to measure AVC load permits to diffrentiate those with truly severe AS from those with moderate or pseudo-severe AS. It should nonetheless be emphasized that the prognostic implications thereof seems to be less in this population than in patients with severe HG-AS. As shown in **Figure 4**, the event-free survival of patients with severe paradoxical LG-AS and high AVC load is indeed significantly better than that of similar patients with severe HG-AS.

Study Limitations

This study has limitations that should be acknowledged. First, we had to exclude a significant number of patients from the outcome analyses because they were already scheduled to undergo surgery at the time of their MDCT evaluation. Nevertheless, we were still able to assess clinical outcomes in 188 patients including a large number of patients with concordant or discordant echocardiographic AS grading. Second, we did not perform subgroups analyses in patients with bicuspid vs. tricuspid valves. This is because of the relative inability of echocardiography to accurately identify bicuspid valves when they are heavily calcified (30). This can potentially be problematic when assessing AVC load by use the Agatston score, since bicuspid valves are usually larger than tricuspid valves and therefore tend to display larger Agatston scores than tricuspid valves. As previously shown, this limitation can be easily overcome by use of AVC density instead of absolute AVC score (16). Finally, we did not investigate the potential impact of AVC load on post-operative or -interventional outcomes. Some studies have recently indicated that the presence and amount of calcium in the left ventricular outflow tract was an important determinant of outcomes after transcatheter aortic valve replacement (TAVR) (31). Unfortunately, the small number of patients undergoing TAVR in our study precluded any meaningful statistical analysis. Further studies will be needed to address this issue.

CONCLUSIONS

Assessment of AVC load accurately identifies truly severe AS and provides powerful prognostic information. Our data further indicate that patients with discordant AS grading consist in a heterogenous group, as evidenced by their large range of AVC load. MDCT allows to differentiate between truly severe and pseudo-severe AS in this population as well, although the prognostic implications thereof are not as pronounced as in patients with concordant AS grading.

SHORT SUMMARY

Using a standardized MDCT scanning protocol, we identified optimal AVC load criteria for diagnosing truly severe AS. In patients with concordant echocardiographic results, 4-year event-free survival was considerably better with low AVC load by these criteria than with high AVC load. In patients with discordant AS grading, between 36 and 55% of them met AVC load criteria for severe AS. Yet, the prognostic implications thereof was less pronounced than in patients with concordant AS grading.

DATA AVAILABILITY STATEMENT

The raw data supporting the conclusions of this article can be made available by the authors, without undue reservation.

ETHICS STATEMENT

The studies involving human participants were reviewed and approved by Comité d'éthique hospitalo-facultaire. The patients/participants provided their written informed consent to participate in this study.

AUTHOR CONTRIBUTIONS

JB and J-LV have performed the statistical analysis, wrote the initial, and final versions of the manuscript. All authors have contributed to data acquisition, data analysis, and drafting of the manuscript.

FUNDING

This study was funded by grants from the Fonds National de Recherche Scientifique (Brussels, Belgium, CDR 23597851, and PDR T.0115.16). AS and A-CP are also supported by the Fonds National de la Recherche Scientifique (Brussels, Belgium).

REFERENCES

1. Connolly HM, Oh JK, Schaff HV, Roger VL, Osborn SL, Hodge DO, et al. Severe aortic stenosis with low transvalvular gradient and severe left ventricular dysfunction: result of aortic valve replacement in 52 patients. *Circulation*. (2000) 101:1940–6. doi: 10.1161/01.CIR.101.16.1940
2. Hachicha Z, Dumesnil JG, Bogaty P, Pibarot P. Paradoxical low-flow, low-gradient severe aortic stenosis despite preserved ejection fraction is associated with higher afterload and reduced survival. *Circulation*. (2007) 115:2856–64. doi: 10.1161/CIRCULATIONAHA.106.668681
3. Dumesnil JG, Pibarot P, Carabello B. Paradoxical low flow and/or low gradient severe aortic stenosis despite preserved left ventricular ejection fraction: implications for diagnosis and treatment. *Eur Heart J*. (2010) 31:281–9. doi: 10.1093/eurheartj/ehp361
4. Barasch E, Fan D, Chukwu EO, Han J, Passick M, Petillo F, et al. Severe isolated aortic stenosis with normal left ventricular systolic function and low transvalvular gradients: pathophysiologic and prognostic insights. *J Heart Valve Dis*. (2008) 17:81–8.
5. Mehrotra P, Jansen K, Flynn AW, Tan TC, Elmariah S, Picard MH, et al. Differential left ventricular remodelling and longitudinal function distinguishes low flow from normal-flow preserved ejection fraction low-gradient severe aortic stenosis. *Eur Heart J*. (2013) 34:1906–14. doi: 10.1093/eurheartj/eht094
6. Herrmann S, Stork S, Niemann M, Lange V, Strotmann JM, Frantz S, et al. Low-gradient aortic valve stenosis myocardial fibrosis and its influence on function and outcome. *J Am Coll Cardiol*. (2011) 58:402–12. doi: 10.1016/j.jacc.2011.02.059
7. Adda J, Mielot C, Giorgi R, Cransac F, Zirphile X, Donal E, et al. Low-flow, low-gradient severe aortic stenosis despite normal ejection fraction is associated with severe left ventricular dysfunction as assessed by speckle-tracking echocardiography: a multicenter study. *Circ Cardiovasc Imaging*. (2012) 5:27–35. doi: 10.1161/CIRCIMAGING.111.967554
8. Clavel MA, Dumesnil JG, Capoulade R, Mathieu P, Senechal M, Pibarot P. Outcome of patients with aortic stenosis, small valve area, and low-flow, low-gradient despite preserved left ventricular ejection fraction. *J Am Coll Cardiol*. (2012) 60:1259–67. doi: 10.1016/j.jacc.2011.12.054
9. Lancellotti P, Magne J, Donal E, Davin L, O'Connor K, Rosca M, et al. Clinical outcome in asymptomatic severe aortic stenosis: insights from the new proposed aortic stenosis grading classification. *J Am Coll Cardiol*. (2012) 59:235–43. doi: 10.1016/j.jacc.2011.08.072
10. Eleid MF, Sorajja P, Michelena HI, Malouf JF, Scott CG, Pellikka PA. Flow-gradient patterns in severe aortic stenosis with preserved ejection fraction: clinical characteristics and predictors of survival. *Circulation*. (2013) 128:1781–9. doi: 10.1161/CIRCULATIONAHA.113.003695
11. Maes F, Boulif J, Pierard S, de Meester C, Melchior J, Gerber B, et al. Natural history of paradoxical low-gradient severe aortic stenosis. *Circ Cardiovasc Imaging*. (2014) 7:714–22. doi: 10.1161/CIRCIMAGING.113.001695
12. Rezzoug N, Vaes B, Pasquet A, Gerber B, de Meester C, Van Pottelbergh G, et al. Prevalence and prognostic impact of valve area-gradient patterns in patients $\geq$ 80 years with woderate-to-severe aortic stenosis (from the prospective BELFRAIL Study). *Am J Cardiol*. (2015) 116:925–32. doi: 10.1016/j.amjcard.2015.05.062
13. Tribouilloy C, Rusinaru D, Charles V, Boulif J, Maes F, Levy F, et al. Progression of low-gradient, low-flow, severe aortic stenosis with preserved left ventricular ejection fraction. *Am J Cardiol*. (2015) 116:612–7. doi: 10.1016/j.amjcard.2015.05.023
14. Jander N, Minners J, Holme I, Gerdts E, Boman K, Brudi P, et al. Outcome of patients with low-gradient "severe" aortic stenosis and preserved ejection fraction. *Circulation*. (2011) 123:887–95. doi: 10.1161/CIRCULATIONAHA.110.983510
15. Messika-Zeitoun D, Aubry MC, Detaint D, Bielak LF, Peyser PA, Sheedy PF, et al. Evaluation and clinical implications of aortic valve calcification measured by electron-beam computed tomography. *Circulation*. (2004) 110:356–62. doi: 10.1161/01.CIR.0000135469.82545.D0
16. Boulif J, Gerber B, Slimani A, Lazam S, de Meester C, Pierard S, et al. Assessment of aortic valve calcium load by multidetector computed tomography. Anatomical validation, impact of scanner settings and incremental diagnostic value. *J Cardiovasc Comput Tomogr*. (2017) 11:360–6. doi: 10.1016/j.jcct.2017.07.004
17. Baumgartner H, Falk V, Bax JJ, De Bonis M, Hamm C, Holm PJ, et al. 2017 ESC/EACTS Guidelines for the management of valvular heart disease. *Eur Heart J*. (2017) 38:2739–91. doi: 10.5603/KP.2018.0013
18. Clavel MA, Messika-Zeitoun D, Pibarot P, Aggarwal SR, Malouf J, Araoz PA, et al. The complex nature of discordant severe calcified aortic valve disease grading: new insights from combined Doppler echocardiographic and computed tomographic study. *J Am Coll Cardiol*. (2013) 62:2329–38. doi: 10.1016/j.jacc.2013.08.1621
19. Aggarwal SR, Clavel MA, Messika-Zeitoun D, Cueff C, Malouf J, AraozcPA, et al. Sex differences in aortic valve calcification measured by multidetector computedctomography in aortic stenosis. *Circ Cardiovasc Imaging*. (2013) 6:40–7. doi: 10.1161/CIRCIMAGING.112.980052
20. Cueff C, Serfaty JM, Cimadevilla C, Laissy JP, Himbert D, Tubach F, et al. Measurement of aortic valve calcification using multislice computed tomography: correlation with haemodynamic severity of aortic stenosis and clinical implication for patients with low ejection fraction. *Heart*. (2011) 97:721–6. doi: 10.1136/hrt.2010.198853
21. Agatston AS, Janowitz WR, Hildner FJ, Zusmer NR, Viamonte M, Jr., Detrano R. Quantification of coronary artery calcium using ultrafast computed tomography. *J Am Coll Cardiol*. (1990) 15:827–32. doi: 10.1016/0735-1097(90)90282-T
22. Pawade T, Clavel MA, Tribouilloy C, Dreyfus J, Mathieu T, Tastet L, et al. Computed tomography aortic valve calcium scoring in patients with aortic stenosis. *Circ Cardiovasc Imaging*. (2018) 11:e007146. doi: 10.1161/CIRCIMAGING.117.007146
23. Nishimura RA, Otto CM, Bonow RO, Carabello BA, Erwin JP, III, Guyton RA, et al. 2014 AHA/ACC guideline for the management of patients with valvular heart disease: executive summary: a report of the American College of Cardiology/American Heart Association Task Force on Practice Guidelines. *J Am Coll Cardiol*. (2014) 63:2438–88. doi: 10.1016/j.jacc.2014.02.537
24. Shavelle DM, Budoff MJ, Buljubasic N, Wu AH, Takasu J, Rosales J, et al. Usefulness of aortic valve calcium scores by electron beam computed tomography as a marker for aortic stenosis. *Am J Cardiol*. (2003) 92:349–53. doi: 10.1016/S0002-9149(03)00646-5
25. Kizer JR, Gefter WB, deLemos AS, Scoll BJ, Wolfe ML, Mohler ER, III. Electron beam computed tomography for the quantification of aortic valvular calcification. *J Heart Valve Dis*. (2001) 10:361–6.
26. Thaden JJ, Nkomo VT, Suri RM, Maleszewski JJ, Soderberg DJ, Clavel MA, et al. Sex-related differences in calcific aortic stenosis: correlating clinical and echocardiographic characteristics and computed tomography aortic valve calcium score to excised aortic valve weight. *Eur Heart J*. (2016) 37:693–9. doi: 10.1093/eurheartj/ehv560
27. Clavel MA, Pibarot P, Messika-Zeitoun D, Capoulade R, Malouf J, Aggarval S, et al. Impact of aortic valve calcification, as measured by MDCT, on survival

in patients with aortic stenosis: results of an international registry study. *J Am Coll Cardiol*. (2014) 64:1202–13. doi: 10.1016/j.jacc.2014.05.066

28. Kamperidis V, van Rosendael PJ, Katsanos S, van der Kley F, Regeer M, Al Amri I, et al. Low gradient severe aortic stenosis with preserved ejection fraction: reclassification of severity by fusion of Doppler and computed tomographic data. *Eur Heart J*. (2015) 36:2087–96. doi: 10.1093/eurheartj/ehv188
29. Maes F, Pierard S, de Meester C, Boulif J, Amzulescu M, Vancraeynest D, et al. Impact of left ventricular outflow tract ellipticity on the grading of aortic stenosis in patients with normal ejection fraction. *J Cardiovasc Magn Reson*. (2017) 19:37. doi: 10.1186/s12968-017-0344-8
30. Pouleur A-C, le Polain de Waroux J-B, Pasquet A, Vanoverschelde J-L, Gerber BJ. Aortic valve area assessment: multidetector CT compared with cine MR imaging and transthoracic and transesophageal echocardiography. *Radiology*. (2007) 244:745–54. doi: 10.1148/radiol.2443061127
31. Pollari F, Hitzl W, Vogt F, Cuomo M, Schwab J, Söhn C, et al. Aortic valve calcification as a risk factor for major complications and reduced survival after transcatheter replacement. *J Cardiovasc Comput Tomogr*. (2020) 14:307–13. doi: 10.1016/j.jcct.2019.12.001

Conflict of Interest: The authors declare that the research was conducted in the absence of any commercial or financial relationships that could be construed as a potential conflict of interest.

frontiers in Cardiovascular Medicine

REVIEW
published: 26 May 2021
doi: 10.3389/fcvm.2021.677977

Molecular and Mechanical Mechanisms of Calcification Pathology Induced by Bicuspid Aortic Valve Abnormalities

*Hail B. Kazik[1], Harkamaljot S. Kandail[2], John F. LaDisa Jr.[1,3,4] and Joy Lincoln[4,5]**

[1] Department of Biomedical Engineering, Marquette University and Medical College of Wisconsin, Milwaukee, WI, United States, [2] Cardio Consulting, Warwick, United Kingdom, [3] Division of Cardiovascular Medicine, Department of Medicine, Medical College of Wisconsin, Milwaukee, WI, United States, [4] Section of Pediatric Cardiology, The Herma Heart Institute, Children's Wisconsin, Milwaukee, WI, United States, [5] Department of Pediatrics, Medical College of Wisconsin, Milwaukee, WI, United States

OPEN ACCESS

Edited by:
Maximillian A. Rogers, Brigham and Women's Hospital and Harvard Medical School, United States

Reviewed by:
Philippe Sucosky, Kennesaw State University, United States
Salah A. Mohamed, University Medical Center Schleswig-Holstein, Germany

***Correspondence:**
Joy Lincoln
jlincoln@mcw.edu

Specialty section:
This article was submitted to Heart Valve Disease, a section of the journal Frontiers in Cardiovascular Medicine

Received: *08 March 2021*
Accepted: *29 April 2021*
Published: *26 May 2021*

Citation:
Kazik HB, Kandail HS, LaDisa JF Jr and Lincoln J (2021) Molecular and Mechanical Mechanisms of Calcification Pathology Induced by Bicuspid Aortic Valve Abnormalities. Front. Cardiovasc. Med. 8:677977. doi: 10.3389/fcvm.2021.677977

Bicuspid aortic valve (BAV) is a congenital defect affecting 1–2% of the general population that is distinguished from the normal tricuspid aortic valve (TAV) by the existence of two, rather than three, functional leaflets (or cusps). BAV presents in different morphologic phenotypes based on the configuration of cusp fusion. The most common phenotypes are Type 1 (containing one raphe), where fusion between right coronary and left coronary cusps (BAV R/L) is the most common configuration followed by fusion between right coronary and non-coronary cusps (BAV R/NC). While anatomically different, BAV R/L and BAV R/NC configurations are both associated with abnormal hemodynamic and biomechanical environments. The natural history of BAV has shown that it is not necessarily the primary structural malformation that enforces the need for treatment in young adults, but the secondary onset of premature calcification in ∼50% of BAV patients, that can lead to aortic stenosis. While an underlying genetic basis is a major pathogenic contributor of the structural malformation, recent studies have implemented computational models, cardiac imaging studies, and bench-top methods to reveal BAV-associated hemodynamic and biomechanical alterations that likely contribute to secondary complications. Contributions to the field, however, lack support for a direct link between the external valvular environment and calcific aortic valve disease in the setting of BAV R/L and R/NC BAV. Here we review the literature of BAV hemodynamics and biomechanics and discuss its previously proposed contribution to calcification. We also offer means to improve upon previous studies in order to further characterize BAV and its secondary complications.

Keywords: hemodynamic, biomechanic, calcific aortic valve disease (CAVD), wall shear stress, fluid-structure interaction simulation

INTRODUCTION

Bicuspid aortic valve (BAV) is the most common congenital heart malformation with an estimated prevalence of 1–3%, and a male predominance of 3:1 (1). As compared to a normal tricuspid aortic valve (TAV) containing three leaflets (or cusps), the BAV forms with only two functional cusps as the result of abnormal valvulogenesis (2). The abnormal structural geometry and resulting adverse hemodynamic environment associated with the BAV offers complexity to the disease that has yet to be fully characterized, but likely has a negative influence on the structure-function relationships normally exhibited by the TAV.

The TAV is an avascular structure connected to the aortic root, containing three semilunar cusps that open and close to maintain unidirectional forward blood flow from the left ventricle to the aorta. The cusps are named according to their location relative to the coronary artery ostia: the left coronary (L), right coronary (R), and non-coronary (NC) (3). Each cusp is comprised of three highly organized layers of extracellular matrix (ECM), which help the valve withstand a range of hemodynamic forces as it opens and closes over 100,000 times a day (1) (**Figure 1**). The fibrosa layer is situated on the aortic side of the cusp and enriched with circumferentially-aligned collagen fibers that provide structural integrity to the valve. On the opposite surface is the ventricularis layer, containing radially-aligned elastin fibers to facilitate cusp motion during valve opening and recoil during valve closure. A proteoglycan-rich spongiosa layer is situated between the fibrosa and ventricularis, and provides deformability to the cusps as well as lubrication to adjacent layers (1). The ECM structure is synthesized and maintained by valve interstitial cells (VICs) that reside within the core of the cusps as quiescent fibroblast-like cells in the absence of disease. Encapsulating the valve cusp is a single layer of valve endothelial cells (VECs) between VICs and the hemodynamic environment (1). It has been shown previously that although VICs and VECs have minimal physical contact *in situ*, the two cell populations molecularly communicate through paracrine signaling to maintain ECM homeostasis and prevent disease (4–7). Previous mechanobiology studies have additionally demonstrated that VECs are mechanosensitive, allowing them to sense and respond to mechanical stimuli from the hemodynamic environment (8, 9). Together, the ECM and cellular components of the valve create an integrated and balanced connective tissue that responds to mechanical stimuli from the hemodynamic environment to maintain normal valve structure and function throughout life.

In cases of abnormal valve development, two of the three cusps fuse, leading to a bicuspid anatomy with unequal sized cusps that often contain a region of fibrous thickening at the fusion site, known as a raphe (10). The bicuspid aortic valve (BAV) exists in different morphologic phenotypes (**Figure 2**), which have been classified by different naming systems. Under the Sievers classification system, BAV morphotypes are categorized by the number of fibrous raphes present as well as the cusps that are fused together. Based on the number of raphes, BAV is classified as: Type 0 (no raphe present), Type 1 (one raphe present), and Type 2 (two raphes present). Types 1 and 2 are further categorized on the basis of cusp fusion relative to the coronary artery origins, where R/L is the fusion between right and left coronary cusps, R/NC is the fusion between right and non-coronary cusps, and L/NC between the left and non-coronary cusps (2, 11) (**Figure 2**). Type 1 occurs with a frequency of 90% of all BAV cases where R/L is the most common configuration (accounting for 80% of Type 1), followed by R/NC (17%), and L/NC (∼2%) (11).

A genetic etiology of the BAV structural malformation is widely acknowledged and supported by studies that have established the heritability of BAV as up to 89%, indicating an almost genetically determined disease (12). Despite this, the genes and mechanisms underlying the developmental origins of forming two, rather than three cusps are largely unknown and remain poorly understood. *In vivo* models corroborated by human genetic studies have identified a few candidate genes potentially involved in the causal molecular mechanisms of BAV including *NOTCH1, GATA* family members (*GATA4, GATA5*, and *GATA6*) as well as *ROBO4*, *eNOS, NKX2.5*, and *SMAD* (13–15).

The severity of BAV ranges from lifelong asymptomatic disease in older adults to severe complications in childhood. However, it is not necessarily the structural malformation of BAV that necessitates clinical intervention but rather the development of BAV-associated secondary complications including aortopathy (aortic dilatation, aneurysm, dissection, and coarctation) and valvulopathy (calcific aortic valve disease (CAVD), aortic stenosis, and regurgitation) (16–18). The presence of a congenital BAV malformation is a major risk factor for developing these secondary complications, and over 50% of young adults (>35 years old) with BAV develop early onset CAVD that can progress to severe aortic stenosis within 10–12 years (16, 17, 19). As a comparison, CAVD in the TAV population affects ∼25% of individuals over the age of 65 with slower progression to severe aortic stenosis (20–30 years) (18, 20–22). Calcification is thought to be an active process involving inflammation, endothelial dysfunction, ECM remodeling, and VIC phenotypic changes resulting in the formation of calcium nodules preferentially on the fibrosa layer, which stiffens the valve cusps leading to stenosis (20, 22, 23). Despite a higher prevalence of CAVD in the BAV R/L configuration, calcification is more frequent and rapid in the BAV R/NC configuration, (24) yet it is unclear why.

To date, the cause of secondary complications in BAV remains unknown. Proponents of a genetic theory hypothesize that the underlying gene mutations responsible for the structural malformation and heritability of BAV are the primary contributors to associated secondary complications. However, in addition there are a growing number of studies supporting the implications of altered hemodynamic and biomechanical influences in BAV. Abnormal mechanical stimuli imposed on the valve may disrupt the normal mechanoregulation of cellular processes responsible for valve homeostasis and subsequently lead to disease. Therefore, the role of hemodynamics and biomechanics in BAV cannot be neglected in the efforts to delineate causal mechanisms of BAV-associated complications.

BAV, and associated complications present a large clinical burden for which there are inadequate treatment options

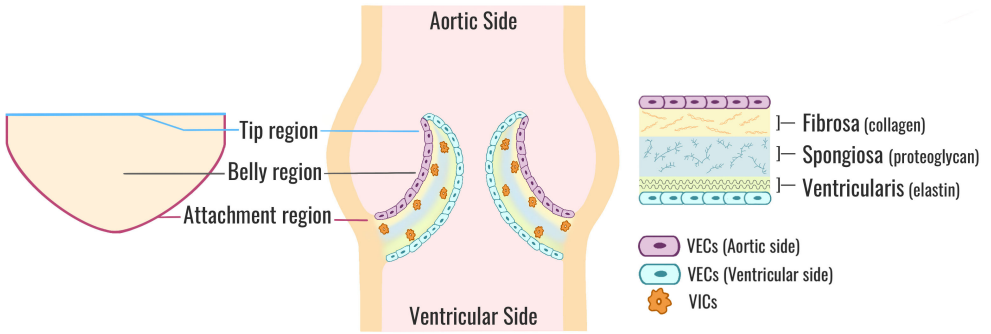

FIGURE 1 | Aortic valve cusp structure. A cross-sectional view of a normal TAV (center). Each valve cusp is comprised of a highly organized ECM (right) stratified into three layers: a collagen-dense fibrosa layer (aortic side), an elastin-rich ventricularis layer (ventricular side), and a spongiosa layer sandwiched in-between comprised mostly of proteoglycans. VICs are situated within the core of each cusp and maintain ECM synthesis and homeostasis. VECs form a protective monolayer encapsulating the entire cusp. A flattened perspective of a single aortic valve cusp (left) illustrates the locations of the tip, belly, and attachment regions. TAV, tricuspid aortic valve; ECM, extracellular matrix; VICs, valve interstitial cells; VECs, valve endothelial cells.

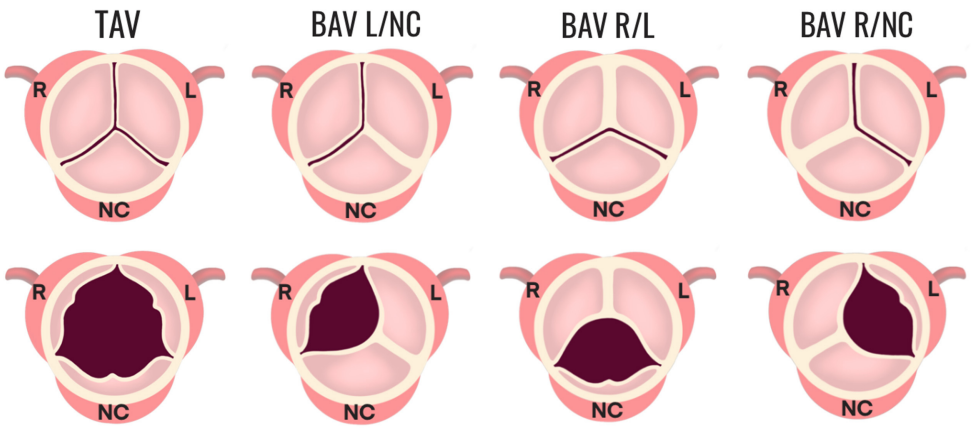

FIGURE 2 | Morphologic phenotypes in BAV. The configuration of a normal TAV is shown compared to three configurations of BAV Type 1 (one fibrous raphe). BAV R/L is the fusion between the R and L coronary cusps and is the most common, accounting for 80% of Type 1. BAV R/NC is the fusion between the R and NC cusps (occurring in 17% of Type 1 cases), and BAV L/NC is the fusion the between L and NC cusps (~1%). BAV, bicuspid aortic valve; R, right; L, left; NC, non-coronary.

currently available. Less invasive options for BAV patients with CAVD and aortic stenosis including balloon aortic valvuloplasty often lead to early symptomatic recurrence. While more invasive approaches such as transcatheter or surgical aortic valve replacement can be associated with suboptimal long-term outcomes (25, 26). Furthermore, calcification and aortic stenosis may go undiagnosed until end-stage when treatments options are further limited (27). Therefore, BAV and its complications warrant the need for novel mechanistic-based therapies that prevent or halt the progression of calcification and aortic stenosis in BAV patients. In order to do this, the field must delineate the temporal and spatial pathobiology of this multifactorial, complex disease by integrating the impact of the hemodynamic environment on molecular and cellular changes within the bicuspid valve and surrounding tissue that drive secondary complications.

HEMODYNAMIC AND BIOMECHANICAL INFLUENCES IN BAV

There is growing evidence from fluid and solid mechanics studies demonstrating the presence of an altered hemodynamic and biomechanical environment in patients with a normally functioning BAV, which may contribute to the pathogenesis of secondary complications, such as calcification at a later time (10, 13, 28–35). The indices derived from these studies describe the hemodynamic environment and mechanical stimuli imposed on normal and diseased valves at the level of orifice area, velocity jets, transvalvular pressure gradients, as well as vortical and helical structure formation (36–41). Fluid mechanics studies have also quantified indices of wall shear stress (WSS) which is defined as the frictional force exerted from blood flow, while solid mechanics studies have assessed cusp biomechanics through measurement of stress and strain (28, 29, 32, 33,

35, 42–44). However, quantification of these indices and data directly supporting a contributing role in the onset of premature calcification remain limited.

Several methods have been employed to quantify the mechanical stimuli imposed on the BAV and uncover mechanisms influencing aortic and valvular pathology in this patient cohort. In this review, the approaches have been generally classified into three types: assessment through available clinical imaging modalities (i.e., *in vivo*), numerical simulations using image-based models (i.e., *in silico*), and bench-top approaches (i.e., *in vitro*, *ex vivo*). The use of these methods have provided significant advancements toward our understanding of mechanical stimuli from BAV, although as discussed below, challenges remain in accurately replicating the associated complex hemodynamic and mechanical environment.

Clinical (*in vivo*) methods including echocardiography, cardiac magnetic resonance imaging (MRI), and computed tomography (CT) often serve as the basis for computational modeling, and have been used independently in the past to describe patient-specific valve morphology and valvular performance (37–40, 45–47). These studies are most often reproduced from an adult cohort with fewer studies focusing on pediatric cases. Recently, 4D flow (temporal phase-contrast MRI with three-directional velocity encoding) has been used to obtain velocity profiles on a patient-specific basis. In principle, this could overcome some of the limitations associated with the assumptions inherent in numerical modeling, but it comes at the cost of spatiotemporal resolution (48). For example, 4D flow has been shown to underestimate WSS, which has been previously related to pathology in BAV and other vascular beds (39).

Experimental techniques such as particle image velocimetry (PIV) and laser doppler velocimetry (LDV) have been used in bench-top approaches to quantify velocity jet magnitude and direction as well as turbulence characteristics like vortical and helical formation (13, 43). Bench-top approaches may provide greater consideration of tissue material properties with the use of excised aortic valves when compared to numerical modeling. However, the use of LDV in such studies for example, is limited to velocity measurements at only a single point and while PIV can provide in-plane or even 3D velocity measurements, it is often difficult to fully replicate physiologic pressure and flow waveforms, patient-specific valve anatomy, and/or compliance of the aortic root in a bench-top approach.

Numerical methods including computational fluid dynamics (CFD) and fluid-structure interaction (FSI) simulations have been applied to BAV modeling with the goal of providing high spatial and temporal resolution (28, 29, 32, 33, 42). When accurately considering the geometric modeling process (28, 49) the result can be detailed indices that are challenging to obtain from imaging alone. Despite recent capabilities in computational modeling using CFD and FSI, many prior studies have relied on idealized assumptions regarding valve geometry, boundary conditions, and/or tissue material properties. Moreover, previous BAV studies have primarily focused on modeling the BAV R/L configuration in the adult population.

Multi-disciplinary studies coupling advanced imaging methods with state-of-the-art computational modeling are underway to create even better representations of the native and pathologic hemodynamic environments of the aortic valve. These studies attempt to address the limitations of the above approaches. A recent study by Kandail et al. (50) investigated hemodynamic alterations possible with one of the most commonly implemented transcatheter aortic valve replacement (TAVR) devices used clinically. The authors reconstructed aortic geometry from clinical imaging, virtually deployed the TAVR device, and implemented physiologically representative boundary conditions while incorporating realistic material properties for the aorta and valve. Although this model was used to study valvular flow in a different setting, it demonstrated a robust approach aimed at addressing many limitations of numerical modeling that may better replicate the physiologic environment. Due to the compounding assumptions necessary for accurate modeling and complexity of BAV hemodynamics, it is imperative that future studies of BAV patients employ similar approaches rooted in realism to link indices to mechanism of pathology.

Hemodynamic Influences on Valvular Performance in BAV

Hemodynamic indices describing the structural geometry, valvular performance, and other hemodynamic influences have been more prominently identified in adults than pediatric patients, but nonetheless have better informed clinical decisions about BAV severity, treatment, and their implications in secondary complications (37, 38, 40, 41, 45–47). **Figure 3** is a diagrammatic comparison of these features in different BAV configurations compared to a normal TAV (also see **Table 1**). While a normal TAV is characterized by having a wider, closer-to-round valve orifice, BAV R/L and BAV R/NC have been shown through flow visualization and imaging studies to exhibit an elliptical, clam-shell shaped valve orifice (28, 44, 45). The effective orifice area in BAV is also significantly smaller than in a normal TAV (BAV values of 1.21–2.28 cm^2 vs. TAV of 2.90–4.26 cm^2) (28, 29, 32, 51–53). The reduced effective orifice area ultimately results in a higher velocity jet with magnitudes reaching 2.0–5.0 m/s as compared to 1.1–2.3 m/s in a normal TAV based on computational, *in vitro*, and imaging studies (28, 29, 33, 36, 43, 54). Consequently, more severe cases of BAV are accompanied by a transvalvular pressure gradient as high as 60 mmHg in adult and pediatric BAV patients, (46) which is a frequently used clinical metric to indicate the severity of stenosis (e.g., >40 mmHg) (52). Factors including cusp geometry and stiffer tissue properties such as in cases with a raphe, are potential contributors to the impaired mobility observed in the fused cusp of BAV (2, 44). This leads to an eccentric systolic velocity jet through the valve that is skewed toward the non-fused cusp and impinges on the downstream wall of the aorta. The direction of the velocity jet, however, is dependent on the valve fusion pattern. Whereas a normal TAV geometry has a systolic velocity jet aligned centrally through the ascending aorta, the velocity jet in BAV R/L is directed toward the non-coronary cusp and impinges on the right-anterior aortic wall, while the velocity jet in BAV R/NC is directed toward the left coronary cusp and

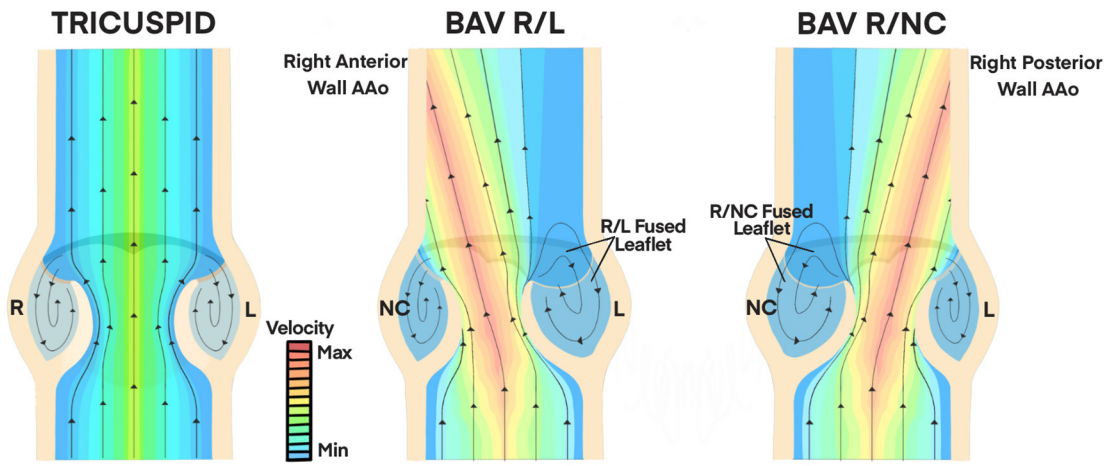

FIGURE 3 | Hemodynamic Influences on Valvular Performance in BAV. A normal TAV features a centrally-aligned velocity jet through the valve orifice at physiologic magnitudes (1.1 to 2.3 m/s, minimum velocity range). Symmetrical vortices form in the cusp sinus of TAV which lead to synchronous closure of valve cusps. BAV R/L and BAV R/NC configurations have skewed velocity jets with magnitudes of 2.0 to 5.0 m/s (maximum velocity range) through the valve orifice due to asymmetric cusp geometry and impaired mobility of the fused cusp (28, 29, 32, 51–53). This is directed toward the right anterior wall of the AAo in BAV R/L and toward the right posterior AAo wall in BAV R/NC. Asymmetrical vortex formation leads to a smaller, faster vortex in the non-fused cusp sinus and a larger, slower vortex in the fused cusp sinus that extends further into the AAo (36–38, 40, 41, 47). AAo, ascending aorta; BAV, bicuspid aortic valve; R, right; L, left; NC, non-coronary.

TABLE 1 | Summary of hemodynamic and biomechanical influences in TAV, BAV R/L, and BAV R/NC.

Indices	Normal TAV	BAV R/L Configuration	BAV R/NC Configuration	References
Hemodynamics Studies				
Valve Orifice Shape/Size	Circular, round orifice, large valve opening area	Elliptical, clamshell-shaped orifice, reduced opening area	Elliptical, clamshell-shaped orifice, reduced opening area	(28, 36)
Systolic Jet Velocity/Direction	Centrally-aligned velocity jet at physiologic magnitudes	High velocity jet skewed towardz right-anterior wall of AAo	High velocity skewed towardz right-posterior wall AAo	(36, 41, 47, 55)
Vortex and Helical Structures	Symmetrical vortical structures in cusp sinuses Absence of abnormal helical flow downstream in AAo	Larger, low velocity vortex in fused cusp sinus; smaller, high velocity vortex in non-fused sinus Right-handed helical flow in AAo	Larger, low velocity vortex in fused cusp sinus; smaller, high velocity vortex in non-fused sinus Left-handed helical flow in AAo	(13, 29, 32, 33, 43, 53)
Cusp Wall Shear Stress (WSS)	High magnitude & unidirectional WSS on ventricularis Low magnitude & oscillatory WSS on fibrosa Magnitude gradually decreases from tip to attachment region	High magnitude & unidirectional WSS on ventricularis of fused and non-fused cusps Elevated WSS on non-fused cusp fibrosa; Sub-physiologic WSS on fused cusp fibrosa	*	(28, 29, 34, 42, 53, 56, 57)
Biomechanics Studies				
Stress/Strain	Cusp stretch and strain are greatest during diastole and in the radial direction High strain along tip region and high von Mises stress along attachment and commissural region	Increased radial strain on fused cusp while circumferential strain is similar to TAV High principal stress on the fused leaflet in attachment and commissural region	*	(28, 29)

TAV, tricuspid aortic valve; BAV, bicuspid aortic valve; R, right coronary; L, left coronary; NC, noncoronary; AAo, ascending aorta.
**Limited data to support conclusions.*

impinges on the right-posterior aortic wall (36–38, 40, 41, 47). The asymmetrical cusp geometry and jet eccentricity in BAV gives rise to abnormal vortical structures in the cusp sinuses. Computational and *in vitro* studies indicate the presence of symmetrical vortices forming in the cusp sinuses of a normal TAV subsequently lead to synchronous closure of the valve cusps (13, 29, 32, 33, 43, 53, 54). Conversely, BAV R/L appears to most often feature a small vortex forming in the non-fused cusp sinus and a larger vortex in the fused cusp sinus that extends further downstream in the aorta (13, 29, 32, 33, 43, 51, 53).

In BAV, WSS indices are largely applicable to VECs that form an impermeable endothelium over the valve cusps. WSS indices act as mechanical stimuli that are ultimately transduced through signaling events via mechanotransduction (58). The vector components of magnitude and direction add to the complexity of some WSS indices, as both are thought to uniquely affect the process (58). The underlying mechanisms of mechanotransduction activated by WSS indices, and their implications in valve pathology are not fully understood, but studies discussed later in this review suggest that altered WSS in BAV could be the reason behind secondary complications such as premature calcification (30). Therefore, further quantifying patterns of WSS in TAV and BAV will likely help elucidate a role in the pathogenesis and acceleration of disease.

Associated literature point to several WSS indices of potential interest in BAV. WSS magnitude quantified as an average value over the cardiac cycle is most often denoted in the literature as time-averaged WSS (TAWSS), or temporal shear magnitude (TSM) (29, 58). Temporal shear gradient (TSG) is another WSS index which describes the time derivative of WSS magnitude at a given point (29, 59). WSS directionality is expressed in terms of oscillatory shear index (OSI), where an OSI of 0.0 is purely unidirectional and an OSI of 0.5 is equally bidirectional (33).

To date, a large number of studies examining indices of WSS in BAV have focused on its distribution in the ascending aorta, mainly in determining its potential role in aortic dilatation and aneurysm (36–38, 40, 41, 47, 54, 55). However, only a handful of studies have been dedicated to distinguishing WSS alterations on the valve cusps (28, 29, 32, 33, 42). Compared to the adult literature, very few studies have determined WSS abnormalities in the ascending aorta of pediatric BAV patients, (40, 45, 46, 55) and even fewer studies have attempted to characterize these alterations on the pathology of the valve cusps. Additionally, for the limited number of studies that have focused on cusp WSS in BAV, most have neglected to consider the implications of coronary blood flow on sinus hemodynamics and cusp mechanics. In fact, a recent *in vitro* study by Flemister et al. (60) using a bioprosthetic TAV highlighted the distinguishable WSS patterns in each cusp sinus when physiologic coronary flow waveforms were included (60). Their study revealed higher velocity and vorticity in the right and non-coronary sinuses compared to the left coronary sinus. Results also revealed a greater likelihood of higher WSS magnitudes in the left coronary and right coronary sinuses (60). These findings further underscore the importance of implementing coronary flow in future BAV studies to accurately replicate native flow conditions and local pressure gradients that result in distinguishable WSS patterns of different BAV configurations. It is also worth noting that studies to date have mostly characterized cusp WSS for BAV R/L (Type 1) fusion with no consideration of BAV R/NC anatomy. Though BAV R/L (Type 1) is the most common BAV configuration, the R/NC fusion pattern is associated with more frequent and accelerated progression of CAVD (24). Collectively addressing the current unmet needs for comparing BAV R/L and BAV R/NC configurations along with the inclusion of coronary flow and consideration of the pediatric population in future BAV studies may greatly enhance our understanding of BAV hemodynamics and biomechanics.

In the adult BAV population, Chandra et al. (33) employed a 2D FSI study comparing local WSS patterns on valve cusps in idealized models of normal TAV and BAV R/L. This approach imposed physiologic transvalvular pressure (diastolic/systolic ratio of 2:1) as a traction condition at the outlet. Results indicated that regardless of valve anatomy, WSS on the cusps is side-specific and site-specific. More specifically, the ventricularis is subjected to high magnitudes of WSS featuring mostly unidirectional, pulsatile flow while the fibrosa is subjected to lower magnitudes of WSS and exhibiting bi-directional, oscillatory flow. Additionally, the authors showed that WSS on any given cusp can vary along the tip, belly, and attachment regions. The BAV R/L model was marked by the existence of abnormal WSS patterns due to the cusp asymmetry. These findings were further substantiated in a follow-up study, this time using 3D FSI models in idealized adult TAV and BAV R/L and imposing a similar transvalvular pressure waveform as a traction condition at the inlet and outlet (29). In all cases, there was a similar spatial distribution of WSS on both cusp surfaces. The tip region was exposed to high magnitudes of WSS, while the belly and attachment regions were exposed to lower magnitudes. On the ventricularis, BAV R/L cusps were subjected to high WSS magnitudes on the belly and tip regions (TSM ranging between 12.3 and 44.7 dyn/cm^2) when compared to TAV cusps (TSM from 5.8 to 19.9 dyn/cm^2). TSG on the ventricularis was lower on the base and belly region of BAV cusps compared to TAV and greater in the tip region of BAV cusps. The BAV fibrosa was subjected to overall lower TSG than TAV with the exception of the base of the non-fused BAV cusp which exhibited higher TSG. These same regions on TAV and BAV R/L cusps experienced mostly unidirectional WSS (OSI $<$ 0.06). While the base of the fused BAV R/L cusp experienced bidirectional WSS (OSI $=$ 0.30), the base of the non-fused BAV R/L cusp and TAV cusps experience closer to unidirectional WSS (OSI $<$ 0.14). Conversely, the fibrosa in all models were exposed to systemically lower WSS magnitudes than the ventricularis, but featured greater variability in regionality and directionality due to valve geometry. Compared to the fibrosa of TAV cusps (TSM from 0.8 to 3.5 dyn/cm^2), the non-fused cusp in BAV R/L experienced elevated WSS (TSM $>$ 3.8 dyn/cm^2) while the fused cusp experienced sub-physiologic WSS (TSM $<$ 1.3 dyn/cm^2). WSS is bidirectional (OSI $>$ 0.14) on the fibrosa of TAV cusps and BAV R/L fused cusps, but unidirectional on the fibrosa of the non-fused BAV type I (OSI $<$ 0.03). Similar findings were attained in a highly sophisticated study conducted by Emendi et al. (28) who created a patient-specific FSI model of adult BAV R/L and compared the computationally-derived cusp WSS to values obtained by 4D flow MRI. This study reaffirmed the presence of WSS elevations on the ventricularis of BAV R/L cusps, with the non-fused cusp experiencing the highest magnitudes of WSS concentrated to the tip region (146 dyn/ cm^2) and decreasing toward the belly and attachment regions. Further, it aligned with previous studies describing systemically lower WSS magnitude on the fibrosa of each cusp, where the fused cusp exhibited much lower WSS compared to

the non-fused cusp. Although this study showed that coupling advanced cardiac imaging and computational modeling can provide realistic predictions of the *in vivo* flow environment, unfortunately results were not compared with a normal control valve to better appreciate the differences in values for WSS in diseased valves. Other computational models have outlined WSS alterations with respect to valve cusp angle and size (32) as well as applying realistic anisotropic-hyperelastic tissue properties of the valve cusps (35). These models revealed similar spatial distributions and WSS overloads in BAV models compared to TAV, although the latter study reported peak average WSS magnitudes of up to 280 and 420 dyn/cm^2 on the cusp fibrosa and ventricularis, respectively, which are significantly higher than levels reported by other studies.

An *in-vitro* flow study with modified porcine BAV and TAV models described the shear stress on valve cusps through measurement of Reynold's shear stress, and viscous shear stress (43). These parameters ultimately indicated regions of high fluctuations, suggesting unsteady interaction between the altered flow and valve cusps. The same group demonstrated in a later study that the fibrosa of the BAV cusp experiences greater fluctuations in WSS compared to TAV cusps (13). This manifested as both magnitude variability in WSS across different cardiac cycles as well as high-frequency fluctuations within the same cardiac cycle. This was more profound on the non-fused cusp in comparison to the fused cusp due to the higher jet velocity and accompanying vortex in that sinus.

Additional studies have further compared the hemodynamic environment in normally functioning BAV and TAV models and show the presence of abnormal patterns of WSS in BAV (34, 42, 53, 56, 57). **Table 1** provides a summary highlighting these key findings. Together with mechanobiology studies discussed later in this review showing the influence of WSS in mechanotransduction pathways to maintain valve health, the role of abnormal WSS and hemodynamic environment present in BAV cannot be neglected as a potential contributor to secondary complications.

Biomechanical Influences on Valvular Performance in BAV

Besides fluid mechanics indices such as WSS, aortic valve tissue is exposed to a combination of normal, bending, tensile, and compressive stresses as the valve opens and closes during each cardiac cycle (30). Perturbations to these stresses are hypothesized to impact the function of VICs and VECs, eventually leading to valve tissue remodeling, inflammation, and calcification (30). Although several solid mechanics studies have described the stresses and strains in a normal TAV, limited data is published in the setting of BAV. The few studies (28, 29, 35, 44, 61, 62) available considering stress and strain in BAV have quantified the solid mechanics induced stress in a number of ways including: maximum in-plane principal stress, von Mises equivalent strain, and cusp stretch.

Robicsek et al. (44) was one of the first groups to investigate biomechanical stresses on cusp motion, contact, folding, and creasing in BAV. They conducted a simulation with dissected human aortic roots of BAV morphology (one 10-year-old male and two 24-year-old males) and noted excessive folding and creasing of the valve cusps. Although this was thought to be reflective of the cusp deformation stresses, the stress and strain were not quantitatively measured. Moreover, the differences between fused and non-fused cusps were not differentiated or compared to those of a normal TAV (61).

One *in vitro* study showed that while BAV and TAV cusps deformed similarly during diastole, they had significantly different deformation patterns during mid-to-late systole (61). As a result, the authors reported increased cusp strain in BAV compared to TAV during this time point, with the fused BAV cusps experiencing 24% higher strain in the radial direction (parallel to the direction of blood flow) than the normal TAV cusps. There were less significant changes in the circumferential strain at this time point.

Several computational studies modeling BAV have demonstrated the non-physiologic creasing of the conjoint cusp as well as the propensity for increased stress in all BAV cusps, with particularly high concentrations at the cusp fusion site and attachment regions (10, 29, 32, 34, 62). In contrast to the former *in vitro* study, these computational studies indicated higher stress and strain during diastole when the valves are closed rather than mid-to-late systole when the valves are open. An FSI study modeling BAV R/L and normal TAV measured the equivalent von Mises strain distribution and stretch on valve cusps throughout the cardiac cycle (29). Cusp strain increased from the base to tip regions in all valve geometries. However, concentration of strain varied spatially in the tip region between valve models: near the commissures in TAV, across the entire coaptation region of the fused BAV cusp, and in more focal areas in the tip region of the non-fused BAV cusp. Regardless of valve anatomy, cusp stretch in the radial direction was higher than in the circumferential direction and, like cusp strain, was greater during diastole and increased from the base to tip region. The BAV cusps had 3% higher radial deformation than TAV cusps with little change in the circumferential deformation. The patient-specific study by Emendi et al. (28) confirmed that principal stress was highest on both cusp surfaces of BAV R/L during diastole and revealed higher stress on the fused cusp (maximum value of 322 kPa) compared to the non-fused cusp. Another notable FSI study (35) determined that the stress imposed on fused and non-fused cusps in BAV R/L is highly dependent on cusp size and fusion angles, suggesting that cusp stresses will vary greatly from patient to patient. **Table 1** summarizes the key findings from solid mechanics studies.

In addition to the hemodynamic influences in BAV, there are clearly disturbances to the biomechanical environment which may also interfere with the normal mechanosensitive regulation of valve structure and function as shown in mechanobiology studies described in the next section.

CALCIFICATION IN BAV

While physiologic stress is necessary to maintain valve homeostasis by influencing cell phenotype, gene expression, and

protein activation in the aortic valve, altered or pathological stress may interfere with the normal responses to physiologic stress or even activate disease-inducing pathways, including those leading to calcification (63). Calcification is characterized by the appearance of calcific nodules on the aortic surface (fibrosa) of aortic valve cusps (8, 23, 64). While the underlying mechanisms of calcification are still largely unknown, it is thought to be an active process whereby VICs exhibit osteoblast-like characteristics in the presence of an inflammatory response, valve endothelial dysfunction, and ECM remodeling (8, 20, 23, 31). The development of calcific nodules stiffens the cusps limiting their mobility, and ultimately leading to aortic stenosis and heart failure (23, 27, 65). Currently there are no therapeutic options directly targeting calcification or preventing the formation of calcific nodules (27). The only suitable treatment for patients with severe CAVD and AS is valve replacement (27).

Mechanisms That Prevent Calcification in Healthy Valves

VECs are a mechanosensitive cell population which utilize a variety of sensing mechanisms such as integrins and glycocalyx to transduce extracellular mechanical stimuli through various downstream signal transduction pathways and cause transcriptional changes (8). In the absence of hemodynamic disturbances, the TAV experiences physiological turnover of the valve ECM that is largely mediated by quiescent VICs. In turn, overlying VECs contribute to this homeostatic process by secreting "protective" growth factors and molecules to underlying VICs to maintain their quiescence, and prevent osteogenic-like processes (66). The anti-calcific factors emanating from VECs include endothelial NO synthase (eNOS) and transforming growth factor β1 (Tgfβ1) that have been shown to target Notch1 and Sox9 in VICs respectively, to prevent pro-calcific changes (5, 7). Additionally, the mechanosensitive capacity of VECs allows them to sense hemodynamic and biomechanical stimuli from the surrounding environment and it is thought that physiologic levels of these stimuli are required to maintain normal function and secretion of anti-calcific factors by VECs. However, in a diseased state, the stimuli imposed on VECs may be affected and potentially lead to reduced expression of anti-calcific factors, or activation of pro-calcific pathways.

Hemodynamic and Biomechanical Influences on Calcification

VECs are known to be sensitive to WSS and strain and also play a role in preventing calcification by VICs (5, 7). However, it is unclear at this point what the downstream responses are to physiologic and pathologic stresses in VECs, and if these responses either affect the ability of VECs to prevent calcification or lead to activation of pro-calcific pathways. The mechanobiology studies reviewed below have tried to answer these questions by considering the response of VECs and VICs to both WSS and strain.

The fibrosa is known to be more vulnerable to calcification than the ventricularis (2, 60). However, in the TAV, the non-coronary cusp fibrosa is preferentially calcified whereas the fused cusp fibrosa in BAV is more prone to calcification (28–30, 60). Interestingly, both of these regions experience lower magnitude and more oscillatory WSS than regions less prone to calcification (67, 68). Additionally, while there are extensive studies in the vascular endothelium observing disease localized to regions of low and oscillatory WSS, less is known about how the valvular endothelium responds to such conditions (30, 31, 69). Despite these correlations, there are limited studies establishing the role of WSS in VECs and particularly how abnormal WSS present in BAV may contribute to valvular disease such as calcification.

In vitro and *ex vivo* studies have used different bioreactors to apply physiologic and non-physiologic WSS onto the valve cusps and examine the relationship between WSS and valve homeostasis (30, 31, 69–71). For example, one study applied non-physiologic WSS conditions representative of BAV (31), while other studies (69) have defined non-physiologic WSS as being outside the normal ranges for TAV. The parallel-plate system is capable of applying uniform, laminar WSS to valve tissue and earlier studies using this approach demonstrated that exposure to either steady or pulsatile WSS can affect ECM synthesis in porcine aortic valve cusps (70, 71). Sucosky et al. (69) implemented the cone-and-plate system which is capable of imposing uni-directional and more complex oscillatory WSS (69). In this *ex vivo* study, the fibrosa and ventricularis of healthy porcine aortic valve cusps were exposed to physiologic WSS (low magnitude and oscillatory WSS on the fibrosa; high magnitude and laminar WSS on the ventricularis) as well as non-physiologic WSS. To model non-physiologic WSS, the fibrosa and ventricularis were exposed to conditions normally experienced by the opposite surface. Inflammatory markers including VCAM-1, ICAM-1, TGF-β1 and BMP-2 were highly upregulated on the fibrosa when exposed to non-physiologic WSS, while expression of these markers remained relatively unchanged on the ventricularis. There were no significant changes under physiologic WSS conditions. The upregulation of pro-inflammatory pathways on the fibrosa only in response to non-physiologic WSS led this group to believe that disease initiation could be side-specific and influenced by altered WSS (69). In a follow up *ex vivo* study, improvements to the cone-and-plate system allowed both sides of the valve cusps to be exposed to different WSS conditions simultaneously (31). This design more closely replicated the *in vivo* flow environment of the aortic valve and was used to distinguish between TAV and BAV R/L configurations. FSI-derived WSS conditions of a normal TAV and BAV R/L model were imposed simultaneously on the fibrosa and ventricularis of porcine aortic valve cusps. Overall, cusps exposed to WSS conditions of a normal TAV and non-fused cusp of BAV R/L maintained valve homeostasis. However, cusps exposed to WSS conditions of BAV R/L were marked by fibrosa endothelial activation (noted by ICAM and VCAM upregulation), pro-inflammatory paracrine signaling (indicated by elevated expression of TGF-β1 and BMP-4), and ECM remodeling (via increased expression of MMP-2, MMP-9, cathepsin L, cathepsin S). Following VIC

osteoblast-like differentiation, elevated levels of the bone matrix protein osteocalcin were also detected on the fibrosa and spongiosa when exposed to fused BAV WSS. Additionally, despite immunoblotting data suggesting an increase in Runx2 and α-SMA expression upon exposure to fused and non-fused BAV cusp WSS, the results were not statistically significant when compared to fresh controls (31).

eNOS is a shear-sensitive gene known to be upregulated in endothelial cells in response to laminar WSS and downregulated in response to oscillatory WSS (8). One study indicated markedly higher expression of eNOS on the ventricularis of excised calcified and non-calcified human aortic valves compared with the fibrosa and additionally that calcified valves overall expressed less eNOS than non-calcified valves (9). This agreed well with the known propensity for calcification on the fibrosa (2, 8, 30). The same group used the cone-and-plate system to impose side-specific physiologic WSS on the ventricularis and fibrosa of porcine aortic valve cusps (72). Using cGMP as a quantitative marker for NO signaling, it was noted that cGMP production increased on both surfaces when exposed to WSS compared to static conditions. cGMP was significantly higher on the ventricularis exposed to unidirectional, pulsatile WSS compared to the fibrosa which was exposed to lower and oscillatory shear stress.

Several other WSS-sensitive genes have been identified and are hypothesized to play a role in calcification, but to date remain unsubstantiated. For example, the Wnt/β-catenin pathway is a potential marker for calcification and known to be regulated by shear stress in endothelial cells, but there is no evidence to directly link this pathway and valvular WSS as causative in CAVD (8). Several miRNAs sensitive to WSS that are linked to calcification have also been identified such as: miRNA-30b which prevents signaling pathways involved in VICs osteogenic differentiation, miRNA-141 which was shown to block TGF-β1 and BMP-2 signaling, and miRNA-486-5p which is known to alter cell phenotype in response to shear stress (8, 73).

These findings suggest that altered WSS may induce inflammation, regulate endothelial function, mediate ECM remodeling, and upregulate osteogenesis-related proteins, all of which contribute to calcification in the aortic valve. See **Table 2** for a summary of these findings. While many shear-sensitive markers have been identified in vascular endothelial cells and to a lesser degree in VECs, only a few studies consider these markers in response to WSS conditions of BAV. Furthermore, while BAV R/L has been represented in such studies, the BAV R/NC configuration has yet to be explored. This could be explained by the lack of data regarding WSS conditions specific to the BAV R/NC configuration.

Findings from biomechanics studies show that the array of stress and strain experienced by a normal TAV is significantly altered in BAV (28, 29, 35, 61). The following mechanobiology studies suggest that deviations from physiologic strain may contribute to calcification through the increase in pro-inflammatory markers and by mediating ECM remodeling in the aortic valve (74–77). These findings are based on *ex vivo* and *in vitro* methods utilizing uniaxial and biaxial stretch simulations to replicate native aortic valve deformations. While both physiologic and non-physiologic strain has been examined, these conditions are not BAV-specific and therefore do not directly address the role of strain in BAV complications.

An *in vitro* study described the role of mechanical strain in porcine VECs when exposed to cyclic equibiaxial strains of 0–5, 0–10, and 0–20% for 24 h, where 10% was considered to be in the physiologic range (76). Cyclic strain was shown to regulate pro-inflammatory markers including VCAM, ICAM, as well as endothelial leukocyte adhesion molecule (E-selectin) in response to strain. Significant upregulation of VCAM-1, ICAM-1, and E-selectin were measured at cyclic strains of 0–5% and 0–20% compared to 0–10% strain and controls. The VEC monolayer in 0–5% and 0–20% strains also presented with decreased integrity and increased cell death compared to 0–10% strain. A follow-up *in vitro* study investigated how mechanical strain affects inflammatory response in porcine VICs at cyclic strains of 0%, 5%, 10%, 15%, and 20% (75). At static (non-physiologic) culture conditions, VICs highly expressed VCAM-1 as well as multiple other inflammatory markers after 2 hours. Upon exposure to strain, levels of these markers dropped, however, VCAM-1 remained upregulated in cells strained at 5% and 10% compared to 15% and 20%. An *ex vivo* study demonstrated that cyclic stretch can regulate expression of BMPs in porcine aortic valve cusps which were exposed to 10% and 15% stretch for 3, 7, and 14 days in osteogenic media containing TGF-β1 (74). After 3 days, BMP-2, BMP-4, and Runx2 were preferentially expressed on the fibrosa in response to 10% and 15% stretch compared to the ventricularis and also greater at 15% stretch compared to 10%. Additionally it was observed that aortic valve cell apoptosis increased when stretched at 15% after 7 days compared to 10% stretch. Introducing BMP antagonist noggin to the media blocked osteogenesis-related activity in the cusps including Runx2, alkaline phosphate, and osteocalcin expression. Elevated cyclic stretch was shown in another study to alter ECM remodeling in aortic valve cusps (77). In this study, circumferentially-aligned porcine aortic valve cusps were stretched to 10% (considered physiologic in this study) and 15%, 20% (pathological) in a tensile stretch bioreactor for 24 and 48 h. Expression of ECM remodeling enzymes MMP-1, MMP-2, MMP-9 and cathepsin L, S and K were quantified in addition to cell proliferation and apoptosis. Cusps exposed to cyclic stretch of 10% yielded expression levels of ECM remodeling enzymes similar to controls. At 15% stretch, cusps demonstrated upregulation MMP-1, MMP-2, MMP-9, cathepsin K, S expression whereas cathepsin L expression was downregulated. There was similar trend seen at 20% stretch but was less prominent. An increase in cellular proliferation and apoptosis at 15% and 20% cyclic stretch suggested that strain of this magnitude disrupted normal valve homeostasis. The findings from these studies are summarized in **Table 2**.

Mechanobiology studies observing strain in the aortic valve have illustrated its ability to regulate processes including inflammation and ECM remodeling (74–77). The physiologic and non-physiologic strain conditions employed in these studies were not BAV specific and therefore may not fully reflect the extent that strain plays a role in BAV. Additional studies imposing the strain conditions experienced by BAV

TABLE 2 | Summary of WSS and Stretch/Strain dependent marker expression in TAV and BAV.

Markers	WSS-dependent Expression	Stretch/Strain-dependent Expression	References
Inflammatory Paracrine Signaling	Altered WSS on fibrosa, but not the ventricularis upregulates TGF-β1 & BMP-2 Simultaneous exposure of ventricularis and fibrosa to BAV fused cusp WSS upregulates TGF-β1 & BMP-4	↑ BMP-2, BMP-4 expression with higher cusp stretch; preferentially expressed on fibrosa vs. ventricularis	(31, 69, 74)
Endothelial Activation	ICAM & VCAM are upregulated on fibrosa, but not ventricularis when exposed to altered WSS Simultaneous exposure of ventricularis and fibrosa to BAV fused cusp WSS upregulates ICAM & VCAM	↑ expression of VCAM-1, ICAM-1, & E-selectin in VECs when exposed to sub-physiologic and supraphysiologic strain ↑ expression of VCAM-1 in VICs when exposed to sub-physiologic strain	(31, 72, 75, 76)
ECM Remodeling	Exposure to BAV fused cusp WSS upregulates MMP-2, MMP-9, Cathepsin L, and Cathepsin S	↑ expression of MMP-1, MMP-2, MMP-9, cathepsin K, cathepsin S and ↓ expression of cathepsin L in response to higher cusp stretch	(31, 77)
Osteoblast-like Differentiation	Elevated osteocalcin on fibrosa upon exposure to BAV fused cusp WSS	↑ Runx2 expression at higher cusp stretch, preferentially on fibrosa	(31, 74)
NO Signaling	↑ eNOS expression on ventricularis (high magnitude & unidirectional WSS) vs. fibrosa (low & oscillatory)	*	(72)

No known reported data to support conclusions.

WSS, wall shear stress; BAV, bicuspid aortic valve; ECM, extracellular matrix; VECs, valve endothelial cells; VICs, valve interstitial cells; NO, nitric oxide; eNOS, endothelial nitric oxide synthase; BMP, bone morphogenic protein; TGF-β, transforming growth factor beta; ICAM, intercellular cell adhesion molecule; VCAM, vascular cell adhesion molecule.

may provide greater insight to the mechanisms of BAV associated complications.

It is important to note that although mechanobiology studies have provided insight to many differentially expressed genes and pathways responsive to WSS and strain, evidence to implicate them as causal mechanisms in BAV-associated complications is lacking. Further, while these mechanisms have been identified in *ex vivo* and *in vitro* studies, it is imperative that future studies attempt to recapitulate the hemodynamic and biomechanical environment using *in vivo* BAV models in order to corroborate the findings from *in vitro* and *ex vivo* studies.

DISCUSSION

BAV and its secondary complications pose a significant health care burden for which there are limited therapeutic options. Findings from hemodynamics studies have shown that BAV experiences a range of abnormalities compared to TAV including skewed velocity jets with higher magnitude, a greater transvalvular pressure gradient, asymmetrical vortical structures in the cusp sinuses, and abnormal helical formation in the ascending aorta. BAV is also subjected to abnormal WSS patterns which are side-specific and site-specific. Importantly, the fibrosa of the fused cusp (most prone to calcification) experiences lower magnitude and more oscillatory WSS than the fibrosa of TAV cusps. Additionally, the ventricularis in BAV is subjected to overall higher magnitude WSS compared to TAV cusps. Biomechanics studies comparing the structural-induced alterations in BAV have shown increased strain and radial cusp stretch compared to TAV with little difference in circumferential stretch. Mechanobiology studies have revealed that the WSS and strain imposed on VECs can regulate inflammatory response, endothelial function, ECM remodeling, and VIC phenotype which are all contributing processes leading to calcification.

Although we have a greater understanding of the hemodynamic and biomechanical environment of BAV from the clinical imaging studies, numerical modeling, and bench-top approaches employed in the studies above, the data available are not currently sufficient to directly show causality for BAV-associated secondary complications such as calcification. Deepening our understanding of these complex mechanisms will require more comprehensive studies using advanced cardiac imaging modalities and more realistic FSI simulations. For example, if the lack of data surrounding the BAV configuration most prone to developing calcification (BAV R/NC) were more extensively studied, resulting data may provide insight related to the underlying mechanisms of CAVD. Similarly, the pediatric population should now be studied using state-of-the-art computational studies to describe the hemodynamic and biomechanical environment of BAV in its earlier stages before the onset of calcification. Inclusion of these aspects in future investigations may elucidate the mechanisms responsible for secondary complications in BAV.

AUTHOR CONTRIBUTIONS

HKaz performed literature review and drafted the article. HKan, JLi, and JLa contributed to revising and editing the manuscript. All authors read and approved the final manuscript.

FUNDING

This work was supported by NIH/NHLBI R01HL132801 and R01HL127033 (JLi), 1R01HL142955 (JLa), and Advancing a Healthier Wisconsin (9520519) (JLi).

REFERENCES

1. Menon V, Lincoln J. The genetic regulation of aortic valve development and calcific disease. *Front Cardiovasc Med.* (2018) 5:162. doi: 10.3389/fcvm.2018.00162
2. Sievers HH, Schmidtke C. A classification system for the bicuspid aortic valve from 304 surgical specimens. *J Thoracic Cardiovasc Surg.* (2007) 133:1226–33. doi: 10.1016/j.jtcvs.2007.01.039
3. Hinton RB, Yutzey KE. Heart valve structure and function in development and disease. *Ann Rev Physiol.* (2011) 73:29–46. doi: 10.1146/annurev-physiol-012110-142145
4. Anstine LJ, Bobba C, Ghadiali S, Lincoln J. Growth and maturation of heart valves leads to changes in endothelial cell distribution, impaired function, decreased metabolism and reduced cell proliferation. *J Mol Cell Cardiol.* (2016) 100:72–82. doi: 10.1016/j.yjmcc.2016.10.006
5. Bosse K, Hans CP, Zhao N, Koenig SN, Huang N, Guggilam A, et al. Endothelial nitric oxide signaling regulates Notch1 in aortic valve disease. *J Mol Cell Cardiol.* (2013) 60:27–35. doi: 10.1016/j.yjmcc.2013.04.001
6. Hjortnaes J, Shapero K, Goettsch C, Hutcheson JD, Keegan J, Kluin J, et al. Valvular interstitial cells suppress calcification of valvular endothelial cells. *Atherosclerosis.* (2015) 242:251–60. doi: 10.1016/j.atherosclerosis.2015.07.008
7. Huk DJ, Austin BF, Horne TE, Hinton RB, Ray WC, Heistad DD, et al. Valve endothelial cell-derived Tgfβ1 signaling promotes nuclear localization of Sox9 in interstitial cells associated with attenuated calcification. *Arterioscler Thromb Vasc Biol.* (2016) 36:328–38. doi: 10.1161/ATVBAHA.115.306091
8. Fernández Esmerats J, Heath J, Jo H. Shear-sensitive genes in aortic valve endothelium. *Antioxid Redox Signal.* (2016) 25:401–4. doi: 10.1089/ars.2015.6554
9. Butcher JT, Nerem RM. Valvular endothelial cells regulate the phenotype of interstitial cells in co-culture: effects of steady shear stress. *Tissue Eng.* (2006) 12:905–15. doi: 10.1089/ten.2006.12.905
10. Conti CA, della Corte A, Votta E, del Viscovo L, Bancone C, de Santo LS, et al. Biomechanical implications of the congenital bicuspid aortic valve: a finite element study of aortic root function from *in vivo* data. *J Thorac Cardiovasc Surg.* (2010) 140: 890–6. doi: 10.1016/j.jtcvs.2010.01.016
11. Liu T, Xie M, Lv Q, Li Y, Fang L, Zhang L, et al. Bicuspid aortic valve: an update in morphology, genetics, biomarker, complications, imaging diagnosis and treatment. *Front Physiol.* (2019) 10:1921. doi: 10.3389/fphys.2018.01921
12. Cripe L, Andelfinger G, Martin LJ, Shooner K, Benson DW. Bicuspid aortic valve is heritable. *J Am Coll Cardiol.* (2004) 44:138–43. doi: 10.1016/j.jacc.2004.03.050
13. Yap CH, Saikrishnan N, Tamilselvan G, Vasilyev N, Yoganathan AP, Yoganathan AP, et al. The congenital bicuspid aortic valve can experience high-frequency unsteady shear stresses on its leaflet surface. *Am J Physiol Heart Circ Physiol.* (2012) 303:721–31. doi: 10.1152/ajpheart.00829.2011
14. Bravo-Jaimes K, Prakash SK. Genetics in bicuspid aortic valve disease: where are we? *Prog Cardiovasc Dis.* (2020) 63:398–406. doi: 10.1016/j.pcad.2020.06.005
15. Gould RA, Aziz H, Woods CE, Seman-Senderos MA, Sparks E, Preuss C, et al. ROBO4 variants predispose individuals to bicuspid aortic valve and thoracic aortic aneurysm. *Nat Genet.* (2019) 51:42–50. doi: 10.1038/s41588-018-0265-y
16. Fedak PWM, Verma S, David TE, Leask RL, Weisel RD, Butany J. Clinical and pathophysiological implications of a bicuspid aortic valve. *Circulation.* (2002) 106:900–4. doi: 10.1161/01.CIR.0000027905.26586.E8
17. Tzemos N. Outcomes in adults with bicuspid aortic valves. *JAMA.* (2008) 300:1317–25. doi: 10.1001/jama.300.11.1317
18. Atkins SK. Etiology of bicuspid aortic valve disease: focus on hemodynamics. *World J Cardiol.* (2014) 6:1227. doi: 10.4330/wjc.v6.i12.1227
19. Siddiqui J, Brizard CP, Konstantinov IE, Galati J, Wheaton G, Cheung M, et al. Outcomes after operations for bicuspid aortic valve disease in the pediatric population. *Ann Thorac Surg.* (2013) 96:2175–83. doi: 10.1016/j.athoracsur.2013.07.130
20. O'Brien KD. Pathogenesis of calcific aortic valve disease: a disease process comes of age (and a good deal more). *Arterioscler Thromb Vasc Biol.* (2006) 26:1721–8. doi: 10.1161/01.ATV.0000227513.13697.ac
21. Nkomo VT, Gardin JM, Skelton TN, Gottdiener JS, Scott CG, Enriquez-Sarano M. Burden of valvular heart diseases: a population-based study. *Lancet.* (2006) 368:1005–11. doi: 10.1016/S0140-6736(06)69208-8
22. Stewart BF, Siscovick D, Lind BK, Gardin JM, Gottdiener JS, Smith VE, et al. Clinical factors associated with calcific aortic valve disease fn1fn1this study was supported in part by contracts NO1-HC85079 through HC-850086 from the National Heart, Lung, and Blood Institute, National Institutes of Health, Bethesda, Maryland. *J Am Coll Cardiol.* (1997) 29:630–4. doi: 10.1016/S0735-1097(96)00563-3
23. Rajamannan NM, Evans FJ, Aikawa E, Grande-Allen KJ, Demer LL, Heistad DD, et al. Calcific aortic valve disease: Not simply a degenerative process: a review and agenda for research from the national heart and lung and blood institute aortic stenosis working group. *Circulation.* (2011) 124:1783–91. doi: 10.1161/CIRCULATIONAHA.110.006767
24. Beppu S, Suzuki S, Matsuda H, Ohmori F, Nagata S, Miyatake K. Rapidity of progression of aortic stenosis in patients with congenital bicuspid aortic valves. *Am J Cardiol.* (1993) 71:322–7. doi: 10.1016/0002-9149(93)90799-I
25. Elbadawi A, Saad M, Elgendy IY, Barssoum K, Omer MA, Soliman A, et al. Temporal trends and outcomes of transcatheter versus surgical aortic valve replacement for bicuspid aortic valve stenosis. *JACC Cardiovasc Interv.* (2019) 12:1811–22. doi: 10.1016/j.jcin.2019.06.037
26. Boe BA, Zampi JD, Kennedy KF, Jayaram N, Porras D, Foerster SR, et al. PEDIATRIC AND CONGENITAL FOCUS Acute Success of Balloon Aortic Valvuloplasty in the Current Era A National Cardiovascular Data Registry Study. *JACC Cardiovasc Interv.* (2017) 10:1717–26. doi: 10.1016/j.jcin.2017.08.001
27. Lindman BR, Clavel MA, Mathieu P, Iung B, Lancellotti P, Otto CM, et al. Calcific aortic stenosis. *Nat Rev Dis Primers.* (2016) 2:16006. doi: 10.1038/nrdp.2016.6
28. Emendi M, Sturla F, Ghosh RP, Bianchi M, Piatti F, Pluchinotta FR, et al. Patient-specific bicuspid aortic valve biomechanics: a magnetic resonance imaging integrated fluid–structure interaction approach. *Ann Biomed Eng.* (2020) 49:627–41. doi: 10.1007/s10439-020-02571-4
29. Cao K, Sucosky P. Computational comparison of regional stress and deformation characteristics in tricuspid and bicuspid aortic valve leaflets. *Int J Numer Method Biomed Eng.* (2017) 33. doi: 10.1002/cnm.2798
30. Arjunon S, Rathan S, Jo H, Yoganathan AP. Aortic valve: mechanical environment and mechanobiology. *Ann Biomed Eng.* (2013) 41:1331–46. doi: 10.1007/s10439-013-0785-7
31. Sun L, Chandra S, Sucosky P. *Ex Vivo.* evidence for the contribution of hemodynamic shear stress abnormalities to the early pathogenesis of calcific bicuspid aortic valve disease. *PLoS ONE.* (2012) 7:e48843. doi: 10.1371/journal.pone.0048843
32. Marom G, Kim HS, Rosenfeld M, Raanani E, Haj-Ali R. Fully coupled fluid-structure interaction model of congenital bicuspid aortic valves: effect of asymmetry on hemodynamics. *Med Biol Eng Comput.* (2013) 51:839–48. doi: 10.1007/s11517-013-1055-4
33. Chandra S, Rajamannan NM, Sucosky P. Computational assessment of bicuspid aortic valve wall-shear stress: implications for calcific aortic valve disease. *Biomech Model Mechanobiol.* (2012) 11:1085–96. doi: 10.1007/s10237-012-0375-x
34. Jermihov PN, Jia L, Sacks MS, Gorman RC, Gorman JH, Chandran KB. Effect of geometry on the leaflet stresses in simulated models of congenital bicuspid aortic valves. *Cardiovasc Eng Technol.* (2011) 2:48–56. doi: 10.1007/s13239-011-0035-9
35. Lavon K, Halevi R, Marom G, ben Zekry S, Hamdan A, Joachim Schäfers H, et al. Fluid–structure interaction models of bicuspid aortic valves: the effects of nonfused cusp angles. *J Biomech Eng.* (2018) 140. doi: 10.1115/1.4038329
36. Barker AJ, Markl M, Bürk J, Lorenz R, Bock J, Bauer S, et al. Bicuspid aortic valve is associated with altered wall shear stress in the ascending aorta. *Circ Cardiovasc Imaging.* (2012) 5:457–6. doi: 10.1161/CIRCIMAGING.112.973370
37. van Ooij P, Potters WV, Collins J, Carr M, Carr J, Malaisrie SC, et al. Characterization of abnormal wall shear stress using 4D flow MRI in human bicuspid aortopathy. *Ann Biomed Eng.* (2015) 43:1385–97. doi: 10.1007/s10439-014-1092-7
38. van Ooij P, Markl M, Collins JD, Carr JC, Rigsby C, Bonow RO, et al. Aortic valve stenosis alters expression of regional aortic wall shear stress: new insights from a 4-Dimensional Flow Magnetic Resonance Imaging Study of 571 Subjects. *J Am Heart Assoc.* (2017) 6:e005959. doi: 10.1161/JAHA.117.005959

39. Piatti F, Pirola S, Bissell M, Nesteruk I, Sturla F, della Corte A, et al. Towardz the improved quantification of *in vivo* abnormal wall shear stresses in BAV-affected patients from 4D-flow imaging: Benchmarking and application to real data. *J Biomech.* (2017) 50:93–101. doi: 10.1016/j.jbiomech.2016.11.044
40. Piatti F, Sturla F, Bissell MM, Pirola S, Lombardi M, Nesteruk I, et al. 4D flow analysis of BAV-related fluid-dynamic alterations: evidences of wall shear stress alterations in absence of clinically-relevant aortic anatomical remodeling. *Front Physiol.* (2017) 8:441. doi: 10.3389/fphys.2017.00441
41. Mahadevia R, Barker AJ, Schnell S, Entezari P, Kansal P, Fedak PWM, et al. Bicuspid aortic cusp fusion morphology alters aortic three-dimensional outflow patterns, wall shear stress, and expression of aortopathy. *Circulation.* (2014) 129:673–82. doi: 10.1161/CIRCULATIONAHA.113.003026
42. Cao K, BukaC M, Sucosky P. Three-dimensional macro-scale assessment of regional and temporal wall shear stress characteristics on aortic valve leaflets. *Comput Method Biomech Biomed Eng.* (2016) 19:603–13. doi: 10.1080/10255842.2015.1052419
43. Saikrishnan N, Yap CH, Milligan NC, Vasilyev NV, Yoganathan AP. *In vitro* characterization of bicuspid aortic valve hemodynamics using particle image velocimetry. *Ann Biomed Eng.* (2012) 40:1760–75. doi: 10.1007/s10439-012-0527-2
44. Robicsek F, Thubrikar MJ, Cook JW, Fowler B. The congenitally bicuspid aortic valve: how does it function? Why does it fail? *Ann Thorac Surg.* (2004) 77:177–85. doi: 10.1016/S0003-4975(03)01249-9
45. Nanda NC, Gramiak R, Manning J, Mahoney EB, Lipchik EO, Deweese JA. Echocardiographic recognition of the congenital bicuspid aortic valve. *Circulation*. (1974). 49:870–5. doi: 10.1016/0002-9149(74)90901-1
46. Fowles RE, Martin RP, Abrams JM, Schapira JN, French JW, Popp RL. Two-dimensional echocardiographic features of bicuspid aortic valve. *Chest.* (1979) 75:434–40. doi: 10.1378/chest.75.4.434
47. Rodríguez-Palomares JF, Dux-Santoy L, Guala A, Kale R, Maldonado G, Teixidó-Turà G, et al. Aortic flow patterns and wall shear stress maps by 4D-flow cardiovascular magnetic resonance in the assessment of aortic dilatation in bicuspid aortic valve disease. *J Cardiovasc Magn Reson.* (2018) 20:28. doi: 10.1186/s12968-018-0451-1
48. Markl M, Schnell S, Barker AJ. 4D flow imaging: current status to future clinical applications. *Curr Cardiol Rep.* (2014) 16:481. doi: 10.1007/s11886-014-0481-8
49. Doost SN, Ghista D, Su B, Zhong L, Morsi YS. Heart blood flow simulation: a perspective review. *BioMed Eng Online.* (2016) 15:101. doi: 10.1186/s12938-016-0224-8
50. Kandail HS, Trivedi SD, Shaikh AC, Bajwa TK, O'Hair DP, Jahangir A, et al. Impact of annular and supra-annular CoreValve deployment locations on aortic and coronary artery hemodynamics. *J Mech Behav Biomed Mater.* (2018) 86:131–42. doi: 10.1016/j.jmbbm.2018.06.032
51. Saikrishnan N, Mirabella L, Yoganathan AP. Bicuspid aortic valves are associated with increased wall and turbulence shear stress levels compared to trileaflet aortic valves. *Biomech Model Mechanobiol.* (2015) 14:577–88. doi: 10.1007/s10237-014-0623-3
52. Seaman C, Akingba AG, Sucosky P. Steady flow hemodynamic and energy loss measurements in normal and simulated calcified tricuspid and bicuspid aortic valves. *J Biomech Eng.* (2014) 136:doi: 10.1115/1.4026575
53. Mei S, de Souza Júnior FSN, Kuan MYS, Green NC, Espino DM. Hemodynamics through the congenitally bicuspid aortic valve: a computational fluid dynamics comparison of opening orifice area and leaflet orientation. *Perfusion.* (2016) 31:683–90. doi: 10.1177/0267659116656775
54. Viscardi F, Vergara C, Antiga L, Merelli S, Veneziani A, Puppini G, et al. Comparative finite element model analysis of ascending aortic flow in bicuspid and tricuspid aortic valve. *Artif Organs.* (2010) 34:1114–20. doi: 10.1111/j.1525-1594.2009.00989.x
55. Hope MD, Hope TA, Meadows AK, Ordovas KG, Urbania TH, Alley MT, Higgins CB. Bicuspid aortic valve: Four-dimensional MR evaluation of ascending aortic systolic flow patterns. *Radiology.* (2010) 255:53–61. doi: 10.1148/radiol.09091437
56. Liu J, Shar JA, Sucosky P. Wall shear stress directional abnormalities in BAV aortas: toward a new hemodynamic predictor of aortopathy? *Front Physiol.* (2018) 9:993. doi: 10.3389/fphys.2018.00993
57. Richards KE, Deserranno D, Donal E, Greenberg NL, Thomas JD, Garcia MJ, et al. Influence of structural geometry on the severity of bicuspid aortic stenosis. *Am J Physiol Heart Circ Physiol.* (2004) 287:1410–6. doi: 10.1152/ajpheart.00264.2003
58. Mahmoudi M, Farghadan A, McConnell D, Barker AJ, Wentzel JJ, Budoff MJ, et al. The story of wall shear stress in coronary artery atherosclerosis: biochemical transport and mechanotransduction. *J Biomech Eng.* (2020) 143. doi: 10.1115/1.4049026
59. White CR, Haidekker M, Bao X, Frangos JA. Temporal Gradients in Shear, but Not Spatial Gradients, Stimulate Endothelial Cell Proliferation. (2001). Available at: http://www.circulationaha.org doi: 10.1161/01.CIR.103.20.2508
60. Flemister DC, Hatoum H, Guhan V, Zebhi B, Lincoln J, Crestanello J, Dasi LP. Effect of Left and right coronary flow waveforms on aortic sinus hemodynamics and leaflet shear stress: correlation with calcification locations. *Ann Biomed Eng.* (2020) 48:2796–808. doi: 10.1007/s10439-020-02677-9
61. Szeto K, Pastuszko P, Álamo JCD, Lasheras J, Nigam V. Bicuspid aortic valves experience increased strain as compared to tricuspid aortic valves. *World J Pediatr Congenit Heart Surg.* (2013) 4:362–66. doi: 10.1177/2150135113501901
62. Katayama S, Umetani N, Hisada T, Sugiura S. Bicuspid aortic valves undergo excessive strain during opening: a simulation study. *J Thorac Cardiovasc Surg.* (2013) 145:1570–6. doi: 10.1016/j.jtcvs.2012.05.032
63. Rathan S, Ankeny CJ, Arjunon S, Ferdous Z, Kumar S, Fernandez Esmerats J, et al. Identification of side- and shear-dependent microRNAs regulating porcine aortic valve pathogenesis. *Sci Rep.* (2016) 6:25397. doi: 10.1038/srep25397
64. Osman L, Yacoub MH, Latif N, Amrani M, Chester AH. Role of human valve interstitial cells in valve calcification and their response to atorvastatin. *Circulation.* (2006) 114(Suppl. 1):I547–52. doi: 10.1161/CIRCULATIONAHA.105.001115
65. Lerman DA, Prasad S, Alotti N. Calcific aortic valve disease: molecular mechanisms and therapeutic approaches. *Eur Cardiol Rev.* (2015) 10:108–12. doi: 10.15420/ecr.2015.10.2.108
66. Shapero K, Wylie-Sears J, Levine RA, Mayer JE, Bischoff J. Reciprocal interactions between mitral valve endothelial and interstitial cells reduce endothelial-to-mesenchymal transition and myofibroblastic activation. *J Mol Cell Cardiol.* (2015) 80:175–85. doi: 10.1016/j.yjmcc.2015.01.006
67. Braddock M, Schwachtgen J-L, Houston P, Dickson MC, Lee MJ, Campbell CJ. Fluid shear stress modulation of gene expression in endothelial cells. *News Physiol Sci.* (1998) 13:241–6. doi: 10.1152/physiologyonline.1998.13.5.241
68. Butcher JT, Simmons CA, Warnock JN. Review: mechanobiology of the aortic heart valve. (2008) 17:62–73.
69. Sucosky P, Balachandran K, Elhammali A, Jo H, Yoganathan AP. Altered shear stress stimulates upregulation of endothelial VCAM-1 and ICAM-1 in a BMP-4- and TGF-β1-dependent pathway. *Arterioscler Thromb Vasc Biol.* (2009) 29:254–60. doi: 10.1161/ATVBAHA.108.176347
70. Weston MW, Yoganathan AP. Biosynthetic activity in heart valve leaflets in response to *in vitro* flow environments. *Ann Biomed Eng.* (2001) 29:752–63. doi: 10.1114/1.1397794
71. Platt M, Xing Y, Jo H, Yoganathan AP. Cyclic pressure and shear stress regulate matrix metalloproteinases and cathepsin activity in porcine aortic valves. *J Heart Valve Dis.* (2006) 15:622–9.
72. Richards J, El-Hamamsy I, Chen S, Sarang Z, Sarathchandra P, Yacoub MH, et al. Side-specific endothelial-dependent regulation of aortic valve calcification: interplay of hemodynamics and nitric oxide signaling. *Am J Pathol.* (2013) 182:1922–31. doi: 10.1016/j.ajpath.2013.01.037
73. Holliday CJ, Ankeny RF, Jo H, Nerem RM. Discovery of shear- and side-specific mRNAs and miRNAs in human aortic valvular endothelial cells. *Am J Physiol Heart Circ Physiol.* (2011) 301:856–67. doi: 10.1152/ajpheart.00117.2011
74. Balachandran K, Sucosky P, Jo H, Yoganathan AP. Elevated cyclic stretch induces aortic valve calcification in a bone morphogenic protein-dependent manner. *Am J Pathol.* (2010) 177:49–57. doi: 10.2353/ajpath.2010.090631

75. Smith KE, Metzler SA, Warnock JN. Cyclic strain inhibits acute pro-inflammatory gene expression in aortic valve interstitial cells. *Biomech Model Mechanobiol.* (2010) 9:117–25. doi: 10.1007/s10237-009-0165-2
76. Metzler SA, Pregonero CA, Butcher JT, Burgess SC, Warnock JN. Cyclic strain regulates pro-inflammatory protein expression in porcine aortic valve endothelial cells. *J Heart Valve Dis.* (2008) 17:571–7.
77. Balachandran K, Sucosky P, Jo H, Yoganathan AP. Elevated cyclic stretch alters matrix remodeling in aortic valve cusps: implications for degenerative aortic valve disease. *Am J Physiol Heart Circ Physiol.* (2009) 296:756–64. doi: 10.1152/ajpheart.00900.2008

Conflict of Interest: The authors declare that the research was conducted in the absence of any commercial or financial relationships that could be construed as a potential conflict of interest.

frontiers in Cardiovascular Medicine

MINI REVIEW
published: 11 June 2021
doi: 10.3389/fcvm.2021.688513

Label-Free Multiphoton Microscopy for the Detection and Monitoring of Calcific Aortic Valve Disease

*Ishita Tandon, Kyle P. Quinn and Kartik Balachandran**

Department of Biomedical Engineering, University of Arkansas, Fayetteville, AR, United States

Calcific aortic valve disease (CAVD) is the most common valvular heart disease. CAVD results in a considerable socio-economic burden, especially considering the aging population in Europe and North America. The only treatment standard is surgical valve replacement as early diagnostic, mitigation, and drug strategies remain underdeveloped. Novel diagnostic techniques and biomarkers for early detection and monitoring of CAVD progression are thus a pressing need. Additionally, non-destructive tools are required for longitudinal *in vitro* and *in vivo* assessment of CAVD initiation and progression that can be translated into clinical practice in the future. Multiphoton microscopy (MPM) facilitates label-free and non-destructive imaging to obtain quantitative, optical biomarkers that have been shown to correlate with key events during CAVD progression. MPM can also be used to obtain spatiotemporal readouts of metabolic changes that occur in the cells. While cellular metabolism has been extensively explored for various cardiovascular disorders like atherosclerosis, hypertension, and heart failure, and has shown potential in elucidating key pathophysiological processes in heart valve diseases, it has yet to gain traction in the study of CAVD. Furthermore, MPM also provides structural, functional, and metabolic readouts that have the potential to correlate with key pathophysiological events in CAVD progression. This review outlines the applicability of MPM and its derived quantitative metrics for the detection and monitoring of early CAVD progression. The review will further focus on the MPM-detectable metabolic biomarkers that correlate with key biological events during valve pathogenesis and their potential role in assessing CAVD pathophysiology.

Keywords: calcific aortic valve disease, multiphoton microscopy, valve interstitial cell metabolism, aortic stenosis, early diagnosis

OPEN ACCESS

Edited by:
Katherine Yutzey, Cincinnati Children's Hospital Medical Center, United States

Reviewed by:
Laura Iop, University of Padua, Italy
Adrien Lupieri, Brigham and Women's Hospital and Harvard Medical School, United States

****Correspondence:***
Kartik Balachandran
kbalacha@uark.edu

Specialty section:
This article was submitted to Heart Valve Disease, a section of the journal Frontiers in Cardiovascular Medicine

Received: *31 March 2021*
Accepted: *17 May 2021*
Published: *11 June 2021*

Citation:
Tandon I, Quinn KP and Balachandran K (2021) Label-Free Multiphoton Microscopy for the Detection and Monitoring of Calcific Aortic Valve Disease. Front. Cardiovasc. Med. 8:688513. doi: 10.3389/fcvm.2021.688513

INTRODUCTION

Calcific aortic valve disease (CAVD) is the most common heart valve disease, with a prevalence of 25% in those 65 years and above (1). Additionally, 75% patients with congenital bicuspid aortic valve disease develop CAVD by the age of 30 years (2, 3). CAVD is a progressive disease with complex pathophysiology (4), and is associated with a 50% elevated risk of fatal cardiovascular pathologies resulting in more than 15,000 deaths annually in North America alone (5). The only available standard of care is valve replacement surgery (6), as early detection, prevention, and mitigation strategies are underdeveloped (7). Several techniques such as echocardiography, cardiac magnetic resonance imaging, and computed tomography are clinically employed for the diagnosis and monitoring of CAVD (8, 9), while newer techniques such as positron emission tomography are

gaining traction (9). However, there remains a need for a multimodal technique capable of performing early detection and monitoring of CAVD progression.

Multiphoton microscopy (MPM) is well-suited to provide non-invasive assessments of tissue structure and function. The most commonly used MPM technique, two-photon excited fluorescence (TPEF) microscopy, employs the use of two photons of near-infrared (NIR) wavelengths to excite fluorophores, which offers advantages such as intrinsic depth sectioning, less photobleaching, and label-free imaging of various endogenous fluorophores (10–13). These characteristics make TPEF suitable for non-destructive, non-invasive, spatiotemporal imaging of live cells and tissue samples, both *in vitro* and *in vivo* (10, 12, 13). MPM has been shown to be useful for generating high-resolution image-based data but also quantitative metrics that can be correlated with biologically-relevant features and events ranging from sub-cellular scales up to gross tissue morphology (10, 13–18).

TPEF allows for quantification of the endogenous fluorescence of the cellular co-factors flavin adenine dinucleotide (FAD) and the reduced forms of nicotinamide adenine dinucleotide (NADH) and nicotinamide adenine dinucleotide phosphate (NADPH). NAD(P)H and FAD play key roles as electron carriers in various metabolic pathways, including glycolysis, the tricarboxylic acid cycle, and the electron transport chain in mitochondria (11, 12, 19, 20). The ratio of the fluorescence intensity of these factors [e.g., FAD/(FAD+NAD(P)H)], called optical redox ratio (ORR), can reveal insights into the interplay between glucose catabolism and oxidative phosphorylation (11, 12, 19–21). NAD(P)H autofluorescence can also be used to assess the mitochondrial organization via the mitochondrial fractal dimension (FD) parameter (20, 22, 23).

In addition to spatially-resolved fluorescence measurements of NAD(P)H, measurements of the time between excitation and emission can provide additional insights into cell metabolism through fluorescence lifetime imaging (FLIM). This technique involves estimating the fluorescence lifetime decay rates, which are sensitive to microenvironmental changes such as pH or protein binding (11). Of note, FLIM of NAD(P)H can be used to distinguish its bound and free states through a biexponential least-squares fit of the lifetime decay curves (11, 19, 24–26). Free NAD(P)H has a mean lifetime of 0.3–0.4 ns, while protein-bound NAD(P)H has a mean lifetime of 1.9–5.7 ns (11). The proportion of free NAD(P)H tends to increase when cells are undergoing glycolysis, while bound NAD(P)H often increases with increases in the rate of oxidative phosphorylation. FLIM is advantageous because it is independent of fluorophore concentration, laser intensity fluctuations, and the effects of tissue adsorption and scattering (18, 19, 24–27).

Second harmonic generation (SHG) imaging is another powerful MPM technique used to assess non-centrosymmetric molecules like fibrillary collagen (17, 28–30). SHG is sensitive to collagen fiber amount, length, diameter, density, and orientation (31–33) and has been used in various research applications including dermatology, oncology, neurology, and cardiovascular disorders (17, 28–34). Apart from measuring collagen via SHG, TPEF imaging has been used to assess elastic fiber content, density, and length to characterize cardiovascular pathophysiology (17, 30, 35). MPM-based coherent Raman imaging techniques, such as coherent anti-Stokes Raman spectroscopy (CARS), have also provided a powerful tool to visualize lipid droplet organization, concentration, and size (24–26, 29, 36–38). SHG and CARS imaging of collagen, calcium, and lipids can be performed simultaneously with TPEF microscopy (11, 13, 20, 39, 40) and could be potentially used to characterize optical signatures associated with CAVD progression.

There are relatively few studies that have applied MPM for the study of aortic valves and its pathophysiology. MPM-based approaches combining TPEF, SHG and CARS, for label-free imaging of an aortic valve have been previously demonstrated (41). TPEF has been used to assess aortic valve interstitial cell (VIC) proliferation (21, 42), osteogenesis (43), and valve calcification *in vitro* and *ex vivo* (39). TPEF autofluorescence ratios have shown potential in assessing CAVD progression *ex vivo* (44). SHG has also been used to quantify collagen remodeling in valve tissues (45). This review outlines how label-free MPM metrics have been employed to assess key events of CAVD progression, in valvular and non-valvular cells, tissues, and disease models. We then summarize the challenges and future directions for MPM as a tool to study valve disease.

MPM-BASED DETECTION OF MARKERS FOR VALVE DISEASE IN OTHER PATHOLOGIES

Multiple events contribute to CAVD progression. Some known hallmarks or markers of CAVD include endothelial damage, endothelial-to-mesenchymal transformation, oxidative stress, lipid deposition and oxidation, inflammation, collagen remodeling, and mineralization (4–7, 46–48). Multiple studies have employed label-free MPM techniques and metrics to assess similar events and biomarkers in other diseases and models as discussed below.

Monitoring of Inflammation and Reactive Oxygen Species

Multiple studies as described here have employed multimodal MPM approach by combining CARS, TPEF, and SHG to assess inflammation. NAD(P)H imaging via TPEF has been shown to be useful in identifying macrophages and CARS has been used to detect foam cells during spinal cord injury (38, 49, 50). MPM has also been used to assess inflammation in blood vessels to identify morphological differences between healthy

Abbreviations: CARS, Coherent anti-Stokes Raman Spectroscopy; CAVD, Calcific Aortic Valve Disease; EVs, Extracellular Vesicles; FAD, Flavin Adenine Dinucleotide; FD, Fractal Dimension; FLIM, Fluorescence lifetime imaging; hMSCs, Human mesenchymal stem cells; MPM, Multiphoton Microscopy; NAD(P)H, Nicotinamide Adenine (phosphorylated) Dinucleotide Reduced; ORR, Optical Redox Ratio; ROS, Reactive Oxygen Species; SHG, Second Harmonic Generation; TPEF, Two-Photon Excited Fluorescence; VICs, Valve Interstitial Cells.

and tumor tissues, lymphocytes, collagen fiber bundles, and endothelial damage (51, 52). Reactive oxygen species (ROS) are a primary cause of endothelial damage and tissue injury leading to inflammatory diseases (53), and are key modulators of cell metabolism (54). Correlation between cell metabolism and ROS has been well-characterized in cancers (55). Given ROS-mediated inflammation and lipid oxidation are key drivers of early CAVD initiation (56–58), imaging metabolic and morphological changes of cells as well as oxidized lipids via MPM to infer inflammation (24, 59), may serve as a powerful early detection tool to detect CAVD initiation.

Monitoring of Extracellular Vesicles and Apoptotic Calcification

Immune signaling, apoptosis, and Ca^{2+} ion flux are closely associated with mitochondrial dysfunction and CAVD progression (60). Apoptotic VICs have been shown to present ectonucleotide pyrophosphatase/phosphodiesterase-1 (eNPP1)-containing extracellular vesicles (EVs) on their cell membrane, where these EVs are thought to promote mineralization (61). Recently, label-free FLIM has been utilized to image EVs isolated from macrophages and cancer cells (62). NAD(P)H lifetime determined by FLIM has also been used to assess apoptosis and shown to change before cleaved caspase-3 activation and mitochondrial dysfunction (27, 63). These results suggest a potential avenue for using FLIM to characterize apoptosis, and therefore EV-mediated dystrophic mineralization during CAVD progression.

Monitoring of Extracellular Matrix Structure and Phenotypic Differentiation

MPM has been used to monitor the osteogenic, adipogenic and chondrogenic differentiation of human mesenchymal stem cells (hMSCs) using various MPM-based metrics, including ORR, mitochondrial organization within the cell, collagen SHG, and FLIM of NAD(P)H and FAD (19, 20, 64). These studies suggest that the assessment of the heterogeneity of the cell population, their capability for collagen synthesis and remodeling, and variation in their differential potential can be assessed via MPM techniques (20, 64, 65). Considering the utility of TPEF and CARS to detect adipogenic differentiation of hMSCs and assess lipid amount, organization, orientation, and concentration (20, 25, 26, 36, 64), MPM-based imaging of lipid deposition may be useful in monitoring CAVD progression. MPM imaging has already been used to visualize elastin and collagen microstructures in heart valves using TPEF and SHG, respectively (17, 30, 45, 66).

MPM IN AORTIC VALVE PATHOLOGY AND PHYSIOLOGY

Ex vivo Characterization of Calcification

TPEF autofluorescence at 800 nm excitation and 460 and 525 nm emission was associated with mineralization in $ApoE^{-/-}$ mice, calcified human valves, and calcific nodules generated *in vitro*, using a ratiometric approach, a result also corroborated by CARS imaging (39). While the fluorescence emission at 525 nm was associated with mineralization, spectral analysis revealed that fluorescence emission at 460 nm was associated with collagen (39).

Recently, we have evaluated multiple ratios of autofluorescence intensity at various stages of disease in a mouse model of CAVD (44). In that study, autofluorescence intensities at specific two-photon excitation and emission wavelengths, represented as $A_{excitation/emission}$, were considered, including $A_{810/525}$, $A_{810/460}$, $A_{860/525}$, and $A_{755/460}$. We found that the $[A_{860/525}/(A_{755/460}+A_{860/525})]$ autofluorescence ratio rather than $[A_{810/525}/(A_{810/460}+A_{810/525})]$ was more sensitive to CAVD progression (44). These TPEF autofluorescence ratios correlated negatively with proliferation, osteogenic differentiation, collagen remodeling, and calcium deposition. Indeed, reduced autofluorescence ratio at 16 weeks served as a predictor for increased calcification in the valve at 28 weeks (44). In another study, assessment of collagen remodeling via SHG revealed that during CAVD, collagen fibers in the spongiosa layer increased in number, width, and density while collagen fibers of the fibrosa became relatively shorter (45) (**Figures 1A,B**). SHG imaging also revealed decreased collagen amount and altered fiber alignment in different regions of aortic valve leaflets in an $ApoE^{-/-}$ mice based CAVD model (66). In the same study, lipid droplets (**Figure 1C**) and cholesterol crystals were identified within cells (**Figure 1D**) and plaques (**Figure 1E**) in aortic valve leaflets via CARS imaging (66).

In vitro Characterization of VIC Pathophysiology

Our lab has previously reported that when VICs underwent a pathogenic phenotype shift, they experienced a decrease in ORR, suggesting a possible link between VIC pathology and its metabolic state (21, 42, 43, 67). TPEF imaging of VICs under quiescent and osteogenic conditions revealed that the ORR decreased during early osteogenic differentiation (**Figure 1F**) and correlated with gene expression of osteogenic markers. However, FD, a marker inversely proportional to mitochondrial clustering, increased at later time points and correlated with gene expression of osteogenic and structural markers as assessed by qRT-PCR. FD also correlated with nuclear morphology which was assessed via TPEF fluorescence maps (43). In another study, VICs subjected to conditions mimicking hypertensive pressures exhibited decreased ORR (21). Even in a more valve mimetic three-dimensional environment with physiological and pathological stretch, VIC ORR correlated negatively with proliferation (42). These studies demonstrate the *in vitro* utility of TPEF in assessing VIC structure, function, and phenotype during CAVD progression.

BIOLOGICAL RELEVANCE OF MPM-BASED METRICS TO VALVE DISEASE

During disease, stress, differentiation, or other pathophysiological conditions, cells undergo increased

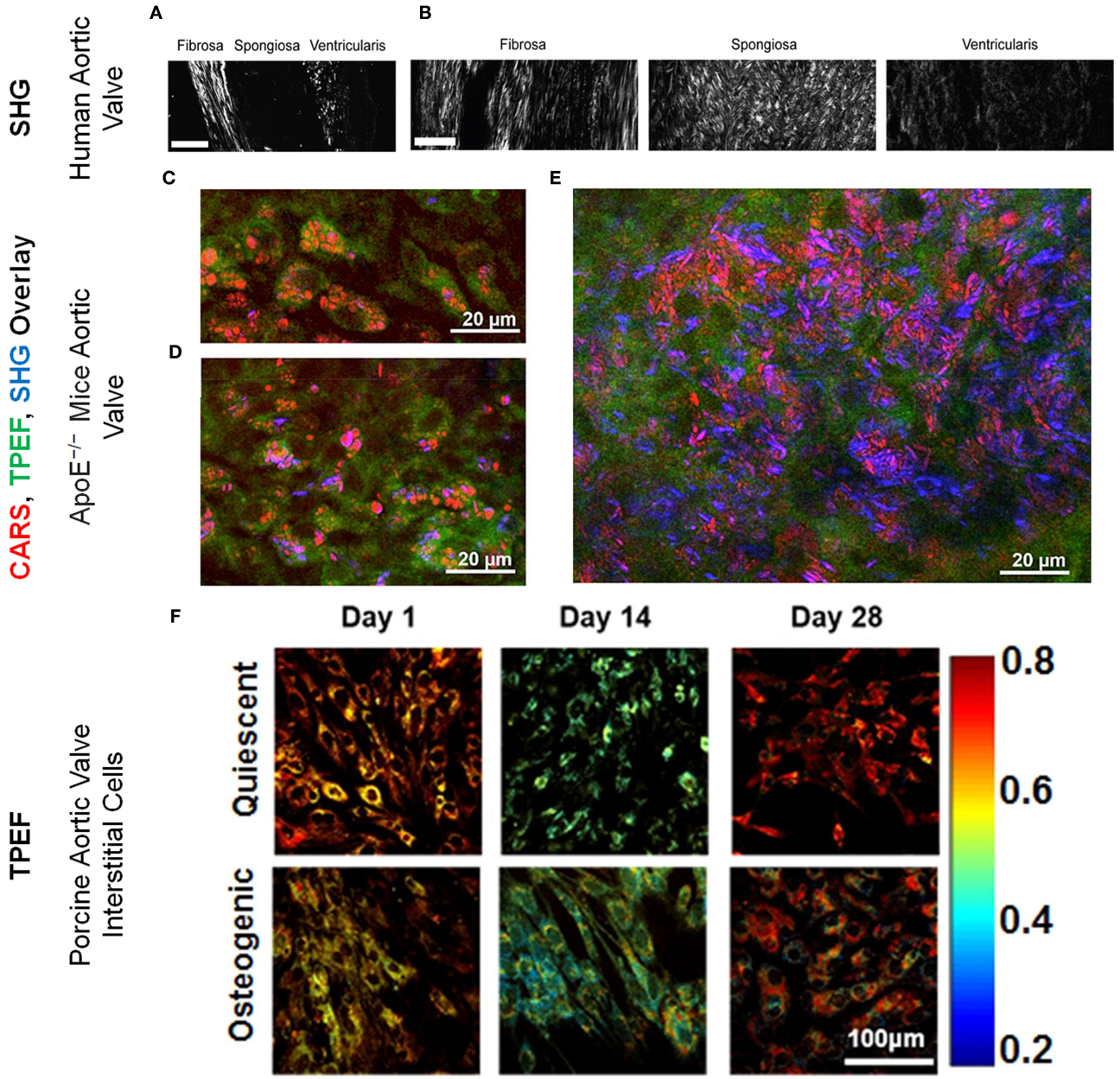

FIGURE 1 | Collagen microarchitecture in **(A)** healthy and **(B)** diseased aortic valve leaflets imaged via SHG imaging. Scale bar = 50 μm. These figure panels were adapted from Hutson et al. (45) under an open access Creative Commons CC BY license. Aortic valve (acoronary) leaflet regions of ApoE$^{-/-}$ mice imaged via CARS (red; lipids and cholesterol), TPEF (green; cells) and SHG (blue; collagen) showing **(C)** lipid droplets and **(D)** cholesterol crystals within the cells and **(E)** lipid droplets and cholesterol crystals in the plaques. These figure panels were adapted from Jannasch et al. (66) under an open access Creative Commons CC BY license. **(F)** ORR maps for VICs cultured under quiescent and osteogenic conditions for 1, 14, and 28 days. ORR decreased in osteogenic VICs by 14 days. The color bar represents the value of unitless ORR ranging between 0.2 and 0.8. These figure panels were modified from Tandon et al. (43) under an open access Creative Commons CC BY license.

glycolysis resulting in increased production of NAD(P)H (11, 14, 20). Under physiological conditions, it has been observed that cells are preferential to the process of oxidative phosphorylation for meeting their energy demands, which results in an increase in NAD+ concentrations (11, 14, 20). This ratio of NAD+ and NADH is correlated with the ratio of FAD and NADH autofluorescence as measured by ORR (11, 20). NAD(P)H fluorescence can also be used to assess mitochondrial organization, which has been associated with multiple cardiovascular disorders (20, 23, 63, 68–73).

Mitochondrial Organization in Calcified Valves

Dynamin-related protein-1, a protein responsible for mitochondrial fission was upregulated in stenotic valves, inhibition of which attenuated calcification (60, 74). Mitochondrial fission is known to induce autophagy (75), and inhibiting fission reduced mitochondrial clustering (72). Interestingly, osteogenic VICs showed higher FD implying less mitochondrial clustering as assessed by TPEF imaging of NAD(P)H fluorescence (43) but the specific functional role of mitochondrial clustering in valve pathophysiology is yet to be elucidated.

CAVD Metabolic Profiling via Multi-Omics Approach

The role of cellular metabolism has been widely explored in various cardiovascular disorders (71, 73, 76, 77) and metabolic regulators like osteocalcin, pyruvate dehydrogenase kinase, and adenosine monophosphate-activated protein kinase pathway have been implicated (78–81). These factors and pathways are known to be differentially regulated in diseased aortic valves (82–84). In turn, aortic stenosis has been a known modulator of cardiac metabolism (85). Few studies exist that directly aimed at understanding metabolic changes and their role in CAVD progression (21, 42, 43, 67), while others employed proteomics and found differentially regulated metabolism-related proteins and/or protein clusters associated with aortic valve disease (86–90). Researchers have also employed transcriptomics (83, 91) and multi-omics (92) approaches and revealed differentially expressed factors, which affect cellular metabolism during aortic valve disease.

Metabolic Changes During VIC Pathophysiology

VIC and hMSC osteogenic differentiation showcased similar trends with respect to ORR and FD (20, 43), an observation supported by the recently elucidated stemness characteristics of VICs (65). A glycolytic shift of metabolism during osteogenic differentiation has been speculated to occur due to the increased biosynthetic demand for collagen synthesis and remodeling (20, 67). However, other factors like pyruvate availability in media may also determine the tendency of cells to prefer glycolysis vs. oxidative phosphorylation (19, 20, 64). In our *in vitro* study, increased proliferation associated with decreased ORR in VICs was regulated by the Akt/mTOR signaling pathway (42), which has also been observed in other studies (55, 93). These signaling pathways were also involved in the regulation of ROS-mediated oxidative stress and its effects on cell metabolism and proliferation (54). Reduced ORR suggested increased glycolysis and/or reduced oxidative phosphorylation during VIC proliferation and osteogenesis (11, 20, 42, 43). Indeed, VICs undergoing mineralization were enriched in proteins responsible for maintaining glycolysis and mediators for phosphate metabolism (94). Additionally, peripheral blood gene signatures associated with CAVD revealed increased proliferation and reduced oxidative phosphorylation (95). Additionally, ATPase, an enzyme important for oxidative phosphorylation, was found to be downregulated in stenotic valves (83). Differences observed in the substrate utilization and glycolytic shifts in cardiovascular development and disorders (77, 85), and the extensive MPM-based assessment of hMSCs (19, 20, 64), should inspire further exploration of metabolic imaging in VICs.

Cause-effect relationships between metabolic alterations and VIC pathophysiology and their correlation with disease require further inquiry. On that front, mechanisms, regulators, and diagnostic strategies for vascular inflammation and calcification are at a more advanced stage of being assessed via imaging techniques (59, 79, 80, 96, 97), and efforts to incorporate these associations with valvular calcification may help to get a better understanding of metabolic imaging in CAVD. Further understanding of how metabolic regulators affect MPM metrics with respect to disease stage and severity, in the context of the aortic valve, is required to fully understand the extent of the biological relevance of MPM metrics in the context of CAVD.

CHALLENGES ASSOCIATED WITH CLINICAL TRANSLATION AND FUTURE DIRECTIONS

Despite several advantages, MPM is not devoid of associated limitations. Challenges exist in terms of specificity and resolution for a given fluorophore, dependency of depth penetration on the absorbing and scattering fluorophores, and minimal but existent photobleaching (11, 98). Some of the challenges associated with heart valve imaging are summarized below.

Intrinsic sources of contrast from NAD(P)H, FAD, lipids, collagen, elastin, and mineralization can facilitate MPM-based imaging of CAVD progression (11, 39). However, their overlapping spectra within the visible range can pose challenges in relating measurements to a specific source of contrast (39, 40). Unmixing the fluorescence spectra of each of the aforementioned components within the valve will be important in understanding how these optical signatures relate to disease stage and severity. Additional studies are needed for rigorous *in vitro* and *ex vivo* screening of optical signatures correlated with each CAVD hallmark, including but not restricted to endothelial damage, infiltration of inflammatory cytokines, oxidization of lipids, apoptosis, and collagen remodeling. It should be noted that while some *ex vivo* characterization has been performed (39, 44, 45), *in vivo* analysis is yet to be realized.

MPM-based intravital imaging of the ventricular wall has been performed (15, 16, 99, 100); however, *in vivo* imaging of valves faces challenges due to accessibility, tissue movement, and blood flow (28, 97, 101–104). Limitations of tissue accessibility are being addressed by enhancing flexibility and miniaturization of microendoscopy tools, which will help facilitate preclinical and clinical translation of MPM (28, 101–103, 105). Work is also focused on developing strategies to overcome motion-based artifacts introduced by heartbeat or physiological geometry changes (104). Additionally, researchers have developed algorithms to account for the NIR signal attenuation by blood (97). Indeed, there remain several

TABLE 1 | Summary of label-free MPM techniques and metrics associated with CAVD progression.

CAVD stage	CAVD event	MPM techniques and metabolic metrics	
		Aortic valve disease	**Non-valve disease models**
Initiation (Inflammation)	Endothelial damage	–	*Blood vessels*: Overlay of TPEF (Ex: 810 nm, Em: 428–695 nm) and SHG (Ex: 810 nm, Em: 395–415 nm) (51), CARS (119)
	Macrophages	–	TPEF (presumably FAD and Lipofuscin, Em: 500–550 nm) (50), *Lipid-laden Macrophages*—CARS (52)
	Lipid deposition	–	*Macrophages*—CARS (52), *Adipogenic MSCs*—TPEF (ORR; Lack of endogenous autofluorescence with autofluorescent cells) (20) *Blood vessels*—CARS (51)
	Oxidative stress	–	FLIM (Ex: <760 nm, Em: 440–470 nm) (Long lifetime species in oxidized lipids) and CARS (24, 120)
Progression (VIC dedifferentiation, Fibrosis, Calcification)	Apoptosis	–	*Neurons and astrocytes*—TPEF (ORR increased) (11), FLIM (Ex: <760 nm, Em: 440–470 nm; Increase or decrease of NAD(P)H lifetime dependent on cell type) (11, 27, 63)
	Extracellular vesicles	–	*EVs from macrophages and breast cancer cell lines*—FLIM (Ex: <760 nm, Em: 440–470 nm) (62)
	Hypoxia	–	TPEF (ORR decreased) and FLIM (Ex: <760 nm, Em: 440–470 nm; free/bound NAD(P)H increased) (11, 120)
	Proliferation	TPEF (ORR decreased) (21, 42–44)	TPEF (ORR decreased) and FLIM (Ex: <760 nm, Em: 440–470 nm; NAD(P)H lifetime decreased) (11, 14)
	VIC dedifferentiation	TPEF (ORR decreased early, FD increased later time points) (43, 44)	N/A
	Extracellular matrix remodeling	*Collagen*—SHG (Ex: 890 nm, Em: 425–465 nm), *Elastin*—TPEF (Ex: 760 nm, Em: 420–460 nm), (17, 30, 45, 66)	TPEF and SHG (25, 34, 52, 105, 119)
	Calcification	*Mineralization*—TPEF (Ex: 800 nm, Em: 460 and 525 nm), and CARS (39)	–

challenges before MPM-based techniques can be applied to the valve leaflets *in vivo*.

Recent advances in FLIM and CARS-based imaging of lipid bilayers, oxidized lipids, extracellular vesicles, and oxidative stress (24, 37, 62) have opened new avenues for exploring label-free signatures in CAVD. Lipid infiltration, oxidation, and biosynthesis are associated with CAVD initiation and progression (106, 107), in addition to being key regulators of metabolism (11, 20). Furthermore, hypoxia-mediated collagen remodeling and cell metabolism in CAVD (11, 108–110), can also potentially be assessed by MPM imaging (17, 30, 45, 66). MPM may also prove useful in further assessing the correlation between metabolism and mineralization by imaging cellular metabolism of VICs, EVs, and mineralization of apoptotic bodies (60, 61, 111). Understanding metabolic changes and their mechanisms during heart valve pathophysiology, may therefore open new avenues for therapeutic interventions as well, as it has in other cardiovascular disorders such as heart failure, hypertrophy, and arterial inflammation (71, 73, 76, 77).

CONCLUSION

MPM offers distinct advantages such as label-free detection, quantitative measurements, reduced phototoxicity, and increased depth penetration (10–13) relative to confocal microscopy. While multiple different techniques and biochemical assays have been utilized to assess CAVD progression, most techniques require the use of exogenous labels and dyes, cellular fixation, and lysis which restrict the longitudinal monitoring of live cells and tissues, unlike MPM based imaging (58, 112, 113). MPM offers a label-free non-destructive alternative that will allow conservation of the sample, time, and resources yet providing quantitative data along with spatial mapping of these biomarkers (10, 11, 13, 25, 34). MPM-based metrics have been widely employed in cancer research (18, 114–116), stem cell research (19, 20, 64, 93), wound healing studies (14, 29, 114, 117), other cardiovascular disorders (35, 97, 118, 119) (**Table 1**) and have been explored for clinical translation as well (29, 115, 121, 122). While MPM-based optical signatures and quantitative metrics may hold potential in streamlining *in vitro* and *ex vivo* CAVD detection and monitoring (**Table 1**), much work is required in elucidating distinct optical signatures that correlate with individual disease markers. Additionally, understanding the biological relevance of these biomarkers and their associated regulators is equally important in furthering the therapeutics and diagnostics of CAVD, a disease with no drug-based therapies, or early diagnostic tests (4–7). Advancements in probe design for accessibility and challenges associated with imaging moving objects with multiple confounding autofluorescent and absorbing sources must be overcome for the successful adoption of MPM techniques and metrics for clinical imaging of aortic valves (28, 97, 101–105).

AUTHOR CONTRIBUTIONS

IT and KB conceptualized the manuscript. IT, KPQ, and KB co-wrote the manuscript. All authors approved the submitted version of the article.

FUNDING

This work was supported by the National Science Foundation [CMMI-1452943 to KB; CBET-1846853 to KPQ] and the American Heart Association [19PRE34370061 to IT].

REFERENCES

1. Kodali SK, Velagapudi P, Hahn RT, Abbott D, Leon MB. Valvular heart disease in patients ≥80 years of age. *J Am Coll Cardiol.* (2018) 71:2058–72. doi: 10.1016/j.jacc.2018.03.459
2. Yutzey KE, Demer LL, Body SC, Huggins GS, Towler DA, Giachelli CM, et al. Calcific aortic valve disease. *Arteriosc Thromb Vasc Biol.* (2014) 34:2387–93. doi: 10.1161/ATVBAHA.114.302523
3. Mordi I, Tzemos N. Bicuspid aortic valve disease: a comprehensive review. *Cardiol Res Pract.* (2012) 2012:196037. doi: 10.1155/2012/196037
4. Freeman RV, Otto CM. Spectrum of calcific aortic valve disease: pathogenesis, disease progression, and treatment strategies. *Circulation.* (2005) 111:3316–26. doi: 10.1161/CIRCULATIONAHA.104.486738
5. Roger VL, Go AS, Lloyd-Jones DM, Benjamin EJ, Berry JD, Borden WB, et al. Heart disease and stroke statistics—2012 update: a report from the American Heart Association. *Circulation.* (2012) 125:e2–e220. doi: 10.1161/CIR.0b013e31823ac046
6. Lerman DA, Prasad S, Alotti N. Calcific aortic valve disease: molecular mechanisms and therapeutic approaches. *Eur Cardiol.* (2015) 10:108–12. doi: 10.15420/ecr.2015.10.2.108
7. Maganti K, Rigolin VH, Sarano ME, Bonow RO. Valvular heart disease: diagnosis and management. *Mayo Clinic Proc.* (2010) 85:483–500. doi: 10.4065/mcp.2009.0706
8. Izquierdo-Gómez MM, Hernández-Betancor I, García-Niebla J, Marí-López B, Laynez-Cerdeña I, Lacalzada-Almeida J. Valve calcification in aortic stenosis: etiology and diagnostic imaging techniques. *Biomed Res Int.* (2017) 2017:5178631. doi: 10.1155/2017/5178631
9. Everett RJ, Newby DE, Jabbour A, Fayad ZA, Dweck MR. The role of imaging in aortic valve disease. *Curr Cardiovasc Imaging Rep.* (2016) 9:21. doi: 10.1007/s12410-016-9383-z
10. Larson AM. Multiphoton microscopy. *Nat Photonics.* (2011) 5:1. doi: 10.1038/nphoton.an.2010.2
11. Kolenc OI, Quinn KP. Evaluating cell metabolism through autofluorescence imaging of NAD(P)H and FAD. *Antioxid Redox Signal.* (2017) 30:875–89. doi: 10.1089/ars.2017.7451
12. Bartolome F, Abramov AY. Measurement of mitochondrial NADH and FAD autofluorescence in live cells. *Methods Mol Biol.* (2015) 1264:263–70. doi: 10.1007/978-1-4939-2257-4_23
13. Zipfel WR, Williams RM, Webb WW. Nonlinear magic: multiphoton microscopy in the biosciences. *Nat Biotechnol.* (2003) 21:1369–77. doi: 10.1038/nbt899
14. Jones JD, Ramser HE, Woessner AE, Quinn KP. *In vivo* multiphoton microscopy detects longitudinal metabolic changes associated with delayed skin wound healing. *Commun Biol.* (2018) 1:198. doi: 10.1038/s42003-018-0206-4
15. Jones JS, Small DM, Nishimura N. *In vivo* calcium imaging of cardiomyocytes in the beating mouse heart with multiphoton microscopy. *Front Physiol.* (2018) 9:969. doi: 10.3389/fphys.2018.00969
16. Li W, Nava RG, Bribriesco AC, Zinselmeyer BH, Spahn JH, Gelman AE, et al. Intravital 2-photon imaging of leukocyte trafficking in beating heart. *J Clin Invest.* (2012) 122:2499–508. doi: 10.1172/JCI62970
17. Schenke-Layland K. Non-invasive multiphoton imaging of extracellular matrix structures. *J Biophotonics.* (2008) 1:451–62. doi: 10.1002/jbio.200810045
18. Skala MC, Riching KM, Gendron-Fitzpatrick A, Eickhoff J, Eliceiri KW, White JG, et al. *In vivo* multiphoton microscopy of NADH and FAD redox states, fluorescence lifetimes, and cellular morphology in precancerous epithelia. *Proc Natl Acad Sci U S A.* (2007) 104:19494–9. doi: 10.1073/pnas.0708425104
19. Meleshina AV, Dudenkova VV, Bystrova AS, Kuznetsova DS, Shirmanova MV, Zagaynova EV. Two-photon FLIM of NAD(P)H and FAD in mesenchymal stem cells undergoing either osteogenic or chondrogenic differentiation. *Stem Cell Res Ther.* (2017) 8:15. doi: 10.1186/s13287-017-0484-7
20. Quinn KP, Sridharan GV, Hayden RS, Kaplan DL, Lee K, Georgakoudi I. Quantitative metabolic imaging using endogenous fluorescence to detect stem cell differentiation. *Sci Rep.* (2013) 3:3432. doi: 10.1038/srep03432
21. Lam NT, Muldoon TJ, Quinn KP, Rajaram N, Balachandran K. Valve interstitial cell contractile strength and metabolic state are dependent on its shape. *Integr Biol (Camb).* (2016) 8:1079–89. doi: 10.1039/C6IB00120C
22. Vargas I, Alhallak K, Kolenc OI, Jenkins SV, Griffin RJ, Dings RPM, et al. Rapid quantification of mitochondrial fractal dimension in individual cells. *Biomed Opt Express.* (2018) 9:5269–79. doi: 10.1364/BOE.9.005269
23. Xylas J, Varone A, Quinn KP, Pouli D, McLaughlin-Drubin ME, Thieu HT, et al. Noninvasive assessment of mitochondrial organization in three-dimensional tissues reveals changes associated with cancer development. *Int J Cancer.* (2015) 136:322–32. doi: 10.1002/ijc.28992
24. Datta R, Alfonso-García A, Cinco R, Gratton E. Fluorescence lifetime imaging of endogenous biomarker of oxidative stress. *Sci Rep.* (2015) 5:9848. doi: 10.1038/srep09848
25. Mazumder N, Balla NK, Zhuo G-Y, Kistenev YV, Kumar R, Kao F-J, et al. Label-free non-linear multimodal optical microscopy-basics, development, and applications. *Front Phys.* (2019) 7:170. doi: 10.3389/fphy.2019.00170
26. Ranawat H, Pal S, Mazumder N. Recent trends in two-photon autofluorescence lifetime imaging (2P-FLIM) and its biomedical applications. *Biomed Eng Lett.* (2019) 9:293–310. doi: 10.1007/s13534-019-00119-7
27. Bower AJ, Marjanovic M, Zhao Y, Li J, Chaney EJ, Boppart SA. Label-free *in vivo* cellular-level detection and imaging of apoptosis. *J Biophotonics.* (2017) 10:143–50. doi: 10.1002/jbio.201600003
28. Garofalakis A, Kruglik SG, Mansuryan T, Gillibert A, Thiberville L, Louradour F, et al. Characterization of a multicore fiber image guide for nonlinear endoscopic imaging using two-photon fluorescence and second-harmonic generation. *J Biomed Opt.* (2019) 24:1–12. doi: 10.1117/1.JBO.24.10.106004
29. König K, Breunig HG, Batista A, Schindele A, Zieger M, Kaatz M. Translation of two-photon microscopy to the clinic: multimodal multiphoton CARS tomography of *in vivo* human skin. *J Biomed Opt.* (2020) 25:1–12. doi: 10.1117/1.JBO.25.1.014515
30. Schenke-Layland K, Stock UA, Nsair A, Xie J, Angelis E, Fonseca CG, et al. Cardiomyopathy is associated with structural remodelling of heart valve extracellular matrix. *Eur Heart J.* (2009) 30:2254–65. doi: 10.1093/eurheartj/ehp267
31. Quinn KP, Sullivan KE, Liu Z, Ballard Z, Siokatas C, Georgakoudi I, et al. Optical metrics of the extracellular matrix predict compositional and mechanical changes after myocardial infarction. *Sci Rep.* (2016) 6:35823. doi: 10.1038/srep35823
32. Quinn KP, Georgakoudi I. Rapid quantification of pixel-wise fiber orientation data in micrographs. *J Biomed Opt.* (2013) 18:046003. doi: 10.1117/1.JBO.18.4.046003
33. Liu Z, Pouli D, Sood D, Sundarakrishnan A, Hui Mingalone CK, Arendt LM, et al. Automated quantification of three-dimensional organization of fiber-like structures in biological tissues. *Biomaterials.* (2016) 116:34–47. doi: 10.1016/j.biomaterials.2016.11.041
34. Zipfel WR, Williams RM, Christie R, Nikitin AY, Hyman BT, Webb WW. Live tissue intrinsic emission microscopy using multiphoton-excited native fluorescence and second harmonic generation. *Proc Natl Acad Sci U S A.* (2003) 100:7075–80. doi: 10.1073/pnas.0832308100

35. Megens R, Reitsma S, Schiffers P, Hilgers R, De Mey J, Slaaf D, et al. Two-photon microscopy of vital murine elastic and muscular arteries. *J Vasc Res.* (2006) 44:87–98. doi: 10.1159/000098259
36. Breunig HG, Bückle R, Kellner-Höfer M, Weinigel M, Lademann J, Sterry W, et al. Combined *in vivo* multiphoton and CARS imaging of healthy and disease-affected human skin. *Microsc Res Tech.* (2012) 75:492–8. doi: 10.1002/jemt.21082
37. Bradley J, Pope I, Wang Y, Langbein W, Borri P, Swann K. Dynamic label-free imaging of lipid droplets and their link to fatty acid and pyruvate oxidation in mouse eggs. *J Cell Sci.* (2019) 132:jcs228999. doi: 10.1242/jcs.228999
38. Tamosaityte S, Galli R, Uckermann O, Sitoci-Ficici KH, Koch M, Later R, et al. Inflammation-related alterations of lipids after spinal cord injury revealed by Raman spectroscopy. *J Biomed Opt.* (2016) 21:61008. doi: 10.1117/1.JBO.21.6.061008
39. Baugh LM, Liu Z, Quinn KP, Osseiran S, Evans CL, Huggins GS, et al. Non-destructive two-photon excited fluorescence imaging identifies early nodules in calcific aortic-valve disease. *Nat Biomedl Eng.* (2017) 1:914–24. doi: 10.1038/s41551-017-0152-3
40. Croce AC, Bottiroli G. Autofluorescence spectroscopy and imaging: a tool for biomedical research and diagnosis. *Eur J Histochem.* (2014) 58:2461. doi: 10.4081/ejh.2014.2461
41. Büttner P, Galli R, Jannasch A, Schnabel C, Waldow T, Koch E. Heart valve stenosis in laser spotlights: insights into a complex disease. *Clin Hemorheol Microcirc.* (2014) 58:65–75. doi: 10.3233/CH-141882
42. Lam NT, Tandon I, Balachandran K. The role of fibroblast growth factor 1 and 2 on the pathological behavior of valve interstitial cells in a three-dimensional mechanically-conditioned model. *J Biol Eng.* (2019) 13:45. doi: 10.1186/s13036-019-0168-1
43. Tandon I, Kolenc OI, Cross D, Vargas I, Johns S, Quinn KP, et al. Label-free metabolic biomarkers for assessing valve interstitial cell calcific progression. *Sci Rep.* (2020) 10:10317. doi: 10.1038/s41598-020-66960-4
44. Tandon I, Johns S, Woessner A, Perez J, Cross D, Ozkizilcik A, et al. Label-free optical biomarkers detect early calcific aortic valve disease in a wild-type mouse model. *BMC Cardiovasc Disord.* (2020) 20:521. doi: 10.1186/s12872-020-01776-8
45. Hutson HN, Marohl T, Anderson M, Eliceiri K, Campagnola P, Masters KS. Calcific aortic valve disease is associated with layer-specific alterations in collagen architecture. *PLoS One.* (2016) 11:e0163858. doi: 10.1371/journal.pone.0163858
46. Chester AH. Molecular and cellular mechanisms of valve calcification. *Aswan Heart Centre Sci Pract Ser.* (2011) 2011:4. doi: 10.5339/ahcsps.2011.4
47. Beckmann E, Grau JB, Sainger R, Poggio P, Ferrari G. Insights into the use of biomarkers in calcific aortic valve disease. *J Heart Valve Dis.* (2010) 19:441–52.
48. Leopold JA. Cellular mechanisms of aortic valve calcification. *Circulation Cardiovascular interventions.* (2012) 5:605–14. doi: 10.1161/CIRCINTERVENTIONS.112.971028
49. Galli R, Sitoci-Ficici KH, Uckermann O, Later R, Marečková M, Koch M, et al. Label-free multiphoton microscopy reveals relevant tissue changes induced by alginate hydrogel implantation in rat spinal cord injury. *Sci Rep.* (2018) 8:10841. doi: 10.1038/s41598-018-29140-z
50. Uckermann O, Galli R, Beiermeister R, Sitoci-Ficici KH, Later R, Leipnitz E, et al. Endogenous two-photon excited fluorescence provides label-free visualization of the inflammatory response in the rodent spinal cord. *Biomed Res Int.* (2015) 2015:859084. doi: 10.1155/2015/859084
51. Xi G, Cao N, Guo W, Kang D, Chen Z, He J, et al. Label-free imaging of blood vessels in human normal breast and breast tumor tissue using multiphoton microscopy. *Scanning.* (2019) 2019:5192875. doi: 10.1155/2019/5192875
52. Lim RS, Kratzer A, Barry NP, Miyazaki-Anzai S, Miyazaki M, Mantulin WW, et al. Multimodal CARS microscopy determination of the impact of diet on macrophage infiltration and lipid accumulation on plaque formation in ApoE-deficient mice. *J Lipid Res.* (2010) 51:1729–37. doi: 10.1194/jlr.M003616
53. Mittal M, Siddiqui MR, Tran K, Reddy SP, Malik AB. Reactive oxygen species in inflammation and tissue injury. *Antioxid Redox Signal.* (2014) 20:1126–67. doi: 10.1089/ars.2012.5149
54. Schieber M, Chandel NS. ROS function in redox signaling and oxidative stress. *Curr Biol.* (2014) 24:R453–R62. doi: 10.1016/j.cub.2014.03.034
55. Koundouros N, Poulogiannis G. Phosphoinositide 3-kinase/Akt signaling and redox metabolism in cancer. *Front Oncol.* (2018) 8:160. doi: 10.3389/fonc.2018.00160
56. Alushi B, Curini L, Christopher MR, Grubitzch H, Landmesser U, Amedei A, et al. Calcific aortic valve disease-natural history and future therapeutic strategies. *Front Pharmacol.* (2020) 11:685. doi: 10.3389/fphar.2020.00685
57. Towler DA. Molecular and cellular aspects of calcific aortic valve disease. *Circ Res.* (2013) 113:198–208. doi: 10.1161/CIRCRESAHA.113.300155
58. Miller JD, Weiss RM, Heistad DD. Calcific aortic valve stenosis: methods, models, and mechanisms. *Circ Res.* (2011) 108:1392–412. doi: 10.1161/CIRCRESAHA.110.234138
59. Orndorff RL, Hong N, Yu K, Feinstein SI, Zern BJ, Fisher AB, et al. NOX2 in lung inflammation: quantum dot based *in situ* imaging of NOX2-mediated expression of vascular cell adhesion molecule-1. *Am J Physiol Lung Cell Mol Physiol.* (2014) 306:L260–L8. doi: 10.1152/ajplung.00278.2013
60. Pedriali G, Morciano G, Patergnani S, Cimaglia P, Morelli C, Mikus E, et al. Aortic valve stenosis and mitochondrial dysfunctions: clinical and molecular perspectives. *Int J Mol Sci.* (2020) 21:4899. doi: 10.3390/ijms21144899
61. Bouchareb R, Boulanger MC, Fournier D, Pibarot P, Messaddeq Y, Mathieu P. Mechanical strain induces the production of spheroid mineralized microparticles in the aortic valve through a RhoA/ROCK-dependent mechanism. *J Mol Cell Cardiol.* (2014) 67:49–59. doi: 10.1016/j.yjmcc.2013.12.009
62. Sorrells JE, Martin EM, Aksamitiene E, Mukherjee P, Alex A, Chaney EJ, et al. Label-free characterization of single extracellular vesicles using two-photon fluorescence lifetime imaging microscopy of NAD(P)H. *Sci Rep.* (2021) 11:3308. doi: 10.1038/s41598-020-80813-0
63. Yu J-S, Guo H-W, Wang H-W, Wang C-H, Wei Y-H. Increase of reduced nicotinamide adenine dinucleotide fluorescence lifetime precedes mitochondrial dysfunction in staurosporine-induced apoptosis of HeLa cells. *J Biomed Opt.* (2011) 16:036008. doi: 10.1117/1.3560513
64. Rice WL, Kaplan DL, Georgakoudi I. Two-photon microscopy for non-invasive, quantitative monitoring of stem cell differentiation. *PLoS One.* (2010) 5:e10075. doi: 10.1371/journal.pone.0010075
65. Bogdanova M, Zabirnyk A, Malashicheva A, Enayati KZ, Karlsen TA, Kaljusto M-L, et al. Interstitial cells in calcified aortic valves have reduced differentiation potential and stem cell-like properties. *Sci Rep.* (2019) 9:12934. doi: 10.1038/s41598-019-49016-0
66. Jannasch A, Schnabel C, Galli R, Faak S, Büttner P, Dittfeld C, et al. Optical coherence tomography and multiphoton microscopy offer new options for the quantification of fibrotic aortic valve disease in ApoE$^{-/-}$ mice. *Sci Rep.* (2021) 11:5834. doi: 10.1038/s41598-021-85142-4
67. Kamel PI, Qu X, Geiszler AM, Nagrath D, Harmancey R, Taegtmeyer H, et al. Metabolic regulation of collagen gel contraction by porcine aortic valvular interstitial cells. *J R Soc Interface.* (2014) 11:20140852. doi: 10.1098/rsif.2014.0852
68. Ong S-B, Hausenloy DJ. Mitochondrial morphology and cardiovascular disease. *Cardiovasc Res.* (2010) 88:16–29. doi: 10.1093/cvr/cvq237
69. Barlow CH, Harden WR, 3rd, Harken AH, Simson MB, Haselgrove JC, Chance B, et al. Fluorescence mapping of mitochondrial redox changes in heart and brain. *Crit Care Med.* (1979) 7:402–6. doi: 10.1097/00003246-197909000-00011
70. Mayevsky A, Rogatsky GG. Mitochondrial function *in vivo* evaluated by NADH fluorescence: from animal models to human studies. *Am J Physiol Cell Physiol.* (2007) 292:C615–40. doi: 10.1152/ajpcell.00249.2006
71. Doenst T, Nguyen TD, Abel ED. Cardiac metabolism in heart failure: implications beyond ATP production. *Circ Res.* (2013) 113:709–24. doi: 10.1161/CIRCRESAHA.113.300376
72. Huang P, Yu T, Yoon Y. Mitochondrial clustering induced by overexpression of the mitochondrial fusion protein Mfn2 causes mitochondrial dysfunction and cell death. *Eur J Cell Biol.* (2007) 86:289–302. doi: 10.1016/j.ejcb.2007.04.002
73. Kolwicz SC, Purohit S, Tian R. Cardiac metabolism and its interactions with contraction, growth, and survival of cardiomyocytes. *Circ Res.* (2013) 113:603–16. doi: 10.1161/CIRCRESAHA.113.302095
74. Rogers MA, Maldonado N, Hutcheson JD, Goettsch C, Goto S, Yamada I, et al. Dynamin-related protein 1 inhibition attenuates cardiovascular

calcification in the presence of oxidative stress. *Circ Res.* (2017) 121:220–33. doi: 10.1161/CIRCRESAHA.116.310293
75. Westermann B. Bioenergetic role of mitochondrial fusion and fission. *Biochim Biophys Acta.* (2012) 1817:1833–8. doi: 10.1016/j.bbabio.2012.02.033
76. van der Velden J, Tocchetti CG, Varricchi G, Bianco A, Sequeira V, Hilfiker-Kleiner D, et al. Metabolic changes in hypertrophic cardiomyopathies: scientific update from the Working Group of Myocardial Function of the European Society of Cardiology. *Cardiovasc Res.* (2018) 114:1273–80. doi: 10.1093/cvr/cvy147
77. Gibb AA, Hill BG. Metabolic coordination of physiological and pathological cardiac remodeling. *Circ Res.* (2018) 123:107–28. doi: 10.1161/CIRCRESAHA.118.312017
78. Rashdan NA, Sim AM, Cui L, Phadwal K, Roberts FL, Carter R, et al. Osteocalcin regulates arterial calcification via altered wnt signaling and glucose metabolism. *J Bone Miner Res.* (2020) 35:357–67. doi: 10.1002/jbmr.3888
79. Demer LL, Tintut Y. Inflammatory, metabolic, and genetic mechanisms of vascular calcification. *Arteriosc Thromb Vasc Biol.* (2014) 34:715–23. doi: 10.1161/ATVBAHA.113.302070
80. Leem J, Lee IK. Mechanisms of vascular calcification: the pivotal role of pyruvate dehydrogenase kinase 4. *Endocrinol Metab (Seoul).* (2016) 31:52–61. doi: 10.3803/EnM.2016.31.1.52
81. Crewe C, Schafer C, Lee I, Kinter M, Szweda LI. Regulation of pyruvate dehydrogenase kinase 4 in the heart through degradation by the lon protease in response to mitochondrial substrate availability. *J Biol Chem.* (2017) 292:305–12. doi: 10.1074/jbc.M116.754127
82. Chen J, Lin Y, Sun Z. Deficiency in the anti-aging gene Klotho promotes aortic valve fibrosis through AMPKα-mediated activation of RUNX2. *Aging Cell.* (2016) 15:853–60. doi: 10.1111/acel.12494
83. Bossé Y, Miqdad A, Fournier D, Pépin A, Pibarot P, Mathieu P. Refining molecular pathways leading to calcific aortic valve stenosis by studying gene expression profile of normal and calcified stenotic human aortic valves. *Circ Cardiovasc Genet.* (2009) 2:489–98. doi: 10.1161/CIRCGENETICS.108.820795
84. Rajamannan NM, Subramaniam M, Rickard D, Stock SR, Donovan J, Springett M, et al. Human aortic valve calcification is associated with an osteoblast phenotype. *Circulation.* (2003) 107:2181–4. doi: 10.1161/01.CIR.0000070591.21548.69
85. Heather LC, Howell NJ, Emmanuel Y, Cole MA, Frenneaux MP, Pagano D, et al. Changes in cardiac substrate transporters and metabolic proteins mirror the metabolic shift in patients with aortic stenosis. *PLoS One.* (2011) 6:e26326. doi: 10.1371/journal.pone.0026326
86. Martin-Rojas T, Mourino-Alvarez L, Alonso-Orgaz S, Rosello-Lleti E, Calvo E, Lopez-Almodovar LF, et al. iTRAQ proteomic analysis of extracellular matrix remodeling in aortic valve disease. *Sci Rep.* (2015) 5:17290. doi: 10.1038/srep17290
87. Mourino-Alvarez L, Baldan-Martin M, Sastre-Oliva T, Martin-Lorenzo M, Maroto AS, Corbacho-Alonso N, et al. A comprehensive study of calcific aortic stenosis: from rabbit to human samples. *Dis Model Mech.* (2018) 11:dmm033423. doi: 10.1242/dmm.033423
88. Gil-Dones F, Martín-Rojas T, López-Almodovar LF, Juárez-Tosina R, de la Cuesta F, Álvarez-Llamas G, et al. Development of an optimal protocol for the proteomic analysis of stenotic and healthy aortic valves. *Rev Esp Cardiol.* (2010) 63:46–53. doi: 10.1016/S1885-5857(10)70008-6
89. Oda T, Matsumoto K-i. Proteomic analysis in cardiovascular research. *Surg Today.* (2016) 46:285–96. doi: 10.1007/s00595-015-1169-4
90. Weisell J, Ohukainen P, Näpänkangas J, Ohlmeier S, Bergmann U, Peltonen T, et al. Heat shock protein 90 is downregulated in calcific aortic valve disease. *BMC Cardiovasc Disord.* (2019) 19:306. doi: 10.1186/s12872-019-01294-2
91. Greene CL, Jaatinen KJ, Wang H, Koyano TK, Bilbao MS, Woo YJ. Transcriptional profiling of normal, stenotic, and regurgitant human aortic valves. *Genes (Basel).* (2020) 11:789. doi: 10.3390/genes11070789
92. Schlotter F, Halu A, Goto S, Blaser MC, Body SC, Lee LH, et al. Spatiotemporal multi-omics mapping generates a molecular atlas of the aortic valve and reveals networks driving disease. *Circulation.* (2018) 138:377–93. doi: 10.1161/CIRCULATIONAHA.117.032291
93. Yu JSL, Cui W. Proliferation, survival and metabolism: the role of PI3K/AKT/mTOR signalling in pluripotency and cell fate determination. *Development.* (2016) 143:3050–60. doi: 10.1242/dev.137075
94. Khan K, Yu B, Kiwan C, Shalal Y, Filimon S, Cipro M, et al. The role of Wnt/β-catenin pathway mediators in aortic valve stenosis. *Front Cell Dev Biol.* (2020) 8:862. doi: 10.3389/fcell.2020.00862
95. MacGrogan D, Martínez-Poveda B, Desvignes J-P, Fernandez-Friera L, Gomez MJ, Vilariño EG, et al. Identification of a peripheral blood gene signature predicting aortic valve calcification. *Physiol Genomics.* (2020) 52:563–74. doi: 10.1152/physiolgenomics.00034.2020
96. Hjortnaes J, Butcher J, Figueiredo J-L, Riccio M, Kohler RH, Kozloff KM, et al. Arterial and aortic valve calcification inversely correlates with osteoporotic bone remodelling: a role for inflammation. *Eur Heart J.* (2010) 31:1975–84. doi: 10.1093/eurheartj/ehq237
97. Sheth RA, Tam JM, Maricevich MA, Josephson L, Mahmood U. Quantitative endovascular fluorescence-based molecular imaging through blood of arterial wall inflammation. *Radiology.* (2009) 251:813–21. doi: 10.1148/radiol.2513081450
98. Masters BR. *Confocal Microscopy and Multiphoton Excitation Microscopy the Genesis of live Cell Imaging, Vol. PM161*. Society of Photo-optical Instrumentation Engineers (2006). 230 p. Available online at: http://ezaccess.libraries.psu.edu/login?url=http://dx.doi.org/10.1117/3.660403
99. Matsuura R, Miyagawa S, Fukushima S, Goto T, Harada A, Shimozaki Y, et al. Intravital imaging with two-photon microscopy reveals cellular dynamics in the ischeamia-reperfused rat heart. *Sci Rep.* (2018) 8:15991. doi: 10.1038/s41598-018-34295-w
100. Allan-Rahill NH, Lamont MRE, Chilian WM, Nishimura N, Small DM. Intravital microscopy of the beating murine heart to understand cardiac leukocyte dynamics. *Front Immunol.* (2020) 11:92. doi: 10.3389/fimmu.2020.00092
101. Ducourthial G, Leclerc P, Mansuryan T, Fabert M, Brevier J, Habert R, et al. Development of a real-time flexible multiphoton microendoscope for label-free imaging in a live animal. *Sci Rep.* (2015) 5:18303. doi: 10.1038/srep18303
102. Zhao Y, Sheng M, Huang L, Tang S. Design of a fiber-optic multiphoton microscopy handheld probe. *Biomed Opt Express.* (2016) 7:3425–37. doi: 10.1364/BOE.7.003425
103. König K, Weinigel M, Hoppert D, Bückle R, Schubert H, Köhler MJ, et al. Multiphoton tissue imaging using high-NA microendoscopes and flexible scan heads for clinical studies and small animal research. *J Biophotonics.* (2008) 1:506–13. doi: 10.1002/jbio.200810049
104. Soulet D, Lamontagne-Proulx J, Aubé B, Davalos D. Multiphoton intravital microscopy in small animals: motion artefact challenges and technical solutions. *J Microsc.* (2020) 278:3–17. doi: 10.1111/jmi.12880
105. Huang L, Zhou X, Liu Q, MacAulay CE, Tang S. Miniaturized multimodal multiphoton microscope for simultaneous two-photon and three-photon imaging with a dual-wavelength Er-doped fiber laser. *Biomed Opt Express.* (2020) 11:624–35. doi: 10.1364/BOE.381473
106. Chen HY, Cairns BJ, Small AM, Burr HA, Ambikkumar A, Martinsson A, et al. Association of FADS1/2 locus variants and polyunsaturated fatty acids with aortic stenosis. *JAMA Cardiol.* (2020) 5:694–702. doi: 10.1001/jamacardio.2020.0246
107. Peeters FECM, Meex SJR, Dweck MR, Aikawa E, Crijns HJGM, Schurgers LJ, et al. Calcific aortic valve stenosis: hard disease in the heart: a biomolecular approach towards diagnosis and treatment. *Eur Heart J.* (2017) 39:2618–24. doi: 10.1093/eurheartj/ehx653
108. Folco EJ, Sheikine Y, Rocha VZ, Christen T, Shvartz E, Sukhova GK, et al. Hypoxia but not inflammation augments glucose uptake in human macrophages: implications for imaging atherosclerosis with 18fluorine-labeled 2-deoxy-D-glucose positron emission tomography. *J Am Coll Cardiol.* (2011) 58:603–14. doi: 10.1016/j.jacc.2011.03.044
109. Sapp MC, Krishnamurthy VK, Puperi DS, Bhatnagar S, Fatora G, Mutyala N, et al. Differential cell-matrix responses in hypoxia-stimulated aortic versus mitral valves. *J R Soc Interface.* (2016) 13:20160449. doi: 10.1098/rsif.2016.0449
110. Swaminathan G, Krishnamurthy VK, Sridhar S, Robson DC, Ning Y, Grande-Allen KJ. Hypoxia stimulates synthesis of neutrophil gelatinase-associated lipocalin in aortic valve disease. *Front Cardiovasc Med.* (2019) 6:156. doi: 10.3389/fcvm.2019.00156

111. Kutryb-Zajac B, Jablonska P, Serocki M, Bulinska A, Mierzejewska P, Friebe D, et al. Nucleotide ecto-enzyme metabolic pattern and spatial distribution in calcific aortic valve disease; its relation to pathological changes and clinical presentation. *Clin Res Cardiol.* (2020) 109:137–60. doi: 10.1007/s00392-019-01495-x
112. Rutkovskiy A, Malashicheva A, Sullivan G, Bogdanova M, Kostareva A, Stensløkken K-O, et al. Valve interstitial cells: the key to understanding the pathophysiology of heart valve calcification. *J Am Heart Assoc.* (2017) 6:e006339. doi: 10.1161/JAHA.117.006339
113. Small A, Kiss D, Giri J, Anwaruddin S, Siddiqi H, Guerraty M, et al. Biomarkers of calcific aortic valve disease. *Arteriosc Thromb Vasc Biol.* (2017) 37:623–32. doi: 10.1161/ATVBAHA.116.308615
114. Yew E, Rowlands C, So PTC. Application of multiphoton microscopy in dermatological studies: a mini-review. *J Innov Opt Health Sci.* (2014) 7:1330010. doi: 10.1142/S1793545813300103
115. Perry SW, Burke RM, Brown EB. Two-photon and second harmonic microscopy in clinical and translational cancer research. *Ann Biomed Eng.* (2012) 40:277–91. doi: 10.1007/s10439-012-0512-9
116. Alhallak K, Rebello LG, Muldoon TJ, Quinn KP, Rajaram N. Optical redox ratio identifies metastatic potential-dependent changes in breast cancer cell metabolism. *Biomed Opt Express.* (2016) 7:4364–74. doi: 10.1364/BOE.7.004364
117. Jones JD, Ramser HE, Woessner AE, Veves A, Quinn KP. Quantifying age-related changes in skin wound metabolism using *in vivo* multiphoton microscopy. *Adv Wound Care (New Rochelle).* (2020) 9:90–102. doi: 10.1089/wound.2019.1030
118. Scherschel JA, Rubart M. Cardiovascular imaging using two-photon microscopy. *Microsc Microanal.* (2008) 14:492–506. doi: 10.1017/S1431927608080835
119. Wang HW, Le TT, Cheng JX. Label-free imaging of arterial cells and extracellular matrix using a multimodal CARS microscope. *Opt Commun.* (2008) 281:1813–22. doi: 10.1016/j.optcom.2007.07.067
120. Datta R, Heylman C, George SC, Gratton E. Label-free imaging of metabolism and oxidative stress in human induced pluripotent stem cell-derived cardiomyocytes. *Biomed Opt Express.* (2016) 7:1690–701. doi: 10.1364/BOE.7.001690
121. WANG B-G, KÖNIG K, HALBHUBER K-J. Two-photon microscopy of deep intravital tissues and its merits in clinical research. *J Microsc.* (2010) 238:1–20. doi: 10.1111/j.1365-2818.2009.03330.x
122. König K, Ehlers A, Riemann I, Schenkl S, Bückle R, Kaatz M. Clinical two-photon microendoscopy. *Microsc Res Tech.* (2007) 70:398–402. doi: 10.1002/jemt.20445

Conflict of Interest: The authors declare that the research was conducted in the absence of any commercial or financial relationships that could be construed as a potential conflict of interest.

frontiers in Cardiovascular Medicine

REVIEW
published: 22 June 2021
doi: 10.3389/fcvm.2021.682298

NOTCH Signaling in Aortic Valve Development and Calcific Aortic Valve Disease

Yidong Wang[1]*, *Yuan Fang*[1], *Pengfei Lu*[2], *Bingruo Wu*[2] and *Bin Zhou*[3,4]*

[1] The Institute of Cardiovascular Sciences, School of Basic Medical Sciences, Xi'an Jiaotong University Health Science Center, Xi'an, China, [2] Department of Genetics, Albert Einstein College of Medicine, Bronx, NY, United States, [3] Departments of Genetics, Pediatrics (Pediatric Genetic Medicine), and Medicine (Cardiology), The Wilf Family Cardiovascular Research Institute, Albert Einstein College of Medicine, Bronx, NY, United States, [4] The Einstein Institute for Aging Research, Albert Einstein College of Medicine, Bronx, NY, United States

NOTCH intercellular signaling mediates the communications between adjacent cells involved in multiple biological processes essential for tissue morphogenesis and homeostasis. The *NOTCH1* mutations are the first identified human genetic variants that cause congenital bicuspid aortic valve (BAV) and calcific aortic valve disease (CAVD). Genetic variants affecting other genes in the NOTCH signaling pathway may also contribute to the development of BAV and the pathogenesis of CAVD. While CAVD occurs commonly in the elderly population with tri-leaflet aortic valve, patients with BAV have a high risk of developing CAVD at a young age. This observation indicates an important role of NOTCH signaling in the postnatal homeostasis of the aortic valve, in addition to its prenatal functions during aortic valve development. Over the last decade, animal studies, especially with the mouse models, have revealed detailed information in the developmental etiology of congenital aortic valve defects. In this review, we will discuss the molecular and cellular aspects of aortic valve development and examine the embryonic pathogenesis of BAV. We will focus our discussions on the NOTCH signaling during the endocardial-to-mesenchymal transformation (EMT) and the post-EMT remodeling of the aortic valve. We will further examine the involvement of the NOTCH mutations in the postnatal development of CAVD. We will emphasize the deleterious impact of the embryonic valve defects on the homeostatic mechanisms of the adult aortic valve for the purpose of identifying the potential therapeutic targets for disease intervention.

Keywords: NOTCH, aortic valve development, calcific aortic valve disease, EMT, bicuspid aortic valve

OPEN ACCESS

Edited by:
Lakshmi Prasad Dasi, Georgia Institute of Technology, United States

Reviewed by:
Francesco Pollari, Nürnberg Hospital, Germany
Adrien Lupieri, Brigham and Women's Hospital and Harvard Medical School, United States

***Correspondence:**
Yidong Wang
yidwang119@xjtu.edu.cn
Bin Zhou
bin.zhou@einsteinmed.org

Specialty section:
This article was submitted to Heart Valve Disease, a section of the journal Frontiers in Cardiovascular Medicine

Received: *18 March 2021*
Accepted: *14 May 2021*
Published: *22 June 2021*

Citation:
Wang Y, Fang Y, Lu P, Wu B and Zhou B (2021) NOTCH Signaling in Aortic Valve Development and Calcific Aortic Valve Disease. Front. Cardiovasc. Med. 8:682298. doi: 10.3389/fcvm.2021.682298

INTRODUCTION

The aortic valve ensures the unidirectional flow through the heart to deliver the oxygenated blood and nutrients to the body through cyclic pumping (1, 2). Over an average lifetime, the heart valves open and close over a billion times (2). The constant mechanical stress causes wear and tear of the heart valves that may lead to calcific aortic valve disease (CAVD) when the valve homeostatic mechanism is exhausted by repeated damages (3, 4). CAVD is the third leading cause of heart disease, and its incidence increases with age (5–12). Aortic valve replacement remains the only

effective treatment option available for CAVD, as currently no medicine is able to prevent the disease progression (8, 9).

More than half of the patients with severe CAVD who need aortic valve replacement have a bicuspid aortic valve (BAV), a congenital defect affecting ∼2% of the general population (9, 13, 14). These patients develop CAVD decades earlier than those who have a tri-leaflet aortic valve (1). These observations support that BAV-asociated CAVD has a developmental origin, and its postnatal stenotic progression by calcification is triggered by external stimuli as a second hit after the primary structural defect *in utero* (9). In support of this view of the pathogenesis of CAVD, the developmental defect of the aortic valve can cause abnormal flow dynamics and thereby predispose the valve to endothelial dysfunction and inflammatory activation, leading to earlier calcification in adulthood (9, 15–18). Therefore, better understanding of molecular mechanisms regulating aortic valve development, as well as postnatal aortic valve homeostasis, is required for the development of new therapeutic strategies for CAVD.

During embryogenesis, aortic valve leaflets are made up of valve endocardial cells (VECs) and valve interstitial cells (VICs), with VICs arising from VECs, cardiac neural crest cells (NCCs), or the second heart field (SHF) cardiomyocytes (19–25). Aortic valve development consists of multiple morphological and cellular events that are spatiotemporally coordinated by complex molecular signal networks (1). In the past two decades, researchers have made significant advance in understanding these developmental events and underlying molecular signaling mechanisms by using the experimental approaches including human genetics, animal models, and *in vitro* cell systems. Among the important discoveries, the NOTCH signaling is recognized as an essential molecular regulator of aortic valve development, which plays critical roles at multiple phases of valvulogenesis (26–31). Furthermore, the *NOTCH1* mutations are the first genetic variants identified for congenital BAV and acquired CAVD in human (32). Therefore, we will focus our review on the findings of the roles of NOTCH signaling in aortic valve development and embryonic pathogenesis of BAV, as well as their implications in the postnatal valve homeostasis and CAVD.

MORPHOGENESIS OF THE MAMMALIAN HEART VALVE

The mammalian heart has four valves including atrioventricular (AV) valves and semilunar valves. The AV valves consist of mitral and tricuspid valve, which connects the left or right atrium to the left or right ventricle, and control the blood flow from the atria entering the ventricles (1). The semilunar valves include the aortic and pulmonary valve, which direct the blood flow from the left or right ventricle into the systemic or pulmonary circulation through the aorta or pulmonary artery (1). In all the heart valves, the mature valve leaflets are made up of the surface VECs and the core VICs, which are embedded in the well-organized extracellular matrix (ECM) (4, 8).

During mouse embryogenesis and at embryonic day 7.5 (E7.5), a subset of mesodermal cells located at the anterior part of the primitive streak migrates to the splanchnic mesoderm and forms the cardiac crescent consisting of the first heart field (FHF) and SHF (23–25, 33, 34). At E8.5, the FHF-derived progenitors fuse at the midline of the embryo and become the primitive heart tube, which comprises an outer layer myocardium, an inner layer endocardium, and a sandwiched ECM-rich space, named cardiac jelly (35, 36). The primitive heart tube elongates by adding cells from the SHF to its both ends while simultaneously undergoing rightward looping to form an S-shape primitive heart consisting of the common atrium, AV canal (AVC), common ventricle, and outflow tract (OFT) (37–40). Around E9.5, heart valve development starts with the formation of endocardial cushions within the AVC and OFT regions through endocardial-to-mesenchymal transformation (EMT) (25, 41–43) (**Figure 1**). EMT is regulated by molecular signals from both myocardium and endocardium. In response to the bone morphogenic protein (BMP)/transforming growth factor β (TGF-β) signals from the myocardium, a subset of VECs begins to lose their surface markers of endothelial cells and gain the characteristics of mesenchymal cells (44–47). The transformed VECs then migrate into the cardiac jelly and proliferate to form the VICs of endocardial cushions (47). The cellularized endocardial cushions function as valve primordia, which are subjected to complex remodeling through spatiotemporally regulated proliferation and apoptosis of VICs, as well as tightly controlled synthesis and organization of ECM (41, 42). The remodeling process continues until birth when the cellularized endocardial cushions eventually become the mature heart valves with thin leaflets.

Lineage tracing studies show that the majority of VICs in AV valves are from the endocardial precursor cells through EMT (20). In contrast, VICs in the semilunar valves are from three distinct populations including VECs, NCCs, and the SHF-derived cardiomyocytes (20). Regarding the aortic valve, genetic lineage tracing of NCCs and VECs using *Wnt1*^{Cre} and *Tie2*^{Cre}, respectively, shows that VECs make the major contribution to the primordia of two coronary leaflets of the aortic valve, whereas NCCs have a minor contribution (20). In contrast, the SHF progenitors, known to contribute to the OFT myocardium and which are essential for the OFT development, have been recently shown to be the major cellular origin of the intercalated cushion mesenchyme, which gives rise to the non-coronary leaflet of the aortic valve (19, 21, 22, 48–51). Functional studies in animal models further confirm the lineage tracing results and link the signal dysregulations in these three progenitors to various congenital aortic valve defects, that is, different BAV subtypes (21, 22, 49, 50, 52).

MOLECULAR SIGNALS UNDERLYING EARLY HEART VALVE MORPHOGENESIS

The rightward looping of the primitive heart tube leads to the formation of morphologically distinct atria, AVC, ventricles, and the OFT (36). In addition, the myocardium of these regions is already molecularly and functionally different (47, 53). The myocardium at AVC and OFT provide the crucial molecular signals that induce VECs to undergo EMT (41,

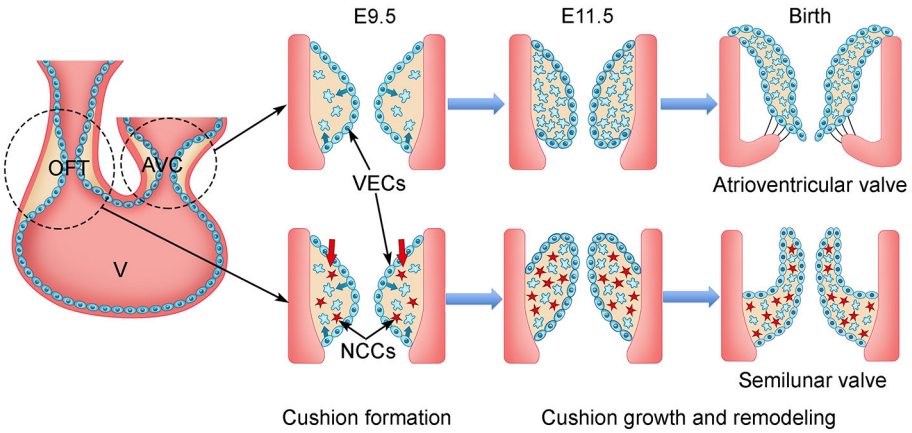

FIGURE 1 | Schematic of cardiac valve development in mice. During mouse embryogenesis, the linear heart tube, composed of outer layer of myocardium (orange) and inner layer of endocardium (blue), undergoes looping beginning at E8.0. The process divides the heart tube into four segments: the atrium, atrioventricular canal (AVC), ventricle (v), and outflow tract (OFT) by E9.5. Two matrix-rich and acellular tissue swellings, named endocardial cushions, are formed within the AVC and OFT regions. In response to the signals from the myocardium, the endocardial cells within the AVC and proximal OFT regions undergo endocardial-to-mesenchymal transformation (EMT). The transformed mesenchymal cells invade the matrix-rich cardiac jelly and proliferate to populate the endocardial cushions within the proximal OFT, while the cardiac neural crest cells (NCCs) migrate into the distal OFT. By E11.5, the AVC and OFT cushions are fully cellularized. After E11.5, the AVC and OFT cushions grow rapidly and undergo intensive remodeling involving spatiotemporal cell proliferation and apoptosis of valve interstitial cells (VICs), as well as dynamic extracellular matrix (ECM) arrangement. The AVC and OFT cushions eventually give rise to the atrioventricular valves (mitral and tricuspid valve) and semilunar valves (aortic and pulmonary valve), respectively. VECs, valve endocardial cells.

45, 47). Biochemical and genetic studies in chick and mouse embryos have identified BMP/TGF-β signaling as a key inducer of EMT (54). Early studies using cultured chicken AVC tissues in a collagen gel assay have demonstrated that TGF-β2 and TGF-β3 are the main cytokines that induce VECs to undergo EMT (55, 56). However, studies in mice have found that only TGF-β2 is required for the initiation of EMT by the AVC explants using the similar collagen gel assay (56), and the *Tgfb2* or *Tgfb3* null mice have no obvious defects in the EMT process and endocardial cushions (57). In contrast, BMP2 and BMP4 are expressed exclusively by the AVC and OFT myocardium, respectively, during early valve development (58–61). Myocardial-specific disruption of *Bmp2* in mice blocks EMT and results in endocardial cushion defects at AVC, suggesting BMP2 is a crucial inducer of EMT (58). Molecular analysis of *Bmp2* knockout embryos by RNA *in situ* hybridization has revealed that loss of *Bmp2* leads to decreased expression of *Tgfb2*, indicating TGF-β2 acts downstream of BMP2 during EMT (58). BMP2 also promotes the expression of *Snai1* and its nuclear stability through inhibiting GSK3β (62). Furthermore, T-box transcriptional factor *Tbx2* is another downstream target of BMP2 and is expressed in the myocardium of AVC and OFT, but absent in the chamber myocardium (63). Molecular analysis has shown that the BMP2-TBX2 signaling axis is essential for specifying the AVC myocardium by repressing the chamber-myocardium gene program (54, 63). Consistently, loss of *Tbx2* in mice results in EMT and endocardial cushion defects at AVC and OFT, whereas overexpression of *Tbx2* induces ectopic expression of *Tgfb2* in the chamber myocardium and ectopic EMT by the chamber endocardial cells (63, 64). Together, the findings of these studies demonstrate local myocardial signals in AVC and OFT that dedicate the cell fate of VECs during EMT to cellularize the endocardial cushions as early valve primordia.

THE NOTCH SIGNALING PATHWAY

In addition to the aforementioned molecular signals from the AVC and OFT myocardium, others and we have studied the functions of NOTCH signaling in heart valve development. The NOTCH signaling pathway is highly conserved across species from zebrafishes to humans (26, 27, 65). It provides a major intercellular signaling mechanism that mediates the crosstalk between adjacent cells. The NOTCH pathway consists of the NOTCH ligands and receptors that are both single-pass transmembrane proteins at the cell surface (**Figure 2**). Mammals have four NOTCH receptors (NOTCH1-4) and five ligands that belong to two families: Serrate/Jagged families (JAG1,2) and Delta (DLL1,3,4) (26, 27, 65). A NOTCH receptor has a large extracellular fragment and a NOTCH intracellular domain (NICD) that contains two nuclear localization signals and a transactivation region. The pre-NOTCH proteins are processed in the Golgi apparatus through proteolytic cleavage mediated by a furin-like convertase. In addition, sugar residues are added to the epidermal growth factor–like repeats of the NOTCH extracellular domain by several glycosyltransferases including the Fringe family proteins and protein O-fucosyltransferases (29–31, 66–68). These posttranslational modifications determine the binding specificity between a NOTCH ligand and its receptor, thereby essential for the proper activation of the NOTCH signaling (69). The mature NOTCH proteins are then transferred to the cell surface and form a heterodimer receptor there through non-covalent interactions (66). The binding of the NOTCH

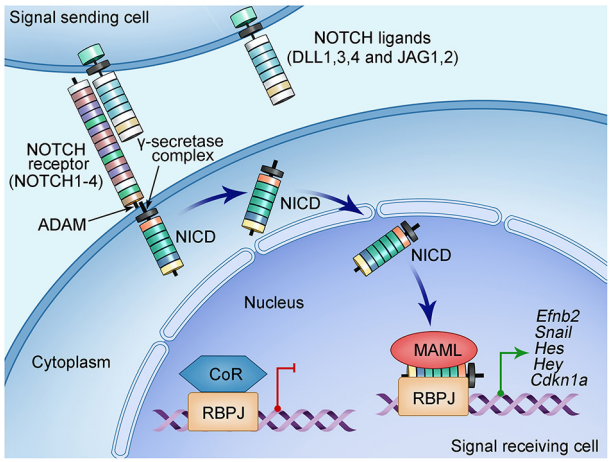

FIGURE 2 | Schematic of NOTCH signaling pathway. NOTCH signaling pathway consists of ligands (DLL1, DLL3, DLL4, and JAG1, JAG2), receptor (NOTCH1-4), nuclear effector RBPJ, and cofactors. Both NOTCH ligands and receptors are type I transmembrane proteins with an extracellular domain consisting of a number of EGF-like repeats modified by sugars essential for the ligand-binding specificity. The NOTCH signal is initiated when the ligand on the surface of the signaling-sending cell binds the NOTCH receptor on the signaling-receiving cell. This ligand–receptor interaction generates a mechanical force that causes the conformational change of the NOTCH receptor, leading to subsequently proteolytic cleavages mediated by disintegrin and metalloproteinase domain-containing protein (ADAM) metalloproteinases and the γ-secretase–presenilin complex. These cleavages on the NOTCH receptor release the NOTCH intracellular domain (NICD), which then translocate into the nucleus and form a transcriptional complex with the DNA-binding protein RBPJ. RBPJ forms a complex with corepressors (CoR) and suppresses the transcription of target genes when NICD is not in the nucleus. The binding of NICD with RBPJ results in the release of CoR, while recruiting the coactivator Mastermind-like protein (MAML), leading to the transcription activation of the target genes such as the HES and HEY families of basic helix–loop–helix transcriptional repressors.

ligand on a signal-sending cell to the NOTCH receptor on a signal-receiving cell leads to the endocytosis of the ligand, the process that generates mechanical force to pull on a NOTCH receptor. This pull action, in turn, triggers the conformational changes, leading to exposure of the S2 site of the receptor being recognized and further cleaved by the ADAM, a disintegrin and metalloproteinase (66). Further cleaving by γ-secretase at S3 site results in the release of the protein fragment NICD (70). The released NICD then shuttles into the nucleus and forms a complex with transcription factor RBPJ. Binding of NICD to RBPJ converts it from a repressor to an activator by releasing its corepressors, allowing recruitment of coactivator Mastermind (MAML) to activate gene expression. The well-known targeted genes include the basic–helix–loop–helix transcriptional factors of the *Hes* and *Hey* families (26, 27, 66).

The activation of the NOTCH signaling regulates multiple cellular functions including fate specification, differentiation, proliferation, apoptosis, and migration during embryogenesis and in adulthood (26). Studies using animal models have led to the identification of many critical roles of the NOTCH signaling in coordinating organ development and maintaining tissue homeostasis. In the cardiovascular system, the NOTCH signaling plays critical roles in early cardiomyocyte differentiation (71–75), ventricular trabeculation (76), cardiac valve formation (52, 59, 77, 78), OFT development (79), and angiogenesis (80), as well as cardiovascular homeostasis (26). The dysregulation of the NOTCH signaling is associated with congenital heart disease (32, 81–83) and several adult cardiovascular disease including atherosclerosis (84), hypertension (85–88), and CAVD (32, 89–91). Next, we will focus our discussion on the roles of the NOTCH signaling in aortic valve development and CAVD.

NOTCH SIGNALING IN EMT AND ENDOCARDIAL CUSHION FORMATION

The NOTCH signaling in the endocardium is critical for the initiation of EMT and endocardial cushion formation (**Figure 3A**). Several NOTCH pathway genes (*Dll4*, *Jag1*, *Notch1*, *Notch4*, *Hey1*, and *Hey2*) are expressed in the endocardium within AVC and OFT regions (i.e., VECs) between E9.0 and E11.5 when EMT takes place in mice (59, 77, 78, 92, 93). Genetic disruption of *Notch1* or *Rbpj* severely blocks EMT and results in hypocellular endocardial cushions in mice (77). A similar phenotype was observed in mice with deletion of *Jag1* using either $Cdh5^{Cre}$ or $Nfatc1^{Cre}$ driver, suggesting *Jag1* is a key ligand inducing the NOTCH signaling during EMT and endocardial cushion formation (59, 93). In contrast, a recent study using $Tie2^{Cre}$ driver demonstrated that *Dll4* but not *Jag1* is the key ligand in this process (78). This discrepancy might be due to different genetic backgrounds and/or *Cre* drivers used in these studies. In addition, the endothelial specific disruption of *Mib1*, an upstream regulator of the NOTCH signaling through modulating the ligand activity, recapitulated the EMT defect observed in the *Notch1* mutant mice (78). Consistent with these *in vivo* findings, the blockage of the NOTCH signaling by either genetic disruption of *Notch1* or *Rbpj* or treating wild-type AVC explants with the NOTCH inhibitor DAPT (*N*-[*N*-(3,5 difluorohenacetyl)-L-alanyl]-*S*-phenylglycine tert-butyl ester) severely impairs the EMT in the *in vitro* collagen gel assays (77).

Mechanistically, the NOTCH signaling directly regulates *Snai1* (*Snail*), which in turn represses the expression of VE cadherin, a major cell–cell adhesive protein expressed in the endothelial cells including VECs (77). Disruption of adhesion junction is prerequisite for VECs to delaminate the endocardial sheet at AVC and OFT, migrate, and invade the cardiac jelly. In addition, *in vitro* studies have demonstrated that *Snai2* (*Slug*) is a direct target of NOTCH1 and represses the expression of VE cadherin during EMT process (94). The EMT defect in the *Snai2* null AVC explants can be rescued by increased expression of *Snai1*, supporting a redundant function between *Snai1* and *Snai2* in regulation of EMT (94). Together, these findings have established a signaling axis consisting of NOTCH-SNAI1/SNAI2-VE cadherin that plays a key role in regulating EMT during endocardial cushion formation and early heart valve development. It is worth to mention that the JAG1/NOTCH

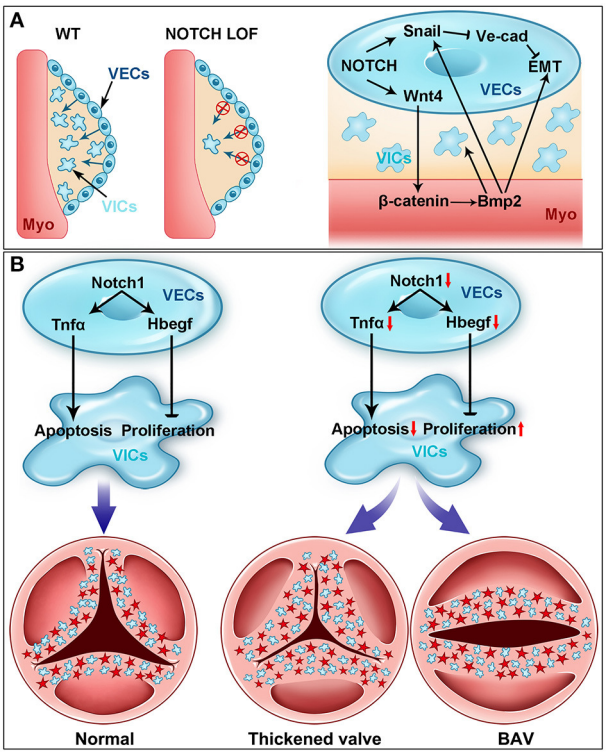

FIGURE 3 | NOTCH signaling in cardiac valve development. **(A)** NOTCH is essential for early heart valve development (i.e., endocardial cushion formation). Cardiac valve development starts with the formation of endocardial cushions through the endocardial-to-mesenchymal transformation (EMT) (blue arrows) process in wild-type (WT) mouse embryos. The EMT process is severely blocked in the NOTCH loss-of-function (LOF) mutant embryos. Mechanistically, NOTCH activates the transcription of *Snail*, which subsequently represses the expression of *VE cadherin*. The downregulation of *VE cadherin* is prerequisite for the endocardial cells to delaminate the endocardial sheet and undergo EMT. NOTCH also induces the expression of *Wnt4* in the endocardium, which activates the canonical WNT signaling in the myocardium (Myo). The activation of WNT signaling in the myocardium promotes the expression of *Bmp2*, which feeds back to the endocardium through *Bmpr1* and regulates the EMT via stabilizing the *Snail* protein in the nucleus. *Bmp2* also promotes the proliferation of mesenchymal cells (MCs) during endocardial cushion formation. **(B)** NOTCH controls the cardiac valve remodeling through regulating the apoptosis and proliferation. NOTCH in the valve endocardial cells (VECs) promotes the expression of *Tnfa*, which subsequently induces the apoptosis of valve interstitial cells (VICs) originated from VECs (blue cells) and NCCs (red cells) during valvulogenesis. On the other hand, NOTCH in VECs directly activates the expression of *Hbegf*, which then inhibits the proliferation of VICs through repressing SMAD signaling. Genetic disruption of the NOTCH signaling pathway results in decreased expression of *Tnfa* and *Hbegf*, leading to the thickened valve leaflets and BAV, the most common congenital heart valve defect.

signaling in the SHF derivatives also critically controls EMT in OFT through interaction with the FGF8-BMP4 signaling (95).

In addition to its VEC autonomous function, the NOTCH1 signaling in VECs also interacts with the signals from the myocardium to regulate EMT during endocardial cushion formation (59, 62). It is noted that while ventricular endocardial cells with ectopic activation of the NOTCH1 signaling acquires an EMT gene program, they are unable to migrate away from the cultured ventricular explants, but invasion can be triggered after additional BMP2 treatment (62). These observations suggest a synergic function between endocardial NOTCH and myocardial BMP signaling in promoting EMT. On the other hand, loss of myocardial *Bmp2* inhibits the expression of *Notch1* in VECs and EMT (58), whereas inhibition of the NOTCH signaling attenuates the invasive phenotype induced by BMP2 in cultured ventricular explants (62). To reveal the endocardial specific functions of the NOTCH1 signaling, we deleted *Notch1* in the endocardial cells of the developing mouse heart by using an *Nfatc1*^{Cre} driver (59). In contrast to the germline *Notch1* null mutants, which have severe overall vascular defects that affect early cardiac morphogenesis (76, 80), our *Notch1* conditional knockout embryos develop normal vascular networks, thereby allowing us to specifically dissect the endocardial-specific roles of NOTCH1 signaling in cardiac development (59). Our studies confirmed that deletion of *Notch1* in the endocardial cells impairs EMT and results in hypocellular endocardial cushions. Furthermore, we show that endocardial NOTCH1 is required for maintaining the myocardial *Bmp2* expression through WNT4-mediated paracrine regulation (59). Our studies demonstrate a NOTCH–WNT–BMP signal axis as a key crosstalk mechanism between endocardium and myocardium essential for EMT and early heart valve development.

As discussed above, mouse embryos with conditional knockout of myocardial *Bmp2* exhibit decreased expression of *Notch1* in the endocardial cells (58). This observation further supports a crosstalk between myocardial BMP and endocardial NOTCH signaling during EMT and endocardial cushion formation. Interestingly, the expression pattern of *Hey1* and *Hey2*, two well-known targets of the NOTCH signaling, is complementary to *Bmp2* (and *Tbx2*) (96–98). Deletion of *Hey1* and *Hey2* simultaneously results in the expansion of AVC myocardium evidenced by the extended expression of *Bmp2* to the atrial myocardium (97, 98). While *Hey1* and *Hey2* are normally expressed by the atrial and ventricular chamber myocardium, respectively, and absent in the AVC myocardium, their chamber expression can be suppressed by the ectopic expression of *Tbx2* (97, 98). In contrast, overexpression of NICD, *Hey1*, or *Hey2* in the chicken heart inhibits the expression of *Bmp2* in AVC (62). These findings support that this negative feedback loop between the endocardial NOTCH and myocardial BMP signaling defines the regional gene program in the chamber and non-chamber myocardium, which regulates the cell fates of VECs during EMT and early heart valve formation (98, 99).

NOTCH SIGNALING IN AORTIC VALVE REMODELING AND EMBRYONIC PATHOGENESIS OF BAV

After EMT, the cellularized endocardial cushions undergo a complex remodeling process and eventually give rise to the valve leaflets and septa, which divide the heart into four chambers in mammals (**Figure 3B**). The remodeling process is coordinated by multiple cell populations, including VECs and VICs of different

embryonic origins in VECs, NCCs, and SHF. Signals from these cells precisely control the spatiotemporal cell proliferation and apoptosis, as well as dynamic ECM production and organization, which together ensure the proper transformation from the blunted bulky valve primordia into the elongated thin valve leaflets (1, 100). Alterations of these signals can cause congenital heart defects. For example, mutations in the NOTCH pathway genes have been identified to be associated with congenital heart defects. In particular, the *NOTCH1* mutations are among the first genetic variants identified for familial BAV in non-syndromic autosomal-dominant human patients (32). Different *NOTCH1* mutations have been observed in BAV patients by several groups (101–104). Furthermore, mutations in *JAG1* or *NOTCH2* cause Alagille syndrome (AGS), which has defects in multiple organs including the heart valves, and mutations in *JAG1* or *NOTCH1* have also been identified for a subset of tetralogy of Fallot patients (81–83).

Gene expression studies with RNA *in situ* hybridization and immunostaining have found that *Notch1* and *Notch4* are expressed in the endothelial cells, whereas *Notch2* and *Notch3* are present in the smooth muscle cells of the aorta and the pulmonary artery. *Jag1* is broadly expressed in the endothelium, the NCC-derived mesenchyme, and the OFT myocardium (79, 95). Inhibition of NOTCH signaling by overexpressing a dominant-negative version of MAML (MNMAML) specifically in the cardiac NCC lineage using the *Pax3*^{Cre} or *Wnt1*^{Cre} driver in mice causes defects in aortic arch patterning and ventricular septum and pulmonary artery stenosis, which reminisce many OFT defects seen in AGS (79, 95). Analysis of the mutant mouse embryos indicates that loss of NOTCH in the cardiac NCC lineage impairs the differentiation of NCC precursors into smooth muscle cells (79), whereas it has no effect on cell proliferation or migration. In addition, the deletion of *Jag1* or the inhibition of NOTCH in the SHF lineage results in defects in the aortic arch and ventricular septum, as well as thickened semilunar valve leaflets where the valve defect is attributed to the decreased cell apoptosis and disorganized ECM (21). Similar defects are present in the mice with the endothelial specific deletion of *Jag1* (93). Furthermore, genetic interactions between the NOTCH pathway genes and other vascular essential genes are observed in the mouse models of cardiac OFT malformations including BAV. For instance, the study of the compound heterozygous mice for *Notch1* and *Nos3* has suggested that genetic interactions between the NOTCH and endothelial nitric oxide synthase (eNOS) signaling pathways are essential for aortic valve remodeling (105).

Pan-endothelial deletion of NOTCH pathway genes using *Tie1*^{Cre} or *Tie2*^{Cre} as a driver in mice causes severe vascular defects that result in embryonic lethality at the middle gestation (80), excluding the investigation of the functions and mechanisms of NOTCH signaling in regulation of aortic valve remodeling after EMT. In addition, Cre drivers including the endocardial specific Cre *Nfatc1*^{Cre} that mediate gene deletion before EMT disrupt genes in VECs and their daughter VICs, thereby complicating the phenotypic interpretation and molecular signaling identification specific to the post-EMT valve remodeling. To overcome these limitations and specifically study the roles of molecular signals in VECs during aortic valve remodeling, we have developed a new Cre driver termed *Nfatc1*^{enCre}, in which the expression of Cre is under the control of an *Nfatc1* gene enhancer (106, 107). Functional validation shows that the *Nfatc1*^{enCre} mice activate the LacZ reporter gene expression specifically in VECs, but not in VICs, beginning around E11.0 (106). We have then generated mouse models with VEC-specific deletion of *Notch1* or *Rbpj*. In contrast to the early lethal phenotype observed in the pan-endothelial *Notch1* or *Rbpj* knockout mice, our VEC-specific *Notch1* mutant mice can survive into adulthood, thereby allowing us to study the role of NOTCH1 signaling in valve remodeling. We have found by echocardiography that the adult VEC *Notch1* conditional knockout mice display increased peak velocity across the aortic valve, indicating a phenotype of aortic valve stenosis (52). Histological and pathological analyses have further indicated that the aortic valves of the mutant mice are thickened, fibrotic, and calcified. In the most severe cases, the cartilage-like structures are present in the leaflets and aortic roots (52). Significantly, some of the mutant mice have developed BAV due to the fusion of the two coronary leaflets (52). These findings demonstrate that the VEC-specific *Notch1* knockout mice recapitulate the common BAV seen in CAVD patients associated with the *NOTCH1* mutations. Thus, the new mouse model offers an excellent opportunity to study the developing mechanism of BAV caused by the *NOTCH1* mutations.

BAV affects ∼2% of general populations and is the most common congenital heart malformation (2, 13, 100, 108, 109). It is associated with a high incidence of CAVD and other cardiac complications including aortic dilation, aneurism, and dissection, which can lead to sudden death (8, 9, 110). A BAV may occur isolated or present in a complex syndrome such as Turner, DiGeorge, or Shone syndrome (111, 112). BAV can be caused by the fusion of two of three leaflets or the absence of any one leaflet and the fusion of the right and left leaflet (R–L) is the most common type present in ∼70% of all the BAV patients (100). Studies using pig (113), hamster (114–117), and mice models (52, 118) have demonstrated that BAV arises from abnormal aortic valve development. As discussed previously, the *NOTCH1* mutations are associated with the common R–L type of BAV in humans (32). In our mouse studies, we find that the VEC-specific deletion of *Notch1* results in BAV due to the fusion of the left and right coronary leaflet during the early post-EMT remodeling of the aortic valve. At the cellular level, loss of *Notch1* in VEC causes increased proliferation but decreased apoptosis of the VICs (**Figure 3B**). In contrast, overactivation of NOTCH in VECs results in decreased proliferation and increased apoptosis of VICs, leading to the hypoplastic valves (52). At the molecular level, we show that NOTCH1 expressed in VECs promotes the expression of *Tnfa*, which subsequently induces the apoptosis of VICs. Of note, similar aortic valve remodeling defect has been found by another study using the same Cre driver to delete *Jag1*, *Notch1*, or *Rbpj*, indicating that the JAG1–NOTCH1 signaling in VECs is required for aortic valve remodeling (78). In this study, loss of NOTCH signaling in VECs leads to increased proliferation of VICs accompanied by decreased expression of *Hbegf*, which is a negative regulator of proliferation through restricting

BMP signaling (119). Further molecular studies demonstrate that *Hbegf* is a direct NOTCH target gene in VECs for the proliferation of VICs, as the supplement of soluble HBEGF to the cultured OFT explants from the *Jag1* mutant embryos can rescue the hyperproliferative phenotype (78). These findings support a dual function of the NOTCH1-regulated signaling from VECs in the apoptosis and proliferation of VICs through tumor necrosis factor α and HBEGF, respectively (**Figure 3B**). These findings are also consistent with the fact that VICs in front of a growing leaflet are highly proliferative, whereas those on the rear side are more likely apoptotic (52). Thus, the NOTCH1 signaling is a critical determinant that controls the balanced proliferation and apoptosis of VICs, which sculpts the endocardial cushions into the thin valve leaflets.

NOTCH SIGNALING IN AORTIC VALVE HOMEOSTASIS AND CALCIFICATION

The aortic valve leaflets, unique tissue microarchitecture with endurant and flexible characteristics essential for a lifelong cyclic function, consist of three layers including fibrosa, spongiosa, and ventricularis (9). The fibrosa layer is located at the aortic side and made up of collagen-rich matrix, VICs, and VECs facing the aortic wall. The spongiosa is the middle layer containing VICs embedded in glycosaminoglycan-rich matrix. The ventricularis layer is rich in elastin fibers and consists of VICs and surface VECs facing the left ventricle (4). VECs on the surface of a leaflet form a barrier that regulate the valve permeability, the adhesion of inflammatory cells, and paracrine or signaling including mechanosensory signals from VECs to VICs (9). VICs are the major cell population in a leaflet, producing ECM and controlling the ECM organization during valve remodeling. In the adult valve, VICs are quiescent under the physiological condition but become activated upon the stimulation by molecular and mechanical signals including the high blood pressure, altered hemodynamics, and inflammatory molecules (9). The activated VICs then undergo transdifferentiation into synthetic myofibroblast and produce many ECM proteins, resulting in pathological ECM remodeling, which makes the valve prone to calcification (5–8).

There is no cure for advanced CAVD patients, except for valve replacement. However, because of high risks of the surgery for the elderly patients and postoperative complications with anticoagulant medicines, the surgical treatment is not suitable for all CAVD patients. Previously considered as a passive consequence of aging (7), CAVD is now recognized as an active disease driven by chronic inflammation (120). Molecular signaling pathways underlying inflammation are thus potential targets for the disease diagnosis and intervention. Signal molecules include eNOS (121), renin–angiotensin system (122–124), NOTCH (89, 90), WNT/β-catenin (122), BMP/TGF-β signaling (122), RANK/RANKL pathway, vitamin K–dependent proteins (125), and microRNAs (9, 126). Here we focus on the NOTCH signaling, whereas the other pathways and molecules are reviewed in recent articles (9, 127).

Since the initial identification of two *NOTCH1* mutations associated with BAV and CAVD by Garg et al. (32), additional *NOTCH1* mutations have been identified in BAV patients by several groups around the world (101, 103, 104). In addition, genome-wide association study has identified several genetic variants in *GATA4/5/6* genes associated with BAV patients (128–130), whereas the targeted disruption of *Gata5* in mice leads to BAV accompanying impaired NOTCH signaling (128, 131, 132). The studies using animal and tissue culture models have further explored the underlying molecular mechanisms. Studies with RNA *in situ* hybridization show that murine *Notch1* mRNA is abundant in VECs and VICs immediately underneath VECs between E11.5 and E13.5 when the intensive valve remodeling is undergoing (32). A similar expression pattern is observed in the adult aortic valves by using the same method. However, antibody staining shows the NOTCH1 protein expression in VECs, but not VICs (52, 78, 89, 92). By using a transgenic mouse line that reports all NOTCH activities via the consensus RBPJ binding sites, we have shown that the NOTCH signaling is highly activated in VECs but absent in VICs during aortic valve development (52). In contrast, in the adult aortic valves, the NOTCH activities are greatly reduced in VECs, whereas some VICs display the NOTCH signals (52). In addition, a reduction of nuclear NOTCH1 activity is seen in the calcified fibrosa when comparing to the non-calcified regions of the diseased valves (90, 133). Together, the dynamic expression pattern of NOTCH1 in the aortic valve indicates potential dual functions in prenatal aortic valve remodeling vs. postnatal homeostasis.

Indeed, the functional studies using mouse models, cultured aortic VICs, and stem cell–derived endothelial cells have collectively revealed the critical roles and mechanisms of NOTCH1 in the regulation of valve calcification. Western diet can induce a 5-fold more calcification in the heterozygous *Notch1* null mice (89). Similarly, after 16 weeks of hyperlipidemic diet feeding, the heterozygous *Rbpj* mice exhibit milder histopathologic features of CAVD including macrophage infiltration, enhanced collagen deposition, pro-osteogenic protein expression, and calcification, but have no obvious hemodynamic changes (91). Endothelial deletion of *Jag1* results in the formation of calcific nodules in the aortic valve of adult mice (93). We have generated and studied a conditional *Notch1* knockout mice model in which *Notch1* was specifically deleted in VECs, and the mutant mice display the typical phenotypes of aortic valve stenosis at a young age of 3 months (52). The mouse CAVD is associated with increased collagen and glycoproteins and calcific nodules. In the most severe case, the cartilage-like structure was seen in the valve leaflet and the annulus (52). Importantly, the mouse CAVD is proceeded with embryonic thickening of the aortic valve leaflets, with a partial penetration of BAV resulting from the fusion of two coronary leaflets resembling the most common form of BAV in humans. In addition, $Nos3^{-/-}$; $Notch1^{+/-}$ mice develop aortic valve disease, indicating a genetic interaction between *Nos3* and *Notch1* in calcific progression (134, 135). In line with these *in vivo* findings, inhibition of NOTCH in cultured aortic VICs from sheep, rat, or pig promotes calcific nodules formation and osteogenic gene expression.

Studies using primary VICs from multiple species and endothelial cells differentiated from the human induced pluripotent stem cells (hiPSCs) of patients with the *NOTCH1* mutations have begun to uncover the deep molecular mechanisms underlying the CAVD progression associated with the *NOTCH1* haploinsufficiency in humans (**Figure 4**). The NOTCH1 signaling activates the expression of *Hey1* and *Hey2*, which in turn represses the transcription of *Runx2*, a key transcriptional regulator of osteoblast cell fate (32). *Bmp2* mediates the induction of osteogenic gene expression and calcification by the NOTCH inhibition (89). Genome-wide screening also finds NOTCH1 positively regulates the expression of matrix Gla protein (MGP), which is known to inhibit calcification through sequestering BMPs (136). In cultured aortic VICs, inhibition of the NOTCH signaling results in decreased expression of *Sox9*, and the loss of *Sox9* function is associated with aortic valve calcification (90). Conversely, the supplementation of *Sox9* is able to attenuate the calcification resulting from the NOTCH inhibition. These findings suggest *Sox9* as another downstream mediator of the NOTCH signaling in the regulation of aortic valve calcification. In a coculture system, nitric oxide (NO) produced by endothelial cells inhibits the calcification of VICs, whereas overexpression of *Notch1* can cancel out the calcification of VICs induced by the NO inhibition (134, 137). Recently, Majumdar et al. report that NO mitigates the aortic valve calcification by activating NOTCH signaling through S-nitrosylation of USP9X (137). These findings support interactions between NO and NOTCH1 in aortic valve calcification. In human studies, analysis of the blood samples from 61 patients with aortic stenosis has revealed an association between the *NOTCH1* variants and the OPG/RANKL/RANK gene program (138). In addition, modeling CAVD in endothelial cells differentiated from hiPSCs by introduction of the *NOTCH1* mutations from patients with BAV and aortic valve stenosis has found that the *NOTCH1* haploinsufficiency leads to the alteration of epigenetic architecture, resulting in derepression of latent pro-osteogenic and proinflammatory gene networks (139). Furthermore, a critical role of the telomere shortening in the initiation of calcific program has been reported in the *Notch1*$^{+/-}$ mice (140). More recently, by using hiPSC technology and machine learning, Theodoris et al. have identified a small molecule XCT790, which is able to correct the gene network changes resulting from the *NOTCH1* haploinsufficiency and to prevent the disease progression in a mouse model of CAVD (141). Although multiple observational studies and randomized controlled trials remain needed, XCT790 represents a promising drug for treating CAVD disease in clinical. Together, these current findings reveal a crucial role of NOTCH1 in aortic valve calcification, while the underlying mechanisms remain an area of intensive investigation.

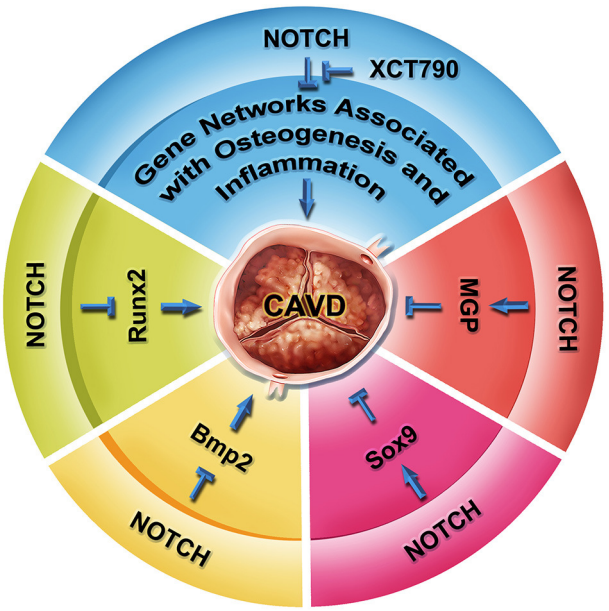

FIGURE 4 | NOTCH signaling in aortic valve homeostasis and CAVD. RUNX2 is a key regulator of osteogenesis, as well as hallmark of CAVD progression. NOTCH represses the transcription of *Runx2* mediated by HEY proteins. NOTCH also represses the expression of *Bmp2* and BMP2-regulated osteoblast-like calcification pathway. Inhibition of NOTCH leads to calcification via a *Sox9*-dependent manner. Conversely, matrix Gla protein MGP suppresses the calcification of soft tissue through antagonizing the BMP signaling. NOTCH positively regulates the transcription of *MGP*. In human iPSC studies, NOTCH1 haploinsufficiency causes gene network change involved in osteogenesis, inflammation, and oxidative stress through an epigenetic mechanism, which can be reversed by a small molecule XCT790. The XCT790 treatment can slow down calcification in the human iPSCs and a mouse model of CAVD.

CONCLUSIONS AND PERSPECTIVES

Heart valve development is a precisely controlled morphogenic process involving cell differentiation, proliferation, apoptosis, and migration, as well as ECM organization. Alteration of molecular signals that regulate this process can cause congenital heart valve defects including BAV, which may lead to CAVD with severe clinical consequences. The structural defects predispose the affected valves to calcification. By using human genetics, animal models, and tissue culture systems, clinicians and basic scientists have worked together and demonstrated the important functions of NOTCH1 in regulation of aortic valve development and CAVD.

The basic and translational research on NOTCH signaling in regulation of aortic valve development and CAVD has led to the identification of a small molecule XCT790 that can halt the disease progression in a mouse model of CAVD. This exemplifies a new avenue for effective drug discovery. However, CAVD is a disease affected by many factors, whereas NOTCH haploinsufficiency contributes to only a small subset of the inheritable cases. Future studies will be needed to broaden the research area to (1) identify additional genetic variants that cause BAV and CAVD using unbiased approaches such as next-generation sequencing, (2) decipher deeper mechanisms underlying disease progression in CAVD patients with or without BAV, and (3) reveal the shared mechanisms among

BAV-associated and acquired CAVD that will facilitate the development of a common therapeutics suitable for all patients. It is expected that combination of clinical studies using advanced next-generation sequencing for large patient cohorts and basic researches with hiPSC technology, machine learning, CRISPR-guided gene editing, and single-cell technologies will uncover new BAV and calcific genes, informing pathogenic mechanisms of CAVD and targeted gene therapeutics for the disease.

AUTHOR CONTRIBUTIONS

YW and BZ wrote the manuscript. PL, BW, and YF read and critically edited the manuscript. YF drew the figures. All authors contributed to the article and approved the submitted version.

FUNDING

Research in the laboratories of YW and BZ was supported by the grants from the National Key R&D Program of China (2019YFA0802300), the National Natural Science Foundation of China (81970266), and Department of Human and Social Affairs of Shaanxi Province in China (2019001) to YW, and the NIH grants National Heart (R01HL078881, R21HL104441, and R01HL111770) to BZ.

REFERENCES

1. Wu B, Wang Y, Xiao F, Butcher JT, Yutzey KE, Zhou B. Developmental mechanisms of aortic valve malformation and disease. *Annu Rev Physiol*. (2017) 79:21–41. doi: 10.1146/annurev-physiol-022516-034001
2. Menon V, Lincoln J. The genetic regulation of aortic valve development and calcific disease. *Front Cardiovasc Med*. (2018) 5:162. doi: 10.3389/fcvm.2018.00162
3. Gould ST, Srigunapalan S, Simmons CA, Anseth KS. Hemodynamic and cellular response feedback in calcific aortic valve disease. *Circ Res*. (2013) 113:186–97. doi: 10.1161/CIRCRESAHA.112.300154
4. Fernandez Esmerats J, Heath J, Jo H. Shear-Sensitive genes in aortic valve endothelium. *Antioxid Redox Signal*. (2016) 25:401–14. doi: 10.1089/ars.2015.6554
5. Towler DA. Molecular and cellular aspects of calcific aortic valve disease. *Circ Res*. (2013) 113:198–208. doi: 10.1161/CIRCRESAHA.113.300155
6. Mathieu P, Boulanger MC. Basic mechanisms of calcific aortic valve disease. *Can J Cardiol*. (2014) 30:982–93. doi: 10.1016/j.cjca.2014.03.029
7. Yutzey KE, Demer LL, Body SC, Huggins GS, Towler DA, Giachelli CM, et al. Calcific aortic valve disease: a consensus summary from the Alliance of Investigators on calcific aortic valve disease. *Arterioscler Thromb Vasc Biol*. (2014) 34:2387–93. doi: 10.1161/ATVBAHA.114.302523
8. Bonow RO, Leon MB, Doshi D, Moat N. Management strategies and future challenges for aortic valve disease. *Lancet*. (2016) 387:1312–23. doi: 10.1016/S0140-6736(16)00586-9
9. Peeters F, Meex SJR, Dweck MR, Aikawa E, Crijns H, Schurgers LJ, et al. Calcific aortic valve stenosis: hard disease in the heart: a biomolecular approach towards diagnosis and treatment. *Eur Heart J*. (2018) 39:2618–24. doi: 10.1093/eurheartj/ehx653
10. Kostyunin AE, Yuzhalin AE, Ovcharenko EA, Kutikhin AG. Development of calcific aortic valve disease: do we know enough for new clinical trials? *J Mol Cell Cardiol*. (2019) 132:189–209. doi: 10.1016/j.yjmcc.2019.05.016
11. Go AS, Mozaffarian D, Roger VL, Benjamin EJ, Berry JD, Blaha MJ, et al. American Heart Association Statistics C and Stroke Statistics S. Heart disease and stroke statistics—2014 update: a report from the American Heart Association. *Circulation*. (2014) 129:e28–292. doi: 10.1161/01.cir.0000442015.53336.12
12. Nkomo VT, Gardin JM, Skelton TN, Gottdiener JS, Scott CG, Enriquez-Sarano M. Burden of valvular heart diseases: a population-based study. *Lancet*. (2006) 368:1005–11. doi: 10.1016/S0140-6736(06)69208-8
13. Hoffman JI, Kaplan S. The incidence of congenital heart disease. *J Am Coll Cardiol*. (2002) 39:1890–900. doi: 10.1016/S0735-1097(02)01886-7
14. Ferreira-Gonzalez I, Pinar-Sopena J, Ribera A, Marsal JR, Cascant P, Gonzalez-Alujas T, et al. Prevalence of calcific aortic valve disease in the elderly and associated risk factors: a population-based study in a Mediterranean area. *Eur J Prev Cardiol*. (2013) 20:1022–30. doi: 10.1177/2047487312451238
15. Ali OA, Chapman M, Nguyen TH, Chirkov YY, Heresztyn T, Mundisugih J, et al. Interactions between inflammatory activation and endothelial dysfunction selectively modulate valve disease progression in patients with bicuspid aortic valve. *Heart*. (2014) 100:800–5. doi: 10.1136/heartjnl-2014-305509
16. Mahadevia R, Barker AJ, Schnell S, Entezari P, Kansal P, Fedak PW, et al. Bicuspid aortic cusp fusion morphology alters aortic three-dimensional outflow patterns, wall shear stress, and expression of aortopathy. *Circulation*. (2014) 129:673–82. doi: 10.1161/CIRCULATIONAHA.113.003026
17. Edlin J, Youssefi P, Bilkhu R, Figueroa CA, Morgan R, Nowell J, et al. Haemodynamic assessment of bicuspid aortic valve aortopathy: a systematic review of the current literature. *Eur J Cardiothorac Surg*. (2019) 55:610–17. doi: 10.1093/ejcts/ezy312
18. Antequera-Gonzalez B, Martinez-Micaelo N, Alegret JM. Bicuspid aortic valve and endothelial dysfunction: current evidence and potential therapeutic targets. *Front Physiol*. (2020) 11:1015. doi: 10.3389/fphys.2020.01015
19. Kirby ML, Gale TF, Stewart DE. Neural crest cells contribute to normal aorticopulmonary septation. *Science*. (1983) 220:1059–61. doi: 10.1126/science.6844926
20. de Lange FJ, Moorman AF, Anderson RH, Manner J, Soufan AT, de Gier-de Vries C, et al. Lineage and morphogenetic analysis of the cardiac valves. *Circ Res*. (2004) 95:645–54. doi: 10.1161/01.RES.0000141429.13560.cb
21. Jain R, Engleka KA, Rentschler SL, Manderfield LJ, Li L, Yuan L, et al. Cardiac neural crest orchestrates remodeling and functional maturation of mouse semilunar valves. *J Clin Invest*. (2011) 121:422–30. doi: 10.1172/JCI44244
22. Lin CY, Lin CJ, Chen CH, Chen RM, Zhou B, Chang CP. The secondary heart field is a new site of calcineurin/Nfatc1 signaling for semilunar valve development. *J Mol Cell Cardiol*. (2012) 52:1096–102. doi: 10.1016/j.yjmcc.2012.01.013
23. Bruneau BG. The developmental genetics of congenital heart disease. *Nature*. (2008) 451:943–8. doi: 10.1038/nature06801
24. Hinton RB, Yutzey KE. Heart valve structure and function in development and disease. *Annu Rev Physiol*. (2011) 73:29–46. doi: 10.1146/annurev-physiol-012110-142145
25. Lin CJ, Lin CY, Chen CH, Zhou B, Chang CP. Partitioning the heart: mechanisms of cardiac septation and valve development. *Development*. (2012) 139:3277–99. doi: 10.1242/dev.063495
26. High FA, Epstein JA. The multifaceted role of Notch in cardiac development and disease. *Nat Rev Genet*. (2008) 9:49–61. doi: 10.1038/nrg2279
27. Niessen K, Karsan A. Notch signaling in cardiac development. *Circ Res*. (2008) 102:1169–81. doi: 10.1161/CIRCRESAHA.108.174318
28. de la Pompa JL. Notch signaling in cardiac development and disease. *Pediatr Cardiol*. (2009) 30:643–50. doi: 10.1007/s00246-008-9368-z
29. MacGrogan D, Nus M, de la Pompa JL. Notch signaling in cardiac development and disease. *Curr Top Dev Biol*. (2010) 92:333–65. doi: 10.1016/S0070-2153(10)92011-5
30. MacGrogan D, Luna-Zurita L, de la Pompa JL. Notch signaling in cardiac valve development and disease. *Birth Defects Res A Clin Mol Teratol*. (2011) 91:449–59. doi: 10.1002/bdra.20815

31. Garg V. Notch signaling in aortic valve development and disease. In: Nakanishi T, Markwald RR, Baldwin HS, Keller BB, Srivastava D, and Yamagishi H, editors. *Etiology and Morphogenesis of Congenital Heart Disease: From Gene Function and Cellular Interaction to Morphology*. Tokyo: Springer (2016). p. 371–6.
32. Garg V, Muth AN, Ransom JF, Schluterman MK, Barnes R, King IN, et al. Mutations in NOTCH1 cause aortic valve disease. *Nature*. (2005) 437:270–4. doi: 10.1038/nature03940
33. Lawson KA, Meneses JJ, Pedersen RA. Clonal analysis of epiblast fate during germ layer formation in the mouse embryo. *Development*. (1991) 113:891–911. doi: 10.1242/dev.113.3.891
34. Tam PP, Parameswaran M, Kinder SJ, Weinberger RP. The allocation of epiblast cells to the embryonic heart and other mesodermal lineages: the role of ingression and tissue movement during gastrulation. *Development*. (1997) 124:1631–42. doi: 10.1242/dev.124.9.1631
35. Abu-Issa R, Kirby ML. Heart field: from mesoderm to heart tube. *Annu Rev Cell Dev Biol*. (2007) 23:45–68. doi: 10.1146/annurev.cellbio.23.090506.123331
36. Vincent SD, Buckingham ME. How to make a heart: the origin and regulation of cardiac progenitor cells. *Curr Top Dev Biol*. (2010) 90:1–41. doi: 10.1016/S0070-2153(10)90001-X
37. Kelly RG, Brown NA, Buckingham ME. The arterial pole of the mouse heart forms from Fgf10-expressing cells in pharyngeal mesoderm. *Dev Cell*. (2001) 1:435–40. doi: 10.1016/S1534-5807(01)00040-5
38. Mjaatvedt CH, Nakaoka T, Moreno-Rodriguez R, Norris RA, Kern MJ, Eisenberg CA, et al. The outflow tract of the heart is recruited from a novel heart-forming field. *Dev Biol*. (2001) 238:97–109. doi: 10.1006/dbio.2001.0409
39. Waldo KL, Kumiski DH, Wallis KT, Stadt HA, Hutson MR, Platt DH, et al. Conotruncal myocardium arises from a secondary heart field. *Development*. (2001) 128:3179–88. doi: 10.1242/dev.128.16.3179
40. Cai CL, Liang X, Shi Y, Chu PH, Pfaff SL, Chen J, et al. Isl1 identifies a cardiac progenitor population that proliferates prior to differentiation and contributes a majority of cells to the heart. *Dev Cell*. (2003) 5:877–89. doi: 10.1016/S1534-5807(03)00363-0
41. Armstrong EJ, Bischoff J. Heart valve development: endothelial cell signaling and differentiation. *Circ Res*. (2004) 95:459–70. doi: 10.1161/01.RES.0000141146.95728.da
42. Combs MD, Yutzey KE. Heart valve development: regulatory networks in development and disease. *Circ Res*. (2009) 105:408–21. doi: 10.1161/CIRCRESAHA.109.201566
43. Lincoln J, Yutzey KE. Molecular and developmental mechanisms of congenital heart valve disease. *Birth Defects Res A Clin Mol Teratol*. (2011) 91:526–34. doi: 10.1002/bdra.20799
44. Markwald R, Eisenberg C, Eisenberg L, Trusk T, Sugi Y. Epithelial-mesenchymal transformations in early avian heart development. *Acta Anat*. (1996) 156:173–86. doi: 10.1159/000147845
45. Schroeder JA, Jackson LF, Lee DC, Camenisch TD. Form and function of developing heart valves: coordination by extracellular matrix and growth factor signaling. *J Mol Med*. (2003) 81:392–403. doi: 10.1007/s00109-003-0456-5
46. Lincoln J, Alfieri CM, Yutzey KE. Development of heart valve leaflets and supporting apparatus in chicken and mouse embryos. *Dev Dyn*. (2004) 230:239–50. doi: 10.1002/dvdy.20051
47. Person AD, Klewer SE, Runyan RB. Cell biology of cardiac cushion development. *Int Rev Cytol*. (2005) 243:287–335. doi: 10.1016/S0074-7696(05)43005-3
48. Xie L, Hoffmann AD, Burnicka-Turek O, Friedland-Little JM, Zhang K, Moskowitz IP. Tbx5-hedgehog molecular networks are essential in the second heart field for atrial septation. *Dev Cell*. (2012) 23:280–91. doi: 10.1016/j.devcel.2012.06.006
49. Leung C, Liu Y, Lu X, Kim M, Drysdale TA, Feng Q. Rac1 Signaling is required for anterior second heart field cellular organization and cardiac outflow tract development. *J Am Heart Assoc*. (2015) 5:e002508. doi: 10.1161/JAHA.115.002508
50. Eley L, Alqahtani AM, MacGrogan D, Richardson RV, Murphy L, Salguero-Jimenez A, et al. A novel source of arterial valve cells linked to bicuspid aortic valve without raphe in mice. *Elife*. (2018) 7:e34110. doi: 10.7554/eLife.34110
51. Mifflin JJ, Dupuis LE, Alcala NE, Russell LG, Kern CB. Intercalated cushion cells within the cardiac outflow tract are derived from the myocardial troponin T type 2 (Tnnt2) Cre lineage. *Dev Dyn*. (2018) 247:1005–17. doi: 10.1002/dvdy.24641
52. Wang Y, Wu B, Farrar E, Lui W, Lu P, Zhang D, et al. Notch-Tnf signalling is required for development and homeostasis of arterial valves. *Eur Heart J*. (2017) 38:675–86. doi: 10.1093/eurheartj/ehv520
53. Eisenberg LM, Markwald RR. Molecular regulation of atrioventricular valvuloseptal morphogenesis. *Circ Res*. (1995) 77:1–6. doi: 10.1161/01.RES.77.1.1
54. Yamada M, Revelli JP, Eichele G, Barron M, Schwartz RJ. Expression of chick Tbx-2, Tbx-3, and Tbx-5 genes during early heart development: evidence for BMP2 induction of Tbx2. *Dev Biol*. (2000) 228:95–105. doi: 10.1006/dbio.2000.9927
55. Boyer AS, Ayerinskas, II, Vincent EB, McKinney LA, Weeks DL, Runyan RB. TGFbeta2 and TGFbeta3 have separate and sequential activities during epithelial-mesenchymal cell transformation in the embryonic heart. *Dev Biol*. (1999) 208:530–45. doi: 10.1006/dbio.1999.9211
56. Camenisch TD, Molin DG, Person A, Runyan RB, Gittenberger-de Groot AC, McDonald JA, et al. Temporal and distinct TGFbeta ligand requirements during mouse and avian endocardial cushion morphogenesis. *Dev Biol*. (2002) 248:170–81. doi: 10.1006/dbio.2002.0731
57. Kaartinen V, Voncken JW, Shuler C, Warburton D, Bu D, Heisterkamp N, et al. Abnormal lung development and cleft palate in mice lacking TGF-beta 3 indicates defects of epithelial-mesenchymal interaction. *Nat Genet*. (1995) 11:415–21. doi: 10.1038/ng1295-415
58. Ma L, Lu MF, Schwartz RJ, Martin JF. Bmp2 is essential for cardiac cushion epithelial-mesenchymal transition and myocardial patterning. *Development*. (2005) 132:5601–11. doi: 10.1242/dev.02156
59. Wang Y, Wu B, Chamberlain AA, Lui W, Koirala P, Susztak K, et al. Endocardial to myocardial notch-wnt-bmp axis regulates early heart valve development. *PLoS ONE*. (2013) 8:e60244. doi: 10.1371/journal.pone.0060244
60. Jiao K, Kulessa H, Tompkins K, Zhou Y, Batts L, Baldwin HS, et al. An essential role of Bmp4 in the atrioventricular septation of the mouse heart. *Genes Dev*. (2003) 17:2362–7. doi: 10.1101/gad.1124803
61. McCulley DJ, Kang JO, Martin JF, Black BL. BMP4 is required in the anterior heart field and its derivatives for endocardial cushion remodeling, outflow tract septation, and semilunar valve development. *Dev Dyn*. (2008) 237:3200–9. doi: 10.1002/dvdy.21743
62. Luna-Zurita L, Prados B, Grego-Bessa J, Luxan G, del Monte G, Benguria A, et al. Integration of a Notch-dependent mesenchymal gene program and Bmp2-driven cell invasiveness regulates murine cardiac valve formation. *J Clin Invest*. (2010) 120:3493–507. doi: 10.1172/JCI42666
63. Harrelson Z, Kelly RG, Goldin SN, Gibson-Brown JJ, Bollag RJ, Silver LM, et al. Tbx2 is essential for patterning the atrioventricular canal and for morphogenesis of the outflow tract during heart development. *Development*. (2004) 131:5041–52. doi: 10.1242/dev.01378
64. Singh R, Hoogaars WM, Barnett P, Grieskamp T, Rana MS, Buermans H, et al. Tbx2 and Tbx3 induce atrioventricular myocardial development and endocardial cushion formation. *Cell Mol Life Sci*. (2012) 69:1377–89. doi: 10.1007/s00018-011-0884-2
65. Rusanescu G, Weissleder R, Aikawa E. Notch signaling in cardiovascular disease and calcification. *Curr Cardiol Rev*. (2008) 4:148–56. doi: 10.2174/157340308785160552
66. MacGrogan D, Munch J, de la Pompa JL. Notch and interacting signalling pathways in cardiac development, disease, and regeneration. *Nat Rev Cardiol*. (2018) 15:685–704. doi: 10.1038/s41569-018-0100-2
67. Stahl M, Uemura K, Ge C, Shi S, Tashima Y, Stanley P. Roles of Pofut1 and O-fucose in mammalian Notch signaling. *J Biol Chem*. (2008) 283:13638–51. doi: 10.1074/jbc.M802027200
68. Shi S, Stanley P. Protein O-fucosyltransferase 1 is an essential component of Notch signaling pathways. *Proc Natl Acad Sci USA*. (2003) 100:5234–9. doi: 10.1073/pnas.0831126100
69. Benedito R, Roca C, Sorensen I, Adams S, Gossler A, Fruttiger M, et al. The notch ligands Dll4 and Jagged1 have opposing effects on angiogenesis. *Cell*. (2009) 137:1124–35. doi: 10.1016/j.cell.2009.03.025

70. Fortini ME. Notch signaling: the core pathway and its posttranslational regulation. *Dev Cell*. (2009) 16:633–47. doi: 10.1016/j.devcel.2009.03.010
71. Rones MS, McLaughlin KA, Raffin M, Mercola M. Serrate and Notch specify cell fates in the heart field by suppressing cardiomyogenesis. *Development*. (2000) 127:3865–76. doi: 10.1242/dev.127.17.3865
72. Schroeder T, Fraser ST, Ogawa M, Nishikawa S, Oka C, Bornkamm GW, et al. Recombination signal sequence-binding protein Jkappa alters mesodermal cell fate decisions by suppressing cardiomyogenesis. *Proc Natl Acad Sci USA*. (2003) 100:4018–23. doi: 10.1073/pnas.0438008100
73. Contakos SP, Gaydos CM, Pfeil EC, McLaughlin KA. Subdividing the embryo: a role for Notch signaling during germ layer patterning in Xenopus laevis. *Dev Biol*. (2005) 288:294–307. doi: 10.1016/j.ydbio.2005.09.015
74. Nemir M, Croquelois A, Pedrazzini T, Radtke F. Induction of cardiogenesis in embryonic stem cells via downregulation of Notch1 signaling. *Circ Res*. (2006) 98:1471–8. doi: 10.1161/01.RES.0000226497.52052.2a
75. Lescroart F, Wang X, Lin X, Swedlund B, Gargouri S, Sanchez-Danes A, et al. Defining the earliest step of cardiovascular lineage segregation by single-cell RNA-seq. *Science*. (2018) 359:1177–81. doi: 10.1126/science.aao4174
76. Grego-Bessa J, Luna-Zurita L, del Monte G, Bolos V, Melgar P, Arandilla A, et al. Notch signaling is essential for ventricular chamber development. *Dev Cell*. (2007) 12:415–29. doi: 10.1016/j.devcel.2006.12.011
77. Timmerman LA, Grego-Bessa J, Raya A, Bertran E, Perez-Pomares JM, Diez J, et al. Notch promotes epithelial-mesenchymal transition during cardiac development and oncogenic transformation. *Genes Dev*. (2004) 18:99–115. doi: 10.1101/gad.276304
78. MacGrogan D, D'Amato G, Travisano S, Martinez-Poveda B, Luxan G, Del Monte-Nieto G, et al. Sequential ligand-dependent notch signaling activation regulates valve primordium formation and morphogenesis. *Circ Res*. (2016) 118:1480–97. doi: 10.1161/CIRCRESAHA.115.308077
79. High FA, Zhang M, Proweller A, Tu L, Parmacek MS, Pear WS, et al. An essential role for Notch in neural crest during cardiovascular development and smooth muscle differentiation. *J Clin Invest*. (2007) 117:353–63. doi: 10.1172/JCI30070
80. Limbourg FP, Takeshita K, Radtke F, Bronson RT, Chin MT, Liao JK. Essential role of endothelial Notch1 in angiogenesis. *Circulation*. (2005) 111:1826–32. doi: 10.1161/01.CIR.0000160870.93058.DD
81. Eldadah ZA, Hamosh A, Biery NJ, Montgomery RA, Duke M, Elkins R, et al. Familial tetralogy of Fallot caused by mutation in the jagged1 gene. *Hum Mol Genet*. (2001) 10:163–9. doi: 10.1093/hmg/10.2.163
82. Li L, Krantz ID, Deng Y, Genin A, Banta AB, Collins CC, et al. Alagille syndrome is caused by mutations in human Jagged1, which encodes a ligand for Notch1. *Nat Genet*. (1997) 16:243–51. doi: 10.1038/ng0797-243
83. Oda T, Elkahloun AG, Pike BL, Okajima K, Krantz ID, Genin A, et al. Mutations in the human Jagged1 gene are responsible for Alagille syndrome. *Nat Genet*. (1997) 16:235–42. doi: 10.1038/ng0797-235
84. Briot A, Civelek M, Seki A, Hoi K, Mack JJ, Lee SD, et al. Endothelial NOTCH1 is suppressed by circulating lipids and antagonizes inflammation during atherosclerosis. *J Exp Med*. (2015) 212:2147–63. doi: 10.1084/jem.20150603
85. Li X, Zhang X, Leathers R, Makino A, Huang C, Parsa P, et al. Notch3 signaling promotes the development of pulmonary arterial hypertension. *Nat Med*. (2009) 15:1289–97. doi: 10.1038/nm.2021
86. Xiao Y, Gong D, Wang W. Soluble JAGGED1 inhibits pulmonary hypertension by attenuating notch signaling. *Arterioscler Thromb Vasc Biol*. (2013) 33:2733–9. doi: 10.1161/ATVBAHA.113.302062
87. Dabral S, Tian X, Kojonazarov B, Savai R, Ghofrani HA, Weissmann N, et al. Notch1 signalling regulates endothelial proliferation and apoptosis in pulmonary arterial hypertension. *Eur Respir J*. (2016) 48:1137–49. doi: 10.1183/13993003.00773-2015
88. Babicheva A, Yuan JX. Endothelial Notch1 in pulmonary hypertension. *Circ Res*. (2019) 124:176–9. doi: 10.1161/CIRCRESAHA.118.314496
89. Nigam V, Srivastava D. Notch1 represses osteogenic pathways in aortic valve cells. *J Mol Cell Cardiol*. (2009) 47:828–34. doi: 10.1016/j.yjmcc.2009.08.008
90. Acharya A, Hans CP, Koenig SN, Nichols HA, Galindo CL, Garner HR, et al. Inhibitory role of Notch1 in calcific aortic valve disease. *PLoS ONE*. (2011) 6:e27743. doi: 10.1371/journal.pone.0027743
91. Nus M, MacGrogan D, Martinez-Poveda B, Benito Y, Casanova JC, Fernandez-Aviles F, et al. Diet-induced aortic valve disease in mice haploinsufficient for the Notch pathway effector RBPJK/CSL. *Arterioscler Thromb Vasc Biol*. (2011) 31:1580–8. doi: 10.1161/ATVBAHA.111.227561
92. Del Monte G, Grego-Bessa J, Gonzalez-Rajal A, Bolos V, De La Pompa JL. Monitoring Notch1 activity in development: evidence for a feedback regulatory loop. *Dev Dyn*. (2007) 236:2594–614. doi: 10.1002/dvdy.21246
93. Hofmann JJ, Briot A, Enciso J, Zovein AC, Ren S, Zhang ZW, et al. Endothelial deletion of murine Jag1 leads to valve calcification and congenital heart defects associated with Alagille syndrome. *Development*. (2012) 139:4449–60. doi: 10.1242/dev.084871
94. Niessen K, Fu YX, Chang L, Hoodless PA, McFadden D, Karsan A. Slug is a direct Notch target required for initiation of cardiac cushion cellularization. *J Cell Biol*. (2008) 182:315–25. doi: 10.1083/jcb.200710067
95. High FA, Jain R, Stoller JZ, Antonucci NB, Lu MM, Loomes KM, et al. Murine Jagged1/Notch signaling in the second heart field orchestrates Fgf8 expression and tissue-tissue interactions during outflow tract development. *J Clin Invest*. (2009) 119:1986–96. doi: 10.1172/JCI38922
96. Kokubo H, Miyagawa-Tomita S, Tomimatsu H, Nakashima Y, Nakazawa M, Saga Y, et al. Targeted disruption of hesr2 results in atrioventricular valve anomalies that lead to heart dysfunction. *Circ Res*. (2004) 95:540–7. doi: 10.1161/01.RES.0000141136.85194.f0
97. Kokubo H, Miyagawa-Tomita S, Nakazawa M, Saga Y, Johnson RL. Mouse hesr1 and hesr2 genes are redundantly required to mediate Notch signaling in the developing cardiovascular system. *Dev Biol*. (2005) 278:301–9. doi: 10.1016/j.ydbio.2004.10.025
98. Kokubo H, Tomita-Miyagawa S, Hamada Y, Saga Y. Hesr1 and Hesr2 regulate atrioventricular boundary formation in the developing heart through the repression of Tbx2. *Development*. (2007) 134:747–55. doi: 10.1242/dev.02777
99. Rutenberg JB, Fischer A, Jia H, Gessler M, Zhong TP, Mercola M. Developmental patterning of the cardiac atrioventricular canal by Notch and Hairy-related transcription factors. *Development*. (2006) 133:4381–90. doi: 10.1242/dev.02607
100. Soto-Navarrete MT, Lopez-Unzu MA, Duran AC, Fernandez B. Embryonic development of bicuspid aortic valves. *Prog Cardiovasc Dis*. (2020) 63:407–18. doi: 10.1016/j.pcad.2020.06.008
101. Mohamed SA, Aherrahrou Z, Liptau H, Erasmi AW, Hagemann C, Wrobel S, et al. Novel missense mutations (p.T596M and p.P1797H) in NOTCH1 in patients with bicuspid aortic valve. *Biochem Biophys Res Commun*. (2006) 345:1460–5. doi: 10.1016/j.bbrc.2006.05.046
102. Oudit GY, Chow CM, Cantor WJ. Calcific bicuspid aortic valve disease in a patient with Cornelia de Lange syndrome: linking altered Notch signaling to aortic valve disease. *Cardiovasc Pathol*. (2006) 15:165–7. doi: 10.1016/j.carpath.2006.02.002
103. McKellar SH, Tester DJ, Yagubyan M, Majumdar R, Ackerman MJ, Sundt TM III. Novel NOTCH1 mutations in patients with bicuspid aortic valve disease and thoracic aortic aneurysms. *J Thorac Cardiovasc Surg*. (2007) 134:290–6. doi: 10.1016/j.jtcvs.2007.02.041
104. McBride KL, Riley MF, Zender GA, Fitzgerald-Butt SM, Towbin JA, Belmont JW, et al. NOTCH1 mutations in individuals with left ventricular outflow tract malformations reduce ligand-induced signaling. *Hum Mol Genet*. (2008) 17:2886–93. doi: 10.1093/hmg/ddn187
105. Koenig SN, Bosse K, Majumdar U, Bonachea EM, Radtke F, Garg V. Endothelial Notch1 is required for proper development of the semilunar valves and cardiac outflow tract. *J Am Heart Assoc*. (2016) 5:e003075. doi: 10.1161/JAHA.115.003075
106. Wu B, Wang Y, Lui W, Langworthy M, Tompkins KL, Hatzopoulos AK, et al. Nfatc1 coordinates valve endocardial cell lineage development required for heart valve formation. *Circ Res*. (2011) 109:183–92. doi: 10.1161/CIRCRESAHA.111.245035
107. Zhou B, Wu B, Tompkins KL, Boyer KL, Grindley JC, Baldwin HS. Characterization of Nfatc1 regulation identifies an enhancer required for gene expression that is specific to pro-valve endocardial cells in the developing heart. *Development*. (2005) 132:1137–46. doi: 10.1242/dev.01640
108. Dutta P, Lincoln J. Calcific aortic valve disease: a developmental biology perspective. *Curr Cardiol Rep*. (2018) 20:21. doi: 10.1007/s11886-018-0968-9

109. Bravo-Jaimes K, Prakash SK. Genetics in bicuspid aortic valve disease: where are we? *Prog Cardiovasc Dis*. (2020) 63:398–406. doi: 10.1016/j.pcad.2020.06.005
110. Martin PS, Kloesel B, Norris RA, Lindsay M, Milan D, Body SC. Embryonic development of the bicuspid aortic valve. *J Cardiovasc Dev Dis*. (2015) 2:248–72. doi: 10.3390/jcdd2040248
111. Siu SC, Silversides CK. Bicuspid aortic valve disease. *J Am Coll Cardiol*. (2010) 55:2789–800. doi: 10.1016/j.jacc.2009.12.068
112. Niaz T, Poterucha JT, Olson TM, Johnson JN, Craviari C, Nienaber T, et al. Characteristic morphologies of the bicuspid aortic valve in patients with genetic syndromes. *J Am Soc Echocardiogr*. (2018) 31:194–200. doi: 10.1016/j.echo.2017.10.008
113. Shaner RF. Abnormal pulmonary and aortic semilunar valves in embryos. *Anat Rec*. (1963) 147:5–13. doi: 10.1002/ar.1091470103
114. Sans-Coma V, Arque JM, Duran AC, Cardo M, Fernandez B. Coronary artery anomalies and bicuspid aortic valves in the Syrian hamster. *Basic Res Cardiol*. (1991) 86:148–53. doi: 10.1007/BF02190547
115. Sans-Coma V, Cardo M, Thiene G, Fernandez B, Arque JM, Duran AC. Bicuspid aortic and pulmonary valves in the Syrian hamster. *Int J Cardiol*. (1992) 34:249–54. doi: 10.1016/0167-5273(92)90021-T
116. Sans-Coma V, Fernandez B, Duran AC, Thiene G, Arque JM, Munoz-Chapuli R, et al. Fusion of valve cushions as a key factor in the formation of congenital bicuspid aortic valves in Syrian hamsters. *Anat Rec*. (1996) 244:490–8. doi: 10.1002/(SICI)1097-0185(199604)244:4<490::AID-AR7>3.0.CO;2-Z
117. Fernandez B, Duran AC, Fernandez-Gallego T, Fernandez MC, Such M, Arque JM, et al. Bicuspid aortic valves with different spatial orientations of the leaflets are distinct etiological entities. *J Am Coll Cardiol*. (2009) 54:2312–8. doi: 10.1016/j.jacc.2009.07.044
118. Lee TC, Zhao YD, Courtman DW, Stewart DJ. Abnormal aortic valve development in mice lacking endothelial nitric oxide synthase. *Circulation*. (2000) 101:2345–8. doi: 10.1161/01.CIR.101.20.2345
119. Iwamoto R, Mine N, Kawaguchi T, Minami S, Saeki K, Mekada E. HB-EGF function in cardiac valve development requires interaction with heparan sulfate proteoglycans. *Development*. (2010) 137:2205–14. doi: 10.1242/dev.048926
120. Manno G, Bentivegna R, Morreale P, Nobile D, Santangelo A, Novo S, et al. Chronic inflammation: A key role in degeneration of bicuspid aortic valve. *J Mol Cell Cardiol*. (2019) 130:59–64. doi: 10.1016/j.yjmcc.2019.03.013
121. El Accaoui RN, Gould ST, Hajj GP, Chu Y, Davis MK, Kraft DC, et al. Aortic valve sclerosis in mice deficient in endothelial nitric oxide synthase. *Am J Physiol Heart Circ Physiol*. (2014) 306:H1302–13. doi: 10.1152/ajpheart.00392.2013
122. Pawade TA, Newby DE, Dweck MR. Calcification in aortic stenosis: the skeleton key. *J Am Coll Cardiol*. (2015) 66:561–77. doi: 10.1016/j.jacc.2015.05.066
123. O'Brien KD, Probstfield JL, Caulfield MT, Nasir K, Takasu J, Shavelle DM, et al. Angiotensin-converting enzyme inhibitors and change in aortic valve calcium. *Arch Intern Med*. (2005) 165:858–62. doi: 10.1001/archinte.165.8.858
124. Cote N, Mahmut A, Fournier D, Boulanger MC, Couture C, Despres JP, et al. Angiotensin receptor blockers are associated with reduced fibrosis and interleukin-6 expression in calcific aortic valve disease. *Pathobiology*. (2014) 81:15–24. doi: 10.1159/000350896
125. Schurgers LJ, Uitto J, Reutelingsperger CP. Vitamin K-dependent carboxylation of matrix Gla-protein: a crucial switch to control ectopic mineralization. *Trends Mol Med*. (2013) 19:217–26. doi: 10.1016/j.molmed.2012.12.008
126. Toshima T, Watanabe T, Narumi T, Otaki Y, Shishido T, Aono T, et al. Therapeutic inhibition of microRNA-34a ameliorates aortic valve calcification via modulation of Notch1-Runx2 signaling. *Cardiovasc Res*. (2019) 116:983–94. doi: 10.1093/cvr/cvz210
127. Akahori H, Tsujino T, Masuyama T, Ishihara M. Mechanisms of aortic stenosis. *J Cardiol*. (2018) 71:215–20. doi: 10.1016/j.jjcc.2017.11.007
128. Alonso-Montes C, Martin M, Martinez-Arias L, Coto E, Naves-Diaz M, Moris C, et al. Variants in cardiac GATA genes associated with bicuspid aortic valve. *Eur J Clin Invest*. (2018) 48:e13027. doi: 10.1111/eci.13027
129. Gharibeh L, Komati H, Bosse Y, Boodhwani M, Heydarpour M, Fortier M, et al. GATA6 regulates aortic valve remodeling, and its haploinsufficiency leads to right-left type bicuspid aortic valve. *Circulation*. (2018) 138:1025–38. doi: 10.1161/CIRCULATIONAHA.117.029506
130. Li RG, Xu YJ, Wang J, Liu XY, Yuan F, Huang RT, et al. GATA4 Loss-of-Function mutation and the congenitally bicuspid aortic valve. *Am J Cardiol*. (2018) 121:469–74. doi: 10.1016/j.amjcard.2017.11.012
131. Laforest B, Andelfinger G, Nemer M. Loss of Gata5 in mice leads to bicuspid aortic valve. *J Clin Invest*. (2011) 121:2876–87. doi: 10.1172/JCI44555
132. Bonachea EM, Chang SW, Zender G, LaHaye S, Fitzgerald-Butt S, McBride KL, et al. Rare GATA5 sequence variants identified in individuals with bicuspid aortic valve. *Pediatr Res*. (2014) 76:211–6. doi: 10.1038/pr.2014.67
133. Kostina A, Shishkova A, Ignatieva E, Irtyuga O, Bogdanova M, Levchuk K, et al. Different Notch signaling in cells from calcified bicuspid and tricuspid aortic valves. *J Mol Cell Cardiol*. (2018) 114:211–9. doi: 10.1016/j.yjmcc.2017.11.009
134. Bosse K, Hans CP, Zhao N, Koenig SN, Huang N, Guggilam A, et al. Endothelial nitric oxide signaling regulates Notch1 in aortic valve disease. *J Mol Cell Cardiol*. (2013) 60:27–35. doi: 10.1016/j.yjmcc.2013.04.001
135. Koenig SN, Bosse KM, Nadorlik HA, Lilly B, Garg V. Evidence of Aortopathy in Mice with Haploinsufficiency of Notch1 in Nos3-Null Background. *J Cardiovasc Dev Dis*. (2015) 2:17–30. doi: 10.3390/jcdd2010017
136. White MP, Theodoris CV, Liu L, Collins WJ, Blue KW, Lee JH, et al. NOTCH1 regulates matrix gla protein and calcification gene networks in human valve endothelium. *J Mol Cell Cardiol*. (2015) 84:13–23. doi: 10.1016/j.yjmcc.2015.04.006
137. Majumdar U, Manivannan S, Basu M, Ueyama Y, Blaser MC, Cameron E, et al. Nitric oxide prevents aortic valve calcification by S-nitrosylation of USP9X to activate NOTCH signaling. *Sci Adv*. (2021) 7:eabe3706. doi: 10.1126/sciadv.abe3706
138. Irtyuga O, Malashicheva A, Zhiduleva E, Freylikhman O, Rotar O, Back M, et al. NOTCH1 mutations in aortic stenosis: association with Osteoprotegerin/RANK/RANKL. *Biomed Res Int*. (2017) 2017:6917907. doi: 10.1155/2017/6917907
139. Theodoris CV, Li M, White MP, Liu L, He D, Pollard KS, et al. Human disease modeling reveals integrated transcriptional and epigenetic mechanisms of NOTCH1 haploinsufficiency. *Cell*. (2015) 160:1072–86. doi: 10.1016/j.cell.2015.02.035
140. Theodoris CV, Mourkioti F, Huang Y, Ranade SS, Liu L, Blau HM, et al. Long telomeres protect against age-dependent cardiac disease caused by NOTCH1 haploinsufficiency. *J Clin Invest*. (2017) 127:1683–88. doi: 10.1172/JCI90338
141. Theodoris CV, Zhou P, Liu L, Zhang Y, Nishino T, Huang Y, et al. Network-based screen in iPSC-derived cells reveals therapeutic candidate for heart valve disease. *Science*. (2021) 371:eabd0724. doi: 10.1126/science.abd0724

Conflict of Interest: The authors declare that the research was conducted in the absence of any commercial or financial relationships that could be construed as a potential conflict of interest.

frontiers in Cardiovascular Medicine

ORIGINAL RESEARCH
published: 26 August 2021
doi: 10.3389/fcvm.2021.709741

Decreased Glucagon-Like Peptide-1 Is Associated With Calcific Aortic Valve Disease: GLP-1 Suppresses the Calcification of Aortic Valve Interstitial Cells

Fan Xiao[1†], Qing Zha[1†], Qianru Zhang[1†], Qihong Wu[2], Zhongli Chen[2], Ying Yang[3], Ke Yang[2] and Yan Liu[1*]*

[1] Department of Cardiology, Shanghai Ninth People's Hospital, Shanghai Jiaotong University School of Medicine, Shanghai, China, [2] Department of Vascular and Cardiology, Ruijin Hospital, Shanghai Jiaotong University School of Medicine, Shanghai, China, [3] Department of Endocrinology, The Second People's Hospital of Yunnan Province, Kunming, China

OPEN ACCESS

Edited by:
Joy Lincoln,
Medical College of Wisconsin,
United States

Reviewed by:
Kristyn Simcha Masters,
University of Wisconsin-Madison,
United States
Ernesto Greco,
Sapienza University of Rome, Italy

***Correspondence:**
Yan Liu
liuyan_ivy@126.com
Ke Yang
ykk_ykkk@126.com

[†]These authors have contributed equally to this work

Specialty section:
This article was submitted to Heart Valve Disease, a section of the journal Frontiers in Cardiovascular Medicine

Received: 14 May 2021
Accepted: 23 July 2021
Published: 26 August 2021

Citation:
Xiao F, Zha Q, Zhang Q, Wu Q, Chen Z, Yang Y, Yang K and Liu Y (2021) Decreased Glucagon-Like Peptide-1 Is Associated With Calcific Aortic Valve Disease: GLP-1 Suppresses the Calcification of Aortic Valve Interstitial Cells. Front. Cardiovasc. Med. 8:709741. doi: 10.3389/fcvm.2021.709741

Objectives: This study explores the concentration and role of glucagon-like peptide-1 (GLP-1) in calcific aortic valve disease (CAVD).

Background: Calcific aortic valve disease is a chronic disease presenting with aortic valve degeneration and mineralization. We hypothesized that the level of GLP-1 is associated with CAVD and that it participates in the calcification of aortic valve interstitial cells (AVICs).

Methods: We compared the concentration of GLP-1 between 11 calcific and 12 normal aortic valve tissues by immunohistochemical (IHC) analysis. ELISA was used to measure GLP-1 in serum of the Control (n = 197) and CAVD groups (n = 200). The effect of GLP-1 on the calcification of AVICs and the regulation of calcific gene expression were also characterized.

Results: The GLP-1 concentration in the calcific aortic valves was 39% less than that in the control non-calcified aortic valves. Its concentration in serum was 19.3% lower in CAVD patients. Multivariable regression analysis demonstrated that GLP-1 level was independently associated with CAVD risk. *In vitro*, GLP-1 antagonized AVIC calcification in a dose- and time-dependent manner and it down-regulated RUNX2, MSX2, BMP2, and BMP4 expression but up-regulated SOX9 expression.

Conclusions: A reduction in GLP-1 was associated with CAVD, and GLP-1 participated in the mineralization of AVICs by regulating specific calcific genes. GLP-1 warrants consideration as a novel treatment target for CAVD.

Keywords: glucagon-like peptide-1, calcific aortic valve disease, calcification, aortic valve interstitial cells, age

INTRODUCTION

Glucagon-like peptide-1 (GLP-1), a hormone of 30 amino acids, is derived from proglucagon (1). It can increase insulin's sensitivity in regulating blood glucose (2), which is an effect that partially reverses aging-related degenerative disease (3). Calcific aortic valve disease (CAVD) is a common and chronic heart valve disease (4) that exhibits aortic valve thickening and calcification (5).

Calcific aortic valve disease involves chronic inflammatory responses (6), lipid accumulation (7, 8), extracellular matrix rebuilding (9, 10), and osteogenic-related gene activation (11, 12). Glucagon-like peptide-1 has shown benefits on cardiovascular function in both preclinical and clinical studies (13–15). Furthermore, a 5-week infusion of GLP-1 (2.5 pmol/kg/min) added to standard therapy in patients with heart function of New York Heart Association class III/IV improved the LV ejection fraction in both diabetic and non-diabetic patients (16). However, the relationship between GLP-1 and CAVD has not been elucidated.

Valve interstitial cells (VICs) are heterogeneous cells that present various phenotypes (myofibroblasts, fibroblasts, and smooth muscle-like cells) and they participate in the physiological function of the aortic valve (17). For instance, the risk factors for CAVD evoke osteogenic signaling, which turn innate quiescent valve interstitial cells (qVICs) into activated valve interstitial cells (aVICs) and facilitate them to differentiate into osteoblastic valve interstitial cells (obVICs) (4, 18, 19). Glucagon-like peptide-1 suppresses vascular smooth muscle cell (VSMC) mineralization by reducing osteogenic gene expression and activating arterial calcification (20). The phenotypic changes in VICs are the main cytological events leading to aortic valve calcification; however, whether GLP-1 regulates the phenotype of VICs is unknown.

In this work, we hypothesized that GLP-1 is differentially regulated in the serum and tissue of CAVD patients and that its concentration is associated with aortic valve calcification.

MATERIALS AND METHODS

Patients

We performed a retrospective study on 200 aortic valves with calcific degeneration (CAVD) and 197 without calcific degeneration between January 2013 and August 2014 in patients recruited from the database of Shanghai Rui Jin Hospital who underwent echocardiographic screening. According to recommendations of the American Society of Echocardiography during hospitalization and patients entered into the screening procedure (21), and underwent standard transthoracic echocardiography and Doppler flow imaging. Calcific aortic valve disease was defined as opaque leaflets with focal areas of mild thickening and increased stiffness with or without an elevated peak trans-aortic valve flow velocity ($\geq$2.0 m/s) (22) (**Figure 1**). Patients with a history of rheumatic disease, endocarditis, or an inflammatory disease were excluded. Detailed medical and family histories were recorded, and fasting blood samples were collected during physical check-up. The diagnosis of type 2 diabetes, hypertension, and coronary artery diseases (CAD)was made according to corresponding criteria of the American Diabetes Association (23), hypertension (24), and CAD (25) guidelines.

Human aortic valves with calcification were obtained from 11 patients who underwent valve replacement. Aortic valve leaflets were collected from the explanted hearts of 12 patients undergoing heart transplantation as normal aortic valves. The study protocol was approved by the Ethics Committee of Ruijin Hospital, Shanghai Jiaotong University School of Medicine, and written informed consent was obtained from all patients.

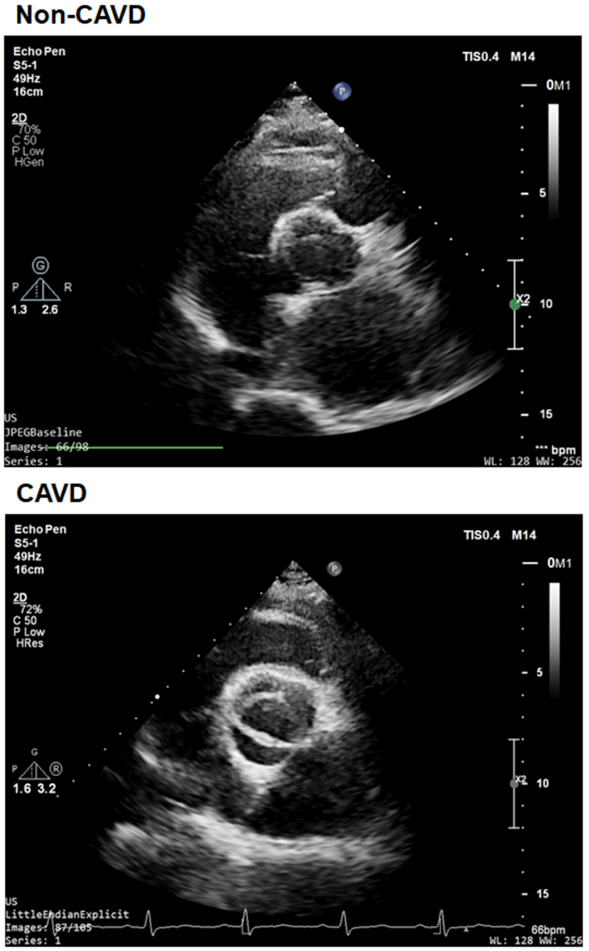

FIGURE 1 | A representative echo image of non-CAVD (upper) and CAVD (bottom).

Reagents and Antibodies

A High Sensitivity GLP-1 Active ELISA Kit (Cat# EZGLPHS-35K, Millipore, MA, USA) was used to measure GLP-1 in serum. Recombinant GLP-1 peptide (Human, Cat #SCP0153), a 3,3′-Diaminobenzidine Liquid Substrate System (Cat# D3939), an Alkaline Phosphatase Diethanolamine (ALP) Activity Kit (Cat# AP0100), Alizarin Red S (Cat# A5533), and a Masson Stain Kit (Cat# HT15) were purchased from Sigma-Aldrich (MO, USA). Primary antibodies were used to detect GLP-1 (Cat# ab22625, Abcam, MA, USA), RUNX2 (Cat# 12556, Cell Signaling Technology, MA, USA), MSX2 (Cat# ab69058, Abcam, MA, USA), SOX9 (Cat# 82630, Cell Signaling Technology, MA, USA), BMP2 (Cat# ab14933, Abcam, MA, USA), BMP4 (Cat# ab39973Abcam, MA, USA), and β-actin (Cat# 4970, Cell Signaling Technology, MA, USA) in immunohistochemical (IHC) or immunoblot assays. The secondary antibodies were

horseradish peroxidase (HRP)-conjugated anti-rabbit antibodies (Cat# 7074, Cell Signaling Technology, MA, USA) or Alexa Fluor 594- or Alexa Fluor 488-conjugated anti-rabbit antibodies (Cat# R37119 or Cat# A27034, Thermo Fisher Scientific, NY, USA). Fetal bovine serum (FBS, Cat# 16000044), DMEM:F12 culture medium, penicillin, and streptomycin were from Gibco BRL (NY, USA).

Primary Aortic Valve Interstitial Cell Culture

Human aortic valve leaflets from the explanted hearts were gathered to culture the primary aortic valve interstitial cells (AVICs) (26). Briefly, valve leaflets were subjected to collagenase digestion and gently scraped to expose the endothelial layer. The leaflets were then cut into microscopic pieces (1–2 mm^2) and cultured in DMEM:F12 (1:1) supplemented with 20% FBS, L-glutamine (2 mmol/L), penicillin (100 U/ml), and streptomycin (100 μg/ml). Cells were grown with 5% CO_2 at 37°C. Upon reaching 80% confluency, the AVICs were passaged using trypsin-EDTA. AVICs between passage 3 and 8 were used for experiments.

Immunohistochemistry

Human calcific ($n = 11$) and non-calcific aortic valves ($n = 12$) were used for histological and immunochemical analysis. Samples were fixed in 4% paraformaldehyde overnight and cut into serial cryosections (5 μm thickness). Sections were used for hematoxylin and eosin (H&E) staining, Alizarin Red S staining, and Masson trichrome staining. Glucagon-like peptide-1 in the valves was detected by IHC using anti-GLP-1 antibody (1:50). After incubation with HRP-conjugated secondary antibodies (1:100), sections were incubated with 3,3′-diaminobenzidine.

The sections of primary AVICs were used for immunofluorescence analysis. The cells were immune-stained with anti-RUNX2 (1:50), anti-MSX2 (1:50), anti-SOX9 (1:50), anti-BMP2 (1:50), or anti-BMP4 (1:50) for 12 h at 4°C and incubated with Alexa Fluor 549- or Alexa Fluor 488-conjugated secondary antibody (1:1,000).

In vitro Calcification of AVICs

Primary AVICs were isolated from the human aortic valve. Aortic valve interstitial cell calcification was induced in osteogenic medium containing DMEM and supplemented with 15% FBS, 50 mg/ml ascorbate-2-phosphate, 10 nM dexamethasone, and 10 mM β-glycerol phosphate (27). The culture medium was changed every 48–72 h, and the cells were harvested for 3 weeks. Aortic valve interstitial cell calcification was determined by Alizarin Red S staining. The cells were washed in distilled water and then exposed to freshly prepared 2% Alizarin Red S (pH to 4.1–4.3) for 5 min (red/orange as positive staining). For quantitative analysis of Alizarin Red S staining, the dye was released from the cell matrix by incubating with cetylpyridinium chloride for 15 min. The released dye was quantified by spectrophotometry at 540 nm. Alkaline Phosphatase Diethanolamine activity was determined using the spectrophotometric measurement of the p-nitrophenol level in the AVICs (28). The amount of Alizarin Red S staining and ALP activity were normalized to the total amount of cellular protein.

TABLE 1 | Baseline characteristics of aortic valves obtained from patients.

Variable	Non-CAVD ($n = 12$)	CAVD ($n = 11$)	*p*
Age, years	62 (58–66)	72 (65–77)	<0.01
BMI, kg/m^2	26 (24–27)	23 (21–25)	0.02
Male, *n* (%)	10 (83)	10 (91)	NS
Smoking status, *n* (%)	2 (17)	3 (27)	NS
Alcohol consumption, *n* (%)	1 (8)	3 (27)	NS
Hypertension, *n* (%)	8 (67)	7 (64)	NS
CHD, *n* (%)	12 (100)	11 (100)	NS
DM, *n* (%)	3 (25)	0 (0)	NS
SBP, mmHg	141 (129–156)	131 (115–143)	NS
DBP, mmHg	80 (71–88)	72 (58–78)	NS
Fasting glucose, mmol/L	4.96 (4.12–5.94)	5.40 (4.88–5.88)	NS
HbA1c, %	6.5 (5.8–7.0)	5.7 (5.5–6.0)	0.03
TG, mmol/L	1.77 (1.06–2.48)	1.35 (0.69–1.96)	NS
TC, mmol/L	4.07 (3.03–4.81)	4.59 (3.37–5.55)	NS
HDL-c, mmol/L	0.88 (0.67–1.06)	1.08 (0.94–1.26)	0.04
LDL-C, mmol/L	2.55 (1.60–3.44)	2.78 (1.77–3.17)	NS
Lp(a), g/L	0.21 (0.07–0.30)	0.30 (0.10–0.31)	NS
BUN, mmol/L	5.17 (4.33–5.80)	6.55 (4.20–8.20)	NS
SCr, μmol/L	83.08 (78–91)	104.55 (76.00–123.00)	NS
eGFR, ml/min	84.18 (81.25–89.88)	67.89 (52.70–88.60)	NS
Cystatin, mg/L	1.10 (0.89–1.20)	1.39 (1.14–1.72)	0.04
Ca, mmol/L	2.22 (2.13–2.32)	2.18 (2.07–2.31)	NS
P, mmol/L	1.17 (1.09–1.29)	0.99 (0.85–1.14)	0.02
Aortic valve area, cm^2	–	0.74 ± 0.07	–
Aortic mean gradient, mmHg	–	47 ± 3	–
Glucose lowering therapy, *n* (%)	3 (25)	0 (0)	NS
Statins, *n* (%)	11 (92)	11 (100)	NS

Continuous variables are presented as the median (25th−75th percentile), and categorical variables are expressed as n (%). For continuous variables, Mann-Whitney U-tests were performed to assess differences. Differences in proportions were analyzed by 2 × 2 chi-square tests.

Quantitative Real-Time PCR

Total RNA was extracted as described above. Briefly, 5 μg of total RNA was reverse-transcribed into cDNA using a reverse transcription system (Promega, WI, USA). PCR amplification was performed with Power SYBR Green PCR Master Mix (Applied Biosystems, CA, USA) in a StepOne system (Applied Biosystems). The oligonucleotides used in quantitative real-time PCR analysis are listed in **Supplementary Table 1**. The gene expression levels were normalized to beta-actin, and the data were analyzed with StepOne software v2.1 (Applied Biosystems).

Western Blot

Cells were lysed with the ProteoJET Mammalian Cell Lysis Reagent (Fermentas, MD, USA) to extract cytoplasmic proteins.

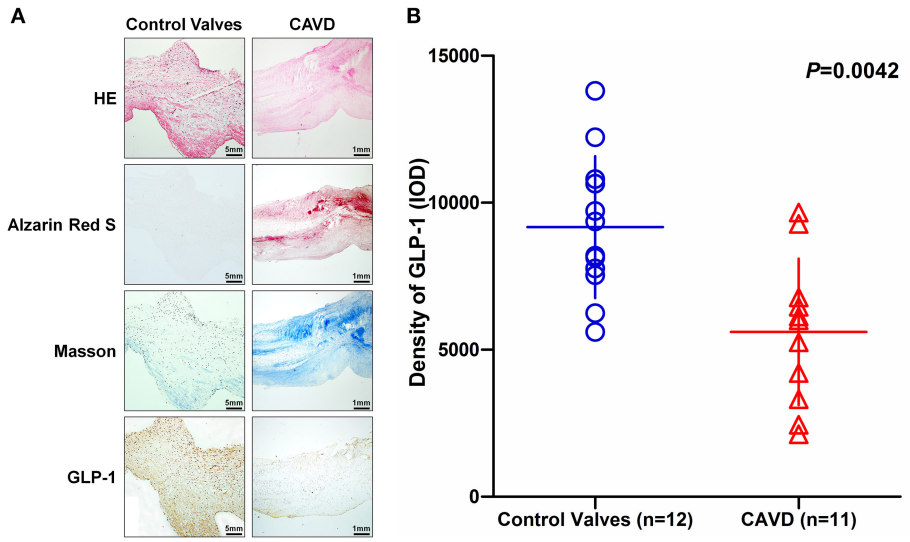

FIGURE 2 | The distribution of GLP-1 in aortic valves with or without calcification. Human aortic valves with calcification ($n = 11$) that underwent valve replacement operation and without calcification ($n = 12$) undergoing heart transplantation were assessed by histological and immunochemical analysis. **(A)** Sections were stained with hematoxylin and eosin, Alizarin Red S, and Masson trichrome staining. IHC stains of GLP-1 and counterstained with hematoxylin. The results of the Non-CAVD valves (left line) are shown at 100× magnification, and the results of CAVD (right line) are shown at 20× magnification. **(B)** The concentration of GLP-1 detected by IHC was determined by assessing its staining with Image-Pro Plus 6.0. The results are shown as the integrated optical density (IOD)/area. The Non-CAVD ($n = 12$) and CAVD valves ($n = 11$) are representative of three independent experiments, and five different fields in each section were detected (the *P*-value was control valves compared with CAVD).

Equal amounts of protein extracts were subjected to 10% SDS/PAGE and blotted onto a poly (vinylidene difluoride) membrane. The membrane was blocked and probed overnight at 4°C with antibodies against RUNX2 (1:1,000), MSX2 (1:1,000), SOX9 (1:100), BMP2 (1:500), BMP4 (1:500), and β-actin (1:2,000), followed by incubation with HRP-conjugated secondary antibodies (1:5,000) for 1 h at room temperature. Blots were developed using an ECL detection system (Millipore, MA, USA). Each image was captured and the intensity of each band was analyzed with Quantity One (Bio-Rad).

Statistical Analysis

We performed statistical analyses with SPSS software (version 20). All tests were two-tailed, and a *p*-value of <0.05 was regarded as statistically significant. Demographic and clinical characteristics were compared between the CAVD and non-CAVD groups. Fisher's exact test was employed for categorical variables, and a two-independent-samples *t*-test or Wilcoxon rank-sum test was employed for numerical variables to evaluate between-group differences. To analyze risk factors for CAVD, candidate variables were decided *a priori* by referral to previous reports. Using these variables, we performed multivariable logistic regression analyses with a backward stepwise selection procedure. Odds ratios (ORs) and 95% CIs were calculated. For ALP and ALZ, repeated-measures ANOVA with the group as a fixed factor was employed to compare the differences between two groups.

RESULTS

Distribution of GLP-1 in Calcific Aortic Valve

Based on the histological analysis, the calcific aortic valve exhibited structural thickening, mineralization and ECM remodeling (**Figure 2A**) and the demographic and clinical characteristics of the study participants were summarized in **Table 1**. The IHC analysis showed that GLP-1 was mainly evenly distributed in the rich region of VICs of control aortic valves, but GLP-1 was prominently distributed in the non-mineralized areas of calcific aortic valves (**Figure 2A**). The integrated optical density (IOD) of the GLP-1 level was calculated in 12 control valves and 11 calcific aortic valves. Compared with the control valves, the concentration of GLP-1 decreased in the calcific aortic valves by 39% (CAVD: 5,606 ± 750.4; vs. Control valves: 9,170 ± 695.9; $P = 0.0042$) (**Figures 2A,B**).

GLP-1 Regulates Calcification of AVICs

Based on the GLP-1 concentration of patients' serum in this study (**Table 2**), we treated AVICs with different doses of GLP-1 to identify the effect of GLP-1 on calcification *in vitro*. Alizarin Red S staining showed that the osteogenic medium (used in the Controls) induced AVIC mineralization, but a higher dose (25–100 pmol/L) of GLP-1 reversed the calcification of AVICs (**Figure 3A**). The Alizarin Red S dilution results [Control = 213.5 ± 9.248 μg/mg; GLP-1 (12.5 pmol/L) = 203.7 ± 7.535 μg/mg vs. Control, $P = 0.318$; GLP-1 (25 pmol/L) = 176.3 ± 5.754 μg/mg vs. Control, $P = 0.033$; GLP-1 (50 pmol/L) = 149.7 ± 7.632 μg/mg vs. Control, $P = 0.007$; GLP-1 (100 pmol/L) = 101.7 ±

TABLE 2 | Clinical characteristics of the control and CAVD groups.

	Control ($n = 197$)	CAVD ($n = 200$)	*P*
Age, yrs	59.02 ± 8.59	74.14 ± 7.67	<0.001
Male, *n* (%)	111 (56.3)	123 (61.5)	NS
Body mass index, kg/m^2	24.65 ± 3.39	25.13 ± 3.46	NS
Active smokers, *n* (%)	59 (29.9)	48 (24.0)	NS
Alcohol, *n* (%)	27 (13.7)	18 (9.0)	NS
Hypertension, *n* (%)	127 (64.5)	154 (77.0)	0.008
Diabetes, *n* (%)	63 (32.0)	61 (30.5)	NS
Coronary heart disease, *n* (%)	134 (68.0)	177 (88.5)	<0.001
Systolic blood pressure, mmHg	77.07 ± 11.70	74.42 ± 11.43	0.023
Diastolic blood pressure, mmHg	131.49 ± 17.73	139.78 ± 20.68	<0.001
Fasting glucose, mmol/L	5.48 ± 1.86	5.52 ± 2.21	NS
HbA1c, %	6.21 ± 1.167	6.38 ± 1.23	NS
Triglycerides, mmol/L	1.78 ± 1.13	1.56 ± 0.86	0.025
Total cholesterol, mmol/L	4.08 ± 1.06	3.91 ± 1.19	NS
LDL, mmol/L	1.13 ± 0.26	1.07 ± 0.29	0.044
HDL, mmol/L	2.39 ± 0.88	2.32 ± 0.98	NS
Lipoprotein(a), g/L	0.12 (0.20)	0.14 (0.30)	0.026
γ-Glutamyl transpeptidase, U/L	19.00 (20.00)	21.00 (14.00)	NS
Blood urea nitrogen, mmol/L	5.06 ± 1.29	6.03 ± 2.40	<0.001
Creatinine, mmol/L	74.07 ± 16.07	86.38 ± 24.25	<0.001
eGFR(CKD-EPI), mL/min	90.39 ± 17.62	72.29 ± 18.23	<0.001
Peak aortic transvalvular velocity, m/s	2.10 ± 0.21	2.14 ± 0.22	NS
Systolic pulmonary artery pressure, mmHg	34.81 ± 2.25	35.21 ± 1.98	NS
Aortic valve mean gradient, mmHg	4.51 ± 1.01	4.72 ± 1.12	NS
Metformin, *n* (%)	35 (17.8)	28 (14.0)	NS
Statin, *n* (%)	163 (82.7)	167 (83.5)	NS
GLP-1, pmol/L	14.00 (9.68)	11.29 (6.75)	<0.001

Values are expressed as the mean ± SD, number (%), or median (interquartile range). CAVD, calcific aortic valve disease; HDL, high-density lipoprotein; LDL, low-density lipoprotein; NS, not significant.

8.950 μg/mg vs. Control, $P = 0.001$] and the activation of ALP [Control=605.5 ± 20.53 U/mg; GLP-1 (12.5 pmol/L) = 595.7 ± 18.26 U/mg vs. Control, $P = 0.513$; GLP-1 (25 pmol/L) = 519.5 ± 12.73 U/mg vs. Control, $P = 0.002$; GLP-1 (50 pmol/L) = 358.7 ± 17.94 U/mg vs. Control, $P = 0.001$; GLP-1 (100 pmol/L) = 218.3 ± 12.41 U/mg vs. Control, $P < 0.001$] also showed that GLP-1 reduced AVIC calcification in a dose-dependent manner (**Figures 3B,C**).

In vitro, the AVICs were calcified over various periods from 7 to 21 days to mimic the process of aged-induced calcification. For further affirming GLP-1 regulated calcification of AVICs with time, we also treated AVICs with 100 pmol/L GLP-1 to identify the time-dependent effect of GLP-1 on calcification from 7 to 21 days. Alizarin Red S staining showed that the extent of calcification rapidly and significantly increased with the time extension (7 days = 129.0 ± 9.2 μg/mg, 14 days = 161.0 ± 6.4 μg/mg, and 21 days = 218.5 ± 7.6 μg/mg compared with 7 days: $P < 0.01$); however, GLP-1 significantly weakened this tendency (respectively, 79.0 ± 7.1, 91.3 ± 10.8, and 108.3 ± 10.5 μg/mg compared with the same groups without GLP-1 treatment: $P < 0.01$) (**Figures 4A,B**). Compared with the Control groups (7 days = 350.8 ± 28.2 U/mg, 14 days = 495.8 ± 37.2 U/mg, 21 days = 624.8 ± 40.9 U/mg, compared with 7 days: $P < 0.01$), a similar effect of GLP-1 with age (GLP-1: 7 days = 147.2 ± 21.3 U/mg, 14 days = 174.3 ± 19.1 U/mg, and 21 days = 212.8 ± 26.5 U/mg compared with same groups without GLP-1 treatment: $P < 0.01$) was demonstrated in the ALP activation test (**Figure 4C**).

GLP-1 Regulated Calcification-Related Gene Expression

Many genes participated in AVIC mineralization, RUNX2 (29), MSX2 (30), and SOX9 (31) act as nuclear transcription factors to regulate downstream gene transcription. For example, the target genes BMP2 and BMP4 (32) promoted calcification of AVICs. Thus, we tested whether GLP-1 inhibited AVIC calcification by regulating the expression of these genes. First, the mRNA levels of *RUNX2*, *MSX2*, *SOX9*, *BMP2,* and *BMP4* were detected by real-time PCR. Glucagon-like peptide-1 decreased the transcription of *RUNX2* by 62% (Control = 1.01 ± 0.02 vs. GLP-1 = 0.38 ± 0.04, $P < 0.01$), *MSX2* by 54% (Control = 1.00 ± 0.02 vs. GLP-1 = 0.46 ± 0.06, $P < 0.01$), *BMP2* by 46% (Control = 1.00 ± 0.01 vs. GLP-1 = 0.54 ± 0.06, $P < 0.01$), and *BMP4* by 59% (Control = 1.01 ± 0.03 vs. GLP-1 = 0.41 ± 0.02, $P < 0.01$) but increased *SOX9* 2.01-fold (Control = 1.00 ± 0.02 vs. GLP-1 = 2.01 ± 0.14, $P < 0.01$) (**Figure 5A**). Second, the distributions of RUNX2, MSX2, SOX9, BMP2, and BMP4 were identified by immunofluorescence in AVICs. RUNX2, MSX2, and SOX9 were located in the nucleus; BMP2 and BMP4 were expressed throughout the cells. GLP-1 also reduced the levels of RUNX2, MSX2, BMP2, and BMP4 but induced SOX9 (**Figure 5B**). Finally, the concentrations of these proteins were measured by western blot and analyzed by the IOD value (ratio of proteins/β-actin). GLP-1 decreased the expression of RUNX2 by 49% (Control = 2.21 ± 0.09 vs. GLP-1 = 1.12 ± 0.17, $P < 0.01$), MSX2 by 53% (Control = 1.75 ± 0.08 vs. GLP-1 = 0.83 ± 0.07, $P < 0.01$), BMP2 by 57% (Control = 1.38 ± 0.13 vs. GLP-1 = 0.60 ± 0.10, $P < 0.01$), and BMP4 by 48% (Control = 1.70 ± 0.09 vs. GLP-1 = 0.89 ± 0.16, $P < 0.01$) but increased SOX9 1.98-fold (Control = 0.90 ± 0.13 vs. GLP-1 = 1.78 ± 0.13, $P < 0.01$) (**Figure 5C**).

Clinical Characteristics and GLP-1 Level in Serum of Non-CAVD and CAVD Groups

Previous results showed the concentration of GLP-1 decreased in valves of CAVD patients. *In vitro*, GLP-1 reversed mmineralization of AVICs with dose- and time-dependent manner, and GLP-1 downregulated pro-calcification genes expression but upregulated anti-calcification genes expression. The serum of CAVD ($n = 200$) and non-CAVD ($n = 197$) were

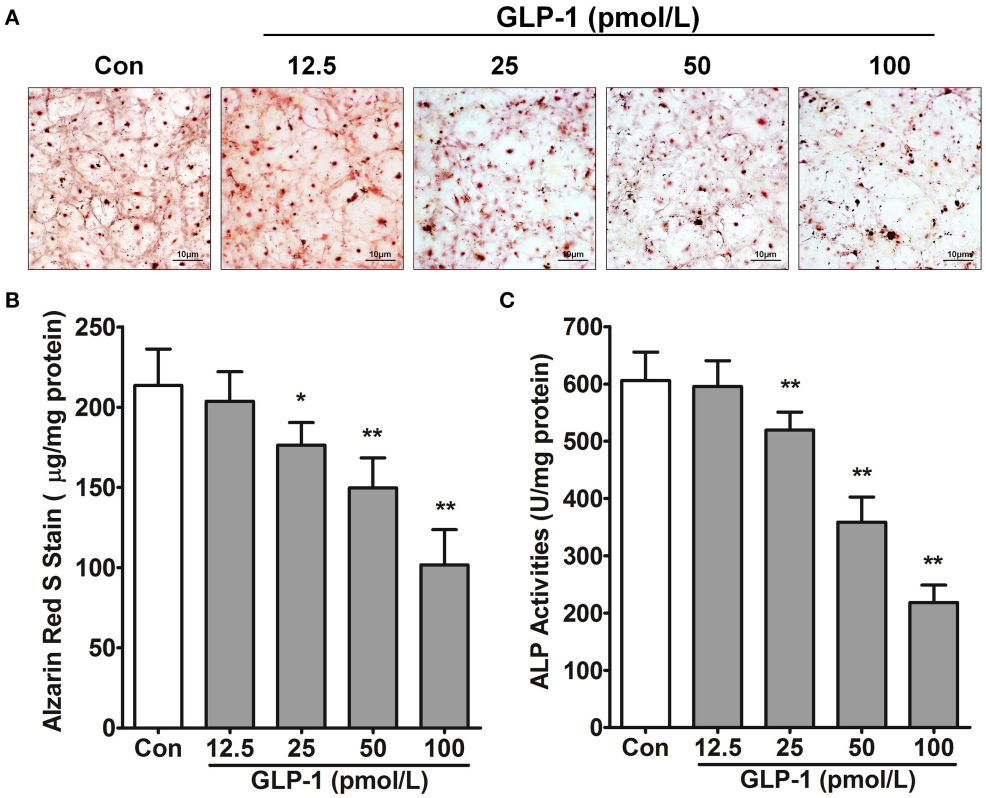

FIGURE 3 | GLP-1 inhibits AVIC calcification. In osteogenic medium, the primary AVICs were incubated with increasing doses (12.5, 25, 50, and 100 pmol/L for 21 days) of GLP-1. The group without the GLP-1 treatment was used as a control (Con). **(A)** Alizarin Red S was used to stain the calcification cells. The pictures were taken using Image-Pro Plus 6.0. Alizarin Red S staining is shown at 400× magnification. **(B)** Quantification of Alizarin Red S staining. **(C)** Quantification of ALP activation in AVICs. The dye was extracted and quantified as described in the Methods section ($n = 6$, mean ± SD, $^{*}P < 0.05$, $^{**}P < 0.01$ compared with Con).

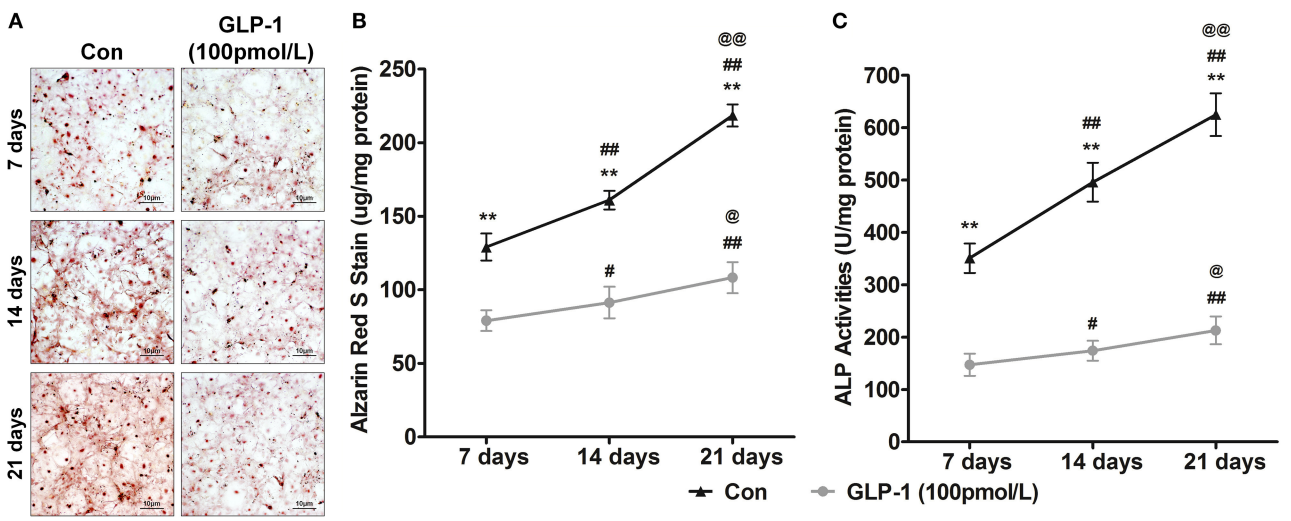

FIGURE 4 | GLP-1 postpones the age-induced mineralization of AVICs. To determine the effect of GLP-1 on age-induced mineralization in AVICs, primary AVICs were cultured for 7, 14, and 21 days in osteogenic medium plus GLP-1 (100 pmol/L) or not. The group without the GLP-1 treatment was used as a control (Con). **(A)** Alizarin Red S stained the calcification cells, and the pictures were taken using Image-Pro Plus 6.0. Alizarin Red S staining is shown at 400× magnification. **(B)** Quantification of Alizarin Red S staining. **(C)** Quantification of ALP activation in AVICs. The dye was extracted and quantified as described in the Methods section ($n = 6$, mean ± SD, $^{**}P < 0.01$ compared with Con; $^{\#}P < 0.05$, $^{\#\#}P < 0.01$ compared with 7-day culture; $^{@}P < 0.05$, $^{@@}P < 0.01$ compared with 14-day culture).

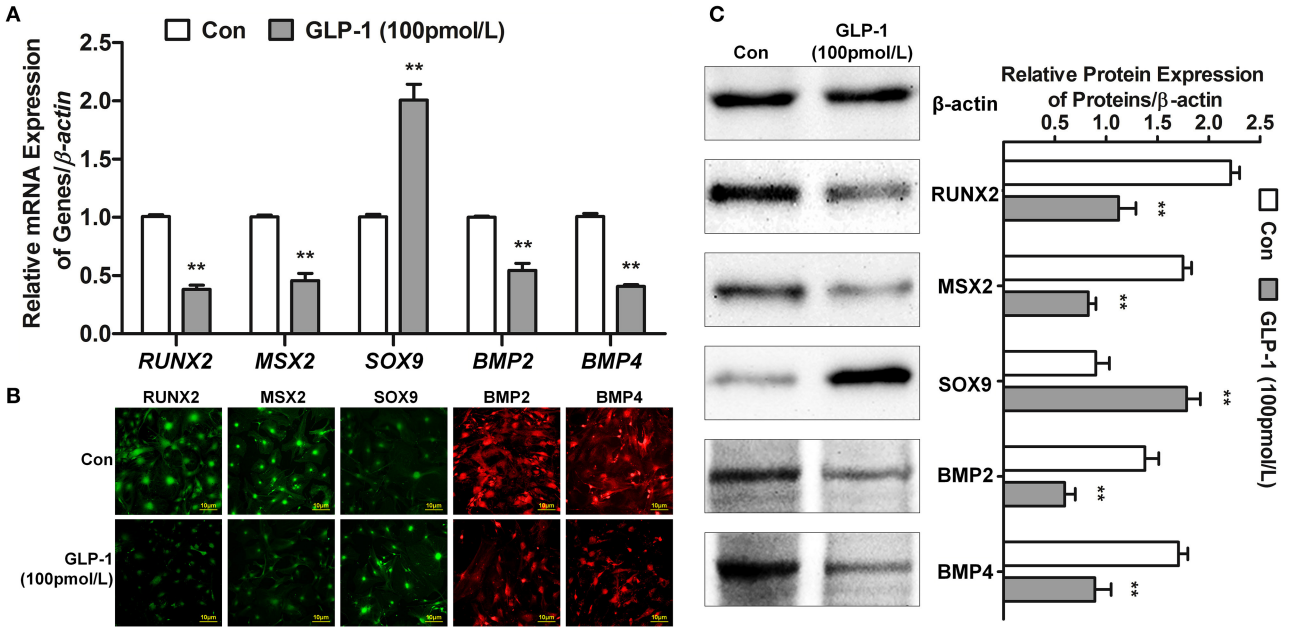

FIGURE 5 | GLP-1 regulates the expression of calcification-related genes. The primary AVICs were stimulated with or without GLP-1 (100 pmol/L) for 21 days in osteogenic medium. The group without the GLP-1 treatment was used as a control (Con). (A) *RUNX2*, *MSX2*, *SOX9*, *BMP2,* and *BMP4* were detected by real-time PCR. **(B)** The protein expression and location of RUNX2, MSX2, SOX9, BMP2, and BMP4 were determined by immunofluorescence analysis. RUNX2, MSX2, and SOX9 were assessed using Alexa Fluor 488-conjugated secondary antibody (Green); BMP2 and BMP4 were assessed using Alexa Fluor 549-conjugated secondary antibody (Red). **(C)** RUNX2, MSX2, SOX9, BMP2, and BMP4 were detected by western blot. The results are representative of three independent experiments. Real-time PCR **(A)** and western blot **(C)** quantified as relative units (genes or proteins/β-actin) ($n = 3$, mean ± SD, $^{**}P < 0.01$ compared with Con).

collected to analysis the relationship of GLP-1 concentration and CAVD.

The demographic and clinical characteristics of the study participants were summarized in **Table 2**. Compared with the non-CAVD group, the patients in the CAVD group had a higher age range (non-CAVD: 59.02 ± 8.59 years vs. CAVD: 74.14 ± 7.67 years; $P < 0.001$), percentage of hypertension (non-CAVD: 64.5% vs. CAVD: 77.0%; $P = 0.008$), and rate of coronary heart disease (non-CAVD: 68.0% vs. CAVD: 88.5%; $P < 0.001$). There were no significant difference in sex, body mass index (BMI), active smoking, alcohol, percentage of diabetes, fasting glucose, HbA1c or γ-glutamyl transpeptidase between the two groups. The diastolic blood pressure was significantly higher in the CAVD group (Non-CAVD: 131.49 ± 17.73 vs. CAVD: 139.78 ± 20.68; $P < 0.001$), but the systolic blood pressure was significantly lower (Non-CAVD: 77.07 ± 11.70 vs. CAVD: 74.42 ± 11.43; $P = 0.023$). Calcific aortic valve disease patients had higher lipoprotein (A) [Non-CAVD: 0.12 (0.20) vs. CAVD: 0.14 (0.30); P = 0.026] and lower triglycerides [Non-CAVD: 1.78 ± 1.13 vs. CAVD: 1.56 ± 0.86; $P = 0.025$] and LDL (Non-CAVD: 1.13 ± 0.26 vs. CAVD: 1.07 ± 0.29; $P = 0.044$), but not total cholesterol or HDL. Renal and blood urea nitrogen (Non-CAVD: 5.06 ± 1.29 mmol/L vs. CAVD: 6.03 ± 2.40 mmol/L; $P < 0.001$), creatinine (Non-CAVD: 74.07 ± 16.07 mmol/L vs. CAVD: 86.38 ± 24.25 mmol/L; $P < 0.001$), and eGFR (CKD-EPI) (Non-CAVD: 90.39 ± 17.62 ml/min vs. CAVD: 72.29 ± 18.23 ml/min; $P < 0.001$) exhibited significant pathogenic propensity changes. No significant difference was observed in terms of the medication treatment between the Non-CAVD and CAVD groups.

Serum Similar to the IHC result for calcific aortic valves, serum GLP-1 was significantly reduced in the CAVD group [Non-CAVD: median = 14.00 pmol/L (25th−75th percentile 9.34–19.02 pmol/L; range 0.38–39.37 pmol/L) vs. CAVD: median = 11.29 pmol/L (25th−75th percentile 8.17–14.92 pmol/L; range 0.05–31.93 pmol/L), $P < 0.001$] (**Table 2**).

GLP-1 as an Independent Factor for CAVD

Based on the multivariable regression analysis, age (OR = 1.255; 95% CI 1.199–1.313), fasting glucose (OR = 0.824; 95% CI, 0.702–0.968), HbA1c (OR = 1.542; 95% CI, 1.171–2.031), HDL (OR = 0.142; 95% CI, 0.045–0.443), BUN (OR = 1.270; 95% CI, 1.032–1.563), and GLP-1 (OR = 0.889; 95% CI, 0.844–0.936) were independently associated with CAVD risk (Model 1 in **Table 3**). When the GLP-1 quartile (median = 12.31 pmol/L, 25th−75th percentiles 8.68–16.73 pmol/L; range 0.05–39.37 pmol/L) in the Non-CAVD and CAVD groups was included in Model 2 (baseline characteristics of the Non-CAVD and CAVD groups according to GLP-1 level, see **Supplementary Table 2**), the association between age, fasting glucose, HbA1c, HDL, BUN, and CAVD remained significant. Compared with the lowest quartile, the OR-values of the other quartiles decreased from 0.818 to 0.115. However, only the highest quartile (OR = 0.115; 95% CI, 0.045–0.291) was significantly associated with lower risk of CAVD (Model 2 in **Table 3**).

Age represented a remarkable risk factor for CAVD and it presented the largest difference from the Non-CAVD group in this study. Therefore, the interaction between GLP-1 quartile and age as covariates was analyzed by multivariable regression analysis. In this analysis, age, fasting glucose, HbA1c, HDL, and BUN remained independent risk factors associated with CAVD. Compared with the lowest quartile, higher GLP-1 reduced the aged-induced risk of pathogenesis from 0.996 to 0.966 (**Table 4**). Only the fourth quartile (OR = 0.966; 95% CI, 0.953–0.980) was significantly associated with CAVD (**Table 4**).

DISCUSSION

Although some clinical, genetic, and animal studies have led to a partial understanding of CAVD, truly important advancements in the disease management (such as optimal diagnosis and treatment strategies) remain out of reach. This area of study thus requires further investigations, especially regarding endogenous protective factors. In this study, we found that GLP-1, a negative independent risk factor, was decreased in aortic valve and serum of CAVD patients. Glucagon-like peptide-1 is also associated with reduced the odds of CAVD and inhibited AVIC mineralization by regulating calcification related-genes. Thus, GLP-1 exhibited protective characteristics to antagonize CAVD.

The present study found that age, hypertension, systolic blood pressure, diastolic blood pressure, CAVD, triglycerides, LDL, lipoprotein (A), blood urea nitrogen, creatinine, and eGFR (CKD-EPI) (as pathogenic factors) significantly differed between the Non-CAVD and CAVD groups (**Table 2**). Among these indicators, age (33), hypertension (4), blood pressure (4), CAD (34), lipoprotein (A) (35), and renal function (36) have been reported to participate in and show pathogenicity associated with CAVD. However, there has been little research regarding the protective factors of CAVD. For these reasons, we focused on GLP-1, which has beneficial effects and is associated with LV diastolic function (37), heart rate (38), cardiac remodeling (39), blood pressure (38), lipid profile (40), and cardiovascular disease independent of adiposity or diabetes (41). Notably, the role of GLP-1 had not been reported in CAVD. We found that the level of GLP-1 was not only decreased in the serum of the CAVD group (**Table 2**) but was also reduced in calcified aortic valves (**Figure 2**). Thus, GLP-1 may be associated with CAVD; as expected, multivariable regression analysis found that GLP-1 was a negative independent factor for CAVD (OR = 0.922; 95% CI, 0.887–0.958) (**Table 3**) and significantly weakened the odds risk of CAVD. These results indicate that the variation in GLP-1 concentration affects CAVD. To determine the influence of GLP-1 concentration on CAVD, GLP-1 concentration was divided into quartiles. The patients with the highest quartile of GLP-1 showed the lowest rate of CAVD (31.3%, $P < 0.001$; **Supplementary Table 2**), and the highest quartile showed a significantly strong negative correlation with CAVD risk (OR = 0.115; 95% CI, 0.045–0.291), which demonstrated that a high dose of GLP-1 exerted an antagonistic effect on the odds risk of CAVD (**Table 3**). Thus, GLP-1 is a novel protective factor negatively associated with CAVD, and decreases in GLP-1 lead to the progressive calcification of the aortic valve.

Glucagon-like peptide-1 is an incretin hormone that is secreted into the serum by enteroendocrine L-cells (distal ileum and colon) and K-cells (duodenum and jejunum) (42); however, we found GLP-1 in non-mineralized aortic valve regions with or without calcified lesions, which indicates that GLP-1 was secreted from intestinal cells and recruited to the aortic valve to influence the function of AVICs. Glucagon-like peptide-1 localizes to interstitial spaces and tissues to regulate metabolic diseases, such as diabetes and obesity (43, 44); GLP-1 also regulates cell functions to protect against cardiovascular disease. *In vitro* and *in vivo* atherosclerosis studies demonstrate that GLP-1 promotes vasodilatation and suppresses the inflammatory response in endothelial cells, inhibits lipid uptake and inflammatory activity in macrophages, and represses the proliferation of smooth muscle cell (SMCs) to prevent atherosclerosis progression (45). In arterial calcification, similar to bone formation, VSMCs differentiate to the osteoblastic phenotype to play a key role in arterial calcification; however, GLP-1 inhibits osteoblastic differentiation and calcification in human VSMCs (20). There are several similarities between CAVD and arterial calcification; however, AVIC heterogenization and mineralization are key components of the cytopathology in CAVD, and these components differ from those in arterial calcification. In this study, the level of GLP-1 decreased by 19.3% in CAVD serum (**Table 2**) and 39% in calcified aortic valve (**Figure 2**), which indicated that a reduction in GLP-1 in the aortic valve caused AVIC calcification. However, whether GLP-1 can reverse CAVD by regulating AVIC osteoblastic differentiation and calcification was not known. To investigate this, we added various doses of GLP-1 to AVICs during the standard process of calcification. Glucagon-like peptide-1 significantly attenuated the density of Alizarin Red S and the activation of ALP at higher doses (**Figure 3**), which demonstrated that GLP-1 could attenuate CAVD by preventing the mineralization of AVICs. Considering this plus the results of **Table 3**, we hypothesized that high GLP-1 weakens the risk of CAVD. Our results indicate that GLP-1 inhibits the calcification of AVICs to exert its protective function in CAVD.

Calcific aortic valve disease is a chronic degenerative disease that has multiple risk factors, including diabetes (46), hypertension (4), dyslipidemia (36), and kidney disease (47). The Multi-Ethnic Study of Atherosclerosis (MESA) found that non-Hispanic whites had the highest frequency of CAVD, followed by Hispanics and blacks, which indicates that CAVD presents racial differences (48). Our study in a Chinese population found that age, fasting glucose, HbA1c, HDL, BUN, and GLP-1 were independent risk factors for CAVD, which indicates that age, diabetes, dyslipidemia and renal insufficiency were associated with CAVD in a Chinese population.

Although multiple pathogenic factors take part in CAVD, age is an important and irreversible risk factor and has the strongest correlation with CAVD (48). A previous study showed that more than 50% of patients with aortic valve calcification were older than 75 years, whereas severe stenosis was found in 2–3% of this elderly population (49). And some reports

TABLE 3 | Multivariable regression analysis for the risk of CAVD.

	Variable	B	S.E.	OR (95% CI)	*P*
Model 1	Age	0.227	0.023	1.255 (1.199–1.313)	<0.001
	Fasting glucose	−0.193	0.082	0.824 (0.702–0.968)	0.018
	HbA1c	0.433	0.14	1.542 (1.171–2.031)	0.002
	HDL	−1.954	0.582	0.142 (0.045–0.443)	0.001
	BUN	0.239	0.106	1.270 (1.032–1.563)	0.024
	GLP-1	−0.118	0.027	0.889 (0.844–0.936)	<0.001
	Constant	−14.442	1.831		<0.001
Model 2	Age	0.235	0.024	1.265 (1.207–1.325)	<0.001
	Fasting glucose	−0.21	0.083	0.810(0.689–0.953)	0.011
	HbA1c	0.422	0.142	1.525 (1.154–2.016)	0.003
	HDL	−2.027	0.597	0.132 (0.041–0.424)	0.001
	BUN	0.214	0.107	1.239 (1.005–1.527)	0.045
	GLP-1[a]				<0.001
	GLP-1[a] (8.69–12.31)	−0.201	0.418	0.818 (0.361–1.855)	0.631
	GLP-1[a] (12.32–16.73)	−0.821	0.436	0.440 (0.187–1.034)	0.06
	GLP-1[a] (16.74–39.37)	−2.162	0.474	0.115 (0.045–0.291)	<0.001
	Constant	−15.333	1.905		<0.001

Variable(s) entered in Model 1: Age, Male, Body mass index, Active smoker, Alcohol, Hypertension, Systolic blood pressure, Diastolic blood pressure, Diabetes, Fasting glucose, HbA1c, Coronary heart disease, Triglycerides, Total cholesterol, LDL, HDL, Lipoprotein(a), γ-glutamyl transpeptidase, Blood urea nitrogen, Creatinine, eGFR (CKD-EPI) and GLP-1. GLP-1[a] was transformed by dividing GLP-1 into quartiles. GLP-1[a] was a categorical variable in the model, with the lowest quartile (0.050–8.785) as a reference category. Variable(s) entered in Model 2: Age, Male, Body mass index, Active smoker, Alcohol, Hypertension, Systolic blood pressure, Diastolic blood pressure, Diabetes, Fasting glucose, HbA1c, Coronary heart disease, Triglycerides, Total cholesterol, LDL, HDL, Lipoprotein(a), γ-glutamyl transpeptidase, Blood urea nitrogen, Creatinine, eGFR (CKD-EPI), GLP-1[a]. B: unstandardized B coefficient.

TABLE 4 | Multivariable regression analysis for the risk of GLP-1 interacting with Age in CAVD.

Variable	B	S.E.	OR (95% CI)	*P*
Age	0.251	0.026	1.285 (1.222–1.351)	<0.001
Fasting glucose	−0.222	0.084	0.801 (0.679–0.944)	0.008
HbA1c	0.437	0.143	1.549 (1.170–2.050)	0.002
HDL	−2.071	0.601	0.126 (0.039–0.409)	0.001
BUN	0.221	0.108	1.247 (1.010–1.540)	0.040
GLP-1[a] * Age				<0.001
GLP-1[a] (8.69–12.31) * Age	−0.004	0.007	0.996 (0.983–1.009)	0.550
GLP-1[a] (12.32–16.73) * Age	−0.013	0.007	0.987 (0.974–1.000)	0.055
GLP-1[a] (16.74–39.37) * Age	−0.034	0.007	0.966 (0.953–0.980)	<0.001
Intercept	−16.334	1.962		<0.001

*GLP-1[a] was transformed by dividing GLP-1 into quartiles. GLP-1[a] was a categorical variable in the model, GLP [a] * age as an interaction term with the lowest quartile (0.05–8.68) by age as a reference category. Variable(s) entered in multivariable regression analysis: age, male, body mass index, active smoker, alcohol, hypertension, systolic blood pressure, diastolic blood pressure, diabetes, fasting glucose, HbA1c, coronary heart disease, triglycerides, total cholesterol, LDL, HDL, Lipoprotein(a), γ-glutamyl transpeptidase, Blood urea nitrogen, creatinine, eGFR (CKD-EPI), GLP-1[a] by age. B: unstandardized B coefficient.*

shown with aged, AVICs can form calcium node (50). In our experiments, we found in extended-duration *in vitro* calcification culture, the mineralization level of AVICs increased (**Figure 4**). These results illustrate that age plays a key role in CAVD mineralization. Moreover, we previously found an effect of GLP-1 on neuroprotection via its reversal of age-induced neurodegeneration, such as that in Alzheimer's and Parkinson's diseases (51).We observed that GLP-1 not only inhibited mineralization but also reduced time-dependent calcification in AVICs from 7 to 21 days (**Figure 4**). These results demonstrate that the leading risk factor of CAVD may can be attenuated by GLP-1.

RUNX2, MSX2, SOX9, BMP2, and BMP4 are important proteins related to calcification. RUNX2 is an osteogenic and chondrogenic transcription factor that is regulated in multiple manners (52). RUNX2 is upregulated in atherosclerotic calcification and endochondral mineralization programs (29). Hydrogen peroxide activates osteogenic Cbfa1/RUNX2 (53) and MSX2/Wnt signaling (30), thereby enhancing mineralization. Miller et al. also found that both of these regulatory cascades were activated in calcifying human aortic valves (54). Acharya et al. (31) demonstrated that Notch1 maintains SOX9 expression to inhibit osteogenic mineralization in AVICs. BMP2 and BMP4 increase the secretion of OPN by upregulating ALP, resulting in the degradation of tissue pyrophosphate (32). Glucagon-like peptide-1 attenuates osteoblastic differentiation and calcification by inhibiting ALP, osteocalcin (OC), and RUNX2 in human VSMCs (20), but whether GLP-1 regulates the expression of MSX2, SOX9, BMP2, and BMP4 remains unknown. As we observed in this study, GLP-1 decreased the expression of RUNX2, MSX2, BMP2, and BMP4 but increased the expression of SOX9 in AVICs (**Figure 5**), which were first suggested a relationship between GLP-1 and these genes in the AVIC calcification process. These results indicate that GLP-1 reversed mineralization in AVICs via two pathways, first by inhibiting the expression of osteogenic genes and second by promoting the expression of anti-osteogenic genes. These results indicate that GLP-1 reversed mineralization in AVICs via two pathways, first by inhibiting the expression of osteogenic genes and second by promoting the expression of anti-osteogenic genes.

This study showed that the level of GLP-1 decreased in both the local calcific aortic valve and in the serum of CAVD patients and that this decrease was associated with age. This indicated that GLP-1 could have value in predicting the occurrence and development of CAVD.

STUDY LIMITATIONS

In this study, we examined the role of GLP-1 in CAVD; however, some *in vivo* experiments and details of the molecular mechanism were lacking. We found HDL and fasting glucose to be negative independent risk factors associated with CAVD. HDL has anti-oxidative and anti-inflammatory properties, but

the role of HDL in CAVD is not clear. Interestingly, our study found that fasting glucose was associated with a reduced risk of CAVD and that high glucose reversed AVIC calcification (data not shown); however, the mechanisms of these effects remain unknown. HDL and fasting glucose in CAVD will be investigated in further studies. Moreover, as a single center cross-sectional study with retrospective characteristic, it might be susceptible to center biases or recall bias. Also, as a retrospective study, the study only indicated associations but not formulate causal relationships. Although we took multiple clinical important cofounders into consideration, it might be possible that unknown potential factors may be missed and it might interfere in our findings. Finally, CAVD was only assessed by echocardiography. Cardiac computed tomography is also another useful approach to quantify aortic valve calcium burden. Finally, although we carefully controlled for the major known confounders, unknown factors may still have interfered in our findings.

Therefore, the results remained to be further confirmed in larger sample size study with prospective randomized controlled designs.

CONCLUSION

Valve tissue and serum from CAVD patients were characterized with lower level of GLP-1. Clinical and cellular evidence suggests that GLP-1 participates in the pathological calcification of the aortic valve. Calcific aortic valve disease is highly prevalent in the elderly, and there are currently no absolute effective treatments to reverse its progression. This study reveals some novel characteristics of GLP-1 and its potential therapeutic value for CAVD.

DATA AVAILABILITY STATEMENT

The raw data supporting the conclusions of this article will be made available by the authors, without undue reservation.

ETHICS STATEMENT

The studies involving human participants were reviewed and approved by Shanghai Ninth People's Hospital+Shanghai Jiaotong University School of Medicine. The patients/participants provided their written informed consent to participate in this study. The animal study was reviewed and approved by Shanghai Ninth People's Hospital+Shanghai Jiaotong University School of Medicine.

AUTHOR CONTRIBUTIONS

YL and KY designed the study, performed data analysis and interpretation, and drafted the manuscript. FX, QZha, and QZhang performed data collection and analysis. FX, QW, and YY contributed to interpretation, drafting, and editing the manuscript. YL and KY provided study design, interpretation, wrote and edited manuscript, are the guarantors of this work and takes full responsibility for the work as a whole, including the study design, access to data, and the decision to submit and publish the manuscript. All authors contributed to conception and design, acquisition of data or analysis and interpretation of data, drafting the article or revising it critically for important intellectual content, and gave final approval of the version to be published.

FUNDING

This work was supported by grants from the Natural Science Foundation of China (81770384, 82070401, 81760734, and 81800339), the Natural Science Foundation of Yunnan Province (No. 2017FA048), the fund of Diabetic Innovation Team (2019HC002), and Endocrine Clinical Medical Center of Yunnan Province (No. ZX2019-02-02). The fund of medical leader in Yunnan Province (No. L-201609). Fundamental research program funding of Ninth People's Hospital affiliated to Shanghai Jiao Tong University School of Medicine (No. JYZZ100).

ACKNOWLEDGMENTS

We would like to thank Dr. Ying Huang and her associates in the core facility unit (School of Medicine, Shanghai Jiao Tong University) for their professional support in imaging capture and processing.

SUPPLEMENTARY MATERIAL

The Supplementary Material for this article can be found online at: https://www.frontiersin.org/articles/10.3389/fcvm.2021.709741/full#supplementary-material

REFERENCES

1. Baggio LL, Drucker DJ. Biology of incretins: GLP-1 and GIP. *Gastroenterology*. (2007). 132:2131–57. doi: 10.1053/j.gastro.2007.03.054
2. Tahrani AA, Bailey CJ, Del Prato S, Barnett AH. Management of type 2 diabetes: new and future developments in treatment. *Lancet*. (2011). 378:182–97. doi: 10.1016/S0140-6736(11)60207-9
3. Li Y, Perry T, Kindy MS, Harvey BK, Tweedie D, Holloway HW, et al. GLP-1 receptor stimulation preserves primary cortical and dopaminergic neurons in cellular and rodent models of stroke and Parkinsonism. *Proc Natl Acad Sci USA*. (2009). 106:1285–90. doi: 10.1073/pnas.0806720106
4. Rajamannan NM, Evans FJ, Aikawa E, Grande-Allen KJ, Demer LL, Heistad DD, et al. Calcific aortic valve disease: not simply a degenerative process: A review and agenda for research from the National Heart and Lung and Blood Institute Aortic Stenosis Working Group. Executive summary: Calcific aortic valve disease-2011 update. *Circulation*. (2011). 124:1783–91. doi: 10.1161/CIRCULATIONAHA.110.006767
5. Otto CM, Kuusisto J, Reichenbach DD, Gown AM, O'Brien KD. Characterization of the early lesion of 'degenerative' valvular aortic stenosis. Histological and immunohistochemical studies. *Circulation*. (1994) 90:844–53. doi: 10.1161/01.CIR.90.2.844

6. Zeng Q, Jin C, Ao L, Cleveland JC Jr, Song R, Xu D, et al. Cross-talk between the Toll-like receptor 4 and Notch1 pathways augments the inflammatory response in the interstitial cells of stenotic human aortic valves. *Circulation*. (2012). 126:S222–30. doi: 10.1161/CIRCULATIONAHA.111.083675
7. Shavelle DM, Takasu J, Budoff MJ, Mao S, Zhao XQ, O'Brien KD. HMG CoA reductase inhibitor (statin) and aortic valve calcium. *Lancet*. (2002). 359:1125–6. doi: 10.1016/S0140-6736(02)08161-8
8. Bouchareb R, Mahmut A, Nsaibia MJ, Boulanger MC, Dahou A, Lepine JL, et al. Autotaxin derived from lipoprotein (A) and valve interstitial cells promotes inflammation and mineralization of the aortic valve. *Circulation*. (2015). 132:677–90. doi: 10.1161/CIRCULATIONAHA.115.016757
9. Freeman RV, Otto CM. Spectrum of calcific aortic valve disease: pathogenesis, disease progression, and treatment strategies. *Circulation*. (2005). 111:3316–26. doi: 10.1161/CIRCULATIONAHA.104.486738
10. Merryman WD. Insights into (the interstitium of) degenerative aortic valve disease. *J Am Coll Cardiol*. (2008). 51:1415; author reply 1416. doi: 10.1016/j.jacc.2007.11.068
11. Wirrig EE, Hinton RB, Yutzey KE. Differential expression of cartilage and bone-related proteins in pediatric and adult diseased aortic valves. *J Mol Cell Cardiol*. (2011). 50:561–9. doi: 10.1016/j.yjmcc.2010.12.005
12. Yetkin E, Waltenberger J. Molecular and cellular mechanisms of aortic stenosis. *Int J Cardiol*. (2009). 135:4–13. doi: 10.1016/j.ijcard.2009.03.108
13. Munaf M, Pellicori P, Allgar V, Wong K. A meta-analysis of the therapeutic effects of glucagon-like peptide-1 agonist in heart failure. *Int J Pept*. (2012). 2012:249827. doi: 10.1155/2012/249827
14. Hausenloy DJ, Whittington HJ, Wynne AM, Begum SS, Theodorou L, Riksen N, et al. Dipeptidyl peptidase-4 inhibitors and GLP-1 reduce myocardial infarct size in a glucose-dependent manner. *Cardiovasc Diabetol*. (2013). 12:154. doi: 10.1186/1475-2840-12-154
15. Woo JS, Kim W, Ha SJ, Kim JB, Kim SJ, Kim WS, et al. Cardioprotective effects of exenatide in patients with ST-segment-elevation myocardial infarction undergoing primary percutaneous coronary intervention: results of exenatide myocardial protection in revascularization study. *Arterioscler Thromb Vasc Biol*. (2013). 33:2252–60. doi: 10.1161/ATVBAHA.113.30 1586
16. Sokos GG, Nikolaidis LA, Mankad S, Elahi D, Shannon RP. Glucagon-like peptide-1 infusion improves left ventricular ejection fraction and functional status in patients with chronic heart failure. *J Card Fail*. (2006). 12 694–9. doi: 10.1016/j.cardfail.2006.08.211
17. Liu AC, Joag VR, Gotlieb AI. The emerging role of valve interstitial cell phenotypes in regulating heart valve pathobiology. *Am J Pathol*. (2007). 171:1407–18. doi: 10.2353/ajpath.2007.070251
18. Jian B, Narula N, Li QY, Mohler ER, III, Levy RJ. Progression of aortic valve stenosis: TGF-beta1 is present in calcified aortic valve cusps and promotes aortic valve interstitial cell calcification via apoptosis. *Ann Thorac Surg*. (2003). 75:457–65; discussion 465–6. doi: 10.1016/S0003-4975(02)04312-6
19. Galeone A, Brunetti G, Oranger A, Greco G, Di Benedetto A, Mori G, et al. Aortic valvular interstitial cells apoptosis and calcification are mediated by TNF-related apoptosis-inducing ligand. *Int J Cardiol*. (2013). 169:296–304. doi: 10.1016/j.ijcard.2013.09.012
20. Zhan JK, Wang YJ, Wang Y, Tang ZY, Tan P, Huang W, et al. The protective effect of GLP-1 analogue in arterial calcification through attenuating osteoblastic differentiation of human VSMCs. *Int J Cardiol*. (2015). 189:188–93. doi: 10.1016/j.ijcard.2015.04.086
21. Baumgartner H, Hung J, Bermejo J, Chambers JB, Edvardsen T, Goldstein S, et al. Recommendations on the echocardiographic assessment of aortic valve stenosis: a focused update from the European Association of Cardiovascular Imaging and the American Society of Echocardiography. *J Am Soc Echocardiogr*. (2017). 30:372–92. doi: 10.1016/j.echo.2017.02.009
22. American College of Cardiology/American Heart Association Task Force on Practice Guidelines; Society of Cardiovascular Anesthesiologists; Society for Cardiovascular Angiography Interventions; Society of Thoracic Surgeons; Bonow RO, Carabello BA, Kanu C, et al. ACC/AHA 2006 guidelines for the management of patients with valvular heart disease: a report of the American College of Cardiology/American Heart Association Task Force on Practice Guidelines (writing Committee to Revise the 1998 guidelines for the management of patients with valvular heart disease) developed in collaboration with the Society of Cardiovascular Anesthesiologists endorsed by the Society for Cardiovascular Angiography and Interventions and the Society of Thoracic Surgeons. *J Am Coll Cardiol*. (2006). 48:e1–148. doi: 10.1161/CIRCULATIONAHA.106. 176857
23. Puavilai G, Chanprasertyotin S, Sriphrapradaeng A. Diagnostic criteria for diabetes mellitus and other categories of glucose intolerance: 1997 criteria by the Expert Committee on the Diagnosis and Classification of Diabetes Mellitus (ADA), 1998 WHO consultation criteria, and 1985 WHO criteria. *World Health Organization. Diabetes Res Clin Pract*. (1999). 44:2–6. doi: 10.1016/S0168-8227(99)00008-X
24. Chobanian AV, Bakris GL, Black HR, Cushman WC, Green LA, Izzo JL, et al. Seventh report of the joint national committee on prevention, detection, evaluation, and treatment of high blood pressure. *Hypertension*. (2003). 42:1206–52. doi: 10.1161/01.HYP.0000107251.49515.c2
25. Taylor AJ, Cerqueira M, Hodgson JM, Mark D, Min J, O'Gara P, et al. ACCF/SCCT/ACR/AHA/ASE/ASNC/NASCI/SCAI/SCMR 2010 appropriate use criteria for cardiac computed tomography. A report of the American College of Cardiology Foundation Appropriate Use Criteria Task Force, the Society of Cardiovascular Computed Tomography, the American College of Radiology, the American Heart Association, the American Society of Echocardiography, the American Society of Nuclear Cardiology, the North American Society for Cardiovascular Imaging, the Society for Cardiovascular Angiography and Interventions, and the Society for Cardiovascular Magnetic Resonance. *J Am Coll Cardiol*. (2010). 56:1864–94. doi: 10.1016/j.jacc.2010.07.005
26. Mohler ER, III, Chawla MK, Chang AW, Vyavahare N, Levy RJ, et al. Identification and characterization of calcifying valve cells from human and canine aortic valves. *J Heart Valve Dis*. (1999). 8:254–60.
27. Mathieu P, Voisine P, Pepin A, Shetty R, Savard N, Dagenais F. Calcification of human valve interstitial cells is dependent on alkaline phosphatase activity. *J Heart Valve Dis*. (2005). 14:353–7.
28. Osman L, Yacoub MH, Latif N, Amrani M, Chester AH. Role of human valve interstitial cells in valve calcification and their response to atorvastatin. *Circulation*. (2006). 114:I547–52. doi: 10.1161/CIRCULATIONAHA.105.001115
29. Tyson KL, Reynolds JL, McNair R, Zhang Q, Weissberg PL, Shanahan CM. Osteo/chondrocytic transcription factors and their target genes exhibit distinct patterns of expression in human arterial calcification. *Arterioscler Thromb Vasc Biol*. (2003). 23:489–94. doi: 10.1161/01.ATV.0000059406.92165.31
30. Lai CF, Shao JS, Behrmann A, Krchma K, Cheng SL, Towler DA. TNFR1-activated reactive oxidative species signals up-regulate osteogenic Msx2 programs in aortic myofibroblasts. *Endocrinology*. (2012). 153:3897–910. doi: 10.1210/en.2012-1216
31. Acharya A, Hans CP, Koenig SN, Nichols HA, Galindo CL, Garner HR, et al. Inhibitory role of Notch1 in calcific aortic valve disease. *PLoS ONE*. (2011). 6:e27743. doi: 10.1371/journal.pone.0027743
32. Steitz SA, Speer MY, McKee MD, Liaw L, Almeida M, Yang H, et al. Osteopontin inhibits mineral deposition and promotes regression of ectopic calcification. *Amer J Pathol*. (2002). 161:2035–46. doi: 10.1016/S0002-9440(10)64482-3
33. Nkomo VT, Gardin JM, Skelton TN, Gottdiener JS, Scott CG, Enriquez-Sarano M. Burden of valvular heart diseases: a population-based study. *Lancet*. (2006). 368:1005–11. doi: 10.1016/S0140-6736(06)69208-8
34. Pohle K, Maffert R, Ropers D, Moshage W, Stilianakis N, Daniel WG, et al. Progression of aortic valve calcification: association with coronary atherosclerosis and cardiovascular risk factors. *Circulation*. (2001). 104:1927–32. doi: 10.1161/hc4101.097527
35. Hung MY, Witztum JL, Tsimikas S. New therapeutic targets for calcific aortic valve stenosis: the lipoprotein(a)-lipoprotein-associated phospholipase A2-oxidized phospholipid axis. *J Am Coll Cardiol*. (2014). 63:478–80. doi: 10.1016/j.jacc.2013.08.1639
36. Stewart BF, Siscovick D, Lind BK, Gardin JM, Gottdiener JS, Smith VE, et al. Clinical factors associated with calcific aortic valve disease. Cardiovascular Health Study. *J Am Coll Cardiol*. (1997). 29:630–4. doi: 10.1016/S0735-1097(96)00563-3
37. Nathanson D, Zethelius B, Berne C, Lind L, Andren B, Ingelsson E, et al. Plasma levels of glucagon like peptide-1 associate

with diastolic function in elderly men. *Diabet Med*. (2011). 28:301–5. doi: 10.1111/j.1464-5491.2010.03207.x
38. Trahair LG, Horowitz M, Stevens JE, Feinle-Bisset C, Standfield S, Piscitelli D, et al. Effects of exogenous glucagon-like peptide-1 on blood pressure, heart rate, gastric emptying, mesenteric blood flow and glycaemic responses to oral glucose in older individuals with normal glucose tolerance or type 2 diabetes. *Diabetologia*. (2015). 58:1769–78. doi: 10.1007/s00125-015-3638-0
39. DeNicola M, Du J, Wang Z, Yano N, Zhang L, Wang Y, et al. Stimulation of glucagon-like peptide-1 receptor through exendin-4 preserves myocardial performance and prevents cardiac remodeling in infarcted myocardium. *Am J Physiol Endocrinol Metab*. (2014). 307:E630–43. doi: 10.1152/ajpendo.00109.2014
40. Fisher M. Glucagon-like peptide 1 receptor agonists and cardiovascular risk in type 2 diabetes: a clinical perspective. *Diabetes Obes Metab*. (2015). 17:335–42. doi: 10.1111/dom.12380
41. Yamaoka-Tojo M, Tojo T, Takahira N, Matsunaga A, Aoyama N, Masuda T, et al. Elevated circulating levels of an incretin hormone, glucagon-like peptide-1, are associated with metabolic components in high-risk patients with cardiovascular disease. *Cardiovasc Diabetol*. (2010). 9:17. doi: 10.1186/1475-2840-9-17
42. Cabou C, Burcelin R. GLP-1, the gut-brain, and brain-periphery axes. *Rev Diabet Stud*. (2011). 8:418–31. doi: 10.1900/RDS.2011.8.418
43. Moran-Ramos S, Tovar AR, Torres N. Diet: friend or foe of enteroendocrine cells–how it interacts with enteroendocrine cells. *Adv Nutr*. (2012). 3:8–20. doi: 10.3945/an.111.000976
44. Moss C, Dhillo WS, Frost G, Hickson M. Gastrointestinal hormones: the regulation of appetite and the anorexia of ageing. *J Hum Nutr Diet*. (2012). 25:3–15. doi: 10.1111/j.1365-277X.2011.01211.x
45. Mita T, Watada H. Glucagon like peptide-1 and atherosclerosis. *Cardiovasc Hematol Agents Med Chem*. (2012). 10:309–18. doi: 10.2174/187152512803530388
46. Katz R, Wong ND, Kronmal R, Takasu J, Shavelle DM, Probstfield JL, et al. Features of the metabolic syndrome and diabetes mellitus as predictors of aortic valve calcification in the Multi-Ethnic Study of Atherosclerosis. *Circulation*. (2006). 113:2113–9. doi: 10.1161/CIRCULATIONAHA.105.598086
47. Ix JH, Shlipak MG, Katz R, Budoff MJ, Shavelle DM, Probstfield JL, et al. Kidney function and aortic valve and mitral annular calcification in the Multi-Ethnic Study of Atherosclerosis (MESA). *Am J Kidney Dis*. (2007). 50:412–20. doi: 10.1053/j.ajkd.2007.05.020
48. Nasir K, Katz R, Takasu J, Shavelle DM, Detrano R, Lima JA, et al. Ethnic differences between extra-coronary measures on cardiac computed tomography: Multi-Ethnic Study of Atherosclerosis (MESA). *Atherosclerosis*. (2008). 198:104–14. doi: 10.1016/j.atherosclerosis.2007.09.008
49. Lindroos M, Kupari M, Heikkila J, Tilvis R. Prevalence of aortic valve abnormalities in the elderly: an echocardiographic study of a random population sample. *J Am Coll Cardiol*. (1993). 21:1220–5. doi: 10.1016/0735-1097(93)90249-Z
50. Schnitzler JG, Ali L, Groenen AG, Kaiser Y, Kroon J. Lipoprotein(a) as orchestrator of calcific aortic valve stenosis. *Biomolecules*. (2019). 9:760. doi: 10.3390/biom9120760
51. Holscher C. Central effects of GLP-1: new opportunities for treatments of neurodegenerative diseases. *J Endocrinol*. (2014). 221:T31–41. doi: 10.1530/JOE-13-0221
52. Steitz SA, Speer MY, Curinga G, Yang HY, Haynes P, Aebersold R, et al. Smooth muscle cell phenotypic transition associated with calcification: upregulation of Cbfa1 and downregulation of smooth muscle lineage markers. *Circ Res*. (2001). 89:1147–54. doi: 10.1161/hh2401.101070
53. Byon CH, Javed A, Dai Q, Kappes JC, Clemens TL, Darley-Usmar VM, et al. Oxidative stress induces vascular calcification through modulation of the osteogenic transcription factor Runx2 by AKT signaling. *J Biol Chem*. (2008). 283:15319–27. doi: 10.1074/jbc.M800021200
54. Miller JD, Chu Y, Brooks RM, Richenbacher WE, Pena-Silva R, Heistad DD. Dysregulation of antioxidant mechanisms contributes to increased oxidative stress in calcific aortic valvular stenosis in humans. *J Amer Coll Cardiol*. (2008). 52:843–50. doi: 10.1016/j.jacc.2008.05.043

Conflict of Interest: The authors declare that the research was conducted in the absence of any commercial or financial relationships that could be construed as a potential conflict of interest.

Publisher's Note: All claims expressed in this article are solely those of the authors and do not necessarily represent those of their affiliated organizations, or those of the publisher, the editors and the reviewers. Any product that may be evaluated in this article, or claim that may be made by its manufacturer, is not guaranteed or endorsed by the publisher.

frontiers in Cardiovascular Medicine

ORIGINAL RESEARCH
published: 30 August 2021
doi: 10.3389/fcvm.2021.687885

Radiation Induces Valvular Interstitial Cell Calcific Response in an *in vitro* Model of Calcific Aortic Valve Disease

Manon Meerman[1†], Rob Driessen[2,3†], Nicole C. A. van Engeland[2,3,4†], Irith Bergsma[2,3], Jacco L. G. Steenhuijsen[5], David Kozono[6], Elena Aikawa[7], Jesper Hjortnaes[1†] and Carlijn V. C. Bouten[2,3*†]*

[1] Department of Cardiothoracic Surgery, Heart and Lung Division, Leiden University Medical Center, Leiden, Netherlands, [2] Department of Biomedical Engineering, Soft Tissue Engineering and Mechanobiology (STEM), Eindhoven University of Technology, Eindhoven, Netherlands, [3] Institute for Complex Molecular Systems (ICMS), Eindhoven University of Technology, Eindhoven, Netherlands, [4] Åbo Akademi University, Faculty of Science and Engineering, Molecular Biosciences, Turku, Finland, [5] Department of Radiotherapy, Catherina Ziekenhuis Eindhoven, Eindhoven, Netherlands, [6] Department of Radiation Oncology, Dana-Farber Cancer Institute and Harvard Medical School, Boston, MA, United States, [7] Center for Interdisciplinary Cardiovascular Sciences, Cardiovascular Medicine, Brigham and Women's Hospital and Harvard Medical School, Boston, MA, United States

OPEN ACCESS

Edited by:
Katherine Yutzey, Cincinnati Children's Hospital Medical Center, United States

Reviewed by:
Kristyn Simcha Masters, University of Wisconsin-Madison, United States
Kartik Balachandran, University of Arkansas, United States

***Correspondence:**
Jesper Hjortnaes
j.hjortnaes@lumc.nl
Carlijn V. C. Bouten
c.v.c.bouten@tue.nl

[†] These authors have contributed equally to this work

Specialty section:
This article was submitted to Heart Valve Disease, a section of the journal Frontiers in Cardiovascular Medicine

Received: *30 March 2021*
Accepted: *13 August 2021*
Published: *30 August 2021*

Citation:
Meerman M, Driessen R, van Engeland NCA, Bergsma I, Steenhuijsen JLG, Kozono D, Aikawa E, Hjortnaes J and Bouten CVC (2021) Radiation Induces Valvular Interstitial Cell Calcific Response in an in vitro Model of Calcific Aortic Valve Disease. Front. Cardiovasc. Med. 8:687885. doi: 10.3389/fcvm.2021.687885

Background: Mediastinal ionizing radiotherapy is associated with an increased risk of valvular disease, which demonstrates pathological hallmarks similar to calcific aortic valve disease (CAVD). Despite advances in radiotherapy techniques, the prevalence of comorbidities such as radiation-associated valvular disease is still increasing due to improved survival of patients receiving radiotherapy. However, the mechanisms of radiation-associated valvular disease are largely unknown. CAVD is considered to be an actively regulated disease process, mainly controlled by valvular interstitial cells (VICs). We hypothesize that radiation exposure catalyzes the calcific response of VICs and, therefore, contributes to the development of radiation-associated valvular disease.

Methods and Results: To delineate the relationship between radiation and VIC behavior (morphology, calcification, and matrix turnover), two different *in vitro* models were established: (1) VICs were cultured two-dimensional (2D) on coverslips in control medium (CM) or osteogenic medium (OM) and irradiated with 0, 2, 4, 8, or 16 Gray (Gy); and (2) three-dimensional (3D) hydrogel system was designed, loaded with VICs and exposed to 0, 4, or 16 Gy of radiation. In both models, a dose-dependent decrease in cell viability and proliferation was observed in CM and OM. Radiation exposure caused myofibroblast-like morphological changes and differentiation of VICs, as characterized by decreased αSMA expression. Calcification, as defined by increased alkaline phosphatase activity, was mostly present in the 2D irradiated VICs exposed to 4 Gy, while after exposure to higher doses VICs acquired a unique giant fibroblast-like cell morphology. Finally, matrix turnover was significantly affected by radiation exposure in the 3D irradiated VICs, as shown by decreased collagen staining and increased MMP-2 and MMP-9 activity.

Conclusions: The presented work demonstrates that radiation exposure enhances the calcific response in VICs, a hallmark of CAVD. In addition, high radiation exposure induces differentiation of VICs into a terminally differentiated giant-cell fibroblast. Further studies are essential to elucidate the underlying mechanisms of these radiation-induced valvular changes.

Keywords: aortic valve disease, radiotherapy, extracellular matrix, *in vitro* modeling, valvular interstitial cells

INTRODUCTION

Despite ongoing technical advances, radiotherapy for treating malignancies in the thoracic region, including lung cancer, thymoma, and lymphoma, is still associated with an increased risk of cardiovascular disease (1, 1–4). As a consequence of exposure of the heart and great vessels to radiation, patients receiving radiotherapy have an increased risk of developing pericarditis, coronary artery disease, cardiomyopathy, and valvular disease years after initial exposure (2, 3, 5–8). Moreover, this risk is even higher in patients receiving radiotherapy before the age of 21 (5, 9). Aortic valve disease represents the majority of radiation-induced valvular diseases (4, 10, 11). Within 20 years after mantle radiation for lymphoma, the incidence of aortic valve stenosis is as high as 16% (12). The only effective treatment for aortic valve stenosis is surgical replacement of the diseased valve (13), however, surgical risks are significantly increased in patients that received chest radiotherapy (14).

Radiation-associated aortic valve disease demonstrates pathological hallmarks similar to calcific aortic valve disease (CAVD) (11, 15, 16). Generally, CAVD is characterized by initial fibrotic thickening of the aortic valve leaflets, which progresses into mineralization of the valve and eventually causes aortic valve leaflet dysfunction due to aortic valve stenosis (17). Traditionally, CAVD was believed to be a passive disease, culminating from years of wear and tear. However, developing insights into the disease have changed these views, and CAVD is now considered to be an active disease process (17). One of the key players in CAVD are resident valvular interstitial cells (VICs) (18). In the normal, healthy aortic valve, VICs represent quiescent fibroblast-like cells, which can differentiate into myofibroblast-like cells upon exposure to environmental stimuli (18, 19). These activated VICs, characterized by alpha smooth muscle actin (αSMA) expression, can remodel the extracellular matrix (ECM) by expressing matrix metalloproteinases (MMPs) or depositing ECM proteins such as collagen (19). The interplay between the quiescent and activated state of VICs is essential in maintaining valvular tissue homeostasis, and provides for the ability of heart valves to adapt to changes in functional demand (20, 21).

The fibrocalcific response observed in early CAVD is thought to be a consequence of persistent activation of VICs (18). In addition, histological studies of end-stage stenotic aortic valves have demonstrated the presence of osteoblast-like cells (21, 22). Numerous reports demonstrated that activated VICs can also differentiate into osteoblast-like cells and actively deposit calcium in the valve interstitium (21). This osteoblast-like differentiation is characterized by the loss of the αSMA expression and the elevation of bone markers, including the transcription factors Runx2 and Osterix, and increased alkaline phosphatase (ALP) activity (23). The temporal relationship of these VIC phenotypes and how they relate to CAVD onset or even progression in humans is not completely understood (20, 21, 24).

Radiation-associated valvular disease cannot merely be equated to CAVD. Specific cellular and ECM responses to ionizing radiation used in radiotherapy have been well documented. Exposure to radiation has shown to activate stromal fibroblasts (25). In addition, increased activation and production of transforming growth factor beta (TGFβ) has been reported as a result of radiation exposure to vessels and myocardium, which in turn leads to increased collagen deposition (26, 27). Explanted heart valves have shown the presence of terminally differentiated atypical giant-cell like fibroblasts, which also have been observed in the skin after radiation therapy (28, 29).

Despite ongoing advances in radiotherapy procedures, the incidence of radiation-induced CAVD is still expected to rise in the future. New radiotherapy techniques are efficient in sparing the heart from radiation exposure while delivering adequate radiation doses to the target area, but improved treatments also increase the number of long-time survivors, thus increasing the number-at-risk (3, 4, 30, 31). To our knowledge, only one other study examined the effects of radiation on the aortic valve in cell culture, but no studies to date have been conducted using three-dimensional (3D) cell culture models of CAVD (32). Such models allow for systematic manipulation of experimental conditions, including radiation dose, and detailed monitoring and analysis of the radiation effects. The aim of this work is to investigate the relationship between radiation and the development of CAVD, using two-dimensional (2D) and three-dimensional (3D) *in vitro* models of the disease. We hypothesize that radiation catalyzes the calcific response of VICs. The work presented here is an initial step in the ongoing research focused on unraveling the effects of radiation exposure on the development of CAVD.

Abbreviations: ALP, alkaline phosphatase; αSMA, alpha smooth muscle actin; ATP, adenosine triphosphate; CAVD, calcific aortic valve disease; CM, control medium; ECM, extracellular matrix; GelMA, methacrylated gelatin; Gy, Gray; HAMA, methacrylated hyaluronic acid; MMP, matrix metalloproteinase; OM, osteogenic medium; RT-PCR, real-time polymerase chain reaction; VIC, valve interstitial cells; Runx2, runt-related transcription factor 2; TGFβ, transforming growth factor beta.

MATERIALS AND METHODS

To investigate the effects of radiation on aortic valvular cells and tissue mimics, two *in vitro* models were used. First, the effects of radiation were evaluated on 2D samples containing VICs. VICs, isolated from porcine aortic valves, were cultured on coverslips in either control medium (CM) or osteogenesis permissive medium (OM) and exposed to increasing doses of radiation. Afterwards, cells were kept in culture and analyzed for cell viability and proliferation by measuring adenosine triphosphate (ATP) and DNA content. VIC morphology and differentiation were assessed with RT-PCR and immunohistochemical staining. Osteogenesis in the irradiated VICs was determined by measuring ALP activity. Next, to better mimic the microenvironment of the cells, a methacrylated hyaluronic acid (HAMA) – methacrylatedgelatin (GelMA) 3D hydrogel system was designed and seeded with porcine VICs. 3D hydrogels, cultured in either CM or OM, were then exposed to 0, 4, or 16 Gy of radiation. Experimental setup of the 3D experiments, including the different radiation doses used, were based on data from the 2D experiments. After irradiation of the cell-laden 3D hydrogel constructs, a compaction assay was performed to determine the effect of radiation on hydrogel structure. DNA content was measured to assess cell viability. The hydrogels were cut into sections and stained for DNA damage and various markers to evaluate VIC differentiation. Matrix turnover was analyzed by measuring MMP-2 and MMP-9 activity, measuring gene expression of collagen-encoding genes and immunofluorescent stainings of collagen expression.

Valvular Interstitial Cell Isolation and Culture

Porcine aortic VICs were isolated from porcine aortic valve leaflets by sequential collagenase/elastase digestion as described previously (33). The cells were cultured in normal growth medium containing Dulbecco's Modified Eagle Medium (DMEM) with high glucose and pyruvate (Gibco, Life Technologies, Grand Island, NY, USA), supplemented with 10% fetal bovine serum (FBS) and 1% penicillin/streptomycin (P/S) (both Gibco) at 37°C and 5% CO_2. This medium condition was also used as CM. The cells were cultured until 70–80% confluency was reached, and then passaged. For all experiments, cells between passage three and six were used. For immunofluorescence, cells were seeded on gelatin-coated coverslips. Cells from three different donors were used for the 2D experiments and another three donors were used for the 3D hydrogel experiments.

Hydrogel Fabrication

For the 3D experiments, hybrid hydrogels were fabricated from HAMA and GelMA as reported previously (33), using photo-crosslinking. Briefly, VICs were resuspended in the prepolymer solution, consisting of 1 wt% HAMA and 5 wt% GelMA, in a concentration of 10 million cells/mL. Then, 50 μl of the cell-laden polymer solution was added between two spacers with a height of 450 μm. The cell-laden polymer solutions were then subjected to UV light (wavelength 360 nm) of 2.5 mW/cm^2 for 30 seconds (Omnicure S2000, EXFO Photonic Solutions Inc, Ontario, Canada). The resulting VIC-laden hydrogels were then transferred to well plates for culturing in either CM or OM. OM consisted of CM supplemented with 10 mM β-glycerophosphate, 10 ng/mL ascorbic acid, and 10 nM dexamethasone (Sigma-Aldrich, St. Louis, MO, USA). The effects of radiation on hydrogel composition were evaluated by performing a compaction assay.

Irradiation

For the 2D irradiation experiments, VICs were plated at a seeding density of 10.000/cm^2 24 h before irradiation. Prior to irradiating the cells, medium was changed to CM or OM. The cells were irradiated with 0, 2, 4, 8, and 16 Gy (0.90 Gy/min) with a Gammacell 40 Exactor Cs-137 irradiator (Best Therotronics, Ottawa, Ontario, Canada). Using the linear-quadratic model (34) with an α/β ratio of 3 Gy for normal tissue late effects, a single 4 Gy dose would be estimated to have the biological effect of a total of 8.5 Gy delivered over 30 fractions, in keeping with modern radiotherapy techniques that seek to lower cardiac dose when treating adjacent organs such as the lung. A single 16 Gy dose would be estimated to have the biological effect of a total of 60 Gy delivered over 30 fractions, which would result from full exposure of the valve to therapeutic doses. After irradiation, cells were kept in culture for 1, 2, 7, or 14 days, depending on the type of analysis.

The 3D hydrogels were fabricated three days before irradiation. Prior to irradiation of the hydrogels, medium was changed to CM with HEPES buffer. The hydrogels were irradiated with 0, 4, and 16 Gy with an Elekta linear accelerator of the hospital. The radiation doses were given from two directions [anterior-posterior-posterior-anterior (AP-PA)] with an instantaneous dose-rate of around 6 Gy/min. The mean dose-rate during irradiation was 4 Gy/min for the 4 Gy group (total treatment time: 1 min) and 5.3 Gy for the 16 Gy group (total treatment time: 3 min). After irradiation, medium was changed to CM or OM and hydrogels were kept in culture for 1, 3, 8, 15, and 21 days, depending on the type of analysis. The control groups of both experiments (0 Gy) were transported to the location of irradiation together with the treated groups.

Cell Viability and Proliferation

To assess cell viability after irradiation, the ATP content of the cells in the 2D models was measured at day 2 using a luminescent cell viability assay (Progema, Madison, WI). The DNA content was measured in both the 2D and 3D models using the Quant-iT PicoGreen Kit (Life Technologies).

Histological and Immunofluorescent Stainings

Samples from different time points were used for histological and immunofluorescence analysis. To assess immediate radiation-induced DNA damage in the 3D hydrogels, they were sacrificed 30 to 60 min after irradiation. The hydrogels were fixed in 3.7% formaldehyde solution (Sigma-Aldrich) and kept in 30% sucrose solution overnight at 4°C. The VIC-laden hydrogels were then frozen in optimal cutting temperature (OCT) compound and 10 μm cross-sections were obtained

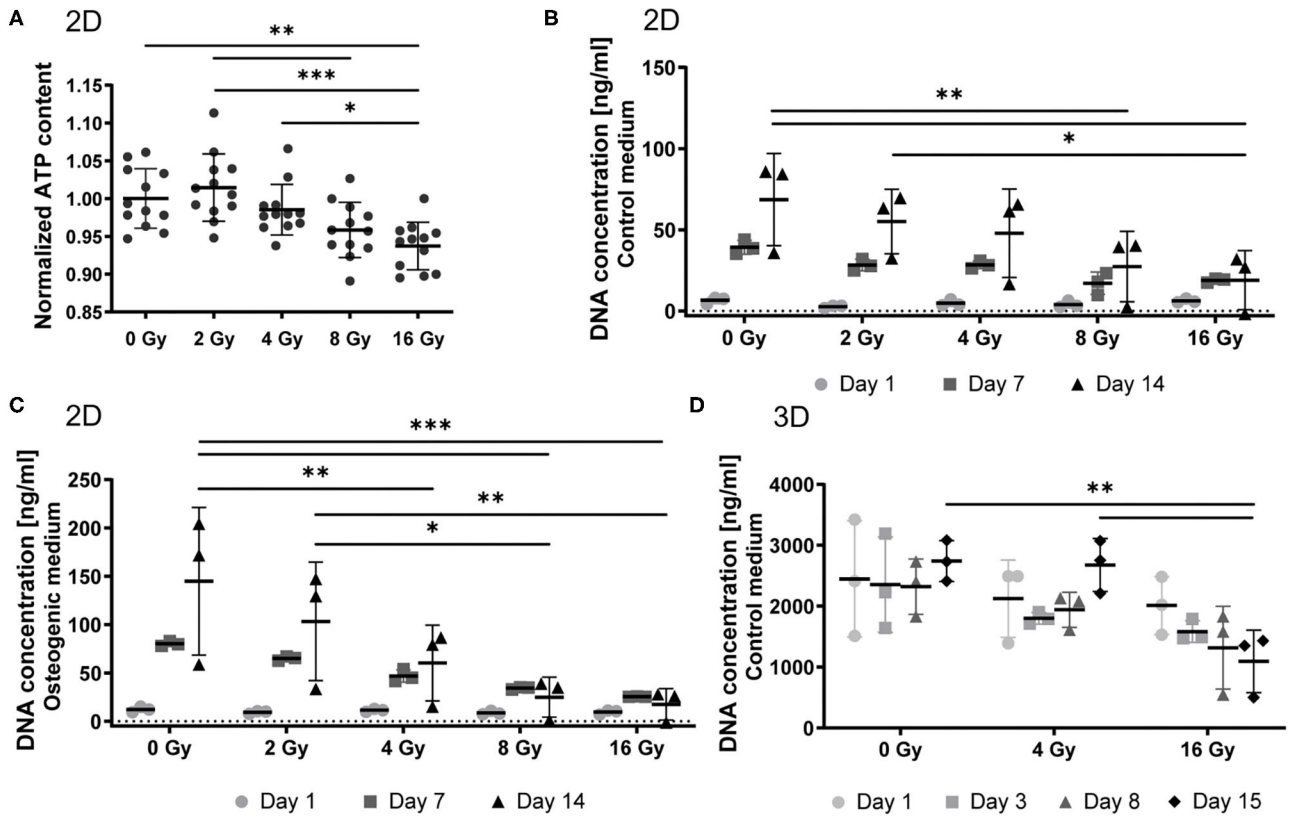

FIGURE 1 | Radiation affects cell viability and proliferation in a dose-dependent manner. **(A)** Quantification of ATP content in 2D VICs exposed to 0, 2, 4, 8, and 16 Gy after 48 h and normalized for DNA content, $n = 12$. **(B–D)** Quantification of proliferation by measurement of the DNA content after 1, 7, and 14 days post radiation for 2D groups in control **(B)** and osteogenic **(C)** medium, and 1, 3, 8, and 15 days post radiation for 3D groups in control medium **(D)**. Significance is represented as *($P < 0.05$), **($P < 0.01$), and ***($P < 0.001$), $n = 3$.

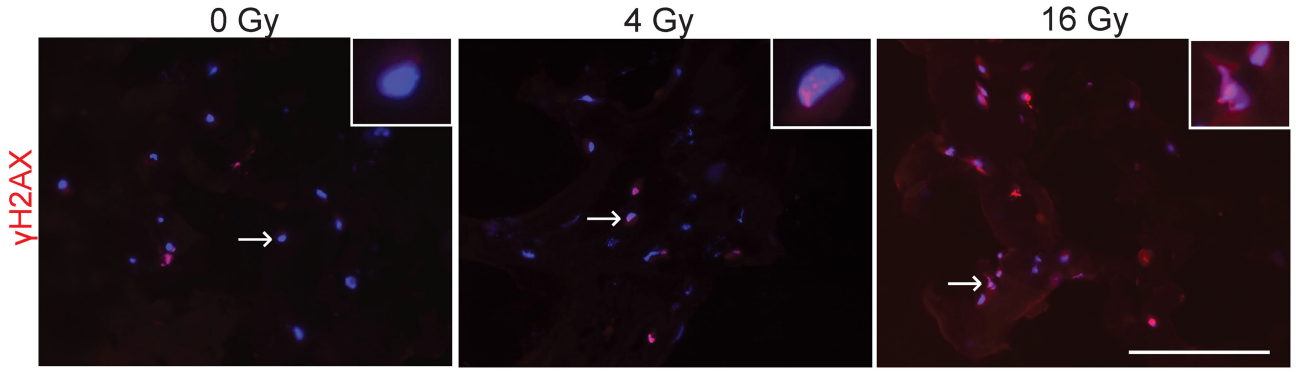

FIGURE 2 | Radiation causes DNA damage. Representative immunofluorescent stained sections of 3D hydrogel samples treated with 0 Gy, 4 Gy, and 16 Gy of radiation. Samples were fixated 30–60 minutes after radiation and stained for γH2AX (red) and cell nuclei (blue). Inserts show higher magnification of cell nuclei indicated by the arrow. Scale bars represent 100 μm.

using a cryostat. Sections were treated with peroxide for antigen retrieval, permeabilized with 0.5% Triton X-100 (Sigma-Aldrich) and blocked with 3% bovine serum albumin (BSA) for 30 min. In order to detect radiation-induced DNA-damage, the sections were stained for γH2AX (Ab22551, Abcam), a marker for double-strand DNA breaks, by incubating the sections with anti-γH2AX antibodies for 1 h at room temperature. Sections were counterstained with 4', 6-diamidino-2-phenylindole (DAPI) (Life Technologies) to visualize cell nuclei. Sections were washed, mounted in Mowiol (Sigma-Aldrich) and analyzed using fluorescence microscopy (Axiovert 200M; Carl Zeiss).

At 14 days post-irradiation, VICs in 2D culture were fixed with ice-cold methanol for 30 min. Immunofluorescence staining for αSMA and collagen was performed using anti-human αSMA antibodies (Clone 1A4, Dako, Carpinteria, CA, USA) and a fluorescent probe (CNA35) for live monitoring of collagen, as previously reported by us (35). Sections were counterstained with DAPI (Life Technologies). At 15 days the hydrogel sections were stained for αSMA, vimentin (Ab20346, Abcam), collagen type I (c2456, Sigma Aldrich) and collagen type III (Ab7778, Abcam). ALP activity was visualized with a 5-bromo-4-chloro-3-indolyl phosphate/nitroblue tetrazolium (BCIP/NBT) solution (Amresco, Kaysville, UT, USA) and an eosin counterstaining (Sigma Aldrich).

Quantification of Alkaline Phosphatase Activity in the 2D Models

Alkaline phosphatase (ALP) activity in the 2D irradiated VICs were quantified using a colorimetric assay kit (Biovision, Milpitas, CA) on day 1, 7 and 14, and normalized to DNA content.

Real-Time Polymerase Chain Reaction

To quantify mRNA expression of irradiated VICs, RT-PCR was performed RNA was isolated with a RNeasy kit (Qiagen, Valencia, CA, USA) on day 1, 7, and 14 after irradiation. From the extracted RNA, complementary DNA was made with oligo-(dT)12-18 primers and SuperScript II reverse transcriptase (Life Technologies). RT-PCR was performed using SYBR Green (BioRad, Hercules, CA, USA) for *ACTA2* (cell activation), *COL1A1* and *COL3A1* (cell functionality), *VIM* (mesenchymal differentiation) and the housekeeping gene glyceraldehyde 3-phosphate dehydrogenase (GAPDH). The following primer sequences were used: *ACTA2*: F:5′-AGTGCGACATTGACAT CAGG-3′ and R:5′-CTGGAAGGTGGACAGAGAGG-3′; *COL1A1*: F:5′CCAAGAGGAGGGCCAAGAAGAAGG-3′ and R:5′-GGGGCAGACGGGGCAGCACTC-3′, *COL3A1*: F:5′CCTGGACGAGATGGAAACCC-3′ and R:5′-ATTTTCAC CACGATCGCCCT-3′, *VIM:* F:5′-AGCAGTATGAGAGTGT GGCC-3′ and R:5′CTTCCATTTCCCGCATCTGG-3′, and *GAPDH*: F:5′-CCCAGAAGACTGTGGATGG-3′, R:5′- ACCT GGTCCTCAGTGTAGCC-3′. mRNA expression was quantified using the comparative Ct method.

Quantification of Matrix Metalloproteinase Activity

To assess the relative difference in MMP activity, gelatin zymography was used. The hydrogels were disrupted with a mikro-dismembrator and loaded into a gelatin co-polymerized SDS-PAGE gel. SDS was removed from the gel by 2.5% Triton X-100 incubation. Subsequently, the gel was incubated in digestion buffer (50 mM TRIS, 4.8 mM $CaCl_2$, pH = 8.5) overnight at 37°C for enzymatic digestion. Next the zymogram was stained for 2 hours with 0.1% (w/v) Brilliant Blue R in 4% (v/v) methanol and 10% (v/v) acetic acid in water followed by de-staining in 4% (v/v) methanol and 10% (v/v) acetic acid in water for 1 h. The zymogram was imaged with a Proxima AQ-4 scanner (Isogen Life Science). Band intensities were analyzed using ImageJ (U.S. National Institute of Health). The MMP activity was normalized to DNA content.

Statistical Analysis

Data are presented as mean ± standard deviation (SD) unless indicated otherwise. To evaluate differences between groups, a one-way ANOVA was performed. For *post-hoc* testing, the Bonferroni test was used. $P < 0.05$ was considered as statistically significant.

RESULTS

Radiation Affects Cell Viability and Proliferation in a Dose-Dependent Manner

VICs were cultured on 2D coverslips and exposed to 0, 2, 4, 8, and 16 Gy of radiation. To evaluate cellular viability, we performed an ATP activity assay. ATP content of VICs decreased upon exposure to increasing radiation doses (**Figure 1A**). We observed a 7% decrease in cell viability in the 16 Gy group, compared to the control group (0 Gy). Next, we determined the proliferation response of the 2D irradiated VICs by quantifying DNA content at several time points after radiation (**Figures 1B,C**). The proliferative activity of these VICs decreased upon increased radiation doses, following a similar trend to cellular viability, establishing a dose-dependent response of VICs to radiation. A similar dose-dependent trend was seen in the irradiated VICs encapsulated in 3D hydrogels, whereby DNA content decreased for the 16 Gy groups 15 days post-exposure, compared to the groups that were exposed to 0 or 4 Gy (**Figure 1D**).

To evaluate potential DNA damaging effects of radiation exposure, 3D hydrogel sections were stained for γH2AX to detect radiation-induced double stranded DNA breaks (**Figure 2**). These stainings showed that in the groups exposed to 4 and 16 Gy, more γH2AX foci are present and have an increased intensity compared to the control group (0 Gy). Our results suggest that radiation causes dose-dependent DNA damage in VICs.

Radiation Causes Myofibroblast-Like Morphological Changes and Differentiation of VICs

To assess different characteristics of the 2D and 3D irradiated VICs, immunohistochemistry and gene expression analyses (RT-PCR) were performed. VICs demonstrated a myofibroblast-like phenotype when cultured in both CM (**Figure 3A**) and OM (**Figure 4A**), characterized by αSMA expression. In both conditions, the number of cells in each well decreased when exposed to increasing radiation doses. Conversely, the cellular size of VICs visually increased upon exposure to higher radiation doses. After exposure to higher radiation doses (16 Gy), VICs were visually observed to adapt a giant cell-like fibroblast phenotype (**Figures 3A**, **4A**).

In addition, a decrease in the number of αSMA-positive cells was observed in both CM and OM when exposed to increasing doses of radiation, compared to the control group

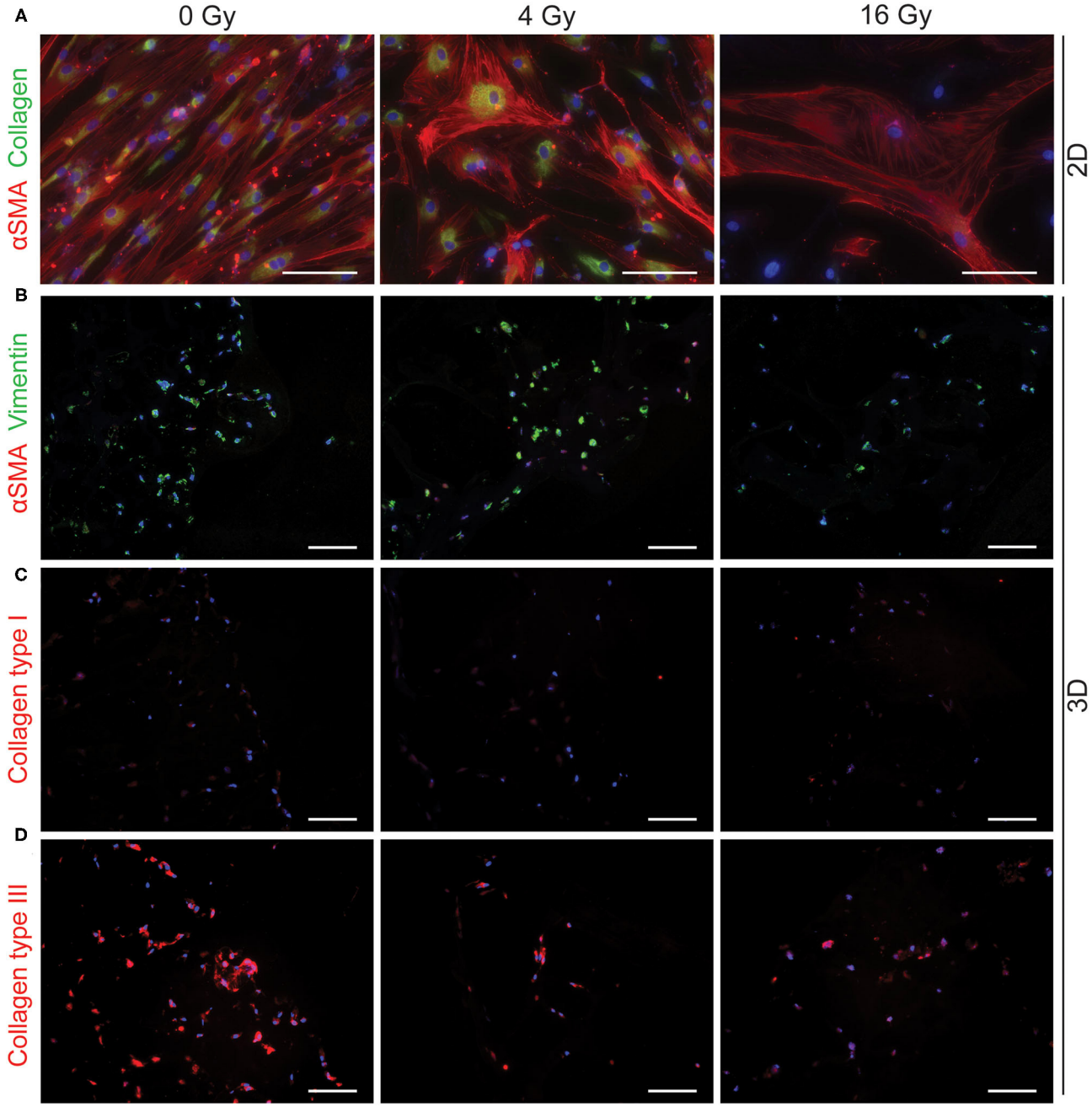

FIGURE 3 | Radiation adversely affects cell morphology in control medium. Staining of 2D cell cultures 14 days after 0 Gy, 4 Gy, and 16 Gy of radiation treatment for αSMA (red) and collagen (green) **(A)**. Sections of 3D hydrogels are stained for αSMA (red) and vimentin (green) **(B)**, collagen type I **(C)**, and collagen type III **(D)**. Nuclei are visualized in blue. Scale bars represents 50 μm in 2D cultures and 100 μm in 3D cultures.

(0 Gy) (**Figures 3A**, **4A**). These observations were confirmed by RT-PCR, where αSMA expression followed a similar trend (**Figure 5A**). No differences between groups were observed at day 1 after irradiation, but a clear decrease in αSMA expression was seen at day 7 post-exposure. In the 3D hydrogels, less αSMA-positive cells were present in both culture conditions compared to the 2D VICs (**Figures 3B**, **4B**). However, no clear difference could be observed between the three radiation doses after 15 days. Nonetheless, gene expression analysis showed that 16 Gy, but not 4 Gy, causes a significant decrease in αSMA expression in 3D irradiated VICs (**Figure 6**).

Radiation Causes Osteogenesis in VICs

To assess the effects of radiation on osteogenesis in VICs, the activity of early osteogenic marker alkaline phosphatase (ALP) was measured at day 14 of cell culture. To visualize ALP activity,

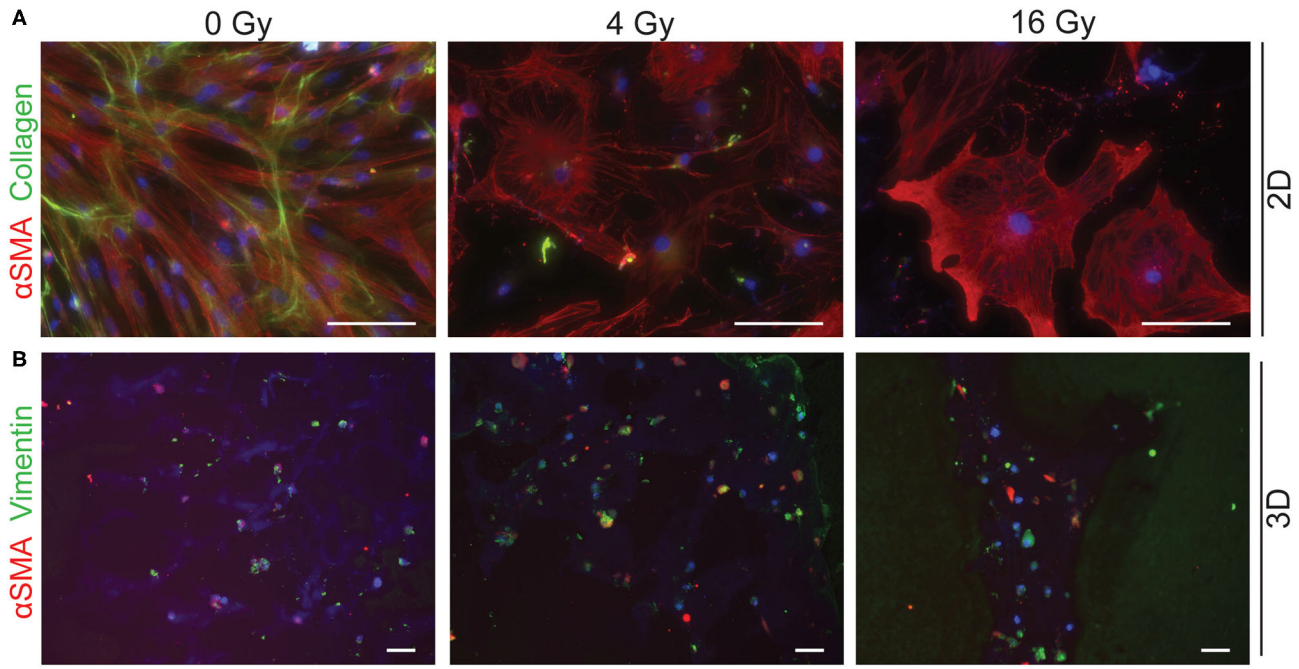

FIGURE 4 | Radiation adversely affects cell morphology in osteogenic medium. Staining of 2D cell cultures for αSMA (red) and collagen (green) 14 days after 0 Gy, 4 Gy, and 16 Gy of radiation treatment **(A)**. Sections of 3D hydrogels are stained for αSMA (red) and vimentin (green) **(B)**. Nuclei are visualized in blue. Scale bars represents 50 μm in 2D cultures and 100 μm in 3D cultures.

VICs were stained with BCIP/NBT, resulting in a dark blue staining due to ALP hydrolyzing BCIP (**Figures 7A,B**). We demonstrated that ALP activity is present in 2D cultured VICs at day 14 of culture and quantified ALP at that day. No ALP activity was observed in the CM groups, apart from the groups that were exposed to high radiation doses (16 Gy). However, when cultured in OM, VICs showed ALP activity predominantly in the group exposed to 4 Gy. Upon exposure to 16 Gy, less ALP-positive cells were observed (**Figure 7C**).

Matrix Turnover in 3D Hydrogels Changes After Radiation Exposure

In the 2D irradiated VICs, we observed a decrease in collagen staining at day 14 of culture, which remained present in a lesser amount after irradiation with 4 Gy but was obsolete at higher radiation doses (**Figures 3A,C,D**). This was confirmed by gene expression of collagen type 1 (*COL1A1*), which showed a decline in expression alongside increasing radiation doses, both in 2D culture (**Figure 5B**) and in the 3D hydrogels (**Figure 6**). In the 3D hydrogels, MMP2 and MMP9 activity also increased over time with higher radiation doses (**Figure 8**).

DISCUSSION

The presented work focused on studying mechanisms of radiation-associated valvular disease using both 2D and 3D established *in vitro* platforms to study CAVD (33, 36). We demonstrated that *in vitro*, radiation exposure induces a decrease in cell viability and proliferation of cultured VICs in a dose-dependent manner. In addition, we showed decreased myofibroblast-like differentiation of VICs when exposed to increasing radiation doses, both in control and osteogenic media. However, an increase in early osteogenic activity was observed upon increasing radiation doses in an osteogenic environment. Next, we visually observed morphological transformation of VICs into a giant cell-like fibroblast phenotype after exposure to higher doses of radiation in osteogenic medium. Finally, we showed that ECM remodeling was affected by radiation exposure. While deposition of new ECM proteins, such as collagen type I and III, was decreased after radiation exposure, MMP activity was induced. In sum, these results suggest that radiation exposure catalyzes the calcific response of VICs as observed in CAVD.

However, these outcomes should be interpreted carefully. After exposure of 2D and 3D VICs to higher doses of radiation (8 and 16 Gy), we observed not only a decreased viability and proliferation, but also a marked change in cell morphology as was apparent by the giant fibroblast-like aspect they obtain after 14 days of culture. Previous studies have reported on these atypical giant-sized fibroblasts in skin, indicating their terminal differentiation (28). Although we have not evaluated DNA damage at this stage, other work has demonstrated that high doses of radiation are associated with increased cellular damage (37) that could suggest the abnormal morphological changes of the VICs in our work. Importantly, these abnormal cells exhibited ALP activity, a marker for early osteogenesis (38). Additional analysis of the mineralization potential of these

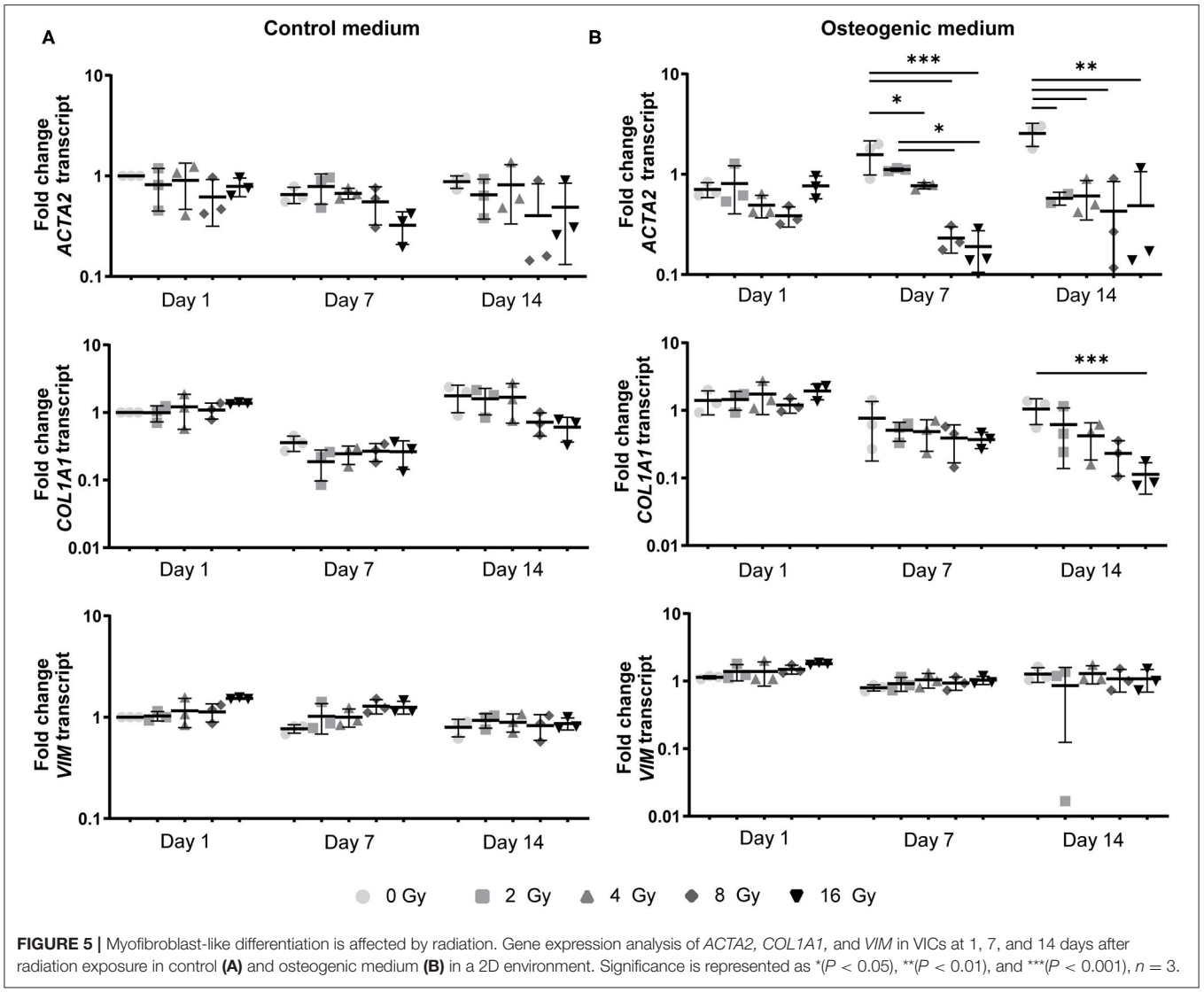

FIGURE 5 | Myofibroblast-like differentiation is affected by radiation. Gene expression analysis of *ACTA2, COL1A1,* and *VIM* in VICs at 1, 7, and 14 days after radiation exposure in control **(A)** and osteogenic medium **(B)** in a 2D environment. Significance is represented as *($P < 0.05$), **($P < 0.01$), and ***($P < 0.001$), $n = 3$.

giant cells is still warranted, but our results already indicate that radiation may induce an osteogenic VIC phenotype *in vitro*. VICs have a higher radio-resistant capacity than most cancer cell lines (39). Nevertheless, they do follow a similar dose-dependent pattern to other cancer cell line studies (39). Osteogenic activity was only observed in VICs cultured in osteogenic medium and exposed to high doses of radiation, supporting our hypothesis that radiation accelerates the osteoblast-like differentiation of VICs, but only when exposed to an osteogenic environment.

VICs are essential in maintaining structural and functional integrity of the aortic valve by continuous remodeling of the ECM through deposition of matrix components, such as collagen, and matrix degradation through increased MMP activity. Our results indicate that ECM remodeling is significantly affected by radiation exposure. The data show that the deposition of newly formed collagen was decreased with exposure to higher radiation doses. On the other hand, MMP-2 and MMP-9 proteolytic activity was increased with increasing radiation doses, suggesting that matrix degradation does continue to occur. The elevation of MMP activity after radiation exposure has already been extensively reported in patients receiving radiotherapy for various types of cancer, including breast cancer and malignant gliomas (40–42). Our findings are therefore in line with other studies that examined the effects of radiation on MMP function. However, further studies are needed to unravel the role of these proteases on the pathogenesis and progression of radiation-associated valvular disease. These findings also emphasize the importance of using 3D models in this context, since these models enable the possibility to study the interplay between VICs and their environment.

Few reports have investigated radiation-associated CAVD (27, 32). Studying the VIC response in conventional *in vitro* models is not sufficient to recapitulate all events that may occur *in vivo*. To overcome this challenge, hydrogel micro-engineering has emerged as a powerful tool to create 3D tissue models recapitulating the VIC micro-environment

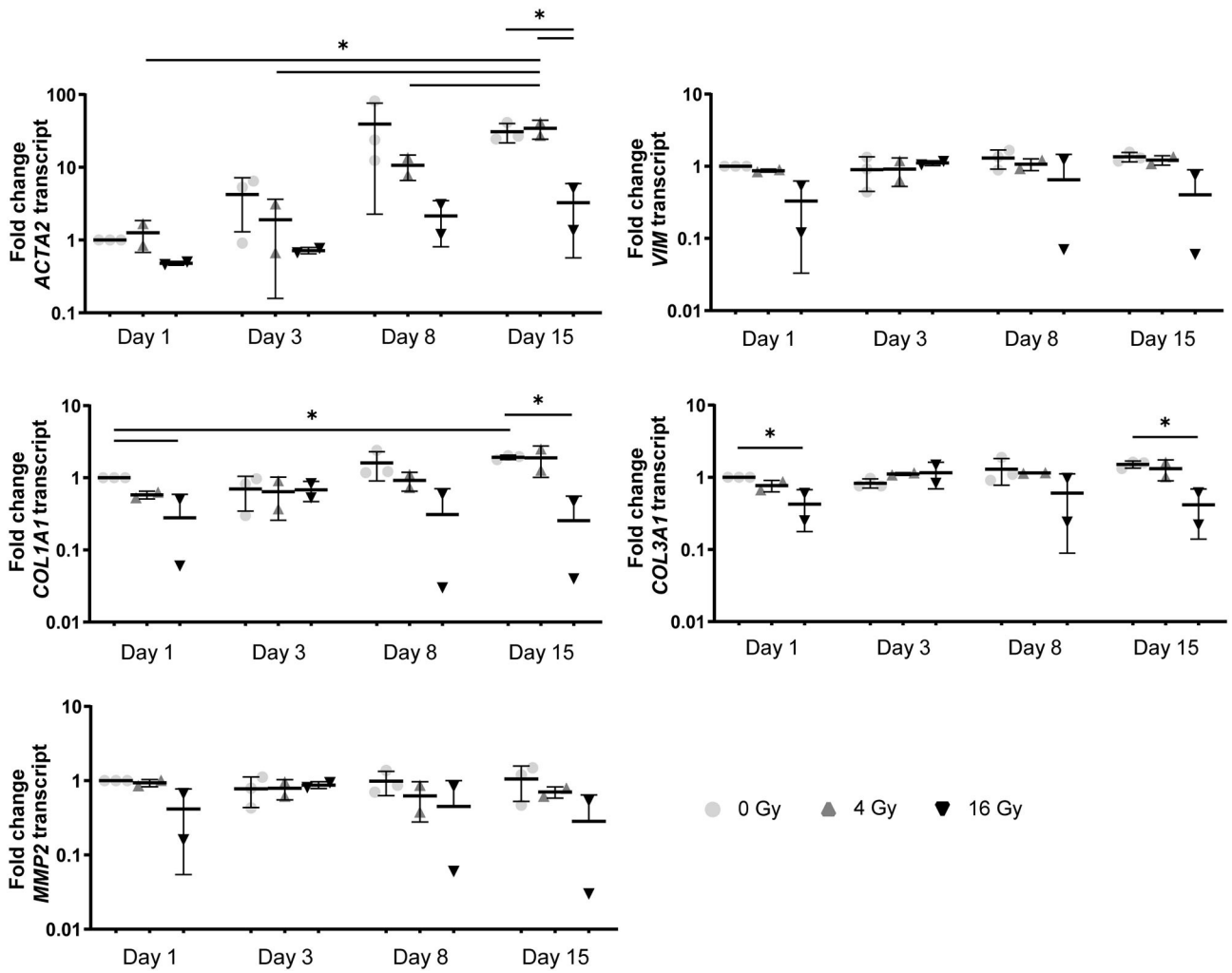

FIGURE 6 | In a 3D environment radiation exposure to 16 Gy, but not 4 Gy, induces changes in VIC differentiation. Gene expression analysis *ACTA2, VIM, COL1A1, COL3A1,* and *MMP2* in VICs at 1, 3, 8, and 15 days post radiation in control medium in 3D hydrogels. Significance is represented as *($P < 0.05$), **($P < 0.01$), and ***($P < 0.001$), $n = 3$.

in vitro. We have previously demonstrated that combining hyaluronic acid and collagen by UV photo-crosslinking, a 3D environment can be created that mimics the micro-environment of the aortic valve (33, 36). Since this system facilitates VIC quiescence, it could offer a valuable platform to study the effects of radiation on valvular tissue as it may occur *in vivo*, since culturing VICs on stiff culture plates has been associated with myofibroblastic activation of the cells (33). Our results demonstrate that the hydrogel structure seems to be unaffected by radiation exposure, as measured by changes in compaction. Possibly, elasticity and porosity of the hydrogels should also be evaluated in future assays. Moreover, the VICs that were being irradiated in this study were quiescent before irradiation, which more accurately mimics *in vivo* conditions than when VICs are cultured on stiff culture plates and thus already become activated prior to irradiation.

Because of our observations that VICs in culture develop into atypical giant cell-like fibroblasts when exposed to higher doses of radiation (8 and 16 Gy), but retain their native morphology at 4 Gy, we chose to expose the VIC-laden hydrogels to only lower and higher doses (4 and 16 Gy, respectively). Although radiotherapy is mostly conducted in a fractionated manner, 4 Gy is within the therapeutic range that patients undergoing radiotherapy receive. In addition, exposure to 16 Gy caused VICs to express osteogenic activity even in normal growth medium, potentially accentuating the accelerated mineralization observed in patients.

In non-radiation associated CAVD, mechanical stress is thought to be one of the initiators of calcification of the valve (43). This type of stress can induce lesions in the fibrosa layer of the aortic valve, eventually leading to the development of CAVD (18). Radiation can also cause microfractures in collagen (44). Therefore, such microlesions in irradiated heart valves

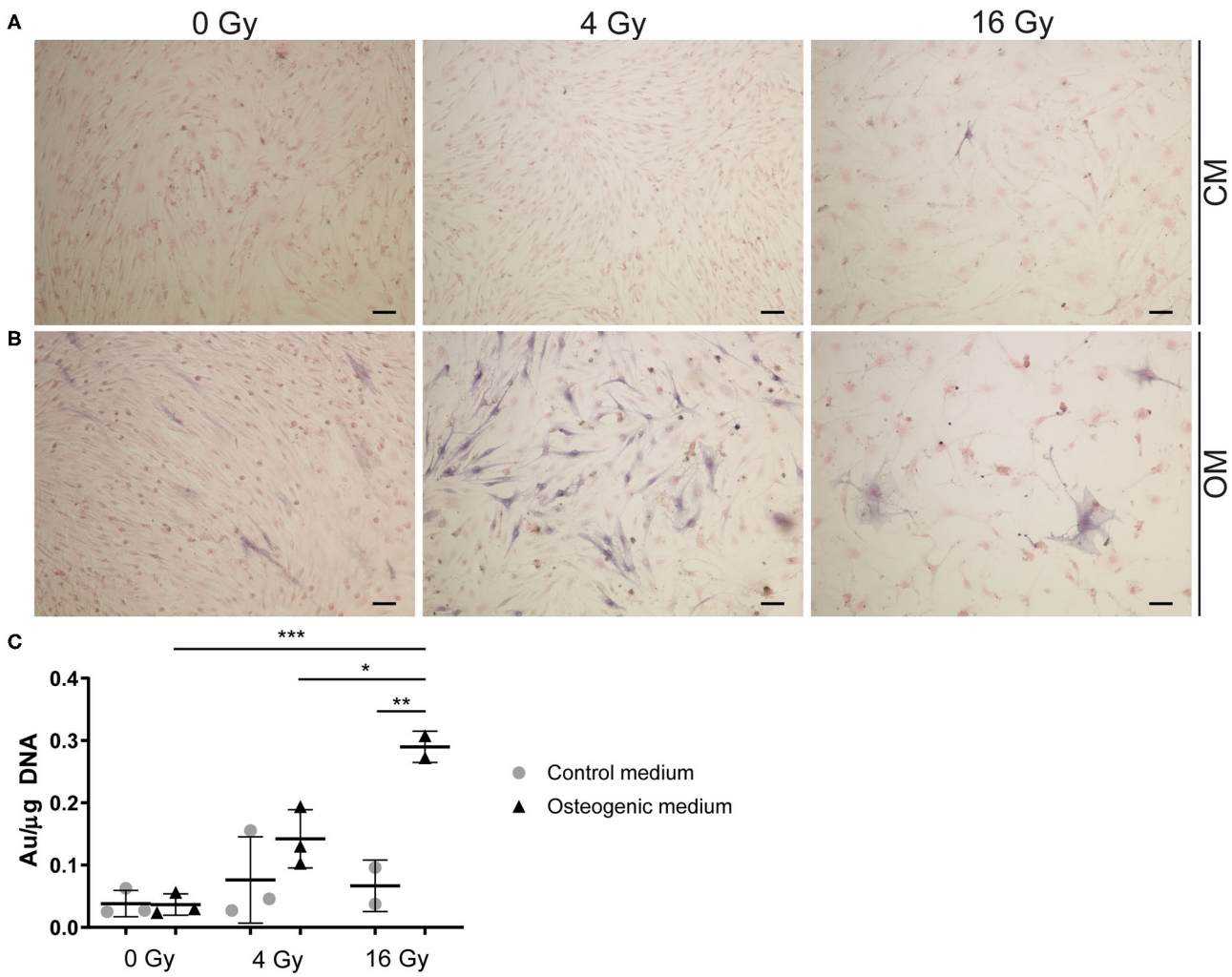

FIGURE 7 | Radiation increases alkaline phosphatase activity. **(A,B)** Staining of VICs in 2D culture for ALP in dark blue and the cytoplasm in pink. Cells were cultured in control **(A)** or osteogenic **(B)** medium. For radiation treatment 0, 4, and 16 Gy were used. **(C)** Quantification of ALP activity in VICs exposed to radiation in control medium (CM) and osteogenic medium (OM). Significance is represented with *($P < 0.05$), **($P < 0.01$), and ***($P < 0.001$), $n = 3$.

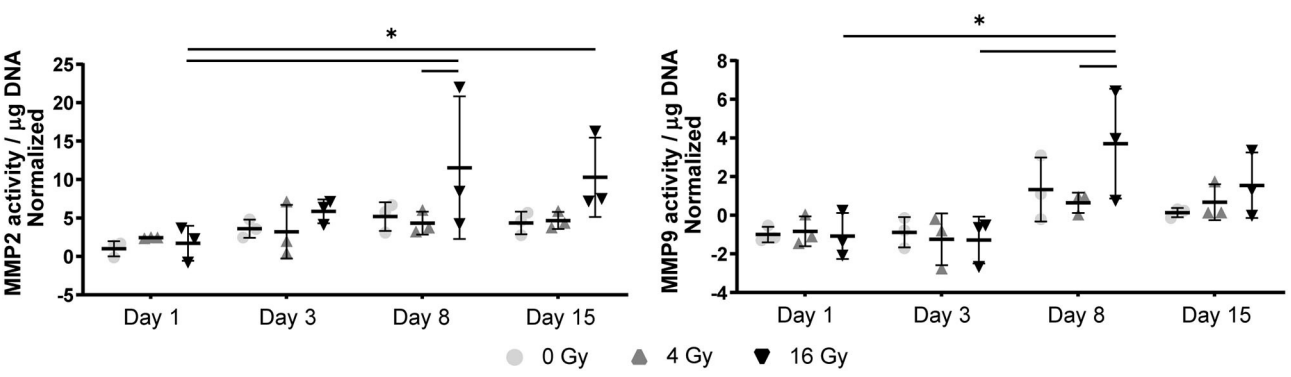

FIGURE 8 | MMP activity in 3D hydrogels increases with higher radiation dose and with time. Quantification of matrix metalloproteinase (MMP) 2 and 9 activity in the hydrogels at day 1, 3, 8, and 15 post radiation. MMP activity is normalized to background activity from the medium in cell-free hydrogels. Significance is represented with *($P < 0.05$), **($P < 0.01$), and ***($P < 0.001$), $n = 3$.

can be one of the key mechanisms in valvular heart disease after radiation therapy. Although compaction analysis showed no effect of radiation on the hydrogels, it is not ruled out that there is damage to the ECM proteins in the hydrogel. Structural analysis of the hydrogels exposed to radiation is therefore needed to investigate these possible mechanisms.

To date, little is known about the relationship between VICs and radiotherapy. To our knowledge, only one other study examined the effects of radiation exposure on VICs. Nadlonek et al. demonstrated an increase in osteoblast-like differentiation of VICs *in vitro*, when exposed to radiation (32). However, only one dose of radiation was used in this study. In order to further adjust dose regimens and protocols of radiotherapy in the future, it is essential to consider the variation of effects radiotherapy may have on tissue. Over the past few decades, great progress has been made in the context of radiotherapy effectiveness and safety (3, 4, 30, 31). With current standards, gamma radiation can better focus on targeted tissue and surrounding tissues can be spared from the damaging effects of radiation. Because of these developments, it is now possible to use higher doses of radiation targeted to a smaller area. However, these new techniques such as inverse-planned intensity modulated radiation therapy (IMRT), used for instance in breast cancer treatment, still involve radiation beams passing through the heart and exposing it to radiation (45, 46). In addition, indirect damage by reactive oxygen species (ROS) as a consequence of irradiation may occur in otherwise shielded areas (47, 48). Radiation-induced valvular disease remains an important issue in patients receiving radiotherapy.

We hypothesized that radiation accelerates the calcific response in the aortic valve. This work demonstrates that radiation exposure enhances loss of the myofibroblast-like phenotype of VICs and promotes their mineralization activity. In addition, we demonstrate that ECM remodeling, one of the most important functions of VICs in maintaining homeostasis of the aortic heart valve, is severely affected by radiation exposure. This might explain the late onset valvular deterioration that is seen in patients decades after receiving mediastinal radiotherapy. Lastly, this work emphasizes the importance of tissue-engineered 3D models of the valvular microenvironment for understanding key processes of radiation-associated CAVD, as they may occur *in vivo*. Further research using such models in direct comparison with *in vivo* data is required to draw clinically relevant conclusions on the development and progression of radiation-associated CAVD of the human aortic valve.

DATA AVAILABILITY STATEMENT

The original contributions presented in the study are included in the article/**Supplementary Material**, further inquiries can be directed to the corresponding author/s.

ETHICS STATEMENT

Ethical review and approval was not required for the animal study because in this work, porcine valvular interstitial cells (VICs) were used from rest material from pigs sacrificed at a slaughterhouse. Therefore, it was not necessary to obtain ethical approval from an ethics committee upon using these cells.

AUTHOR CONTRIBUTIONS

JH, RD, NE, and CB designed the experiments and RD, NE, JH, and IB performed the experiments. JS performed the radiation in the Catharina Hospital, Eindhoven. Data analysis, interpretation and creation of figures was performed by MM, RD, NE, IB, JH, EA, CB, and DK. The manuscript was written by MM, RD, NE, and JH. JH and CB supervised the project and secured funding. All authors have read, commented, and agreed to the content of the manuscript.

FUNDING

This work was supported by the Netherlands Heart Foundation (NHF-2011T024) and the Netherlands Scientific Council (NWO-92003572) (to JH); the Ministry of Education, Culture and Science for the Gravitation Program 024.003.013 Materials Driven Regeneration (to CB); and NIH grants R01 HL136431, R01 HL141917 and R01 HL147095 (to EA).

SUPPLEMENTARY MATERIAL

The Supplementary Material for this article can be found online at: https://www.frontiersin.org/articles/10.3389/fcvm.2021.687885/full#supplementary-material

Supplemental Figure 1 | Gelatin zymography bands for active MMP-9 (82 kDa) and active MMP-2 (62 kDa) measured 1, 3, 8 and 15 days post radiation (with 0 Gy, 4 Gy or 16 Gy). Three donors were included for every condition and non-radiated empty hydrogels (without VICs) were used as a negative control.

REFERENCES

1. McGale P, Darby SC, Hall P, Adolfsson J, Bengtsson NO, Bennet AM, et al. Incidence of heart disease in 35,000 women treated with radiotherapy for breast cancer in Denmark and Sweden. *Radiother Oncol.* (2011) 100:167–75. doi: 10.1016/j.radonc.2011.06.016
2. Van Nimwegen FA, Schaapveld M, Janus CPM, Krol ADG, Petersen EJ, Raemaekers JMM, et al. Cardiovascular disease after hodgkin lymphoma treatment 40-year disease risk. *JAMA Intern Med.* (2015) 175:1007–17. doi: 10.1001/jamainternmed.2015.1180
3. Ratosa I, Ivanetic Pantar M. Cardiotoxicity of mediastinal radiotherapy. *Reports Pract Oncol Radiother.* (2019) 24:629–43. doi: 10.1016/j.rpor.2019.09.002
4. Lewis GD, Farach A. Cardiovascular toxicities of radiation therapy. *Methodist Debakey Cardiovasc J.* (2019) 15:274–81. doi: 10.14797/mdcj-15-4-274
5. Aleman BMP, van den Belt-Dusebout AW, Klokman WJ. Van't Veer MB, Bartelink H, van Leeuwen FE. Long-term cause-specific mortality of patients treated for Hodgkin's disease. *J Clin Oncol Off.* (2003) 21:3431–9. doi: 10.1200/JCO.2003.07.131

6. Hancock SL, Tucker MA, Hoppe RT. Factors affecting late mortality from heart disease after treatment of Hodgkin's disease. *JAMA*. (1993) 270:1949–55.
7. Cella L, Liuzzi R, Conson M, Torre G, Caterino M, De Rosa N, et al. Dosimetric predictors of asymptomatic heart valvular dysfunction following mediastinal irradiation for Hodgkin's lymphoma. *Radiother Oncol J Eur Soc Ther Radiol Oncol.* (2011) 101:316–21. doi: 10.1016/j.radonc.2011.08.040
8. Jaworski C, Mariani JA, Wheeler G, Kaye DM. Cardiac complications of thoracic irradiation. *J Am Coll Cardiol.* (2013) 61:2319–28. doi: 10.1016/j.jacc.2013.01.090
9. van Nimwegen FA, Ntentas G, Darby SC, Schaapveld M, Hauptmann M, Lugtenburg PJ, et al. Risk of heart failure in survivors of Hodgkin lymphoma: effects of cardiac exposure to radiation and anthracyclines. *Blood.* (2017) 129:2257–65. doi: 10.1182/blood-2016-09-740332
10. Heidenreich PA, Hancock SL, Lee BK, Mariscal CS, Schnittger I. Asymptomatic cardiac disease following mediastinal irradiation. *J Am Coll Cardiol.* (2003) 42:743–9. doi: 10.1016/s0735-1097(03)00759-9
11. van Rijswijk JW, Farag ES, Bouten CVC, de Boer OJ, van der Wal A, de Mol BAJM, et al. Fibrotic aortic valve disease after radiotherapy: an immunohistochemical study in breast cancer and lymphoma patients. *Cardiovasc Pathol.* (2020) 45:107176. doi: 10.1016/j.carpath.2019.107176
12. Hull MC, Morris CG, Pepine CJ, Mendenhall NP. Valvular dysfunction and carotid, subclavian, and coronary artery disease in survivors of hodgkin lymphoma treated with radiation therapy. *JAMA.* (2003) 290:2831–7. doi: 10.1001/jama.290.21.2831
13. Hammermeister KE, Sethi GK, Henderson WG, Oprian C, Kim T, Rahimtoola S, et al. comparison of outcomes in men 11 years after heart-valve replacement with a mechanical valve or bioprosthesis. Veterans affairs cooperative study on valvular heart disease. *N Engl J Med.* (1993) 328:1289–96. doi: 10.1056/NEJM199305063281801
14. Crestanello JA, McGregor CGA, Danielson GK, Daly RC, Dearani JA, Orszulak TA, et al. Mitral and tricuspid valve repair in patients with previous mediastinal radiation therapy. *Ann Thorac Surg.* (2004) 78:826–31. doi: 10.1016/j.athoracsur.2004.04.008
15. Veinot JP, Edwards WD. Pathology of radiation-induced heart disease: a surgical and autopsy study of 27 cases. *Hum Pathol.* (1996) 27:766–73. doi: 10.1016/S0046-8177(96)90447-5
16. Tamura A, Takahara Y, Mogi K, Katsumata M. Radiation-induced valvular disease is the logical consequence of irradiation. *Gen Thorac Cardiovasc Surg.* (2007) 55:53–6. doi: 10.1007/s11748-006-0070-x
17. Yutzey KE, Demer LL, Body SC, Huggins GS, Towler DA, Giachelli CM, et al. Calcific aortic valve disease - a consensus summary from the alliance of investigators on calcific aortic valve disease. *Arterioscler Thromb Vasc Biol.* (2014) 34:2387–93. doi: 10.1161/ATVBAHA.114.302523
18. Aikawa E, Libby P. A rock and a hard place chiseling away at the multiple mechanisms of aortic stenosis. *Circulation.* (2017) 135:1951–5. doi: 10.1161/CIRCULATIONAHA.117.027776
19. Rabkin E, Hoerstrup SP, Aikawa M, Mayer JEJ, Schoen FJ. Evolution of cell phenotype and extracellular matrix in tissue-engineered heart valves during *in-vitro* maturation and *in-vivo* remodeling. *J Heart Valve Dis.* (2002) 11:308–14.
20. Liu AC, Joag VR, Gotlieb AI. The emerging role of valve interstitial cell phenotypes in regulating heart valve pathobiology. *Am J Pathol.* (2007) 171:1407–18. doi: 10.2353/ajpath.2007.070251
21. Rutkovskiy A, Malashicheva A, Sullivan G, Bogdanova M, Kostareva A, Stensløkken KO, et al. Valve interstitial cells: the key to understanding the pathophysiology of heart valve calcification. *J Am Heart Assoc.* (2017) 6:1–23. doi: 10.1161/JAHA.117.006339
22. Otto CM, Kuusisto J, Reichenbach DD, Gown AM, O'Brien KD. Characterization of the early lesion of "degenerative" valvular aortic stenosis. Histological and immunohistochemical studies. *Circulation.* (1994) 90:844–53. doi: 10.1161/01.cir.90.2.844
23. Mohler ER. 3rd, Gannon F, Reynolds C, Zimmerman R, Keane MG, Kaplan FS. Bone formation and inflammation in cardiac valves. *Circulation.* (2001) 103:1522–8. doi: 10.1161/01.cir.103.11.1522
24. Di Vito A, Donato A, Presta I, Mancuso T, Brunetti FS, Mastroroberto P, et al. Extracellular matrix in calcific aortic valve disease: architecture, dynamic and perspectives. *Int J Mol Sci.* (2021) 22:913. doi: 10.3390/ijms22020913
25. Qayyum MA, Insana MF. Stromal responses to fractionated radiotherapy. *Int J Radiat Biol.* (2012) 88:383–92. doi: 10.3109/09553002.2012.660301
26. de Cortie K, Russell NS, Coppes RP, Stewart FA, Scharpfenecker M. Bone marrow-derived macrophages incorporate into the endothelium and influence vascular and renal function after irradiation. *Int J Radiat Biol.* (2014) 90:769–77. doi: 10.3109/09553002.2014.920967
27. Herskind C, Rodemann HP. Spontaneous and radiation-induced differentiationof fibroblasts. *Exp Gerontol.* (2000) 35:747–55. doi: 10.1016/s0531-5565(00)00168-6
28. Lara PC, Russell NS, Smolders IJ, Bartelink H, Begg AC, Coco-Martin JM. Radiation-induced differentiation of human skin fibroblasts: relationship with cell survival and collagen production. *Int J Radiat Biol.* (1996) 70:683–92. doi: 10.1080/095530096144572
29. Russell NS, Lara PC, Grummels A, Hart AA, Coco-Martin JM, Bartelink H, et al. *In vitro* differentiation characteristics of human skin fibroblasts: correlations with radiotherapy-induced breast fibrosis in patients. *Int J Radiat Biol.* (2000) 76:231–40. doi: 10.1080/095530000138880
30. Duma MN, Baumann R, Budach W, Dunst J, Feyer P, Fietkau R, et al. Heart-sparing radiotherapy techniques in breast cancer patients: a recommendation of the breast cancer expert panel of the German society of radiation oncology (DEGRO). *Strahlentherapie und Onkol.* (2019) 195:861–71. doi: 10.1007/s00066-019-01495-w
31. Piroth MD, Baumann R, Budach W, Dunst J, Feyer P, Fietkau R, et al. Heart toxicity from breast cancer radiotherapy: current findings, assessment, and prevention. *Strahlentherapie und Onkol.* (2018) 195:1–12. doi: 10.1007/s00066-018-1378-z
32. Nadlonek NA, Weyant MJ Yu JA, Cleveland JCJ, Reece TB, Meng X, et al. Radiation induces osteogenesis in human aortic valve interstitial cells. *J Thorac Cardiovasc Surg.* (2012) 144:1466–70. doi: 10.1016/j.jtcvs.2012.08.041
33. Hjortnaes J, Camci-Unal G, Hutcheson JD, Jung SM, Schoen FJ, Kluin J, et al. Directing valvular interstitial cell myofibroblast-like differentiation in a hybrid hydrogel platform. *Adv Healthc Mater.* (2015) 4:121–30. doi: 10.1002/adhm.201400029
34. Barendsen GW. Dose fractionation, dose rate and iso-effect relationships for normal tissue responses. *Int J Radiat Oncol Biol Phys.* (1982) 8:1981–97. doi: 10.1016/0360-3016(82)90459-x
35. Krahn KN, Bouten CVC, van Tuijl S, van Zandvoort MAMJ, Merkx M. Fluorescently labeled collagen binding proteins allow specific visualization of collagen in tissues and live cell culture. *Anal Biochem.* (2006) 350:177–85. doi: 10.1016/j.ab.2006.01.013
36. Hjortnaes J, Goettsch C, Hutcheson JD, Camci-Unal G, Lax L, Scherer K, et al. Simulation of early calcific aortic valve disease in a 3D platform: a role for myofibroblast differentiation. *J Mol Cell Cardiol.* (2016) 94:13–20. doi: 10.1016/j.yjmcc.2016.03.004
37. Offit K, Gilad S, Paglin S, Kolachana P, Roisman LC, Nafa K, et al. Rare variants of ATM and risk for Hodgkin's disease and radiation-associated breast cancers. *Clin cancer Res an Off J Am Assoc Cancer Res.* (2002) 8:3813–9.
38. Aikawa E, Nahrendorf M, Figueiredo J-L, Swirski FK, Shtatland T, Kohler RH, et al. Osteogenesis associates with inflammation in early-stage atherosclerosis evaluated by molecular imaging *in vivo*. *Circulation.* (2007) 116:2841–50. doi: 10.1161/CIRCULATIONAHA.107.732867
39. Concin N, Zeillinger C, Stimpfel M, Schiebel I, Tong D, Wolff U, et al. p53-dependent radioresistance in ovarian carcinoma cell lines. *Cancer Lett.* (2000) 150:191–9. doi: 10.1016/s0304-3835(99)00393-6
40. Zhou W, Yu X, Sun S, Zhang X, Yang W, Zhang J, et al. Increased expression of MMP-2 and MMP-9 indicates poor prognosis in glioma recurrence. *Biomed Pharmacother.* (2019) 118:109369. doi: 10.1016/j.biopha.2019.109369
41. Olivares-Urbano MA, Griñán-Lisón C, Zurita M. del Moral R, Ríos-Arrabal S, Artacho-Cordón F, et al. Matrix metalloproteases and TIMPs as prognostic biomarkers in breast cancer patients treated with radiotherapy: A pilot study. *J Cell Mol Med.* (2020) 24:139–48. doi: 10.1111/jcmm.14671
42. Artacho-Cordón F, Ríos-Arrabal S, Lara PC, Artacho-Cordón A, Calvente I, Núñez MI. Matrix metalloproteinases: Potential therapy to prevent the development of second malignancies after breast radiotherapy. *Surg Oncol.* (2012) 21:143–51. doi: 10.1016/j.suronc.2012.06.001
43. Butcher JT, Simmons CA, Warnock JN. Mechanobiology of the aortic heart valve. *J Heart Valve Dis.* (2008) 17:62–73.

44. Sarathchandra P, Smolenski RT, Yuen AHY, Chester AH, Goldstein S, Heacox AE, et al. Impact of γ-irradiation on extracellular matrix of porcine pulmonary valves. *J Surg Res.* (2012) 176:376–85. doi: 10.1016/j.jss.2011.10.011
45. Taylor CW, Zhe W, Macaulay E, Jagsi R, Duane F, Darby SC. Exposure of the heart in breast cancer radiation therapy: A systematic review of heart doses published during 2003 to 2013. *Int J Radiat Oncol Biol Phys.* (2015) 93:845–53. doi: 10.1016/j.ijrobp.2015.07.2292
46. Taylor CW, Kirby AM. Cardiac side-effects from breast cancer radiotherapy. *Clin Oncol.* (2015) 27:621–9. doi: 10.1016/j.clon.2015.06.007
47. Sylvester CB, Abe J, Patel ZS, Grande-Allen KJ. Radiation-induced cardiovascular disease: mechanisms and importance of linear energy transfer. *Front Cardiovasc Med.* (2018) 5:1–9. doi: 10.3389/fcvm.2018.00005
48. Caron J, Nohria A. Cardiac toxicity from breast cancer treatment: can we avoid this? *Curr Oncol Rep.* (2018) 20:1–8. doi: 10.1007/s11912-018-0710-1

Conflict of Interest: The authors declare that the research was conducted in the absence of any commercial or financial relationships that could be construed as a potential conflict of interest.

frontiers in Cardiovascular Medicine

ORIGINAL RESEARCH
published: 30 August 2021
doi: 10.3389/fcvm.2021.736303

Angiogenic Secretion Profile of Valvular Interstitial Cells Varies With Cellular Sex and Phenotype

Victoria Nelson[1], *Vaidehi Patil*[1], *LaTonya R. Simon*[1], *Kelsey Schmidt*[1], *Chloe M. McCoy*[1] *and Kristyn S. Masters*[1,2,3]*

[1] Department of Biomedical Engineering, University of Wisconsin-Madison, Madison, WI, United States, [2] Department of Medicine, University of Wisconsin School of Medicine and Public Health, Madison, WI, United States, [3] Department of Materials Science and Engineering, University of Wisconsin-Madison, Madison, WI, United States

Angiogenesis is a hallmark of fibrocalcific aortic valve disease (CAVD). An imbalance of pro- and anti-angiogenic factors is thought to play a role in driving this disease process, and valvular interstitial cells (VICs) may act as a significant source of these factors. CAVD is also known to exhibit sexual dimorphism in its presentation, and previous work suggested that VICs may exhibit cellular-scale sex differences in the context of angiogenesis. The current study sought to investigate the production of angiogenesis-related factors by male and female VICs possessing quiescent (qVIC) or activated (aVIC) phenotypes. Production of several pro-angiogenic growth factors was elevated in porcine aVICs relative to qVICs, with sex differences found in both the total amounts secreted and their distribution across media vs. lysate. Porcine valvular endothelial cells (VECs) were also sex-separated in culture and found to behave similarly with respect to metabolic activity, viability, and tubulogenesis, but male VECs exhibited higher proliferation rates than female VECs. VECs responded to sex-matched media conditioned by VICs with increased tubulogenesis, but decreased proliferation, particularly upon treatment with aVIC-derived media. It is likely that this attenuation of proliferation resulted from a combination of decreased basic fibroblast growth factor and increased thrombospondin-2 (TSP2) secreted by aVICs. Overall, this study indicates that VICs regulate angiogenic VEC behavior via an array of paracrine molecules, whose secretion and sequestration are affected by both VIC phenotype and sex. Moreover, strong sex differences in TSP2 secretion by VICs may have implications for understanding sexual dimorphism in valve fibrosis, as TSP2 is also a powerful regulator of fibrosis.

Keywords: sexual dimorphism, valvular endothelial cells, calcific aortic valve disease, valvular interstitial cell, angiogenesis, thrombospondin

OPEN ACCESS

Edited by:
Joy Lincoln,
Medical College of Wisconsin,
United States

Reviewed by:
Adrian Chester,
The Magdi Yacoub Institute,
United Kingdom
Kartik Balachandran,
University of Arkansas, United States
Joshua D. Hutcheson,
Florida International University,
United States

***Correspondence:**
Kristyn S. Masters
kmasters@wisc.edu

Specialty section:
This article was submitted to Heart Valve Disease, a section of the journal Frontiers in Cardiovascular Medicine

Received: *05 July 2021*
Accepted: *09 August 2021*
Published: *30 August 2021*

Citation:
Nelson V, Patil V, Simon LR, Schmidt K, McCoy CM and Masters KS (2021) Angiogenic Secretion Profile of Valvular Interstitial Cells Varies With Cellular Sex and Phenotype. Front. Cardiovasc. Med. 8:736303. doi: 10.3389/fcvm.2021.736303

INTRODUCTION

Calcific aortic valve disease (CAVD) is the most common type of heart valve disease in the Western world (1). It is associated with mild to severe valve leaflet thickening and calcification and is driven by active pathobiological processes including chronic inflammation, fibrosis, and angiogenesis (1, 2). CAVD is more prevalent in men and exhibits sexual dimorphism in its presentation, where females with CAVD have more fibrosis, while males have more calcification (3–5).

Healthy aortic heart valves are not vascularized, so any angiogenesis in the valve is considered pathological. Angiogenesis is thought to be both a consequence of CAVD and a factor in its progression. During early stages of CAVD, valve thickening causes diffusion limitations that can signal the need for vascularization. These vessels can then act as a source of stimuli that further regulate pathological processes in the valve, such as chronic inflammation (6). Valvular endothelial cells (VECs) line the blood-contacting surfaces of the valve and may serve as a source of cells for valvular neovascularization (7). Imbalances in pro- and anti-angiogenic factors are thought to be a driving factor in their dysfunction (8) and, ultimately, the development of angiogenesis seen in CAVD (6).

Meanwhile, valvular interstitial cells (VICs) are the dominant cell type throughout the bulk of the valve and are believed to play a role in mediating these angiogenic processes. VICs are active in secreting soluble biomolecules and synthesizing extracellular matrix (ECM) components to regulate and remodel the valve environment (9, 10). VICs are primarily present in a quiescent (qVIC) phenotype in the healthy aortic valve, and they can be activated to a myofibroblastic, or activated (aVIC), phenotype in response to injury or pathological insult (10). Recent work has shown that VICs isolated from human valves with CAVD display pro-angiogenic properties and can differentiate into a perivascular phenotype (11).

Crosstalk between VICs and VECs has been described in the context of VIC homeostasis and disease, and VICs can stimulate angiogenic sprouting by VECs (7). However, relatively little remains known about paracrine angiogenic interactions between VICs and VECs and how they vary with VIC phenotype. Additionally, the crosstalk between these cells has not been studied in the context of cellular-scale sex differences. A previous microarray analysis of male and female VICs found that angiogenesis was one of seven biological process categories overrepresented in male VICs (12), suggesting that VIC behavior in the context of angiogenesis could differ with sex. Moreover, no previous studies have examined whether VEC behavior is dependent upon cellular-scale sex. These gaps in knowledge motivated the current work, wherein we quantify the secretion of angiogenic factors by both male and female qVICs and aVICs and then characterize the effects of these paracrine factors on angiogenesis-related activity of sex-matched VECs. Improved characterization of angiogenesis in CAVD could lead to a better understanding of CAVD pathogenesis and could inform the development of pharmacological CAVD treatments.

METHODS

VIC Isolation

Valvular interstitial cells (VICs) were isolated from male and female porcine aortic valves (Hoesly's Meats, New Glarus, WI) and cultured separately by sex. Aortic valve leaflets were excised from porcine hearts, and VICs were immediately isolated via collagenase digestion, as described previously (13). The cells were then plated on a 10 cm tissue culture plate, refed with growth medium on Day 1 and then every other day after that until they reached 70-90% confluency. Cells were then passaged onto either normal tissue culture plates to continue as activated VICs (aVICs) or collagen-coated plates to culture into quiescent VICs (qVICs), according to published protocols (14). Briefly, qVICs were generated via culture in low-glucose DMEM supplemented with 2% FBS, 100 U/mL penicillin (P4333; Sigma), 100 μg/mL streptomycin (P4333; Sigma), bFGF (10 ng/mL; Peprotech, Rocky Hill, NJ) and 5.25 mg/mL insulin (I0516; Sigma). Generation of qVIC vs. aVIC cultures was validated by qRT-PCR for alpha smooth muscle actin (ACTA2), where aVICs were confirmed by a minimum 10-fold increase in ACTA2 gene expression as previously described (14). All VICs were refed every other day and subcultured until passage three, at which point they were seeded for experiments. For each sex, each experiment used VICs pooled from $N = 3$ pigs; all experiments were repeated a minimum of two times, with each repeat using N=3 pigs that did not overlap with previous donor pools. All VICs were used as fresh isolates and never frozen down.

VEC Isolation

Valvular endothelial cells (VECs) were isolated from male and female porcine aortic valves (Hoesly's Meats, New Glarus, WI) and cultured separately by sex. Aortic leaflets were dissected and washed twice in an M199 solution containing 100 U/mL penicillin (P4333; Sigma), 100 μg/mL streptomycin (P4333; Sigma), and 200 mM L-glutamine solution (G7513; Sigma). The leaflets were then incubated in a 37°C water bath in a PBS solution including 60 U/mL collagenase type 2 (Worthington Biochemical Corp., Lakewood, NJ), penicillin (100 U/mL), and streptomycin (100 μg/L) for 120 minutes. Leaflets were separated from the enzyme solution by passing through a 100 μm cell strainer and then added to PBS pre-warmed to 37°C and vortexed for 60 seconds to dislodge the VECs from the tissue matrix. The cell solution was separated from the leaflets by passing through a 100 μm cell strainer and pelleted via centrifugation at 1,000 rpm for 10 min. The cell pellet was resuspended in 10 mL EGM-2 basal growth medium (CC3162; Lonza), and the cells were then plated on 10 cm plates coated with 2% gelatin in sterile deionized water for expansion. After expansion, cells were prepared for fluorescence-activated cell sorting (FACS). Briefly, cells were detached using TrypLE (ThermoFisher), pelleted, and then resuspended in FACS buffer (0.5% BSA, 2 mM EDTA, 20 mM HEPES in PBS). Cells were counted, incubated with FITC-conjugated anti-CD-31 (5 μL per 10^6 cells, MCA1746F; BioRad, Hercules, CA) at 4°C for 30 mins, counterstained with DAPI (1 μg/mL), and washed. FACS was performed using a BD FACSAria (BD Biosciences, Franklin Lakes, NJ) to select for live cells positively stained for CD-31. VECs were used between passages three and seven. Each batch of VECs was from a single donor, and each experiment was repeated 2-4 times, using a new donor each time (for a total of $N = 3$–5 separate donors, with $n = 3$ samples/condition per donor).

Angiogenic Growth Factor Secretion Profile of VICs

Male and female aVICs and qVICs were seeded in 10 cm dishes at a density of 50,000 cells/cm^2 and cultured in standard growth

medium (low-glucose DMEM with 10% FBS and 1% penicillin-streptomycin solution) for 48 h. The aVICs were cultured on 10 cm tissue culture coated plates while qVICs were cultured on 10 cm collagen-coated plates in order to retain their qVIC phenotype for the duration of the experiment. Seven ELISAs were run on the conditioned culture media and culture lysate (collected in RIPA buffer, 89900; ThermoFisher): endothelin-1 (DY1160; R&D Systems, Minneapolis, MN), platelet derived growth factor-A (PDGF-A, DY221; R&D), vascular endothelial growth factor-A (VEGF-A, DY293B; R&D), basic fibroblast growth factor (bFGF, DY233; R&D), epidermal growth factor (EGF, DY236; R&D), insulin-derived growth factor-1 (IGF-1, DY291; R&D), and thrombospondin-2 (TSP2, DTSB20; R&D), all per manufacturer's instructions. The media and lysate were differentially diluted in the sample dilution buffer specific to each ELISA kit such that all sample absorbance readings fell within the dynamic range of each ELISA. A Quant-iT™ PicoGreen™ dsDNA Assay (P11496; Thermo Fisher Scientific) was performed on the lysate to normalize to cell number across all samples.

Heparan Sulfate *in situ* ELISA

Heparan sulfate proteoglycan-2 (HSPG2) deposition was assayed by semi-quantitative immunocytochemical detection. Cells were fixed in 10% neutral buffered formalin (Sigma), endogenous peroxidase activity was quenched with 0.3% hydrogen peroxide in methanol for 1 h, and samples blocked overnight in 3% goat serum. Samples were then incubated with monoclonal mouse anti-HSPG2 antibody (ab23418, Abcam, Waltham, MA) for 2 h followed by a series of washes with 1X PBS and labeling with a horseradish peroxidase-linked goat anti-mouse secondary antibody (polyclonal, 0.5 μg/mL; Sigma) for 40 min. After washing, samples were incubated in 1-Step Turbo-TMB ELISA substrate solution (ThermoFisher) and the reaction stopped after 5 min through the addition of 2 N sulfuric acid (ThermoFisher). Color development was proportional to HSPG2 content and measured with a plate reader. Background signal was determined by following the same procedure without incubating in primary antibody solution. This background absorbance was subtracted from the samples for the respective culture condition. Corrected absorbance values were normalized to total cell number determined by DAPI staining.

VEC Proliferation

Proliferation of VECs at baseline and in response to VIC-conditioned media was analyzed using a Click-iT EdU cell proliferation assay (C10337; Thermo Fisher Scientific). Male and female aVICs and qVICs were seeded at 50,000 cells/cm^2 in 10 cm plates and cultured as described above, with conditioned media collected after 48 h. VIC growth medium was also placed in dishes without cells for 48 h to generate a matched negative control comprised of unconditioned, but incubated, media. Male and female VECs were seeded at 21,000 cells/cm^2 in 48-well plates coated with 2% gelatin. VECs were allowed to grow for 8 h prior to refeeding with VIC-conditioned (or unconditioned) media, and then cultured overnight. VECs were incubated with EdU solution for 2 h and then fixed with 4% paraformaldehyde. Detection of EdU was performed following manufacturer instructions with a Hoechst® 33342 counterstain. Images were taken on a Zeiss Axiovert.A1 inverted microscope and analyzed manually, with percent proliferation expressed as the number of EdU-positive cells divided by the total cell number in each field of view at three fields of view per well and with three wells per condition. Proliferation experiments were also repeated in the presence of a neutralizing antibody to CD36, which acts as the receptor for TSP-2 (Clone FA6-152, Stem Cell Technologies, Vancouver, Canada), or an isotype control (mouse IgG1 K, 550878, BD Biosciences, Franklin Lakes, NJ), which were added to VECs at a concentration of 5 μg/mL for 30 min prior to refeeding with conditioned medium.

VEC Tubulogenesis

Male and female aVICs and qVICs were seeded in 10 cm dishes at a density of 50,000 cells/cm^2 and cultured in standard growth medium as described above. Conditioned media was collected from VICs after 48 h of culture. VIC growth medium was also placed in dishes without cells for 48 h to generate a matched negative control comprised of unconditioned, but incubated, media. Male and female VECs were seeded at 62,000 cells/cm^2 in 96-well plates coated with 8–11 mg/mL growth factor-reduced Matrigel (354230; Corning) and allowed to attach for 30 min. The conditioned VIC media was then applied to VECs in a sex-matched manner (i.e., media from male VICs applied to male VECs). The VECs were cultured in the VIC-conditioned (or unconditioned) media for 4 h prior to analyzing tubulogenesis. The positive control was cultured in EGM-2 media supplemented with VEGF to ensure that the cells at that density would form tubes. Images were taken at three fields of view per well and with three wells per condition on the Zeiss AxioVert.A1 inverted microscope and analyzed through WIMASIS (Córdoba, Spain).

VEC Viability and Metabolic Activity

To assess VEC viability, male and female VECs were seeded at 10,000 cells/well in a 96 well plate and cultured for 72 h. Cells were then washed in PBS and incubated for 30 min in Live/Dead stain (L3224, ThermoFisher) at concentrations of 2 μM Calcein AM and 4 μM EthD-1. Cells were then imaged on a Zeiss Observer Z1, with three images taken per well, $n = 3$ wells per condition. Images were analyzed using Fiji with a macro from Allevi by 3D Systems to count live and dead cells; viability is expressed as % live cells. VEC metabolic activity was measured using CellTiter-Glo (G7570, Promega, Madison, WI). For this assay, male and female VECs were seeded in opaque-walled 96 well plates at a density of 10,000 cells/well and cultured for ∼72 h. Cells were equilibrated at room temperature for 30 min prior to adding 100 μL CellTiter-Glo solution to the 100 μL cell culture medium already present in the wells. The plates were placed on an orbital shaker for 2 min, incubated statically for 10 min at room temperature for the signal to stabilize, and then luminescence read on a plate reader.

Western Blot

Male and female aVICs and qVICs were cultured as described above for 48 h, at which point cell lysates were collected using Pierce RIPA buffer. A microBCA assay (ThermoFisher) was

conducted to determine protein concentration for each sample. Samples were diluted to the same protein concentration and then denatured in a 70°C water bath for 10 min with Novex™ Tris-Glycine SDS Sample Buffer (LC2676; ThermoFisher). The samples were loaded into a 4–12% Tris-glycine gel and electrophoresis performed using a XCell SureLock Mini-Cell system (EI0001; Thermo Fisher Scientific) was run at 200 V for 30 min. The gel was blotted onto a PVDF membrane overnight at 4°C at 16 V. The membrane was blocked in 5% w/v milk in PBST for 90 min at room temperature and then incubated with anti-chondromodulin-1 antibody (MAB41681, R&D) at a dilution of 1:1,000 at 4°C overnight. The membrane was then washed in TBST and incubated with an HRP conjugated secondary antibody at a dilution of 1:10,000 for 1h at room temperature, followed by washing with TBST, exposing to the ECL substrate, and imaging on the Bio-Rad ChemiDoc XRS imaging system (1708265; Bio-Rad).

RESULTS

Angiogenic Factor Secretion Profile Varies With Cell Sex and Phenotype

VIC secretion of seven factors known to participate in the promotion of angiogenesis was analyzed by ELISA. VEGF is the most commonly studied pro-angiogenic growth factor and was detected in the media and lysate of male and female qVICs and aVICs (**Figure 1A**). Sex differences in VEGF secretion were evident in qVICs only, with female qVICs secreting more VEGF than males. In general, the aVIC phenotype was associated with increased VEGF production by both male and female cells. A similar phenotype-dependent trend was observed for PDGF. For this growth factor, greater amounts of PDGF were found in aVIC cultures for each sex, compared to their qVIC counterpart (**Figure 1B**). However, PDGF secretion varied with sex for only one condition, where male aVICs had more PDGF in the media fraction compared to female aVICs.

bFGF (or FGF-2) is another growth factor that is a potent mitogen and pro-angiogenic agent (15). VIC secretion of bFGF tended to follow an opposite trend than what was observed for VEGF and PDGF, in that an activated VIC phenotype was associated with decreased bFGF production (**Figure 1C**). Although media levels of bFGF did not vary with sex, significantly less bFGF was found in the lysate of male qVICs compared to female qVICs, leading to a difference in bFGF totals between male and female qVICs. Endothelin-1 is not as commonly examined as a direct pro-angiogenic factor, but can be a potent EC mitogen (16); it was included in our study because an initial qualitative angiogenic factor screen (not shown) showed high levels of ET-1 in the media. Similar to the results described for VEGF and PDGF, ET-1 production tended to be significantly increased in aVICs compared to qVICs, and this was true across both sexes (**Figure 1D**). Additionally, a consistent sex-dependent effect was observed, where male aVICs produced more ET-1 than female aVICs.

Finally, EGF and IGF-1 round out the suite of factors that are frequently associated with pro-angiogenic actions (17, 18). These two molecules were not consistently found in detectable quantities in both the media and lysate of the cell phenotypes/sexes examined. Specifically, EGF was not present within the detection limits of the assay, while IGF-1 was found in female qVIC media and male qVIC lysate, although at the lower assay detection limit in both.

Sequestration of Angiogenic Factors Varies With Cell Sex and Phenotype

Examination of the distribution of growth factors between media and lysate also uncovered sex- and phenotype-dependent trends (**Figure 2A**). Amongst qVICs, the fraction of each pro-angiogenic factor present in the media remained similar across both males and females. However, this was not the case for aVICs; for 3 of the 4 factors detected (PDGF, bFGF, ET-1), male aVICs had a significantly increased proportion of the molecule present in the media compared to female aVICs.

An alternative way of describing this change is that male aVICs had smaller amounts of sequestered growth factors relative to female aVICs. Because growth factor sequestration is highly dependent upon the extracellular matrix environment, we also evaluated whether sexual dimorphism in ECM secretion could be influencing these results. Heparan sulfate proteoglycans are generally responsible for growth factor binding (19), so an *in situ* ELISA for HSPG2 was performed. The HSPG2 ELISA results were consistent with the growth factor secretion profiles (**Figure 2B**); specifically, male aVIC cultures had less HSPG2 than female aVIC cultures, which could contribute to the lower amounts of sequestered factors in the male aVIC cultures.

Baseline Valvular Endothelial Cell Behavior Exhibits Little Sex-Dependence

Before we could examine the impact of angiogenic factors secreted by male and female VICs on the function of sex-matched VECs, we first needed to characterize whether VECs exhibited sex-dependent angiogenic behaviors at baseline. Because VECs have not previously been separated by sex in culture, basic cell viability and metabolic activity were also quantified. As shown in **Figures 3A,B**, neither ATP activity nor viability were affected by cellular-scale VEC sex. Proliferation and *in vitro* tubulogenesis were then evaluated as measures more directly related to angiogenic activity. The proliferation of male VECs tended to be significantly higher than the proliferation of female VECs (**Figure 3C**), while tubulogenesis was similar across male and female VECs (**Figure 3D**).

VIC-Conditioned Media Increases Tubulogenesis but Decreases VEC Proliferation

As demonstrated in **Figure 1**, VICs secrete numerous pro-angiogenic factors, so we hypothesized that VIC-conditioned media would promote angiogenic outcomes in VECs. This hypothesis appeared to hold true for tubulogenesis, where media conditioned by VICs tended to promote formation of more and longer VEC tubules compared to unconditioned media (**Figures 4A,B**). Sex differences were not observed in these

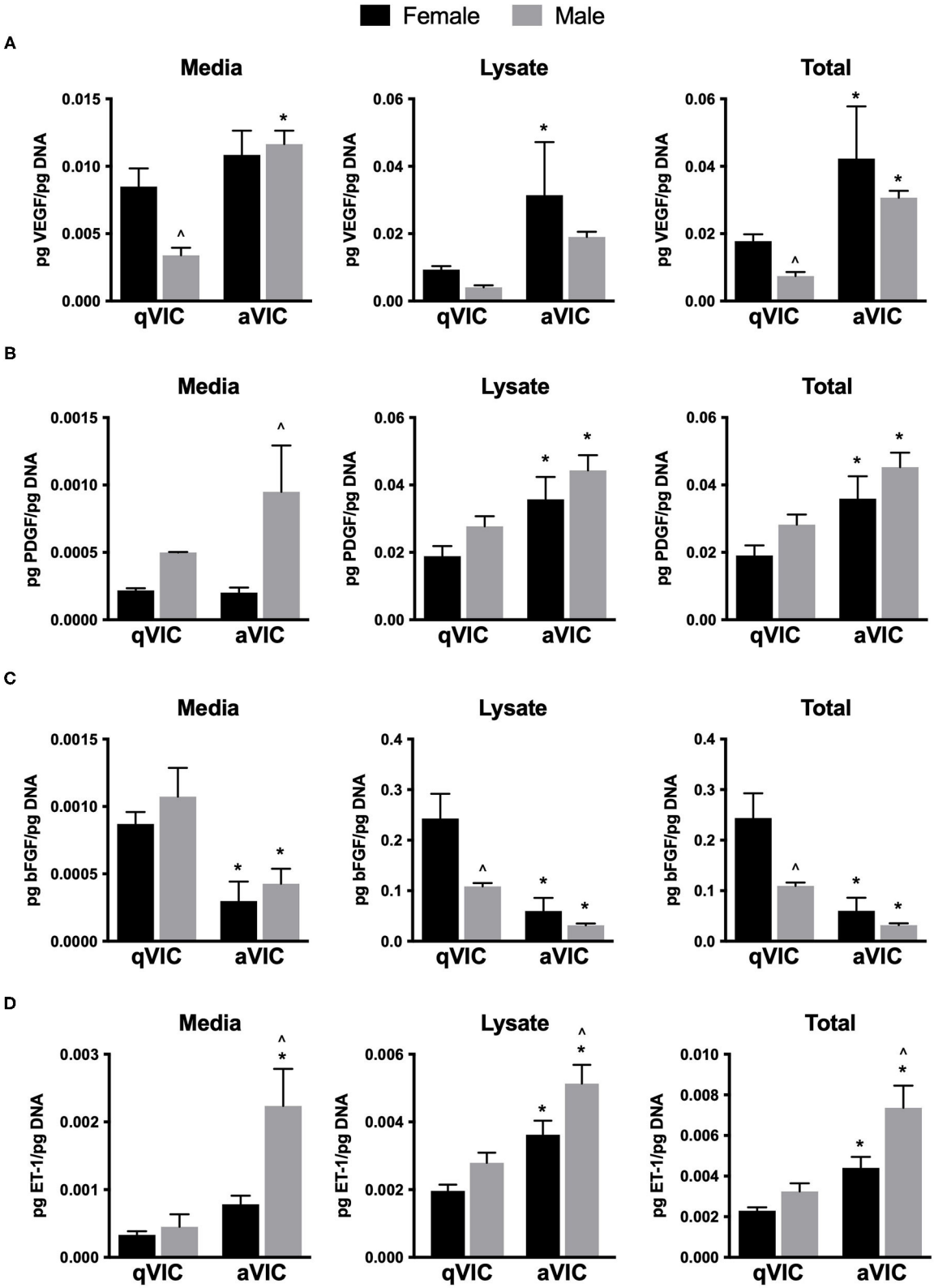

FIGURE 1 | Production of pro-angiogenic factors by male and female qVICs and aVICs. **(A)** vascular endothelial growth factor (VEGF), **(B)** platelet derived growth factor-A (PDGF), **(C)** basic fibroblast growth factor (bFGF), and **(D)** endothelin-1 (ET-1). $^{*}p < 0.05$ vs. sex-matched qVIC level; $\hat{}p < 0.05$ vs. female VIC of same phenotype by two-way ANOVA with Tukey's post *hoc* test. $N = 3$ pigs per sex, $n = 3$ wells per condition.

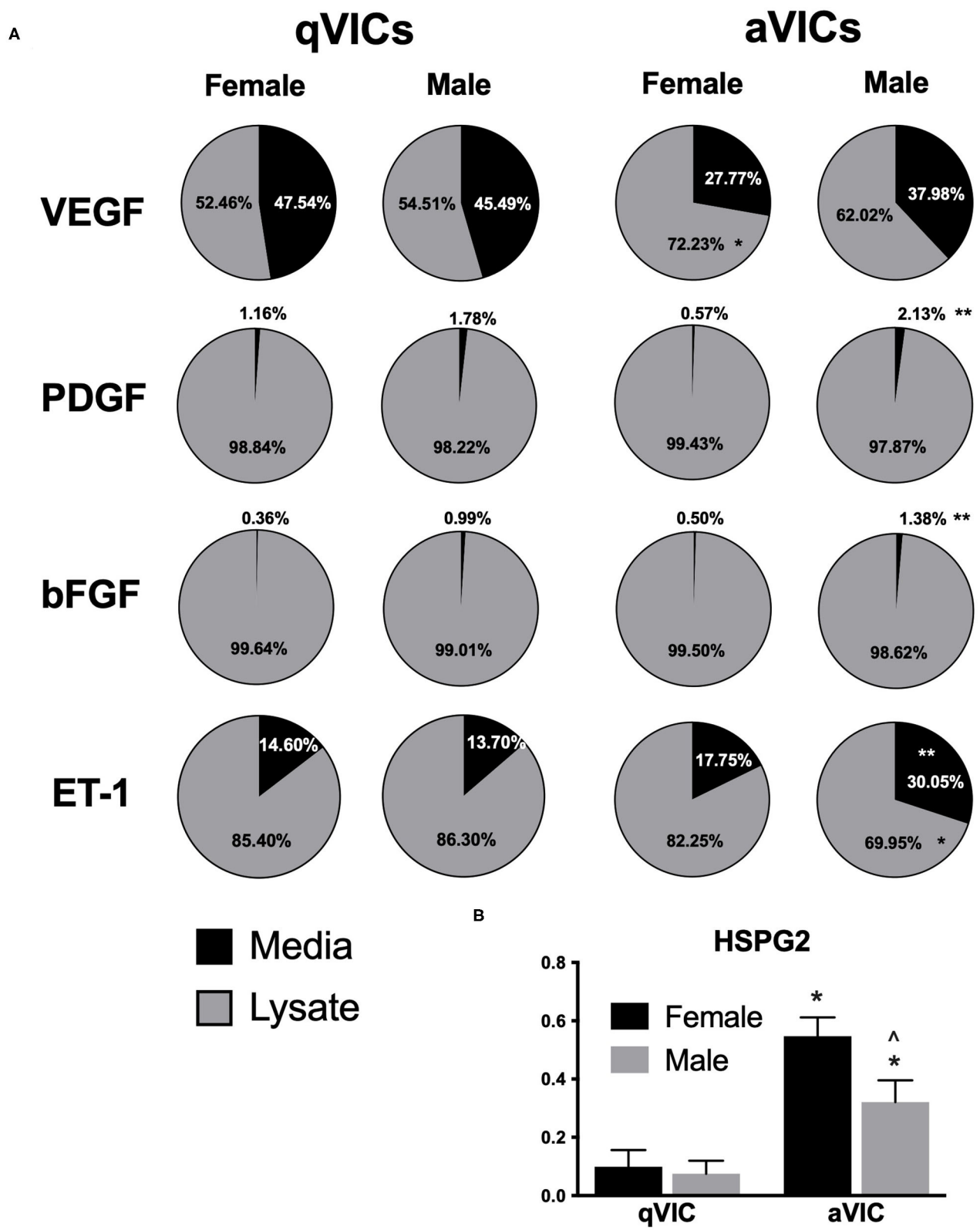

FIGURE 2 | Distribution of pro-angiogenic factors across media and lysate from male and female qVICs and aVICs. **(A)** Percent of total growth factor found in media vs. lysate for VEGF, PDGF, bFGF, and ET-1. *$p < 0.05$ vs. sex-matched qVIC level; **$p < 0.05$ vs. female VIC of same phenotype. **(B)** Heparan sulfate proteoglycan 2 (HSPG2) found in extracellular matrix of male and female qVIC and aVIC cultures. *$p < 0.05$ vs. sex-matched qVIC level; ^$p < 0.05$ vs. female VIC of same phenotype by two-way ANOVA with Tukey's post *hoc* test. $N = 3$ pigs per sex, $n = 3$ wells per condition.

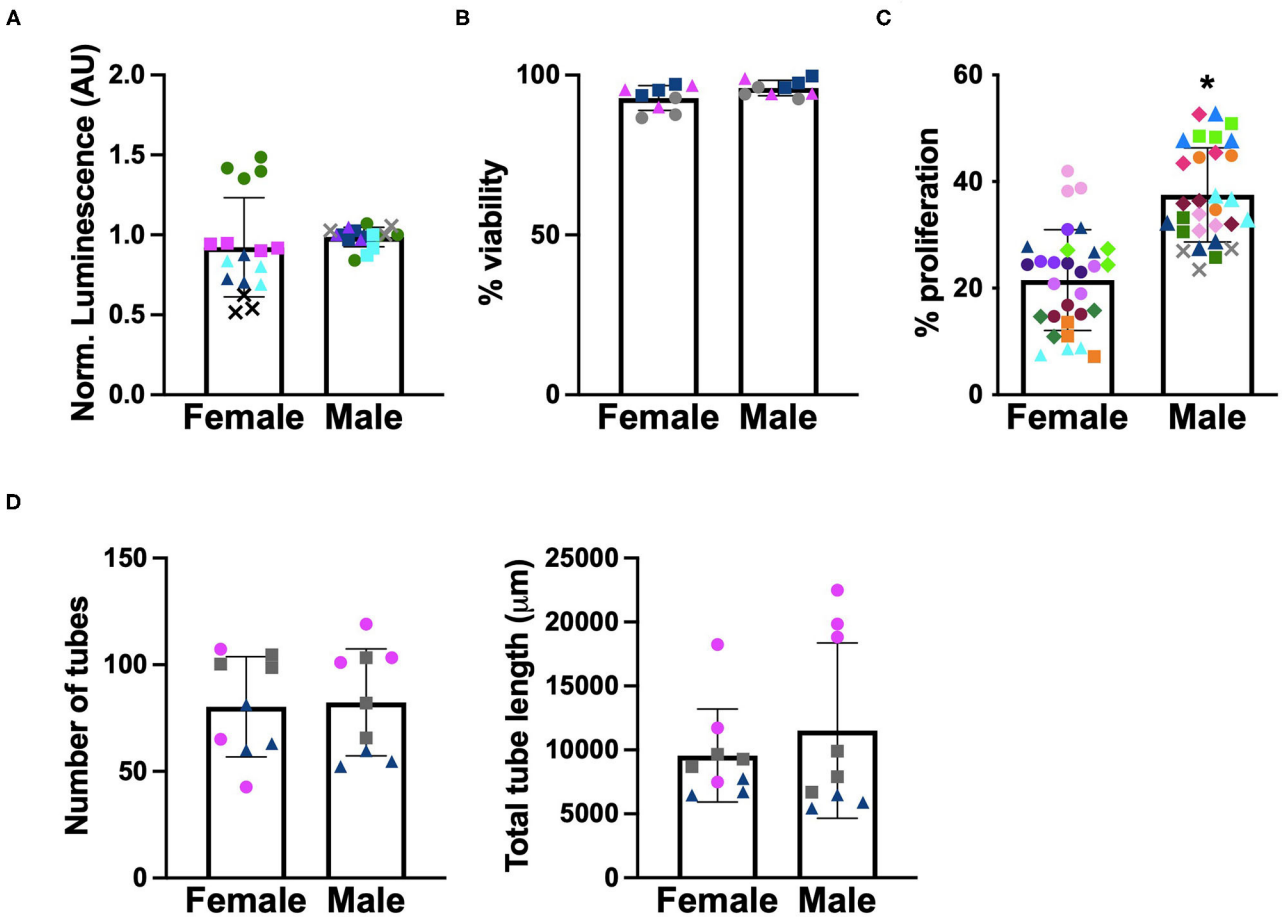

FIGURE 3 | Sex differences in baseline characterization of VECs. **(A)** ATP activity, **(B)** viability, **(C)** proliferation, and **(D)** tubulogenesis. Different marker shapes indicate different donors; different colors within the same marker shape indicate different runs with the same donor. *$p < 0.05$ vs. female VECs by Welch's t-test. $N =$ 3–4 pigs per sex, $n = 3$ wells per condition.

results, suggesting that the differences in angiogenic secretion profiles of male and female VICs were not sufficient to drive sexual dimorphism in downstream events.

aVICs are the dominant VIC phenotype in diseased valves, and this phenotype tended to secrete more of these factors than qVICs in our study. Thus, we had also hypothesized that media conditioned by aVICs would show greater ability to increase angiogenic activity in VECs compared to media conditioned by qVICs. However, this was not the case, as tubulogenesis in VEC cultures treated with aVIC media was typically lower than when VECs were treated with qVIC media.

Analysis of VEC proliferation after treatment with VIC-conditioned media also yielded somewhat unexpected results. Specifically, all VIC-conditioned media decreased VEC proliferation relative to the unconditioned control (**Figure 4C**). Proliferation was lowest in VECs treated with aVIC-conditioned media. Given that the baseline (unconditioned media) proliferation of male VECs is significantly higher than female VECs, the magnitude of the decrease in proliferation upon application of aVIC-conditioned media was greater for males (8-fold) than for females (3-fold).

Anti-angiogenic Factors Are Secreted by VICs

The suppressive effects of VIC-conditioned media on VEC proliferation led us to postulate that the media may be enriched in anti-proliferative factors. Thrombospondin-2 (TSP2) and chrondromodulin-1 (Chm1) are known to be anti-angiogenic molecules (8, 20, 21), so we evaluated their presence in our VIC cultures. TSP2 secretion was highly dependent upon both VIC sex and phenotype. Greater amounts of TSP2 were secreted by female VICs relative to males, and TSP2 production was elevated by approximately 2-fold in aVICs of both sexes, compared to their qVIC counterparts (**Figure 5A**). The distribution of TSP2 across media and lysate fractions was similar across all four conditions (**Figure 5B**). Chm1 was detected only in the culture lysate and was found to be decreased in aVIC cultures, without exhibiting any sex-dependence (**Figure 5C**).

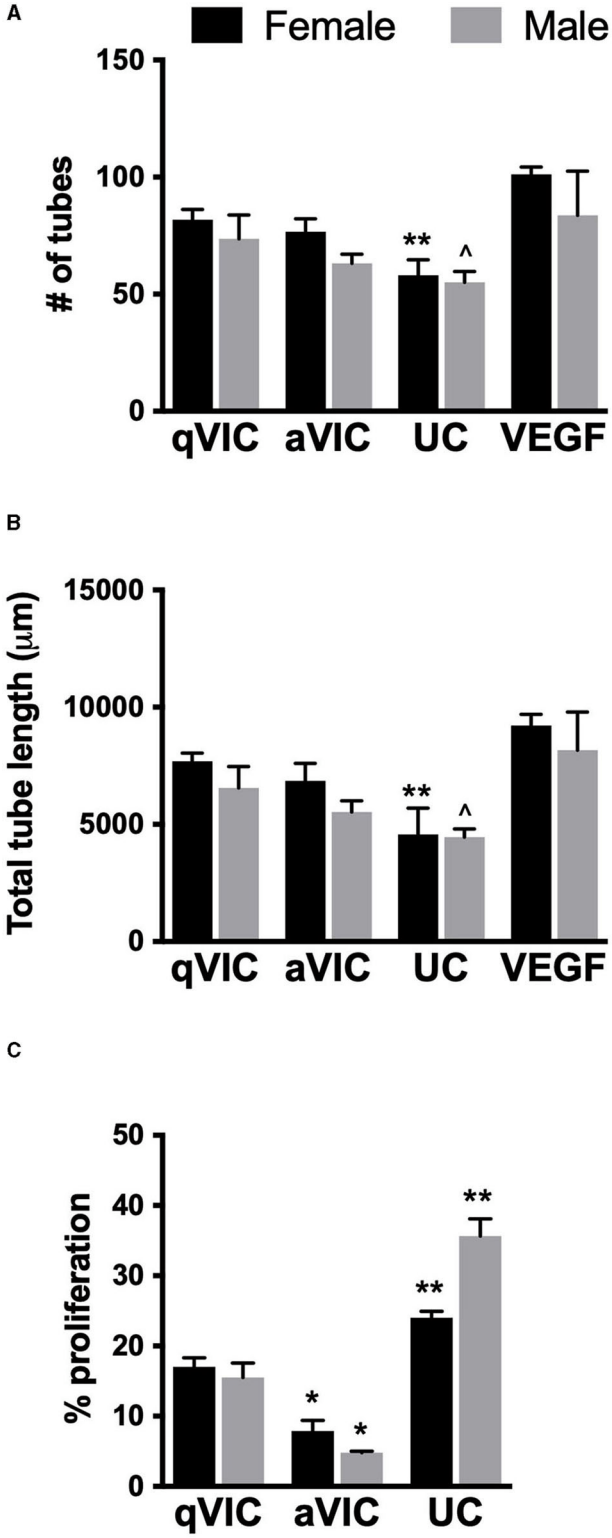

FIGURE 4 | Effect of VIC-conditioned media on VEC function. **(A)** Number, **(B)** length of tubules formed by VECs in tubulogenesis assay, and **(C)** VEC proliferation. *$p < 0.05$ vs. sex-matched qVIC condition; **$p < 0.05$ vs. sex-matched aVIC and qVIC conditions by two-way ANOVA with Tukey's post *hoc* test. UC = unconditioned media. $N = 3$–4 pigs per sex, $n = 3$ wells per condition.

VIC-Secreted TSP2 Is Partially Responsible for Suppressing VEC Proliferation

Observationally, it appeared that levels of TSP2 in the media (**Figure 5A**) inversely correlated with the proliferation trends seen with conditioned media (**Figure 4B**). Thus, we sought to understand whether this factor was responsible for driving the suppression of VEC proliferation seen upon treatment with aVIC-conditioned medium. There are no small molecule inhibitors of TSP2 itself, so a blocking antibody to CD36, the receptor that recognizes TSP2, was used to block cellular recognition of the TSP2 in VIC-conditioned medium. As seen in **Figure 6**, blocking CD36 partially recovered VEC proliferation compared to the isotype control in the female condition. The blocking was effective only in females, which is also where we had found higher levels of TSP2 in the conditioned medium.

DISCUSSION

The precise role of angiogenesis in CAVD is not yet understood, but it is hypothesized to promote CAVD pathogenesis by contributing to the recruitment of inflammatory cells (22), and could potentially serve as a target for slowing the progression of fibrocalcific events (11). Our characterization found that VIC expression of a myofibroblastic phenotype was associated with increased expression of many angiogenesis-related factors. Moreover, although sexual dimorphism in CAVD has been recognized (4, 5, 23, 24), few studies have characterized cellular-scale sex differences in valvular cells. In this work, we found intrinsic differences in the growth factor secretion profile of male and female VICs, as well as the proliferative behaviors of VECs. Overall, our results do not indicate a single dominant VIC-secreted factor in regulating angiogenic VEC outcomes, but they do point toward VIC phenotype being highly influential with respect to modulating angiogenesis on both the molecular and functional (e.g., VEC behavior) scale. Cellular-scale sex also significantly influenced VIC angiogenic secretion profiles, but it was ultimately associated with only modest changes in VEC behavior outcomes.

In the early stages of valve thickening, the majority of VICs are thought to still be in a qVIC phenotype (25). However, during later stages of CAVD, when neovascularization becomes evident, activated VICs (aVICs) represent the dominant phenotype. The potential contribution of different VIC phenotypes to angiogenic events is not well understood, as the ability to intentionally generate and maintain qVIC cultures is a relatively recent development (13, 14). In previous work, *ex vivo* cultures of small valve explants revealed that more capillary-like outgrowths occurred in stenotic valve cultures compared to non-stenotic (26). A recent study also showed that VICs from valves with CAVD were more pro-angiogenic than VICs from healthy valves (11). Although that study did not explicitly culture the VICs from healthy valves as qVICs, their finding that diseased VICs secreted more VEGF into the media than healthy VICs was consistent with our results showing increased secretion of VEGF by aVICs compared to qVICs.

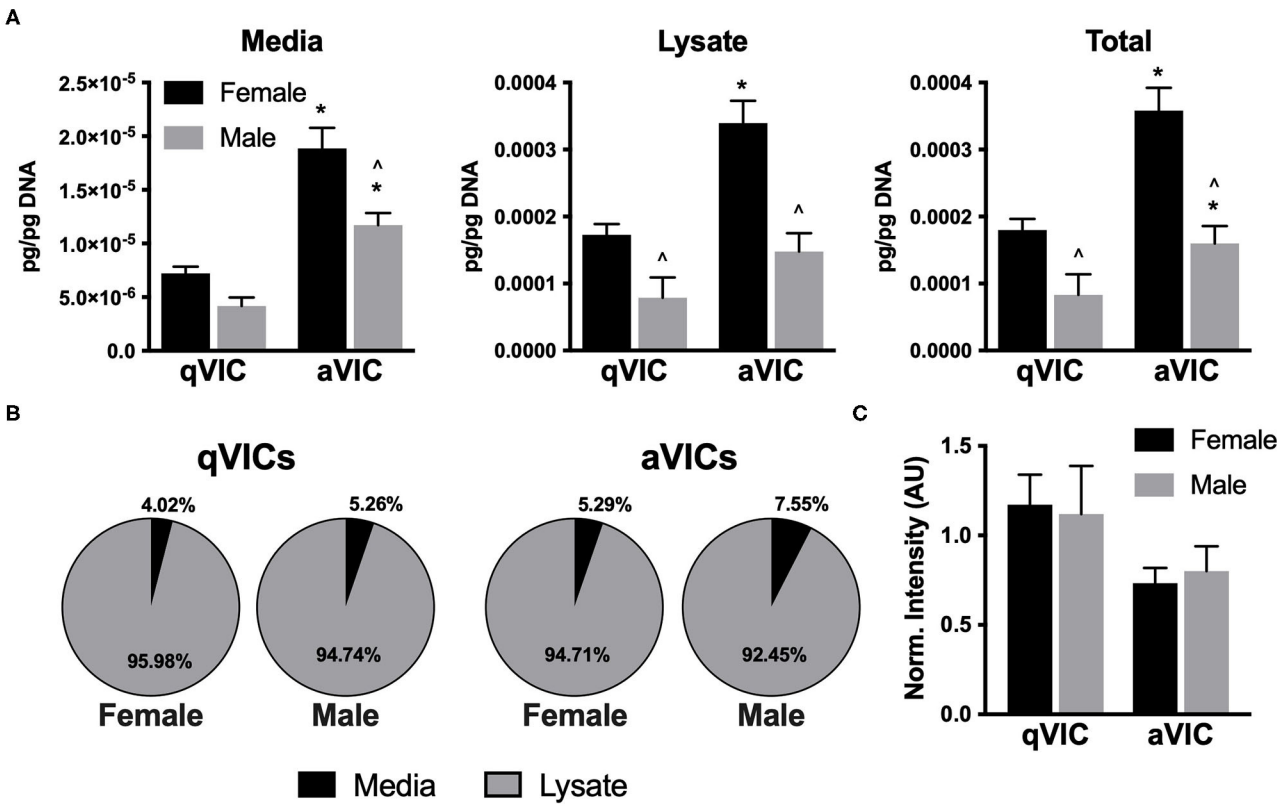

FIGURE 5 | Production of anti-angiogenic factors by VICs. **(A)** Production and **(B)** distribution of thrombospondin-2 (TSP2) in VIC cultures. **(C)** Western blot quantification of chondromodulin-1 in VIC lysates. *$p < 0.05$ vs. sex-matched qVIC level; ^$p < 0.05$ vs. female VIC of same phenotype by two-way ANOVA with Tukey's post *hoc* test. $N = 3$ pigs per sex, $n = 3$ wells per condition.

However, in contrast with the aforementioned VIC angiogenesis study, our results indicated that media conditioned by pathological VICs attenuated endothelial cell proliferation compared to media from healthy VICs (11). This difference between studies may be affected by using a different endothelial cell source, where the prior work used endothelial colony forming cells (ECFCs) isolated from umbilical cord blood, while our endothelial cells were adult VECs. Differences in donor age and type of cell may contribute to variations in their proliferative and angiogenic capacities and responses to stimuli. Additionally, the valves and VICs in all previous work were pooled from both males and females, so sex differences could not be examined. With respect to the decreased VEC proliferation seen in our work, we hypothesize that it was due to a combination of decreased bFGF and increased anti-proliferative factors (of which TSP2 is only one such molecule) in the aVIC media. It is important to note that the proliferation of VECs induced by aVIC-conditioned media was not just lower than the qVIC condition, but also lower than the negative (non-conditioned) control. This finding suggested that there was an anti-proliferative force at play, rather than just differences in bFGF, which caused us to focus our follow-up efforts on TSP2. Blocking the receptor for TSP2 was found to modestly recover VEC proliferation in the female aVIC-conditioned medium, indicating that the high TSP2 levels in female aVICs were partially responsible for the anti-proliferative effects. Because this study focused on examining factors that were primarily associated with angiogenesis, Chm-1 and TSP2 were the first molecules we investigated in the context of negative VEC regulation. However, there are many anti-proliferative molecules secreted by VICs that are not necessarily prominent in angiogenesis, and our previous work revealed sexual dimorphism in VIC gene expression of some of these (e.g., serpinB2, apoliprotein E) (12). Our current findings motivate further study into VIC secretion of such proliferation-regulating molecules and their sex-dependent impact on VECs.

Many of the trends observed in our study are consistent with histological observations of human valves with CAVD. For example, VEGF and ET-1 are elevated in sclerotic valves (27), which aligns with our finding of increased VEGF and ET-1 production by aVICs compared to qVICs. Studies of human plasma also indicate higher levels of ET-1 in males compared to females (28), which is matched by our VIC observations. TSP2 is upregulated in CAVD (29) while chondromodulin-1 is downregulated (30), which also mirrors our *in vitro* trends. One outlier in our findings was bFGF, in that it was the only pro-angiogenic factor we tested that decreased in aVICs. It is not known how this compares to the case of human valves, as it

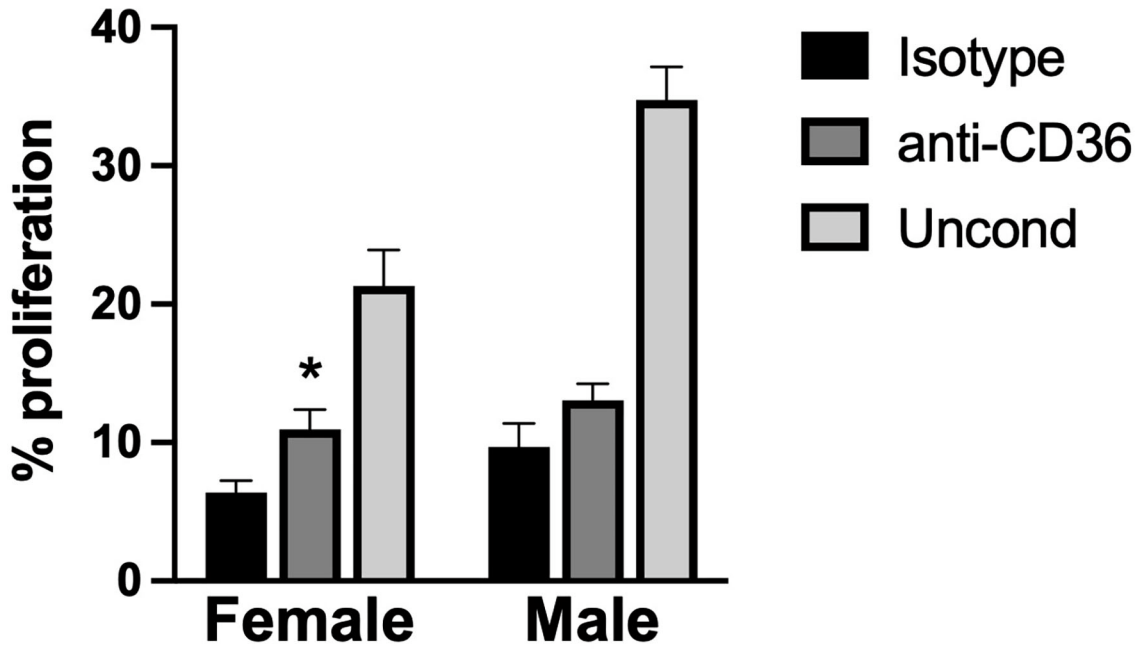

FIGURE 6 | VEC proliferation upon blocking TSP2 in VIC-conditioned media. VEC proliferation was measured following treatment with an antibody against CD36, to block VEC recognition of TSP2, or an isotype control. *$p < 0.05$ vs. sex-matched isotype control. $N = 3$ pigs per sex, $n = 3$ wells per condition.

does not appear that diseased human valves have been tested for bFGF. In our work, although the media used for qVIC and aVIC experiments was not supplemented with bFGF, it is possible that the previous exposure of qVICs to bFGF-supplemented media during qVIC expansion induced a lasting upregulation of endogenous bFGF secretion, since bFGF is known to induce its own expression (31).

The current study also examined the total growth factor content of VIC cultures (i.e., not only growth factor present in the media), which has not previously been characterized. For all growth factors examined, the majority of the biomolecule was present in the lysate fraction, which represents growth factors that had been secreted and were bound to the ECM, as well as growth factors that were still located in the intracellular space. One interesting outcome that emerged was a lesser fraction of growth factor in male VIC lysates compared to females. This difference motivated us to examine whether male and female VICs differed in their production of the ECM component that is most commonly responsible for growth factor sequestration. In fact, male VICs produced less HSPG2 than female VICs, which could contribute to the lower abundance of growth factors in male VIC lysates. Differences in ECM production by male and female aVICs have not previously been documented, but have the potential to affect numerous processes related to CAVD progression.

Although the molecules examined in this study are commonly associated with angiogenesis, regulation of this behavior is not their only role. Notably, several of the molecules that we quantified are also known to be potent regulators of fibrosis. For example, TSP2 is known to be powerfully pro-fibrotic (32), as it regulates molecules related to collagen fibrillogenesis, crosslinking, and degradation (33, 34). Thus, while its upregulation in diseased cells and tissues may seem counterintuitive from an angiogenesis perspective, it does align with the increase in fibrosis seen in CAVD. Our TSP2 findings are particularly interesting in the context of CAVD sexual dimorphism, as TSP2 levels were over 2-fold higher in female aVICs compared to male aVICs, a trend that aligns with fibrosis being more prevalent in female valves compared to male valves (4). In fact, the largest sex differences observed across all molecules quantified in the present study were found in TSP2. Thus, although our data related to angiogenesis did not reveal very strong sex-related associations, our TSP2 findings may have implications for understanding sexual dimorphism in valvular fibrosis.

Of course, this study is not without limitations. The VICs were cultured on 2-dimensional tissue culture polystyrene, which does not mimic the physical or biochemical properties of the native valve. It is possible that the growth factor secretion profiles may differ in ECM-based environments with different biophysical properties (35). Moreover, although porcine valves exhibit a high degree of similarity to human valves, the angiogenic behavior of human valve cells may differ from the porcine valve cells studied herein. Also, while numerous growth factors relevant to angiogenesis were quantified in this work, there may be other influential pro- or anti-angiogenic biomolecules that are produced by VICs. This study also raises several avenues to pursue in future work regarding CAVD angiogenesis and sexual

dimorphism. For example, macrophages are known to be a potent driver of angiogenic processes (36), so VICs are unlikely to be the only source of angiogenic factors in the context of the diseased valve. Once the valve has been infiltrated by inflammatory cells, it is possible that VICs may play a lesser role in driving angiogenesis. Another issue raised by this work is the existence of sexual dimorphism in VEC function and how it may affect valvular susceptibility to disease. Cellular-scale sex differences have been documented in ECs from other tissue sources (37); the current work examined only a few VEC functions, but motivates an expanded study on this topic for future work. Finally, the mechanism for the cellular-scale sex differences noted herein is not yet known. Potential hypotheses to examine in future work include chromosome complement or cellular memory of sex hormones (38).

DATA AVAILABILITY STATEMENT

The original contributions presented in the study are included in the article/supplementary material, further inquiries can be directed to the corresponding author.

AUTHOR CONTRIBUTIONS

KS, CM, and KM conceived of the ideas. VN, VP, LS, KS, CM, and KM had various roles in designing and performing the experiments. VN, VP, and KM analyzed the data. All authors approved of the manuscript.

FUNDING

This work was supported by a grant from the NIH (R01 HL141181 to KM) and the UW-Madison Graduate Engineering Research Scholars (GERS) Program. This material is based upon work supported by the National Science Foundation under Grant No. 1400815. Any opinions, findings, and conclusions or recommendations expressed in this material are those of the author(s) and do not necessarily reflect the views of the National Science Foundation. Performance of experiments herein was also supported by the University of Wisconsin Carbone Cancer Center Grant P30 CA014520.

REFERENCES

1. Rajamannan NM, Evans FJ, Aikawa E, Grande-Allen KJ, Demer LL, Heistad DD, et al. Calcific aortic valve disease: not simply a degenerative process: A review and agenda for research from the National Heart and Lung and Blood Institute Aortic Stenosis Working Group. Executive summary: Calcific aortic valve disease-2011 update. *Circulation*. (2011) 124:1783–91. doi: 10.1161/CIRCULATIONAHA.110.006767
2. Freeman RV, Otto CM. Spectrum of calcific aortic valve disease: pathogenesis, disease progression, and treatment strategies. *Circulation.* (2005) 111:3316–26. doi: 10.1161/CIRCULATIONAHA.104.486738
3. Cote N, Clavel MA. Sex differences in the pathophysiology, diagnosis, and management of aortic stenosis. *Cardiol Clin.* (2020) 38:129–38. doi: 10.1016/j.ccl.2019.09.008
4. Simard L, Cote N, Dagenais F, Mathieu P, Couture C, Trahan S, et al. Sex-related discordance between aortic valve calcification and hemodynamic severity of aortic stenosis: is valvular fibrosis the explanation? *Circ Res.* (2017) 120:681–91. doi: 10.1161/CIRCRESAHA.116.309306
5. Voisine M, Hervault M, Shen M, Boilard AJ, Filion B, Rosa M, et al. Age, sex, and valve phenotype differences in fibro-calcific remodeling of calcified aortic valve. *J Am Heart Assoc.* (2020) 9:e015610. doi: 10.1161/JAHA.119.015610
6. Soini Y, Salo T, Satta J. Angiogenesis is involved in the pathogenesis of nonrheumatic aortic valve stenosis. *Hum Pathol.* (2003) 34:756–63. doi: 10.1016/S0046-8177(03)00245-4
7. Arevalos CA, Berg JM, Nguyen JM, Godfrey EL, Iriondo C, Grande-Allen KJ. Valve interstitial cells act in a pericyte manner promoting angiogensis and invasion by valve endothelial cells. *Ann Biomed Eng.* (2016) 44:2707–23. doi: 10.1007/s10439-016-1567-9
8. Hakuno D, Kimura N, Yoshioka M, Fukuda K. Role of angiogenetic factors in cardiac valve homeostasis and disease. *J Cardiovasc Transl Res.* (2011) 4:727–40. doi: 10.1007/s12265-011-9317-8
9. Bogdanova M, Zabirnyk A, Malashicheva A, Enayati KZ, Karlsen TA, Kaljusto ML, et al. Interstitial cells in calcified aortic valves have reduced differentiation potential and stem cell-like properties. *Sci Rep.* (2019) 9:12934. doi: 10.1038/s41598-019-49016-0
10. Liu AC, Joag VR, Gotlieb AI. The emerging role of valve interstitial cell phenotypes in regulating heart valve pathobiology. *Am J Pathol.* (2007) 171:1407–18. doi: 10.2353/ajpath.2007.070251
11. Gendron N, Rosa M, Blandinieres A, Sottejeau Y, Rossi E, Van Belle E, et al. Human aortic valve interstitial cells display proangiogenic properties during calcific aortic valve disease. *Arterioscler Thromb Vasc Biol.* (2021) 41:415–29. doi: 10.1161/ATVBAHA.120.314287
12. McCoy CM, Nicholas DQ, Masters KS. Sex-related differences in gene expression by porcine aortic valvular interstitial cells. *PLoS ONE.* (2012) 7:e39980. doi: 10.1371/journal.pone.0039980
13. Latif N, Quillon A, Sarathchandra P, McCormack A, Lozanoski A, Yacoub MH, et al. Modulation of human valve interstitial cell phenotype and function using a fibroblast growth factor 2 formulation. *PLoS ONE.* (2015) 10:e0127844. doi: 10.1371/journal.pone.0127844
14. Porras AM, Engeland NC, Marchbanks E, McCormack A, Yacoub MH, Bouten CV, et al. Robust generation of quiescent porcine valvular interstitial cell cultures. *J Am Heart Assoc.* (2017) 6:e005041. doi: 10.1161/JAHA.116.005041
15. Yoshida A, Anand-Apte B, Zetter BR. Differential endothelial migration and proliferation to basic fibroblast growth factor and vascular endothelial growth factor. *Growth Factors.* (1996) 13:57–64. doi: 10.3109/08977199609034566
16. Dong F, Zhang X, Wold LE, Ren Q, Zhang Z, Ren J. Endothelin-1 enhances oxidative stress, cell proliferation and reduces apoptosis in human umbilical vein endothelial cells: role of ETB receptor, NADPH oxidase and caveolin-1. *Br J Pharmacol.* (2005) 145:323–33. doi: 10.1038/sj.bjp.0706193
17. Lopez-Lopez C, LeRoith D, Torres-Aleman I. Insulin-like growth factor I is required for vessel remodeling in the adult brain. *Proc Natl Acad Sci U S A.* (2004) 101:9833–8. doi: 10.1073/pnas.0400337101
18. van Cruijsen H, Giaccone G, Hoekman K. Epidermal growth factor receptor and angiogenesis: Opportunities for combined anticancer strategies. *Int J Cancer.* (2005) 117:883–8. doi: 10.1002/ijc.21479
19. Forsten-Williams K, Chu CL, Fannon M, Buczek-Thomas JA, Nugent MA. Control of growth factor networks by heparan sulfate proteoglycans. *Ann Biomed Eng.* (2008) 36:2134–48. doi: 10.1007/s10439-008-9575-z
20. Zhang X, Lawler J. Thrombospondin-based antiangiogenic therapy. *Microvasc Res.* (2007) 74:90–9. doi: 10.1016/j.mvr.2007.04.007
21. Zhu S, Qiu H, Bennett S, Kuek V, Rosen V, Xu H, et al. Chondromodulin-1 in health, osteoarthritis, cancer, and heart disease. *Cell Mol Life Sci.* (2019) 76:4493–502. doi: 10.1007/s00018-019-03225-y
22. Mathieu P, Bouchareb R, Boulanger MC. Innate and adaptive immunity in calcific aortic valve disease. *J Immunol Res.* (2015) 2015:851945. doi: 10.1155/2015/851945

23. Porras AM, McCoy CM, Masters KS. Calcific aortic valve disease: a battle of the sexes. *Circ Res.* (2017) 120:604–6. doi: 10.1161/CIRCRESAHA.117.310440
24. Summerhill VI, Moschetta D, Orekhov AN, Poggio P, Myasoedova VA. Sex-specific features of calcific aortic valve disease. *Int J Mol Sci.* (2020). 21:5620. doi: 10.3390/ijms21165620
25. Porras AM, Shanmuganayagam D, Meudt JJ, Krueger CG, Hacker TA, Rahko PS, et al. Development of Aortic Valve Disease in Familial Hypercholesterolemic Swine: Implications for Elucidating Disease Etiology. *J Am Heart Assoc.* (2015) 4:e002254. doi: 10.1161/JAHA.115.002254
26. Chalajour F, Treede H, Ebrahimnejad A, Lauke H, Reichenspurner H, Ergun S. Angiogenic activation of valvular endothelial cells in aortic valve stenosis. *Exp Cell Res.* (2004) 298:455–64. doi: 10.1016/j.yexcr.2004.04.034
27. Peltonen T, Taskinen P, Napankangas J, Leskinen H, Ohtonen P, Soini Y, et al. Increase in tissue endothelin-1 and ETA receptor levels in human aortic valve stenosis. *Eur Heart J.* (2009) 30:242–9. doi: 10.1093/eurheartj/ehn482
28. Miyauchi T, Yanagisawa M, Iida K, Ajisaka R, Suzuki N, Fujino M, et al. Age- and sex-related variation of plasma endothelin-1 concentration in normal and hypertensive subjects. *Am Heart J.* (1992) 123:1092–3. doi: 10.1016/0002-8703(92)90734-D
29. Pohjolainen V, Mustonen E, Taskinen P, Napankangas J, Leskinen H, Ohukainen P, et al. Increased thrombospondin-2 in human fibrosclerotic and stenotic aortic valves. *Atherosclerosis.* (2012) 220:66–71. doi: 10.1016/j.atherosclerosis.2011.10.003
30. Yoshioka M, Yuasa S, Matsumura K, Kimura K, Shiomi T, Kimura N, et al. Chondromodulin-I maintains cardiac valvular function by preventing angiogenesis. *Nat Med.* (2006) 12:1151–9. doi: 10.1038/nm1476
31. Wang D, Mayo MW, Baldwin AS. Jr. *Basic fibroblast growth factor transcriptional autoregulation requires EGR-1 Oncogene.* (1997) 14:2291–9. doi: 10.1038/sj.onc.1201069
32. Reinecke H, Robey TE, Mignone JL, Muskheli V, Bornstein P, Murry CE. Lack of thrombospondin-2 reduces fibrosis and increases vascularity around cardiac cell grafts. *Cardiovasc Pathol.* (2013) 22:91–5. doi: 10.1016/j.carpath.2012.03.005
33. Calabro NE, Barrett A, Chamorro-Jorganes A, Tam S, Kristofik NJ, Xing H, et al. Thrombospondin-2 regulates extracellular matrix production, LOX levels, and cross-linking via downregulation of miR-29. *Matrix Biol.* (2019) 82:71–85. doi: 10.1016/j.matbio.2019.03.002
34. Bornstein P, Armstrong LC, Hankenson KD, Kyriakides TR, Yang Z. Thrombospondin 2, a matricellular protein with diverse functions. *Matrix Biol.* (2000) 19:557–68. doi: 10.1016/S0945-053X(00)00104-9
35. Mabry KM, Payne SZ, Anseth KS. Microarray analyses to quantify advantages of 2D and 3D hydrogel culture systems in maintaining the native valvular interstitial cell phenotype. *Biomaterials.* (2015) 74:31–41. doi: 10.1016/j.biomaterials.2015.09.035
36. Graney PL, Ben-Shaul S, Landau S, Bajpai A, Singh B, Eager J, et al. Macrophages of diverse phenotypes drive vascularization of engineered tissues. *Sci Adv*. (2020). 6(18):eaay6391 doi: 10.1126/sciadv.aay6391
37. Stanhewicz AE, Wenner MM, Stachenfeld NS. Sex differences in endothelial function important to vascular health and overall cardiovascular disease risk across the lifespan. *Am J Physiol Heart Circ Physiol.* (2018) 315:H1569–H88. doi: 10.1152/ajpheart.00396.2018
38. Regitz-Zagrosek V, Kararigas G. Mechanistic Pathways of Sex Differences in Cardiovascular Disease. *Physiol Rev*. (2017) 97:1–37. doi: 10.1152/physrev.00021.2015

Conflict of Interest: The authors declare that the research was conducted in the absence of any commercial or financial relationships that could be construed as a potential conflict of interest.

Publisher's Note: All claims expressed in this article are solely those of the authors and do not necessarily represent those of their affiliated organizations, or those of the publisher, the editors and the reviewers. Any product that may be evaluated in this article, or claim that may be made by its manufacturer, is not guaranteed or endorsed by the publisher.

frontiers in Cardiovascular Medicine

REVIEW
published: 17 September 2021
doi: 10.3389/fcvm.2021.734175

Calcific Aortic Stenosis—A Review on Acquired Mechanisms of the Disease and Treatments

Banafsheh Zebhi[1], *Mohamad Lazkani*[2] *and David Bark Jr.*[3,4]*

[1] Department of Mechanical Engineering, Colorado State University, Fort Collins, CO, United States, [2] Medical Center of the Rockies, University of Colorado Health, Loveland, CO, United States, [3] Department of Pediatrics, Washington University in Saint Louis, Saint Louis, MO, United States, [4] Department of Biomedical Engineering, Washington University in Saint Louis, Saint Louis, MO, United States

Calcific aortic stenosis is a progressive disease that has become more prevalent in recent decades. Despite advances in research to uncover underlying biomechanisms, and development of new generations of prosthetic valves and replacement techniques, management of calcific aortic stenosis still comes with unresolved complications. In this review, we highlight underlying molecular mechanisms of acquired aortic stenosis calcification in relation to hemodynamics, complications related to the disease, diagnostic methods, and evolving treatment practices for calcific aortic stenosis.

Keywords: calcific aortic stenosis, prosthetic heart valve, basilica, transcatheter heart valve, hemodynamics, coronary obstruction

OPEN ACCESS

Edited by:
Katherine Yutzey, Cincinnati Children's Hospital Medical Center, United States

Reviewed by:
Joshua D. Hutcheson, Florida International University, United States
Ernesto Greco, Sapienza University of Rome, Italy

***Correspondence:**
David Bark Jr.
bark@wustl.edu

Specialty section:
This article was submitted to Heart Valve Disease, a section of the journal Frontiers in Cardiovascular Medicine

Received: *30 June 2021*
Accepted: *18 August 2021*
Published: *17 September 2021*

Citation:
Zebhi B, Lazkani M and Bark D Jr. (2021) Calcific Aortic Stenosis—A Review on Acquired Mechanisms of the Disease and Treatments. Front. Cardiovasc. Med. 8:734175. doi: 10.3389/fcvm.2021.734175

INTRODUCTION

Calcific aortic stenosis (AS) is the most common valve disease in developed countries (1, 2), in which valves thicken and stiffen, and in some cases nodular deposits form, limiting valve function. This may result in valve regurgitation with concomitant stenosis. Calcific AS is a progressive disease that advances with age (3, 4), affecting ∼0.2% of people 50–59 years of age and increasing to 9.8% for 80–89 years (5, 6). As the general population has become older, the prevalence of calcific AS has increased, igniting multiple improvements in its management (2). In addition to new diagnostic imaging techniques emerging, novel prosthetic valves have been developed as an effective treatment for calcific AS. To date, pharmacotherapy has not been shown to slow down the progression of the disease, or to reverse the calcification process (2). In this review we highlight engineering perspectives toward recent advancements in the treatment of AS, underlying molecular pathways and mechanisms of the calcification process, clinical characteristics, hemodynamics, complications of calcific AS, diagnoses, and common treatment practices for calcific AS.

AORTIC VALVE STRUCTURE AND CALCIFICATION

Aortic valve (AV) leaflets consist of three layers: the ventricularis layer is elastin-rich and located on the ventricular side; the spongiosa is made of proteoglycans that provide lubrication for the other layers; and a fibrosa layer made of a dense collagen network is on the aortic side of the valve (7, 8), which provides much of the structural support in response to mechanical forces (9). These 3 layers are filled with valvular interstitial cells (VICs), and the entire layered structure is covered by endothelial cells (10) (**Figure 1**). The fibrosa layer is particularly prone to calcification (11), while alterations to the endothelial barrier function could impact propensity

for calcification. For years, calcification was thought to be a passive degenerative process in which calcium accumulates on leaflets (4, 12–17), where old age, male gender, diabetes mellitus, coronary artery disease, chronic renal disease, hypertension, hypercholesterolemia, and smoking are known to increase the risk for AV calcification (18). Now, it is understood that calcification is a complex process involving mechanobiology, molecular signaling, tissue remodeling, and inflammation as the AV opens and closes billions of times during a lifetime.

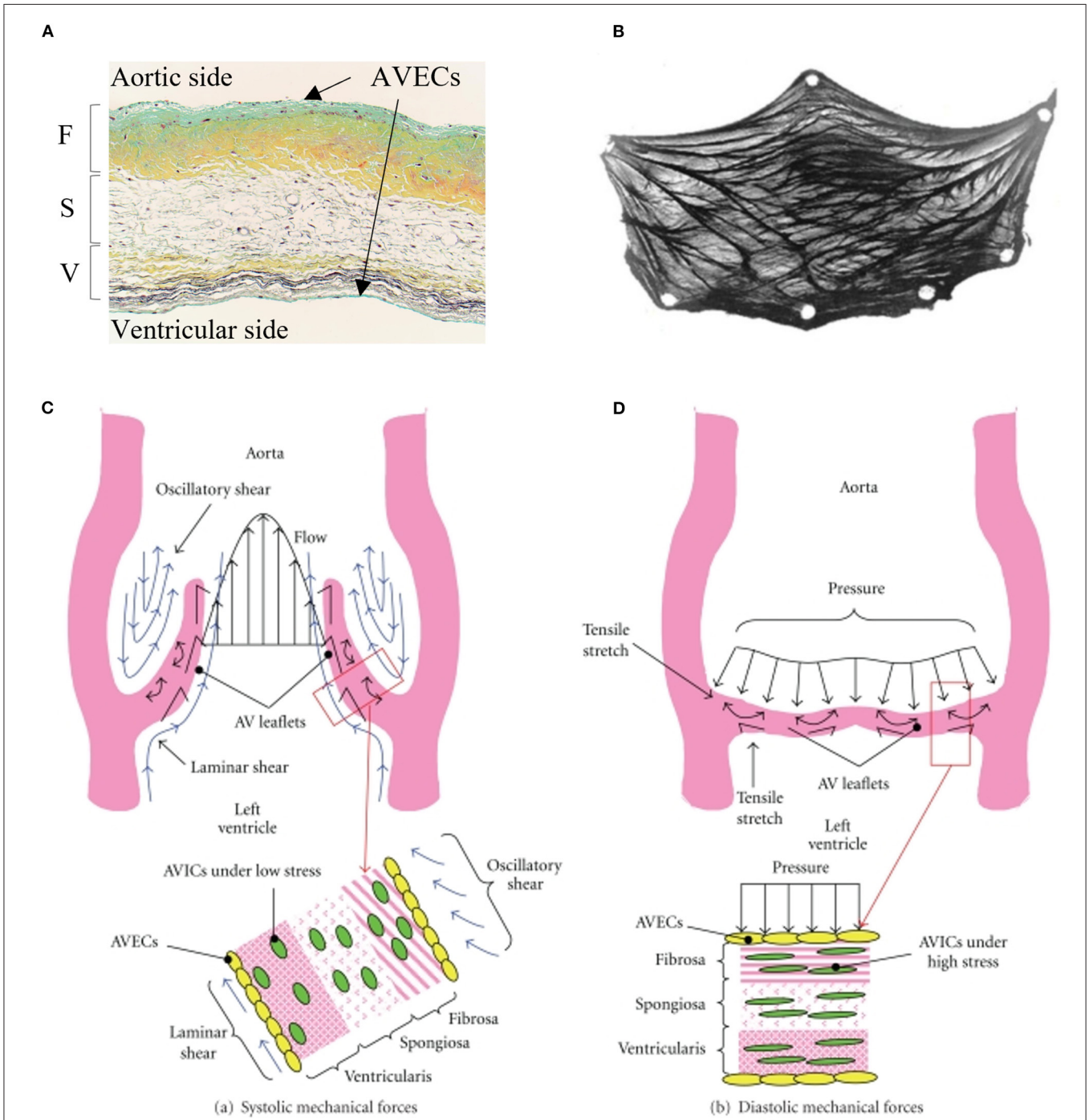

FIGURE 1 | Microscopic and macroscopic overview of aortic valve tissue structure: **(A)** histological section of the aortic valve leaflet showing three layers: fibrosa (F), spongiosa (S), and ventricularis (V) covered by valvular interstitial cells (VICs) and valvular endothelial cells (VlvECs). **(B)** excised view of the aortic valve leaflet demonstrating fiber structure. Schematic of stress experienced by aortic valve leaflets and valvular cells during **(C)** systole, and **(D)** diastole. **(A)** is from Fishbein et al. **(B)** is from Driessen et al. **(C,D)** are from Balachandran et al. with permission.

HEMODYNAMICS AND ENDOTHELIAL CELL MECHANOTRANSDUCTION

Due to the sensitivity to hemodynamics (blood flow), endothelial cells may contribute to calcification and AS by responding to shear stress experienced on the cells' apical side (**Figure 1**). Indicating a potential link, calcium formation is more common in the non-coronary cusp, where surrounding fluid wall shear stress is lower relative to coronary cusps (1). Endothelial cells respond to shear stress by changing their morphology, gene regulation, protein expression, transendothelial transport, alignment, and release of molecules and proteins from the surface (19). These processes can occur as endothelial cells convert mechanical stimuli to biochemical signals to elicit biological responses, known as mechanotransduction, briefly summarized below.

Vascular endothelial cells sense their environment through ion channels (which allows membrane depolarization and cell signaling), integrins, intercellular junction proteins, caveolae, the glycocalyx, G protein-coupled receptors (GPCRs), and tyrosine kinase receptors (20, 21), However, only some of these mechanosensors have been observed for valvular endothelial cells (further explained below). Integrins function as signaling receptors and play a crucial role in transmitting physical mechanical forces between the extracellular matrix and the actin cytoskeleton via focal adhesion complexes. In one example, valvular endothelial cell morphological alignment perpendicular to the direction of flow involves β1 integrin, vinculin and focal adhesion kinase and depends on Rho-kinase and calpain (19). GPCRs are also highly sensitive to changes in flow and activate downstream signaling by binding to extracellular ligands (22). The glycocalyx is a mediator for cell-cell adhesion and works as a trap for ions and antibodies that translate to downstream signaling pathways (20). Using these mechanosensors (and others), mechanical forces are transmitted to the nucleus and can change the nuclear morphology, stiffness, and gene expression (23). Mechanotransduction in relation to AS calcification continues to be explored and only a brief description of some findings are presented here.

INFLAMMATION MECHANISM IN AORTIC VALVE CALCIFICATION

Multiple studies indicate a role for an innate and adaptive immune response that leads to calcification. This largely initiates with dysregulated valvular endothelial cells, progresses to excessive remodeling of the leaflet ECM, changes in tissue stiffness, tissue mineralization, osteogenesis (formation of bone), and eventually lead to late-stage calcification (24, 25).

The endothelium is most responsive to the magnitude and directionality of fluid shear stress. Physiological unidirectional shear stress is protective by downregulating adhesion proteins, vascular cell adhesion molecule 1 (VCAM-1), platelet endothelial cell adhesion molecule-1 (PECAM-1), and chemokines IL-1β and IL-8. It also leads to expression of nitric oxide (NO), which can help prevent thrombotic responses that could otherwise play a role in calcification (8). Notch signaling is increased, which helps prevent calcification (26, 27). There is also increased expression of osteoprotegrin (OPG), which regulates aortic valve calcification by inhibiting receptor activator of the nuclear factor κB ligand (RANKL) signaling (28, 29). Under oscillatory shear stress, VCAM-1, intercellular adhesion molecule 1 (ICAM-1), endothelial selectin (E-selectin), VEGF, and TGFβ are upregulated, which leads to increased oxidative stress and inflammatory agents such as bone morphogenic protein (BMP)-4 and cytokines: IL-1β and INFγ. TGFβ and VEGF can induce cell proliferation, fibrosis, and promotes calcification by enhancing irreversible tissue thickening and stiffening (19). Increased BMP-2 and BMP-4 can upregulate osteogenic pathways involving the Msx2 transcription factor that activates Wnt/LDL receptor-related protein 5 (Lrp5)/β-catenin signaling (30, 31), and the Runx2/Cbfa1 transcription factor (31, 32) that leads to differentiation of the VICs to an osteoblast-like phenotype. Altogether, low and oscillatory shear stress found in stagnating regions of aortic valve leaflets are linked to signaling changes in the endothelium that lead to proinflammatory responses that could be linked to calcification.

Endothelial cell responses can also lead to low-density lipoprotein (LDL) deposition in response to altered mechanical forces, which can induce inflammation (25, 33). LDL and lipoprotein (a) derived from cholesterol colocalize in the calcified valve tissue in early calcification (34). Plasma lipoprotein (a) is an independent risk factor of AS identified through genome-wide association studies (34–36). Furthermore, apolipoprotein H (APOH) was identified as a novel locus for lipoprotein (a) levels (36). Despite the link of LDL with calcification, studies have found that LDL suppression or lipid-lowering therapy with statins (anti-inflammatory and antioxidant agents) do not slow down the progression of disease even when given at early stages of calcification (37–41).

Macrophages are found in calcified AV leaflets, likely entering through trans-endothelial migration involving ICAM and VCAM (37). In response to activated endothelial cells, macrophages release pro-osteogenic cytokines like IL-1β, IL-6, tumor necrosis factor-α (TNF-α), and RANKL, all of which could contribute to calcification. Activated macrophages produce enzymes that can cause interstitial cell activation, changes in gene expression, and differentiation to osteoblasts, which then leads to excess synthesis and remodeling of collagen fibers in the fibrosa (11) (**Figure 2**). Cytokines can promote cell proliferation and ECM remodeling. Some fibroblasts can differentiate to activated myofibroblasts (42). The activation of myofibroblasts further induces inflammation through the expression of BMP, MMP-2, and MMP-9 and releases TNF-α and TGF-β1 and eventually differentiate to osteoblast-like phenotype (43). TNF-α activates nuclear factor-κB (NF-κB) pathways which leads to expression of proinflammatory genes (44–46). Via activation of NF-κB, T cell activation amplifies the inflammatory response by producing cytokine interferon- (IFN-γ) and TNF-α. Macrophages (along with vascular smooth muscle cells) also release calcification-prone extracellular vesicles (EVs) (47, 48). Excessive production of EVs lead to microcalcification. Overall, macrophages can

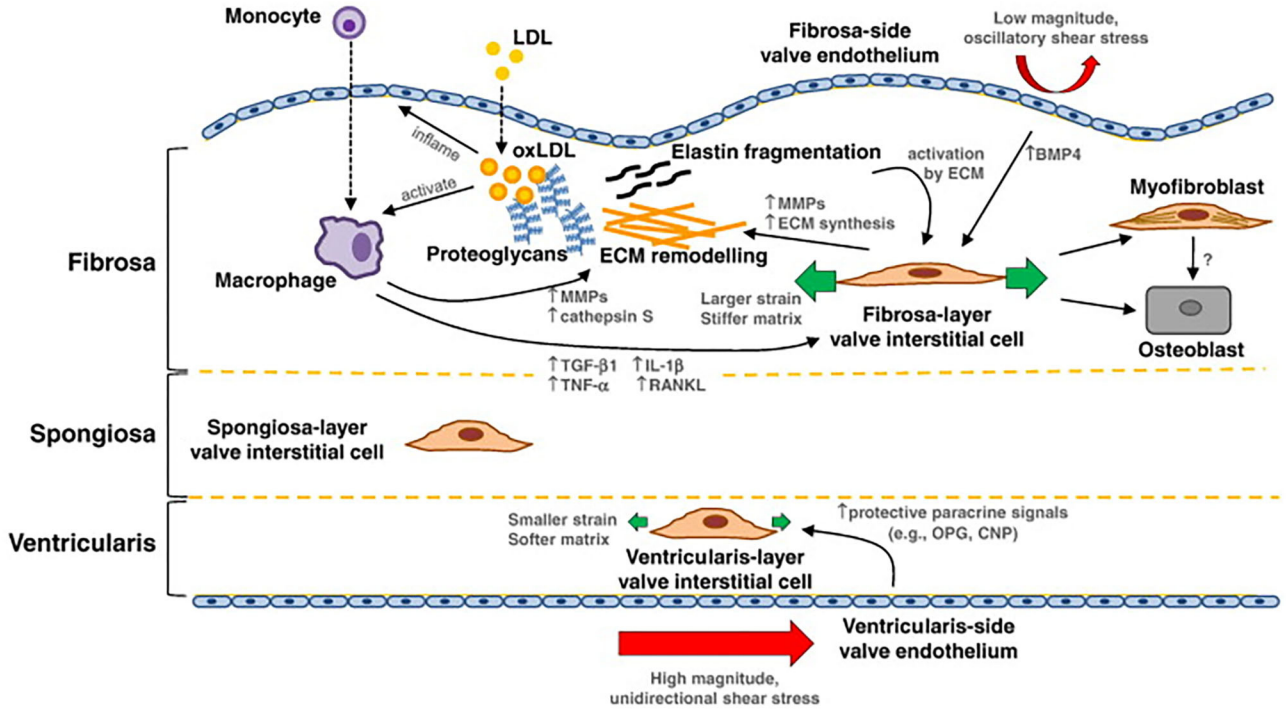

FIGURE 2 | Summary of mechanotransduction and pathway of valvular calcification: in the fibrosa layer, the oxidated LDL (oxLDL) can inflame the endothelial cells, bind to monocytes, and activate macrophages. Activated macrophages mediate extracellular matrix (ECM) remodeling and molecular signaling that can potentiate valvular interstitial cell (VIC) pathological differentiation to myofibroblast and osteoblast cells. The ECM further affects VIC activation and differentiation; activated VICs synthesize and remodel the ECM, and produce cytokines, like TGF-β1. Interstitial and endothelial cells on each layer of the tissue exhibit a different phenotype. On the ventricular side, endothelial cells experience high magnitude and unidirectional shear stress, which may inhibit pathological differentiation of the local VICs. Image is from Yip et al. with permission.

initiate a number of proinflammatory events that can lead to calcification in response to endothelial signals.

PHARMACOTHERAPIES

Currently there is no approved pharmaceutical treatment for calcific aortic valve stenosis, but literature provides possible future pharmacological approaches in human and animal models. A review by Myasoedova et al. (49) showed that oxidized low density lipoprotein (Ox-LDL), oxidized phospholipids (Ox-PL), lipoprotein associated phospholipase A2 (Lp-PLA2), Lp(a), proprotein convertase subtilisin/kexin type 9 (PCSK9), high density lipoprotein (HDL), the purinergic receptor 2Y2 (P2Y2R), sodium-dependent phosphate cotransporter (PiT-1), dipeptidyl peptidase-4 (DDP-4) are targetable components for prevention and treatment of calcific AS in human. In efforts to target calcific AS, antisense oligonucleotides (ASOs) 2nd generation [inhibitor of apo(a) mRNA translation] was introduced as a new selective Lp(a) inhibitor (50, 51). Niacin (nicotinic acid) therapy helps to lower LDL and Lp(a) (52) and increase HDL (53). Since statins exhibit limited benefit to calcific AS, the lowering of LDL may not provide benefit. Also, a trial study showed that extended-release niacin (ERN) does not reduce the risk of cardiovascular disease despite the favorable effect on lowering Lp(a) (54). PCSK9 (involve in regulating blood cholesterol) inhibitors can significantly lower LDL and plasma Lp(a) (55, 56) and reduce the risk of cardiovascular disease, but have an unclear impact on calcific AS. Sodium phosphonoformate (PFA) as a PiT-1 inhibitor can inhibit calcification in human VICs (57). DDP-4 inhibitors inhibit progression of calcific AS by blocking insulin-like growth factors and osteogenic activities in VICs. Additionally, some animal studies suggest that calcification can be reversible. Miller et al. (58) showed that a "genetic switch" in Reversa mice can reduce plasma lipid and oxidative stress and halt the progression of the calcific AS. P2Y2R promotes expression of carbonic anhydrase CAXII, which acidifies the extracellular space and promotes calcification regression by resorbing minerals in mice (59). There is ongoing effort to develop pharmacotherapies for calcific AS, but due to the complex processes involved, this is a challenging undertaking.

CLINICAL AND HEMODYNAMIC CHARACTERISTICS OF AORTIC STENOSIS

Severe AS can result in serious problems. Patients can experience heart murmur, chest pain, shortness of breath, fatigue and syncope. Pressure overload can occur in the left ventricle, and when left untreated, this can lead to hypertrophy (60). Presence of

long-term pressure overload can even eventually lead to systolic failure and congestive heart failure. AS can also further create bleeding complications described below.

Aortic stenosis severity can be assessed based on valve flow velocity, valve orifice area, and the pressure gradient across the valve (61, 62). The common flow condition for severe stenosis is defined as a peak aortic velocity $\geq$ 4 (m/s), pressure gradient $\geq$40 (mmHg), and AV area <1 (cm^2) (63); however, 5–10% of the patients with severe stenosis have low flow (low cardiac output), low pressure gradient <40 (mmHg) due to reduced left ventricle ejection fraction (LVEF) (<40%) (62), and 10–35% with severe stenosis have paradoxical (Stage 3D Severe AS) low flow and low pressure gradient due to LV hypertrophy (with normal EF). These variations of hemodynamics make the diagnosis and decision making for treatment of AS difficult; therefore other parameters have also been used to make accurate decisions when treating AS; this includes both subjective clinical symptoms and objective data, such as valvulateral impedance, AV resistance, projected AV area at normal flow, and calcium score (62, 63). A review by Saikrishnan et al. (62) provides a comprehensive summary of metrics, units, methods of measurement and the cut-off points for severe AS. In order to score AS, maximum velocity and pressure gradient are measured, and valve effective orifice area (EOA) is calculated.

Blood flow through the valve can be characterized using techniques and imaging modalities described below. Blood flowing from left ventricle outflow tract (LVOT), passing through a stiff narrow valve opening, creates a jet with maximum velocity at vena contracta (VC). VC is a location where fluid pathlines converge, and the velocity is the highest. The area of the VC is known as the EOA. Using Doppler echocardiography, pressure drop is approximated using a simplified Bernoulli equation, assuming that proximal velocity is negligible, $\Delta P = 4v^2$, where ΔP is the transaortic valve pressure gradient (between VC and LVOT), and v is maximum velocity of blood (64) (**Figure 3**). EOA is calculated using the continuity equation; the volume flow rate passing through LVOT equals to the flow rate passing through VC, i.e., $EOA \cdot VTI_{VC} = CSA_{LVoT} \cdot VTI_{LVoT}$, where VTI_{VC} and VTI_{LVoT} are the velocity time integrals measured from the parasternal long-axis view at the location of LVOT and VC, and EOA and CSA_{LVoT} are cross sectional areas of VC and LVOT (62, 64, 65). In rare cases when there are discrepancies in Doppler echocardiography measurements, cardiac catheterization is used to obtain a more accurate measurement of pressure directly from the blood vessel. Using the Gorlin equation, the geometric orifice area (GOA) is calculated from the flow rate and the pressure drop between the LVOT and VC, which is related to the EOA through the contraction coefficient. The GOA the area formed by free edges of the leaflets when valves are fully opened. Thus, catheterization measurements are performed at peak systole. A review by Saikrishnan et al. (62) provides a detailed description of diagnostic modalities and formulations. Calcific AS can be additionally assessed by computed tomography (CT) which provides high-resolution assessment of calcification, and enables accurate measurement of leaflet anatomy and annulus geometry. Calcific deposits have higher density compared with surrounding soft tissues. CT imaging uses attenuation coefficients expressed

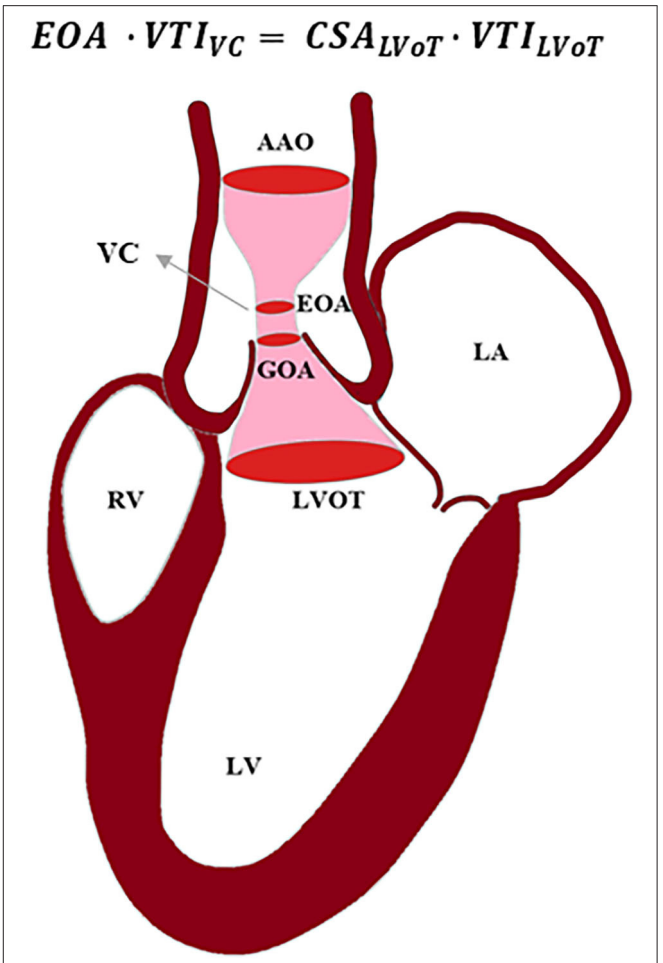

FIGURE 3 | Schematic of blood passing through a stenosed aortic valve. Using continuity equation, the effective orifice area (EOA) can be calculated based on velocity time integral (VTI) at vena contracta (VC), cross-sectional area (CSA) of left ventricle outflow tract (LVOT), and VTI at LVOT. AAO, ascending aorta; LA, left atrium; LV, left ventricle; RV, right ventricle; GOA, geometric orifice area.

by Hounsfield unit (HU). High density calcific deposits have a high attenuation value (>130 HU) which makes the calcific area appear bright in the image. A calcium score is quantified by multiplying calcified area by Hounsfield unit, and is known as Agatston score (66, 67). Different Agatston scores are used for men and women to diagnose severe stenosis (68–70). Recent studies highlighted that calcification deposits are more prevalent in men, while fibrosis may be more significantly involved in valvular dysfunction in women (71–73); presence of estrogen in women inhibits aortic valve calcification via suppression of RANKL signaling (74, 75) and suppression of TGFβ-dependent ECM production (76). Animal studies showed that sex-related differences in calcific aortic valve disease are due to different pathogenetic and signaling pathways in male and female (72).

In addition to impacting energy loss and hemodynamics, an aortic stenosis has a significant impact on the hemostatic capacity

of blood. It can lead to gastrointestinal, skin, and mucosal bleeding, which may, in-part, be attributed to acquired von Willebrand syndrome (AVWS) also known as Heydes Syndrome (77–81). It appears as though the AVWS stems from turbulence that can occur in an aortic stenosis, whereas it is often alleviated once a diseased valve is replaced, eliminating pathological flow (78, 82–86).

CALCIFIC AORTIC VALVE STENOSIS TREATMENT

At late stages of calcific AS, no therapies can manage the progression of calcification and the only effective treatment is valve repair or replacement (61).

Valve Repair

Valve repair surgery can be used and is one of the oldest cardiovascular surgical interventions dating back to the early 1920s (87). Native aortic valve (root and leaflets) repair comes with low mortality risk and is free of most valve-related complications, yet durability of treatments remained limited and reoperation is often required in the short term (88). This has largely fallen out of favor in modern practice and is not utilized often, except in some centers.

Valvuloplasty

Balloon aortic valvuloplasty (BAV) is a catheter-based technique that dilates native valve's narrowed opening by delivering and inflating a balloon at the site of stenosed valve through femoral artery (89). BAV increases leaflet mobility by creating a fracture in calcified lesions, expanding the aortic annulus and separating calcified commissures (90). It has become a tool that can even be used in fetal aortic stenosis, to avoid progression into a more complex congenital heart malformation (91–94). Use of an oversized balloon can cause infractions in the valve ring, separation between leaflets and the root, and leaflet tearing (90). Additionally, balloon inflation may cause complications like coronary ostia occlusion that could lead to myocardial ischemia and dysfunction of left ventricle. BAV procedures do not provide long term improvements in adults, as the dilated valve can become restenosed; therefore, BAV is a temporary improvement option and a bridge to SAVR or TAVR for patients who are at high risk and need an urgent intervention (95). Utilization of BAV is also practiced as a palliative treatment option in terminal patients with <1-year life expectancy to improve quality of life in the short term, often seen in the hospice population.

Valve Replacement

Surgical aortic valve replacement (SAVR) has become the most common treatment for severe calcific aortic stenosis in which patients undergo an open-heart surgery to replace their aortic valve with a mechanical or a bioprosthetic valve; in this procedure calcified native leaflets are cut and removed. The mechanical or bioprosthetic valve is subsequently sutured to the aortic root. SAVR improves symptoms and survival, but it comes with risks of thrombosis in mechanical valves that can cause stroke or heart attack, or in the case of bioprosthetic valves, durability is an issue with these valves often calcifying over time (96). Initially, in older patients who are inoperable or are at high risk for surgery, transcatheter aortic valve replacement (TAVR) was an alternative option. However, this option is now common practice for lower risk patients, as the devices and procedures have advanced with equal to improved outcomes compared to SAVR (97, 98). The first in-human TAVR was performed in 2002 (99); since then, more than 50,000 TAVR interventions have been done worldwide (100). TAVR is a less invasive technology in which a stented valve is delivered to the location of native valve through a catheter and is expanded to replace the calcified native aortic valve and leaflets.

Current guidelines set by the American College of Cardiology (ACC) and American Heart Association (AHA) advocate for Aortic Valve Replacement in the setting of symptomatic severe aortic stenosis. Timing of intervention depends on the development of clinical symptoms once the valve is classified as severe. The main reason is due to durability of bioprosthetic valves. Due to the relative development of TAVR being in its infancy within the last decade, long term durability has not been well-established, although expert consensus agree 10 years is a reasonable time frame before expected degeneration and failure of the bioprosthesis. However, investigators are currently attempting to determine the benefit of treatment of severe aortic stenosis before the development of symptoms and potentially remodeling and other stressful changes to the heart. An ongoing study titled Evaluation of Transcatheter Aortic Valve Replacement Compared to Surveillance for Patients With Asymptomatic Severe Aortic Stenosis (EARLY TAVR) trial is ongoing to address the timing of intervention in severe aortic stenosis (101–104). Furthermore, there is another school of thought that goes beyond waiting for symptoms with severe AS, but in fact challenges the traditional belief to only treat severe AS. A clinical trial is being developed, called PROGRESS: Management of Moderate Aortic Stenosis by Clinical Surveillance or TAVR. As such, investigators are now looking to examine the benefit of treating moderate AS with TAVR intervention, although facing the same challenges regarding the issue of durability.

SAVR and TAVR have various advantages. A study of 699 high-risk patients with severe aortic stenosis who were randomly treated with SAVR and TAVR in PARTNER 1 trial showed that 1-year mortality rates were similar between the transcatheter and surgically treated groups (24.2% TAVR vs. 26.8% SAVR), but hemodynamics and post-operative outcomes were significantly different. The transcatheter group had a shorter hospitalization with a slightly better mean AV pressure gradient and mean AV area at 1-year. However, vascular complications were significantly higher in the transcatheter group at 1-month (11% TAVR vs. 3.2% SAVR). The rate of major strokes at 1-year were more than twice as high in the transcatheter group (5.1% TAVR vs. 2.4% SAVR). Moderate and severe paravalvular regurgitation was more frequent in the transcatheter group than in the surgical group at 1-year (6.8% TAVR vs. 1.9% SAVR). Meanwhile, major bleeding was more frequent in the surgical group (19.5% SAVR vs. 9.3% TAVR) (105). Other follow-up studies have confirmed similar mortality rates and post-procedural outcomes; at 5 years, Gleason et al. (106) reported mortality rates of 55.3 and 55.4%

for TAVR and SAVR, respectively, and Mack et al. (107) reported that risk of death at 5 years increases to 67.8% in TAVR and 62.4% in SAVR.

In low-risk patients, with severe aortic stenosis that were randomly treated with SAVR and TAVR in PARTNER 3 trial, TAVR was associated with significantly lower risk of mortality at 1 year (2.1% TAVR vs. 3.5% SAVR) and life threatening bleeding (3.9% TAVR vs. 11.2% SAVR); no significant differences in stroke (3.0% TAVR vs. 4.2% SAVR), major vascular complications (3.6% TAVR vs. 2.4% SAVR), and myocardial infarction (1.7% TAVR vs. 2.1% SAVR); and significantly higher moderate to severe paravalvular leak (PVL) (3.6% TAVR vs. 1.7% SAVR) (108). With 3 trials (PARTNER 1, 2, and 3), TAVR vs. SAVR have been studied in high-, intermediate-, and low-risk patients.

The TAVR utilization among underserved and underrepresented populations are lower. This was initially thought to be related to lower incident of AS among Black and Hispanic populations (109), but further studies suggested that this might be due to limited accesses to care, low socioeconomic status, and treatment biases in the non-White population (109–112). This calls the need for advance clinical care accessible to all patients regardless of their race and ethnicity.

MECHANICAL HEART VALVES

Currently implanted mechanical heart valves (MHVs) typically have a bileaflet structure in shape of two disks made of pyrolytic carbon that can open pivotally. MHVs are highly durable when compared with other artificial heart valves; they can last up to 25 years in patients without major complications, but they have high risk of thrombosis (96). High durability makes these valves more suitable for patients younger than age 50, as MHVs have a lower risk of reoperation (113).

Fluid high shear stress in the hinge region of these valves can initiate thrombotic events (114–117). Patients treated with mechanical valves need a lifelong anticoagulant drug therapy to prevent thrombosis and thromboembolism (118); however these drugs increase the risk of bleeding, stroke, systemic embolism, cardiac tamponade and death (119). Therefore, multiple groups are attempting to improve the blood-material interactions through surface treatments (120–123). However, the hemodynamic impact on blood from the hinge remains a concern, even with these treatments.

BIOPROSTHETIC HEART VALVES

Bioprosthetic heart valves (BHV) are made of porcine or bovine pericardium. They have the advantage of being less thrombotic, requiring only short-term anticoagulation after surgery. The main disadvantage of BHVs is that they often require reoperation due to structural valve deterioration and calcification, making the average BHV lifetime only ∼15 years. In recent years, BHVs durability has been improved by anti-calcification and anti-mineralization treatments. Therefore, nowadays BHVs are more commonly recommended for implantation, even in younger patients, due to their improved durability and lower risk of structural deterioration (124). Otherwise, pediatric patients previously exhibited severe complications with calcification of BHVs.

TRANSCATHETER HEART VALVES

Transcatheter heart valves (THVs) are gaining traction due to novel designs and delivery systems to replace the calcified aortic valve. In TAVR procedures, TAVs are deployed to the location of a calcified aortic valve with stent expansion through one of two main mechanisms: balloon expansion or self-expansion through shape memory alloys. The stent permanently opens the native valve by pushing against calcified leaflets. Some of the most frequent complications occurring with TAVR procedures are TAV malpositioning, coronary obstruction, paravalvular leak, crimped-induced leaflet damage, thrombosis, conduction abnormalities, and prosthetic-patient mismatch (125). There are also less common, but potentially fatal complications including valve embolization and annular rupture. TAV crimping causes significant structural changes and damages in leaflet tissue that affects the durability of the tissue, and can lead to early thrombosis, early calcification and endocarditis in tissue (126). Prosthetic-patient mismatch is a condition in which EOA of the TAV is too small relative to patient's body size (127) causing elevated flow resistance at the valve which should be overcome by increased pressure in the heart (125).

Valve positioning has an important role in TAV hemodynamics; it has been suggested that TAV be positioned about 5 mm below the annulus of the valve for the best outcome (128); however, the deployment site is dependent on the type of the TAV and in recent years, many attempts have been made to customize TAV deployment according to the patient-specific aortic root anatomy. If the implant is too-high or a too-low, it can result in moderate to severe paravalvular aortic regurgitation (AR) or PVL (128). The malpositioned TAV can be manually repositioned; if ineffective, an alternative solution is to deploy a second TAV inside the first TAV, this is known as valve-in-valve (ViV) procedure (128). Using new generation of TAVR devices, ViV has shown to be very effective in reducing post-procedural AR; a study of 63 patient who had ViV procedure using Edwards Sapien transcatheter valve showed that only 7.9% of the patient still had significant AR after procedure, however, ViV is associated with higher prevalence of cardiac conduction abnormalities which requires permanent pacemaker implantation in patients (129).

Additionally, undersizing a TAV can lead to malpositioning, valve dislodgement, and embolization (130). It has been recommended that slightly oversizing the TAV can minimize PVL without causing injury and rupture in aortic root and annulus (130–134). Another cause of PVL after TAVR procedure for calcified AS is the gap between the TAV and soft tissue resulting from stiffened calcified native leaflets and a calcified annulus (135). The new generation of TAVR devices are designed to reduce some of these complications. Edwards Sapien family of valves are balloon expandable TAVs comprised of a cobalt-chromium frame; an inner and an outer sealing skirts made

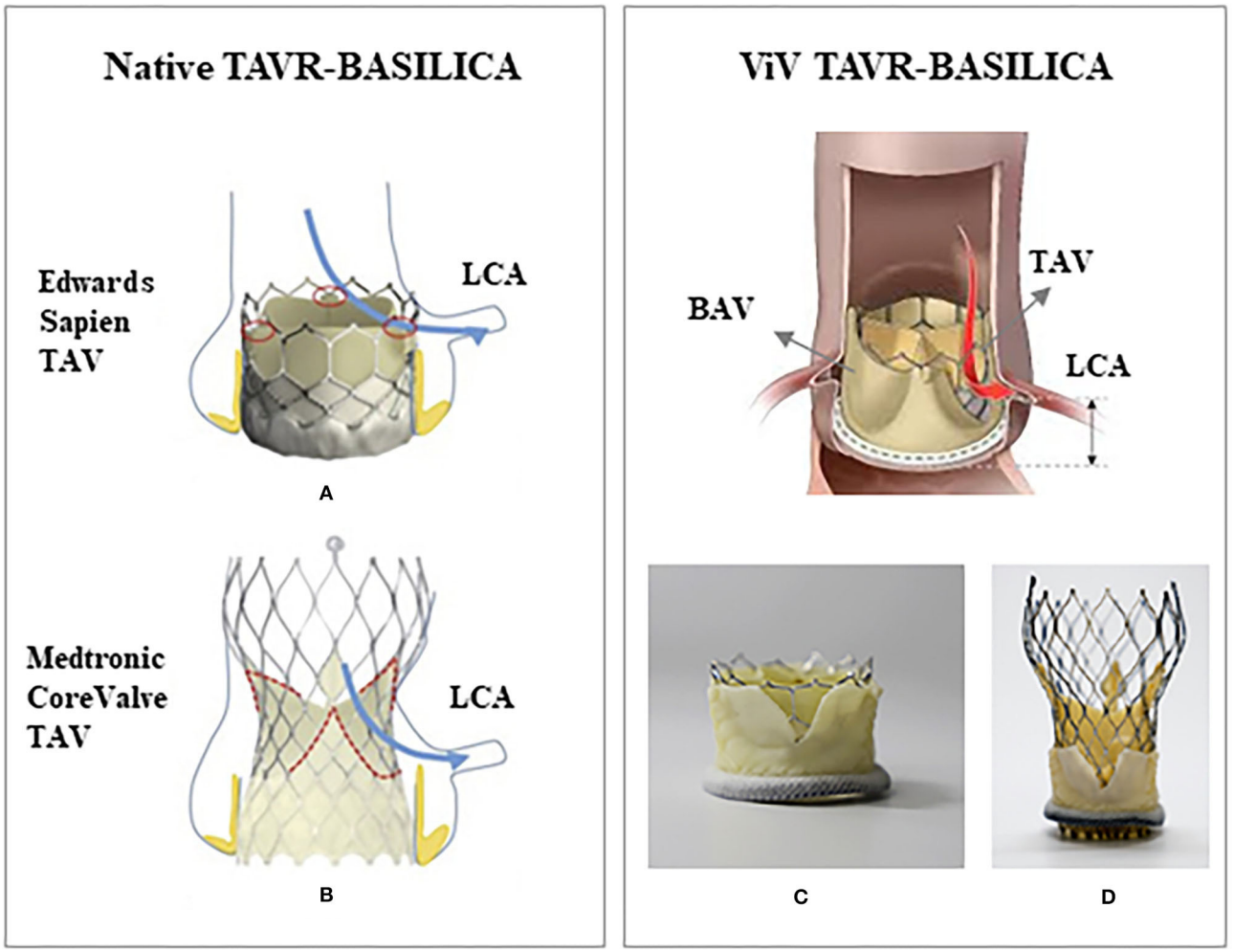

FIGURE 4 | Schematic of a native TAVR-BASILICA and a valve-in-valve TAVR-BASILICA: **(A)** a Edwards Sapien 3 transcatheter aortic valve (TAV) and **(B)** a Medtronic CoreValve Evolut R TAV replaced in a native aortic valve. **(C)** An Edwards Sapien 3 TAV and **(D)** a Medtronic CoreValve Evolut R TAV replaced in a bioprosthetic aortic valve (BAV). Red and blue arrows show the location of the lacerated leaflet (native or bioprosthetic) relative to the left coronary artery (LCA). **(A,B)** are from Krishnaswamy et al. **(C,D)** are from Khodaee et al. with permission.

from polyethylene terephthalate (PET) fabric to reduce PVL; and bovine pericardial leaflet tissue treated with anticalcification treatment, ThermaFix, to reduce mineralization. In contrast, the Medtronic CoreValve family are self-expandable, owing to nitinol stent material, and are comprised of porcine pericardial leaflet tissue with an antimineralization treatment. Numerous studies have investigated performance of Medtronic CoreValve and Edwards Sapien valves with respect to postprocedural PVL. Some reported that moderate to severe post-procedural PVL is more common with Medtronic CoreValve (136–138). However, a recent longitudinal study showed that the severity and frequency of PVL at pre-discharge was significantly higher in Medtronic CoreValve (56.7% Medtronic CoreValve vs. 43.2% Edwrads Sapien, $p = 0.06$), but after 1 year, there was no major differences in frequency and severity of PVL between the two groups, possibly due to coaptation of self-expandable nitinol stent with aortic annulus (139).

Conduction abnormalities can be caused by tissue damage during valve deployment. In general, balloon-expandable valves have lower rates of pacemaker requirements compared to self-expandable TAVs. Studies show that the risk of conduction abnormalities and the need for permanent pacemaker implantation is higher after Medtronic CoreValve implantation compared to Edwards Sapien (140–143), possibly due to the valve design and its self-expansion mechanism; Medtronic CoreValves have a higher height and are implanted deeper into the LVOT. The self-expandable nitinol stent may apply pressure on and below the annulus that could result in atrioventricular node and left bundle branches damage (143, 144).

CORONARY OBSTRUCTION

Surgical bioprosthetic valves are likely to degenerate within 10–20 years (145). Since reoperation is a high-risk procedure for

elderly patients and increases their mortality risk, in recent years, non-invasive implantation of a TAV inside the degenerative bioprosthetic valve has become an alternative intervention for these patients (145–147). However, it may come with the risk of coronary obstruction. Coronary obstruction is a rare consequence of TAVR that occurs during the procedure in <1% of patients, but it is life-threatening (128, 148, 149) as it restricts blood flow circulation in coronary arteries. Coronary obstruction can occur following a TAV implantation in native aortic valve or following a ViV procedure which includes TAV implantation inside another TAV or TAV implantation inside a surgical bioprosthetic valve. Coronary obstruction is more common during ViV procedure (about four times greater) than during TAVR in a native aortic valve (145, 146, 149), and more frequently occurs with use of balloon expandable valves (0.81% balloon expandable vs. 0.34% self-expandable) (149). This is possibly due to the differences in design and deployment mechanism of the transcatheter valves (148, 149). Coronary obstruction following a surgical bioprosthetic ViV procedure occurs more frequently in patients who had stentless or stented valves with bioprosthetic leaflets mounted externally (146). Additionally, it is proposed that coronary obstruction in surgical bioprosthetic ViV procedures is more related to the model and positioning of the surgical bioprosthetic valve, and is independent of the type of TAV, particularly if a surgical valve is implanted in a non-coaxial tilted position, decreasing the distance between leaflets and coronary ostia (148). Other surgical bioprosthetic valve risk factors were supra-annular implantation, high leaflet profile, valve design, stentless valves, or bulky bioprosthetic leaflets (148).

Clinical studies showed that anatomical factors such as low-laying coronary ostium and narrow sinus of Valsava (SOV), narrow sinotubular junction, and low sinus height are associated with coronary occlusion (148, 149), while the left coronary artery (LCA) more commonly becomes obstructed (88.6%) (149). In this study, the average height of LCA ostia in patients with coronary obstruction was 11 mm in men, and 10 mm in women. Most patients with SOV <30 mm and LCA ostium height <12 mm had coronary obstruction (146). Initially, female sex was identified as a risk factor for coronary obstruction (148, 149), but when aortic root dimensions were adjusted to body surface area, female anatomy was no longer an independent factor for coronary obstruction (148, 150).

Coronary obstruction can be caused by calcium deposits, a native leaflet blocking the coronary ostia, a TAV that is positioned too high within the annulus, or through thrombosis (128). In native TAVR procedures, coronary obstruction was linked to presence of bulky calcified lesions on the aortic leaflet blocking the coronary ostium (97.7%); however, the degree of calcification was not a predictor of coronary obstruction (149). Even though the location of the calcification is an important factor in coronary obstruction (148), to-date no study has been done to evaluate coronary obstruction with respect to anatomical features of coronary ostium and the location of the calcium nodules.

Coronary obstruction might be prevented by a novel intervention technique called bioprosthetic or native aortic scallop intentional laceration (BASILICA) (151).

BIOPROSTHETIC OR NATIVE AORTIC SCALLOP INTENTIONAL LACERATION OF CORONARY ARTERY

The first BASILICA human procedure was performed in 2011 during a surgical bioprosthetic ViV procedure in two patients using Edwards Sapien and Medtronic CoreValve to prevent coronary obstruction (147). This technique has been originated from the LAMPOON (Intentional Laceration of the Anterior Mitral leaflet to Prevent left ventricular Outflow Obstruction during transcatheter mitral valve implantation) technique (151). In this procedure, a guiding catheter carrying an electrified wire is directed toward aortic valve through the femoral artery and is positioned at the base of the leaflet; the electrified wire lacerates the leaflet from base to its free edge (152) and creates a split leaflet that would allow blood flow through the coronary arteries. Since the first BASILICA procedure in 2011, some clinical and computational studies have been performed to show the feasibility of BASILICA procedure and to evaluate its overall outcomes and outcomes relative to thrombosis and post-operation coronary obstruction (151–158); however implications of this procedure on outcomes remain unclear (**Figure 4**).

Leaflet thrombosis remains a concern for TAVR after the BASILICA procedure, despite theoretically creating more washout in the target aortic sinus and neosinus. A recent experimental study showed that leaflet laceration can mitigate the risk of thrombosis, while improving washout, with increases in velocity in the sinus and the neosinus by 50% for a Medtronic Evolve ViV, and more than 60% in Edwards Sapien 3 ViV (158). Similarly, a computational study showed that the average blood residence time (BRT) on the leaflets of BASILICA computational model was about 10% less than that in the ViV computational model without leaflet laceration. It has been hypothesized that thrombus is more likely to form in regions with low flow, which can better support fibrin formation due to low advective transport (or increased BRT) (157, 159, 160). Therefore, the BASILICA procedure appears to reduce the risk of leaflet thrombosis in the lacerated leaflets (157). Additionally, a computational study showed that the hemodynamic outcome of a two-leaflet-lacerated BASILICA model is improved when compared with a one-lacerated BASILICA model and the model without laceration, but no significant difference was observed for additional leaflet laceration (three-leaflet-lacerated model) (156). Overall, the BASILICA technique is still relatively new and require additional studies to better understand the benefits and when the procedure may be most effective.

DISCUSSION

As the general population has become older, the prevalence of calcific AS has increased in the recent decades; this has led to extensive research to reveal the complex underlying mechanisms of the valvular calcification, which involves mechanobiology, molecular signals, tissue remodeling, and inflammation, and yet our understanding of this complex process is limited.

Since pharmacotherapy has been ineffective in preventing progression of the calcification, treatment of calcific AS has become narrowed down to surgical and minimally-invasive interventions to repair or replace the native valve; this has led to design and development of artificial valves such as MHVs, BHVs, and TAVs that can mimic the function of the native valve. An immense amount of research has been performed to evaluate the performance of these artificial valves, and to develop better designs that can improve their flaws. Yet, there are undesirable post-interventional outcomes that are related to shortcomings of each valve design.

TAVR has gained favor as procedures and designs have undergone many improvements in recent decades. Despite this, there are still unresolved complications. New procedures aimed at overcoming challenges, like the BASILICA procedure continue to be investigated. Despite precise measurements on a patient's aortic valve anatomy and calcification, calcified lesions continue to complicate TAVR. Other tools like computational modeling have helped surgeons with pre-procedural planning, and with understanding the underlying biomechanics of post-procedural complications. However, these many of these tools continue to be validated. Overall, more studies are required to evaluate the relationships between new procedures and valves with hemodynamics, patient-specific anatomical characteristics, and deployment. This would help surgeons to select patients with suitable characteristics for specific procedures or valves that could improve outcomes.

AUTHOR CONTRIBUTIONS

BZ reviewed the literature and made figures. BZ and DB prepared the manuscript. All authors contributed to the article and approved the submitted version.

REFERENCES

1. Dweck MR, Boon NA, Newby DE. Calcific aortic stenosis: a disease of the valve and the myocardium. *J Am Coll Cardiol.* (2012) 60:1854–63. doi: 10.1016/j.jacc.2012.02.093
2. Lindman BR, Clavel M-A, Mathieu P, Iung B, Lancellotti P, Otto CM, et al. Calcific aortic stenosis. *Nat Rev Dis Primers.* (2016) 2:1–28. doi: 10.1038/nrdp.2016.6
3. Lindman BR, Bonow RO, Otto CM. Current management of calcific aortic stenosis. *Circ Res.* (2013) 113:223–37. doi: 10.1161/CIRCRESAHA.111.300084
4. Otto CM. Calcific aortic stenosis-time to look more closely at the valve. *N Engl J Med.* (2008) 359:1395–8. doi: 10.1056/NEJMe0807001
5. Joseph J, Naqvi SY, Giri J, Goldberg S. Aortic stenosis: pathophysiology, diagnosis, and therapy. *Am J Med.* (2017) 130:253–63. doi: 10.1016/j.amjmed.2016.10.005
6. Eveborn GW, Schirmer H, Heggelund G, Lunde P, Rasmussen K. The evolving epidemiology of valvular aortic stenosis. The Tromsø study. *Heart.* (2013) 99:396–400. doi: 10.1136/heartjnl-2012-302265
7. Sacks MS, Smith DB, Hiester ED. The aortic valve microstructure: effects of transvalvular pressure. *J Biomed Mater Res.* (1998) 41:131–41. doi: 10.1002/(SICI)1097-4636(199807)41:1<131::AID-JBM16>3.0.CO;2-Q
8. Gould ST, Srigunapalan S, Simmons CA, Anseth KS. Hemodynamic and cellular response feedback in calcific aortic valve disease. *Circ Res.* (2013) 113:186–97. doi: 10.1161/CIRCRESAHA.112.300154
9. Stella JA, Sacks MS. On the biaxial mechanical properties of the layers of the aortic valve leaflet. *J Biomech Eng.* (2007) 129:757–66. doi: 10.1115/1.2768111
10. Rutkovskiy A, Malashicheva A, Sullivan G, Bogdanova M, Kostareva A, Stensløkken KO, et al. Valve interstitial cells: the key to understanding the pathophysiology of heart valve calcification. *J Am Heart Assoc.* (2017) 6:e006339. doi: 10.1161/JAHA.117.006339
11. Yip CYY, Simmons CA. The aortic valve microenvironment and its role in calcific aortic valve disease. *Cardiovasc Pathol.* (2011) 20:177–82. doi: 10.1016/j.carpath.2010.12.001
12. Rajamannan NM, Bonow RO, Rahimtoola SH. Calcific aortic stenosis: an update. *Nat Clin Pract Cardiovasc Med.* (2007) 4:254–62. doi: 10.1038/ncpcardio0827
13. Rajamannan NM. Calcific aortic stenosis: lessons learned from experimental and clinical studies. *Arterioscler Thromb Vasc Biol.* (2009) 29:162–8. doi: 10.1161/ATVBAHA.107.156752
14. Rajamannan NM, Evans FJ, Aikawa E, Grande-Allen KJ, Demer LL, Heistad DD, et al. Calcific aortic valve disease: not simply a degenerative process a review and agenda for research from the National Heart and Lung and Blood Institute Aortic Stenosis Working Group. *Circulation.* (2011) 124:1783. doi: 10.1161/CIRCULATIONAHA.110.006767
15. Rajamannan NM, Otto CM. Targeted therapy to prevent progression of calcific aortic stenosis. *Circulation.* (2004) 110:1180–2. doi: 10.1161/01.CIR.0000140722.85490.EA
16. Lerman DA, Prasad S, Alotti N. Calcific aortic valve disease: molecular mechanisms and therapeutic approaches. *Eur Cardiol Rev.* (2015) 10:108. doi: 10.15420/ecr.2015.10.2.108
17. Demer LL, Tintut Y. Vascular calcification: pathobiology of a multifaceted disease. *Circulation.* (2008) 117:2938–48. doi: 10.1161/CIRCULATIONAHA.107.743161
18. Mohler ER, Nichols R, Harvey W, Sheridan M, Waller B, Waller BF. Development and progression of aortic valve stenosis: atherosclerosis risk factors-a causal relationship? A clinical morphologic study. *Clin Cardiol.* (1991) 14:995–9. doi: 10.1002/clc.4960141210
19. Butcher JT, Nerem RM. Valvular endothelial cells and the mechanoregulation of valvular pathology. *Philos Trans R Soc B Biol Sci.* (2007) 362:1445–57. doi: 10.1098/rstb.2007.2127
20. Fernández Esmerats J, Heath J, Jo H. Shear-sensitive genes in aortic valve endothelium. *Antioxid Redox Signal.* (2016) 25:401–14. doi: 10.1089/ars.2015.6554
21. Tarbell JM, Shi Z-D, Dunn J, Jo H. Fluid mechanics, arterial disease, and gene expression. *Annu Rev Fluid Mech.* (2014) 46:591–614. doi: 10.1146/annurev-fluid-010313-141309
22. Katritch V, Cherezov V, Stevens RC. Structure-function of the G protein-coupled receptor superfamily. *Annu Rev Pharmacol Toxicol.* (2013) 53:531–56. doi: 10.1146/annurev-pharmtox-032112-135923
23. Lombardi ML, Jaalouk DE, Shanahan CM, Burke B, Roux KJ, Lammerding J. The interaction between nesprins and sun proteins at the nuclear envelope is critical for force transmission between the nucleus and cytoskeleton. *J Biol Chem.* (2011) 286:26743–53. doi: 10.1074/jbc.M111.233700
24. Aikawa E, Nahrendorf M, Figueiredo J-L, Swirski FK, Shtatland T, Kohler RH, et al. CLINICAL PERSPECTIVE. *Circulation.* (2007) 116:2841–50. doi: 10.1161/CIRCULATIONAHA.107.732867
25. Hjortnaes J, New SE, Aikawa E. Visualizing novel concepts of cardiovascular calcification. *Trends Cardiovasc Med.* (2013) 23:71–9. doi: 10.1016/j.tcm.2012.09.003
26. Nigam V, Srivastava D. Notch1 represses osteogenic pathways in aortic valve cells. *J Mol Cell Cardiol.* (2009) 47:828–34. doi: 10.1016/j.yjmcc.2009.08.008
27. Yutzey KE, Demer LL, Body SC, Huggins GS, Towler DA, Giachelli CM, et al. Calcific aortic valve disease: a consensus summary from the Alliance of Investigators on Calcific Aortic Valve Disease. *Arterioscler Thromb Vasc Biol.* (2014) 34:2387–93. doi: 10.1161/ATVBAHA.114.302523

28. Kawakami R, Nakagami H, Noma T, Ohmori K, Kohno M, Morishita R. RANKL system in vascular and valve calcification with aging. *Inflamm Regen.* (2016) 36:1–6. doi: 10.1186/s41232-016-0016-3
29. Kaden JJ, Bickelhaupt S, Grobholz R, Haase KK, Sarıkoç A, Brueckmann M, et al. Receptor activator of nuclear factor κB ligand and osteoprotegerin regulate aortic valve calcification. *J Mol Cell Cardiol.* (2004) 36:57–66. doi: 10.1016/j.yjmcc.2003.09.015
30. Rajamannan NM, Subramaniam M, Caira F, Stock SR, Spelsberg TC. Atorvastatin inhibits hypercholesterolemia-induced calcification in the aortic valves via the Lrp5 receptor pathway. *Circulation.* (2005) 112:I-229–I-34. doi: 10.1161/01.CIRCULATIONAHA.104.524306
31. O'Brien KD. Pathogenesis of calcific aortic valve disease: a disease process comes of age (and a good deal more). *Arterioscler Thromb Vasc Biol.* (2006) 26:1721–8. doi: 10.1161/01.ATV.0000227513.13697.ac
32. Phimphilai M, Zhao Z, Boules H, Roca H, Franceschi RT. BMP signaling is required for RUNX2-dependent induction of the osteoblast phenotype. *J Bone Miner Res.* (2006) 21:637–46. doi: 10.1359/jbmr.060109
33. Favero G, Paganelli C, Buffoli B, Rodella LF, Rezzani R. Endothelium and its alterations in cardiovascular diseases: life style intervention. *Biomed Res Int.* (2014) 2014:801896. doi: 10.1155/2014/801896
34. Thanassoulis G. Lipoprotein (a) in calcific aortic valve disease: from genomics to novel drug target for aortic stenosis. *J Lipid Res.* (2016) 57:917–24. doi: 10.1194/jlr.R051870
35. Cairns BJ, Coffey S, Travis RC, Prendergast B, Green J, Engert JC, et al. A replicated, genome-wide significant association of aortic stenosis with a genetic variant for lipoprotein (a) meta-analysis of published and novel data. *Circulation.* (2017) 135:1181–3. doi: 10.1161/CIRCULATIONAHA.116.026103
36. Hoekstra M, Chen HY, Rong J, Dufresne L, Yao J, Guo X, et al. Genome-wide association study highlights APOH as a novel locus for lipoprotein (a) levels-brief report. *Arterioscler Thromb Vasc Biol.* (2021) 41:458–64. doi: 10.1161/ATVBAHA.120.314965
37. Passos LS, Lupieri A, Becker-Greene D, Aikawa E. Innate and adaptive immunity in cardiovascular calcification. *Atherosclerosis.* (2020) 306:59–67. doi: 10.1016/j.atherosclerosis.2020.02.016
38. Akin I, Nienaber CA. Is there evidence for statins in the treatment of aortic valve stenosis? *World J Cardiol.* (2017) 9:667. doi: 10.4330/wjc.v9.i8.667
39. Cowell SJ, Newby DE, Prescott RJ, Bloomfield P, Reid J, Northridge DB, et al. A randomized trial of intensive lipid-lowering therapy in calcific aortic stenosis. *N Engl J Med.* (2005) 352:2389–97. doi: 10.1056/NEJMoa043876
40. Chan KL, Teo K, Dumesnil JG, Ni A, Tam J. Effect of Lipid lowering with rosuvastatin on progression of aortic stenosis: results of the aortic stenosis progression observation: measuring effects of rosuvastatin (ASTRONOMER) trial. *Circulation.* (2010) 121:306–14. doi: 10.1161/CIRCULATIONAHA.109.900027
41. Rossebø AB, Pedersen TR, Boman K, Brudi P, Chambers JB, Egstrup K, et al. Intensive lipid lowering with simvastatin and ezetimibe in aortic stenosis. *N Engl J Med.* (2008) 359:1343–56. doi: 10.1056/NEJMoa0804602
42. Freeman RV, Otto CM. Spectrum of calcific aortic valve disease: pathogenesis, disease progression, and treatment strategies. *Circulation.* (2005) 111:3316–26. doi: 10.1161/CIRCULATIONAHA.104.486738
43. Santibáñez JF, Guerrero J, Quintanilla M, Fabra A, Martínez J. Transforming growth factor-β1 modulates matrix metalloproteinase-9 production through the Ras/MAPK signaling pathway in transformed keratinocytes. *Biochem Biophys Res Commun.* (2002) 296:267–73. doi: 10.1016/S0006-291X(02)00864-1
44. Helderman F, Segers D, de Crom R, Hierck BP, Poelmann RE, Evans PC, et al. Effect of shear stress on vascular inflammation and plaque development. *Curr Opin Lipidol.* (2007) 18:527–33. doi: 10.1097/MOL.0b013e3282ef7716
45. Kaden JJ, Dempfle C-E, Grobholz R, Fischer CS, Vocke DC, Kiliç R, et al. Inflammatory regulation of extracellular matrix remodeling in calcific aortic valve stenosis. *Cardiovasc Pathol.* (2005) 14:80–7. doi: 10.1016/j.carpath.2005.01.002
46. Mathieu P, Bouchareb R, Boulanger M-C. Innate and adaptive immunity in calcific aortic valve disease. *J Immunol Res.* (2015) 2015:851945. doi: 10.1155/2015/851945
47. New SE, Goettsch C, Aikawa M, Marchini JF, Shibasaki M, Yabusaki K, et al. Macrophage-derived matrix vesicles: an alternative novel mechanism for microcalcification in atherosclerotic plaques. *Circ Res.* (2013) 113:72–7. doi: 10.1161/CIRCRESAHA.113.301036
48. Kapustin AN, Chatrou ML, Drozdov I, Zheng Y, Davidson SM, Soong D, et al. Vascular smooth muscle cell calcification is mediated by regulated exosome secretion. *Circ Res.* (2015) 116:1312–23. doi: 10.1161/CIRCRESAHA.116.305012
49. Myasoedova VA, Ravani AL, Frigerio B, Valerio V, Moschetta D, Songia P, et al. Novel pharmacological targets for calcific aortic valve disease: prevention and treatments. *Pharmacol Res.* (2018) 136:74–82. doi: 10.1016/j.phrs.2018.08.020
50. Graham MJ, Viney N, Crooke RM, Tsimikas S. Antisense inhibition of apolipoprotein (a) to lower plasma lipoprotein (a) levels in humans. *J Lipid Res.* (2016) 57:340–51. doi: 10.1194/jlr.R052258
51. Tsimikas S, Viney NJ, Hughes SG, Singleton W, Graham MJ, Baker BF, et al. Antisense therapy targeting apolipoprotein (a): a randomised, double-blind, placebo-controlled phase 1 study. *Lancet.* (2015) 386:1472–83. doi: 10.1016/S0140-6736(15)61252-1
52. Stein EA, Raal F. Future directions to establish lipoprotein (a) as a treatment for atherosclerotic cardiovascular disease. *Cardiovasc Drugs Therapy.* (2016) 30:101–8. doi: 10.1007/s10557-016-6654-5
53. Garg A, Sharma A, Krishnamoorthy P, Garg J, Virmani D, Sharma T, et al. Role of niacin in current clinical practice: a systematic review. *Am J Med.* (2017) 130:173–87. doi: 10.1016/j.amjmed.2016.07.038
54. Albers JJ, Slee A, O'Brien KD, Robinson JG, Kashyap ML, Kwiterovich PO, et al. Relationship of apolipoproteins A-1 and B, and lipoprotein (a) to cardiovascular outcomes: the AIM-HIGH trial (Atherothrombosis Intervention in Metabolic Syndrome with Low HDL/High Triglyceride and Impact on Global Health Outcomes). *J Am Coll Cardiol.* (2013) 62:1575–9. doi: 10.1016/j.jacc.2013.06.051
55. Raal FJ, Giugliano RP, Sabatine MS, Koren MJ, Blom D, Seidah NG, et al. PCSK9 inhibition-mediated reduction in Lp (a) with evolocumab: an analysis of 10 clinical trials and the LDL receptor's role [S]. *J Lipid Res.* (2016) 57:1086–96. doi: 10.1194/jlr.P065334
56. Sabatine MS, Giugliano RP, Keech AC, Honarpour N, Wiviott SD, Murphy SA, et al. Evolocumab and clinical outcomes in patients with cardiovascular disease. *N Engl J Med.* (2017) 376:1713–22. doi: 10.1056/NEJMoa1615664
57. Seya K, Furukawa K-I, Chiyoya M, Yu Z, Kikuchi H, Daitoku K, et al. 1-Methyl-2-undecyl-4 (1H)-quinolone, a derivative of quinolone alkaloid evocarpine, attenuates high phosphate-induced calcification of human aortic valve interstitial cells by inhibiting phosphate cotransporter PiT-1. *J Pharmacol Sci.* (2016) 131:51–7. doi: 10.1016/j.jphs.2016.04.013
58. Miller JD, Weiss RM, Serrano KM, Brooks RM, Berry CJ, Zimmerman K, et al. Lowering plasma cholesterol levels halts progression of aortic valve disease in mice. *Circulation.* (2009) 119:2693–701. doi: 10.1161/CIRCULATIONAHA.108.834614
59. Bouchareb R, Côté N, Le Quang K, El Husseini D, Asselin J, Hadji F, et al. Carbonic anhydrase XII in valve interstitial cells promotes the regression of calcific aortic valve stenosis. *J Mol Cell Cardiol.* (2015) 82:104–15. doi: 10.1016/j.yjmcc.2015.03.002
60. Carabello BA. How does the heart respond to aortic stenosis: let me count the ways. *Am Heart Assoc.* (2013) 6:858–60. doi: 10.1161/CIRCIMAGING.113.001242
61. Cowell SJ, Newby DE, Boon NA, Elder AT. Calcific aortic stenosis: same old story? *Age Ageing.* (2004) 33:538–44. doi: 10.1093/ageing/afh175
62. Saikrishnan N, Kumar G, Sawaya FJ, Lerakis S, Yoganathan AP. Accurate assessment of aortic stenosis: a review of diagnostic modalities and hemodynamics. *Circulation.* (2014) 129:244–53. doi: 10.1161/CIRCULATIONAHA.113.002310
63. Kwon S, Gopal A. Hemodynamic classifications of aortic stenosis and relevance to prognosis. *Aortic Stenosis Curr Perspect.* (2019) 1–18. doi: 10.5772/intechopen.86707
64. Baumgartner H, Hung J, Bermejo J, Chambers JB, Evangelista A, Griffin BP, et al. Echocardiographic assessment of valve stenosis: EAE/ASE recommendations for clinical practice. *J Am Soc Echocardiogr.* (2009) 22:1–23. doi: 10.1016/j.echo.2008.11.029
65. Garcia J, Kadem L, Larose E, Clavel M-A, Pibarot P. Comparison between cardiovascular magnetic resonance and transthoracic Doppler

echocardiography for the estimation of effective orifice area in aortic stenosis. *J Cardiovasc Magn Resonance.* (2011) 13:1–9. doi: 10.1186/1532-429X-13-25
66. Agatston AS, Janowitz WR, Hildner FJ, Zusmer NR, Viamonte M, Detrano R. Quantification of coronary artery calcium using ultrafast computed tomography. *J Am Coll Cardiol.* (1990) 15:827–32. doi: 10.1016/0735-1097(90)90282-T
67. Koos R, Mahnken AH, Sinha AM, Wildberger JE, Hoffmann R, Kühl HP. Aortic valve calcification as a marker for aortic stenosis severity: assessment on 16-MDCT. *Am J Roentgenol.* (2004) 183:1813–8. doi: 10.2214/ajr.183.6.01831813
68. Pawade T, Clavel M-A, Tribouilloy C, Dreyfus J, Mathieu T, Tastet L, et al. Computed tomography aortic valve calcium scoring in patients with aortic stenosis. *Circulation.* (2018) 11:e007146. doi: 10.1161/CIRCIMAGING.117.007146
69. Clavel M-A, Messika-Zeitoun D, Pibarot P, Aggarwal SR, Malouf J, Araoz PA, et al. The complex nature of discordant severe calcified aortic valve disease grading: new insights from combined Doppler echocardiographic and computed tomographic study. *J Am Coll Cardiol.* (2013) 62:2329–38. doi: 10.1016/j.jacc.2013.08.1621
70. Clavel M-A, Pibarot P, Messika-Zeitoun D, Capoulade R, Malouf J, Aggarwal SR, et al. Impact of aortic valve calcification, as measured by MDCT, on survival in patients with aortic stenosis: results of an international registry study. *J Am Coll Cardiol.* (2014) 64:1202–13. doi: 10.1016/j.jacc.2014.05.066
71. Voisine M, Hervault M, Shen M, Boilard AJ, Filion B, Rosa M, et al. Age, sex, and valve phenotype differences in fibro-calcific remodeling of calcified aortic valve. *J Am Heart Assoc.* (2020) 9:e015610. doi: 10.1161/JAHA.119.015610
72. Summerhill VI, Moschetta D, Orekhov AN, Poggio P, Myasoedova VA. Sex-specific features of calcific aortic valve disease. *Int J Mol Sci.* (2020) 21:5620. doi: 10.3390/ijms21165620
73. Fleury M-A, Clavel M-A. Sex and race differences in the pathophysiology, diagnosis, treatment, and outcomes of valvular heart diseases. *Can J Cardiol.* (2021) 37:980–91. doi: 10.1016/j.cjca.2021.02.003
74. Osako MK, Nakagami H, Koibuchi N, Shimizu H, Nakagami F, Koriyama H, et al. Estrogen inhibits vascular calcification via vascular RANKL system: common mechanism of osteoporosis and vascular calcification. *Circ Res.* (2010) 107:466–75. doi: 10.1161/CIRCRESAHA.110.216846
75. Harper E, Forde H, Davenport C, Rochfort KD, Smith D, Cummins PM. Vascular calcification in type-2 diabetes and cardiovascular disease: Integrative roles for OPG, RANKL and TRAIL. *Vascul Pharmacol.* (2016) 82:30–40. doi: 10.1016/j.vph.2016.02.003
76. Zhang B, Miller VM, Miller JD. Influences of sex and estrogen in arterial and valvular calcification. *Front Endocrinol.* (2019) 10:622. doi: 10.3389/fendo.2019.00622
77. Gelfand ML, Cohen T, Ackert JJ, Ambos M, Mayadag M. Gastrointestinal bleeding in aortic stenosis. *Am J Gastroenterol.* (1979) 71:30–8.
78. Warkentin TE, Moore JC, Morgan DG. Gastrointestinal angiodysplasia and aortic stenosis. *N Engl J Med.* (2002) 347:858–9. doi: 10.1056/NEJM200209123471122
79. Vincentelli A, Susen S, Le Tourneau T, Six I, Fabre O, Juthier F, et al. Acquired von Willebrand syndrome in aortic stenosis. *N Engl J Med.* (2003) 349:343–9. doi: 10.1056/NEJMoa022831
80. Nkomo VT, Gardin JM, Skelton TN, Gottdiener JS, Scott CG, Enriquez-Sarano M. Burden of valvular heart diseases: a population-based study. *Lancet.* (2006) 368:1005–11. doi: 10.1016/S0140-6736(06)69208-8
81. Yasar SJ, Abdullah O, Fay W, Balla S. Von Willebrand factor revisited. *J Interv Cardiol.* (2018) 31:360–7. doi: 10.1111/joic.12478
82. Susen S, Vincentelli A, Le Tourneau T, Caron C, Zawadzki C, Prat A, et al. Severe aortic and mitral valve regurgitation are associated with von willebrand factor defect. *Am Soc Hematol.* (2005) 106:1790. doi: 10.1182/blood.V106.11.1790.1790
83. Blackshear J, Wysokinska E, Safford R, Thomas C, Shapiro B, Ung S, et al. Shear stress-associated acquired Von Willebrand syndrome in patients with mitral regurgitation. *J Thromb Haemost.* (2014) 12:1966–74. doi: 10.1111/jth.12734
84. Van Belle E, Rauch A, Vincent F, Robin E, Kibler M, Labreuche J, et al. Von Willebrand factor multimers during transcatheter aortic-valve replacement. *N Engl J Med.* (2016) 375:335–44. doi: 10.1056/NEJMoa1505643
85. Van Belle E, Vincent F, Rauch A, Casari C, Jeanpierre E, Loobuyck V, et al. von Willebrand factor and management of heart valve disease: JACC review topic of the week. *J Am Coll Cardiol.* (2019) 73:1078–88. doi: 10.1016/j.jacc.2018.12.045
86. Bortot M, Bark K, Neeves K, Clendenen N, Bark DJ, DiPaola J. Impaired primary hemostasis in patients on cardiopulmonary bypass. *Arterioscler Thromb Vasc Biol.* (2019) 39:A130. doi: 10.1161/atvb.39.suppl_1.130
87. Cohn LH, Tchantchaleishvili V, Rajab TK. Evolution of the concept and practice of mitral valve repair. *Ann Cardiothorac Surg.* (2015) 4:315–21. doi: 10.3978/j.issn.2225-319X.2015.04.09
88. Aicher D, Fries R, Rodionycheva S, Schmidt K, Langer F, Schäfers H-J. Aortic valve repair leads to a low incidence of valve-related complications. *Eur J Cardio Thorac Surg.* (2010) 37:127–32. doi: 10.1016/j.ejcts.2009.06.021
89. Cribier A, Saoudi N, Berland J, Savin T, Rocha P, Letac B. Percutaneous transluminal valvuloplasty of acquired aortic stenosis in elderly patients: an alternative to valve replacement? *Lancet.* (1986) 327:63–7. doi: 10.1016/S0140-6736(86)90716-6
90. Safian RD, Mandell VS, Thurer RE, Hutchins GM, Schnitt SJ, Grossman W, et al. Postmortem and intraoperative balloon valvuloplasty of calcific aortic stenosis in elderly patients: mechanisms of successful dilation. *J Am Coll Cardiol.* (1987) 9:655–60. doi: 10.1016/S0735-1097(87)80061-X
91. Arzt W, Wertaschnigg D, Veit I, Klement F, Gitter R, Tulzer G. Intrauterine aortic valvuloplasty in fetuses with critical aortic stenosis: experience and results of 24 procedures. *Ultrasound Obstetr Gynecol.* (2011) 37:689–95. doi: 10.1002/uog.8927
92. Marshall AC, Tworetzky W, Bergersen L, McElhinney DB, Benson CB, Jennings RW, et al. Aortic valvuloplasty in the fetus: technical characteristics of successful balloon dilation. *J Pediatr.* (2005) 147:535–9. doi: 10.1016/j.jpeds.2005.04.055
93. Tworetzky W, Wilkins-Haug L, Jennings RW, van der Velde ME, Marshall AC, Marx GR, et al. Balloon dilation of severe aortic stenosis in the fetus: potential for prevention of hypoplastic left heart syndrome: candidate selection, technique, and results of successful intervention. *Circulation.* (2004) 110:2125–31. doi: 10.1161/01.CIR.0000144357.29279.54
94. Friedman KG, Margossian R, Graham DA, Harrild DM, Emani SM, Wilkins-Haug LE, et al. Postnatal left ventricular diastolic function after fetal aortic valvuloplasty. *Am J Cardiol.* (2011) 108:556–60. doi: 10.1016/j.amjcard.2011.03.085
95. Kogoj P, Devjak R, Bunc M. Balloon aortic valvuloplasty (BAV) as a bridge to aortic valve replacement in cancer patients who require urgent non-cardiac surgery. *Radiol Oncol.* (2014) 48:62. doi: 10.2478/raon-2013-0078
96. Head SJ, Çelik M, Kappetein AP. Mechanical versus bioprosthetic aortic valve replacement. *Eur Heart J.* (2017) 38:2183–91. doi: 10.1093/eurheartj/ehx141
97. Pibarot P, Salaun E, Dahou A, Avenatti E, Guzzetti E, Annabi M-S, et al. Echocardiographic results of transcatheter versus surgical aortic valve replacement in low-risk patients: the PARTNER 3 trial. *Circulation.* (2020) 141:1527–37. doi: 10.1161/CIRCULATIONAHA.119.044574
98. Braghiroli J, Kapoor K, Thielhelm TP, Ferreira T, Cohen MG. Transcatheter aortic valve replacement in low risk patients: a review of PARTNER 3 and Evolut low risk trials. *Cardiovasc Diagn Ther.* (2020) 10:59. doi: 10.21037/cdt.2019.09.12
99. Cribier A, Eltchaninoff H, Bash A, Borenstein N, Tron C, Bauer F, et al. Percutaneous transcatheter implantation of an aortic valve prosthesis for calcific aortic stenosis: first human case description. *Circulation.* (2002) 106:3006–8. doi: 10.1161/01.CIR.0000047200.36165.B8
100. Kheradvar A, Groves EM, Goergen CJ, Alavi SH, Tranquillo R, Simmons CA, et al. Emerging trends in heart valve engineering: Part II. Novel and standard technologies for aortic valve replacement. *Ann Biomed Eng.* (2015) 43:844–57. doi: 10.1007/s10439-014-1191-5
101. Lancellotti P, Vannan MA. Timing of intervention in aortic stenosis. *N Engl J Med.* (2020) 382:191–3. doi: 10.1056/NEJMe1914382
102. Banovic M, Iung B, Putnik S, Nikolic S, Penicka M, Deja M, et al. Addressing the treatment dilemma in asymptomatic aortic stenosis: the AVATAR trial. *JACC Cardiovasc Imaging.* (2019) 12:1896–7. doi: 10.1016/j.jcmg.2019.07.012
103. James Everett R, Clavel M-A, Pibarot P, Dweck MR. Timing of intervention in aortic stenosis a review of current and future strategies. *Heart.* (2018) 104:2067–76. doi: 10.1136/heartjnl-2017-312304

104. Lindman BR, Dweck MR, Lancellotti P, Généreux P, Piérard LA, O'Gara PT, et al. Management of asymptomatic severe aortic stenosis: evolving concepts in timing of valve replacement. *Cardiovasc Imaging.* (2020) 13:481–93. doi: 10.1016/j.jcmg.2019.01.036
105. Smith CR, Leon MB, Mack MJ, Miller DC, Moses JW, Svensson LG, et al. Transcatheter versus surgical aortic-valve replacement in high-risk patients. *N Engl J Med.* (2011) 364:2187–98. doi: 10.1056/NEJMoa1103510
106. Gleason TG, Reardon MJ, Popma JJ, Deeb GM, Yakubov SJ, Lee JS, et al. 5-Year outcomes of self-expanding transcatheter versus surgical aortic valve replacement in high-risk patients. *J Am Coll Cardiol.* (2018) 72:2687–96. doi: 10.1016/j.jacc.2018.08.2146
107. Mack MJ, Leon MB, Smith CR, Miller DC, Moses JW, Tuzcu EM, et al. 5-year outcomes of transcatheter aortic valve replacement or surgical aortic valve replacement for high surgical risk patients with aortic stenosis (PARTNER 1): a randomised controlled trial. *Lancet.* (2015) 385:2477–84. doi: 10.1016/S0140-6736(15)60308-7
108. Kolte D, Vlahakes GJ, Palacios IF, Sakhuja R, Passeri JJ, Inglessis I, et al. Transcatheter versus surgical aortic valve replacement in low-risk patients. *J Am Coll Cardiol.* (2019) 74:1532–40. doi: 10.1016/j.jacc.2019.06.076
109. Grines CL, Klein AJ, Bauser-Heaton H, Alkhouli M, Katukuri N, Aggarwal V, et al. Racial and ethnic disparities in coronary, vascular, structural, and congenital heart disease. *Catheter Cardiovasc Interv.* (2021) 98:277–94. doi: 10.1002/ccd.29745
110. Alkhouli M, Holmes DR, Carroll JD, Li Z, Inohara T, Kosinski AS, et al. Racial disparities in the utilization and outcomes of TAVR: TVT registry report. *JACC Cardiovasc Interv.* (2019) 12:936–48. doi: 10.1016/j.jcin.2019.03.007
111. Sleder A, Tackett S, Cerasale M, Mittal C, Isseh I, Radjef R, et al. Socioeconomic and racial disparities: a case-control study of patients receiving transcatheter aortic valve replacement for severe aortic stenosis. *J Racial Ethnic Health Disparities.* (2017) 4:1189–94. doi: 10.1007/s40615-016-0325-x
112. Yeung M, Kerrigan J, Sodhi S, Huang P-H, Novak E, Maniar H, et al. Racial differences in rates of aortic valve replacement in patients with severe aortic stenosis. *Am J Cardiol.* (2013) 112:991–5. doi: 10.1016/j.amjcard.2013.05.030
113. Henn MC, Moon MR. Mechanical prosthetic valves. In: Raja S, editor. *Cardiac Surgery*. Cham: Springer (2020). p. 291–8.
114. Alemu Y, Bluestein D. Flow-induced platelet activation and damage accumulation in a mechanical heart valve: numerical studies. *Artif Organs.* (2007) 31:677–88. doi: 10.1111/j.1525-1594.2007.00446.x
115. Wootton DM, Ku DN. Fluid mechanics of vascular systems, diseases, and thrombosis. *Annu Rev Biomed Eng.* (1999) 1:299–329. doi: 10.1146/annurev.bioeng.1.1.299
116. Yun BM, Wu J, Simon HA, Arjunon S, Sotiropoulos F, Aidun CK, et al. A numerical investigation of blood damage in the hinge area of aortic bileaflet mechanical heart valves during the leakage phase. *Ann Biomed Eng.* (2012) 40:1468–85. doi: 10.1007/s10439-011-0502-3
117. Ge L, Dasi LP, Sotiropoulos F, Yoganathan AP. Characterization of hemodynamic forces induced by mechanical heart valves: Reynolds vs. viscous stresses. *Ann Biomed Eng.* (2008) 36:276–97. doi: 10.1007/s10439-007-9411-x
118. Dangas GD, Weitz JI, Giustino G, Makkar R, Mehran R. Prosthetic heart valve thrombosis. *J Am Coll Cardiol.* (2016) 68:2670–89. doi: 10.1016/j.jacc.2016.09.958
119. Kulik A, Rubens FD, Wells PS, Kearon C, Mesana TG, van Berkom J, et al. Early postoperative anticoagulation after mechanical valve replacement: a systematic review. *Ann Thorac Surg.* (2006) 81:770–81. doi: 10.1016/j.athoracsur.2005.07.023
120. Sun T, Tan H, Han D, Fu Q, Jiang L. No platelet can adhere-largely improved blood compatibility on nanostructured superhydrophobic surfaces. *Small.* (2005) 1:959–63. doi: 10.1002/smll.200500095
121. Bark DL, Vahabi H, Bui H, Movafaghi S, Moore B, Kota AK, et al. Hemodynamic performance and thrombogenic properties of a superhydrophobic bileaflet mechanical heart valve. *Ann Biomed Eng.* (2017) 45:452–63. doi: 10.1007/s10439-016-1618-2
122. Leslie DC, Waterhouse A, Berthet JB, Valentin TM, Watters AL, Jain A, et al. A bioinspired omniphobic surface coating on medical devices prevents thrombosis and biofouling. *Nat Biotechnol.* (2014) 32:1134–40. doi: 10.1038/nbt.3020
123. Khorasani M, Mirzadeh H. In vitro blood compatibility of modified PDMS surfaces as superhydrophobic and superhydrophilic materials. *J Appl Polym Sci.* (2004) 91:2042–7. doi: 10.1002/app.13355
124. Johnston DR, Soltesz EG, Vakil N, Rajeswaran J, Roselli EE, Sabik III JF, et al. Long-term durability of bioprosthetic aortic valves: implications from 12,569 implants. *Ann Thorac Surg.* (2015) 99:1239–47. doi: 10.1016/j.athoracsur.2014.10.070
125. Dasi LP, Hatoum H, Kheradvar A, Zareian R, Alavi SH, Sun W, et al. On the mechanics of transcatheter aortic valve replacement. *Ann Biomed Eng.* (2017) 45:310–31. doi: 10.1007/s10439-016-1759-3
126. Alavi SH, Groves EM, Kheradvar A. The effects of transcatheter valve crimping on pericardial leaflets. *Ann Thorac Surg.* (2014) 97:1260–6. doi: 10.1016/j.athoracsur.2013.11.009
127. Del Pino MDCL, Ortiz MR, Ortega MD, Fernández JS, Quero CF, Jiménez ED, et al. Prosthesis-patient mismatch after transcatheter aortic valve replacement: prevalence and medium term prognostic impact. *Int J Cardiovasc Imaging.* (2019) 35:827–36. doi: 10.1007/s10554-018-01519-z
128. Laborde J-C, Brecker SJ, Roy D, Jahangiri M. Complications at the time of transcatheter aortic valve implantation. *Methodist Debakey Cardiovasc J.* (2012) 8:38. doi: 10.14797/mdcj-8-2-38
129. Makkar RR, Jilaihawi H, Chakravarty T, Fontana GP, Kapadia S, Babaliaros V, et al. Determinants and outcomes of acute transcatheter valve-in-valve therapy or embolization: a study of multiple valve implants in the US PARTNER trial (Placement of AoRTic TraNscathetER Valve Trial Edwards SAPIEN Transcatheter Heart Valve). *J Am Coll Cardiol.* (2013) 62:418–30. doi: 10.1016/j.jacc.2013.04.037
130. Fassa A-A, Himbert D, Vahanian A. Mechanisms and management of TAVR-related complications. *Nat Rev Cardiol.* (2013) 10:685. doi: 10.1038/nrcardio.2013.156
131. Barbanti M, Yang T-H, Rodès Cabau J, Tamburino C, Wood DA, Jilaihawi H, et al. Anatomical and procedural features associated with aortic root rupture during balloon-expandable transcatheter aortic valve replacement. *Circulation.* (2013) 128:244–53. doi: 10.1161/CIRCULATIONAHA.113.002947
132. Blanke P, Reinöhl J, Schlensak C, Siepe M, Pache G, Euringer W, et al. Prosthesis oversizing in balloon-expandable transcatheter aortic valve implantation is associated with contained rupture of the aortic root. *Circulation.* (2012) 5:540–8. doi: 10.1161/CIRCINTERVENTIONS.111.967349
133. Willson AB, Webb JG, Freeman M, Wood DA, Gurvitch R, Thompson CR, et al. Computed tomography-based sizing recommendations for transcatheter aortic valve replacement with balloon-expandable valves: comparison with transesophageal echocardiography and rationale for implementation in a prospective trial. *J Cardiovasc Comput Tomogr.* (2012) 6:406–14. doi: 10.1016/j.jcct.2012.10.002
134. Binder RK, Webb JG, Willson AB, Urena M, Hansson NC, Norgaard BL, et al. The impact of integration of a multidetector computed tomography annulus area sizing algorithm on outcomes of transcatheter aortic valve replacement: a prospective, multicenter, controlled trial. *J Am Coll Cardiol.* (2013) 62:431–8. doi: 10.1016/j.jacc.2013.04.036
135. Bernard S, Yucel E. Paravalvular leaks-from diagnosis to management. *Curr Treat Options Cardiovasc Med.* (2019) 21:1–16. doi: 10.1007/s11936-019-0776-6
136. Gilard M, Eltchaninoff H, Iung B, Donzeau-Gouge P, Chevreul K, Fajadet J, et al. Registry of transcatheter aortic-valve implantation in high-risk patients. *N Engl J Med.* (2012) 366:1705–15. doi: 10.1056/NEJMoa1114705
137. Moat NE, Ludman P, de Belder MA, Bridgewater B, Cunningham AD, Young CP, et al. Long-term outcomes after transcatheter aortic valve implantation in high-risk patients with severe aortic stenosis: the UK TAVI (United Kingdom Transcatheter Aortic Valve Implantation) Registry. *J Am Coll Cardiol.* (2011) 58:2130–8. doi: 10.1016/j.jacc.2011.08.050
138. Athappan G, Patvardhan E, Tuzcu EM, Svensson LG, Lemos PA, Fraccaro C, et al. Incidence, predictors, and outcomes of aortic regurgitation after transcatheter aortic valve replacement: meta-analysis and systematic review of literature. *J Am Coll Cardiol.* (2013) 61:1585–95. doi: 10.1016/j.jacc.2013.01.047

139. Gilbert ON, Choi CH, Franzil JL, Caughey M, Qureshi W, Stacey RB, et al. Comparison of paravalvular aortic leak characteristics in the Medtronic CoreValve versus Edwards Sapien Valve: paravalvular aortic leak characteristics. *Catheter Cardiovasc Interv.* (2018) 92:972–80. doi: 10.1002/ccd.27643
140. Franzoni I, Latib A, Maisano F, Costopoulos C, Testa L, Figini F, et al. Comparison of incidence and predictors of left bundle branch block after transcatheter aortic valve implantation using the CoreValve versus the Edwards valve. *Am J Cardiol.* (2013) 112:554–9. doi: 10.1016/j.amjcard.2013.04.026
141. Siontis GC, Jüni P, Pilgrim T, Stortecky S, Büllesfeld L, Meier B, et al. Predictors of permanent pacemaker implantation in patients with severe aortic stenosis undergoing TAVR: a meta-analysis. *J Am Coll Cardiol.* (2014) 64:129–40. doi: 10.1016/j.jacc.2014.04.033
142. Khatri PJ, Webb JG, Rodés-Cabau J, Fremes SE, Ruel M, Lau K, et al. Adverse effects associated with transcatheter aortic valve implantation: a meta-analysis of contemporary studies. *Ann Intern Med.* (2013) 158:35–46. doi: 10.7326/0003-4819-158-1-201301010-00007
143. Karyofillis P, Kostopoulou A, Thomopoulou S, Habibi M, Livanis E, Karavolias G, et al. Conduction abnormalities after transcatheter aortic valve implantation. *J Geriatr Cardiol.* (2018) 15:105–12. doi: 10.11909/j.issn.1671-5411.2018.01.004
144. Khawaja M, Rajani R, Cook A, Khavandi A, Moynagh A, Chowdhary S, et al. Permanent pacemaker insertion after CoreValve transcatheter aortic valve implantation: incidence and contributing factors (the UK CoreValve Collaborative). *Circulation.* (2011) 123:951–60. doi: 10.1161/CIRCULATIONAHA.109.927152
145. Dvir D, Webb J, Brecker S, Bleiziffer S, Hildick-Smith D, Colombo A, et al. Transcatheter aortic valve replacement for degenerative bioprosthetic surgical valves: results from the global valve-in-valve registry. *Circulation.* (2012) 126:2335–44. doi: 10.1161/CIRCULATIONAHA.112.104505
146. Ribeiro HB, Rodés-Cabau J, Blanke P, Leipsic J, Kwan Park J, Bapat V, et al. Incidence, predictors, and clinical outcomes of coronary obstruction following transcatheter aortic valve replacement for degenerative bioprosthetic surgical valves: insights from the VIVID registry. *Eur Heart J.* (2018) 39:687–95. doi: 10.1093/eurheartj/ehx455
147. Gurvitch R, Cheung A, Bedogni F, Webb JG. Coronary obstruction following transcatheter aortic valve-in-valve implantation for failed surgical bioprostheses. *Catheter Cardiovasc Interv.* (2011) 77:439–44. doi: 10.1002/ccd.22861
148. Sultan I, Siki M, Wallen T, Szeto W, Vallabhajosyula P. Management of coronary obstruction following transcatheter aortic valve replacement. *J Card Surg.* (2017) 32:777–81. doi: 10.1111/jocs.13252
149. Ribeiro HB, Webb JG, Makkar RR, Cohen MG, Kapadia SR, Kodali S, et al. Predictive factors, management, and clinical outcomes of coronary obstruction following transcatheter aortic valve implantation: insights from a large multicenter registry. *J Am Coll Cardiol.* (2013) 62:1552–62. doi: 10.1016/j.jacc.2013.07.040
150. Hamdan A, Barbash I, Schwammenthal E, Segev A, Kornowski R, Assali A, et al. Sex differences in aortic root and vascular anatomy in patients undergoing transcatheter aortic valve implantation: a computed-tomographic study. *J Cardiovasc Comput Tomogr.* (2017) 11:87–96. doi: 10.1016/j.jcct.2017.01.006
151. Khan JM, Greenbaum AB, Babaliaros VC, Rogers T, Eng MH, Paone G, et al. The BASILICA trial: prospective multicenter investigation of intentional leaflet laceration to prevent TAVR coronary obstruction. *JACC Cardiovasc Interv.* (2019) 12:1240–52. doi: 10.1016/j.jcin.2019.03.035
152. Khan JM, Dvir D, Greenbaum AB, Babaliaros VC, Rogers T, Aldea G, et al. Transcatheter laceration of aortic leaflets to prevent coronary obstruction during transcatheter aortic valve replacement: concept to first-in-human. *JACC Cardiovasc Interv.* (2018) 11:677–89. doi: 10.1016/j.jcin.2018.01.247
153. Komatsu I, Mackensen GB, Aldea GS, Reisman M, Dvir D. Bioprosthetic or native aortic scallop intentional laceration to prevent iatrogenic coronary artery obstruction. Part 1: how to evaluate patients for BASILICA. *Eurointervention.* (2019) 15:47–54. doi: 10.4244/EIJ-D-19-00057
154. Komatsu I, Mackensen GB, Aldea GS, Reisman M, Dvir D. Bioprosthetic or native aortic scallop intentional laceration to prevent iatrogenic coronary artery obstruction. Part 2: how to perform BASILICA. *Eurointervention.* (2019) 15:55-66. doi: 10.4244/EIJ-D-19-00056
155. Dvir D, Khan J, Kornowski R, Komatsu I, Chatriwalla A, Mackenson GB, et al. Novel strategies in aortic valve-in-valve therapy including bioprosthetic valve fracture and BASILICA. *Eurointervention.* (2018) 14:AB74–AB82. doi: 10.4244/EIJ-D-18-00667
156. Mayo RP, Yaakobovich H, Finkelstein A, Shadden SC, Marom G. Impact of BASILICA on the thrombogenicity potential of valve-in-valve implantations. *J Biomech.* (2021) 118:110309. doi: 10.1016/j.jbiomech.2021.110309
157. Khodaee F, Qiu D, Dvir D, Azadani AN. Reducing the risk of leaflet thrombosis in transcatheter aortic valve-in-valve implantation by BASILICA: a computational simulation study. *Eurointervention.* (2019) 15:67–70. doi: 10.4244/EIJ-D-19-00048
158. Hatoum H, Maureira P, Lilly S, Dasi LP. Impact of leaflet laceration on transcatheter aortic valve-in-valve washout: BASILICA to solve neosinus and sinus stasis. *JACC Cardiovasc Interv.* (2019) 12:1229–37. doi: 10.1016/j.jcin.2019.04.013
159. Rayz V, Boussel L, Ge L, Leach J, Martin A, Lawton M, et al. Flow residence time and regions of intraluminal thrombus deposition in intracranial aneurysms. *Ann Biomed Eng.* (2010) 38:3058–69. doi: 10.1007/s10439-010-0065-8
160. Gorbet MB, Sefton MV. Biomaterial-associated thrombosis: roles of coagulation factors, complement, platelets and leukocytes. *Biomaterials.* (2004) 25:219–41. doi: 10.1016/B978-008045154-1.50025-3

Conflict of Interest: The authors declare that the research was conducted in the absence of any commercial or financial relationships that could be construed as a potential conflict of interest.

frontiers in Cardiovascular Medicine

METHODS
published: 01 October 2021
doi: 10.3389/fcvm.2021.734692

Organ Culture Model of Aortic Valve Calcification

Adrian H. Chester[1,2]*, *Padmini Sarathchandra*[2], *Ann McCormack*[2] *and Magdi H. Yacoub*[1,2]

[1] *Heart Science Centre, Magdi Yacoub Institute, Harefield, United Kingdom,* [2] *National Heart & Lung Institute, Imperial College, Imperial College London, London, United Kingdom*

A significant amount of knowledge has been gained with the use of cell-based assays to elucidate the mechanisms that mediate heart valve calcification. However, cells used in these studies lack their association with the extra-cellular matrix or the influence of other cellular components of valve leaflets. We have developed a model of calcification using intact porcine valve leaflets, that relies upon a biological stimulus to drive the formation of calcified nodules within the valve leaflets. Alizarin Red positive regions were formed in response to lipopolysaccharide and inorganic phosphate, which could be quantified when viewed under polarized light. Point analysis and elemental mapping analysis of electron microscope images confirmed the presence of nodules containing calcium and phosphorus. Immunohistochemical staining showed that the development of these calcified regions corresponded with the expression of RUNX2, osteocalcin, NF-kB and the apoptosis marker caspase 3. The formation of calcified nodules and the expression of bone markers were both inhibited by adenosine in a concentration-dependent manner, illustrating that the model is amenable to pharmacological manipulation. This organ culture model offers an increased level of tissue complexity in which to study the mechanisms that are involved in heart valve calcification.

Keywords: aortic valve, calcification, porcine, adenosine, lipopolysaccharide, osteoblasts, valve interstitial cells, valve calcification model

OPEN ACCESS

Edited by:
Katherine Yutzey, Cincinnati Children's Hospital Medical Center, United States

Reviewed by:
Boudewijn Kruithof, Leiden University Medical Center, Netherlands
Joy Lincoln, Medical College of Wisconsin, United States

***Correspondence:**
Adrian H. Chester
a.chester@imperial.ac.uk

Specialty section:
This article was submitted to Heart Valve Disease, a section of the journal Frontiers in Cardiovascular Medicine

Received: *01 July 2021*
Accepted: *02 September 2021*
Published: *01 October 2021*

Citation:
Chester AH, Sarathchandra P, McCormack A and Yacoub MH (2021) Organ Culture Model of Aortic Valve Calcification. Front. Cardiovasc. Med. 8:734692. doi: 10.3389/fcvm.2021.734692

INTRODUCTION

The development of a medical strategy to treat aortic stenosis is required to alleviate the burden of the increasing numbers of patients who require aortic valve replacement, which is predicted to increase with an aging population (1). The use of pharmacological agents to delay or even remove the need for surgical replacement of diseased valves, or percutaneous implantation, would represent a breakthrough in the treatment of patients with calcific aortic valve disease (2). The translation of information gained from *in vitro* experiments using isolated cells into clinical studies has been hampered by the limitations of available animal models of calcific valve disease (3). This is illustrated by the disappointing results from clinical trials with statins (4, 5), despite data from *in vitro* and *in vivo* studies that supported beneficial effects of statins against the development of valve calcification (6–8).

The use of pathological specimens from humans and cultured cells from humans, sheep and pigs has shed light on the biological mechanisms that mediate the differentiation of valve interstitial cells (VIC) into an osteogenic cell phenotype, which is believed to be the responsible cell phenotype in the development of calcified lesions in the fibrosa layer of the valve (9). Cell-based studies have relied on a variety of endpoints to assess pro-calcifying stimuli, including the expression

of osteogenic markers, evidence of osteogenic signaling and the measurement of calcium using calcium specific dyes, radiolabeled calcium or histochemical staining (Alizarin Red and von Kossa) (10–12). With regards to mineralisation, previous studies have questioned the "calcified nodule" model of valve calcification using cultured porcine VIC, whereby analysis of nodules formed in response to TGF-b1 and osteogenic media, which stained positive for Alizarin Red, failed to show the presence of mineralisation using live-cell imaging micro-Raman spectroscopy (13). While the use of human cells is informative, attempts to standardize conditions to induce calcification have shown the dependence on passage number in the response of osteogenic media containing organic phosphate (14). There is also an influence of the compliance of the substrate on which cells are grown with regards to calcification potential (15).

Based on the experience with vascular calcification (16, 17), and knowledge gained with use of cultured cells to induce calcification with respect to the use of lipopolysaccharide (LPS) and inorganic phosphate (12, 18–20), we set out to establish an organ culture model of valve calcification using intact porcine aortic valve leaflets. Such a model would allow assessment of the response of the VIC while they are in their physiological environment with respect to the 3-D architecture of the extracellular environment and the proximity of valve endothelial cells (VEC).

METHODS

Stimulation of Leaflet Calcification

Porcine hearts were obtained from a local abattoir. Under sterile conditions the aortic valve leaflets were removed from the aortic root and placed immediately in DMEM. Each leaflet was pinned to the base of a 6-well tissue culture plate coated with the silicone elastomer, Sylgard (Sigma) and covered with 3 mL of low glucose DMEM with 0.4% FBS and antibiotics. To induce a calcification response valve leaflets were incubated with LPS and inorganic phosphate (sodium phosphate), with the media being changed every 2–3 days. Experiments were conducted to determine the optimal concentrations of LPS and phosphate, the duration of incubation required, and the variability between different leaflets and within different regions of each leaflet. The experiments were performed in the presence of 0.4 unit/mL pyrophosphatase (Sigma), which reduces levels of pyrophosphate, an endogenous inhibitor of calcification and has been shown to increase the calcifying effect of phosphate in porcine valve cusps (12). Once the conditions for inducing and quantifying a calcification response in the valve leaflets was achieved, the inhibitory effect of increasing concentrations of adenosine was assessed.

Assessment of Leaflet Calcification

Quantification of Calcium Deposition

On completion of the experiment, valve leaflets were fixed in 10% formal saline. Valve leaflets were cut into 3 pieces radially (left, center and right portions of the leaflet) and were processed, mounted in wax blocks sectioned and stained with Alizarin Red. Images were taken under polarized light and image analysis was carried out using Image J (**Figure 1**).

Immunohistochemistry for Calcification Markers

Prior to immunoperoxidase staining, 5 μm thick paraffin wax sections of valve leaflets were dewaxed and rehydrated in water. Antigen retrieval was carried out by immersing the slides in 0.1 M citrate buffer (pH 6) and microwaving for 10 min, the slides were then left in the same buffer for a further 20 min followed by tap water wash. Endogenous peroxidases in the tissue were blocked by incubating with 3% hydrogen peroxide for 5 min. To reduce non-specific binding, the slides were incubated with blocking buffer [3% Bovine serum albumin (BSA, Sigma) + 3% normal horse serum (Vector laboratories)], for 30 min. Slides were then incubated overnight in a moist chamber with antibodies against rabbit polyclonal RUNX2 at 1:200 (Abcam), mouse monoclonal Osteocalcin 1:600 (Abcam), rabbit polyclonal Osteopontin 1:500 (Chemicon), mouse monoclonal NF-kB 1:800 (BD transduction), Rabbit monoclonal cleaved caspase 3 1:200 (R&D systems). Antibody dilutions were made in half-strength blocking buffer. Negative controls consisted of blocking buffer. After thorough washing, all the slides were incubated with VECTASTAIN® Elite® ABC-Peroxidase Kit (R.T.U. Universal) for 30 min for each secondary and tertiary antibody (Vector Laboratories). Specimens were then incubated with DAB (Sigma) for 5 min washed well in tap water, stained the nuclei with Haematoxylin for 1 min and mounted using Aquatex (VWR). Stained slides were scanned using Hamamatsu Nanozoomer.

Elemental Analysis by Energy-Dispersive X-Ray Spectroscopy

10 μm thick paraffin wax sections were dewaxed and rehydrated to water, air-dried, mounted on SEM stubs coated with Gold/Palladium. Elemental analysis was performed by Energy-dispersive X-ray spectroscopy (EDAX) on a JEOL 6,010 analytical scanning electron microscope.

Data Analysis

Photomicrographs of the three sections (left, middle and right) from each leaflet, stained with Alizarin Red and viewed under polarized light, or antibody staining viewed under normal light, were analyzed with Image J. Firstly the area of the leaflet was calculated by tracing around the edge of the section (S_{Area}). The section was then viewed under the Red channel and the threshold adjusted to highlight only areas of positive staining. The area fraction (AF) for the whole field of view was then calculated ($FofV_{Area}$), which was subsequently used to calculate the percentage area of positive staining of the section [(AF x $FofV_{Area}/S_{Area}$) x100]. The mean of the values for three regions of each leaflet was then calculated to give the result for each leaflet. For quantification of antibody staining in **Figure 8**, Image J software was used to calculate the percentage of area stained of photomicrographs of identical size at x40 magnification from regions of whole leaflet sections that were either Alizarin Red positive or negative. Statistical analysis was performed using ANOVA followed by the Dunnett's *post-hoc* test or a *T*-test where appropriate. Numerical data is expressed as the mean ± standard error of the mean. Values for N referred to the number of individual cusps that were studied.

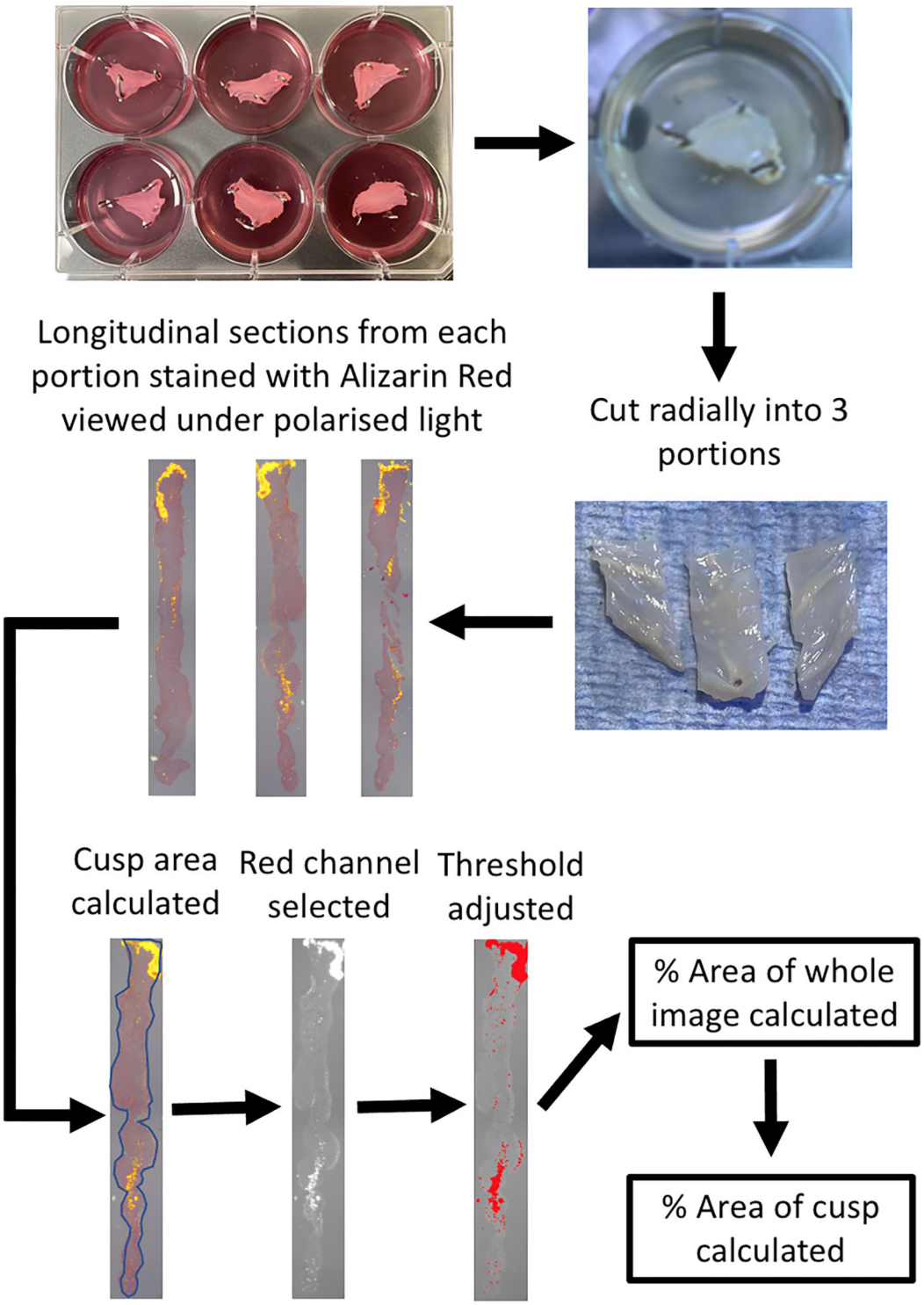

FIGURE 1 | Schematic diagram of the experimental protocol. Following incubation of the pinned-out valve leaflets, they are fixed while still in the wells with 10% formal saline. Each leaflet is cut into 3 portions radially, processed and embedded in wax blocks and cut longitudinal sections cut on a microtome. Alizarin Red staining of a slide from each of the three leaflet portions is viewed under polarized light and then quantified using Image J, to ultimately calculate the percentage of the area of the leaflet that stains for Alizarin Red.

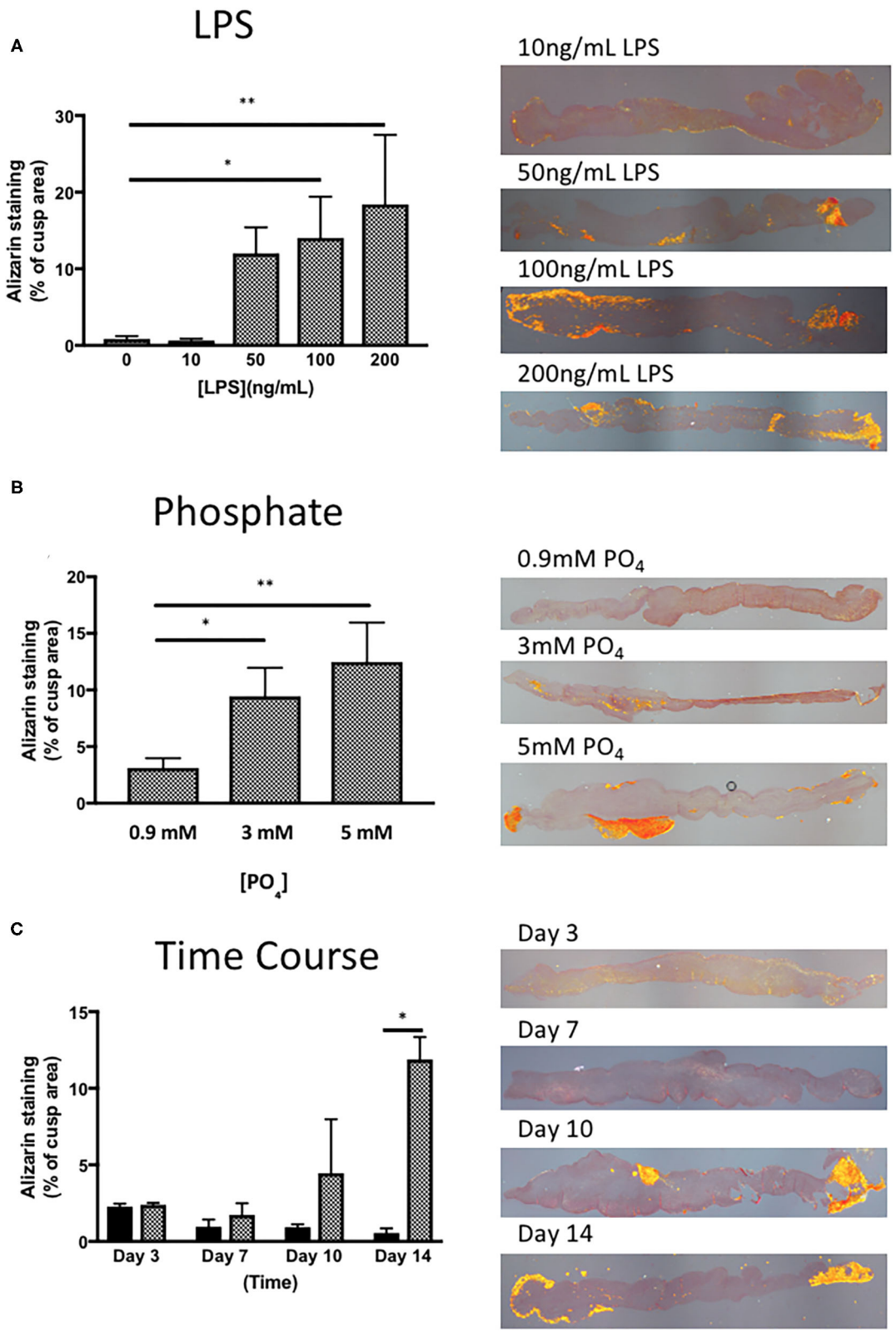

FIGURE 2 | Optimisation of the response of valve leaflets to LPS and phosphate. **(A)** The effect of LPS concentration on calcium accumulation in porcine aortic valve leaflets in culture for 14 days in the presence of 3 mM phosphate (*$p = 0.071$, **$p = 0.003$, ANOVA; $n = 3$) and representative images of sections stained with Alizarin

(Continued)

FIGURE 2 | Red, imaged under polarized light for each concentration of LPS. **(B)** The effect of phosphate concentration on calcium accumulation in porcine aortic valve leaflets in culture for 14 days in the presence of 100 ng/mL LPS (*$P = 0.015$, **$P = 0.001$, ANOVA; $n = 4$) and representative images of sections stained with Alizarin Red, imaged under polarized light for each concentration of phosphate. **(C)** Time course of the effect of culture media (black bars) and 100 ng/mL LPS and 3 mM phosphate (cross-hatched bars) on calcium accumulation in porcine aortic valve leaflets in culture for 3 to 14 days (*$P = 0.001$, 2 way ANOVA, $n = 2$) and representative images of sections stained with Alizarin Red, imaged under polarized light for each time point.

RESULTS

Stimulation of Leaflet Calcification

To identify a suitable concentration of LPS to use, the effect of 10–200 ng/mL of LPS was assessed in the presence of 3 mM phosphate for 14 days. LPS was able to give a concentration-dependent increase in Alizarin Red staining in porcine valve leaflets, where the response of LPS at 10 ng/mL was indistinguishable from the control group (no LPS), while that of 100 & 200 ng/mL showed that 15–20% of the cross-sectional area of the leaflet stained positive for Alizarin Red (**Figure 2A**). In another series of experiments, to optimize the concentration of inorganic phosphate, the concentration of LPS was kept at 100 ng/mL and the concentration varied of phosphate between 0.9 mM and 5 mM (DMEM contains 0.9 mM phosphate) for 14 days. Supplementation of DMEM with 3 mM and 5 mM phosphate gave a progressive increase Alizarin Red staining up to ∼20% of the valve area (**Figure 2B**). Based on the findings of these initial experiments, all subsequent experiment used 100 ng/mL of LPS and 3 mM phosphate. To check if the incubation time of LPS and phosphate was optimal, a time-course experiment over the 14-day period was performed. After 3 and 7-days incubation with 100 ng/mL LPS and 3 mM phosphate, there were no measurable increases in Alizarin Red staining. After 10 days there was marked, but variable increase in calcification, which was further increased after 14-days (**Figure 2C**). These results confirmed that the experiments required at least 14 days of incubation with LPS and phosphate.

Leaflet Specific and Regional Effect of Calcification Response

To check if there was any variation in the calcification response of the left-coronary, right-coronary and non-coronary leaflets, we analyzed the response of each individual leaflet to 100 ng/mL LPS and 3 mM phosphate. Results show that the calcification response did not differ between the three different valve leaflets (**Figure 3A**). To validate the measurement of calcification in the three regions across each leaflet, the response in the left, middle and right portion of each leaflet, in each of the three leaflets was compared. No statistical difference in the response of each region, in each cusp could be seen (**Figure 3B**). It was noteworthy that the right portion of the non-coronary cusp was markedly more variable than the other regions studied.

EDAX Elemental Analysis

Scanning electron microscope images of valve treated with 100 ng/mL LPS and 3 mM phosphate showed electron dense nodules in specific regions of the leaflet, which were not evident in the media only treated tissue (**Figures 4A,B**). Point analysis of LPS/phosphate stimulated valve leaflets by EDAX showed a prominent peak in the spectra for calcium at 3.69 KeV and for phosphorus at 2.01 KeV. In contrast, media treated valve leaflets showed no peak corresponding to calcium or phosphorus. The appearance of silicon in the spectra is due to inadvertent detection of the glass slide (**Figures 4C–F**). In addition to the spectral analysis, the chemical nature of the image seen on the electron micrographs was confirmed with elemental mapping, whereby the presence of calcium and phosphorus coincided with the image of the nodule (**Figure 5**).

Expression of Inflammatory, Calcification and Apoptotic Markers by Immunohistochemistry

To assess if LPS was inducing an inflammatory response in the valve leaflet, the expression of NF-kB was investigated. In untreated leaflets no staining for NF-kB was evident (**Figures 6A,B**). In contrast LPS and phosphate treated leaflets show regional staining, some of which that associated with the cell nuclei (**Figures 6C,D**). By examining the staining in sequential sections of valve leaflets from media treated (**Figures 7A,C,E,G,I**) and LPS and phosphate (**Figures 7B,D,F,H,J**), it was possible to show that areas that showed positive staining for Alizarin Red (**Figure 7B**) were associated with areas of positive staining for osteocalcin, RUNX2, NF-kB and caspase 3 (**Figures 7D,F,H,J**, respectively). Quantification of the staining in Alizarin Red positive areas, compared to areas that were negative for Alizarin Red, show that there were significantly greater levels of staining for osteocalcin, RUNX2, NF-kB and caspase 3 in the calcified areas (**Figures 8A–D**, respectively). The lack of caspase 3 staining in control valves indicated the absence of apoptosis after 14-days incubation in media alone.

Pharmacological Modulation of Porcine Leaflet Calcification

Based on our previous observations, where adenosine was shown to inhibit the expression of osteoblast marker in cultured human VIC (10), we assessed the ability of adenosine to inhibit the calcification of intact porcine leaflets stimulated with 100 ng/mL of LPS and 3 mM phosphate for 14 days. In these experiments, one leaflet from each valve was used as a positive control, while the other two leaflets were treated with adenosine. The effects observed in the adenosine treated leaflets were expressed as a percentage of the positive control for the corresponding valve. Immunohistochemical staining for RUNX2 (**Figures 9A–C**), osteopontin (**Figures 9D–F**) and osteocalcin (**Figures 9G–I**) showed stronger staining in the LPS and phosphate treated leaflets, compared to control. Addition of 10^{-5}M adenosine to LPS and phosphate, resulted in a

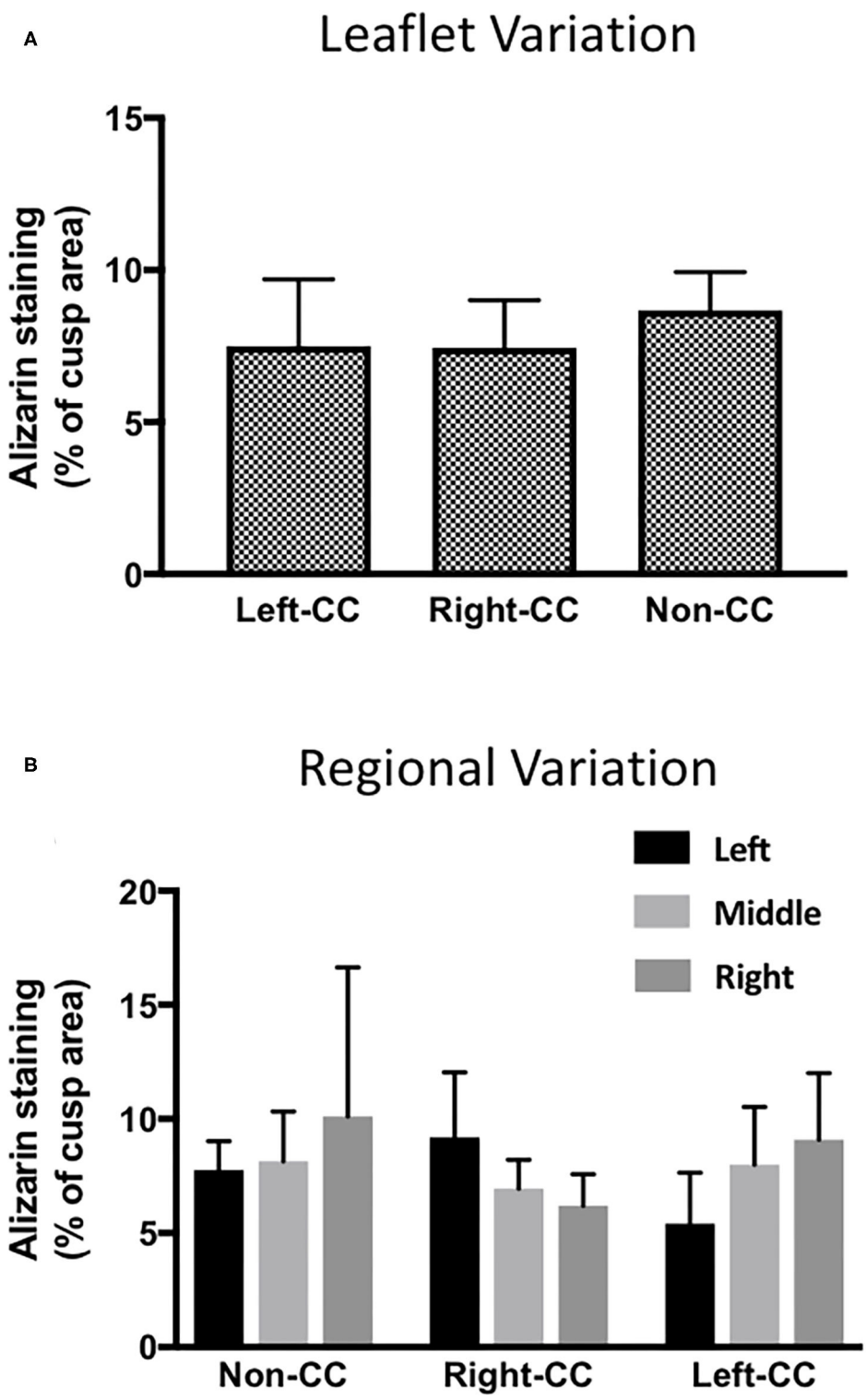

FIGURE 3 | Leaflet-specific and regional effects of LPS and phosphate. **(A)** Leaflet specific effects of 100 ng/mL LPS and 3 mM phosphate on calcium accumulation in the left-, right- and non-coronary leaflets of porcine aortic valves. Values are the mean of the measurement from the three regions of each leaflet ($p > 0.05$, ANOVA; $n = 6$). **(B)** Comparison of the effect of 100 ng/mL LPS and 3 mM in the 3 regions of the left- right- and non-coronary leaflet assessed for calcium accumulation ($p > 0.05$, ANOVA; $n = 6$).

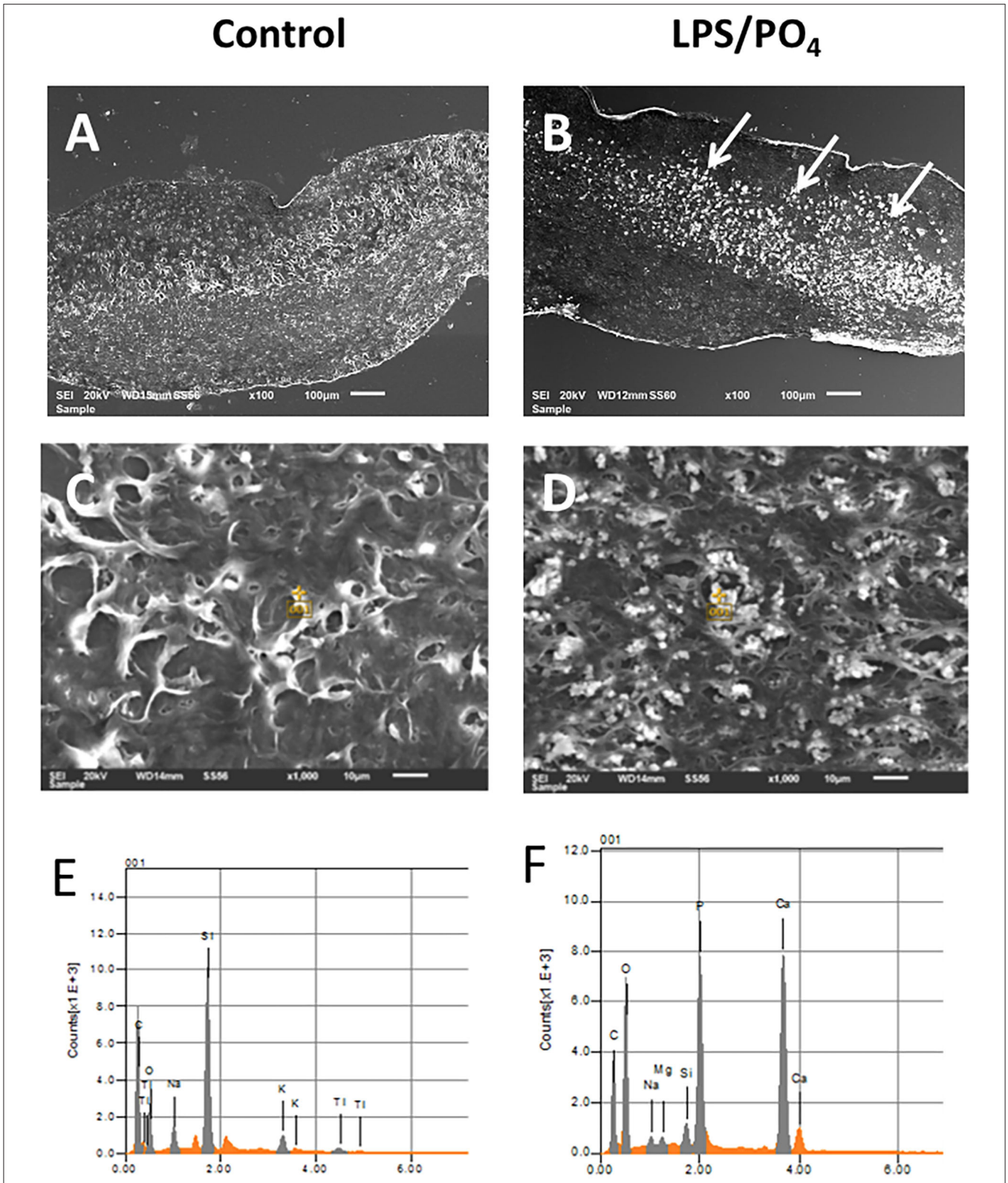

FIGURE 4 | Electron microscopy and EDAX analysis of calcified valve leaflets. Scanning electron micrographs of porcine valve leaflets stimulated with media alone **(A)** or 100 ng/mL LPS and 3 mM phosphate for 14-days **(B)**, with presence of calcified areas (white arrows) (x100 magnification, scale bar = 100 μM). High power view and point analysis (yellow cross) of aortic valve leaflets from control and LPS/PO4 treated valves (x1,000 magnification, scale bar =10 μM) **(C,D)**, and the spectrum showing no calcium or phosphorus peaks in the control **(E)**, but their presence in the LPS/PO4 treated tissue **(F)**.

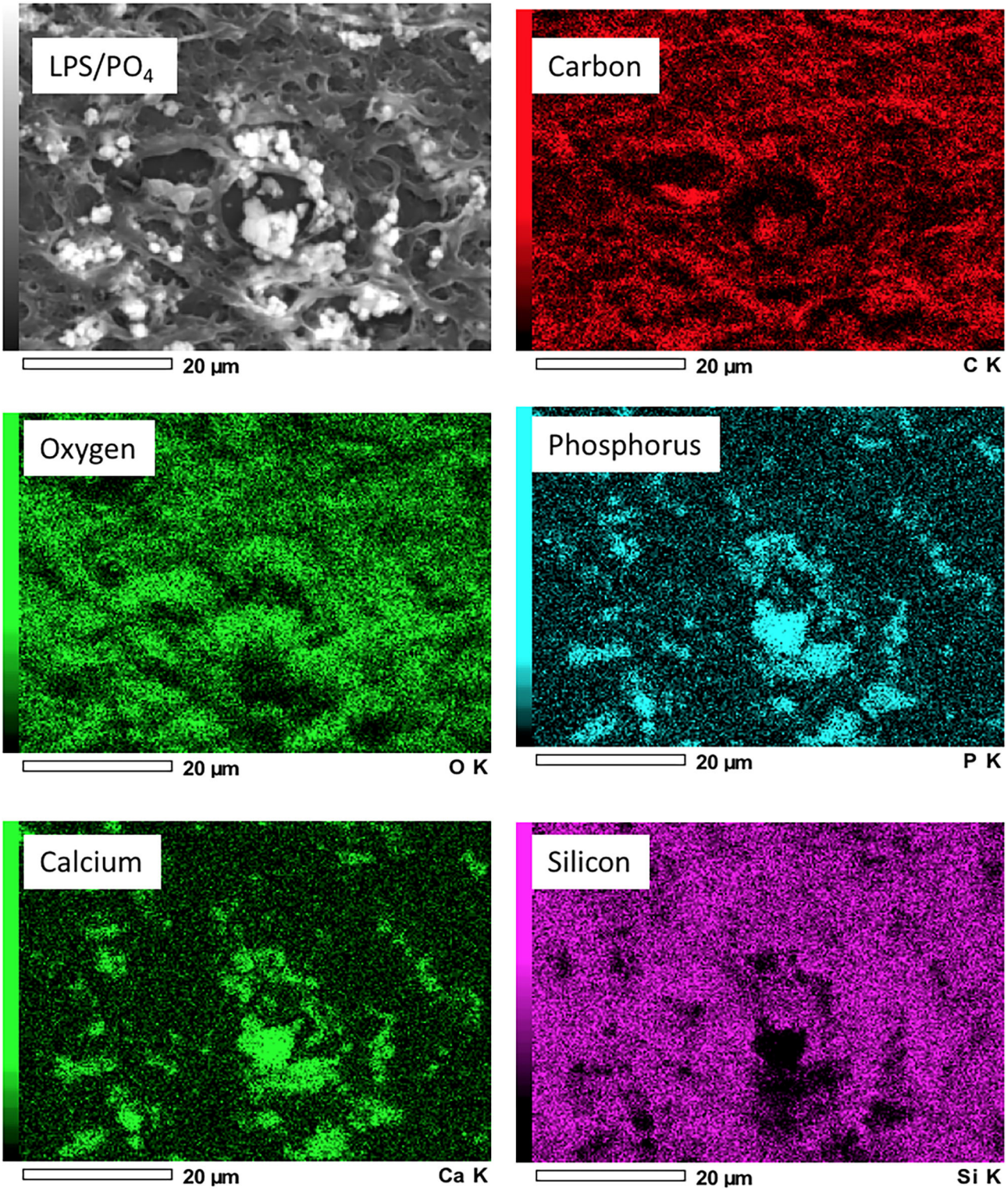

FIGURE 5 | Elemental mapping of LPS and phosphate treated valve leaflets. Scanning electron micrographs showing the elemental distribution of carbon, oxygen, phosphorus, calcium and silicon. Regions of greater electron density corresponding to the distribution of calcium and phosphorus.

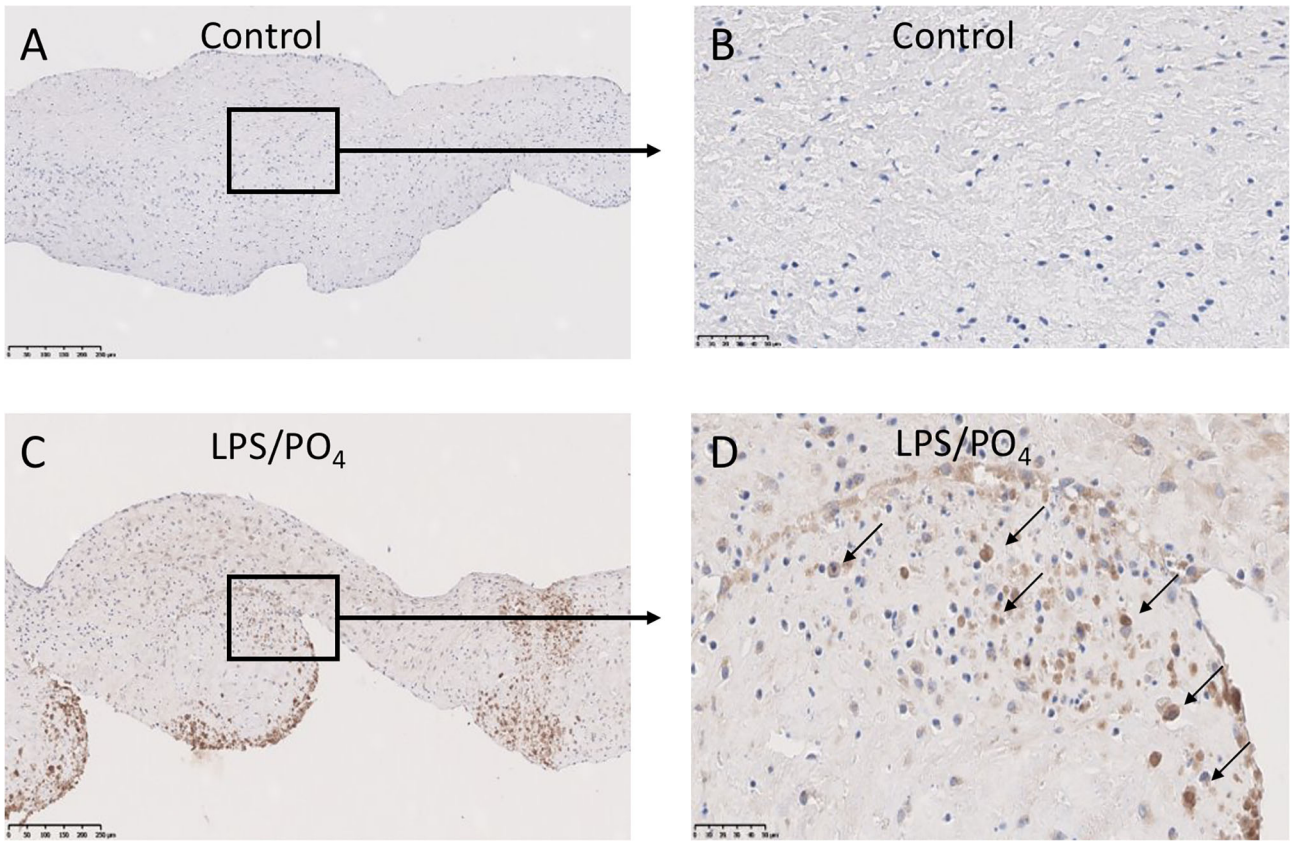

FIGURE 6 | Expression of NF-kB in calcified valve leaflets. Low and high-powered images of immunohistochemical staining for NF-kB in untreated **(A,B)** and 100 ng/mL LPS & 3 mM phosphate treated **(C,D)** valve leaflets. Nuclear expression of NF-kB can be seen in **(D)** (black arrows). **(A,C)** scale bar, 200 μM; **(B,D)** scale bar, 500 μM.

marked reduction in the staining for RUNX2, osteopontin and osteocalcin. Lower concentrations of adenosine (10^{-8} and 10^{-7}M) had no significant effect on the amount of Alizarin Red staining in the leaflets. At concentrations above 10^{-7}M, there was a progressive reduction in the amount of Alizarin Red staining, which reached statistical significance at 10^{-5}M (**Figure 10A**). Corresponding to reductions in Alizarin Red staining, there was also significant reductions in antibody staining for osteocalcin, oeteopontin and RUNX2 in valve leaflets treated with 10^{-5}M adenosine (**Figures 10B–D**, respectively). The areas measured for staining of each antibody were similar in all 3 groups (**Figure 10E**).

DISCUSSION

This study sets out an *ex-vivo* organ culture model of valve calcification that can quantify the level of calcium incorporated into the valve and assess phenotypic changes in the cells that reside in calcified regions. Elemental analysis and mapping showed that the nodules that were visible with the scanning electron microscope were comprised of calcium and phosphorus. The use of intact valve leaflets has the advantage that the VIC are retained in the physiological arrangement with respect to their association with the extracellular matrix and their relationship with the VEC. Intact valve leaflets from pigs and mice have previously been used to assess the effects of pro-calcific stimuli, including inorganic phosphate osteogenic media, osteogenic media supplemented with TGFβ1 and mechanical injury (11, 12, 21–24).

These previous studies have largely relied upon osteogenic media, which contains β-glycerophosphate, dexamethasone, and ascorbic acid, to drive the calcification response. In contrast, this model uses LPS, a TLR4 receptor agonist, to drive the calcification response and the subsequent initiation of an inflammatory response, as evidenced by nuclear expression of NF-kB in the calcified regions. The contribution of specific cell types within the valve leaflet to the response of LPS was not studied, however LPS has previously been shown to stimulate a calcification response in cultured VIC and to augment the effects of calcification of VIC to gamma–interferon (18, 20, 25, 26). Phosphate in combination with inorganic pyrophosphatase has also previously been shown to stimulate increase levels of radiolabeled calcium and the formation of Alizarin Red positive lesions, in intact valve leaflets over an 8-day period (12). Based on these

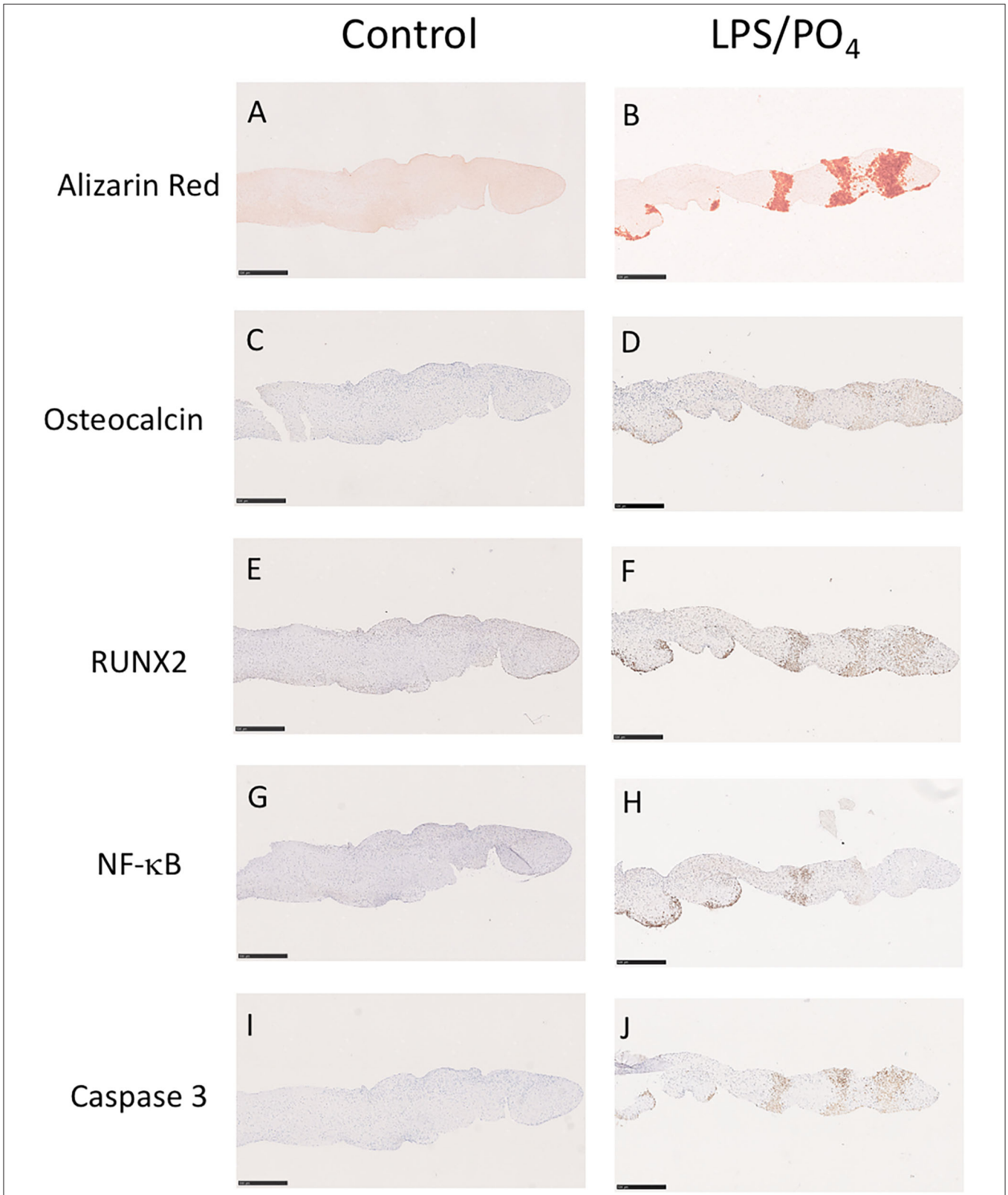

FIGURE 7 | Colocalisation of Alizarin Red staining with osteogenic, inflammatory and apoptotic markers. Sequential sections of a valve leaflet stimulated media alone (left column) or 100 ng/mL LPS and 3 mM phosphate (right column) for 14-days. Histochemical staining for Alizarin Red **(A,B)** co-localizes with regions of immunohistochemical staining for osteocalcin **(C,D)**, RUNX2 **(E,F)**, NF-kB **(G,H)** and caspase 3 **(I,J)**. Scale bar, 500 μM.

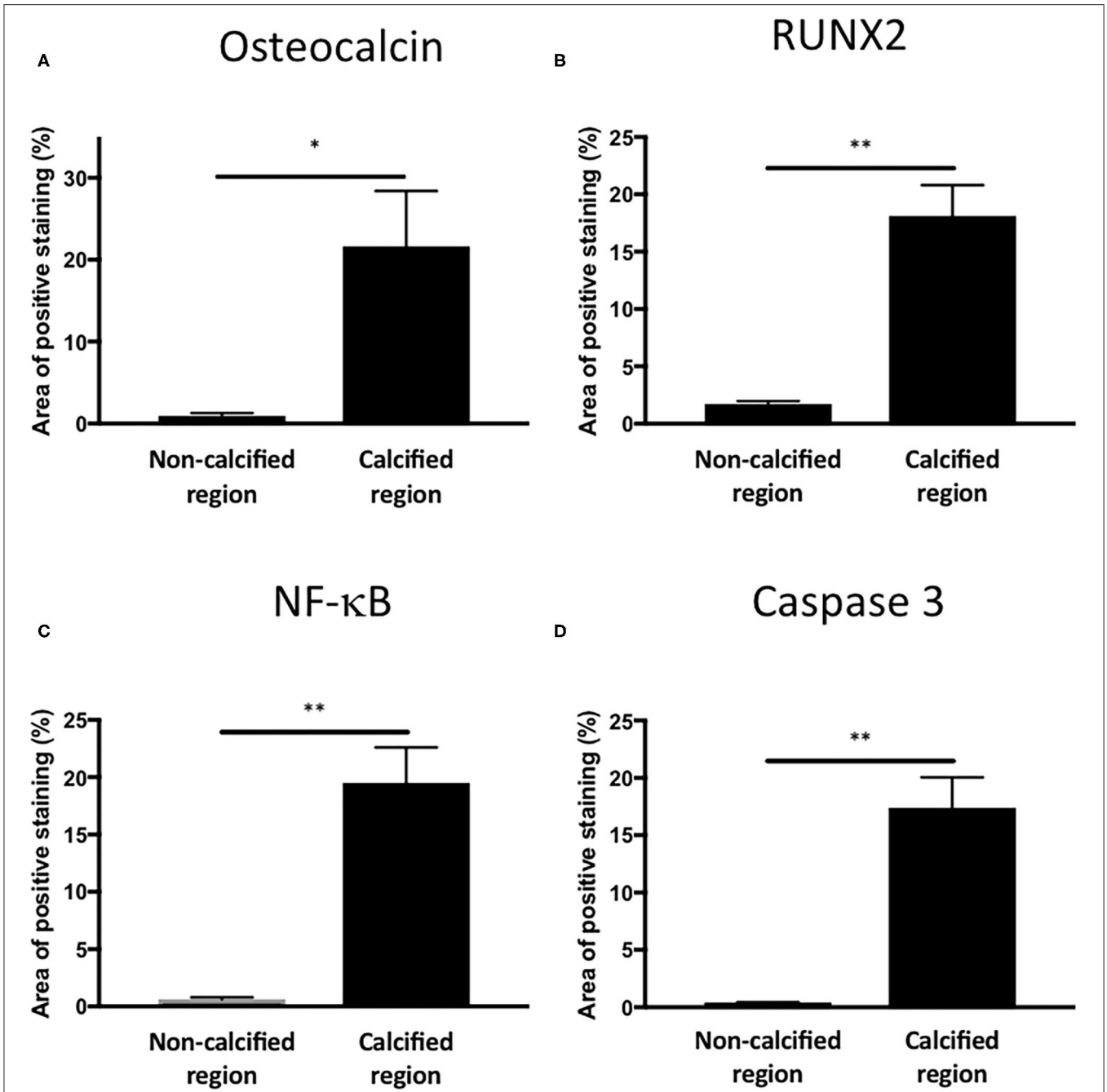

FIGURE 8 | Quantification of osteogenic, inflammatory and apoptotic markers in Alizarin Red positive and negative areas of valve leaflets. Percentage area staining of 1.1 mm^2 regions from non-calcified and calcified regions for **(A)** osteocalcin (*$P = 0.012$, T-Test; $n = 4$), **(B)** RUNX2 (**$P < 0.001$, T-Test; $n = 4$), **(C)** NF-kB (**$P < 0.001$, T-Test; $n = 4$) and **(D)** caspase 3 (**$P < 0.001$, T-Test; $n = 4$).

findings we included pyrophosphatase to block the anti-calcification effect of pyrophosphate in the valve leaflets. We observed an augmentation of the response to 100 ng/mL LPS, with increasing phosphate concentration. Since there was no significant difference in the effect between 3 and 5 mM phosphate, we opted to choose the lower concentration, since this is nearer to the concentration used in previous studies and below the concentration required for phosphate to have a direct effect on calcification (12, 14).

From the analysis of the data on the quantification of the percentage area of each leaflet that showed positive staining with Alizarin Red, we determined that the most accurate way to assess the degree of calcification in each valve leaflet was to sample each leaflet in three areas and calculate the mean of the three

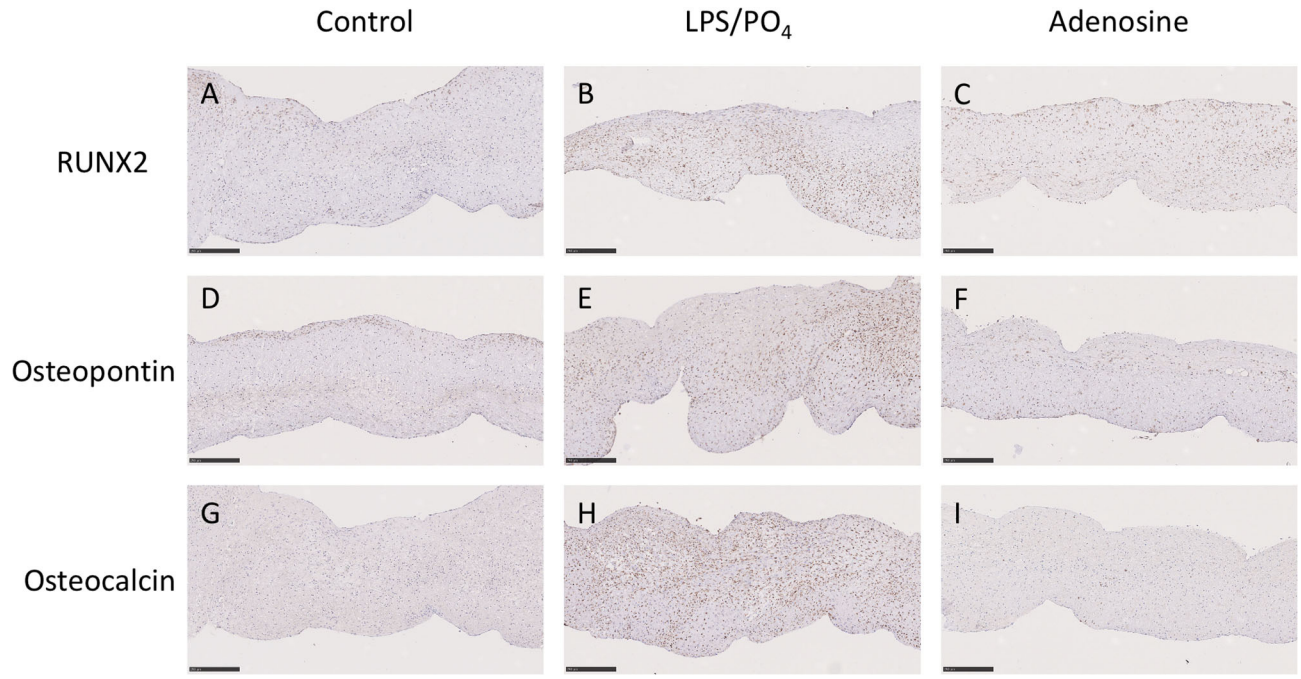

FIGURE 9 | Effect of adenosine on the expression of osteogenic markers. Immunohistochemical staining in media alone (left column), 100 ng/mL LPS 3 μM phosphate treated (center column) and 100 ng/mL LPS 3 mM phosphate and 10^{-5}M adenosine treated (right column) valve leaflets. Section were stained with RUNX2 **(A–C)**, osteopontin **(D–F)** and osteocalcin **(G–I)**. Scale bar, 100 μM.

observations. We were subsequently able to show that there was no bias toward any of the three individual aortic valve leaflets or to left, middle or right regions of each of the cusps. The Alizarin Red staining did not follow a specific pattern, nor was it exclusively associated with the fibrosa layer of the valve leaflets. There was a tendency for the calcification to occur at either end of each cusp. This could be due to the development of tension in the cusp when it was pinned into position in the culture plate or during the 14-day culture period. We aim to extend this model with the use of a stretch bioreactor to investigate the application of cyclic strain on the calcification response of LPS and phosphate. It has been previously shown that strain increased calcified nodule formation and enhances the response to TGFβ1 and BMP (11, 27). The advantage offered by this model includes the ability to quantify changes in cell phenotype and of calcification and adjacent sections of valve leaflets. There was increased expression of osteoblast markers and the osteoblast transcription factor RUNX2, both of which are known to be expressed in calcified valves (28, 29). The presence of caspase-3 in the calcified regions demonstrates a role for apoptosis in the calcification response, suggesting that dystrophic calcification may also be occurring alongside osteogenic calcification. Both osteogenic and dystrophic calcification are features of the disease in human valves (30, 31). This model gives the opportunity to probe for other markers or mediators of calcification via antibody staining and/or western blotting. Recently a multi-omics approach to define the pathogenesis of calcific aortic valve disease has been advocated (32). Comparing the changes induced in this model using transcriptomics, proteomics and metabolomics will define the pathways that mediate the response and allow comparison with cell-based models and pathological samples from humans.

We were also able to show that the calcification response was amenable to pharmacological manipulation with adenosine. Our previous studies have shown an inhibitory effect of osteogenic markers induced by osteogenic media (10). Here we were able to demonstrate an inhibitory effect of adenosine on levels of calcification induced by LPS and phosphate, which was associated with a reduction in osteopontin, osteocalcin and RUNX2 expression. The beneficial effects on adenosine on valve calcification have previously been reported in a murine aortic root challenged with osteogenic media. A_1 and A_{2b} receptors were shown to mediate anti-calcification effects of adenosine, while A_{2a} receptor exacerbated the calcifying effect of osteogenic media (33). The model described in this paper would be amenable to similar receptor antagonist studies.

There are several limitations of the model described in this paper. The effect of LPS and phosphate takes at least 2 weeks to develop. A significant degree of calcification was observed after 10 days in some valves, but overall, the effect was more consistent with a longer incubation time. The data for time-course experiment in **Figure 2C** was based data from only 2 animals. While this experiment was only intended only to provide evidence of the shortest incubation time to give consistent

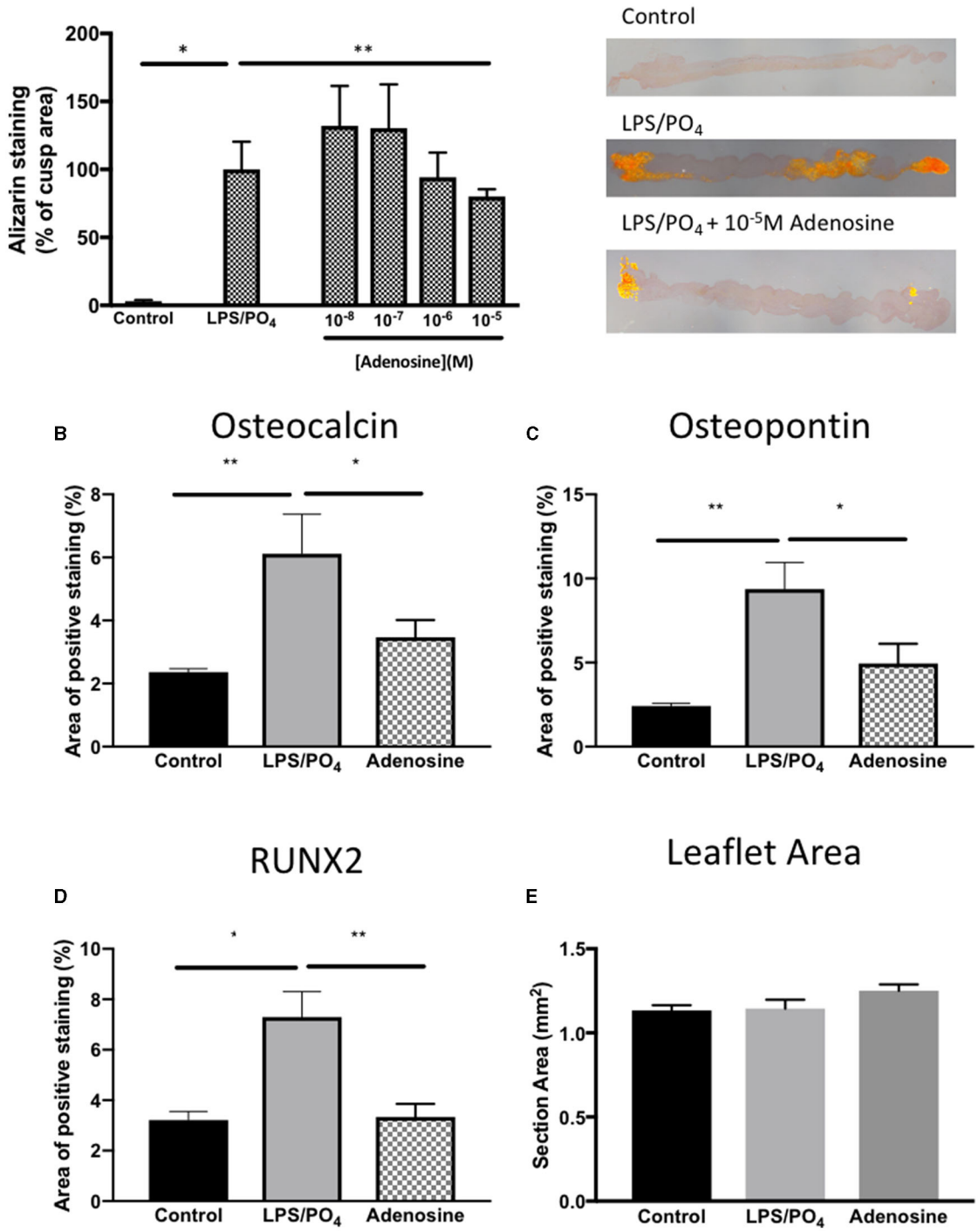

FIGURE 10 | Inhibitory effect of adenosine on calcification and expression of osteogenic markers. Effect of increasing concentrations of adenosine (10^{-8}-10^{-5}M) on the expression of Alizarin Red in sections of valve leaflet response to 100 ng/mL and 3 mM phosphate (*$P = 0.008$, *T*-Test; $n = 8$ and **$P = 0.011$, *T*-Test; $n = 6$) and representative images of sections stained with Alizarin Red imaged under polarized light for each treatment group **(A)**. Quantification of the area of positive staining in control (media alone), 100 ng/mL and 3 mM phosphate and 100 ng/mL & 3 mM phosphate with 10^{-5}M adenosine for **(B)** osteocalcin (**$P = 0.001$, *$P = 0.029$, ANOVA; $n = 11$–15 areas from 3 valves), **(C)** osteopontin (**$P < 0.001$, *$P = 0.029$, ANOVA; $n = 13$–15 areas from 3 valves) and **(D)** RUNX2 (*$P = 0.003$, **$P = 0.001$, ANOVA; $n = 9$–14 areas from 3 valves). **(E)** The mean area per measurement was similar in all 3 groups.

response to LPS and inorganic phosphate, further studies with more samples and longer time points may demonstrate the need for a longer duration for the experiment to give less variation in the response of the leaflets. By keeping each valve leaflet intact, a larger number of hearts are required to run more complex experimental protocols (e.g., concentration-response, antagonist studies). We avoided cutting each valve into smaller pieces, to avoid damage to the endothelial layer and maintain the integrity of the valve structure. Lastly, this model relies on the use of porcine tissue, which may not respond in an identical manner to human tissue. However, this type of study with human tissue would be virtually impossible due to the number of valves that would be required.

This organ culture model relies upon a combination of a biological stimulus and the promoting effects of phosphate to yield a quantifiable calcification response and an opportunity to simultaneously identify changes in the expression of phenotypic markers associated with valve calcification. We demonstrate that the model is amenable to pharmacological modulation by adenosine. The presence of all the cellular components and extracellular matrix will allow future studies to identify new markers and mediators of valve calcification as well as to serve as a tool for pre-clinical assessment of new anti-calcification agents.

DATA AVAILABILITY STATEMENT

The raw data supporting the conclusions of this article will be made available by the authors, without undue reservation.

ETHICS STATEMENT

Ethical review and approval was not required for the animal study because use of porcine hearts obtained from abattoir being slaughtered for food.

AUTHOR CONTRIBUTIONS

AC: devised concept and experimental design, analysis of data, and writing of the paper. PS: histology, EM work, elemental analysis, and writing of the paper. AM: valve tissue preparation and culture, processing samples, and writing of the paper. MY: critical appraisal and writing of the paper. All authors contributed to the article and approved the submitted version.

FUNDING

This study was funded by The Magdi Yacoub Institute.

REFERENCES

1. Yacoub MH, Takkenberg JJ. Will heart valve tissue engineering change the world? *Nat Clin Pract Cardiovasc Med.* (2005) 2:60–1. doi: 10.1038/ncpcardio0112
2. Zheng KH, Tzolos E, Dweck MR. Pathophysiology of aortic stenosis and future perspectives for medical therapy. *Cardiol Clin.* (2020) 38:1–12. doi: 10.1016/j.ccl.2019.09.010
3. Sider KL, Blaser MC, Simmons CA. Animal models of calcific aortic valve disease. *Int J Inflam.* (2011) 2011:364310. doi: 10.4061/2011/364310
4. Cowell SJ, Newby DE, Prescott RJ, Bloomfield P, Reid J, Northridge DB. A randomized trial of intensive lipid-lowering therapy in calcific aortic stenosis. *N Engl J Med.* (2005) 352:2389–97. doi: 10.1056/NEJMoa043876
5. Rossebo AB, Pedersen TR, Boman K, Brudi P, Chambers JB, Egstrup K, et al. Intensive lipid lowering with simvastatin and ezetimibe in aortic stenosis. *N Engl J Med.* (2008) 359:1343–56. doi: 10.1056/NEJMoa0804602
6. Rajamannan NM, Subramaniam M, Caira F, Stock SR, Spelsberg TC. Atorvastatin inhibits hypercholesterolemia-induced calcification in the aortic valves via the Lrp5 receptor pathway. *Circulation.* (2005) 112(Suppl. 9):I229–34. doi: 10.1161/01.CIRCULATIONAHA.104.524306
7. Osman L, Yacoub MH, Latif N, Amrani M, Chester AH. Role of human valve interstitial cells in valve calcification and their response to atorvastatin. *Circulation.* (2006) 114(Suppl. 1):I547–52. doi: 10.1161/CIRCULATIONAHA.105.001115
8. Benton JA, Kern HB, Leinwand LA, Mariner PD, Anseth KS. Statins block calcific nodule formation of valvular interstitial cells by inhibiting alpha-smooth muscle actin expression. *Arterioscler Thromb Vasc Biol.* (2009) 29:1950–7. doi: 10.1161/ATVBAHA.109.195271
9. Rutkovskiy A, Malashicheva A, Sullivan G, Bogdanova M, Kostareva A, Stenslokken KO, et al. Valve interstitial cells: the key to understanding the pathophysiology of heart valve calcification. *J Am Heart Assoc.* (2017) 6:e006339. doi: 10.1161/JAHA.117.006339
10. Osman L, Chester AH, Amrani M, Yacoub MH, Smolenski RT. A novel role of extracellular nucleotides in valve calcification: a potential target for atorvastatin. *Circulation.* (2006) 114(Suppl. 1):I566–72. doi: 10.1161/CIRCULATIONAHA.105.001214
11. Balachandran K, Sucosky P, Jo H, Yoganathan AP. Elevated cyclic stretch induces aortic valve calcification in a bone morphogenic protein-dependent manner. *Am J Pathol.* (2010) 177:49–57. doi: 10.2353/ajpath.2010.090631
12. Rathan S, Yoganathan AP, O'Neill CW. The role of inorganic pyrophosphate in aortic valve calcification. *J Heart Valve Dis.* (2014) 23:387–94.
13. Cloyd KL, El-Hamamsy I, Boonrungsiman S, Hedegaard M, Gentleman E, Sarathchandra P, et al. Characterization of porcine aortic valvular interstitial cell 'calcified' nodules. *PLoS ONE.* (2012) 7:e48154. doi: 10.1371/journal.pone.0048154
14. Goto S, Rogers MA, Blaser MC, Higashi H, Lee LH, Schlotter F, et al. Standardization of human calcific aortic valve disease *in vitro* modeling reveals passage-dependent calcification. *Front Cardiovasc Med.* (2019) 6:49. doi: 10.3389/fcvm.2019.00049
15. Yip CY, Chen JH, Zhao R, Simmons AC. Calcification by valve interstitial cells is regulated by the stiffness of the extracellular matrix. *Arterioscler Thromb Vasc Biol.* (2009) 29:936–42. doi: 10.1161/ATVBAHA.108.182394
16. Akiyoshi T, Ota H, Iijima K, Son BK, Kahyo T, Setou M, et al. A novel organ culture model of aorta for vascular calcification. *Atherosclerosis.* (2016) 244:51–8. doi: 10.1016/j.atherosclerosis.2015.11.005
17. Liu Y, Li J, Han Y, Chen Y, Liu L, Lang J, et al. Advanced glycation end-products suppress autophagy by AMPK/mTOR signaling pathway to promote vascular calcification. *Mol Cell Biochem.* (2020) 471:91–100. doi: 10.1007/s11010-020-03769-9
18. Venardos N, Nadlonek NA, Zhan Q, Weyant MJ, Reece TB, Meng X, et al. Aortic valve calcification is mediated by a differential response of aortic valve interstitial cells to inflammation. *J Surg Res.* (2014) 190:1–8. doi: 10.1016/j.jss.2013.11.373
19. Zheng D, Zang Y, Xu H, Wang Y, Cao X, Wang T, et al. MicroRNA-214 promotes the calcification of human aortic valve interstitial cells through the acceleration of inflammatory reactions with activated MyD88/NF-kappaB signaling. *Clin Res Cardiol.* (2019) 108:691–702. doi: 10.1007/s00392-018-1398-9
20. Parra-Izquierdo I, Castanos-Mollor I, Lopez J, Gomez C, San Roman JA, Sanchez Crespo M, et al. Lipopolysaccharide and interferon-gamma team up to activate HIF-1alpha via STAT1 in normoxia and exhibit

sex differences in human aortic valve interstitial cells. *Biochim Biophys Acta Mol Basis Dis.* (2019) 1865:2168–79. doi: 10.1016/j.bbadis.2019.04.014
21. Richards J, El-Hamamsy I, Chen S, Sarang Z, Sarathchandra P, Yacoub MH, et al. Side-specific endothelial-dependent regulation of aortic valve calcification: interplay of hemodynamics and nitric oxide signaling. *Am J Pathol.* (2013) 182:1922–31. doi: 10.1016/j.ajpath.2013.01.037
22. Zabirnyk A, Perez MDM, Blasco M, Stenslokken KO, Ferrer MD, Salcedo C, et al. A novel *ex vivo* model of aortic valve calcification. A preliminary report. *Front Pharmacol.* (2020) 11:568764. doi: 10.3389/fphar.2020.568764
23. Kruithof BPT, van de Pol V, Los T, Lodder K, Gourabi BM, DeRuiter MC, et al. New calcification model for intact murine aortic valves. *J Mol Cell Cardiol.* (2021) 156:95–104. doi: 10.1016/j.yjmcc.2021.03.003
24. Honda S, Miyamoto T, Watanabe T, Narumi T, Kadowaki S, Honda Y, et al. A novel mouse model of aortic valve stenosis induced by direct wire injury. *Arterioscler Thromb Vasc Biol.* (2014) 34:270–8. doi: 10.1161/ATVBAHA.113.302610
25. Babu AN, Meng X, Zou N, Yang X, Wang M, Song Y, et al. Lipopolysaccharide stimulation of human aortic valve interstitial cells activates inflammation and osteogenesis. *Ann Thorac Surg.* (2008) 86:71–6. doi: 10.1016/j.athoracsur.2008.03.008
26. Meng X, Ao L, Song Y, Babu A, Yang X, Wang M, et al. Expression of functional Toll-like receptors 2 and 4 in human aortic valve interstitial cells: potential roles in aortic valve inflammation and stenosis. *Am J Physiol Cell Physiol.* (2008) 294:C29–35. doi: 10.1152/ajpcell.00137.2007
27. Fisher CI, Chen J, Merryman WD. Calcific nodule morphogenesis by heart valve interstitial cells is strain dependent. *Biomech Model Mechanobiol.* (2013) 12:5–17. doi: 10.1007/s10237-012-0377-8
28. Wirrig EE, Hinton RB, Yutzey KE. Differential expression of cartilage and bone-related proteins in pediatric and adult diseased aortic valves. *J Mol Cell Cardiol.* (2011) 50:561–9. doi: 10.1016/j.yjmcc.2010.12.005
29. O'Brien KD, Kuusisto J, Reichenbach DD, Ferguson M, Giachelli C, Alpers CE, et al. Osteopontin is expressed in human aortic valvular lesions. *Circulation.* (1995) 92:2163–8. doi: 10.1161/01.CIR.92.8.2163
30. Jian B, Narula N, Li QY, Mohler ER, 3rd Levy RJ. Progression of aortic valve stenosis: TGF-beta1 is present in calcified aortic valve cusps and promotes aortic valve interstitial cell calcification via apoptosis. *Ann Thorac Surg.* (2003) 75:457–65; discussion 465–6. doi: 10.1016/S0003-4975(02)04312-6
31. Rajamannan NM, Subramaniam M, Rickard D, Stock SR, Donovan J, Springett M, et al. Human aortic valve calcification is associated with an osteoblast phenotype. *Circulation.* (2003) 107:2181–4. doi: 10.1161/01.CIR.0000070591.21548.69
32. Blaser MC, Kraler S, Luscher TF, Aikawa E. Multi-omics approaches to define calcific aortic valve disease pathogenesis. *Circ Res.* (2021) 128:1371–97. doi: 10.1161/CIRCRESAHA.120.317979
33. Kutryb-Zajac B, Jablonska P, Serocki M, Bulinska A, Mierzejewska P, Friebe D, et al. Nucleotide ecto-enzyme metabolic pattern and spatial distribution in calcific aortic valve disease; its relation to pathological changes and clinical presentation. *Clin Res Cardiol.* (2020) 109:137–60. doi: 10.1007/s00392-019-01495-x

Conflict of Interest: The authors declare that the research was conducted in the absence of any commercial or financial relationships that could be construed as a potential conflict of interest.

Publisher's Note: All claims expressed in this article are solely those of the authors and do not necessarily represent those of their affiliated organizations, or those of the publisher, the editors and the reviewers. Any product that may be evaluated in this article, or claim that may be made by its manufacturer, is not guaranteed or endorsed by the publisher.

frontiers in Cardiovascular Medicine

ORIGINAL RESEARCH
published: 06 January 2022
doi: 10.3389/fcvm.2021.743257

Predictors of Permanent Pacemaker Implantation in Patients After Transcatheter Aortic Valve Replacement in a Chinese Population

Jiaqi Zhang[1,2†], *Chengwei Chi*[2†], *Simiao Tian*[3], *Shulong Zhang*[2*] and *Jihong Liu*[2*]

[1] School of Graduate Studies, Dalian Medical University, Dalian, China, [2] Heart Center, Affiliated Zhongshan Hospital of Dalian University, Dalian, China, [3] Department of Scientific Research, Affiliated Zhongshan Hospital of Dalian University, Dalian, China

OPEN ACCESS

Edited by:
Lakshmi Prasad Dasi,
Georgia Institute of Technology,
United States

Reviewed by:
Paul Human,
University of Cape Town, South Africa
Sarvesh Chelvanambi,
Brigham and Women's Hospital and
Harvard Medical School,
United States

***Correspondence:**
Jihong Liu
8643089@qq.com
Shulong Zhang
zhangshulongmd@sina.com

[†]These authors have contributed equally to this work

Specialty section:
This article was submitted to Heart Valve Disease, a section of the journal Frontiers in Cardiovascular Medicine

Received: 18 July 2021
Accepted: 06 December 2021
Published: 06 January 2022

Citation:
Zhang J, Chi C, Tian S, Zhang S and Liu J (2022) Predictors of Permanent Pacemaker Implantation in Patients After Transcatheter Aortic Valve Replacement in a Chinese Population. Front. Cardiovasc. Med. 8:743257. doi: 10.3389/fcvm.2021.743257

Background: Permanent pacemaker (PPM) implantation is the main complication of transcatheter aortic valve replacement (TAVR). Few studies have evaluated the requirement for PPM implantation due to ECG changes following TAVR in a Chinese population.

Objective: Our study aimed to evaluate the incidence and predictors of PPM implantation in a cohort of Chinese patients with TAVR.

Methods: We retrospectively evaluated 39 consecutive patients with severe native aortic stenosis referred for TAVR with a self-expandable prosthesis, the Venus A valve (Venus MedTech Inc., Hangzhou, China), from 2019 to 2021 at the Heart Center of Affiliated Zhongshan Hospital of Dalian University. Predictors of PPM implantation were identified using logistic regression.

Results: In our study, the incidence of PPM implantation was 20.5%. PPM implantation occurs with higher risk in patients with negative creatinine clearance (CrCl), dyslipidemia, high Society of Thoracic Surgeons (STS) Morbimortality scores, and lead I T wave elevation. TAVR induced several cardiac electrical changes such as increased R wave and T wave changes in lead V5. The main independent predictors of PPM implantation were new-onset left bundle branch block (LBBB) (coef: 3.211, 95% CI: 0.899–7.467, $p = 0.004$) and lead I T wave elevation (coef: 11.081, 95% CI: 1.632–28.083, $p = 0.016$).

Conclusion: New-onset LBBB and lead I T wave elevation were the main independent predictors of PPM implantation in patients undergoing TAVR. Clinical indications such as negative CrCl, dyslipidemia, high STS Morbimortality scores, and an increased T wave elevation before TAVR should be treated with caution to decrease the need for subsequent PPM implantation.

Keywords: aortic stenosis, transcatheter aortic valve replacement, complete atrioventricular block, permanent pacemaker, predictors

INTRODUCTION

Aortic valve stenosis (AVS) has become the most prevalent acquired heart valve disease pathology (1). Transcatheter aortic valve replacement (TAVR) has been proven to be an efficient treatment for patients with severe AVS. Patients who suffer from this disease are at high-to-intermediate surgical risk (2–4). More recently, new randomized trials have broadened the clinical indications for the procedure, with its efficacy in intermediate and low-risk patients also being demonstrated (2–5). There has been a high demand for TAVR since its introduction in China. These figures are expected to exponentially increase due to the increasing age of the population (6).

This is timeous given that the first TAVR procedure has was performed in China in 2010. To date, only 3,500 patients across approximately 100 hospitals have received TAVR. Currently, self-expandable, mechanically expandable, and balloon-expandable aortic valves are clinically used in TAVR procedures in Western countries. Whereas the majority of TAVR cases in China involve self-expandable valves, investigations into the outcome of these valves in patients with AVS are lacking.

With the development of new-generation valves and operating methods, the occurrence of redo heart valve replacement, paravalvular leakage, and blood vessel complications has significantly decreased. Nevertheless, subsequent permanent pacemaker (PPM) implantation on account of complete atrioventricular block (AVB) is one of the most common complications after TAVR as diagnosed by ECG (7).

Therefore, the purpose of our study was to compare the type and frequency of ECG changes before and after TAVR and at one-month follow-up after discharge. We investigated these ECG changes to determine the main predictors of conduction disorders that lead to PPM implantation after TAVR in Chinese patients with self-expandable valves.

METHODS

Study Population

We retrospectively evaluated 47 consecutive patients with severe native aortic stenosis referred for TAVR with the self-expandable Venus A valve (Venus Med Tech Inc., Hangzhou, China) from 2019 to 2021 at the Heart Center of Affiliated Zhongshan Hospital of Dalian University. The exclusion criteria included patients with PPM prior to TAVR ($n = 2$), intraoperative mortality ($n = 1$), valve-in-valve procedures ($n = 3$), and patients where 12-lead ECGs were unavailable ($n = 2$). Considering this, only 39 patients were included in the study. Surgical indications of patients were assessed and decided upon by a multidisciplinary team of doctors consisting of cardiac surgeons, cardiologists, echocardiologists, and anesthetists. A self-expandable aortic valve was deployed using the transfemoral approach in all patients. The study was approved by the ethics committee of Affiliated Zhongshan Hospital of Dalian University. The study also complied with the Declaration of Helsinki. All patients who participated in the study signed written informed consent forms.

Electrocardiogram Analysis

All patients underwent immediate standardized (10 mm = 1 mV, 25 mm/s) 12-lead ECG before and one month post-operation with subsequent retrospective analysis of the data. Parameters included heart rate, rhythm, axis deviation, PR interval, type of AVB, QRS interval, type of bundle-branch block, QT interval, and corrected QT interval (cQT).

Statistical Analysis

Categorical variables are expressed as numbers and percentages. All continuous data were expressed as means ± standard deviation (SD) or medians ± range as appropriate. Categorical variables were compared using Chi-squared or Fisher exact tests. Continuous variables were compared with the Student's *t*-test (2-tailed) or Wilcoxon signed-rank tests as appropriate. To identify predictors of patients with PPM dependency after TAVR, logistic regression, with Firth's correction due to the small sample size, was performed. All analyses were conducted using R (version 3.2.2; R Foundation for Statistical Computing, Vienna, Austria) or SAS Statistics (version 9.4; North Carolina, America). A p-value < 0.05 was considered statistically significant.

RESULTS

The detailed clinical baseline characteristics of patients in total and with or without PPM implantation are shown in **Table 1**. The mean age of the 39 consecutive patients was 75.0 ± 8.6 years, and 53.8% of the study population was male. Nearly 70% of the patients with severe AVS were at intermediate or high surgical risk with New York Heart Association (NYHA) classification III/IV. The average EuroScore II and Society of Thoracic Surgeons (STS) Mortality scores were 7.97 ± 8.53 and 3.18 ± 2.81, respectively. No statistical differences were observed between the two groups with the exception of higher dyslipidemia and worse creatinine clearance (CrCl) in the group with PPM implantation. The STS Morbimortality scores at baseline was much higher among the patients with PPM implantation than among those without PPM implantation (with PPM 20.93 ± 8.72 vs. without PPM 13.96 ± 7.20, $p = 0.025$). Complete AVB (62.5%) was the main indication for patients with PPM implantation after TAVR. In our study, the incidence of PPM implantation was 20.5%. Among patients with PPM implantation within 30 days of undergoing the TAVR procedure, the mean time to PPM implantation after TAVR was 5.8 ± 2.8 days.

As shown in **Table 2**, evaluation of electrocardiographic parameters and echocardiographic characteristics before TAVR were analyzed. At baseline, there were no differences between the two groups based on mean aortic gradient, aortic valvular area, and valvular aortic area indexed to body surface area. Also, left ventricular ejection fraction (LVEF), left ventricular end-diastolic dimension (LVEDD), aortic root diameter (AO), left ventricular posterior wall thickness (PWT), and interventricular septum thickness (IVST) were comparable between the two groups. There was a larger amplitude of the T wave on lead I before TAVR in the patients with PPM implantation than in the patients without PPM implantation (with PPM 0.10 ± 0.17 mv vs. without

TABLE 1 | Baseline characteristics according to the group of study population: Total, without permanent pacemaker (PPM) and with PPM.

	Total ($n = 39$)	Without pacemaker ($n = 31$)	With pacemaker ($n = 8$)	p value
Age, years	75.0 ± 8.6	74.3 ± 9.1	77.9 ± 6.0	0.293
Male gender	21 (53.8)	17 (54.8)	4 (50)	0.807
Heart Failure, NYHA Class I/II	3 (7.7)/8 (20.5)	3 (9.7)/6 (19.4)	0/2(25)	0.642
NYHA Class III/IV	14 (35.9)/14 (35.9)	9 (29)/11(41.3)	5 (62.5)/1(12.5)	0.169
Dyslipidemia	24 (61.5)	16 (51.6)	8 (100)	0.015
DM	13 (33.3)	11 (35.5)	2 (25)	0.694
CrCl, ml/minute	59.58 ± 28.38	74.78 ± 26.94	49.42 ± 26.02	0.022
COPD	3 (7.7)	1 (3.2)	2 (25)	0.101
Stroke	13 (33.3)	10 (32.3)	3 (37.5)	0.779
PVD	12 (30.8)	9 (29)	3 (37.5)	0.682
CAD	23 (59)	20 (64.5)	3 (37.5)	0.235
AF	9 (23.1)	6 (19.4)	3 (37.5)	0.355
Previousvalvular replacement surgery	1 (2.6)	1 (3.2)	0	0.607
Need for urgent aortic valvular intervention	1 (2.6)	0	1 (12.5)	0.205
Risk evaluation:				
EuroScore II	7.97 ± 8.53	6.74 ± 7.59	12.72 ± 10.73	0.077
STS Mortality	3.18 ± 2.81	2.97 ± 3.01	4.00 ± 1.81	0.364
STS Morbimortality	15.39 ± 7.94	13.96 ± 7.20	20.93 ± 8.72	0.025

Data are presented as mean ± SD or n (%) as appropriate. NYHA, New York Heart Association heart failure classification; DM, diabetes mellitus; CrCl, creatinine clearance; COPD, chronic obstructive pulmonary disease; PVD, peripheral vascular disease; CAD, coronary artery disease; AF, atrial fibrillation (paroxysmal or permanent).

PPM −0.07 ± 0.19 mv, $p = 0.028$). No other significant statistical differences were found between the two groups at baseline.

Table 3 shows the pattern of electrocardiographic changes in patients before and after TAVR. Our study did not identify any significant differences in the incidence of electrocardiographic conduction disturbances, such as new-onset atrial fibrillation (AF), new-onset 1st degree AV block, new-onset right bundle branch block (RBBB), or new-onset left anterior fascicular block (LAFB), with the exception of new-onset left bundle branch block (LBBB) (without PPM 22.6% vs. with PPM 75%, $p < 0.001$), as shown in **Table 3**.

Figure 1 summarizes the results involving predictors for patients having PPM implantation after TAVR. The main independent predictors of PPM implantation were new-onset LBBB (coef: 3.211, 95% CI: 0.899–7.467, $p = 0.004$) and T wave magnitude in lead I (coef: 11.081, 95% CI: 1.632–28.083, $p = 0.016$).

DISCUSSION

In the present study of 39 patients with self-expandable valves, we analyzed clinical data, echocardiographic characteristics, and electrocardiographic parameters. Four main findings of our study demonstrated that (1) the total rate of PPM implantation in our consecutive patients was 20.5%; (2) PPM implantation occurs with higher risk in patients with negative CrCl, dyslipidemia, high STS Morbimortality scores, and increased T wave magnitude in lead I; (3) TAVR induced several cardiac electrical changes, such as increased R wave and T wave changes in lead V5; and (4) new-onset LBBB and T wave magnitude in lead I were the main independent predictors of PPM implantation in patients undergoing TAVR.

Indications for PPM Implantation

The most common indication for PPM implantation in those who underwent TAVR was complete AVB in our study, which had also been demonstrated previously (7, 8). Consistent with previous data, a sick sinus syndrome (37.5%), including relevant sinus and bradycardia, was a leading indication in patients who underwent PPM implantation (9).

The anatomic relationship between the aortic valve and the cardiac conduction system is the foundation of the conduction disturbances in patients undergoing TAVR. Anatomically, the proximity of this portion of the atrioventricular node (AVN), the bundle of His, and the membranous part of the interventricular septum makes it more susceptible to conduction disturbances. The left bundle branch is close to the bottom of the interleaflet triangle together with the location of the right coronary leaflets and non coronary aortic valve (10–12). The incidence of complete AVB after TAVR is due to a direct mechanical injury to the AVN and/or the left bundle branch that results in ischemia, edema, and hematoma according to necropsy studies (10). Due to the invention of a self-expandable valve possessing a subannular section, the release of the valve will produce radial force to the left ventricular outflow tract (LVOT). The implantation of a self-expandable valve may lead to conduction block (13). Therefore, it is crucial to improve the surgical manipulations among experienced surgeons in order to decrease the risk of complete AVB after TAVR.

TABLE 2 | Echocardiographic characteristics and electrocardiographic parameters.

	Total ($n = 39$)	Without pacemaker ($n = 31$)	With pacemaker($n = 8$)	p value
Mean aortic gradient (mmHg)	49.85 ± 21.54	52.90 ± 22.03	38.00 ± 15.37	0.081
Aortic valvular area (cm2)	0.67 ± 0.23	0.65 ± 0.24	0.73 ± 0.18	0.409
Valvular aortic area indexed to body surface area (cm2/m2)	0.38 ± 0.14	0.36 ± 0.14	0.42 ± 0.12	0.298
LVEF (%)	51.92 ± 13.05	52.16 ± 13.05	51.00 ± 13.87	0.826
LVEDD (mm)	52.15 ± 9.69	51.39 ± 9.46	55.13 ± 10.64	0.337
AO (mm)	20.10 ± 2.11	20.35 ± 2.14	19.13 ± 1.81	0.144
PWT (mm)	12.54 ± 2.21	12.52 ± 2.31	12.63 ± 1.92	0.903
IVST (mm)	13.44 ± 2.79	13.52 ± 3.04	13.13 ± 1.55	0.729
Heart Rate (bpm)	73.44 ± 15.72	72.65 ± 16.39	76.50 ± 13.27	0.543
Sinus	32 (82.1)	26 (83.9)	6 (75)	0.617
AF	4 (10.3)	2 (6.5)	2 (25)	0.180
Other atrial rhythm	2 (5.1)	2 (6.5)	0	0.461
Abnormal cardiac electric axis	22 (56.4)	17 (54.8)	5(62.5)	0.697
PR Interval (ms)	166.11 ± 47.28	162.21 ± 50.38	185.00 ± 21.64	0.289
1° AVB	5 (12.8)	4 (12.9)	1(12.5)	0.976
S1 (mv)	1.75 ± 0.83	1.80 ± 0.84	1.57 ± 0.78	0.477
S2 (mv)	2.47 ± 1.71	2.44 ± 1.87	2.56 ± 0.99	0.875
S3 (mv)	1.97 ± 1.27	1.98 ± 1.36	1.93 ± 0.92	0.930
R5 (mv)	2.49 ± 1.01	2.48 ± 1.00	2.54 ± 1.09	0.878
R6 (mv)	2.06 ± 0.86	2.05 ± 0.93	2.10 ± 0.59	0.882
I ST (mv)	−0.05 ± 0.07	−0.05 ± 0.08	−0.05 ± 0.04	0.915
aVL ST (mv)	−0.05 ± 0.07	−0.04 ± 0.08	−0.07 ± 0.05	0.326
V5 ST (mv)	−0.10 ± 0.12	−0.10 ± 0.14	−0.11 ± 0.07	0.847
V6 ST (mv)	−0.11 ± 0.12	−0.10 ± 0.13	−0.11 ± 0.06	0.865
T wave in lead I (mv)	−0.03 ± 0.20	−0.07 ± 0.19	0.10 ± 0.17	0.028
T wave in lead avL (mv)	−0.06 ± 0.17	−0.07 ± 0.16	−0.01 ± 0.23	0.322
T wave in lead V5 (mv)	−0.06 ± 0.45	−0.12 ± 0.46	0.17 ± 0.36	0.103
T wave in lead V6 (mv)	−0.04 ± 0.39	−0.05 ± 0.41	−0.002 ± 0.30	0.760
QRS Complex (ms)	104.13 ± 22.97	104.81 ± 24.50	101.50 ± 16.83	0.722
LBBB	3 (7.7)	3 (9.7)	0	0.360
RBBB	5 (12.8)	3 (9.7)	2 (25)	0.268
LAFB	2 (5.1)	1 (3.2)	1 (12.5)	0.372
QT interval (ms)	417.44 ± 56.34	418.58 ± 57.31	413.00 ± 55.91	0.807
cQT interval (ms)	456.21 ± 43.02	451.73 ± 44.97	473.50 ± 30.77	0.206

Data are presented as mean ± SD or n (%) as appropriate. LVEF, left ventricular ejection fraction; LVEDD, left ventricular end-diastolic dimension; AO, aortic root diameter; PWT, left ventricular posterior wall thickness; IVST, interventricular septum thickness; AF, atrial fibrillation; 1° AVB, first degree atrioventricular block; S1, S wave magnitude in lead V1; S2, S wave magnitude in lead V2; S3, S wave magnitude in lead V3; R5, R wave magnitude in lead V5; R6, R wave magnitude in lead V6; I ST, ST-segment in lead I; aVL ST, ST-segment in lead aVL; V5 ST, ST-segment in lead V5; V6 ST, ST-segment in lead V6; LBBB, left bundle branch block; RBBB, right bundle branch block; LAFB, left anterior fascicular block; cQT interval, corrected QT interval.

Abnormal Clinical Indications for PPM Implantation

Patients with a higher burden of PPM implantation following TAVR had a higher prevalence of abnormal clinical indications. Some abnormal clinical data before the procedure may be related to injury within the underlying conduction system during TAVR (11). Du et al. (12) demonstrated that patients with prior LBBB had a relatively higher risk of PPM implantation in the Chinese population. Gaede et al. (9) summarized that patients who already had aortic valve replacement prior to TAVR required a PPM implantation less frequently. Our study showed that severe AVS patients who required PPM following TAVR were likely to present with dyslipidemia and negative CrCl. STS Morbimortality also played an important role in evaluating patients with a high frequency of conduction disturbances after TAVR.

Previous studies have reported that renal dysfunction at baseline predicted a higher increase of myocardial injury after the procedure. Additionally, myocardial injury after TAVR could lead to conduction disturbances, which may contribute to the need for PPM implantation (14–16). Thus, lower average CrCl may lead to worse kidney function at baseline, which plays an important role in patients requiring PPM implantation after TAVR. Lindman et al. (17) showed that elevated blood lipid

parameters were associated with higher risks of calcific AVS. On account of the thickening and remodeling of the aortic valve leaflets, the formation of calcific AVS will cause severe cardiac outflow tract stenosis. Prosthesis implantation may produce radial force to the cardiac outflow tract, which results in conduction block. It is therefore recommended that doctors focus more attention on reducing the risk factors before TAVR to decrease the need for subsequent PPM implantation.

Predictors of PPM Implantation After TAVR

Few studies have evaluated the relationship between new-onset LBBB and the risk of PPM implantation after TAVR. In our cohort, a new-onset LBBB and T wave magnitude in lead I were the predictors for the patients requiring a PPM implantation after TAVR. However, prior RBBB at baseline was identified as an independent predictor in some previous studies (7, 11, 18, 19). In contrast to our study, smaller studies have shown that prior RBBB plays an important role in cardiac conduction system disorders after TAVR (8, 9, 20, 21).

TABLE 3 | Procedural related electrocardiographic conduction disturbances.

	Total ($n = 39$)	Without pacemaker ($n = 31$)	With pacemaker ($n = 8$)	p value
New-onset AF	7 (17.9)	5 (16.1)	2 (25)	0.617
New-onset 1° AVB	8 (20.5)	5 (16.1)	3 (37.5)	0.323
New-onset LBBB	13 (33.3)	7 (22.6)	6 (75)	<0.001
New-onset RBBB	4 (10.3)	4 (12.9)	0	0.284
New-onset LAFB	2 (5.1)	2 (6.5)	0	0.461

Data are presented as mean ± SD or n (%) as appropriate. AF, atrial fibrillation; 1° AVB, first degree atrioventricular block; LBBB, left bundle branch block; RBBB, right bundle branch block; LAFB, left anterior fascicular block.

The predictors of PPM implantation in patients receiving TAVR have been examined in seven studies (9, 12, 22–26). All studies were cohort studies. RBBB prior to TAVR was considered to be a predictor in most of the selected studies (9, 12, 22, 24, 26) in **Table 4**. However, the association of new-onset LBBB with PPM implantation after TAVR has not been fully characterized. A study by Chorianopoulos et al. (22), in which 46 patients with PPM implantation and 83 patients without PPM implantation were enrolled, showed that prior RBBB was the only predictor. A retrospective cohort study by Muillet et al. (23) showed that post-TAVR QRS duration and depth of implantation were the predictors of PPM implantation in patients receiving TAVR. In a cohort study by Luise Gaede et al. (9), in which 176 patients with PPM implantation and 849 patients without PPM implantation were enrolled, not only prior RBBB but also higher MPG and post-dilatation of the prosthesis were observed to be the predictors. A study focusing on 38 Chinese patients with PPM implantation and 218 Chinese patients without PPM implantation showed that prior RBBB, tricuspid aortic valve (TAV), and implantation depth at the non-coronary sinus side were the predictors, especially in Chinese population (12). The study of Kiani S, et al. (24) showed the history of syncope, prior RBBB, QRS duration ≥138 ms, and valve oversizing >15.6% were the predictors. Ferreira T et al. (25) demonstrated that increased H-V interval, which showed in post-TAVR electrophysiological study, was the best predictor of PPM implantation undergoing TAVR. A previous study by Johny Nicolas et al. (26) showed that RBBB before TAVR was the only predictor.

A positive correlation between PPM implantation after TAVR and new-onset LBBB was demonstrated in our study. However, no correlation was found between PPM implantation and prior RBBB or 1° AVB. We attribute the finding to mechanical injury that mainly affected the left bundle branch. Preexisting damage to the right bundle branch may lead to

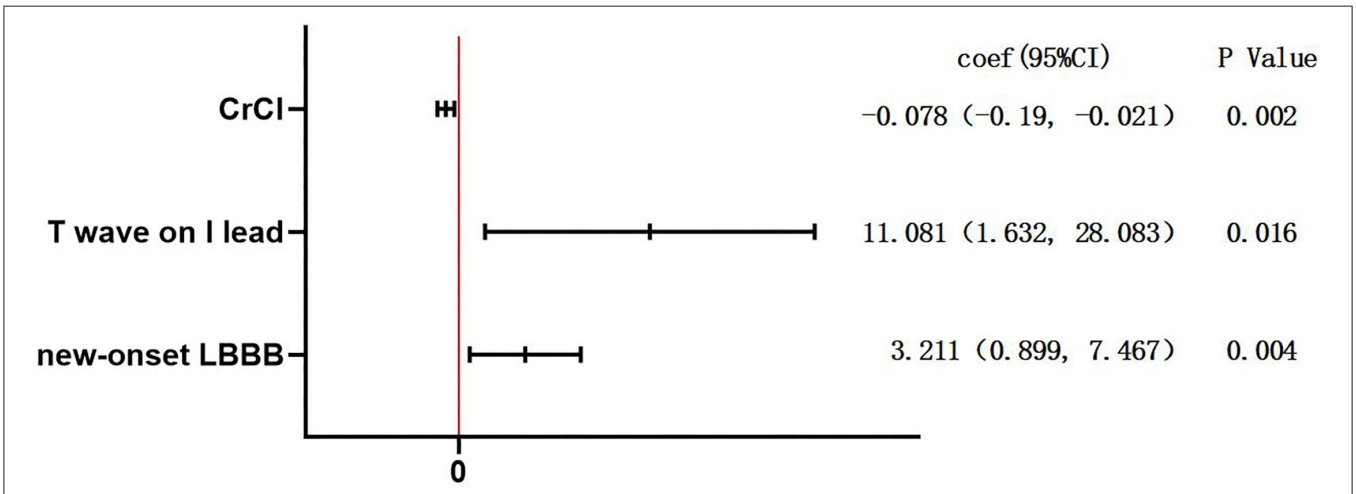

FIGURE 1 | Multiple logistic regression analysis for the predictors of permanent pacemaker (PPM) implantation. To identify predictors of patients with PPM dependency after transcatheter aortic valve replacement (TAVR), logistic regression, with Firth's correction due to the small sample size, was performed. The variables to the right of the red line were predictors of PPM implantation. CrCl, creatinine clearance; LBBB, left bundle branch block.

TABLE 4 | Summary of studies regarding predictors of Permanent Pacemaker Implantation after TAVR.

Authors	Year	Country	Study design	Groups	Numbers of subjects	Predictors	Ref
Chorianopoulos et al. (22)	2012	Germany	Cohort	With PPM	46	prior RBBB	22
				Without PPM	83		
Mouillet et al. (23)	2013	France	Cohort	With PPM	21	Post-TAVR, QRS duration, Depth of implantation	23
				Without PPM	58		
Gaede et al. (9)	2017	Germany	Cohort	With PPM	176	prior RBBB, higher mean aortic gradient and post- dilatation of the prosthesis	9
				Without PPM	849		
Du et al. (12)	2019	China	Cohort	With PPM	38	prior RBBB, TAV, implantation depth at the noncoronary sinus side	12
				Without PPM	218		
Kiani et al. (24)	2019	America	Cohort	With PPM	57	history of syncope, prior RBBB, QRS duration ≥138 ms, valve oversizing >15.6%	24
				Without PPM	721		
Ferreira et al. (25)	2020	France	Cohort	With PPM	21	HV interval	25
				Without PPM	53		
Nicolas et al. (26)	2020	The Netherlands	Cohort	With PPM	132	prior RBBB	26
				Without PPM	790		

PPM, permanent pacemaker; TAVR, transcatheter aortic valve replacement; TAV, tricuspid aortic valve; HV, His to ventricle.

complete AVB when exposed to TAVR. The mechanism of the relationship between T wave magnitude in lead I and PPM implantation is unknown. Meanwhile, other predictors, including the type of the valve and the depth of prosthesis implantation, were not confirmed in our cohort (27–30). To date, no detailed guidelines for the management of new-onset LBBB following TAVR are available. Consequently, any recommendation about the management of new-onset LBBB after TAVR should be treated with caution and further investigation is warranted.

Study Limitations

The limitations of our study are as follows. First, our study had a small sample size and a short follow-up time. The patients undergoing TAVR were also from a single center. The numbers of patients with PPM implantation and without PPM implantation were low, which limits the statistics of the study. However, the data were revised with Firth's correction due to the small sample size. All analyses were conducted using R (version 3.2.2; R Foundation for Statistical Computing, Vienna, Austria) or SAS Statistics (version 9.4; North Carolina, America). Thus, we strongly believe that our findings are reliable. Second, following discharge, we observed the patients only after a one-month follow-up. The interpretation may differ based on six-month or one-year follow-up periods. Finally, other variables, such as the position of the valve and valve type, may have generated a significant variation to the risk of conduction abnormalities after TAVR. Although our study cohort was small, only involved a single center, and was limited to a short follow-up time, we strongly believe that our findings are representative and may assist in providing valuable insight toward future identification of high-risk cases requiring PPM. Hence, our findings about PPM implantation after TAVR contributes to not only patients but also doctors for improving the postoperative quality of life of patients.

CONCLUSIONS

The overall incidence of PPM implantation in our consecutive patients was 20.5%. PPM implantation occurs with higher risk in patients with negative CrCl, dyslipidemia, high STS Morbimortality score, and increased T wave magnitude in lead I. TAVR induced several cardiac electrical changes, such as increased R wave and T wave changes in lead V5. New-onset LBBB and T wave magnitude in lead I were the main independent predictors of PPM implantation in patients undergoing TAVR.

DATA AVAILABILITY STATEMENT

The raw data supporting the conclusions of this article will be made available by the authors, without undue reservation.

ETHICS STATEMENT

The studies involving human participants were reviewed and approved by the Ethics Committee of Affiliated Zhongshan Hospital of Dalian University. The patients/participants provided their written informed consent to participate in this study.

AUTHOR CONTRIBUTIONS

JZ, CC, and ST: conceptualization and methodology. JZ and CC: investigation and writing—original draft. JZ: writing—review and English editing. ST, SZ, and JL: supervision. All authors contributed to the article and approved the submitted version.

SUPPLEMENTARY MATERIAL

The Supplementary Material for this article can be found online at: https://www.frontiersin.org/articles/10.3389/fcvm.2021.743257/full#supplementary-material

REFERENCES

1. Goody PR, Hosen MR, Christmann D, Niepmann ST, Zietzer A, Adam M, et al. Aortic valve stenosis: from basic mechanisms to novel therapeutic targets. *Arterioscler Thromb Vasc Biol.* (2020) 40:885–900. doi: 10.1161/ATVBAHA.119.313067
2. Arora S, Vavalle JP. Transcatheter aortic valve replacement in intermediate and low risk patients-clinical evidence. *Ann Cardiothorac Surg.* (2017) 6:493–7. doi: 10.21037/acs.2017.07.01
3. Smith CR, Leon MB, Mack MJ, Miller DC, Moses JW, Svensson LG, et al. Transcatheter versus surgical aortic-valve replacement in high-risk patients. *N Engl J Med.* (2011) 364:2187–98. doi: 10.1056/NEJMoa1103510
4. Leon MB, Smith CR, Mack M, Miller DC, Moses JW, Svensson LG, et al. Transcatheter aortic-valve implantation for aortic stenosis in patients who cannot undergo surgery. *N Engl J Med.* (2010) 363:1597–607. doi: 10.1056/NEJMoa1008232
5. Chamandi C, Barbanti M, Munoz-Garcia A, Latib A, Nombela-Franco L, Gutiérrez-Ibanez E, et al. Long-term outcomes in patients with new-onset persistent left bundle branch block following TAVR. *JACC Cardiovasc Interv.* (2019) 12:1175–84. doi: 10.1016/j.jcin.2019.03.025
6. Thaden JJ, Nkomo VT, Enriquez-Sarano M. The global burden of aortic stenosis. *Prog Cardiovasc Dis.* (2014) 56:565–71. doi: 10.1016/j.pcad.2014.02.006
7. Nazif TM, Dizon JM, Hahn RT, Xu K, Babaliaros V, Douglas PS, et al. Predictors and clinical outcomes of permanent pacemaker implantation after transcatheter aortic valve replacement: the PARTNER (Placement of AoRtic TraNscathetER Valves) trial and registry. *JACC Cardiovasc Interv.* (2015) 8:60–9. doi: 10.1016/j.jcin.2014.07.022
8. Erkapic D, De Rosa S, Kelava A, Lehmann R, Fichtlscherer S, Hohnloser SH. Risk for permanent pacemaker after transcatheter aortic valve implantation: a comprehensive analysis of the literature. *J Cardiovasc Electrophysiol.* (2012) 23:391–7. doi: 10.1111/j.1540-8167.2011.02211.x
9. Gaede L, Kim WK, Liebetrau C, Dörr O, Sperzel J, Blumenstein J, et al. Pacemaker implantation after TAVI: predictors of AV block persistence. *Clin Res Cardiol.* (2018) 107:60–9. doi: 10.1007/s00392-017-1158-2
10. Auffret V, Puri R, Urena M, Chamandi C, Rodriguez-Gabella T, Philippon F, et al. Conduction disturbances after transcatheter aortic valve replacement: current status and future perspectives. *Circulation.* (2017) 136:1049–69. doi: 10.1161/CIRCULATIONAHA.117.028352
11. Chen S, Chau KH, Nazif TM. The incidence and impact of cardiac conduction disturbances after transcatheter aortic valve replacement. *Ann Cardiothorac Surg.* (2020) 9:452–67. doi: 10.21037/acs-2020-av-23
12. Du F, Zhu Q, Jiang J, Chen H, Liu X, Wang J. Incidence and predictors of permanent pacemaker implantation in patients who underwent transcatheter aortic valve replacement: observation of a chinese population. *Cardiology.* (2020) 145:27–34. doi: 10.1159/000502792
13. Tzamtzis S, Viquerat J, Yap J, Mullen MJ, Burriesci G. Numerical analysis of the radial force produced by the Medtronic-CoreValve and Edwards-SAPIEN after transcatheter aortic valve implantation (TAVI). *Med Eng Phys.* (2013) 35:125–30. doi: 10.1016/j.medengphy.2012.04.009
14. De Marzo V, Crimi G, Vercellino M, Benenati S, Pescetelli F, Della Bona R, et al. Impact of bioprosthetic valve type on peri-procedural myocardial injury and mortality after transcatheter aortic valve replacement. *Heart Vessels.* (2021). doi: 10.2459/JCM.0000000000001178
15. Stundl A, Schulte R, Lucht H, Weber M, Sedaghat A, Shamekhi J, et al. Periprocedural myocardial injury depends on transcatheter heart valve type but does not predict mortality in patients after transcatheter aortic valve replacement. *JACC Cardiovasc Interv.* (2017) 10:1550–60. doi: 10.1016/j.jcin.2017.05.029
16. Nara Y, Watanabe Y, Kataoka A, Nakashima M, Hioki H, Nagura F, et al. Incidence, predictors, and midterm clinical outcomes of myocardial injury after transcatheter aortic-valve implantation. *Int Heart J.* (2018) 59:1296–302. doi: 10.1536/ihj.17-645
17. Lindman BR, Clavel MA, Mathieu P, Iung B, Lancellotti P, Otto CM. et al. Calcific aortic stenosis. *Nat Rev Dis Primers.* (2016) 2:16006. doi: 10.1038/nrdp.2016.6
18. Mauri V, Reimann A, Stern D, Scherner M, Kuhn E, Rudolph V, et al. Predictors of Permanent Pacemaker Implantation After Transcatheter Aortic Valve Replacement With the SAPIEN 3. *JACC Cardiovasc Interv.* (2016) 9:2200–9. doi: 10.1016/j.jcin.2016.08.034
19. Keßler M, Gonska B, Seeger J, Rottbauer W, Wöhrle J. Predictors of permanent pacemaker implantation after transfemoral aortic valve implantation with the Lotus valve. *Am Heart J.* (2017) 192:57–63. doi: 10.1016/j.ahj.2017.07.011
20. Fraccaro C, Buja G, Tarantini G, Gasparetto V, Leoni L, Razzolini R, et al. Incidence, predictors, and outcome of conduction disorders after transcatheter self-expandable aortic valve implantation. *Am J Cardiol.* (2011) 107:747–54. doi: 10.1016/j.amjcard.2010.10.054
21. Boerlage-Van Dijk K, Kooiman KM, Yong ZY, Wiegerinck EM, Damman P, Bouma BJ, et al. Predictors and permanency of cardiac conduction disorders and necessity of pacing after transcatheter aortic valve implantation. *Pacing Clin Electrophysiol.* (2014) 37:1520–9. doi: 10.1111/pace.12460
22. Chorianopoulos E, Krumsdorf U, Pleger ST, Katus HA, Bekeredjian R. Incidence of late occurring bradyarrhythmias after TAVI with the self-expanding CoreValve(®) aortic bioprosthesis. *Clin Res Cardiol.* (2012) 101:349–55. doi: 10.1007/s00392-011-0398-9
23. Mouillet G, Lellouche N, Lim P, Meguro K, Yamamoto M, Deux J, et al. Patients without prolonged QRS after TAVI with CoreValve device do not experience high-degree atrio-ventricular block. *Catheter Cardiovasc Interv.* (2013) 81:882–7. doi: 10.1002/ccd.24657
24. Kiani S, Kamioka N, Black GB, Lu MLR, Lisko JC, Rao B, et al. Development of a risk score to predict new pacemaker implantation after transcatheter aortic valve replacement. *JACC Cardiovasc Interv.* (2019) 12:2133–42. doi: 10.1016/j.jcin.2019.07.015
25. Ferreira T, Da Costa A, Cerisier A, Vidal N, Guichard JB, Romeyer C, et al. Predictors of high-degree conduction disturbances and pacemaker implantation after transcatheter aortic valve replacement: Prognostic role of the electrophysiological study. *Pacing Clin Electrophysiol.* (2021) 44:843–55. doi: 10.1111/pace.14225
26. Nicolas J, Guedeney P, Claessen BE, Mehilli J, Petronio AS, Sartori S, et al. Incidence, predictors and clinical impact of permanent pacemaker insertion in women following transcatheter aortic valve implantation: Insights from a prospective multinational registry. *Catheter Cardiovasc Interv.* (2021) 98:E908–17. doi: 10.1002/ccd.29807
27. Schymik G, Tzamalis P, Bramlage P, Heimeshoff M, Würth A, Wondraschek R, et al. Clinical impact of a new left bundle branch block following TAVI implantation: 1-year results of the TAVIK cohort. *Clin Res Cardiol.* (2015) 104:351–62. doi: 10.1007/s00392-014-0791-2
28. Husser O, Pellegrini C, Kessler T, Burgdorf C, Thaller H, Mayr NP, et al. Predictors of permanent pacemaker implantations and new-onset conduction abnormalities with the SAPIEN 3 balloon-expandable transcatheter heart valve. *JACC Cardiovasc Interv.* (2016) 9:244–54. doi: 10.1016/j.jcin.2015.09.036
29. Rodríguez-Olivares R, van Gils L, El Faquir N, Rahhab Z, Di Martino LF, van Weenen S, et al. Importance of the left ventricular outflow tract in the need for pacemaker implantation after transcatheter aortic valve replacement. *Int J Cardiol.* (2016) 216:9–15. doi: 10.1016/j.ijcard.2016.04.023
30. Manuel AM, Almeida J, Guerreiro C, Dias T, Barbosa A, Teixeira P, et al. The effects of transcatheter aortic valve implantation on cardiac electrical properties. *Rev Port Cardiol (Engl Ed).* (2020) 39:431–40. doi: 10.1016/j.repc.2020.02.011

Conflict of Interest: The authors declare that the research was conducted in the absence of any commercial or financial relationships that could be construed as a potential conflict of interest.

frontiers | Frontiers in Cardiovascular Medicine

ORIGINAL RESEARCH
published: 19 July 2022
doi: 10.3389/fcvm.2022.770065

Increased TGFβ1 and SMAD3 Contribute to Age-Related Aortic Valve Calcification

*Mrinmay Chakrabarti[1], Aniket Bhattacharya[1,2], Mengistu G. Gebere[1], John Johnson[1], Zeeshan A. Ayub[1], Ioulia Chatzistamou[3], Narendra R. Vyavahare[4] and Mohamad Azhar[1,5]**

[1] Department of Cell Biology and Anatomy, School of Medicine, University of South Carolina, Columbia, SC, United States, [2] Department of Neuroscience and Cell Biology, Child Health Institute of New Jersey Rutgers-Robert Wood Johnson Medical School, New Brunswick, NJ, United States, [3] Department of Pathology, Microbiology, and Immunology, School of Medicine, University of South Carolina, Columbia, SC, United States, [4] Biomedical Engineering, Clemson University, Clemson, SC, United States, [5] William Jennings Bryan Dorn VA Medical Center, Columbia, SC, United States

OPEN ACCESS

Edited by:
Katherine Yutzey,
Cincinnati Children's Hospital Medical Center, United States

Reviewed by:
Robert J. Levy,
Children's Hospital of Philadelphia, United States
Brendan Martin Corcoran,
University of Edinburgh, United Kingdom

***Correspondence:**
Mohamad Azhar
Mohamad.Azhar@uscmed.sc.edu

Specialty section:
This article was submitted to Heart Valve Disease, a section of the journal Frontiers in Cardiovascular Medicine

Received: 03 September 2021
Accepted: 20 June 2022
Published: 19 July 2022

Citation:
Chakrabarti M, Bhattacharya A, Gebere MG, Johnson J, Ayub ZA, Chatzistamou I, Vyavahare NR and Azhar M (2022) Increased TGFβ1 and SMAD3 Contribute to Age-Related Aortic Valve Calcification. Front. Cardiovasc. Med. 9:770065. doi: 10.3389/fcvm.2022.770065

Aims: Calcific aortic valve disease (CAVD) is a progressive heart disease that is particularly prevalent in elderly patients. The current treatment of CAVD is surgical valve replacement, but this is not a permanent solution, and it is very challenging for elderly patients. Thus, a pharmacological intervention for CAVD may be beneficial. In this study, we intended to rescue aortic valve (AV) calcification through inhibition of TGFβ1 and SMAD3 signaling pathways.

Methods and Results: The *klotho* gene, which was discovered as an aging-suppressor gene, has been observed to play a crucial role in AV calcification. The *klotho* knockout ($Kl^{-/-}$) mice have shorter life span (8–12 weeks) and develop severe AV calcification. Here, we showed that increased TGFβ1 and TGFβ-dependent SMAD3 signaling were associated with AV calcification in $Kl^{-/-}$ mice. Next, we generated *Tgfb1*- and *Smad3*-haploinsufficient $Kl^{-/-}$ mice to determine the contribution of TGFβ1 and SMAD3 to the AV calcification in $Kl^{-/-}$ mice. The histological and morphometric evaluation suggested a significant reduction of AV calcification in $Kl^{-/-}$; $Tgfb1^{\pm}$ mice compared to $Kl^{-/-}$ mice. *Smad3* heterozygous deletion was observed to be more potent in reducing AV calcification in $Kl^{-/-}$ mice compared to the $Kl^{-/-}$; $Tgfb1^{\pm}$ mice. We observed significant inhibition of *Tgfb1*, *Pai1*, *Bmp2, Alk2*, *Spp1*, and *Runx2* mRNA expression in $Kl^{-/-}$; $Tgfb1^{\pm}$ and $Kl^{-/-}$; $Smad3^{\pm}$ mice compared to $Kl^{-/-}$ mice. Western blot analysis confirmed that the inhibition of TGFβ canonical and non-canonical signaling pathways were associated with the rescue of AV calcification of both $Kl^{-/-}$; $Tgfb1^{\pm}$ and $Kl^{-/-}$; $Smad3^{\pm}$ mice.

Conclusion: Overall, inhibition of the TGFβ1-dependent SMAD3 signaling pathway significantly blocks the development of AV calcification in $Kl^{-/-}$ mice. This information is useful in understanding the signaling mechanisms involved in CAVD.

Keywords: *Tgfb* = transforming growth factor beta, *Smad3*, Klotho, CAVD (calcific aortic valve disease), aortic valve calcification

INTRODUCTION

Calcific aortic valve disease (CAVD) is a progressive heart disease in which aortic valve sclerosis progresses to aortic valve stenosis with severe calcification and impaired leaflet function (1–5). The aortic valve (AV) calcification affects 25% of the population over 65 years of age and about 50% of those over 85 years (2). Surgical valve replacement is the most effective treatment for valvular heart disease (6). Old age and chronic kidney disease (CKD) are important risk factors for CAVD (1). The serum levels of klotho (KL) decrease in CKD patients with heart valve calcification and therefore klotho is considered an independent risk factor for CAVD in CKD (7). The *klotho* gene (*Kl*) is identified as an anti-aging gene in mice that prolongs the life span (8). Since its serendipitous discovery, *klotho* has drawn significant attention owing to its potential role in aging, chronic kidney disease (CKD), and several cardiovascular diseases (9, 10). Earlier investigations indicated that *klotho* expresses predominantly in the distal tubular epithelial cells of the kidney (11, 12). Another study has confirmed klotho expression in human artery and cardiac myocytes (10). Functions of klotho include regulation of energy metabolism, anti-inflammatory and anti-oxidative effects, modulation of ion transport, and regulation of mineral metabolism (13). Several reports also endorsed the protective role of *klotho* in several organs as well as reversal of disease mechanisms including cardiovascular disease (14). The *Kl* encodes a single-pass transmembrane protein of 135 kDa. The klotho protein is clipped on the cell surface by membrane-anchored proteases and the entire extracellular domain (∼130 kDa) is released into the systemic circulation (8, 15, 16). Thus, klotho protein exists in two forms: membrane-bound klotho and secreted klotho (10, 17). More probably, membrane klotho solely serves as a co-receptor for the binding to fibroblast growth factor 23 (FGF23) (18). FGF23 is a bone-derived hormone that acts on kidney to stimulate phosphate elimination into urine and inhibit vitamin D synthesis, thereby modulating negative phosphate balance (19, 20). One significant characteristic of FGF23 is that it has very poor affinity to FGF receptors (21, 22). Binding of membrane klotho generates a constitutive binary complex with FGF receptors (FGFRs) which creates a *de novo* high-affinity binding site for FGF23 (22). Thus, FGF23 requires membrane klotho to bind to its cognate FGF receptors and exert its biological activity (22). The klotho ($Kl^{-/-}$) and/or *Fgf23* ($Fgf23^{-/-}$) knockout mice exhibit many key aspects associated with human CAVD including, premature aging, kidney disease, increased serum phosphate levels (i.e., hyperphosphatemia), and increased osteogenic gene expression (7, 23, 24). The $Kl^{-/-}$ mice die by 12 weeks of age due to multiple age-related complications. The $Kl^{-/-}$ mice develop calcific nodules in the AV hinge and aortic annulus, but they do not show significant AV leaflet thickening, extracellular matrix (ECM) disorganization, or inflammation (25). In addition, the $Kl^{-/-}$ mice also develop ectopic calcification of aorta and kidneys (26). It has been reported that valve interstitial cells (VIC) in the calcified AV hinge in $Kl^{-/-}$ mice become activated and express several pro-calcific markers, including COX2, RUNX2, osteopontin (OPN1/SPP1), and alkaline phosphatase (ALP). Recently, $Kl^{-/-}$ mice have been successfully used in preclinical testing of potential new drugs for AV calcification (27). Since CKD is associated with klotho and human CAVD (28) and the AV calcification in $Kl^{-/-}$ mice resembles human CAVD (29), the $Kl^{-/-}$ mice are useful mouse models for investigating the mechanisms involved in pathogenesis of CAVD (29, 30).

Surgical specimens of the aortic valve (AV) obtained from older patients with CAVD have increased levels of transforming growth factor beta1 (TGFβ1) (31–37). Elevated TGFβ1 levels are frequently observed during vascular calcification and CKD (38–40) and contribute to the progression of calcification of cardiovascular tissues (41, 42). Both AV calcification and vascular calcification are regarded as the crucial risk factors in CKD and are associated with cardiovascular and all-cause morbidity and mortality (43) (44). The AV calcification is an active process with some parallels to physiological bone formation (3, 45). A critical role is attributed to vascular smooth muscle cells (VSMC) and VIC, which can differentiate and convert into myofibroblasts, osteoblast, and chondroblast-like phenotypes (46, 47). Osteoblasts or chondrogenic VSMCs/VICs actively promote valvular or vascular tissue mineralization (25, 48). Although the intracellular signaling pathways that control this trans-differentiation into myofibroblasts, osteoblasts, or chondrocytes are yet not understood completely (49). Human myxomatous valve disease (MMVD) is characterized by increased VIC proliferation, leaflet thickening, increased proteoglycan expression, and ECM remodeling (50). Cell proliferation is unaffected and αSMA expression is reduced in calcified AV of $Kl^{-/-}$ mice (25), suggesting that VIC activation or MMVD is not present in $Kl^{-/-}$ mice. TGFβ1 plays a crucial role in both myofibroblasts and osteogenic trans-differentiation of the VSMCs/VICs and induces cellular senescence through the upregulation of plasminogen activator inhibitor (*Pai1*) (38, 47). Moreover, TGFβ1-dependent osteoinductive signaling involves altered expression of the chondrogenic transcription factor SRY-Box 9 (SOX9), which is involved in AV calcification (51–54).

Increased levels of TGFβ ligands can contribute to cell degeneration, inflammation, metabolic malfunction, tissue fibrosis, and calcification. While the roles of TGFβ signaling depend on cellular contexts, age-related changes are also a potential context, and therefore the relationship between TGFβ signaling and klotho, which is involved in cellular senescence and aging-related diseases such as CAVD, warrants serious attention. There are many investigations that showed that $Kl^{-/-}$ mice can induce calcification in aortic valves (25, 27, 55, 56). The AV of $Kl^{\pm}$ mice do not show any calcification, although a high-fat diet resulted in collagen-I deposition and fibrosis of the aortic valve cusps on the aortic side (57). The signaling mechanisms of AV calcification in klotho deficient mice are still unclear and require further investigations. In this work, we investigated the impact of reduced TGFβ signaling on the AV calcification in $Kl^{-/-}$ mice. We observed that partial inhibition of TGFβ signaling through haploinsufficiency of *Tgfb1* and *Smad3* improves the pathological condition of the AV calcification in klotho-deficient mice.

MATERIALS AND METHODS

Ethics Statement

All animal procedures were performed according to the Guidelines for the Care and Use of Laboratory Animals published by the National Institutes of Health and were approved by the Institutional Animal Care and Use Committee (IACUC) of the University of South Carolina. Mice were euthanized by an overdose of isoflurane in a sealed container as approved by the IACUC.

Mouse Strains

$Kl^{\pm}$ (B6;129S5-Kl^{TM1Lex}/*Mmucd*, Stock# 011732) mice were obtained from the Mutant Mouse Resource and Research Centers (MMRRC) supported by the NIH. These mice were first backcrossed on to C57BL/6 background for more than nine generations. First, the $Kl^{\pm}$; $Tgfb1^{\pm}$ and $Kl^{\pm}$; $Smad3^{\pm}$ mice were generated in our mouse facility by the genetic crossing of the $Kl^{\pm}$ (B6) to $Tgfb1^{\pm}$ (50% 129SvJ and 50% CF-1) (58) and $Smad3^{\pm}$ (129/SvJ) (59) mice. Self-crossing of $Kl^{\pm}$; $Tgfb1^{\pm}$ and $Kl^{\pm}$; $Smad3^{\pm}$ male and female mice resulted in the generation of wild-type control ($Kl^{+/+}$, $Kl^{+/+}$; $Tgfb1^{+/+}$, and $Kl^{+/+}$; $Smad3^{+/+}$), $Kl^{-/-}$, $Kl^{-/-}$; $Tgfb1^{\pm}$, and $Kl^{-/-}$; $Smad3^{\pm}$ mice. Before starting each study, we collected the tail at the age of 3 weeks and genomic DNAs were extracted for each animal and confirmed the genotype using gene-specific primers for *Kl*, *Tgfb1*, and *Smad3* (**Table 1**). PCR genotyping was done as described earlier (60–62).

Tissue Collection and Processing for Histology

Wild-type controls $Kl^{-/-}$, $Kl^{-/-}$; $Tgfb1^{\pm}$, and $Kl^{-/-}$; $Smad3^{\pm}$ mice were sacrificed, and aortic valve tissues were collected for histological, immunohistochemical, morphometric, and molecular analyses. The whole heart of each mouse was perfused with 1XPBS and later fixed in 4% paraformaldehyde in PBS (Fisher Scientific, Waltham, MA, United States) for 48 h. Then, tissues were dehydrated in 70, 95, and 100% ethanol (Fisher Scientific, Waltham, MA, United States) and cleared with xylene (Fisher Scientific, Waltham, MA, United States). Paraffin-embedded hearts were sectioned using an RM2245 Leica microtome (Leica Biosystems, Buffalo Grove, IL, United States) and 7 μm thick serial sections through the aortic roots including annulus, aortic leaflets and hinge, and a portion of the sinus of Valsalva were collected for various histological and morphometric evaluation. Multiple serial sections from each animal were used for quantifying structural or histological changes using the NIH Image J (Fiji) software.

TABLE 1 | Primer sequence for PCR amplification.

Sl. No	Primer name	Sequence (5′–3′)	Amplified gene
1.	KL01	GCAGCGCATCGCCTTCTATC	*Klotho*
2.	KL02	ATGCTCCAGACATTCTCAGC	
3.	KL03	GATGGGGTCGACGTCA	
4.	KL04	TAAAGGAGGAAAGCCATTGTC	
5.	IMF36	AGGACCTGGGTTGGAAGTG	*Tgfb1*
6.	IMR36	CTTCTCCGTTTCTCTGTCACCCTAT	
7.	IMF11	GCCGAGAAAGTATCCATCAT	
8.	IMF-37	CGGCGAGGATCTCGTCGTGACCCA	*Smad3*
9.	IMR-37	GCGATACCGTAAAGCACGAGGAAG	
10.	IMF-38	GGATGGTCGGCTGCAGGTGTCC	
11.	IMR-38	TGTTGAAGGCAAACTCACAGAGC	

TABLE 2 | List of qPCR primers.

Sl. No	Target gene	Biorad unique assay ID
1.	Tgfb1, mouse	qMmuCED0044726
2.	Tgfbr2, mouse	qMmuCID0015359
3.	Alk2, mouse	qMmuCID0040095
4.	Pai1, mouse	qMmuCID0027303
5.	Bmp2, mouse	qMmuCID0014251
6.	SPP1, mouse	qMmuCED0040763
7.	Runx2, mouse	qMmuCID0005205
8.	B2m, mouse	qMmuCID0040553

Histology

All histological staining procedures were performed according to the protocol provided by the manufacturers. Before various histological staining procedures, the tissues were de-paraffinized and rehydrated. Hematoxylin and eosin staining (H&E staining) was carried out using Harris' hematoxylin (Cat # HS-400) and Eosin (Sigma, Cat # HT110380). Tissue sections were kept in alizarin red stain (American MasterTech Scientific, Lodi, CA, United States) for 5 min for detection of calcium deposits. For alizarin red staining, tissue sections were fixed and dehydrated with −20°C cold acetone (Thermo Fisher Scientific, Waltham, MA, United States) and cleared with an acetone/xylene solution (50% acetone and 50% Safe Clear II Xylene substitute, both purchased from Thermo Fisher Scientific, Waltham, MA, United States). Alcian blue stain kit (catalog # KTABP2.5) was used to detect proteoglycans. The Verhoeff's Elastin staining kit (Cat# KTVEL) was used for elastic fiber (black color) and collagens (red color) staining. Collagens were also detected by using the Manson's Trichrome 2,000 stain kit (cat # KTMTR2PT). All kits for detecting proteoglycans, collagens, and elastin fibers were purchased from the American MasterTech Scientific (Lodi, CA, United States). At the end of each staining, the tissue slides were mounted with a permanent mounting medium (Vector Laboratories, Burlingame, CA, United States). All tissue sections were subsequently visualized and photographed in low and high magnifications under bright field optics on the Nikon Optiphot-2 (equipped with AxioCam MRc Camera) and EVOS TM FL Auto Imaging System (Thermo Fisher Scientific, Inc., Grand Island, NY, United States). Morphometric quantification of signal intensity was done on multiple serial sections from each animal per group by using the NIH- Image J (Fiji) software.

Immunohistochemistry

Paraformaldehyde-fixed paraffin-embedded serial sections representing annulus, aortic leaflets and hinge, and a portion of the sinus of Valsalva were used for immunohistochemistry. Sections were de-paraffined and hydrated with two changes in 1X PBS and one change in deionized water (5 min each). Heat-mediated antigen retrieval was performed by dipping the slides in a mildly boiling 1X citric acid buffer (catalog no. S1700; Agilent Dako, Santa Clara, CA, United States) for 10 min in a microwave, cooled to room temperature, and rinsed in PBS. Endogenous peroxidases were blocked with freshly prepared 0.5% H_2O_2/methanol for 30 min, followed by non-specific epitope blocking with 5% goat serum/0.1% Tween/0.02% sodium

azide in PBS for 20 min. Avidin and Biotin blocking was done as per the manufacturer's recommendation (Cat# SP-2001, Vector Labs, Burlingame, CA, United States), followed by overnight incubation at 4°C in anti-pSMAD2 (1:3000, Millipore, Burlington, MA, United States) (61). Slides were then washed and incubated with appropriate biotinylated secondary antibody (1:200) for 30 min, followed by Avidin-Biotin complex (Cat# PK-6100, Vectastain Elite ABC HRP kit) for 30 min, washed in PBS, and finally developed with DAB/H_2O_2. Nuclei were counterstained with hematoxylin and sections were dehydrated through graded ethanol series, cleared in xylene, and mounted. Both low- and high-magnification images were taken under bright field optics on the Nikon Optiphot-2 (equipped with AxioCam MRc Camera). Morphometric quantification of pSMAD2-stained average area (μm^2) was done on multiple serial sections from each animal per group by using the NIH-Image J software.

RNA Isolation, cDNA Synthesis, and Quantitative PCR

The AV tissue was dissected manually from wild-type, $Kl^{-/-}$, $Kl^{-/-}$; $Tgfb1^{\pm}$, and $Kl^{-/-}$; $Smad3^{\pm}$ mice. The AV tissue contained aortic roots including annulus, aortic leaflets and hinge, and a portion of the sinus of Valsalva. Five individual biological samples from each group were analyzed for gene expression study. Total RNA was isolated from the AV tissue of wild-type and $Kl^{-/-}$, $Kl^{-/-}$; $Tgfb1^{\pm}$, and $Kl^{-/-}$; $Smad3^{\pm}$ mice using Trizol (Invitrogen/ThermoFisher, Grand Island, NY, United States) and miRNeasy micro kit (Qiagen, Germantown, MD, United States) according to the manufacturer's protocols. cDNA was generated from 500 ng total RNA using an RT-PCR kit according to the instructions provided by the manufacturer (Bio-Rad Laboratories, Inc.). cDNA was then diluted 10 times and later subjected to quantitative PCR amplification (Bio-Rad CFX) using pre-validated gene-specific primers procured from the vendor (Bio-Rad Laboratories, Inc., Hercules, CA, United States) (**Table 2**). Approximately, 10 ng of cDNA was used for each 20 μl qPCR reaction. Following qPCR analyses, the cycle count threshold (Ct) was normalized to species-specific housekeeping genes (*B2m*; purchased from Bio-Rad, Inc.) and the $2^{\wedge -\Delta Ct}$ values were determined and graphically presented. Statistically significant differences in gene expression levels were determined using Student's *t*-test, indicated in the figure legends, on at least three or more independent experiments with $p < 0.05$ considered significant.

Western Blot Analysis

Three independent "pooled" samples of the AV tissue from each group of mice were used for western blotting. The AV tissues in each sample were "pooled" from two individual mice for each genotype (wild-type, $Kl^{-/-}$, $Kl^{-/-}$; $Tgfb1^{\pm}$, and $Kl^{-/-}$; $Smad3^{\pm}$). Thus, each independent pooled sample consists of two biological replicates (n = 6 per genotype). The AV tissue contained aortic roots including annulus, aortic leaflets and hinge, and a portion of the sinus of Valsalva. The AV tissue was cut into small pieces and homogenized using Wheaton tapered tissue grinders (Thermo Fisher Scientific, Rockford, IL, United States) in M-PER mammalian protein extraction reagent (Thermo Fisher Scientific) with a complete mini protease inhibitor cocktail (Sigma-Aldrich, St. Louis, Louis, MO, United States) and Halt protease and phosphatase inhibitor single-use cocktail (Thermo Fisher Scientific, Rockford, IL, United States) as per the manufacturer's protocol. Homogenized tissue lysates were subjected to brief sonication for 20 s on ice and then kept at room temperature for 20 min. Then, centrifugation was performed at 15,000 rpm for 20 min at 4°C and the supernatants were collected. Total protein concentration in the supernatant was determined using the Pierce BCA protein assay kit (Thermo Scientific, Rockford, IL, United States). Samples were stored at −80°C until further use. Western blotting was performed with equal amounts of protein samples and the primary IgG antibodies against phospho-SMAD2 (Cell Signaling Technology, Danvers, MA, United States Cat #3108), SMAD2 (Cell Signaling, Cat #5339), phospho-SMAD3 (Cell Signaling, Cat #9520), SMAD3 (Cell Signaling, Cat #9523), phospho-SMAD1/5 (Cell Signaling, Cat #9516), SMAD1/5 (Cell Signaling, Cat #9743), phospho-p38 (Cell Signaling, Cat #4511), p38 (Cell Signaling, Cat #8690), phospho-ERK1/2 (Cell Signaling, Cat #4370), and ERK1/2 (Cell Signaling, Cat #4695) at a dilution of 1:1000. Primary IgG antibodies against all these proteins were purchased from Cell Signaling Technology, Inc. (Danvers, MA, United States). The horseradish peroxidase-conjugated anti-mouse or anti-rabbit secondary IgG antibody (Cell Signaling, Cat # 7074) was used at 1:5000 dilution to detect a primary IgG antibody. Western blots were incubated with Clarity western ECL detection reagents (Bio-Rad Laboratories, United States) and exposed to X-OMAT AR films (Eastman Kodak, Rochester, NY, United States) for autoradiography. The autoradiograms were scanned on an EPSON Scanner using Photoshop software (Adobe Systems, Seattle, WA, United States). β-actin, clone AC-15, monoclonal primary antibody (Sigma-Aldrich, St. Louis, MO, United States) was used as a loading control to compare equal loading in the SDS-PAGE. We quantified our results *via* densitometric analysis using NIH Image J (Fiji) software. Quantitative densitometric analysis normalized the expression levels of phosphorylated proteins with their non-phosphorylated/total forms or β-actin. Microsoft Excel was used for recording and managing the raw data. Statistics were performed using pair-wise comparisons between the groups, utilizing analysis of variance and unpaired two-tailed Student's *t*-test (GraphPad Prism 9 Software, San Diego, CA). Data were reported as means ± *SD* of the mean. Probability values < 0.05 were considered significant.

RESULTS

Increased *Tgfb1* Expression and SMAD3 Activation Are Associated With the Calcification of the Aortic Valve in Klotho Knockout Mice

We collected tissues from the aortic valve from 8- to 10-week-old wild-type and $Kl^{-/-}$ mice and performed alizarin red staining of tissue sections to determine calcification in the aortic valve

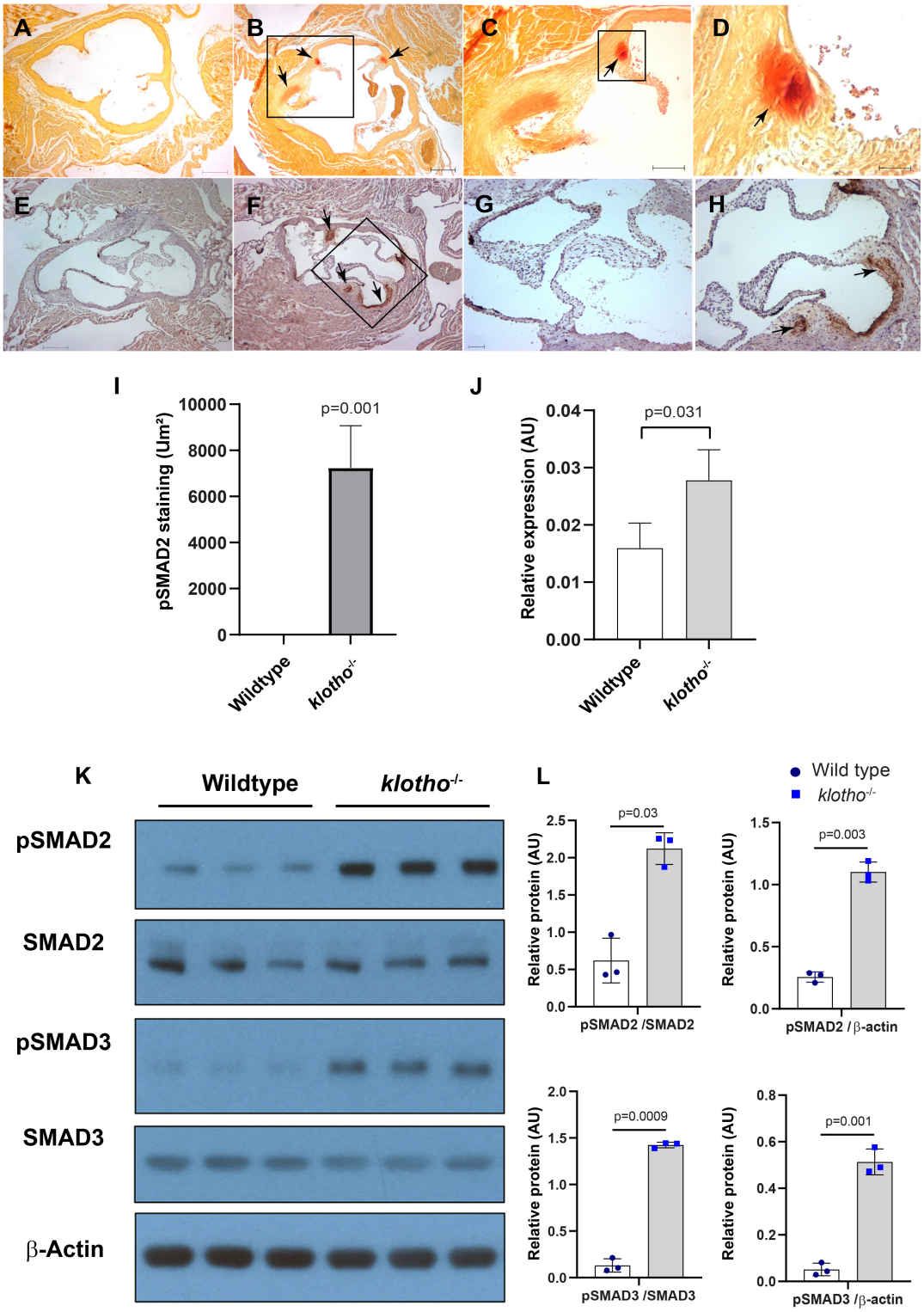

FIGURE 1 | The klotho (*Kl*) genetic deletion leads to calcification in the aortic valve hinge and annulus with upregulation of *Tgfb1* and TGFβ-dependent SMAD2 signaling in 10–12-week-old mice. **(A–D)** Alizarin red staining of wild-type **(A)** and $Kl^{-/-}$ **(B–D)** mice. Scale bars = **(A–B)** 200 μm; **(C)** 100 μm; **(D)** 50 μm. **(E–I)** Immunohistochemistry showing localized pSMAD2 levels in AV hinge and aortic annulus of wild-type **(E,G)** and $Kl^{-/-}$ **(F,H)**. The pSMAD2-stained area was quantified using NIH Image J software **(I)**. **(J)** qPCR study to quantify *Tgfb1* expression in the pooled and micro-dissected tissue samples of AV and annulus from wild-type and $Kl^{-/-}$ mice. **(K)** Western blotting analyses showing levels of phosphorylated SMADs (p SMAD2, pSMAD3), total SMADs (SMAD2, SMAD3), and β-actin in micro-dissected and pooled tissue samples containing AV and annulus from wild-type and $Kl^{-/-}$ mice. **(L)** Densitometric analysis quantifying band intensities of western blots. The densitometry graphs of pSMAD2 and pSMAD3 were normalized with total or non-phosphorylated form of the proteins or β-actin. Values indicate mean ± SD, and significant "*p*-values" between wild-type and $Kl^{-/-}$ groups were given on the top of histograms.

area. Our alizarin red staining confirmed the presence of calcific nodules in the AV hinge and aortic annulus of the $Kl^{-/-}$ mice (n = 12) (**Figures 1A–D**). There was no AV calcification seen in the control mice, which included $Kl^{+/+}$ and $Kl^{\pm}$ mice. Immunohistochemistry analysis indicated that increased phosphorylated SMAD2 (pSMAD2) was associated with AV calcification in the hinge and aortic annulus (n = 6) (**Figures 1E–I**). We tested if the *Tgfb1* mRNA level was upregulated in the AV tissue of $Kl^{-/-}$ mice by qPCR analysis. The data indicated significant upregulation of *Tgfb1* mRNA expression (n = 5, p = *0.031*) in $Kl^{-/-}$ mice compared to the wild-type control (**Figure 1J**). Next, we determined if the increased *Tgfb1* mRNA expression level is consistent with the induction of the downstream TGFβ signaling molecules at the protein level. We analyzed the downstream TGFβ signaling pathway molecules in tissue samples collected from the AV tissue of wild-type and $Kl^{-/-}$ mice. Since phosphorylation of SMAD2 and SMAD3 is typically used as a surrogate for TGFβ signaling, western blot analysis was used to quantify both phosphorylated and total (no-phosphorylated) SMAD and SMAD3. The data showed statistically significant induction of activated forms of the SMAD2 (i.e., pSMAD2) and SMAD3 (i.e., pSMAD3) (TGFβ-specific SMADs), in $Kl^{-/-}$ mice when compared to wild-type mice (n = 6) (**Figures 1K,L**).

Genetic Inactivation of TGFβ Signaling Pathway Components Improved Structural Features and Extracellular Matrix Organization of Aortic Valve in Klotho-Deficient Mice

Histological staining was carried out to examine the morphological, cellular, and structural changes in the AV tissue of 8–10-week-old $Kl^{-/-}$ mice following the partial genetic deletion of TGFβ1 and SMAD3 genes (**Figures 2A–H**). Histological examination of H&E-stained serial tissue sections confirmed calcified nodules in the AV hinge and annulus in the $Kl^{-/-}$ mice (n = 12) (**Figures 2A,B**). Morphometric quantitative analysis indicated no significant changes in the overall thickening of AV leaflets in $Kl^{-/-}$ mice compared to wild-type mice (n = 6) (**Figure 2I**). Histological and morphometric evaluation of $Kl^{-/-}$;$Tgfb1^{\pm}$ mice showed partial improvement in the overall tissue structure of the AV hinge and annulus compared to $Kl^{-/-}$ mice (n = 6) (**Figures 2A–C,I**). Similar analysis of $Kl^{-/-}$;$Smad3^{\pm}$ mice revealed a complete rescue of the AV hinge and aortic annulus (**Figures 2A–D,I**). Alcian blue staining was used to observe chondrogenic differentiation and proteoglycans or glycosaminoglycans (GAGs) distribution in the AV hinge and aortic annulus in all four groups of mice (n = 6–12). The

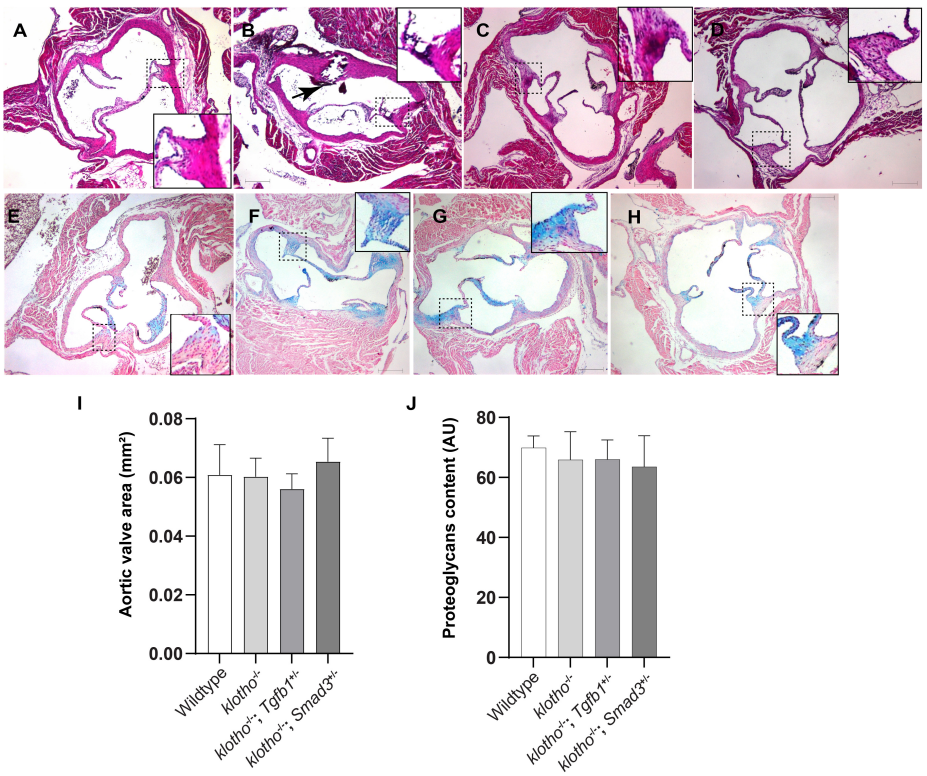

FIGURE 2 | Effect of lowering of TGFβ1 and SMAD3 on AV structure and proteoglycan (GAG) distribution in 10- to 12-week-old $Kl^{-/-}$ mice. **(A–D)** Hematoxylin and eosin (H&E) staining and **(E–H)** Alcian blue staining of wild-type, $Kl^{-/-}$, $Kl^{-/-}$;$Tgfb1^{\pm}$, and $Kl^{-/-}$;$Smad3^{\pm}$ mice showing aortic valve histology and proteoglycans distribution. A magnified view showing further details of the boxed region is presented for each image. **(I–J)** Quantitative analysis of AV area in H&E-stained **(I)** and proteoglycans content in alcian blue-stained **(J)** images. Quantification of AV area and GAG content was done on multiple serial sections from each animal per group by using NIH- Image J software. Values indicate mean ± *SD* (n = 5). Scale bars = **(A–H)** 200 μm.

data indicated abnormal proteoglycans in the AV hinge and aortic annulus in both $Kl^{-/-}$ (n = 12) and $Kl^{-/-}$;$Tgfb1^{\pm}$ (n = 6) mice compared to wild-type or $Kl^{-/-}$;$Smad3^{\pm}$ mice (n = 12), but morphometric quantification did not reveal any significant changes in the overall proteoglycans content (n = 6) (**Figures 2E–H,J**). Finally, we determined collagen and elastic fibers' organization through the VVG staining of serial sections (n = 6–12) (**Figures 3A–J**). The quantitative analysis did not reveal any significant changes in overall collagen content (**Figure 3I**). Histological assessment of high-powered images and morphometric evaluation showed dysregulated elastic fiber organization in the AV hinge of $Kl^{-/-}$ mice (n = 12), which was significantly rescued by partial genetic deletion of *Smad3* (n = 12) but not *Tgfb1* (n = 6) (**Figures 3A–H,J**).

Haploinsufficiency of *Tgfb1* and *Smad3* Significantly Reduced Vascular Calcification in Klotho-Deficient Mice

We generated $Kl^{-/-}$;$Tgfb1^{\pm}$ and $Kl^{-/-}$;$Smad3^{\pm}$ mice to confirm the effect of TGFβ1 and canonical SMAD3-dependent TGFβ signaling pathways on AV calcification in klotho-deficient mice. Histological and quantitative analyses of alizarin red-stained serial sections through aortic roots including annulus, aortic leaflets and hinge, and a portion of the sinus of Valsalva of the 8- to 10-week-old wild-type, $Kl^{-/-}$, $Kl^{-/-}$;$Tgfb1^{\pm}$ and $Kl^{-/-}$;$Smad3^{\pm}$ were performed (n = 6–12) (**Figures 4A–I**). There was no AV calcification in wild-type mice (**Figures 4A,E**). The $Kl^{-/-}$ mice showed calcific nodules in the AV hinge (n = 12, p = *0.002*) (**Figures 4A,B,E,F,I**). Interestingly, the overall extent of the calcification in the AV hinge was less in $Kl^{-/-}$;$Tgfb1^{\pm}$ mice compared to the $Kl^{-/-}$ mice (n = 6, p = *0.01*) (**Figures 4A–C,E–G,I**). Importantly, the AV calcification was almost completely rescued in $Kl^{-/-}$;$Smad3^{\pm}$ mice (n = 12, p = *0.002*) (**Figures 4A–I**).

Heterozygous Deletion of *Tgfb1* and *Smad3* Blocks the Expression of Genes Involved in Aortic Valve Calcification

We have investigated the impact of partial genetic deletion of *Tgfb1* and *Smad3* on the expression of genes involved in TGFβ (*Tgfb1, Pai1*) and BMP (*Bmp2, Alk2*) signaling

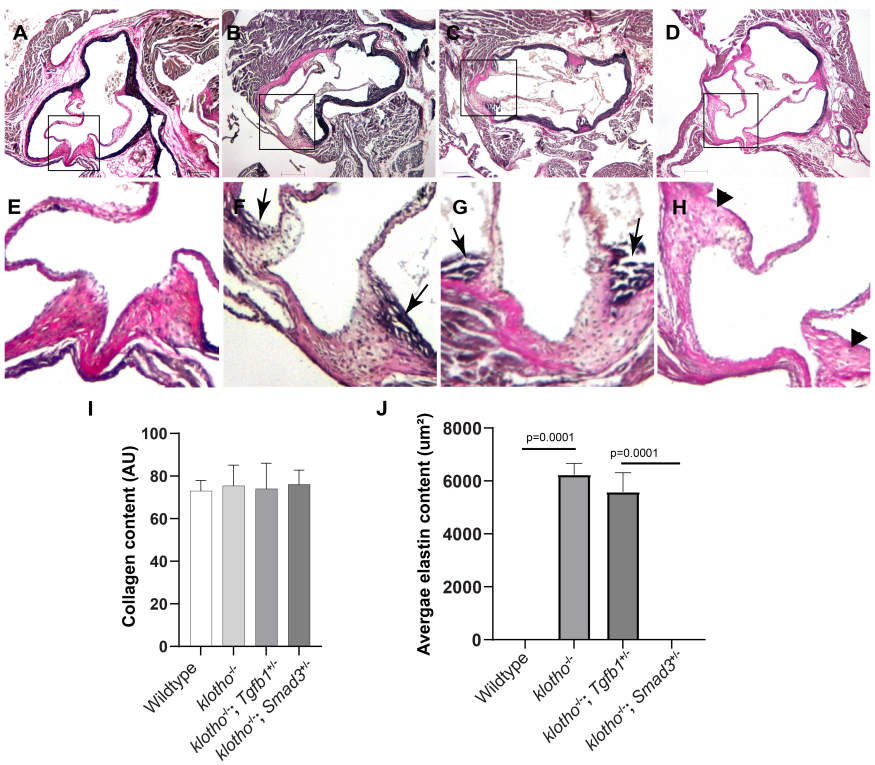

FIGURE 3 | Effect of *Tgfb1* and *Smad3* heterozygous deletion on collagen and elastin fibers in the aortic valve of 10–12-week-old $Kl^{-/-}$ mice. **(A–H)** Verhoeff-Van Gieson (VVG) staining of tissue sections through the aortic valve and annulus of wild-type **(A,E)**, $Kl^{-/-}$ **(B,F)**, $Kl^{-/-}$;$Tgfb1^{\pm}$ **(C,G)**, and $Kl^{-/-}$;$Smad3^{\pm}$ **(D,H)** mice. Magnified images of the boxed area **(A–D)** are given in **(E–H)**. Arrows indicate the presence of abnormal elastin fibers in $Kl^{-/-}$ **(F)** and $Kl^{-/-}$;$Tgfb1^{\pm}$ **(G)** mice. VVG stains elastin in black and collagen fibers in red color. **(I)** Histogram showing total collagen content in the aortic valve, including leaflets, annulus, and AV hinge. Quantification of collagen fibers content was done by measuring the intensity of collagen staining on multiple serial sections from each animal per group by using NIH-Image J software. Values indicate mean ± *SD* (n = 5). **(J)** Histogram showing the average area containing the elastin fibers in the AV hinge. Quantification of elastin fibers content was done by measuring the average area in the AV hinge with elastin staining on multiple serial sections from each animal per group by using NIH-Image J software. Values indicate mean ± *SD* (n = 5), and significant "p-values" were given on the top of histograms. Scale bars: **(A–H)** 200 μm.

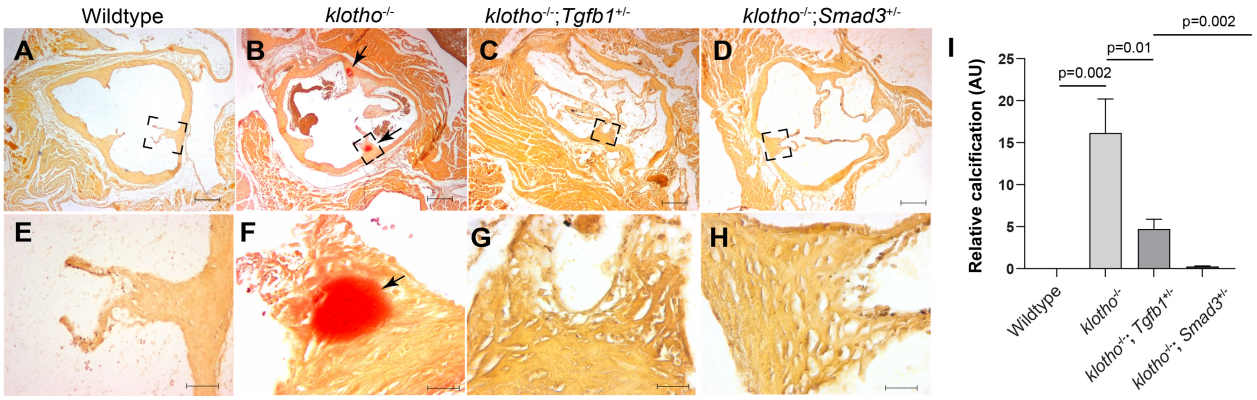

FIGURE 4 | Partial genetic inactivation of *Tgfb1* and *Smad3* inhibits AV calcification in 10–12-week-old $Kl^{-/-}$ mice. **(A–H)** Alizarin red staining of aortic valve in wild-type **(A,E)**, $Kl^{-/-}$ **(B,F)**, $Kl^{-/-}$;$Tgfb1^{\pm}$ **(C,G)**, and $Kl^{-/-}$;$Smad3^{\pm}$ **(D,H)** mice. Images **(E–H)** are the magnified views of the corresponding boxed region **(A–D)**. Scale bars = **(A–D)**, 200 μm; **(E–F)**, 50 μm. **(I)** Quantitative analysis of calcification. Quantification of calcification was done on multiple serial sections from each animal per group by using NIH-Image J software. Values indicate mean ± *SD*, and significant "*p*-values" were given on the top of histograms.

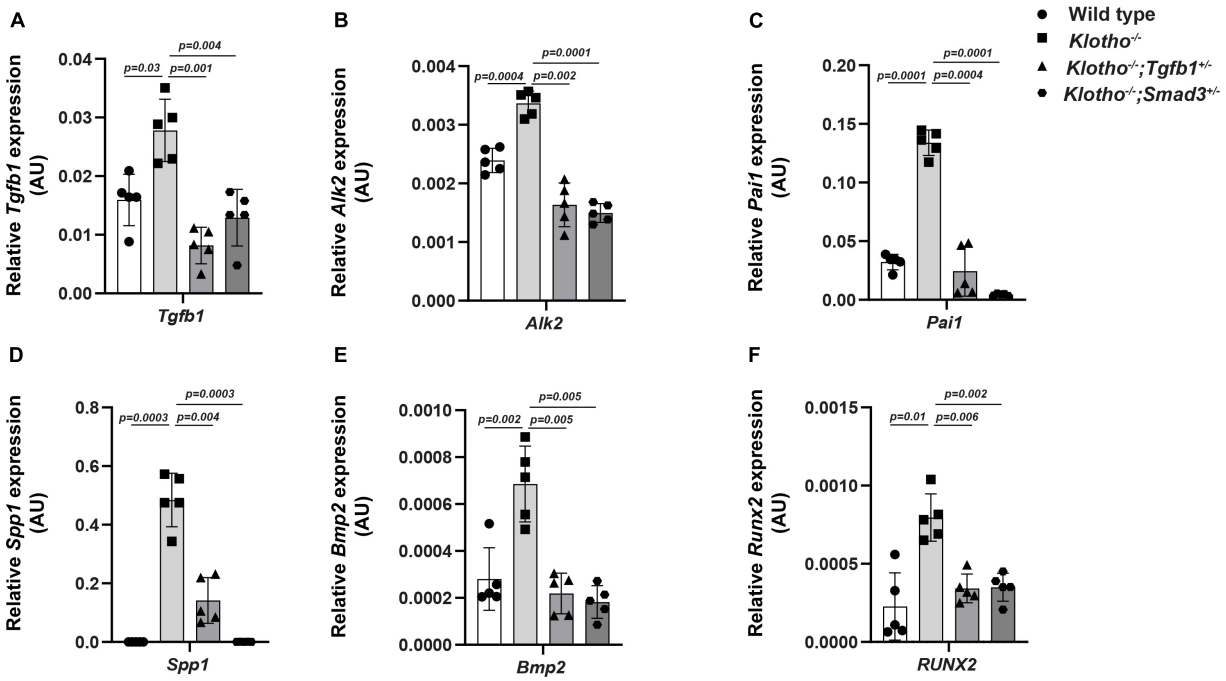

FIGURE 5 | Effect of partial genetic deletion of *Tgfb1* and *Smad3* on key genes involved in TGFβ and BMP signaling, and AV calcification. The qPCR analysis of selected genes in micro-dissected pooled tissue samples representing AV leaflets and hinge and aortic annulus of wild-type, $Kl^{-/-}$, $Kl^{-/-}$;$Tgfb1^{\pm}$, and $Kl^{-/-}$;$Smad3^{\pm}$ mice. Expression levels of *Tgfb1* (TGFβ ligand) **(A)**, *Alk2* (BMP Type I receptor) **(B)**, *Pai1* (TGFβ target gene) **(C)**, *Spp1* (calcification marker) **(D)**, *Bmp2* (BMP ligand) **(E)**, and *Runx2* (osteoblast differentiation marker) **(F)** were quantified. Triplicate samples from each of the five different biological replicates ($n = 5$) were analyzed. Quantitative data are shown as mean ± *SD* ($n = 5$). Two-sided Student's *t*-test (unpaired) was used. Significant comparisons are indicated on the top of each histogram.

and osteoblast differentiation (*Spp1, Runx2*) during CAVD development and progression in $Kl^{-/-}$ mice. The qPCR analysis was performed on aortic valve tissue containing aortic roots including annulus, sinus of Valsalva, and aortic leaflets and hinge from individual 8- to 10-week-old wild-type, $Kl^{-/-}$, $Kl^{-/-}$;$Tgfb1^{\pm}$, and $Kl^{-/-}$;$Smad3^{\pm}$ mice ($n = 5$) (**Figure 5**). We observed significant increase in the *Tgfb1* ($p = 0.03$), *Pai1* ($p = 0.0001$), *Bmp2* ($p = 0.002$), *Alk2* ($p = 0.0004$), *Spp1* ($p = 0.0003$), and *Runx2* ($p = 0.01$) mRNA expression in the AV tissue from the $Kl^{-/-}$ mice compared to wild-type mice (**Figure 5**). Partial genetic inhibition of *Tgfb1* and *Smad3* significantly inhibited the expression of all these genes. Heterozygous *Smad3* deletion was observed to be more potent in reducing the expression of *Pai1* and *Spp1* genes

in $Kl^{-/-}$ mice compared to partial *Tgfb1* ligand inhibition (**Figures 5C,D**).

Partial Genetic Deletion of *Tgfb1* and *Smad3* Blocks Aortic Valve Calcification by Reducing Both Canonical and Non-canonical TGFβ Signaling Pathways

We observed significant induction of TGFβ receptor-dependent phosphorylation of serine/threonine residues of TGFβ SMADs (i.e., pSMAD2 and pSMAD3), TGFβ/BMP SMAD1/5 (i.e., pSMAD1/5), and non-SMAD pathways (i.e., p38 MAPK, ERK1/2 MAPK) in the AV tissue from the $Kl^{-/-}$ mice (n = 6) (**Figure 6**). Our immunoblot analyses of AV tissues from the wild-type control, $Kl^{-/-}$, $Kl^{-/-}$;*Tgfb1*$^{\pm}$, and $Kl^{-/-}$;*Smad3*$^{\pm}$ mice indicated that haploinsufficiency of *Tgfb1* and *Smad3* reduced the activation of these molecules in the $Kl^{-/-}$ mice (**Figure 6A**). There was no significant change in the total amount of the SMAD2, SMAD3, SMAD1/5, p38, ERK1/2 (ERK1 (top band), 44 KDa; ERK2 (bottom band), 42 KDa), and β-actin

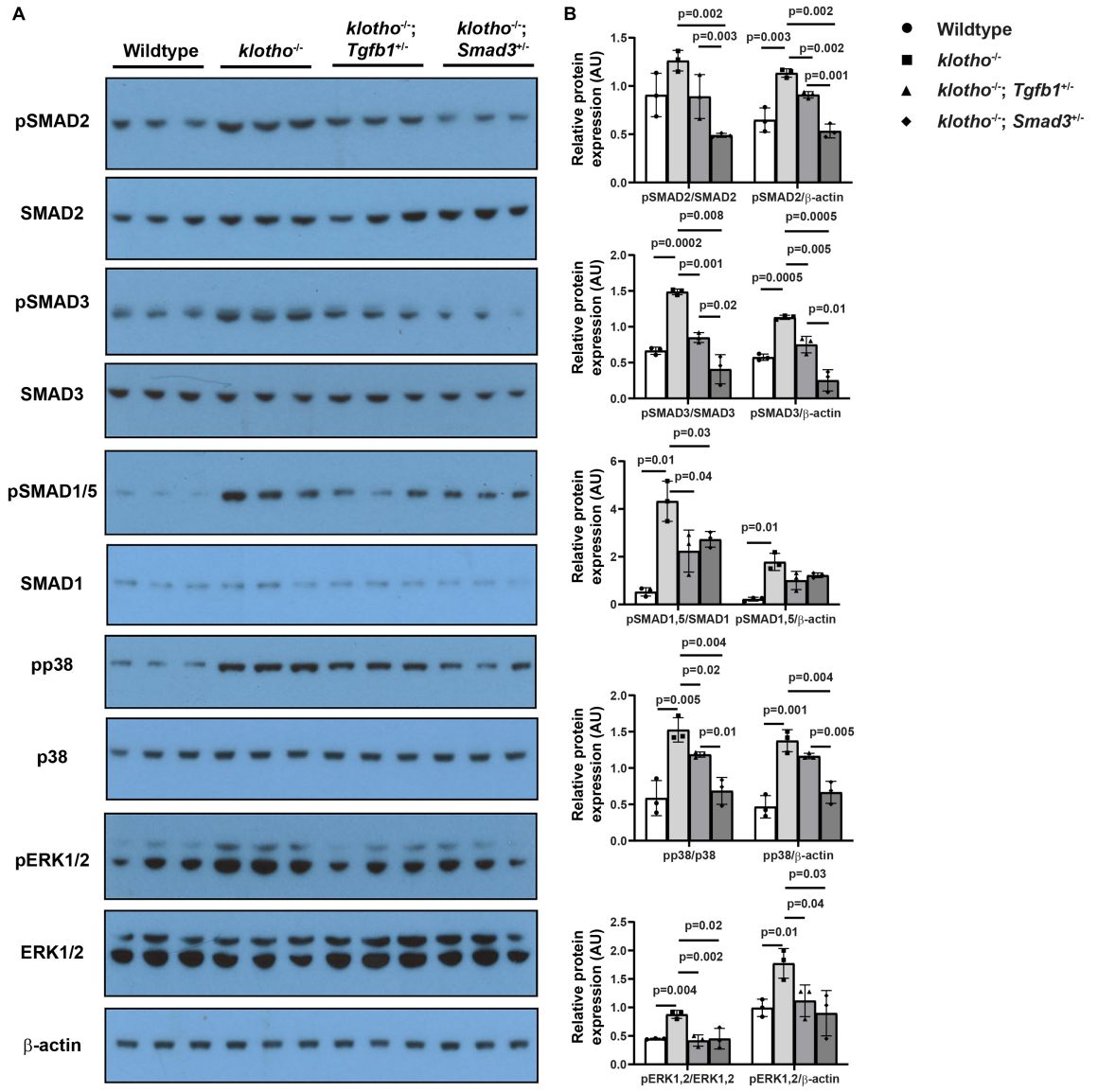

FIGURE 6 | Haploinsufficiency of *Tgfb1* and *Smad3* inhibits canonical and non-canonical TGFβ signaling in the aortic valve of $Kl^{-/-}$ mice. **(A)** Western blot analysis on three different micro-dissected pooled tissues, from two to three hearts/sample, representing AV leaflets and hinge area and aortic annulus of 10–12-week-old wild-type, $Kl^{-/-}$, $Kl^{-/-}$;*Tgfb1*$^{\pm}$, and $Kl^{-/-}$;*Smad3*$^{\pm}$ mice showing protein levels of the phosphorylated forms of canonical and non-canonical pathway molecules (pSMAD2, pSMAD3, pSMAD1/5, pp38, and pERK1/2) and their non-phosphorylated/total forms (SMAD2, SMAD3, SMAD1/5, p38, and ERK1/2). A common and independent β-actin blot (bottom) was also used for normalizing the data. **(B)** Densitometric quantification of phosphorylated proteins after normalization to total non-phosphorylated proteins or β-actin. Numerical data (mean ± *SD*) from three pooled samples are presented as scatter plots with bar. The *p*-values are shown on top of the histograms.

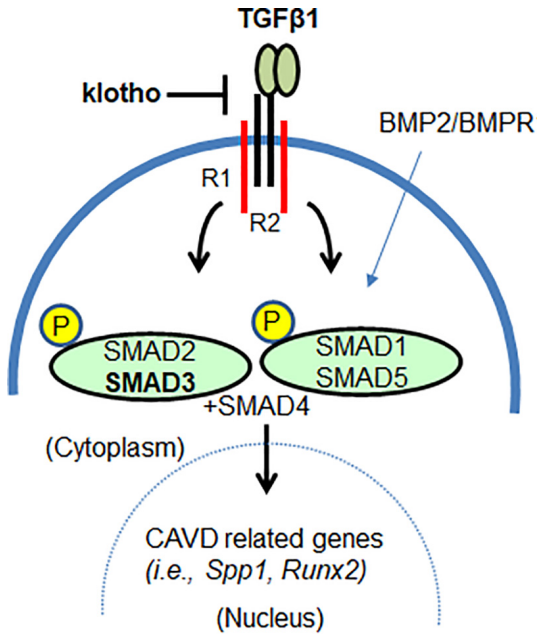

FIGURE 7 | The klotho as a mediator of TGFβ1-dependent SMAD3 signaling in AV calcification. SMAD3 can mediate klotho-dependent TGFβ1 signaling. Lowering TGFβ1-dependent SMAD3 signaling also lowers SMAD1/5 signaling. Thus, klotho functions, in part, as a mediator by restraining or attenuating the augmented TGFβ/BMP signaling and TGFβ-regulated transcription of genes involved in CAVD.

proteins in the wild-type control, $Kl^{-/-}$, $Kl^{-/-}$;$Tgfb1^{\pm}$, and $Kl^{-/-}$;$Smad3^{\pm}$ mice (**Figure 6A**). Quantitative densitometric analysis comparing the expression levels of phosphorylated proteins with their non-phosphorylated/total forms or β-actin revealed similar results (**Figure 6B**). Collectively, partial *Smad3* deletion was more potent than heterozygous deletion of *Tgfb1* in reducing the activation of SMAD2/3/5, p38, and ERK1/2 MAPK during aortic valve calcification in klotho-deficient mice (**Figures 6A,B**).

DISCUSSION

The klotho deficiency has been shown to cause age-related calcification of AV hinge and aortic annulus in mice (25). The $Kl^{-/-}$ mice also exhibit increased expression of many key osteogenic genes involved in human CAVD (25, 63). We demonstrated that upregulation of TGFβ1 and SMAD3 are involved in AV calcification in klotho-deficient mice. The data also indicate that calcific nodule formation in the aortic valve of klotho-deficient mice is associated with increased *Tgfb1* expression and elevated levels of activated forms of SMAD2, SMAD3, SMAD1/5, p38, and ERK1/2 MAPK.

Importantly, partial genetic ablation of *Tgfb1* or *Smad3* significantly decreases the expression of *Tgfb1* and both canonical (SMAD-dependent) and non-canonical (MAPK-mediated) TGFβ signaling pathways and blocks the pathological progression of the AV calcification in $Kl^{-/-}$ mice. Collectively, while *Tgfb1* haploinsufficiency significantly improved the structural and ECM features, *Smad3* haploinsufficiency almost fully reversed pathological structural changes and disrupted elastin fiber organization in the aortic valve of klotho-deficient mice. Dysregulated elastin fibers in the AV leaflet hinge in $Kl^{-/-}$ mice are consistent with a recent report by Gomez-Stallons et al. (64) showing increased elastin fragmentation and loss of elastin integrity in postmortem leaflet patients with CAVD.

Haploinsufficiency of *Smad3* has been observed to be more potent in inhibiting aortic valve calcification compared to *Tgfb1* ligand inhibition. This is consistent the notion that signaling from TGFβ1 and/or other TGFβ ligands could be effectively blocked by partial deletion of *Smad3*. Thus, the effect of lowering TGFβ1 on SMAD2/3 activation and AV calcification rescue may be somewhat less pronounced in $Kl^{-/-}$;$Tgfb1^{\pm}$ mice as compared to $Kl^{-/-}$;$Smad3^{\pm}$ mice. This may be due to functional compensation of the loss of TGFβ1 by other TGFβ ligands (i.e., TGFβ2, 3) and SMAD2. All three TGFβ ligands (TGFβ1, TGFβ2, and TGFβ3) interact with TGFβ Type I and II receptors and lead to activation of SMAD3 and SMAD2. Activated SMAD2/3 with SMAD4 translocate to the nucleus and regulate TGFβ target genes (e.g., *Pai1*) (36, 65). Increased levels of TGFβ1 (31) and pSMAD2 and PAI1 (66) are associated with CAVD. PAI1 is a known TGFβ target, and therefore, its expression was reduced along with the AV calcification rescue in response to partial inactivation of *Tgfb1* ($Kl^{-/-}$;$Tgfb1^{\pm}$ mice) or *Smad3* ($Kl^{-/-}$;$Smad3^{\pm}$ mice) in klotho-deficient mice. Wirrig et al. have reported increased expression of *Spp1* and *Runx2* in AV tissue of the $Kl^{-/-}$ mice (55). Gomez-Stallons et al. (56) (ATVB) have reported that *Spp1, Bmp2,* and *Runx2* are increased in $Kl^{-/-}$ AV tissue (56). Our results indicating significant rescue of CAVD and expression of these genes in $Kl^{-/-}$ mice by partial genetic deletion of *Tgfb1* or *Smad3* are consistent with these published findings. It remains unclear if SMAD2 and SMAD3 play a redundant or unique role in AV calcification in CAVD.

There are several experimental limitations in this study. The effect of sex is not specifically addressed. The levels of active and latent TGFβ1 protein are not determined. Since most widely used anti-TGFβ1 antibodies (2G7, 1D11) cross-react to TGFβ3 and not TGFβ2 ligands (67), this study only demonstrated upregulation of *Tgfb1* transcript levels in the aortic valve of $Kl^{-/-}$ mice. Regardless of these limitations, the molecular data indicate that both TGFβ1 and SMAD3 contribute to the expression of critical genes involved in the pathogenesis of CAVD. Collectively, our findings represent novel genetic approaches for blocking the progression of CAVD.

Another important piece of information that emerged from this study is the effect of lowering TGFβ1 or SMAD3 on BMP signaling pathway in CAVD. TGFβs and the BMPs are members of the TGFβ family (68). It is well established that increased BMP signaling contributes to AV calcification in $Kl^{-/-}$ mice. It has been reported that both *Bmp2* and pSMAD1/5 levels are increased in AV tissue of $Kl^{-/-}$ mice and that genetic inactivation of BMP receptor Bmpr1a in the aortic valve interstitial cells can prevent AV calcification (56). It is

remarkable to find that lowering of TGFβ1 as well as SMAD3 has significantly reduced the expression of BMP ligand (*Bmp2*) and BMP Type I receptor (*Alk2*) and activation of BMP-dependent SMAD (pSMAD1/5). Constitutively active mutants of ALK2 have been identified as causative of Fibrodysplasia Ossificans Progressiva (FOP), which is an extremely rare heritable disorder of connective tissues characterized by progressive heterotopic ossification in various skeletal sites (69). It is known that TGFβ1 *via* TGFβ Type I receptor can interact with ALK2 resulting in the simultaneous activation of SMAD2/3 and SMAD1/5 (70, 71). Also, *Alk2* deletion can reduce both SMAD2/3 and SMAD1/5 in cushion mesenchymal cells during heart development (72). Importantly, lowering pSMAD3 (this study) or pSMAD1/5 (56) has a similar effect in blocking AV calcification in $Kl^{-/-}$ mice, suggesting crosstalk between TGFβ and BMP pathways in maintaining AV homeostasis (**Figure 7**). It is noteworthy that SMAD7, an inhibitory SMAD and TGFβ target gene, binds to and blocks all type I receptors in the TGFβ family, whereas SMAD6 shows preferential binding and inhibitory activity toward the BMP type I receptors ALK3 and ALK6 (73). Both SMAD 6 and 7 cooperate in suppressing the physiological BMP signaling during the differentiation of mesenchymal progenitor cells to osteoblasts (74). This is due to rapid and direct induction of *Smad6* expression by the primary BMP stimulus, followed by activation of autocrine TGFβ signaling, which then induces a second wave of *Smad7* expression that, together with the preexisting SMAD6, shuts down BMP receptor activity in a more sustained manner and limits the rate of differentiation to osteoblasts (74). Whether the negative regulation of TGFβ and BMP pathway *via* SMAD7 is failed in $Kl^{-/-}$ mice remains a potential area of future investigation.

This study indicates that the haploinsufficiency of *Smad3* is more effective than *Tgfb1* heterozygous deletion in decreasing the activation of p38 MAPK in AV tissue of klotho-deficient mice. Improper activation of p38 or ERK MAPKs is a precursor of constitutive SMAD2/3 signaling associated with aortopathy (75, 76). TGFβ-activation of the SMAD2/3 requires the kinase activity of the TGFβRI, while the TGFβRI kinase activity is not required for the TGFβ-induced oligomerization of the TGFβRII/TGFβRI complex, where the TRAF6 binding to the TGFβRI results in the activation of TAK1-p38 MAPK pathway. Thus, TGFβ activation of TGFβRII/TGFβRI-complex leads to (a) the TGFβRI-kinase-dependent activation of SMAD2/3 and (b) the TGFβRII/TGFβRI-hetero-oligomerization which will cause a rapid activation of TRAF6 resulting in p38 MAPK pathway activation. It is possible that changes in the non-canonical TGFβ pathway may be a primary determinant of AV calcification in $Kl^{-/-}$ mice. Thus, the exact contribution of the non-canonical (non-SMAD) TGFβ pathway in the AV calcification requires further investigation.

Overall, our findings suggest that klotho is an important mediator of TGFβ signaling *in vivo* in adult aortic valves (**Figure 7**). Both TGFβ1 and TGFβ-dependent canonical (pSMAD2/3) and non-canonical (p38 MAPK, ERK1/2 MAPK) pathways are activated in the absence of klotho. This suggests that klotho restrains TGFβ ligand-receptor-dependent TGFβ signaling and that increased TGFβ-induced activation of SMAD2/3 and/or SMAD1/5 somehow drives the AV calcification in klotho-deficient mice. This is consistent with the observation that partial genetic inactivation of TGFβ1 and *SMAD3* (this study), and BMPR1A (56) can block the development and progression of AV calcification in klotho-deficient animals. Our observations are further supported by *in vitro* evidence that klotho can bind to the TGFβ Type II receptor complex, thereby contributing to the inhibition of TGFβ1 signaling (22, 77). In conclusion, our results demonstrated that inhibition of TGFβ signaling by selectively targeting TGFβ1 or SMAD3 could inhibit AV calcification. This information will be useful in designing safer treatments for CAVD.

DATA AVAILABILITY STATEMENT

The raw data supporting the conclusions of this article will be made available by the authors, without undue reservation.

ETHICS STATEMENT

The animal study was reviewed and approved by the IACUC University of South Carolina.

AUTHOR CONTRIBUTIONS

MA: conceptualization and supervision. MC, AB, MG, IC, ZA, and JJ: methodology. MC, AB, IC, and MA: formal analysis. MC and MA: writing—original draft preparation. IC and MA writing—review and editing. MA and NV: funding acquisition. All authors have read and agreed to the submitted version of the manuscript.

FUNDING

This work was supported by the Transformative Research Seed Grant Initiative, Bob Price Instrumentation Resource Facility Endowment Fund, and ASPIRE-II (Advanced Support Program for Integration of Research Excellence-II- Office of the Vice President for Research) from the University of South Carolina, and the National Institutes of Health (grant nos. R01HL126705, R01HL145064, and 1P20GM103641) (Center for Dietary Supplements and Inflammation; Prakash Nagarkatti and Mitzi Nagarkatti).

ACKNOWLEDGMENTS

We thank the Instrumentation Resource Facility at the University of South Carolina School of Medicine and the Dorn VA Medical Center for the instrumentation support.

REFERENCES

1. Lindman BR, Clavel MA, Mathieu P, Iung B, Lancellotti P, Otto CM, et al. Calcific aortic stenosis. *Nat Rev Dis Primers.* (2016) 2:16006. doi: 10.1038/nrdp.2016.6
2. Yutzey KE, Demer LL, Body SC, Huggins GS, Towler DA, Giachelli CM, et al. Calcific aortic valve disease: a consensus summary from the alliance of investigators on calcific aortic valve disease. *Arterioscler Thromb Vasc Biol.* (2014) 34:2387–93. doi: 10.1161/ATVBAHA.114.302523
3. Rajamannan NM, Evans FJ, Aikawa E, Grande-Allen KJ, Demer LL, Heistad DD, et al. Calcific aortic valve disease: not simply a degenerative process: a review and agenda for research from the National Heart and Lung and Blood Institute Aortic Stenosis Working Group. Executive summary: calcific aortic valve disease-2011 update. *Circulation.* (2011) 124:1783–91. doi: 10.1161/CIRCULATIONAHA.110.006767
4. Dutta P, Lincoln J. Calcific aortic valve disease: a developmental biology perspective. *Curr Cardiol Rep.* (2018) 20:21. doi: 10.1007/s11886-018-0968-9
5. Wu B, Wang Y, Xiao F, Butcher JT, Yutzey KE, Zhou B. Developmental Mechanisms of Aortic Valve Malformation and Disease. *Annu Rev Physiol.* (2016) 79:21–41. doi: 10.1146/annurev-physiol-022516-034001
6. Bui HT, Khair N, Yeats B, Gooden S, James SP, Dasi LP. Transcatheter heart valves: a biomaterials perspective. *Adv Healthc Mater.* (2021) 10:e2100115. doi: 10.1002/adhm.202100115
7. Chen Y, Chen YX, Huang C, Duan ZB, Xu CY. The clinical value of klotho and FGF23 in cardiac valve calcification among patients with chronic kidney disease. *Int J Gen Med.* (2021) 14:857–66. doi: 10.2147/IJGM.S299197
8. Kurosu H, Yamamoto M, Clark JD, Pastor JV, Nandi A, Gurnani P, et al. Suppression of aging in mice by the hormone Klotho. *Science.* (2005) 309:1829–33. doi: 10.1126/science.1112766
9. Jadhav S, Tripathi S, Chandrekar A, Waikar SS, Hsiao LL. A novel antibody for the detection of alternatively spliced secreted KLOTHO isoform in human plasma. *PLoS One.* (2021) 16:e0245614. doi: 10.1371/journal.pone.0245614
10. Lim K, Lu TS, Molostvov G, Lee C, Lam FT, Zehnder D, et al. Vascular Klotho deficiency potentiates the development of human artery calcification and mediates resistance to fibroblast growth factor 23. *Circulation.* (2012) 125:2243–55. doi: 10.1161/CIRCULATIONAHA.111.053405
11. Matsumura Y, Aizawa H, Shiraki-Iida T, Nagai R, Kuro-o M, Nabeshima Y. Identification of the human klotho gene and its two transcripts encoding membrane and secreted klotho protein. *Biochem Biophys Res Commun.* (1998) 242:626–30. doi: 10.1006/bbrc.1997.8019
12. Kato Y, Arakawa E, Kinoshita S, Shirai A, Furuya A, Yamano K, et al. Establishment of the anti-Klotho monoclonal antibodies and detection of Klotho protein in kidneys. *Biochem Biophys Res Commun.* (2000) 267:597–602. doi: 10.1006/bbrc.1999.2009
13. Hu MC, Kuro-o M, Moe OW. Renal and extrarenal actions of Klotho. *Semin Nephrol.* (2013) 33:118–29. doi: 10.1016/j.semnephrol.2012.12.013
14. Kuro OM. The Klotho proteins in health and disease. *Nat Rev Nephrol.* (2019) 15:27–44. doi: 10.1038/s41581-018-0078-3
15. Chen CD, Podvin S, Gillespie E, Leeman SE, Abraham CR. Insulin stimulates the cleavage and release of the extracellular domain of Klotho by ADAM10 and ADAM17. *Proc Natl Acad Sci USA.* (2007) 104:19796–801. doi: 10.1073/pnas.0709805104
16. Bloch L, Sineshchekova O, Reichenbach D, Reiss K, Saftig P, Kuro-o M, et al. Klotho is a substrate for alpha-, beta- and gamma-secretase. *FEBS Lett.* (2009) 583:3221–4. doi: 10.1016/j.febslet.2009.09.009
17. Donate-Correa J, Mora-Fernandez C, Martinez-Sanz R, Muros-de-Fuentes M, Perez H, Meneses-Perez B, et al. Expression of FGF23/KLOTHO system in human vascular tissue. *Int J Cardiol.* (2013) 165:179–83. doi: 10.1016/j.ijcard.2011.08.850
18. Imura A, Iwano A, Tohyama O, Tsuji Y, Nozaki K, Hashimoto N, et al. Secreted Klotho protein in sera and CSF: implication for post-translational cleavage in release of Klotho protein from cell membrane. *FEBS Lett.* (2004) 565:143–7. doi: 10.1016/j.febslet.2004.03.090
19. Consortium A. Autosomal dominant hypophosphataemic rickets is associated with mutations in FGF23. *Nat Genet.* (2000) 26:345–8. doi: 10.1038/81664
20. Shimada T, Hasegawa H, Yamazaki Y, Muto T, Hino R, Takeuchi Y, et al. FGF-23 is a potent regulator of vitamin D metabolism and phosphate homeostasis. *J Bone Miner Res.* (2004) 19:429–35. doi: 10.1359/JBMR.0301264
21. Yu X, Ibrahimi OA, Goetz R, Zhang F, Davis SI, Garringer HJ, et al. Analysis of the biochemical mechanisms for the endocrine actions of fibroblast growth factor-23. *Endocrinology.* (2005) 146:4647–56. doi: 10.1210/en.2005-0670
22. Doi S, Zou Y, Togao O, Pastor JV, John GB, Wang L, et al. Klotho inhibits transforming growth factor-beta1 (TGF-beta1) signaling and suppresses renal fibrosis and cancer metastasis in mice. *J Biol Chem.* (2011) 286:8655–65. doi: 10.1074/jbc.M110.174037
23. Kuro-o M, Matsumura Y, Aizawa H, Kawaguchi H, Suga T, Utsugi T, et al. Mutation of the mouse klotho gene leads to a syndrome resembling ageing. *Nature.* (1997) 390:45–51.
24. Linefsky JP, O'Brien KD, Katz R, de Boer IH, Barasch E, Jenny NS, et al. Association of serum phosphate levels with aortic valve sclerosis and annular calcification: the cardiovascular health study. *J Am Coll Cardiol.* (2011) 58:291–7. doi: 10.1016/j.jacc.2010.11.073
25. Cheek JD, Wirrig EE, Alfieri CM, James JF, Yutzey KE. Differential activation of valvulogenic, chondrogenic, and osteogenic pathways in mouse models of myxomatous and calcific aortic valve disease. *J Mol Cell Cardiol.* (2012) 52:689–700. doi: 10.1016/j.yjmcc.2011.12.013
26. Hu MC, Shi M, Zhang J, Quinones H, Griffith C, Kuro-o M, et al. Klotho deficiency causes vascular calcification in chronic kidney disease. *J Am Soc Nephrol.* (2011) 22:124–36.
27. Dutta P, Kodigepalli KM, LaHaye S, Thompson JW, Rains S, Nagel C, et al. KPT-330 prevents aortic valve calcification via a novel C/EBPbeta signaling pathway. *Circ Res.* (2021) 128:1300–16. doi: 10.1161/CIRCRESAHA.120.318503
28. Piers LH, Touw HR, Gansevoort R, Franssen CF, Oudkerk M, Zijlstra F, et al. Relation of aortic valve and coronary artery calcium in patients with chronic kidney disease to the stage and etiology of the renal disease. *Am J Cardiol.* (2009) 103:1473–7. doi: 10.1016/j.amjcard.2009.01.396
29. Thubrikar MJ, Aouad J, Nolan SP. Patterns of calcific deposits in operatively excised stenotic or purely regurgitant aortic valves and their relation to mechanical stress. *Am J Cardiol.* (1986) 58:304–8.
30. Menon V, Lincoln J. The genetic regulation of aortic valve development and calcific disease. *Front Cardiovasc Med.* (2018) 5:162. doi: 10.3389/fcvm.2018.00162
31. Jian B, Narula N, Li QY, Mohler ER III, Levy RJ. Progression of aortic valve stenosis: TGF-beta1 is present in calcified aortic valve cusps and promotes aortic valve interstitial cell calcification via apoptosis. *Ann Thorac Surg.* (2003) 75:457–65. doi: 10.1016/s0003-4975(02)04312-6
32. Clark-Greuel JN, Connolly JM, Sorichillo E, Narula NR, Rapoport HS, Mohler ER III, et al. Transforming growth factor-beta1 mechanisms in aortic valve calcification: increased alkaline phosphatase and related events. *Ann Thorac Surg.* (2007) 83:946–53. doi: 10.1016/j.athoracsur.2006.10.026
33. Derynck R, Jarrett JA, Chen EY, Eaton DH, Bell JR, Assoian RK, et al. Human transforming growth factor-beta complementary DNA sequence and expression in normal and transformed cells. *Nature.* (1985) 316:701–5.
34. Akhurst RJ, Hata A. Targeting the TGFbeta signalling pathway in disease. *Nat Rev Drug Discov.* (2012) 11:790–811.
35. Mu Y, Gudey SK, Landstrom M. Non-Smad signaling pathways. *Cell Tissue Res.* (2012) 347:11–20.
36. Heldin CH, Moustakas A. Signaling receptors for TGF-beta family members. *Cold Spring Harb Perspect Biol.* (2016) 8:a022053.
37. Shull MM, Ormsby I, Kier AB, Pawlowski S, Diebold RJ, Yin M, et al. Targeted disruption of the mouse transforming growth factor-beta 1 gene results in multifocal inflammatory disease. *Nature.* (1992) 359:693–9.
38. Luong TTD, Estepa M, Boehme B, Pieske B, Lang F, Eckardt KU, et al. Inhibition of vascular smooth muscle cell calcification by vasorin through interference with TGFbeta1 signaling. *Cell Signal.* (2019) 64:109414. doi: 10.1016/j.cellsig.2019.109414
39. Musial K, Zwolinska D. Novel indicators of fibrosis-related complications in children with chronic kidney disease. *Clin Chim Acta.* (2014) 430:15–9. doi: 10.1016/j.cca.2013.12.031
40. Vianna HR, Soares CM, Silveira KD, Elmiro GS, Mendes PM, de Sousa Tavares M, et al. Cytokines in chronic kidney disease: potential link of MCP-1 and dyslipidemia in glomerular diseases. *Pediatr Nephrol.* (2013) 28:463–9. doi: 10.1007/s00467-012-2363-x
41. Voelkl J, Lang F, Eckardt KU, Amann K, Kuro OM, Pasch A, et al. Signaling pathways involved in vascular smooth muscle cell calcification during hyperphosphatemia. *Cell Mol Life Sci.* (2019) 76:2077–91.

42. Voelkl J, Cejka D, Alesutan I. An overview of the mechanisms in vascular calcification during chronic kidney disease. *Curr Opin Nephrol Hypertens.* (2019) 28:289–96.
43. Shanahan CM, Crouthamel MH, Kapustin A, Giachelli CM. Arterial calcification in chronic kidney disease: key roles for calcium and phosphate. *Circ Res.* (2011) 109:697–711.
44. Hoevelmann J, Mahfoud F, Lauder L, Scheller B, Bohm M, Ewen S. Valvular heart disease in patients with chronic kidney disease. *Herz.* (2021) 46:228–33.
45. Alves RD, Eijken M, van de Peppel J, van Leeuwen JP. Calcifying vascular smooth muscle cells and osteoblasts: independent cell types exhibiting extracellular matrix and biomineralization-related mimicries. *BMC Genomics.* (2014) 15:965. doi: 10.1186/1471-2164-15-965
46. Voelkl J, Luong TT, Tuffaha R, Musculus K, Auer T, Lian X, et al. SGK1 induces vascular smooth muscle cell calcification through NF-kappaB signaling. *J Clin Invest.* (2018) 128:3024–40. doi: 10.1172/JCI96477
47. Walker GA, Masters KS, Shah DN, Anseth KS, Leinwand LA. Valvular myofibroblast activation by transforming growth factor-beta: implications for pathological extracellular matrix remodeling in heart valve disease. *Circ Res.* (2004) 95:253–60.
48. Steitz SA, Speer MY, Curinga G, Yang HY, Haynes P, Aebersold R, et al. Smooth muscle cell phenotypic transition associated with calcification: upregulation of Cbfa1 and downregulation of smooth muscle lineage markers. *Circ Res.* (2001) 89:1147–54. doi: 10.1161/hh2401.101070
49. Alesutan I, Feger M, Tuffaha R, Castor T, Musculus K, Buehling SS, et al. Augmentation of phosphate-induced osteo-/chondrogenic transformation of vascular smooth muscle cells by homoarginine. *Cardiovasc Res.* (2016) 110:408–18. doi: 10.1093/cvr/cvw062
50. Rabkin E, Aikawa M, Stone JR, Fukumoto Y, Libby P, Schoen FJ. Activated interstitial myofibroblasts express catabolic enzymes and mediate matrix remodeling in myxomatous heart valves. *Circulation.* (2001) 104:2525–32.
51. Leibrock CB, Alesutan I, Voelkl J, Pakladok T, Michael D, Schleicher E, et al. NH4Cl treatment prevents tissue calcification in klotho deficiency. *J Am Soc Nephrol.* (2015) 26:2423–33.
52. Alesutan I, Musculus K, Castor T, Alzoubi K, Voelkl J, Lang F. Inhibition of phosphate-induced vascular smooth muscle cell osteo-/chondrogenic signaling and calcification by bafilomycin a1 and methylamine. *Kidney Blood Press Res.* (2015) 40:490–9. doi: 10.1159/000368524
53. Huk DJ, Austin BF, Horne TE, Hinton RB, Ray WC, Heistad DD, et al. Valve endothelial cell-derived Tgfbeta1 signaling promotes nuclear localization of sox9 in interstitial cells associated with attenuated calcification. *Arterioscler Thromb Vasc Biol.* (2016) 36:328–38. doi: 10.1161/ATVBAHA.115.306091
54. Peacock JD, Levay AK, Gillaspie DB, Tao G, Lincoln J. Reduced sox9 function promotes heart valve calcification phenotypes in vivo. *Circ Res.* (2010) 106:712–9.
55. Wirrig EE, Gomez MV, Hinton RB, Yutzey KE. COX2 inhibition reduces aortic valve calcification in vivo. *Arterioscler Thromb Vasc Biol.* (2015) 35:938–47. doi: 10.1161/ATVBAHA.114.305159
56. Gomez-Stallons MV, Wirrig-Schwendeman EE, Hassel KR, Conway SJ, Yutzey KE. Bone morphogenetic protein signaling is required for aortic valve calcification. *Arterioscler Thromb Vasc Biol.* (2016) 36:1398–405.
57. Chen J, Lin Y, Sun Z. Deficiency in the anti-aging gene Klotho promotes aortic valve fibrosis through AMPKalpha-mediated activation of RUNX2. *Aging Cell.* (2016) 15:853–60. doi: 10.1111/acel.12494
58. Azhar M, Runyan RB, Gard C, Sanford LP, Miller ML, Andringa A, et al. Ligand-specific function of transforming growth factor beta in epithelial-mesenchymal transition in heart development. *Dev Dyn.* (2009) 238:431–42. doi: 10.1002/dvdy.21854
59. Daniel SG, Ball CL, Besselsen DG, Doetschman T, Hurwitz BL. Functional changes in the gut microbiome contribute to transforming growth factor beta-deficient colon cancer. *mSystems.* (2017) 2:e00065–17. doi: 10.1128/mSystems.00065-17
60. Chakrabarti M, Al-Sammarraie N, Gebere MG, Bhattacharya A, Chopra S, Johnson J, et al. Transforming growth factor beta3 is required for cardiovascular development. *J Cardiovasc Dev Dis.* (2020) 7:19.
61. Bhattacharya A, Al-Sammarraie N, Gebere MG, Johnson J, Eberth JF, Azhar M. Myocardial TGFbeta2 is required for atrioventricular cushion remodeling and myocardial development. *J Cardiovasc Dev Dis.* (2021) 8:26.
62. Azhar M, Yin M, Bommireddy R, Duffy JJ, Yang J, Pawlowski SA, et al. Generation of mice with a conditional allele for transforming growth factor beta 1 gene. *Genesis.* (2009) 47:423–31.
63. Wirrig EE, Hinton RB, Yutzey KE. Differential expression of cartilage and bone-related proteins in pediatric and adult diseased aortic valves. *J Mol Cell Cardiol.* (2011) 50:561–9. doi: 10.1016/j.yjmcc.2010.12.005
64. Gomez-Stallons MV, Tretter JT, Hassel K, Gonzalez-Ramos O, Amofa D, Ollberding NJ, et al. Calcification and extracellular matrix dysregulation in human postmortem and surgical aortic valves. *Heart.* (2019) 105:1616–21. doi: 10.1136/heartjnl-2019-314879
65. Azhar M, Ware SM. Genetic and developmental basis of cardiovascular malformations. *Clin Perinatol.* (2016) 43:39–53.
66. Weiss RM, Ohashi M, Miller JD, Young SG, Heistad DD. Calcific aortic valve stenosis in old hypercholesterolemic mice. *Circulation.* (2006) 114:2065–9.
67. Angelov SN, Hu JH, Wei H, Airhart N, Shi M, Dichek DA. TGF-beta (Transforming Growth Factor-beta) signaling protects the thoracic and abdominal aorta from angiotensin II-induced pathology by distinct mechanisms. *Arterioscler Thromb Vasc Biol.* (2017) 37:2102–13. doi: 10.1161/ATVBAHA.117.309401
68. Morikawa M, Derynck R, Miyazono K. TGF-beta and the TGF-beta family: context-dependent roles in cell and tissue physiology. *Cold Spring Harb Perspect Biol.* (2016) 8:a021873.
69. Culbert AL, Chakkalakal SA, Theosmy EG, Brennan TA, Kaplan FS, Shore EM. Alk2 regulates early chondrogenic fate in fibrodysplasia ossificans progressiva heterotopic endochondral ossification. *Stem Cells.* (2014) 32:1289–300. doi: 10.1002/stem.1633
70. Daly AC, Randall RA, Hill CS. Transforming growth factor beta-induced Smad1/5 phosphorylation in epithelial cells is mediated by novel receptor complexes and is essential for anchorage-independent growth. *Mol Cell Biol.* (2008) 28:6889–902. doi: 10.1128/MCB.01192-08
71. Flanders KC, Heger CD, Conway C, Tang B, Sato M, Dengler SL, et al. Brightfield proximity ligation assay reveals both canonical and mixed transforming growth factor-beta/bone morphogenetic protein Smad signaling complexes in tissue sections. *J Histochem Cytochem.* (2014) 62:846–63. doi: 10.1369/0022155414550163
72. Wang J, Sridurongrit S, Dudas M, Thomas P, Nagy A, Schneider MD, et al. Atrioventricular cushion transformation is mediated by ALK2 in the developing mouse heart. *Dev Biol.* (2005) 286:299–310.
73. Goto K, Kamiya Y, Imamura T, Miyazono K, Miyazawa K. Selective inhibitory effects of Smad6 on bone morphogenetic protein type I receptors. *J Biol Chem.* (2007) 282:20603–11. doi: 10.1074/jbc.M702100200
74. Maeda S, Hayashi M, Komiya S, Imamura T, Miyazono K. Endogenous TGF-beta signaling suppresses maturation of osteoblastic mesenchymal cells. *EMBO J.* (2004) 23:552–63. doi: 10.1038/sj.emboj.7600067
75. Carta L, Smaldone S, Zilberberg L, Loch D, Dietz HC, Rifkin DB, et al. p38 MAPK is an early determinant of promiscuous Smad2/3 signaling in the aortas of fibrillin-1 (Fbn1)-null mice. *J Biol Chem.* (2009) 284:5630–6. doi: 10.1074/jbc.M806962200
76. Holm TM, Habashi JP, Doyle JJ, Bedja D, Chen Y, van Erp C, et al. Noncanonical TGFbeta signaling contributes to aortic aneurysm progression in Marfan syndrome mice. *Science.* (2011) 332:358–61.
77. Sugiura H, Yoshida T, Shiohira S, Kohei J, Mitobe M, Kurosu H, et al. Reduced Klotho expression level in kidney aggravates renal interstitial fibrosis. *Am J Physiol Renal Physiol.* (2012) 302:F1252–64.

Conflict of Interest: The authors declare that the research was conducted in the absence of any commercial or financial relationships that could be construed as a potential conflict of interest.

frontiers | Frontiers in Cardiovascular Medicine

TYPE Original Research
PUBLISHED 25 October 2022
DOI 10.3389/fcvm.2022.742850

OPEN ACCESS

EDITED BY
Lakshmi Prasad Dasi,
Georgia Institute of Technology,
United States

REVIEWED BY
Veronika Myasoedova,
Monzino Cardiology Center (IRCCS),
Italy
Sarvesh Chelvanambi,
Department of Medicine, Brigham
and Women's Hospital and Harvard
Medical School, United States
Cécile Oury,
University of Liège, Belgium
Borja Fernández,
University of Malaga, Spain
Anna Malashicheva,
Institute of Cytology, Russia

*CORRESPONDENCE
Vidu Garg
vidu.garg@nationwidechildrens.org
Uddalak Majumdar
uddalak2005@gmail.com

SPECIALTY SECTION
This article was submitted to
Heart Valve Disease,
a section of the journal
Frontiers in Cardiovascular Medicine

RECEIVED 16 July 2021
ACCEPTED 30 September 2022
PUBLISHED 25 October 2022

CITATION
Majumdar U, Choudhury TZ,
Manivannan S, Ueyama Y, Basu M and
Garg V (2022) Single-cell
RNA-sequencing analysis of aortic
valve interstitial cells demonstrates
the regulation of integrin signaling by
nitric oxide.
Front. Cardiovasc. Med. 9:742850.
doi: 10.3389/fcvm.2022.742850

Single-cell RNA-sequencing analysis of aortic valve interstitial cells demonstrates the regulation of integrin signaling by nitric oxide

Uddalak Majumdar [1,2]*, Talita Z. Choudhury[1,2], Sathiyanarayanan Manivannan[1,2], Yukie Ueyama[1,2], Madhumita Basu[1,2,3] and Vidu Garg [1,2,3,4]*

[1]Center for Cardiovascular Research, Nationwide Children's Hospital, Columbus, OH, United States, [2]The Heart Center, Nationwide Children's Hospital, Columbus, OH, United States, [3]Department of Pediatrics, The Ohio State University, Columbus, OH, United States, [4]Department of Molecular Genetics, The Ohio State University, Columbus, OH, United States

Calcific aortic valve disease (CAVD) is an increasingly prevalent condition among the elderly population that is associated with significant morbidity and mortality. Insufficient understanding of the underlying disease mechanisms has hindered the development of pharmacologic therapies for CAVD. Recently, we described nitric oxide (NO) mediated S-nitrosylation as a novel mechanism for preventing the calcific process. We demonstrated that NO donor or an S-nitrosylating agent, S-nitrosoglutathione (GSNO), inhibits spontaneous calcification in porcine aortic valve interstitial cells (pAVICs) and this was supported by single-cell RNA sequencing (scRNAseq) that demonstrated NO donor and GSNO inhibited myofibroblast activation of pAVICs. Here, we investigated novel signaling pathways that are critical for the calcification of pAVICs that are altered by NO and GSNO by performing an in-depth analysis of the scRNA-seq dataset. Transcriptomic analysis revealed 1,247 differentially expressed genes in pAVICs after NO donor or GSNO treatment compared to untreated cells. Pathway-based analysis of the differentially expressed genes revealed an overrepresentation of the integrin signaling pathway, along with the Rho GTPase, Wnt, TGF-β, and p53 signaling pathways. We demonstrate that *ITGA8* and *VCL*, two of the identified genes from the integrin signaling pathway, which are known to regulate cell-extracellular matrix (ECM) communication and focal adhesion, were upregulated in both *in vitro* and *in vivo* calcific conditions. Reduced expression of these genes after treatment with NO donor suggests that NO inhibits calcification by targeting myofibroblast adhesion and ECM remodeling. In addition, withdrawal of NO donor after 3 days of exposure revealed that NO-mediated transcriptional and translational regulation is a transient event

and requires continuous NO exposure to inhibit calcification. Overall, our data suggest that NO and S-nitrosylation regulate the integrin signaling pathway to maintain healthy cell-ECM interaction and prevent CAVD.

KEYWORDS

calcific aortic valve disease, nitric oxide, S-nitrosylation, single cell RNA-sequencing, integrin signaling, extracellular matrix (ECM)

Introduction

Calcific aortic valve disease (CAVD) is defined by the thickening of the aortic valve leaflets with the deposition of calcific nodules. The estimated global prevalence of CAVD is 12.6 million with greater than 100,000 deaths per year (1). The Global Burden of Disease Study 2019 found that newly diagnosed cases of CAVD increased ∼3.5-fold from 1990, with nearly 600,000 cases in 2019. (2). Despite its correlation with aging, calcification has been demonstrated to be an active disease process and not a degenerative process (3). However, the mechanisms underlying disease progression are not clearly understood and as a result, no effective therapies have been developed to prevent or cure CAVD in humans (4, 5).

A healthy aortic valve opens and closes to its full extent during each cardiac cycle to maintain proper unidirectional blood flow and prevent regurgitation. The structure and composition of the leaflet allow the valve to withstand the oscillating hemodynamic forces associated with each cardiac contraction. Heart valves are composed of valve endothelial cells (VECs), valve interstitial cells (VICs), and extracellular matrix (ECM). VICs are interspersed within the ECM, and the VICs and ECM are encapsulated by a single layer of VECs. Bidirectional communication between VECs, VICs, and ECM is important for the maintenance of a healthy valve. The present and previous studies have demonstrated that VEC-derived nitric oxide (NO), a second messenger molecule, is important for the inhibition of calcification in VICs (6–9). VECs modulate the proliferation and differentiation of VICs to maintain a quiescent VIC phenotype by reducing the expression of α-smooth muscle actin (αSMA), while the osteogenic phenotype of VICs is defined by the increased expression of RUNX2 (9, 10). Studies have shown that porcine aortic valve interstitial cells (pAVICs) when cultured on stiff surfaces express increased αSMA, which can be inhibited by co-culturing with porcine aortic valve endothelial cells (pAVECs) (11). The addition of L-NAME, a NO synthase (NOS) blocker, abrogates this VEC-dependent inhibition of αSMA expression (11). Regulation by VECs is dependent on blood flow and associated shear stress, which can also regulate NO production (12, 13). Exposure to L-arginine, a NOS substrate, can prevent lipopolysaccharide (LPS)-induced bone-related alkaline phosphatase expression and calcification of collagen matrix in bovine aortic valve interstitial cells (AVICs) (14). Recently, we observed NO donor can suppress both αSMA and RUNX2 expression in pAVICs (7). *In vivo* and *in vitro* studies have demonstrated that NO can activate NOTCH1 signaling, and loss of function mutations in *NOTCH1* are associated with CAVD in humans (6, 15). We have also demonstrated aortic valve thickening in *Notch1* haploinsufficient mice in a $Nos3^{-/-}$ background (6, 16). Recently, we described a mechanism by which NO activates NOTCH1 signaling and prevents CAVD that requires S-nitrosylation, a NO-dependent post-translational modification of target proteins (7). Utilizing mass spectrometric screening, we identified USP9X, a deubiquitinase, as one of the S-nitrosylated targets that can activate NOTCH1 signaling. We further demonstrated that the deletion of *Usp9x* from VECs and VEC-derived VICs in mice leads to thickened, calcified aortic valves which are stenotic (7). Although the involvement of the NO-dependent sGC/cGMP pathway in the inhibition of calcification of VICs has been described by others, we did not observe activation of this pathway in pAVICs culture condition after NO donor treatment (9, 17–19).

To understand the molecular mechanism of NO-dependent inhibition of CAVD, we utilized *in vitro* pAVICs (6). We observed spontaneous calcification of pAVICs when cultured on the stiff surface of tissue culture plastic plates. This calcification was prevented when cultured in presence of NO donor and the S-nitrosylating agent, S-nitrosoglutathione (GSNO) (7). Therefore, the pAVICs, cultured in presence of NO donor or GSNO represent a healthy state, whereas, the untreated cells represent a disease condition. It has been previously reported that the myofibroblast activation in pAVICs is initiated by increasing the stiffness of the culture conditions (20, 21). We demonstrated NO donor and GSNO can inhibit this stiffness associated myofibroblast activation and subsequent calcification. VICs are surrounded by ECM *in vivo*, and the ECM functions to maintain the proper healthy environment for VICs. We previously reported the presence of disorganized ECM with increased deposition of proteoglycan in *Usp9x* mutant mice, an *in vivo* model of CAVD

(7). However, the role of NO in the regulation of ECM is not well-understood.

Communication between the valve cells and ECM is critical for the optimal function of the valve. In this context, cell surface receptors play critical roles in maintaining ECM homeostasis and reduced stiffness. Healthy VICs are responsible for the turnover of ECM and respond to extracellular mechanical and chemical stimuli (22). VICs communicate with the ECM through integrins and non-integrin membrane receptors, which play a regulatory role in stiffness-dependent calcification (20, 23). Integrins are transmembrane proteins comprising heterodimers of α and β subunits. Dysregulation in this integrin specificity has been observed in CAVD along with multiple other diseases including cancer, atherosclerosis, and kidney, and liver diseases (24, 25). Integrin receptors bind to their specific ECM partner proteins by recognizing distinct peptide sequences and blocking of this interaction has been shown to lead to calcific nodule formation (19). This suggests that the ECM-influenced calcification may be regulated by integrin-ECM interactions (20). For example, integrin α5β1 and αvβ3, which are both minimally expressed in quiescent VICs, bind to fibronectin by recognizing RGD peptide motif, but with myofibroblast activation, the expression and ECM binding of both of these receptors is increased (20, 25, 26). On the other hand, the 67-kD non-integrin protein receptor interacts with the laminin-derived YIGSR peptide motif. Blocking of this interaction leads to increase calcific nodule formation in pAVICs, suggesting its inhibitory role in calcification (20). Other integrin receptors, such as α2β1 bind to collagen-derived DEGA peptide motif, important for force generation in the valve leaflets (27, 28). Blocking of α2β1 integrins or actin polymerization abolished force generation that suggests VIC-collagen coupling *via* α2β1 is necessary for force generation in the valve leaflet (28). In addition, elevated expression of other collagen-binding integrin receptors α1β1 and α3β1 were also observed in diseased valves (25, 29). Certain integrin-ligand interactions play important role in the initiation of osteoblast differentiation and mineralization (30). This interaction between ECM ligands and integrin receptors initiates downstream signaling pathways by activating Ras or MAPK (31). After binding to ECM ligands, integrin receptors transmit extracellular mechano-signals inside the cells by recruiting focal adhesion proteins, which establish the connection to the actin cytoskeleton. In addition, α-smooth muscle actin (αSMA; *ACTA2*), expressed in myofibroblasts allows cells to generate enhanced cellular forces, which can also be transmitted back to the ECM *via* integrins (32). These mechanical forces prompt VICs to be activated and to differentiate into myofibroblasts, which then secrete growth factors and also ECM components. The role of transforming growth factors (TGF) has been implicated in valve development and calcification (33–37). Our published analysis of single-cell RNA sequencing (scRNAseq) data from pAVICs demonstrates that NO donor and GSNO prevent the myofibroblast activation and calcification by downregulating αSMA, Vimentin, Calponin, and Transgelin expression (7). However, our previous analysis was limited to the examination of genes that are important for myofibroblast activation. We did not examine the altered cellular signaling pathways, which are modulated by NO donor or GSNO to inhibit calcification.

In this report, we have analyzed scRNAseq data to identify the altered cellular signaling pathways that prevent spontaneous myofibroblast activation and calcification of pAVICs in response to NO signaling. We found an overrepresentation of the integrin signaling pathway in NO donor and GSNO-treated conditions. This finding was further confirmed in our recently described murine model of calcification. We also have demonstrated that altered gene expression in pAVICs after NO donor and GSNO treatment is temporary and is dependent on continuous NO exposure. Overall, our data suggest that NO and S-nitrosylation of target proteins maintain healthy VIC-ECM interactions and prevent calcification by regulation of integrin signaling pathway members.

Materials and methods

Porcine aortic valve interstitial cell culture and treatments

Valve interstitial cells were collected from juvenile pig valve leaflets as previously described (7). Briefly, valve leaflets were digested with collagenase (Worthington Biochemical# LS004176) for 5°min at 37°C and the VEC layer was removed gently with a sterile swab. After VEC layer removal, valve leaflets were digested with collagenase for 15 h at 37°C to dislodge VICs. Isolated pAVICs were cultured in a VIC-specific medium as previously described (7). pAVICs were passaged with trypsin-EDTA and only cells between passages three and seven were used in this study. pAVICs were cultured on a stiff surface of plastic tissue culture plates in Media-199 (ThermoFisher, Waltham, MA, United States, #11150059) supplemented with 10% fetal bovine serum (FBS) for 5 days or as otherwise noted. To expose pAVICs to the NO donor or S-nitrosylating agent, cell culture media was supplemented with either detaNONOate (150 μm) (FisherScientific, Pittsburgh, PA, United States, #AC328651000), or S-nitrosoglutathione (GSNO: 200 μm) (MilliporeSigma, Burlington, MA, United States, #N4148) and was refreshed daily.

To test and validate whether the effect of NO is long-lasting, pAVICs were cultured for 3 days with detaNONOate (150 μm) and then without detaNONOate either for additional 2 days (scRNAseq) or an additional 2, 5, and 8 days (Western Blot). This pAVICs culture condition will be designated as "NO donor

withdrawal." In this experiment 5 days culture of pAVICs with and without detaNONOate, and GSNO were utilized as control.

To culture pAVICs in osteogenic media, Media 199 was supplemented with ascorbate-2-phosphate (50 μg/ml; Sigma-Aldrich, Burlington, MA, United States, #49752), 10 nM dexamethasone (Sigma-Aldrich, Burlington, MA, United States, #D4902), and 10 μm β-glycerol phosphate (Sigma-Aldrich, Burlington, MA, United States, #G9422).

Single-cell RNA sequencing and analyses

For this study, we examined published single-cell data (GEO accession no: GSE161123). The methods for single-cell sequencing were already described previously (7). Briefly, we utilized >85% viable pAVICs to generate 10 × Genomics 3′ v2 chemistry-based libraries using 10 × Genomics Chromium controller (~2,000 target cell recovery/group) following the manufacturer's instructions. All libraries were sequenced (150 bp paired-end) in the Illumina HiSeq4000 platform and 10× Genomics' Cell Ranger pipeline was used to demultiplex and generate FASTQ files. Data was mapped to the pig genome Sscrofa11 with Y sequences from WTSI_X_Y_pig V2 (GCF_000003025.6_Sscrofa11.1_genomic.fna) and gene annotation (GCF_000003025.6_Sscrofa11.1_genomic_genes.filtered.gtf) from NCBI.[1] Cell ranger aggregate was used to combine scRNA-seq data with different treatments (control, GSNO, NO donor, and NO donor withdrawal) that yield a total of 7,037 cells (control: 1,683, GSNO: 1966, NO donor: 1,485, and NO donor withdrawal: 1,903 cells). We recovered an average expression of 3,397 genes per cell. Seurat (version 3.0) was used for data processing, identification, and normalization of genes with the highest variability. Common differentially expressed genes among NO donor and GSNO compared to control were selected using criteria $p_{\text{adjusted}} \leq 0.05$ and $\text{Log}_2\text{FC} \geq 0.6$ or ≤ -0.6 (at least 50% up or down-regulated genes). For all of the samples, the base means cut-off of 100 was utilized to filter differentially expressed genes. The volcano plot was created using ggplot2 (3.2.1) package of R. Heatmap and violin plots were created using Ryabhatta App (38). The chord diagram was generated using http://www.datasmith.org online tool. PANTHER pathway analysis was performed using the functional classification of *Homo sapiens* PANTHER 16.0 release. In addition, we imported mouse (P30) aortic valve data (39) from the Gene Expression Omnibus database (GSE117011). To compare the gene expression of mouse aortic valve and pAVICs, mouse gene names were replaced with corresponding porcine homolog's gene names downloaded from BioMart (Ensemble[2]) as previously described (7). To compare the trends in the gene expression change across different treatments, a normalized, average expression from the four treatments was used. Normalized, average expression values for each of the 1,247 genes were calculated using the "AverageExpression" function of Seurat. Spearman distances were calculated for each of the pairs of culture conditions using the "Dist" function in the R package "amap" (version 0.8.18). Heatmap was drawn using the R package Pheatmap (version 1.0.12) based on the distance matrix output of the Dist function.

1 https://www.ncbi.nlm.nih.gov/assembly/GCF_000003025.6/

2 https://useast.ensembl.org/info/data/biomart/index.html

RNA purification and quantitative real-time polymerase chain reaction

RNA was isolated from pAVICs using TRIzol Reagent (ThermoFisher Scientific, Waltham, MA, United States, #15596018) following the manufacturer's protocol. Approximately 0.5–1.0 μg of RNA was used for reverse transcription using SuperScript VILO cDNA Synthesis Kit (ThermoFisher Scientific, Waltham, MA, United States, #11754-050). For the quantification of gene expression, real-time PCR was performed using the Applied Biosystems 7,500 real-time polymerase chain reaction (PCR). SYBR Green-based (Thermo Fisher Scientific# 4385612) quantitative real-time (RT) PCR was performed to calculate mean relative gene expression after normalization of C_t values to glyceraldehyde 3-phosphate dehydrogenase (*GAPDH*) using the $^{\Delta\Delta}$ Ct method. *GAPDH* has previously been utilized as a control gene for normalization in aortic valve leaflets (40). All primer sequences are provided in **Supplementary Data 2**.

Experimental mouse model

Animal experiments using mice were approved by the Institutional Animal Care and Use Committee (IACUC) at the Research Institute at Nationwide Children's Hospital. *Usp9x*$^{fl/fl}$ mice were obtained from Charles River Laboratories, Italy, originally generated by Ozgene Pty Ltd., Australia. *Usp9x*$^{fl/fl}$ female mice were bred with *Tie2*^{Cre} male mice (Jax# 008863), to generate *Cre*$^{+}$ (experimental) and *Cre*$^{-}$ (control) male (*Usp9x*$^{fl/Y}$; *Tie2*^{Cre}) mice as described previously (7). Genotyping was performed at P10 for *Cre*. After 6 weeks, mice were fed a high-fat western diet (Envigo, Indianapolis, IN, United States, #TD.88137) until 24 weeks of age. Prior to euthanasia, female mice underwent echocardiograms following our previously described protocol (7). Only male mice were utilized for subsequent studies. Mice were euthanized to collect hearts for immunohistological analyses. After euthanasia, hearts were perfused with phosphate-buffered saline (PBS), removed, and fixed in 4% paraformaldehyde (PFA) at 4°C overnight. After fixation, the hearts were embedded in paraffin and sectioned for further analysis.

Immunofluorescence and immunohistochemistry *in vitro* and *in vivo*

For immunofluorescence staining, cultured pAVICs were fixed with 2.5% PFA at 4°C for 15 min and permeabilized with Phosphate-Buffered Saline Triton (PBST, PBS containing 0.1% TritonX100). After permeabilization, non-specific immunoreactions were blocked using 1% BSA in PBST for 1 h at room temperature and incubated overnight with primary antibodies against ITGA8 (Santa Cruz Biotechnology, Dallas, TX, United States, #sc-365798). After primary antibody incubation, cells were washed with PBST and incubated with Alexa Fluor-594 conjugated anti-mouse secondary antibody (ThermoFisher Scientific, Waltham, MA, United States, #A21203) for 1 h at room temperature in the dark. Nuclei were stained with DAPI (1.5 μg/ml; Sigma-Aldrich, Burlington, MA, United States, #D9542). An Olympus IX51 microscope attached to Olympus DP74 camera was used to capture Images. The expression of ITGA8 was quantified by using ImageJ software. To measure the expression of the protein of interest "RawIntDen," which represents the "Fluorescent intensity" were measured for the whole image, followed by counting the number of cells by counting the nuclei (DAPI) in the same image. Expression of the target protein was represented as the average of fluorescent intensity/number of cells of multiple fields. Triplicate experiments were performed for statistical analysis.

For immunofluorescence imaging of tissue sections, a similar protocol was performed. First, the tissue sections were deparaffinized, using xylene and grades of ethanol, followed by antigen retrieval using citrate-based Antigen Unmasking solution (Vector Laboratories, Newark, CA, United States, #H-3300) following the manufacturer's protocol. After antigen retrieval, non-specific immunoreactions were blocked by treating the tissue sections with 1% bovine serum albumin (BSA) in PBST for 1 h. For ITGA8, the primary antibody (1:50; Santa Cruz Biotechnology, Dallas, TX, United States, #sc-365798) was incubated overnight at 4°C, followed by washing with PBST. Sections were incubated with anti-mouse secondary antibody conjugated to Alexa Fluor 594 (1:200 and 1:200; ThermoFisher Scientific, Waltham, MA, United States, #A21203) for 1 h at room temperature. VECTASHIELD® HardSet™ Antifade Mounting Medium with DAPI (Vector Laboratories, Newark, CA, United States, #H-1500) was used for nuclei staining. An Olympus BX51 microscope attached to an Olympus DP74 camera was used for imaging.

For immunohistochemistry (IHC), tissue sections were deparaffinized in xylene and rehydrated with ethanol and PBS before antigen retrieval. Sections were incubated with 3% H_2O_2 at room temperature for 10 min and blocked with 2% normal goat serum (Vector Laboratories, Newark, CA, United States, #S-1,000) in TBST (Tris-buffered saline containing 0.1% Tween-20) for 1 h. After blocking, sections were incubated with primary antibody for VCL (1:50, Santa Cruz Biotechnology, Dallas, TX, United States, #sc-73614) overnight at 4°C. Following this, sections were incubated with SignalStain Boost anti-Mouse IHC Detection Reagent (Cell Signaling Technology, #8114) at room temperature for 45 min. Visualization was performed using SignalStain DAB Substrate Kit (Cell Signaling Technology, Danvers, MA, #8059) and imaged using a Keyence BZ-X800 Fluorescence microscope.

Western blot analysis

Cell lysates were prepared from cultured cells in RIPA Lysis and Extraction Buffer (ThermoFisher Scientific, Waltham, MA, United States, #89900) supplemented with Halt Protease Inhibitor Cocktail (ThermoFisher Scientific, Waltham, MA, United States, #87785). Lysates were centrifuged at 15,871 g for 15 min at 4°C and the supernatants were collected. Pierce BCA Protein Assay Kit (ThermoFisher Scientific, Waltham, MA, United States, #23227) was used to estimate protein concentration. Approximately 10–25 μg of the cell lysates were mixed with 6X Laemmli SDS-Sample Buffer (Boston Bioproducts, Milford, MA, United States, #BP-111R) containing β-mercaptoethanol and boiled for 5 min. Protein samples were separated in 4–20% Mini-PROTEAN® TGX™ Precast Gels (Bio-Rad, Hercules, CA, United States, #4561094), transferred into a polyvinylidene difluoride membrane (Bio-Rad, Hercules, CA, United States, #1620177), and blocked with 5% non-fat milk in TBS containing 0.1% Tween®-20. Membranes were probed with primary antibodies against ITGA8 (1:500; Santa Cruz Biotechnology, Dallas, TX, United States, #sc-365798), VCL (1:500; Santa Cruz Biotechnology, Dallas, TX, United States, #sc-25336), SMA (1:200; Abcam# ab18147), VIM (1:1,000; Cell Signaling Technology# 5741S), and GAPDH (1:1,000; Novus Biologicals, Centennial, CO, United States, #NB300-221). After the primary antibodies probing, membranes were further probed with anti-rabbit and anti-mouse secondary antibodies conjugated with HRP (1:4,000; Vector Laboratories, Newark, CA, United States, #PI-1000, PI-2000). After probing with the secondary antibody, Pierce ECL Western Blotting Substrate (ThermoFisher Scientific, Waltham, MA, United States, #32106) or SuperSignal West Dura Extended Duration Substrate (ThermoFisher Scientific, Waltham, MA,United States, #34075) was used to develop western blots. Restore™ Western Blot Stripping Buffer (Thermo Scientific# 21059) was used for re-probing with different primary antibodies following the manufacturer's protocol. Protein levels were quantified by

densitometric analysis using ImageJ software and normalized to GAPDH.

Statistics

All the experiments were performed at least in triplicate. Mann Whitney test was performed to compare two groups and one-way analysis of variance (ANOVA) was performed to compare more than two groups to determine statistical significance using the GraphPad Prism 8 software package. For all analyses, $p \leq 0.05$ were considered statistically significant.

Study approval

This study was approved by the Institutional Animal Care and Use Committee at NCH (protocol AR16-00053) and conducted per the NIH's Guide for the Care and Use of Laboratory Animals (41).

Results

Nitric oxide transcriptionally regulates key signaling pathways for calcification in porcine aortic valve interstitial cells

We previously reported that pAVICs calcify spontaneously when cultured on a stiff surface. NO and GSNO can prevent this spontaneous calcification by inhibiting the activation of myofibroblast genes. To further confirm our observation, we cultured pAVICs in osteogenic media for 5 days in the presence and absence of NO donor and GSNO. We observed calcification of pAVICs in osteogenic media can also be inhibited by NO donor and GSNO (**Supplementary Figure 1**). Similar to this observation, we previously reported that NO reduces the protein expression of an osteogenic marker, RUNX2 in ratAVICs, cultured in osteogenic media (7). These observations in different *in vitro* calcific conditions strengthen our hypothesis that NO can inhibit valve calcification. To evaluate the NO or S-nitrosylation-dependent transcriptional regulation of cultured pAVICs, scRNAseq analysis of NO donor-treated, GSNO-treated, and untreated pAVICs was performed (7). Since, heart valves are composed of different cell types including subpopulations of VECs, VICs, immune cells, and melanocytes, bulk RNAseq cannot differentiate the cellular response to NO donor and GSNO (39, 42). However, we did not observe VECs or immune cells, or melanocytes and any separate identity of VIC-subpopulations in our pAVICs culture (7). Our transcriptomic analysis revealed activation of several myofibroblast genes in absence of NO donor and GSNO, among which *ACTA2* (αSMA) was found to be the most significantly upregulated gene (7). However, this analysis was limited to the identification of myofibroblast gene activation. In this report, we have analyzed the scRNAseq data to identify altered cellular signaling pathways that are responsive to NO. Unbiased clustering of the gene expression from all of these cells using Uniform Manifold Approximation and Projection (UMAP) demonstrated three distinct populations (**Figure 1A**). NO donor and GSNO treated pAVIC populations were similar in their cellular transcriptomic profiles but distinctly separate from the untreated control pAVICs. This data suggests that the NO-dependent transcriptional regulation of pAVICs is predominantly *via* S-nitrosylation (**Figure 1A**) based on the chemical and biological aspects of GSNO, which is considered an S-nitrosylating agent (43). Since NO exerts its cellular activity to a greater extent *via* S-nitrosylation, the effects of GSNO and NO donors are overlapping (**Figure 1A**). In addition, we previously demonstrated that GSNO produces an insignificant amount of NO in pAVICs culture (7). This observation also reduces the possibility of NO-dependent tyrosine nitration, another protein modification that is primarily associated with the oxidative stress-dependent generation of peroxynitrite, a highly reactive nitrogen species (RNS) (44).

To investigate the transcriptional changes involved in calcification using this *in vitro* system, we evaluated common differentially expressed genes after NO and GSNO treatment compared to untreated control with $p_{adjusted} \leq 0.05$ and $Log_2FC \geq 0.6$ or ≤ -0.6 (at least 50% increase or decrease in fold change). We considered differentially expressed genes after filtering the expression with a base mean cut-off of 100 for all of the samples. Using these filter criteria, we obtained 1,247 transcripts for protein-coding genes, among them 427 were upregulated and 820 were downregulated (**Figure 1B** and **Supplementary Data 1**). PANTHER pathway analysis of these 1,247 genes identified 15 pathways with at least > 10 genes (**Figure 1C**). These pathways include integrin signaling (*ITGA8, VCL, COL1A1, COL1A2, ACTA2, ACTN1, ACTG1*) with the maximum number of affected genes, followed by Rho GTPase, Wnt (*DVL1*), TGF-β (*TGFB2, TGFB3, TGFBR2*), and p53 signaling pathways. Interestingly, all of these pathways have been identified to be involved in the initiation and progression of calcification and this data suggests that these pathways are regulated by NO in the setting of CAVD (45–47). NO-dependent regulation of the integrin signaling pathway that regulates ECM by modulating actin cytoskeleton and focal adhesions has already been demonstrated in cancer and inflammatory conditions (48–51). The formation of the actin cytoskeleton and focal adhesions are also regulated by Rho family GTPases, which were also identified in the PANTHER analysis (**Figure 1C**). Overall, this data indicates that NO and S-nitrosylation can modulate

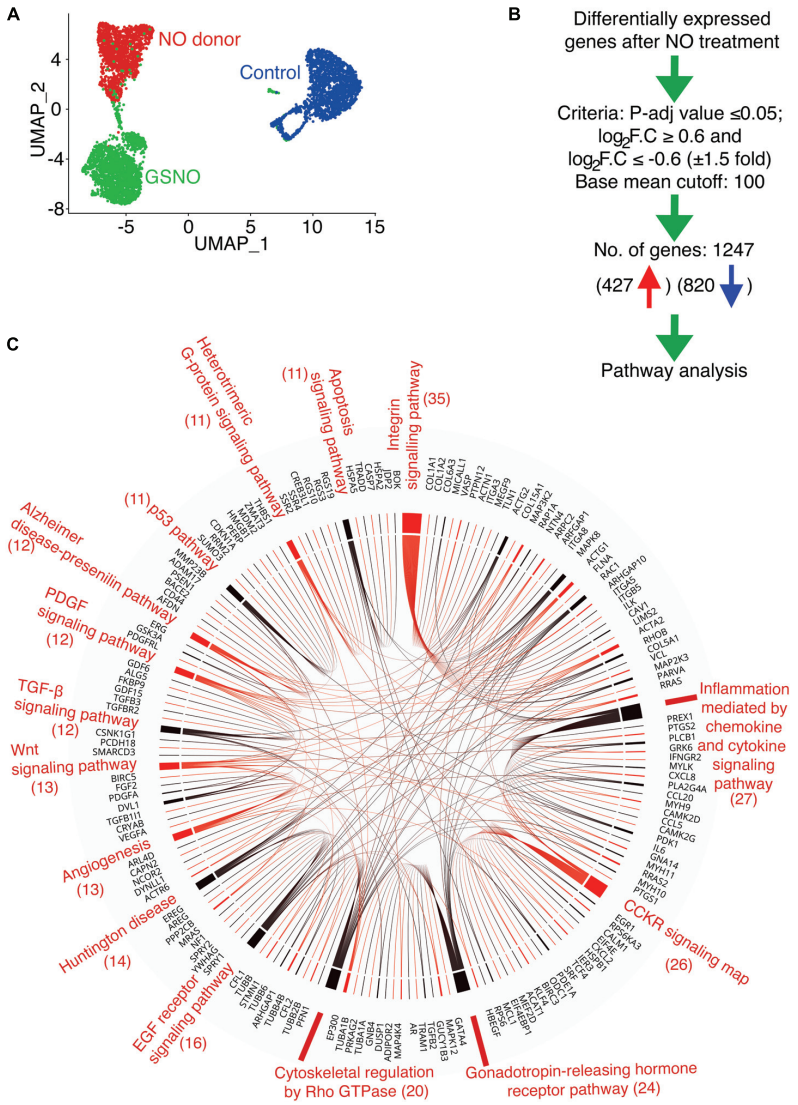

FIGURE 1
Identification of altered signaling pathway in porcine aortic valve interstitial cells (pAVICs) exposed to nitric oxide (NO) donor or S-nitrosoglutathione (GSNO) by single-cell RNA sequencing (scRNA-seq). **(A)** Uniform Manifold Approximation and Projection (UMAP) plot of scRNA-seq expression data displays three distinct populations of pAVICs cultured in the absence (control; blue) and presence of NO donor (red) or GSNO (green) for 5 days. **(B)** The flow chart represents the filtering criteria for the selection of differentially expressed genes. **(C)** Chord plot illustrates overrepresented signaling pathways (at least > 10 genes) and corresponding differentially expressed genes identified by PANTHER pathway analysis. The number of genes is mentioned in parentheses identified in each pathway.

multiple cellular signaling pathways and supports the utility of cultured pAVICs as an *in vitro* model of valve calcification.

Nitric oxide and S-nitrosoglutathione alters the integrin signaling pathway in porcine aortic valve interstitial cells

In addition to PANTHER pathway analysis, we utilized WebGestalt (WEB-based GEne SeT AnaLysis Toolkit) to evaluate overrepresented pathways based on their false discovery rate (FDR) (**Supplementary Figures 2A,B**; 52). Interestingly we observed that the Integrin signaling pathway was the top significantly enriched pathway with eight upregulated and 24 downregulated genes after NO donor and GSNO treatment as shown in the heatmap (**Figure 2A**). The altered gene expression pattern between the NO donor treated and untreated control was striking while the gene expression changes after GSNO treatment demonstrated an "intermediate" pattern between these two conditions. As both NO donor and GSNO equally prevented calcification *in vitro* (7), this suggested

that a partial rescue of the gene expression profile was sufficient to inhibit calcification. In addition to the integrin signaling pathway, the Rho GTPase pathway was also discovered as a significantly altered pathway (**Supplementary Figure 2B**). As described earlier, the Rho GTPase pathway functions together with the integrin signaling pathway to modulate the response of VICs to altered ECM and vice versa in CAVD (45). Notably, among these 32 differentially expressed genes in the integrin signaling pathway, the protein products of nine genes were identified as S-nitrosylated in VICs either calcific or non-calcific conditions after NO treatment (**Figure 2B**; 7).

To validate the involvement of the integrin signaling pathway, we evaluated the expression of three out of eight upregulated and eight out of 24 downregulated genes. These genes represent at least one-third of the identified genes of the integrin signaling pathway using quantitative RT-PCR. Expression of these genes demonstrated similar and significant transcriptional expression as observed by scRNAseq (**Figures 2A,C**). These genes encode for ECM proteins (e.g., *COL1A1, COL1A2*: collagens), focal adhesion proteins (e.g., *TLN1*: talin, *VCL*: vinculin), and also integrins (*ITGA5, ITGA8, ITGB5*: integrins α and β subunits). The heterodimer of integrin β5 (*ITGB5*) and αv (integrin αvβ5) are expressed in fibroblasts and endothelial cells, whereas integrin α8 (*ITGA8*) and β1 (integrin α8β1) are expressed in smooth muscle cells (SMC) (24). The role of ITGA8 has been linked to aortic calcification in a murine model of atherosclerosis (53). Therefore, we were particularly interested in *ITGA8* expression in this study as a critical gene altered by NO. We examined the expression of Integrin α8 (ITGA8) in cultured pAVICs using immunofluorescence (**Figures 2D,E**). We observed reduced expression of ITGA8 in pAVICs after NO donor and GSNO exposure compared to untreated control, following a similar trend observed in our scRNAseq data. Interestingly, we observed upregulation of *ITGB5* and downregulation of *ITGA8* after NO donor and GSNO treatment suggesting that NO and GSNO inhibit the expression of SMC genes in VICs and allow VICs to maintain a more, quiescent fibroblast-like phenotype (**Figure 2A**). Overall, our data suggest that NO and S-nitrosylation-mediated modulation of the integrin signaling pathway may be associated with the progression of CAVD.

Expression of integrin signaling pathway members was perturbed in the murine calcific aortic valve

As discussed above, a heterodimeric combination of integrins receptors determines ECM binding specificity and downstream signal transduction. Integrins recruit focal adhesion proteins, such as VCL that mechanically connect the ECM and cytoskeleton, to balance a force between cellular stress fibers and ECM (32). The role of VCL has previously been reported in both valvular and vascular endothelial morphological alignment (54). Endothelial cells sense the hemodynamics in their environment and contribute to calcification by responding to the shear stress experienced on the cells' apical side (55). To test the expression of these integrin pathway genes, we combined our data with previously published scRNAseq data of mouse adult aortic valves at P30 as described previously (7, 39). We did not observe significant expression of *ITGA8* and *VCL* in healthy aortic VICs in wild-type mice (**Figure 3A**). However, both of these genes were highly expressed in pAVICs, cultured on the stiff surface, and downregulated after treatment with NO donor and GSNO (**Figure 2C**). To test whether this increase in integrin pathway genes is specific to pAVICs *in vitro* culture condition or it has any *in vivo* relevance, we utilized our newly described CAVD murine model in which *Usp9x* was deleted in endothelial and endothelial-derived cells (7). Since *Usp9x* is located in X-chromosome, therefore conditional deletion of the gene from endothelial and endothelial-derived VICs will be homozygous in male ($Usp9x^{fl/Y}$; $Tie2^{Cre+}$), and heterozygous in female ($Usp9x^{fl/Wt}$; $Tie2^{Cre+}$) mice. Aortic velocity was measured in female mice by echocardiography, and we observed incomplete penetrance of a stenotic phenotype in these 24 weeks old mice (p = 0.4498) (**Supplementary Figure 3**). Therefore, $Usp9x^{fl/Wt}$; $Tie2^{Cre+}$ female mice were not used in this study as a model of calcification. Notably in humans, males also develop calcification more often than females (56, 57). We examined the expression of ITGA8 and VCL in the aortic valve of $Usp9x^{fl/Y}$; $Tie2Cre^{+}$ murine model in comparison to Cre^{-} control (**Figures 3B,C**). Immunofluorescence imaging demonstrated increased expression of ITGA8 in calcific valves (**Figure 3B**). Immunohistochemistry also demonstrated increased VCL expression in the aortic valve of $Usp9x^{fl/Y}$; $Tie2Cre^{+}$ mice (**Figure 3C**). Interestingly, higher expression of ITGA8 was observed in the myocardium of $Usp9x^{fl/Y}$, $Tie2Cre^{-}$, compared to $Usp9x^{fl/Y}$, $Tie2Cre^{+}$ mice (**Supplementary Figure 4**). This data indicates that elevated expression of ITGA8 is valve specific in response to calcification signaling events. Therefore, both our *in vivo* and *in vitro* observation demonstrates altered expression of integrin signaling pathway members, which suggests perturbed cell-ECM communication during CAVD.

Nitric oxide-dependent integrin pathway regulation is transient

Our data suggest that the effect of NO on the cellular signaling pathway is dependent on the NO-mediated post-translational modification, S-nitrosylation. S-nitrosylation is a reversible protein modification and can initiate or inhibit cellular signaling processes. To test whether the effect of NO on these signaling pathways is long-lasting, pAVICs were cultured for 3 days in presence of a NO donor, followed by culturing

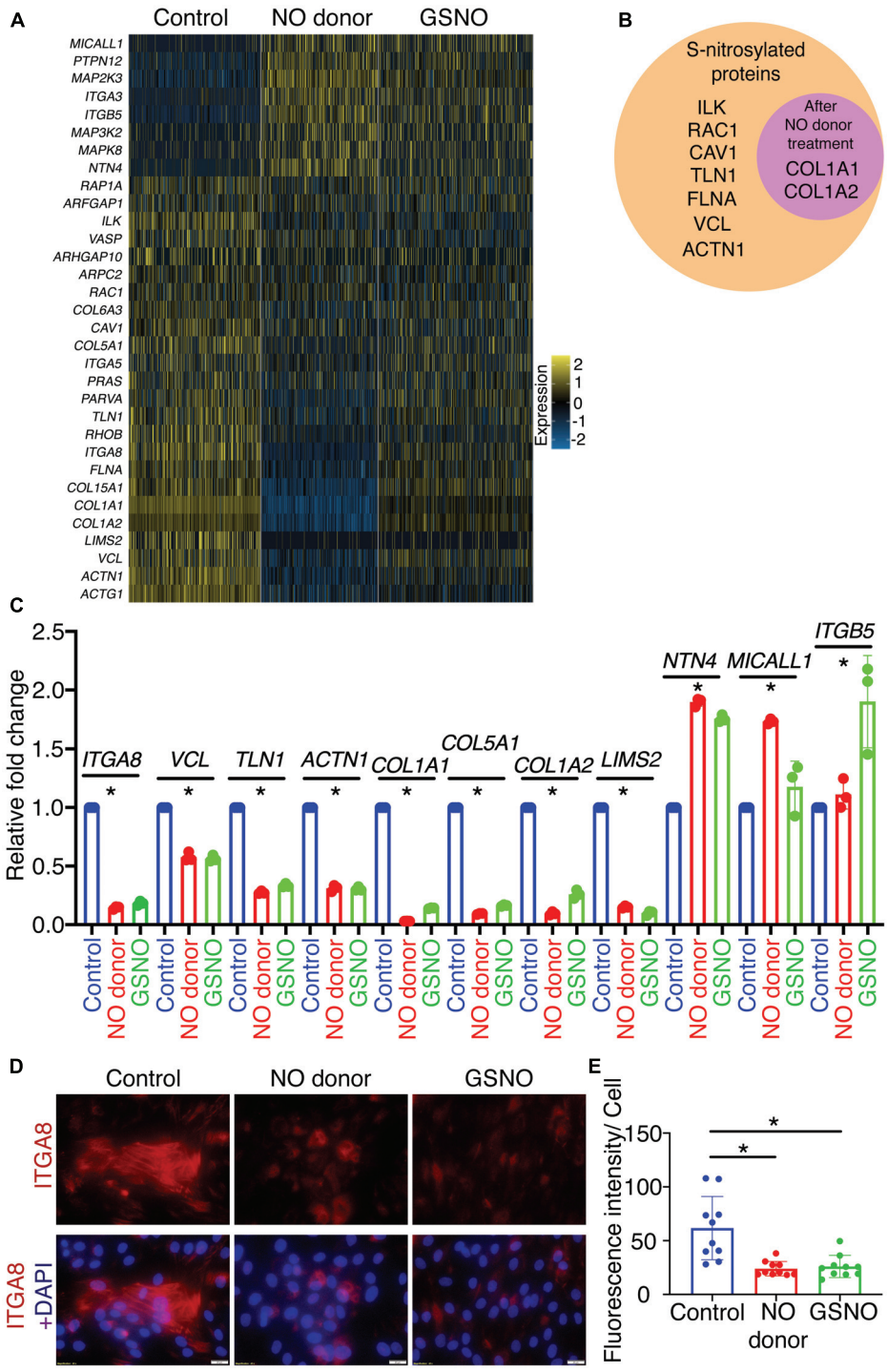

FIGURE 2
Identification and validation of differentially expressed genes involved in integrin signaling pathway in porcine aortic valve interstitial cells (pAVICs) exposed to nitric oxide (NO) donor or S-nitrosoglutathione (GSNO). **(A)** Heatmap represents *Z*-scored expression of 32 differentially expressed genes involved in the integrin signaling pathway in individual cells from control, NO donor, and GSNO treated pAVICs. **(B)** Diagram representing the protein product of differentially regulated integrin pathway genes, which were S-nitrosylated in valve interstitial cells (VICs). The circle inside represents S-nitrosylated proteins enriched after NO donor treatment. **(C)** Transcriptional expression of 11 representative genes from the integrin signaling pathway was estimated in control, NO donor, and GSNO-treated pAVICs by quantitative real time polymerase chain reaction (RT-PCR). **(D)** Immunofluorescence images represent the decreased expression of ITGA8 (red) with NO donor and GSNO when compared to untreated control pAVICs, co-stained with nuclear DAPI (blue). Scale bar: 20 μm. **(E)** The graph shows the quantification of fluorescence intensity of ITGA8 expression in control, NO donor, and GSNO treated pAVICs normalized to the number of cells. *Indicates $p \leq 0.05$.

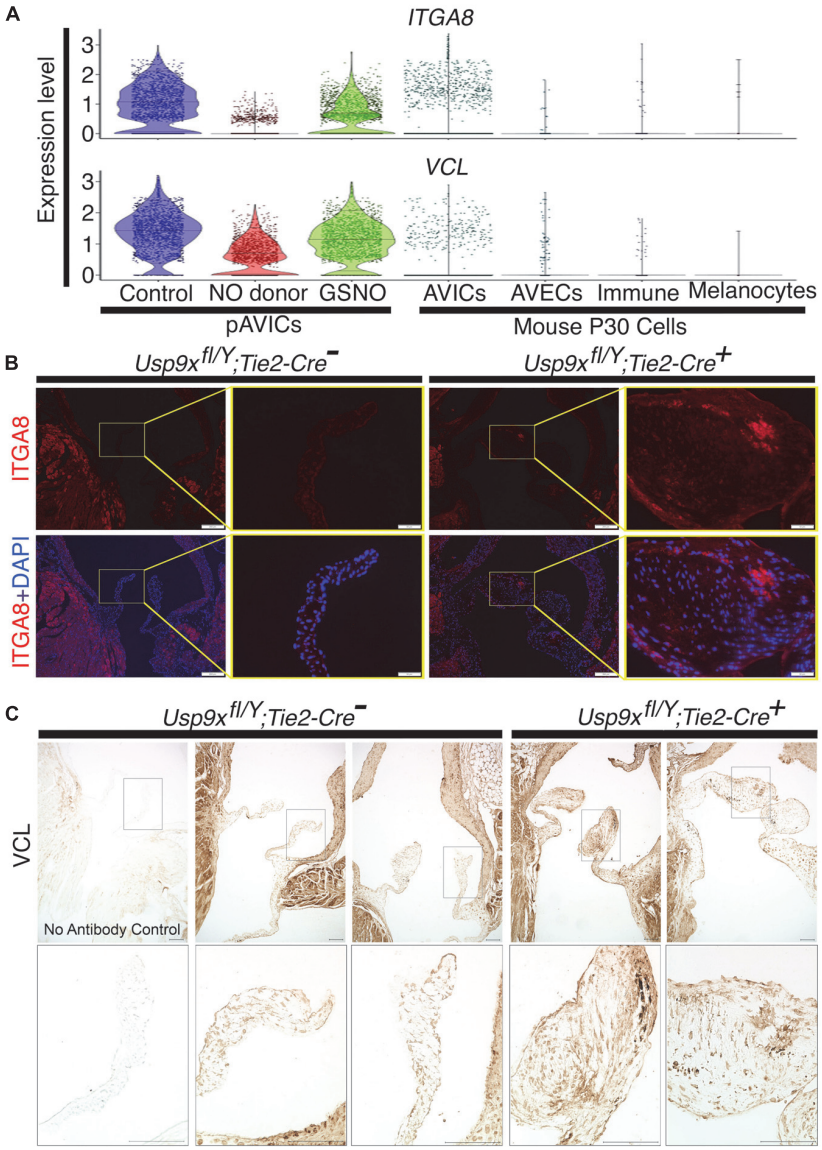

FIGURE 3
Increased expression of ITGA8 and vinculin (VCL) in calcified mouse aortic valve. **(A)** Violin plots demonstrate the expression of *ITGA8* and *VCL* in porcine aortic valve interstitial cells (pAVICs) and mouse P30 aortic valve cells. **(B)** Immunofluorescence staining of aortic valve sections demonstrates the increase of ITGA8 (Integrin α8; red) expression in calcific conditions (*Usp9x*$^{fl/Y}$*; Tie2-Cre*$^{+}$) compared to (*Usp9x*$^{fl/Y}$*; Tie2-Cre*$^{-}$) controls (n = 2) and co-stained with nuclear DAPI (blue). Arrows indicate the representative area of expression of ITGA8. Yellow boxes indicate the magnified area of the tissue sections shown right of each image. Scale bar: 100 μm. **(C)** Immunohistochemistry of aortic valve sections demonstrate increased expression of VCL in (*Usp9x*$^{fl/Y}$*; Tie2-Cre*$^{+}$) compared to (*Usp9x*$^{fl/Y}$*; Tie2-Cre*$^{-}$) controls (n = 2). Negative control with no primary antibody is shown in the first column. Boxes indicate the magnified area of tissue sections shown below each image. Scale bar: 100 μm.

cells without a NO donor for two more days. Hereafter, this pAVICs culture condition will be designated as "NO donor withdrawal." The scRNAseq data after NO donor withdrawal was analyzed in comparison to the transcriptomic data in the presence and absence of NO donor and GSNO for 5 days. In this study, we considered 1,247 identified protein-coding genes based on *P*-value and fold changes (**Figure 1**). We examined the correlative distance between each culture condition and observed the expression pattern of these 1,247 genes after NO donor withdrawal was similar to untreated control [Spearman distance (SD) = 2.3×10^8] (**Figures 4A,B**). Not surprisingly, NO donor and GSNO treatment show similar expression profiles (SD = 1.78×10^8). This data again is consistent with the finding that the NO-dependent transcriptional regulation in pAVICs is predominantly exerted by S-nitrosylation and this effect is transient.

To validate this observation in protein level, we cultured pAVICs for 3 days in presence of NO donor and then

10.3389/fcvm.2022.742850

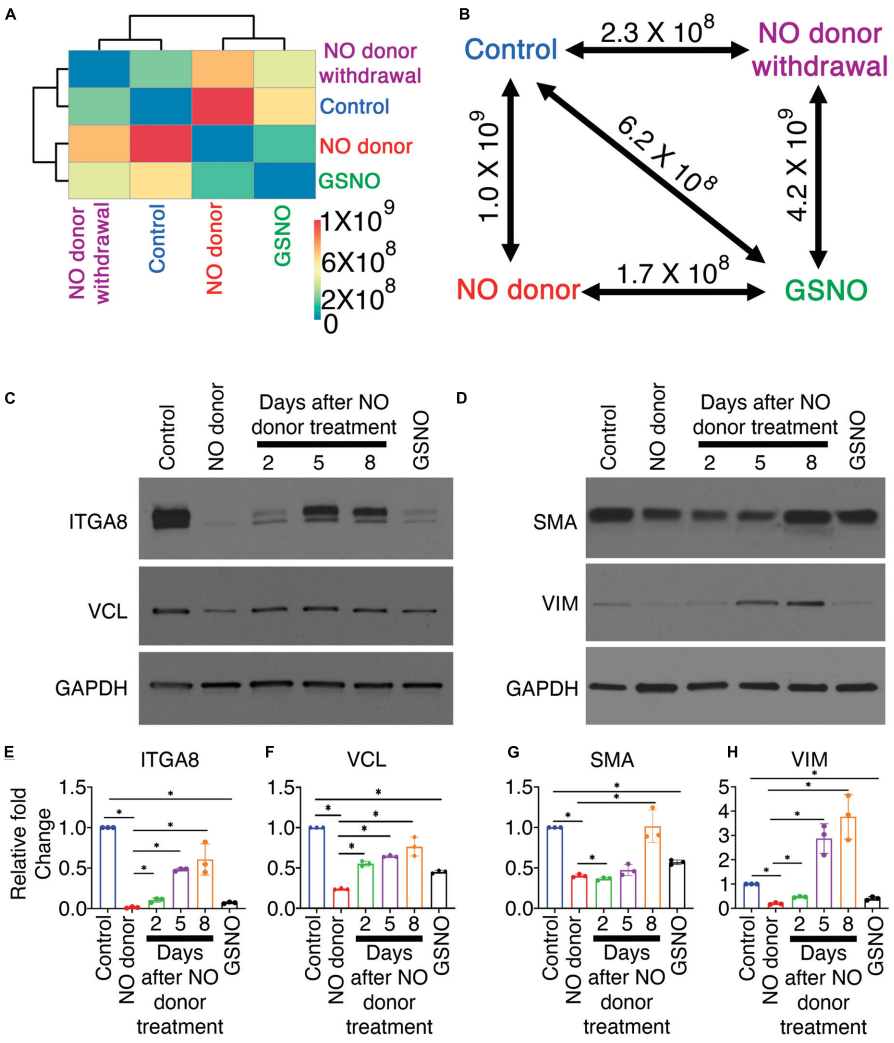

FIGURE 4

Nitric oxide (NO)-dependent transcriptional responses in porcine aortic valve interstitial cells (pAVICs) are short-lived. **(A)** Heatmap showing the Spearman distance between different pairs of culture conditions calculated based on the normalized average expression of 1,247 selected genes of pAVICs, cultured for 5 days in the absence (control) and presence of NO donor or S-nitrosoglutathione (GSNO) or a culture condition where NO donor was present for first 3 days and absent for remaining 2 days (NC). **(B)** Diagram represents the Spearman distance between groups and is denoted as Spearman distance (SD), comparing any two-culture condition marked by a double-headed arrow. **(C,D)** Immunoblots show expressions of ITGA8 (Integrin α8), VCL (vinculin), SMA (smooth muscle actin), and VIM (vimentin) in pAVICs, cultured for 5 days in the absence and presence of NO donor, GSNO, and without NO donor after 3 days of NO donor treatment. After 3 days of NO donor treatment, pAVICs were cultured for additional 2, 5, and 8 days without NO donor. Glyceraldehyde 3-phosphate dehydrogenase (GAPDH) was utilized as a loading control. **(E–H)** Graphs show quantification of ITGA8, VCL, SMA, and VIM, respectively, from immunoblots shown in panel **(C,D)**. *Indicates $P \leq 0.05$.

without NO donor for additional 2, 5, and 8 days. We examined the protein expression of ITGA8 and VCL by western blot after NO donor withdrawal in comparison to untreated control, NO donor, and GSNO-treated pAVICs (Figure 4C). Both ITGA8 and VCL protein expression was reduced after NO donor and GSNO treatment but increased again after NO donor withdrawal (Figures 4C,E,F). Interestingly, the restoration of the expression profile of a gene after NO donor withdrawal appeared to be slower at the translational level compared to the transcriptional level (Figures 4A,C). This is possibly due to the reversibility of S-nitrosylation modification, which is removed slowly from the target proteins in the absence of NO. This observation indicates that the effect of NO and subsequent S-nitrosylation on keeping VICs healthy is a temporary event. Continuous NO exposure, either from endogenous or external sources is necessary to keep VICs healthy and quiescent fibroblast behavior.

We previously demonstrated that pAVICs undergo myofibroblast activation spontaneously and NO can inhibit this

activation by downregulation of *ACTA2* (SMA: smooth muscle actin) and *VIM* (Vimentin) expression at the transcriptional level (7). Here, we found the protein expression of SMA and VIM were also reduced after NO donor and GSNO treatment compared to untreated control. Similar to integrin pathway members, SMA and VIM expression was also increased after NO donor withdrawal (**Figures 4D,G,H**). SMA and VIM are both structural proteins important for generating forces, which are transmitted to the ECM *via* integrins and focal adhesion proteins. NO, and GSNO can inhibit the altered expression of ECM remodeling genes, both at the transcriptional and translational levels.

Discussion

In this study, we evaluated the transcriptional changes of cultured pAVICs in the presence and absence of NO donor and GSNO. Differentially expressed genes from various signaling pathways were identified in presence of NO donor and GSNO compared to untreated control. We considered 1,247 significantly ($P_{adjusted} \leq 0.05$) expressed genes with at least 1.5-fold up or down-regulation for pathway enrichment analysis. Our analysis revealed the involvement of integrin, Rho GTPase, Wnt, TGF-β, and p53 signaling pathways in the process of calcification. We detected the highest number of genes involved in the integrin signaling pathway were differentially expressed after NO donor and GSNO treatments. We verified the expression of integrin pathway members and their temporal regulation by NO donor utilizing both pAVICs culture and a murine model of calcification. Overall, our study suggests that NO regulates the cell-ECM interaction by modulating the integrin pathway, which subsequently leads to calcification *via* dysregulated cellular signaling.

With analysis of our scRNAseq data from cultured pAVICs exposed to NO donor and GSNO, we identified eight upregulated and 24 downregulated genes that encode for important components of this signaling pathway, including different integrins, collagens, and focal adhesion proteins (**Figure 1C**). Interestingly, the expression of these genes after GSNO treatment was in between NO donor treated and untreated control (**Figure 2A**). This observation generates a possibility of involvement of molecular pathways other than S-nitrosylation. It is important to note that we previously demonstrated that the NO-dependent sGC/cGMP pathway is not activated in pAVICs after NO donor treatment (7). Possibly the differences in gene expression profile between NO donors and GSNO are due to differential redox status, which was not investigated and is beyond the scope of this study. In addition to S-nitrosylation, another NO-dependent post-translational modification is tyrosine nitration, which also plays an important role in regulating protein structure and activity (58–60). Nitration of tyrosine residues is classically produced by peroxynitrite, generated by the reaction of NO and oxygen radicals, associated with oxidative stress. Traditionally, it was thought to be an irreversible, degenerative process that leads to protein degradation (61–63). However, there is accumulating evidence demonstrating its reversible nature in certain conditions, qualifying this modification as an inducer of cellular signaling, similar to phosphorylation-dephosphorylation or S-nitrosylation- denitrosylation (58–60). The functional role of tyrosine nitration in the context of calcification needs to be studied further. On the other hand, S-nitrosylation is an established redox-dependent reversible protein modification, important for various cellular signaling. However, aberrant production of ROS and RNS leads to alteration in protein folding and function *via* dysregulated S-nitrosylation and tyrosine nitration. Dysregulation of these protein modifications is already implicated in aging, cancer, diabetes, and also neurodegenerative, cardiovascular, pulmonary and musculoskeletal diseases (64, 65). Therefore, a regulated balance of NO production and cellular redox status is required to propagate healthy cell-ECM interaction.

We verified similar changes in the expression of integrins (e.g., ITGA8) and focal adhesion proteins (e.g., VCL) in the murine calcified aortic valve, as observed in scRNAseq (**Figures 2**, **3**). Previously we described thickened and stenotic aortic valve with a disorganized matrix in *Usp9x*$^{fl/fl}$; *Tie2-Cre*$^{+}$ mouse (7). It is well-known that the production of NO by endothelial NOS is dependent on blood flow (12, 13). It can be speculated that thickened valve leaflets would initiate disturbed blood flow patterns across the valve, which would also lead to perturbed NO production. Since NO is a freely diffusible molecule, but short-lived, it cannot travel from the endothelial cells to the interstitial cells located far (aortic side) from the laminar shear flow side (ventricular side) in the thickened valve. It is notable that the aortic side of the aortic valve experience oscillatory shear flow (66). We previously demonstrated that S-nitrosylation is predominantly present in the ventricular side of the aortic valve and the atrial side of the mitral valve, both of which experience the laminar shear flow (7). Therefore, we suggest that the perturbed blood flow through the thickened and stenotic aortic valve in our murine model of CAVD leads to insufficient NO production, followed by perturbation of the integrin signaling pathway and ECM turnover in VICs.

Integrins demonstrate binding specificity toward various ECM proteins and transduce intracellular signals. This signaling is determined by the ECM composition and stiffness, which regulate cellular phenotypes (24). We observed differential expression of integrin genes (*ITGA3,5* and *8*) between control and NO-treated pAVICs (**Figure 1C**). The protein product of these three genes heterodimerizes with integrin β1. All of these integrin heterodimers α3β1, α5β1, and α8β1 play important roles in promoting myofibroblast activation and developing fibrotic conditions (67–70). In addition, we observed differential expression of various collagens (*COL1A1, COL1A2,*

COL15A1, COL6A3, COL5A1) (**Supplementary Figure 2A**), which constitutes the largest fraction of the ECM, both in the valve and in the myocardium. After binding to ECM, integrins interact with the cytoskeleton *via* focal adhesion proteins, which were also differentially expressed (*VCL, TLN1*) after NO and GSNO treatment (**Figure 1C**). Interestingly, two collagens (*COL1A1, COL1A2*), which were transcriptionally downregulated (**Figure 2A** and **Supplementary Figure 2A**) were also S-nitrosylated in the non-calcific condition after NO donor treatment (**Figure 2B**). This data suggests a possible feedback inhibition of ECM genes at the transcriptional level by S-nitrosylation. However, the mechanism of this feedback regulation requires further investigation.

In addition, changes in the expression of the cytoskeletal genes including *ACTA2, ACTN1*, and *ACTG1* (**Figure 1C**) were observed after NO donor and GSNO treatment. The cytoskeletal response toward ECM is mediated by the Rho family of GTPases, which were also differentially expressed (*RHOB, RAC1*) in NO donor and GSNO-treated cells (**Figure 1C**). Intracellular forces generated by the actin cytoskeleton are transmitted back to the ECM to alter its organization. This triggers the activation of TGF-β, which can further promote myofibroblast activation (71). TGF-β also regulates the Wnt signaling pathway by repressing GSK3β, which results in the degradation of cytoplasmic β-catenin in cooperation with disheveled (DVL). We found differential expression of TGF-β and Wnt pathway genes (*TGFB2, TGFB3, TGFBR2, DVL1*) (**Figure 1C** and **Supplementary Data 1**), which have well-established roles in cardiac development and disease (47, 72). Overall, our scRNAseq analysis indicates that NO can globally regulate intracellular signaling pathways in VICs and its extracellular communication with ECM to maintain healthy VICs.

Healthy VICs reflect a quiescent fibroblast type which becomes activated to a myofibroblast-like state when cultured on a stiff surface of a tissue culture plate (20, 21, 73). We have demonstrated that NO donor and GSNO can inhibit the myofibroblast activation of pAVICs (7). However, it is not clear whether activated pAVICs can differentiate back to a fibroblast-like state. Interestingly, we observed increased expression of *TCF21*, a cardiac fibroblast marker after NO donor exposure (**Supplementary Figure 5**). It has been demonstrated before that S-nitrosylation and TCF21^{+} cells are present predominantly in the laminar shear flow side (ventricular side) of the healthy aortic valve (7, 39). This data indicates a possible correlation between NO-mediated S-nitrosylation and the maintenance of a healthy fibroblast-type state defined by TCF21 expression. An increase of *TCF21* in presence of NO (**Supplementary Figure 5**) also indicates that NO can reverse the myofibroblast toward a fibroblast-type state in an *in vitro* setting. Further studies are required to determine if there is a reduction of TCF21^{+} cells in the aortic valve of murine models of CAVD.

Analysis of our scRNAseq data revealed that NO-dependent regulation of the integrin signaling pathway is important for the communication between cells and ECM. However, cultured pAVICs on tissue culture plates do not have a proper ECM. Therefore, the effect of ECM remodeling during the progression of calcification cannot be identified in this *in vitro* condition, which is a major drawback of this model system. Although we verified the expression of some genes *in vivo* mouse model, the conclusion of this study is limited to the identification of altered cellular signaling pathways and gene expression, which are related to cell-ECM interaction. It has previously been reported that myofibroblast activation and calcification of pAVICs are influenced by the stiffness of the culture plates, which possibly mimics the very advanced stages of CAVD (21, 74, 75). Interestingly, NO donor and GSNO can prevent this myofibroblast activation and calcification of pAVICs, cultured on a stiff surface. This effect of NO donor and GSNO on the pAVICs is transcriptional and not influenced by the stiffness of its culture condition. This generates the possibility of therapeutic agents, which can continuously produce NO, and would have the potential to preserve the healthy status of VICs. This puts NO donors and GSNO as potential therapeutic agents which may fix or decelerate the progression of CAVD by altering diseased VICs and ECM *via* regulation of integrin and other involved signaling pathways.

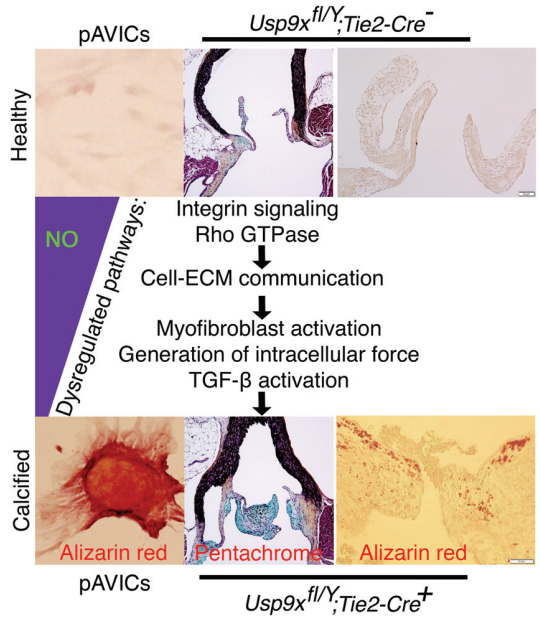

FIGURE 5
Nitric oxide (NO) inhibits the process of aortic valve calcification. Schematic showing the proposed model where calcification is initiated with reduced NO availability that perturbs integrin signaling pathway, cell-extracellular matrix (ECM) interactions, followed by dysregulation of various cellular signaling pathways.

Overall, we are proposing that uninterrupted and adequate NO production is required to inhibit CAVD by keeping VICs in a quiescent fibroblast state which regulates healthy ECM turnover (**Figure 5**). Insufficient bioavailability of NO leads to dysregulated integrin signaling, ECM turnover, and remodeling, which generates mechanical forces both by ECM and VICs. These mechanical forces induce dysregulation of multiple downstream cellular pathways, including the TGF-β and Wnt pathways contributing to aortic valve calcification (**Figure 5**).

Data availability statement

The datasets presented in this study can be found in online repositories. The names of the repository/repositories and accession number(s) can be found below: https://www.ncbi.nlm.nih.gov/geo/, GSE161123.

Ethics statement

The animal study was reviewed and approved by Institutional Animal Care and Use Committee (IACUC) at the Research Institute at Nationwide Children's Hospital.

Author contributions

VG and UM: conceived the project and designed the experiments. UM, YU, and TC: performed and analyzed the experiments. MB: performed scRNA-seq library preparation. SM: processed the scRNAseq datasets and developed Ryabhatta app. UM, TC, and VG: wrote the manuscript with input from all authors. All authors contributed to the article and approved the submitted version.

Funding

This work was supported by funding from National Heart, Lung, and Blood Institute grants: R01 HL132801 (VG), R01 HL121797 (VG), NHLBI Postdoctoral Fellowship T32 HL098039 (SM), and AHA/Children's Heart Foundation grant 18CDA34110330 (MB).

Acknowledgments

We thank members of the Biomorphology Core at Nationwide Children's Hospital for histology support and Emily Cameron for maintenance of mouse colony.

Conflict of interest

The authors declare that the research was conducted in the absence of any commercial or financial relationships that could be construed as a potential conflict of interest.

Publisher's note

Supplementary material

The Supplementary Material for this article can be found online at: https://www.frontiersin.org/articles/10.3389/fcvm.2022.742850/full#supplementary-material

SUPPLEMENTARY FIGURE 1
Alizarin red staining of calcific nodules of porcine aortic valve interstitial cells (pAVICs) cultured on plastic tissue culture plates in osteogenic media in the presence and absence of nitric oxide (NO) donor and S-nitrosoglutathione (GSNO).

SUPPLEMENTARY FIGURE 2
The maximum number of differentially expressed genes involved in the integrin signaling pathway in porcine aortic valve interstitial cells (pAVICs) exposed to nitric oxide (NO) donor or S-nitrosoglutathione (GSNO). **(A)** Volcano plot of $\log_2$(Fold change) vs. −log10(*P*-value), demonstrating differential expression of upregulated (blue) and downregulated (cyan) genes between NO donor treated and untreated pAVICs. Genes identified from integrin signaling pathway have been marked. ITGA8 is one of the most significantly downregulated gene after NO donor treatment. **(B)** Graph describes overrepresented pathway analysis considering $-\log_{10}$ (FDR) and $\log_2$ (enrichment ratio) using WebGestalt online tool. Integrin signaling pathway, cytoskeletal regulation of Rho GTPase and CCKR signaling pathway were significant based on −log10(FDR). Intensity in color scale (top left corner) indicates number of genes identified in each pathway.

SUPPLEMENTARY FIGURE 3
The aortic velocity of female *Usp9x*$^{fl/wt}$, *Tie2Cre*$^{-}$, and *Usp9x*$^{fl/wt}$, *Tie2Cre*$^{+}$ mice by echocardiography.

SUPPLEMENTARY FIGURE 4
Higher expression of ITGA8 was observed in the myocardium of *Usp9x*$^{fl/Y}$, *Tie2Cre*$^{-}$, compared to *Usp9x*$^{fl/Y}$, *Tie2Cre*$^{+}$ mice.

SUPPLEMENTARY FIGURE 5
Nitric oxide (NO) donor induces the expression of the cardiac fibroblast gene, *TCF21*, in porcine aortic valve interstitial cells (pAVICs). Violin plots show increased expression of *TCF21* in pAVICs after NO donor treatment compared to untreated control.

SUPPLEMENTARY DATA 1
Differentially expressed genes in porcine aortic valve interstitial cells (pAVICs) after nitric oxide (NO) donor and S-nitrosoglutathione (GSNO) treatment compared to untreated cells.

SUPPLEMENTARY DATA 2
List of primers used to identify gene expression by quantitative real time polymerase chain reaction (RT-PCR).

References

1. Yadgir S, Johnson CO, Aboyans V, Adebayo OM, Adedoyin RA, Afarideh M, et al. Global, regional, and National burden of calcific aortic valve and degenerative mitral valve diseases, 1990-2017. *Circulation.* (2020) 141:1670–80. doi: 10.1161/CIR.0000000000000848

2. Yi B, Zeng W, Lv L, Hua P. Changing epidemiology of calcific aortic valve disease: 30-year trends of incidence, prevalence, and deaths across 204 countries and territories. *Aging.* (2021) 13:12710–32. doi: 10.18632/aging.202942

3. Freeman RV, Otto CM. Spectrum of calcific aortic valve disease: pathogenesis, disease progression, and treatment strategies. *Circulation.* (2005) 111:3316–26. doi: 10.1161/CIRCULATIONAHA.104.486738

4. Hutcheson JD, Aikawa E, Merryman WD. Potential drug targets for calcific aortic valve disease. *Nat Rev Cardiol.* (2014) 11:218–31. doi: 10.1038/nrcardio.2014.1

5. Rogers MA, Aikawa E. Cardiovascular calcification: artificial intelligence and big data accelerate mechanistic discovery. *Nat Rev Cardiol.* (2019) 16:261–74. doi: 10.1038/s41569-018-0123-8

6. Bosse K, Hans CP, Zhao N, Koenig SN, Huang N, Guggilam A, et al. Endothelial nitric oxide signaling regulates Notch1 in aortic valve disease. *J Mol Cell Cardiol.* (2013) 60:27–35. doi: 10.1016/j.yjmcc.2013.04.001

7. Majumdar U, Manivannan S, Basu M, Ueyama Y, Blaser MC, Cameron E, et al. Nitric oxide prevents aortic valve calcification by S-nitrosylation of USP9X to activate NOTCH signaling. *Sci Adv.* (2021) 7:eabe3706. doi: 10.1126/sciadv.abe3706

8. Kennedy JA, Hua X, Mishra K, Murphy GA, Rosenkranz AC, Horowitz JD. Inhibition of calcifying nodule formation in cultured porcine aortic valve cells by nitric oxide donors. *Eur J Pharmacol.* (2009) 602:28–35. doi: 10.1016/j.ejphar.2008.11.029

9. Richards J, El-Hamamsy I, Chen S, Sarang Z, Sarathchandra P, Yacoub MH, et al. Side-specific endothelial-dependent regulation of aortic valve calcification: interplay of hemodynamics and nitric oxide signaling. *Am J Pathol.* (2013) 182:1922–31. doi: 10.1016/j.ajpath.2013.01.037

10. Butcher JT, Nerem RM. Valvular endothelial cells regulate the phenotype of interstitial cells in co-culture: effects of steady shear stress. *Tissue Eng.* (2006) 12:905–15. doi: 10.1089/ten.2006.12.905

11. Gould ST, Matherly EE, Smith JN, Heistad DD, Anseth KS. The role of valvular endothelial cell paracrine signaling and matrix elasticity on valvular interstitial cell activation. *Biomaterials.* (2014) 35:3596–606. doi: 10.1016/j.biomaterials.2014.01.005

12. Boo YC, Jo H. Flow-dependent regulation of endothelial nitric oxide synthase: role of protein kinases. *Am J Physiol Cell Physiol.* (2003) 285:C499–508. doi: 10.1152/ajpcell.00122.2003

13. Joannides R, Haefeli WE, Linder L, Richard V, Bakkali EH, Thuillez C, et al. Nitric oxide is responsible for flow-dependent dilatation of human peripheral conduit arteries in vivo. *Circulation.* (1995) 91:1314–9. doi: 10.1161/01.CIR.91.5.1314

14. Bertacco E, Millioni R, Arrigoni G, Faggin E, Iop L, Puato M, et al. Proteomic analysis of clonal interstitial aortic valve cells acquiring a pro-calcific profile. *J Proteome Res.* (2010) 9:5913–21. doi: 10.1021/pr100682g

15. Garg V, Muth AN, Ransom JF, Schluterman MK, Barnes R, King IN, et al. Mutations in NOTCH1 cause aortic valve disease. *Nature.* (2005) 437:270–4. doi: 10.1038/nature03940

16. Koenig SN, Bosse K, Majumdar U, Bonachea EM, Radtke F, Garg V. Endothelial notch1 is required for proper development of the semilunar valves and cardiac outflow tract. *J Am Heart Assoc.* (2016) 5:e003075. doi: 10.1161/JAHA.115.003075

17. Kanno Y, Into T, Lowenstein CJ, Matsushita K. Nitric oxide regulates vascular calcification by interfering with TGF- signalling. *Cardiovasc Res.* (2008) 77:221–30. doi: 10.1093/cvr/cvm049

18. Yip CY, Blaser MC, Mirzaei Z, Zhong X, Simmons CA. Inhibition of pathological differentiation of valvular interstitial cells by C-type natriuretic peptide. *Arterioscler Thromb Vasc Biol.* (2011) 31:1881–9. doi: 10.1161/ATVBAHA.111.223974

19. Blaser MC, Wei K, Adams RLE, Zhou YQ, Caruso LL, Mirzaei Z, et al. Deficiency of natriuretic peptide receptor 2 promotes bicuspid aortic valves, aortic valve disease, left ventricular dysfunction, and ascending aortic dilatations in mice. *Circ Res.* (2018) 122:405–16. doi: 10.1161/CIRCRESAHA.117.311194

20. Gu X, Masters KS. Regulation of valvular interstitial cell calcification by adhesive peptide sequences. *J Biomed Mater Res A.* (2010) 93:1620–30. doi: 10.1002/jbm.a.32660

21. Yip CY, Chen JH, Zhao R, Simmons CA. Calcification by valve interstitial cells is regulated by the stiffness of the extracellular matrix. *Arterioscler Thromb Vasc Biol.* (2009) 29:936–42. doi: 10.1161/ATVBAHA.108.182394

22. Tomasek JJ, Gabbiani G, Hinz B, Chaponnier C, Brown RA. Myofibroblasts and mechano-regulation of connective tissue remodelling. *Nat Rev Mol Cell Biol.* (2002) 3:349–63. doi: 10.1038/nrm809

23. Valiente-Alandi I, Schafer AE, Blaxall BC. Extracellular matrix-mediated cellular communication in the heart. *J Mol Cell Cardiol.* (2016) 91:228–37. doi: 10.1016/j.yjmcc.2016.01.011

24. Bachmann M, Kukkurainen S, Hytonen VP, Wehrle-Haller B. Cell adhesion by integrins. *Physiol Rev.* (2019) 99:1655–99. doi: 10.1152/physrev.00036.2018

25. Schroer AK, Merryman WD. Mechanobiology of myofibroblast adhesion in fibrotic cardiac disease. *J Cell Sci.* (2015) 128:1865–75. doi: 10.1242/jcs.162891

26. Benton JA, Fairbanks BD, Anseth KS. Characterization of valvular interstitial cell function in three dimensional matrix metalloproteinase degradable PEG hydrogels. *Biomaterials.* (2009) 30:6593–603. doi: 10.1016/j.biomaterials.2009.08.031

27. Staatz WD, Fok KF, Zutter MM, Adams SP, Rodriguez BA, Santoro SA. Identification of a tetrapeptide recognition sequence for the alpha 2 beta 1 integrin in collagen. *J Biol Chem.* (1991) 266:7363–7. doi: 10.1016/S0021-9258(20)89455-1

28. Stephens EH, Durst CA, Swanson JC, Grande-Allen KJ, Ingels NB, Miller DC. Functional coupling of valvular interstitial cells and collagen Via $\alpha 2\beta 1$ integrins in the mitral leaflet. *Cell Mol Bioeng.* (2010) 3:428–37. doi: 10.1007/s12195-010-0139-6

29. Afek A, Shoenfeld Y, Manor R, Goldberg I, Ziporen L, George J, et al. Increased endothelial cell expression of alpha3beta1 integrin in cardiac valvulopathy in the primary (Hughes) and secondary antiphospholipid syndrome. *Lupus.* (1999) 8:502–7. doi: 10.1191/096120399678840873

30. Schneider GB, Zaharias R, Stanford C. Osteoblast integrin adhesion and signaling regulate mineralization. *J Dent Res.* (2001) 80:1540–4. doi: 10.1177/00220345010800061201

31. Brancaccio M, Hirsch E, Notte A, Selvetella G, Lembo G, Tarone G. Integrin signalling: the tug-of-war in heart hypertrophy. *Cardiovasc Res.* (2006) 70:422–33. doi: 10.1016/j.cardiores.2005.12.015

32. Baker EL, Zaman MH. The biomechanical integrin. *J Biomech.* (2010) 43:38–44. doi: 10.1016/j.jbiomech.2009.09.007

33. Clark-Greuel JN, Connolly JM, Sorichillo E, Narula NR, Rapoport HS, Mohler ER III, et al. Transforming growth factor-beta1 mechanisms in aortic valve calcification: increased alkaline phosphatase and related events. *Ann Thorac Surg.* (2007) 83:946–53. doi: 10.1016/j.athoracsur.2006.10.026

34. Jian B, Narula N, Li QY, Mohler ER III, Levy RJ. Progression of aortic valve stenosis: TGF-beta1 is present in calcified aortic valve cusps and promotes aortic valve interstitial cell calcification via apoptosis. *Ann Thorac Surg.* (2003) 75:457–65. doi: 10.1016/S0003-4975(02)04312-6

35. Jenke A, Kistner J, Saradar S, Chekhoeva A, Yazdanyar M, Bergmann AK, et al. Transforming growth factor-beta1 promotes fibrosis but attenuates calcification of valvular tissue applied as a three-dimensional calcific aortic valve disease model. *Am J Physiol Heart Circ Physiol.* (2020) 319:H1123–41. doi: 10.1152/ajpheart.00651.2019

36. Varshney R, Murphy B, Woolington S, Ghafoory S, Chen S, Robison T, et al. Inactivation of platelet-derived TGF-beta1 attenuates aortic stenosis progression in a robust murine model. *Blood Adv.* (2019) 3:777–88. doi: 10.1182/bloodadvances.2018025817

37. Chakrabarti M, Al-Sammarraie N, Gebere MG, Bhattacharya A, Chopra S, Johnson J, et al. Transforming growth factor beta3 is required for cardiovascular development. *J Cardiovasc Dev Dis.* (2020) 7:19. doi: 10.3390/jcdd7020019

38. Manivannan SN, Garg V. Natian and ryabhatta—graphical user interfaces to create, analyze and visualize single-cell transcriptomic datasets. *bioRxiv.* [Preprint]. (2021). doi: 10.1101/2021.06.17.448424

39. Hulin A, Hortells L, Gomez-Stallons MV, O'Donnell A, Chetal K, Adam M, et al. Maturation of heart valve cell populations during postnatal remodeling. *Development.* (2019) 146:dev173047. doi: 10.1242/dev.173047

40. Hutcheson JD, Schlotter F, Creager MD, Li X, Pham T, Vyas P, et al. Elastogenesis correlates with pigment production in murine aortic valve leaflets. *Front Cardiovasc Med.* (2021) 8:678401. doi: 10.3389/fcvm.2021.678401

41. National Research Council, Division on Earth and Life Studies, Institute for Laboratory Animal Research, Committee for the Update of the Guide for the Care and Use of Laboratory Animals. *Guide for the Care and Use of Laboratory Animals.* 8th ed. Washington, DC: The National Academies Press (2011).

42. Blaser MC, Kraler S, Luscher TF, Aikawa E. Multi-omics approaches to define calcific aortic valve disease pathogenesis. *Circ Res.* (2021) 128:1371–97. doi: 10.1161/CIRCRESAHA.120.317979

43. Broniowska KA, Diers AR, Hogg N. S-nitrosoglutathione. *Biochim Biophys Acta.* (2013) 1830:3173–81. doi: 10.1016/j.bbagen.2013.02.004

44. Bartesaghi S, Radi R. Fundamentals on the biochemistry of peroxynitrite and protein tyrosine nitration. *Redox Biol.* (2018) 14:618–25. doi: 10.1016/j.redox.2017.09.009

45. Gu X, Masters KS. Role of the Rho pathway in regulating valvular interstitial cell phenotype and nodule formation. *Am J Physiol Heart Circ Physiol.* (2011) 300:H448–58. doi: 10.1152/ajpheart.01178.2009

46. Gao L, Ji Y, Lu Y, Qiu M, Shen Y, Wang Y, et al. Low-level overexpression of p53 promotes warfarin-induced calcification of porcine aortic valve interstitial cells by activating Slug gene transcription. *J Biol Chem.* (2018) 293:3780–92. doi: 10.1074/jbc.M117.791145

47. Khan K, Yu B, Kiwan C, Shalal Y, Filimon S, Cipro M, et al. The Role of Wnt/beta-Catenin Pathway Mediators in Aortic Valve Stenosis. *Front Cell Dev Biol.* (2020) 8:862. doi: 10.3389/fcell.2020.00862

48. Saisongkorh V, Maiuthed A, Chanvorachote P. Nitric oxide increases the migratory activity of non-small cell lung cancer cells via AKT-mediated integrin alphav and beta1 upregulation. *Cell Oncol.* (2016) 39:449–62. doi: 10.1007/s13402-016-0287-3

49. Gupta SK, Vlahakis NE. Integrin alpha9beta1 mediates enhanced cell migration through nitric oxide synthase activity regulated by Src tyrosine kinase. *J Cell Sci.* (2009) 122:2043–54. doi: 10.1242/jcs.041632

50. Chigaev A, Smagley Y, Sklar LA. Nitric oxide/cGMP pathway signaling actively down-regulates alpha4beta1-integrin affinity: an unexpected mechanism for inducing cell de-adhesion. *BMC Immunol.* (2011) 12:28. doi: 10.1186/1471-2172-12-28

51. Bhopale VM, Yang M, Yu K, Thom SR. Factors associated with nitric oxide-mediated beta2 integrin inhibition of neutrophils. *J Biol Chem.* (2015) 290:17474–84. doi: 10.1074/jbc.M115.651620

52. Liao Y, Wang J, Jaehnig EJ, Shi Z, Zhang B. WebGestalt 2019: gene set analysis toolkit with revamped UIs and APIs. *Nucleic Acids Res.* (2019) 47:W199–205. doi: 10.1093/nar/gkz401

53. Marek I, Canu M, Cordasic N, Rauh M, Volkert G, Fahlbusch FB, et al. Sex differences in the development of vascular and renal lesions in mice with a simultaneous deficiency of Apoe and the integrin chain Itga8. *Biol Sex Differ.* (2017) 8:19. doi: 10.1186/s13293-017-0141-y

54. Butcher JT, Nerem RM. Valvular endothelial cells and the mechanoregulation of valvular pathology. *Philos Trans R Soc Lond B Biol Sci.* (2007) 362:1445–57. doi: 10.1098/rstb.2007.2127

55. Zebhi B, Lazkani M, Bark D Jr. Calcific aortic stenosis-a review on acquired mechanisms of the disease and treatments. *Front Cardiovasc Med.* (2021) 8:734175. doi: 10.3389/fcvm.2021.734175

56. Porras AM, McCoy CM, Masters KS. Calcific aortic valve disease: a battle of the sexes. *Circ Res.* (2017) 120:604–6. doi: 10.1161/CIRCRESAHA.117.310440

57. Rajamannan NM, Evans FJ, Aikawa E, Grande-Allen KJ, Demer LL, Heistad DD, et al. Calcific aortic valve disease: not simply a degenerative process: a review and agenda for research from the National Heart and Lung and Blood Institute Aortic Stenosis Working Group. Executive summary: calcific aortic valve disease-2011 update. *Circulation.* (2011) 124:1783–91. doi: 10.1161/CIRCULATIONAHA.110.006767

58. Adams L, Franco MC, Estevez AG. Reactive nitrogen species in cellular signaling. *Exp Biol Med.* (2015) 240:711–7. doi: 10.1177/1535370215581314

59. Sabadashka M, Nagalievska M, Sybirna N. Tyrosine nitration as a key event of signal transduction that regulates functional state of the cell. *Cell Biol Int.* (2021) 45:481–97. doi: 10.1002/cbin.11301

60. Yakovlev VA, Mikkelsen RB. Protein tyrosine nitration in cellular signal transduction pathways. *J Recept Signal Transduct Res.* (2010) 30:420–9. doi: 10.3109/10799893.2010.513991

61. Gomez-Tortosa E, Gonzalo I, Newell K, Garcia Yebenes J, Vonsattel P, Hyman BT. Patterns of protein nitration in dementia with Lewy bodies and striatonigral degeneration. *Acta Neuropathol.* (2002) 103:495–500. doi: 10.1007/s00401-001-0495-3

62. Burai R, Ait-Bouziad N, Chiki A, Lashuel HA. Elucidating the role of site-specific nitration of alpha-synuclein in the pathogenesis of Parkinson's disease via protein semisynthesis and mutagenesis. *J Am Chem Soc.* (2015) 137:5041–52. doi: 10.1021/ja5131726

63. Ischiropoulos H, Beckman JS. Oxidative stress and nitration in neurodegeneration: cause, effect, or association?. *J Clin Invest.* (2003) 111:163–9. doi: 10.1172/JCI200317638

64. Foster MW, Hess DT, Stamler JS. Protein S-nitrosylation in health and disease: a current perspective. *Trends Mol Med.* (2009) 15:391–404. doi: 10.1016/j.molmed.2009.06.007

65. Pacher P, Beckman JS, Liaudet L. Nitric oxide and peroxynitrite in health and disease. *Physiol Rev.* (2007) 87:315–424. doi: 10.1152/physrev.00029.2006

66. Balachandran K, Sucosky P, Yoganathan AP. Hemodynamics and mechanobiology of aortic valve inflammation and calcification. *Int J Inflam.* (2011) 2011:263870. doi: 10.4061/2011/263870

67. Kim KK, Wei Y, Szekeres C, Kugler MC, Wolters PJ, Hill ML, et al. Epithelial cell alpha3beta1 integrin links beta-catenin and Smad signaling to promote myofibroblast formation and pulmonary fibrosis. *J Clin Invest.* (2009) 119:213–24. doi: 10.1172/JCI36940

68. Wang Z, Collighan RJ, Gross SR, Danen EH, Orend G, Telci D, et al. RGD-independent cell adhesion via a tissue transglutaminase-fibronectin matrix promotes fibronectin fibril deposition and requires syndecan-4/2 alpha5beta1 integrin co-signaling. *J Biol Chem.* (2010) 285:40212–29. doi: 10.1074/jbc.M110.123703

69. Sarrazy V, Koehler A, Chow ML, Zimina E, Li CX, Kato H, et al. Integrins alphavbeta5 and alphavbeta3 promote latent TGF-beta1 activation by human cardiac fibroblast contraction. *Cardiovasc Res.* (2014) 102:407–17. doi: 10.1093/cvr/cvu053

70. Bouzeghrane F, Mercure C, Reudelhuber TL, Thibault G. Alpha8beta1 integrin is upregulated in myofibroblasts of fibrotic and scarring myocardium. *J Mol Cell Cardiol.* (2004) 36:343–53. doi: 10.1016/j.yjmcc.2003.11.007

71. Caraci F, Gili E, Calafiore M, Failla M, La Rosa C, Crimi N, et al. TGF-beta1 targets the GSK-3beta/beta-catenin pathway via ERK activation in the transition of human lung fibroblasts into myofibroblasts. *Pharmacol Res.* (2008) 57:274–82. doi: 10.1016/j.phrs.2008.02.001

72. Azhar M, Brown K, Gard C, Chen H, Rajan S, Elliott DA, et al. Transforming growth factor Beta2 is required for valve remodeling during heart development. *Dev Dyn.* (2011) 240:2127–41. doi: 10.1002/dvdy.22702

73. Rutkovskiy A, Malashicheva A, Sullivan G, Bogdanova M, Kostareva A, Stenslokken KO, et al. Valve interstitial cells: the key to understanding the pathophysiology of heart valve calcification. *J Am Heart Assoc.* (2017) 6:e006339. doi: 10.1161/JAHA.117.006339

74. Chen JH, Simmons CA. Cell-matrix interactions in the pathobiology of calcific aortic valve disease: critical roles for matricellular, matricrine, and matrix mechanics cues. *Circ Res.* (2011) 108:1510–24. doi: 10.1161/CIRCRESAHA.110.234237

75. Ngai D, Lino M, Bendeck MP. Cell-matrix interactions and matricrine signaling in the pathogenesis of vascular calcification. *Front Cardiovasc Med.* (2018) 5:174. doi: 10.3389/fcvm.2018.00174

frontiers | Frontiers in Cardiovascular Medicine

TYPE Original Research
PUBLISHED 23 November 2022
DOI 10.3389/fcvm.2022.1003233

OPEN ACCESS

EDITED BY
Ernesto Greco,
Sapienza University of Rome, Italy

REVIEWED BY
Yuan Zhan,
Huazhong University of Science and Technology, China
Liyuan Han,
University of Chinese Academy of Sciences, China
Jian Zhou,
Fudan University, China
Yi Xue,
Xiamen University, China, in collaboration with reviewer JZ

*CORRESPONDENCE
Xiaojie Xie
xiexj@zju.edu.cn

SPECIALTY SECTION
This article was submitted to Heart Valve Disease, a section of the journal Frontiers in Cardiovascular Medicine

RECEIVED 26 July 2022
ACCEPTED 31 October 2022
PUBLISHED 23 November 2022

CITATION
Yu J, Wang Z, Bao Q, Lei S, You Y, Yin Z and Xie X (2022) Global burden of calcific aortic valve disease and attributable risk factors from 1990 to 2019.
Front. Cardiovasc. Med. 9:1003233.
doi: 10.3389/fcvm.2022.1003233

Global burden of calcific aortic valve disease and attributable risk factors from 1990 to 2019

Jiaye Yu, Zhuo Wang, Qinyi Bao, Shuxin Lei, Yayu You, Zhehui Yin and Xiaojie Xie*

Department of Cardiology, The Second Affiliated Hospital, Zhejiang University School of Medicine, Hangzhou, Zhejiang, China

Background: Calcific aortic valve disease (CAVD) was highly prevalent among developed countries and caused numerous deaths. Based on the Global Burden of Disease 2019, this study was designed to present comprehensive epidemiological information, attributable risks, and relevant factors.

Methods: All data were available online *via* the Global Health Data Exchange (GHDx). In this study, we analyzed the global incidence, prevalence, deaths, and disability-adjusted life years (DALYs) of CAVD across different regions from 1990 to 2019. We applied the estimated annual percentage changes (EAPCs) to evaluate the change trends and their attributable risks. In addition, we explored several relevant factors.

Results: From 1990 to 2019, the incidence cases, prevalence cases, CAVD-related deaths, and DALYs of CAVD gradually increased globally. However, the age-standardized death rate (ASDR) was relatively stable, and the age-standardized DALYs rate gradually declined during the past 30 years. Males and elderly individuals were more likely to suffer from CAVD. High systolic blood pressure (SBP) was the predominant attributable risk of disease burden that presented a global downward trend (death: EAPC = −0.68, 95% CI −0.77∼−0.59, $P < 0.001$; DALYs: EAPC = −0.99, 95% CI −1.09 to −0.89, $P < 0.001$). Alcohol consumption ($R = 0.79$, $P < 0.001$), smoking prevalence ($R = 0.75$, $P < 0.001$), and calcium ($R = 0.72$, $P < 0.001$) showed a positive correlation with the age-standardized incidence rate (ASIR), whereas classic monsoon region ($R = -0.68$, $P < 0.001$) and mean temperature ($R = -0.7$, $P < 0.001$) showed a negative correlation with age-standardized incidence rate (ASIR). Besides, medical and healthcare resources presented a positive correlation with ASIR. Meanwhile, similar relationships were found in age-standardized prevalence rate (ASPR), ASDR, and age-standardized DALY rate (ASDALYR).

Conclusion: CAVD displays widely varied spatial distribution around the world, of which high SDI regions have the highest burdens. Age is a powerful factor and hypertension a predominant attributable risk factor. Moreover, controlling blood pressure, avoiding smoking, reducing alcohol consumption, and so on, could effectively reduce the burden of CAVD.

KEYWORDS

calcific aortic valve disease, Global Burden of Disease Study, disability-adjusted life year, estimated annual percentage change, attributable risk factor

Introduction

Calcific aortic valve disease (CAVD) is defined as a clinical diagnosis of stenosis due to progressive calcification of the valve which causes impaired hemodynamics. Much clinical and laboratory evidence has suggested that the disease was an active process involving chronic inflammation, lipid deposition, and biomineralization (1). Moreover, the clinical evolution of the disease is from aortic sclerosis and asymptomatic aortic stenosis (AS) to symptomatic aortic stenosis. When the valve becomes thickened over the years, it presents severely impaired leaflet motion and vast left ventricular outflow tract obstruction, which causes left ventricular remodeling (1). Finally, thisresults in chronic heart failure.

CAVD is the most common valvular heart disease (VHD) in the western world and high-income countries (2). Furthermore, it is the third most frequent cardiovascular disease after coronary artery disease and hypertension among developed countries (3). The prevalence of CAVD rose sharply with age, especially in those aged over 65 years, and most of those were symptomatic (1). In 2017, there were ∼12.6 million cases of CAVD, increased by 124% from 1990, with 102,700 CAVD-related deaths globally (2). Moreover, rheumatic heart disease (RHD), the most prevalent VHD in the world, showed a downward trend, whereas CAVD presented the fastest increase among non-rheumatic valvular disease (NRVD).

Since life expectancy has extended over the last decades, the prevalence of CAVD was predicted to double within the next half century (4). And as no medication has proved to be effective in stopping the evolution of this disease, aortic valve replacement (AVR) is the only effective therapy for it, which remains a significant financial and physical burden for patients (5, 6). Therefore, more attention should be paid to the existing high burden of CAVD, and prevention is particularly important and cost-effective. In this study, we focused on the global incidence, prevalence, deaths, and disability-adjusted life years (DALYs) of CAVD across different regions (204 countries and territories) from 1990 to 2019. Moreover, we analyzed attributable risks and various covariates to discover underlying attributable risk factors and potential exposure.

Methods

Study data

All data were available in the Global Health Data Exchange (GHDx), an online catalog conducted by the Institute for Health Metrics and Evaluation (IHME). GBD 2019 study estimated epidemiological quantity in 23 age groups, gender groups, and 204 countries and territories for a total of 369 diseases (7, 8). In this study, we extracted the incidence, prevalence, deaths, DALYs, and corresponding age-standardized rates (ASRs) of CAVD and health risk factors attributable to it. We presented the above indicators for 5 socio-demographic index (SDI) regions, 4 World Bank income (WBI) level groups, 21 GBD regions, and 204 countries and territories from 1990 to 2019. Meanwhile, we performed gender and age stratifications. SDI is a socio-demographic indicator comprehensively considering education, national income, and fertility rate (7, 9). Thus, the world is divided into five SDI regions including low, low-middle, middle, high-middle, and high SDI regions. According to gross national income (GNI) per capita calculated by the World Bank Atlas method, there are four WBI regions including low, lower-middle, upper-middle, and high WBI regions (10).

DALYs are the sum of years of life lost (YLLs) (due to premature mortality) and years lived with disability (YLDs). In brief, YLDs comprehensively consider several social preference values, for example, disability weight, age weight, and so on. And the formula to calculate DALYs could be simplified as

$$\mathrm{YLL} = N \times L1$$
$$\mathrm{YLD} = I \times D \times L2$$
$$\mathrm{DALYs} = YLLs + YLDs$$

Where N is the number of premature deaths due to a given disease; L1 is the standard life expectancy loss for each death; I is the number of disabilities; D is thedisability weight; and L2 is the average duration of disease (11).

In addition, the GBD 2019 study provided 87 risk factors for a given disease at regional levels. Three attributable risks of CAVD were found, including lead exposure, high systolic blood pressure (SBP), and a diet high in sodium. The population attributable fraction (PAF) is the estimated fraction of cases that would be attributable to exposure. And the computational formula of PAF is presented as:

PAF = E/O × 100% (where O and E refer to the observed case load and the case load attributable to exposure, respectively) (7, 12). Finally, we analyzed the burden of CAVD and covariates downloaded from the GBD 2019 covariate dataset (https://cloud.ihme.washington.edu/s/b2tQnbsjAyWgeHm?path=%2FGBD%202019%20Covariates), and correlation coefficient (R-value) was calculated for each covariate.

Statistical analysis

Annual incidence cases, prevalence cases, CAVD-related death cases, and DALYs were used to present the disease burden. Meanwhile, corresponding ASRs were applied to exclude the age distribution differences among different populations (13). The estimated annual percentage change (EAPC) of ASR of incidence, prevalence, deaths, and DALYs were used to reflect the trends of disease burden. Based on the equation $Y = \alpha + \beta X + \varepsilon$ [where Y refers to ln(ASR), X refers to the calendar year, and ε represents the error term], EAPC is calculated using the formula $EAPC = 100 \times [\exp(\beta) - 1]$ (14). Therefore, when the EAPC value and its 95% confidence interval (CI) are over zero,

the ASR presents an uptrend and vice versa (15). Furthermore, we calculated spearman's correlation coefficient (R) to explore the correlation between the burden of CAVD (using ASRs) and covariates. Data analysis and visualization were performed by the open-source software R (version 4.1.0). A two-tailed $p < 0.05$ was deemed statistically significant.

Results

The incidence and its trend

Globally, over the past 30 years, the incidence case of CAVD gradually increased by 351% from 130,821 in 1990 to 589,637 cases in 2019 (Table 1). Meanwhile, the age-standardized incidence rate (ASIR) of CAVD increased by 120% from 3.25 (95% UI 2.76∼3.86) per 100,000 in 1990 to 7.13 (95% UI 6.22∼8.15) in 2019 (EAPC = 3.03, 95% CI 2.80∼3.27) (Tables 1, 5). In the socio-demographic factor level, the high SDI region had the highest CAVD burden until 2019 [incidence case: 92,683 in 1990 and 329,823 cases in 2019; ASIR: 9.18 (95% UI 7.65∼11.05) per 100,000 in 1990 and 19.04 (95% UI 16.65∼21.96) in 2019; EAPC = 2.93, 95% CI 2.62∼3.23] (Tables 1, 5). At the same time, high-middle SDI had the fastest increase in the 30 years (ASIR: 2.40 per 100,000 in 1990 and 9.59 in 2019, EAPC = 5.10, 95% CI 4.92∼5.27) (Tables 1, 5). Similar results were found at the WBI level. Among geographical zones, high-income north America and high-income Asia Pacific had the highest ASIR in 1990 (14.32 and 15.12 per 100,000, respectively) while central Europe and Australasia presented the highest ASIR in 2019 (33.16 and 44.39 per 100,000, respectively) (Table 1). Australasia and eastern Europe were the fastest-growing regions (EAPC of Australasia: 7.72, 95% CI 7.51∼7.94; EAPC of Eastern Europe: 7.75, 95% CI 7.33∼8.16) (Table 5). Among 204 countries and territories, the USA and Japan had the highest ASIR in 1990 (15.77 and 17.10 per 100,000, respectively), while Hungary and Slovenia had the highest ASIR in 2019 (56.24 and 62.21 per 100,000, respectively) (Figure 1C; Supplementary Table 1). Germany and Iceland had the fastest increase in ASIR (EAPC = 12.84, 95% CI 10.89∼14.82 and 13.35, 95% CI 10.93∼15.81, respectively) (Figure 1E; Supplementary Table 2). Incidence was positively correlated with age and there were two peaks, one at age 70 to 74 and the other at age over 95 (Figure 1B).

The ASIR was higher in male than female individuals (in 1990: 3.63 per 100,000 in male individuals, 2.88 in female individuals; and in 2019: 7.95 per 100,000 in male individuals, 6.31 in female individuals) globally (Figure 1A, Table 1). This phenomenon was found in five SDI levels, four WBI levels, and most geographical regions. However, in Australasia and high-income Asia Pacific in 1990 and 2019 and western Europe in 2019, the reverse applied. And both sexes shared a quite similar EAPC (3.04, 95% CI 2.87∼3.21 in male and 3.06, 95% CI 2.75∼3.38 in female individuals) (Figure 1D, Table 5). In general, most regions had a rising trend of ASIR from 1990 to 2019 in both genders (Figure 1D, Table 5). Male individuals in Australasia had the most rapid increase in ASIR (EAPC = 7.65, 95% CI 7.33∼7.96) and female individuals in eastern Europe had the highest EAPC of 8.26 (95% CI 7.68∼8.83). Nevertheless, female individuals in southern Sub-Saharan Africa showed the greatest decrease (EAPC: −0.5, 95% CI −0.56∼−0.44).

The prevalence and its trend

In the globe, the prevalence of CAVD cases remarkably increased by 443% from 1,732,988 in 1990 to 9,404,077 cases in 2019 (Table 2). At the same time, the age-standardized prevalence rate (ASPR) of CAVD increased by 120% from 45.54 (95% UI 37.61∼54.67) per 100,000 in 1990 to 116.34 (95% UI 100.39∼134.50) in 2019 (EAPC = 3.65, 95% CI 3.4∼3.91) (Tables 2, 5). Socio-demographic factor subgroup analysis indicated that high SDI regions showed the most prevalence cases (1,324,934 in 1990 and 5,095,444 in 2019) and highest ASPR (126.83 per 100,000 in 1990 and 273.52 in 2019) (Table 2). However, middle SDI regions showed the most rapid increase (EAPC = 8.19, 95% CI 7.9∼8.49) (Table 5). Among WBI levels, the situation was analogous. As for geographical regions, high-income north America and high-income Asia Pacific were the top two regions with the highest ASPR in 1990 (191.35 and 233.42 per 100,000, respectively), but in 2019, they were central Europe and Australasia (ASPR: 608.31 and 649.50 per 100,000, respectively) (Table 2). Meanwhile, Australasia and East Asia had the fastest increase in ASPR (EAPC of Australasia: 10.18, 95% CI 9.7∼10.67; EAPC of East Asia: 11.5, 95% CI 10.86∼12.13) (Table 5). Among 204 countries and territories, the USA and Japan had the highest ASPR in 1990 (210.23 and 261.58 per 100,000, respectively), while Romania and Slovenia were the top two countries with the highest ASPR in 2019 (1,044.49 and 1,080.06 per 100,000, respectively) (Figure 2C; Supplementary Table 1). Furthermore, Germany and Iceland had the fastest rise in ASPR (EAPC = 15.15, 95% CI 12.8∼17.56 and 15.28, 95% CI 12.56∼18.06, respectively) (Figure 2E; Supplementary Table 2). Prevalence was positively correlated with age and peaked at age of 90 to 94 globally (Figure 2B).

The ASPR was higher in male than female individuals (in 1990: 51.19 per 100,000 in male individuals, 40.28 in female individuals, male to female ratio = 1.27; in 2019: 133.38 per 100,000 in male individuals, 99.86 in female individuals, ratio = 1.34) globally (Figure 2A, Table 2). Male and female individuals showed a similar growing trend of ASPR during the past 30 years (EAPC of males: 3.67, 95% CI 3.46∼3.88; EAPC of females: 3.62, 95% CI 3.31∼3.93) (Figure 2D, Table 5). Among five SDI levels, four WBI levels, and 21 GBD regions, there were slight differences in the variation tendency of ASPR in this period (Figures 2A,D, Table 5). However, female individuals in southern sub-Saharan Africa showed a downward trend (EAPC

TABLE 1 The incidence of CAVD in 1990/2019.

	1990						2019					
	Incident cases No *10^3 (95% UI)			ASIR/100,000 No. (95% UI)			Incident cases No *10^3 (95% UI)			ASIR/100,000 No. (95% UI)		
	Male	Female	Both	Male	Female	Both	Male	Female	Both	Male	Female	Both
Global	69.64 (59.32~82.58)	61.18 (50.97~73.84)	130.82 (110.7~156.02)	3.63 (3.11~4.27)	2.88 (2.41~3.45)	3.25 (2.76~3.86)	313.8 (271.31~360.92)	275.83 (239.87~317.14)	589.64 (512.9~677.06)	7.95 (6.92~9.09)	6.31 (5.49~7.26)	7.13 (6.22~8.15)
SDI level												
High SDI	44.82 (37.39~53.93)	47.86 (39.24~58.27)	92.68 (76.42~112.27)	9.9 (8.32~11.84)	8.49 (7~10.28)	9.18 (7.65~11.05)	153.12 (133.19~177.54)	176.7 (152.55~204.1)	329.82 (285.98~381.25)	19.31 (16.87~22.23)	18.66 (16.22~21.66)	19.04 (16.65~21.96)
High-middle SDI	16.38 (13.68~19.36)	10.01 (8.51~11.81)	26.39 (22.29~31.01)	3.17 (2.69~3.72)	1.68 (1.42~1.97)	2.4 (2.04~2.79)	118.39 (98.87~139.91)	74.82 (64.36~86.77)	193.22 (163.54~225.65)	12.25 (10.28~14.34)	6.92 (5.94~8.03)	9.59 (8.14~11.18)
Middle SDI	4.28 (3.62~5.08)	1.91 (1.59~2.32)	6.19 (5.24~7.33)	0.87 (0.75~1.01)	0.4 (0.34~0.48)	0.63 (0.54~0.73)	30.87 (25.84~36.65)	19.07 (15.79~23.07)	49.94 (41.59~59.44)	2.38 (2.01~2.78)	1.42 (1.19~1.69)	1.89 (1.59~2.23)
Low-middle SDI	2.93 (2.49~3.43)	0.98 (0.81~1.18)	3.91 (3.33~4.61)	1.11 (0.96~1.29)	0.44 (0.36~0.52)	0.77 (0.66~0.9)	8.58 (7.37~10)	4.02 (3.41~4.78)	12.6 (10.82~14.6)	1.38 (1.19~1.59)	0.62 (0.53~0.74)	0.98 (0.85~1.14)
Low SDI	1.21 (1.04~1.42)	0.41 (0.34~0.48)	1.62 (1.39~1.88)	1.14 (1~1.3)	0.49 (0.42~0.58)	0.82 (0.71~0.94)	2.72 (2.35~3.18)	1.14 (0.97~1.34)	3.86 (3.34~4.46)	1.14 (0.99~1.31)	0.56 (0.48~0.65)	0.84 (0.73~0.97)
World Bank Income Level												
World Bank High Income	50.53 (42.41~60.72)	52.74 (43.46~64)	103.28 (85.7~124.63)	9.11 (7.7~10.89)	7.62 (6.32~9.2)	8.35 (6.99~10.01)	181.82 (158.47~210.31)	208.85 (179.93~241.29)	390.67 (339.45~451.2)	19.48 (17.02~22.4)	18.68 (16.26~21.64)	19.14 (16.73~22.05)
World Bank Upper Middle Income	11.75 (9.86~13.89)	6.39 (5.45~7.55)	18.14 (15.35~21.22)	1.54 (1.32~1.79)	0.82 (0.7~0.96)	1.18 (1.01~1.37)	108.78 (89.85~129.14)	59.39 (49.83~70.34)	168.17 (139.25~198.69)	6.36 (5.28~7.49)	3.27 (2.75~3.85)	4.81 (4~5.65)
World Bank Lower Middle Income	6.73 (5.73~7.87)	1.77 (1.45~2.19)	8.5 (7.24~9.96)	1.36 (1.16~1.57)	0.4 (0.34~0.49)	0.87 (0.74~1.01)	21.73 (18.47~25.39)	6.82 (5.76~8.11)	28.55 (24.32~33.44)	1.87 (1.6~2.16)	0.61 (0.52~0.72)	1.22 (1.05~1.41)
World Bank Low Income	0.61 (0.53~0.71)	0.26 (0.22~0.31)	0.87 (0.76~1.01)	0.93 (0.83~1.04)	0.46 (0.4~0.53)	0.69 (0.61~0.77)	1.36 (1.18~1.58)	0.69 (0.6~0.81)	2.05 (1.79~2.36)	0.94 (0.84~1.07)	0.51 (0.45~0.59)	0.72 (0.64~0.81)
Region												
Andean Latin America	0.1 (0.09~0.11)	0.05 (0.05~0.06)	0.15 (0.13~0.17)	0.95 (0.84~1.06)	0.51 (0.45~0.59)	0.72 (0.65~0.81)	1.66 (1.43~1.91)	0.49 (0.41~0.57)	2.15 (1.86~2.46)	5.74 (4.98~6.62)	1.62 (1.37~1.9)	3.62 (3.14~4.16)
Australasia	0.49 (0.4~0.59)	0.77 (0.68~0.88)	1.26 (1.1~1.45)	5.07 (4.27~6)	5.83 (5.15~6.55)	5.56 (4.9~6.32)	9.23 (7.82~10.95)	10.95 (9.07~13.09)	20.17 (17.13~23.51)	42.87 (36.65~50.79)	45.8 (38.35~54.49)	44.39 (38.08~51.79)
Caribbean	0.33 (0.3~0.37)	0.11 (0.1~0.13)	0.44 (0.4~0.49)	2.62 (2.36~2.9)	0.85 (0.75~0.96)	1.7 (1.53~1.88)	1.82 (1.55~2.15)	0.53 (0.46~0.61)	2.35 (2.02~2.73)	7.21 (6.13~8.44)	1.94 (1.67~2.23)	4.49 (3.86~5.21)
Central Asia	0.19 (0.15~0.23)	0.14 (0.11~0.18)	0.33 (0.27~0.4)	0.87 (0.72~1.04)	0.5 (0.41~0.63)	0.66 (0.54~0.8)	1.74 (1.43~2.06)	0.9 (0.73~1.07)	2.65 (2.18~3.11)	3.97 (3.28~4.66)	1.87 (1.54~2.21)	2.86 (2.37~3.35)
Central Europe	5.11 (4.3~6.03)	4.69 (3.92~5.52)	9.8 (8.26~11.5)	7.5 (6.34~8.77)	5.71 (4.78~6.71)	6.59 (5.52~7.69)	27.88 (23.58~32.92)	29.4 (25.02~34.63)	57.28 (48.87~67.32)	34.18 (28.97~40.11)	31.88 (27.15~37.4)	33.16 (28.29~38.67)
Central Latin America	0.69 (0.6~0.79)	0.36 (0.31~0.41)	1.05 (0.92~1.2)	1.57 (1.37~1.79)	0.82 (0.72~0.94)	1.19 (1.05~1.35)	3.7 (3.19~4.26)	2.05 (1.75~2.39)	5.75 (4.95~6.62)	3.09 (2.67~3.55)	1.57 (1.35~1.82)	2.29 (1.99~2.63)
Central Sub-Saharan Africa	0.11 (0.1~0.13)	0.05 (0.04~0.06)	0.16 (0.14~0.19)	1.21 (1.06~1.37)	0.7 (0.62~0.8)	0.94 (0.84~1.06)	0.25 (0.22~0.3)	0.16 (0.14~0.18)	0.41 (0.36~0.47)	1.22 (1.08~1.38)	0.76 (0.66~0.85)	0.97 (0.87~1.1)
East Asia	1.72 (1.37~2.18)	1.25 (0.98~1.59)	2.97 (2.37~3.78)	0.4 (0.32~0.49)	0.29 (0.23~0.36)	0.34 (0.28~0.42)	29.75 (23.71~36.34)	26.89 (21.55~33.19)	56.64 (45.3~69.33)	2.77 (2.24~3.32)	2.44 (1.97~2.99)	2.61 (2.11~3.15)
Eastern Europe	6.67 (5.26~8.16)	1.27 (1.02~1.57)	7.93 (6.36~9.59)	5.7 (4.57~6.89)	0.73 (0.6~0.89)	2.9 (2.34~3.48)	57.17 (45.96~69.72)	11.24 (9.06~13.65)	68.42 (55.23~82.91)	42.22 (34.12~50.83)	5.91 (4.74~7.11)	22.58 (18.38~27.04)

(Continued)

10.3389/fcvm.2022.1003233

TABLE 1 (Continued)

	1990						2019					
	Incident cases No *10^3 (95% UI)			ASIR/100,000 No. (95% UI)			Incident cases No *10^3 (95% UI)			ASIR/100,000 No. (95% UI)		
	Male	Female	Both	Male	Female	Both	Male	Female	Both	Male	Female	Both
Eastern Sub-Saharan Africa	0.34 (0.29∼0.39)	0.16 (0.14∼0.19)	0.5 (0.43∼0.57)	1.02 (0.9∼1.15)	0.64 (0.55∼0.74)	0.83 (0.74∼0.95)	0.77 (0.65∼0.91)	0.4 (0.34∼0.47)	1.17 (1.01∼1.35)	1.05 (0.91∼1.2)	0.64 (0.54∼0.74)	0.84 (0.73∼0.96)
High-income Asia Pacific	12.34 (10.17∼14.87)	18.14 (14.91∼22.22)	30.47 (25.25∼36.92)	13.49 (11.28∼16.05)	16.33 (13.56∼19.81)	15.12 (12.61∼18.17)	33.55 (27.93∼40.84)	55.05 (45.3∼66.38)	88.6 (73.61∼107.12)	21.84 (18.59∼25.63)	27.65 (23.31∼33.08)	25.04 (21.32∼29.6)
High-income North America	25.9 (21.23∼31.6)	23 (18.51∼28.36)	48.91 (39.76∼59.97)	16.97 (13.99∼20.58)	11.97 (9.74∼14.71)	14.32 (11.71∼17.4)	64.38 (55.43∼74.66)	59.19 (50.96∼68.17)	123.57 (106.45∼142.33)	23.54 (20.52∼26.98)	17.26 (14.98∼19.67)	20.23 (17.61∼23.2)
North Africa and Middle East	1.6 (1.36∼1.87)	0.43 (0.37∼0.52)	2.04 (1.75∼2.37)	1.76 (1.53∼2.03)	0.6 (0.52∼0.71)	1.19 (1.04∼1.36)	5.25 (4.37∼6.23)	1.82 (1.57∼2.13)	7.07 (5.98∼8.35)	1.98 (1.69∼2.31)	0.89 (0.78∼1.02)	1.46 (1.27∼1.69)
Oceania	0.02 (0.02∼0.03)	0.01 (0.01∼0.01)	0.03 (0.02∼0.03)	1.61 (1.35∼1.93)	0.53 (0.46∼0.6)	1.07 (0.91∼1.26)	0.09 (0.07∼0.1)	0.04 (0.04∼0.05)	0.13 (0.11∼0.15)	2.21 (1.86∼2.63)	1.24 (1.04∼1.45)	1.73 (1.47∼2.04)
South Asia	3.33 (2.8∼3.94)	0.8 (0.65∼0.99)	4.13 (3.48∼4.94)	1.37 (1.16∼1.6)	0.46 (0.38∼0.55)	0.93 (0.79∼1.09)	9.03 (7.66∼10.6)	3.34 (2.74∼4.06)	12.37 (10.49∼14.62)	1.47 (1.25∼1.72)	0.57 (0.47∼0.68)	1.01 (0.85∼1.18)
Southeast Asia	0.44 (0.36∼0.53)	0.28 (0.22∼0.34)	0.71 (0.59∼0.86)	0.41 (0.35∼0.48)	0.24 (0.2∼0.29)	0.32 (0.27∼0.38)	1.88 (1.56∼2.24)	1.42 (1.2∼1.71)	3.29 (2.78∼3.94)	0.64 (0.55∼0.75)	0.45 (0.38∼0.53)	0.54 (0.46∼0.64)
Southern Latin America	0.47 (0.4∼0.55)	0.62 (0.49∼0.92)	1.09 (0.9∼1.43)	2.48 (2.1∼2.87)	2.57 (2.03∼3.86)	2.59 (2.13∼3.46)	4.67 (4.07∼5.45)	4.06 (3.57∼4.63)	8.73 (7.73∼9.92)	12.76 (11.17∼14.78)	8.6 (7.56∼9.83)	10.64 (9.44∼12.08)
Southern Sub-Saharan Africa	0.34 (0.29∼0.41)	0.1 (0.08∼0.12)	0.44 (0.37∼0.52)	2.78 (2.33∼3.35)	0.72 (0.6∼0.85)	1.62 (1.38∼1.91)	4.45 (3.54∼5.51)	0.18 (0.15∼0.22)	4.64 (3.72∼5.7)	14.93 (12.01∼18.1)	0.65 (0.54∼0.77)	7.09 (5.73∼8.6)
Tropical Latin America	1.17 (1∼1.37)	0.78 (0.66∼0.91)	1.95 (1.67∼2.28)	2.66 (2.26∼3.08)	1.79 (1.51∼2.1)	2.22 (1.91∼2.57)	3.95 (3.35∼4.64)	2.64 (2.24∼3.09)	6.59 (5.61∼7.68)	3.5 (2.97∼4.09)	1.99 (1.69∼2.32)	2.71 (2.31∼3.15)
Western Europe	7.92 (6.58∼9.54)	8.03 (6.56∼9.87)	15.95 (13.21∼19.24)	3.33 (2.79∼3.97)	2.56 (2.11∼3.14)	2.96 (2.46∼3.57)	51.77 (43.75∼61.18)	64.74 (54.65∼77.31)	116.51 (98.95∼138.35)	14.25 (12.15∼16.77)	15.41 (13.15∼18.28)	14.9 (12.77∼17.56)
Western Sub-Saharan Africa	0.36 (0.3∼0.43)	0.14 (0.11∼0.17)	0.51 (0.43∼0.6)	0.7 (0.6∼0.83)	0.38 (0.32∼0.46)	0.57 (0.49∼0.66)	0.81 (0.68∼0.97)	0.35 (0.29∼0.42)	1.16 (0.99∼1.37)	0.71 (0.61∼0.84)	0.45 (0.38∼0.53)	0.58 (0.5∼0.67)

CAVD, calcific aortic valve disease; ASIR, the age-standardized incidence rate; SDI, socio-demographic index.

10.3389/fcvm.2022.1003233

= −0.13, 95% CI −0.27∼0) of ASPR while male individuals in this region showed a relatively huge increase (EAPC = 9.62, 95% CI 8.13∼11.14).

The death and its trend

In general, CAVD-related death cases significantly increased from 53,298 in 1990 to 126,827 in 2019 while the age-standardized death rate (ASDR) was relatively stable during the past 30 years (from 1.75 per 100,000 in 1990 to 1.76 in 2019, EAPC = 0.06, 95% CI −0.04∼0.15) (Tables 3, 5). In the SDI level, the high SDI regions had the highest burden until 2019 [death cases: 36,015 in 1990 and 80,211 in 2019, ASDR: 3.46 (95% UI 3.06∼3.84) per 100,000 in 1990 and 3.35 (95% UI 2.75∼3.74) in 2019] (Table 3). At the same time, high-middle SDI regions experienced the most rapid increase in this period (ASDR: 0.93 in 1990 and 1.28 in 2019, EAPC = 1.17, 95% CI

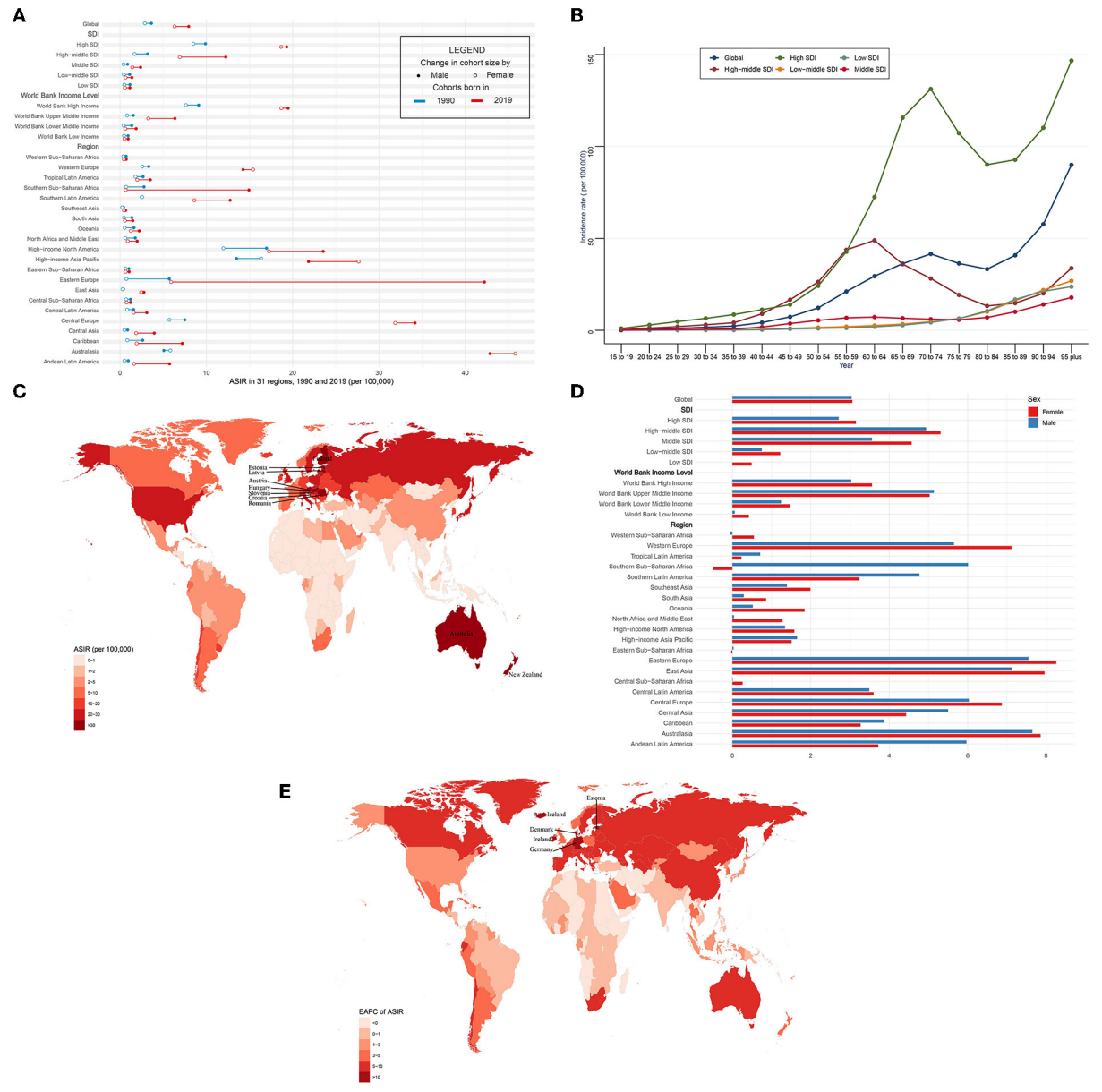

FIGURE 1
ASIR and its trend of CAVD. **(A)** ASIR in 31 regions from 1990 to 2019. **(B)** Incidence rate stratified by age in the globe and 5 SDI regions in 2019. **(C)** ASIR in 204 countries and territories in 2019. **(D)** EAPC of ASIR in 31 regions from 1990 to 2019. **(E)** EAPC of ASIR in 204 countries and territories from 1990 to 2019. CAVD, calcific aortic valve disease; ASIR, the age-standardized incidence rate; SDI, socio-demographic index; EAPC, estimated annual percentage change.

TABLE 2 The prevalence of CAVD in 1990/2019.

	1990						2019					
	Prevalent cases No *10^3 (95% UI)			ASPR/100,000 (95% UI)			Prevalent cases No *10^3 (95% UI)			ASPR/100,000 (95% UI)		
	Male	Female	Both	Male	Female	Both	Male	Female	Both	Male	Female	Both
Global	894.5 (741.59~1067.5)	838.49 (690.26~1016.94)	1732.99 (1431.47~2074.81)	51.19 (42.68~60.91)	40.28 (32.99~48.82)	45.54 (37.61~54.67)	5027.26 (4276.88~5861.59)	4376.82 (3771.24~5082.8)	9404.08 (8079.6~10889.73)	133.38 (113.79~154.58)	99.86 (86.1~115.88)	116.34 (100.39~134.5)
SDI level												
High SDI	632.57 (523.39~760.43)	692.36 (563.23~842.26)	1324.93 (1090~1602.16)	142.6 (117.67~171.17)	113.91 (93.22~137.94)	126.83 (104.61~152.72)	2385.46 (2064.99~2748.14)	2709.98 (2327.88~3211.14)	5095.44 (4402.07~5933.38)	288.07 (250.19~330.79)	256.98 (221.02~300.21)	273.52 (237.08~315.22)
High-middle SDI	230.81 (188.4~277.51)	134.13 (110.52~160.59)	364.93 (300.69~436.29)	48.72 (39.87~58.5)	22.04 (18.22~26.36)	33.9 (27.98~40.44)	2185.22 (1810.72~2589.05)	1384.6 (1166.85~1627.03)	3569.82 (3002.41~4203.73)	234.86 (194.65~277.14)	121.54 (102.65~142.7)	174.53 (147.33~204.54)
Middle SDI	21.52 (16.92~26.64)	8.98 (7~11.44)	30.51 (24.09~37.76)	4 (3.16~4.93)	1.68 (1.31~2.13)	2.82 (2.23~3.49)	403.23 (326.37~489.15)	255.32 (203.74~311.73)	658.55 (529.93~800.78)	32.62 (26.5~39.34)	19.6 (15.69~23.94)	25.93 (20.92~31.47)
Low-middle SDI	7.05 (5.57~8.79)	2.31 (1.77~2.97)	9.36 (7.35~11.71)	2.12 (1.69~2.6)	0.76 (0.59~0.98)	1.45 (1.15~1.79)	43.85 (35.46~53.49)	23.41 (18.56~29.17)	67.26 (54.36~81.97)	6.34 (5.14~7.64)	3.3 (2.63~4.09)	4.78 (3.86~5.82)
Low SDI	2.34 (1.83~2.93)	0.59 (0.43~0.78)	2.93 (2.3~3.72)	1.69 (1.35~2.11)	0.52 (0.39~0.68)	1.12 (0.88~1.38)	7.43 (5.89~9.24)	2.24 (1.69~2.9)	9.68 (7.61~12.14)	2.5 (1.99~3.1)	0.86 (0.66~1.1)	1.67 (1.34~2.07)
World Bank Income Level												
World Bank High Income	720.96 (596.8~862.18)	765.97 (623.9~931.67)	1486.93 (1226.29~1790.77)	132.11 (109.85~158.01)	102.63 (84.23~123.72)	116.01 (95.82~139.03)	2913.58 (2525.2~3353.42)	3314.67 (2856.43~3900.43)	6228.25 (5389.24~7231.3)	295.76 (256.26~338.43)	261.86 (226.25~305.36)	279.68 (242.58~322.69)
World Bank Upper Middle Income	128.86 (103.46~157.41)	63.17 (51.17~76.63)	192.03 (155.18~232.96)	17.74 (14.32~21.54)	7.88 (6.4~9.57)	12.5 (10.17~15.09)	1889.48 (1556.27~2269.7)	1011.97 (832.19~1208.2)	2901.45 (2400.08~3460.03)	117.06 (96.4~140.16)	55.94 (46.06~66.6)	84.88 (70.35~101.1)
World Bank Lower Middle Income	43.31 (34.49~52.59)	8.83 (6.88~11.19)	52.14 (41.82~63.1)	8.29 (6.68~10.07)	1.84 (1.44~2.33)	5.01 (4.02~6.04)	218.05 (174.89~264.45)	47.18 (37.93~57.83)	265.23 (214.14~320.12)	18.79 (15.21~22.79)	4.02 (3.24~4.89)	11.11 (9.01~13.35)
World Bank Low Income	1.16 (0.91~1.45)	0.4 (0.3~0.54)	1.56 (1.22~1.97)	1.4 (1.1~1.73)	0.54 (0.41~0.71)	0.96 (0.76~1.18)	4.08 (3.22~5.04)	1.7 (1.3~2.17)	5.77 (4.54~7.17)	2.34 (1.85~2.88)	1.04 (0.81~1.33)	1.67 (1.32~2.06)
Region												
Andean Latin America	0.56 (0.45~0.69)	0.27 (0.21~0.35)	0.83 (0.66~1.03)	5.25 (4.22~6.41)	2.37 (1.82~3.03)	3.77 (3.02~4.63)	26.25 (22.25~30.53)	7.1 (5.81~8.45)	33.35 (28.25~39.02)	96.53 (81.91~112.71)	24.29 (19.85~28.95)	59.04 (50.07~69.05)
Australasia	4.03 (3.23~5.03)	5.85 (4.83~7.03)	9.88 (8.18~11.83)	38.54 (30.95~47.68)	42.99 (35.39~51.62)	41.77 (34.78~49.88)	145.81 (124.04~176.73)	175.01 (146.24~209.39)	320.82 (272.23~381.06)	641.53 (548.23~771.77)	653.5 (546.89~785.16)	649.5 (552~772.74)
Caribbean	2.64 (2.18~3.2)	0.72 (0.57~0.89)	3.36 (2.75~4.01)	20.63 (17.03~25.03)	5.2 (4.14~6.44)	12.61 (10.3~15.1)	36.64 (30.14~44.78)	8.83 (7.18~10.64)	45.47 (37.69~54.85)	149.46 (123.31~182.28)	32.16 (26.19~38.74)	87.51 (72.62~105.56)
Central Asia	1.91 (1.46~2.38)	1.86 (1.44~2.35)	3.77 (2.96~4.71)	9.8 (7.66~12.16)	6.69 (5.22~8.43)	7.92 (6.22~9.83)	26.75 (21.47~32.02)	14.31 (11.58~17.08)	41.06 (33.49~48.81)	77.22 (62.76~91.41)	34.51 (28.22~40.92)	53.22 (43.89~62.92)
Central Europe	79.88 (66.06~95.09)	74.78 (61.25~89.11)	154.66 (128.34~184.57)	123.97 (102.96~146.99)	87.57 (71.89~104.38)	104.18 (86.62~123.47)	582.72 (493.97~689.09)	677.83 (575.85~802.85)	1260.56 (1067.65~1479.62)	648.83 (551.63~763.85)	566.62 (482.05~673.31)	608.31 (517.94~713.51)
Central Latin America	4.96 (3.98~6)	2.04 (1.61~2.53)	7 (5.59~8.53)	11.78 (9.52~14.38)	4.45 (3.51~5.52)	7.98 (6.44~9.71)	51.88 (43.38~61.48)	25.08 (20.49~30.42)	76.96 (63.86~91.38)	45.83 (38.37~54.3)	19.54 (15.96~23.74)	31.82 (26.45~37.75)
Central Sub-Saharan Africa	0.18 (0.14~0.22)	0.07 (0.05~0.09)	0.25 (0.19~0.32)	1.42 (1.12~1.79)	0.62 (0.46~0.82)	1 (0.79~1.26)	0.58 (0.45~0.75)	0.21 (0.16~0.28)	0.8 (0.62~1.01)	2.03 (1.6~2.54)	0.78 (0.6~0.99)	1.36 (1.08~1.69)
East Asia	9.79 (7.21~13.03)	8.48 (6.28~11.34)	18.27 (13.68~24.32)	2.19 (1.63~2.88)	1.94 (1.45~2.54)	2.1 (1.57~2.74)	466.89 (370.91~566.03)	424.13 (335.82~519.55)	891.02 (707.25~1093.31)	45.83 (36.68~55.4)	39 (30.97~47.63)	42.41 (33.87~51.68)
Eastern Europe	103.55 (81.71~128.12)	18.11 (14.27~22.87)	121.66 (97.12~148.88)	101.46 (81.16~123.89)	10.01 (7.96~12.57)	43.32 (34.79~52.76)	1114.74 (894.48~1351.95)	213.94 (170.2~259.17)	1328.69 (1065.7~1605.21)	843.96 (678.61~1017.4)	98.37 (78.91~118.49)	395.8 (319.64~477)

(Continued)

10.3389/fcvm.2022.1003233

TABLE 2 (Continued)

	1990						2019					
	Prevalent cases No *10^3 (95% UI)			ASPR/100,000 (95% UI)			Prevalent cases No *10^3 (95% UI)			ASPR/100,000 (95% UI)		
	Male	Female	Both	Male	Female	Both	Male	Female	Both	Male	Female	Both
Eastern Sub-Saharan Africa	0.56 (0.44~0.71)	0.2 (0.15~0.27)	0.76 (0.59~0.96)	1.29 (1.02~1.61)	0.56 (0.43~0.73)	0.93 (0.73~1.15)	2.03 (1.55~2.57)	0.57 (0.43~0.76)	2.6 (2~3.27)	2.15 (1.69~2.68)	0.7 (0.53~0.91)	1.4 (1.1~1.74)
High-income Asia Pacific	195.57 (159.86~238.65)	273.98 (222.49~332.08)	469.56 (383.48~566.44)	216.47 (177.61~261.2)	241.28 (196.5~291.56)	233.42 (191.41~280.25)	709.94 (604.2~831.52)	1005.76 (841.19~1215.47)	1715.7 (1450.88~2042.13)	401.97 (341.36~468.6)	402.2 (338.33~481.05)	408.4 (348.93~479.89)
High-income North America	352.7 (287.81~429.14)	334.97 (268.61~413.09)	687.66 (557.97~840.92)	233.74 (190.72~283.24)	158.45 (128.41~193.96)	191.35 (155.87~232.93)	807.35 (704.42~936.66)	685.54 (595.4~793.05)	1492.89 (1305.2~1727.5)	295.58 (258.9~338.66)	200.55 (175.67~230.07)	244.39 (214.46~279.6)
North Africa and Middle East	8.31 (6.49~10.17)	1.38 (1.03~1.79)	9.7 (7.64~11.9)	8.19 (6.48~10.01)	1.51 (1.15~1.96)	4.92 (3.9~6.04)	42.78 (33.73~52.9)	11.52 (8.98~14.41)	54.3 (43.23~66.78)	16.12 (12.82~19.87)	5.15 (4.08~6.4)	10.83 (8.67~13.35)
Oceania	0.09 (0.07~0.11)	0.02 (0.02~0.03)	0.11 (0.09~0.14)	6.54 (5.25~8.28)	1.99 (1.6~2.5)	4.3 (3.49~5.36)	0.68 (0.54~0.83)	0.45 (0.36~0.56)	1.13 (0.9~1.37)	21.01 (17.04~25.69)	16.03 (12.75~19.73)	18.61 (14.95~22.75)
South Asia	6.93 (5.36~8.8)	1.4 (0.99~1.95)	8.33 (6.4~10.64)	2.07 (1.63~2.6)	0.53 (0.39~0.71)	1.34 (1.04~1.67)	23.36 (18.46~29.12)	6.83 (5.06~9.18)	30.19 (23.68~37.63)	3.1 (2.46~3.85)	0.96 (0.72~1.28)	2.03 (1.6~2.52)
Southeast Asia	1.08 (0.8~1.41)	0.71 (0.51~0.96)	1.78 (1.34~2.36)	0.86 (0.65~1.12)	0.55 (0.4~0.72)	0.7 (0.53~0.91)	13.23 (10.27~16.94)	10.75 (8.36~13.78)	23.99 (18.74~30.27)	4.73 (3.76~5.95)	3.43 (2.7~4.37)	4.06 (3.21~5.09)
Southern Latin America	2.62 (2.1~3.23)	2.87 (2.24~3.84)	5.5 (4.39~6.94)	12.4 (9.98~15.27)	11.14 (8.73~14.92)	11.87 (9.53~14.91)	59.7 (50.59~71.86)	42.19 (35.18~50.8)	101.89 (87.12~120.8)	163.8 (139.01~196.84)	89.01 (74.38~106.77)	122.72 (104.78~145.67)
Southern Sub-Saharan Africa	2.18 (1.69~2.73)	0.18 (0.14~0.23)	2.37 (1.84~2.94)	17.15 (13.32~21.26)	1.17 (0.91~1.5)	8.15 (6.36~10.13)	57.02 (43.85~72.95)	0.39 (0.3~0.51)	57.41 (44.28~73.39)	221.92 (171.05~280.83)	1.23 (0.95~1.58)	94.86 (72.97~120.7)
Tropical Latin America	5.29 (4.23~6.47)	2.74 (2.18~3.4)	8.03 (6.43~9.81)	10.75 (8.57~13.09)	5.13 (4.09~6.33)	7.79 (6.23~9.54)	39.09 (31.08~48.19)	19.51 (15.59~24.04)	58.6 (47.23~72.05)	34.55 (27.66~42.42)	14.62 (11.68~17.97)	23.73 (19.16~29.01)
Western Europe	110.62 (88.68~135.53)	107.59 (86.28~133.7)	218.21 (177.74~268.12)	45.56 (36.74~55.61)	30.99 (25~38.25)	37.65 (30.75~45.97)	816.75 (693.15~958.79)	1046.03 (883.03~1250.05)	1862.79 (1577.56~2209.09)	204.08 (172.96~239.05)	203.21 (170.91~241.76)	204.84 (174.62~240.59)
Western Sub-Saharan Africa	1.04 (0.79~1.33)	0.26 (0.19~0.35)	1.3 (1~1.63)	1.82 (1.4~2.31)	0.61 (0.45~0.83)	1.27 (0.99~1.58)	3.06 (2.35~3.91)	0.81 (0.6~1.09)	3.87 (3~4.88)	2.53 (1.95~3.21)	0.84 (0.63~1.12)	1.65 (1.3~2.04)

CAVD, calcific aortic valve disease; ASPR, the age-standardized prevalence rate; SDI, socio-demographic index.

10.3389/fcvm.2022.1003233

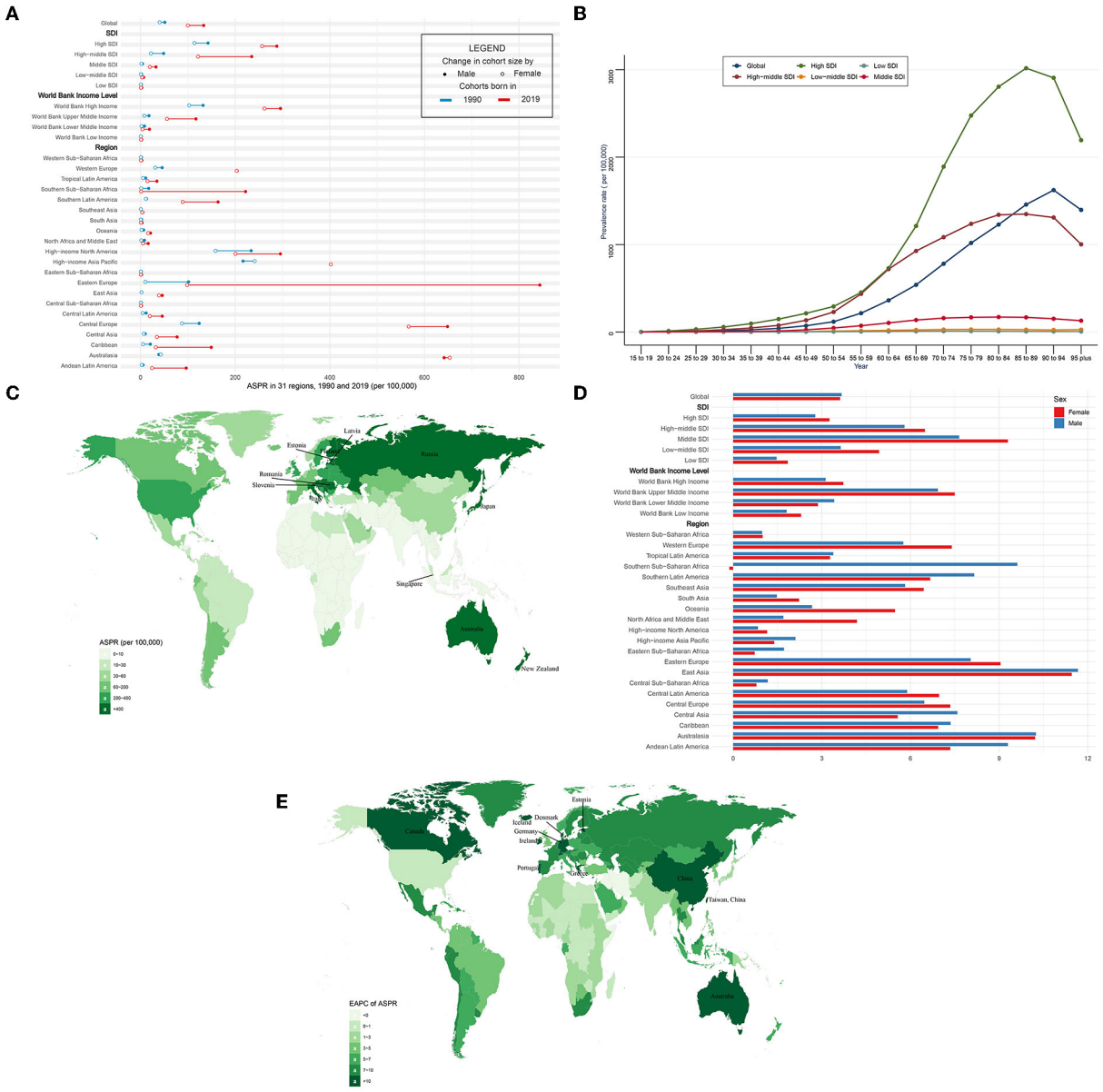

FIGURE 2
ASPR and its trend of CAVD. **(A)** ASPR in 31 regions from 1990 to 2019. **(B)** Prevalence rate stratified by age in the globe and 5 SDI regions in 2019. **(C)** ASPR in 204 countries and territories in 2019. **(D)** EAPC of ASPR in 31 regions from 1990 to 2019. **(E)** EAPC of ASPR in 204 countries and territories from 1990 to 2019. CAVD, calcific aortic valve disease; ASPR, the age-standardized prevalence rate; SDI, socio-demographic index; EAPC, estimated annual percentage change.

0.89∼1.45) (Table 5). Similar results were found at the WBI level. Subgroup analysis by geographical regions showed that western Europe and high-income north America were the top two regions with the highest ASDR (western Europe: 3.59 per 100,000 in 1990 and 4.05 in 2019; high-income north America: 3.56 per 100,000 in 1990 and 3.64 in 2019). Central Europe had the fastest rise in ASDR (EAPC = 4.85, 95% CI 4.43∼5.27), whereas North Africa and the middle east (EAPC = −0.65, 95% CI −0.7∼−0.61) and east Asia (EAPC = −0.54, 95% CI −0.86∼−0.21) showed the fastest decrease in ASDR. Among 204 countries and territories, the highest ASDR was in Cyprus (10.21 per 100,000) in 1990, followed by Norway (5.55 per 100,000) and Bermuda (5.29 per 100,000) (Figure 3C; Supplementary Table 1). Meanwhile, the hugest annual increase of ASDR during the past 30 years was in Poland (EAPC = 9.44, 95% CI 8.09∼10.8), followed by Czechia (EAPC = 8.72, 95% CI 7.78∼9.68) and Estonia (EAPC = 8.6, 95% CI 7.35∼9.87), while the largest annual decrease of ASDR was in Qatar (EAPC

TABLE 3 The death of CAVD in 1990/2019.

	1990						2019					
	Death cases No*10^3 (95% UI)			ASDR/100,000 (95% UI)			Death cases No *10^3 (95% UI)			ASDR/100,000 (95% UI)		
	Male	Female	Both	Male	Female	Both	Male	Female	Both	Male	Female	Both
Global	24.52 (22.44~27.03)	28.78 (24.82~34.07)	53.3 (47.76~59.73)	1.86 (1.69~2.04)	1.62 (1.39~1.91)	1.75 (1.55~1.96)	54.17 (47.77~58.67)	72.65 (57.76~84.3)	126.83 (105.6~141.39)	1.85 (1.58~2.01)	1.66 (1.32~1.92)	1.76 (1.45~1.97)
SDI level												
High SDI	15.18 (14.09~16.49)	20.84 (17.97~24.02)	36.02 (32.13~39.86)	3.97 (3.65~4.31)	3.06 (2.63~3.54)	3.46 (3.06~3.84)	31.77 (27.2~34.65)	48.45 (37.05~56.49)	80.21 (64.3~90.1)	3.62 (3.11~3.96)	3.1 (2.45~3.59)	3.35 (2.75~3.74)
High-middle SDI	4.07 (3.66~4.44)	4.29 (3.58~5.08)	8.36 (7.42~9.21)	1.08 (0.95~1.2)	0.81 (0.67~0.95)	0.93 (0.81~1.04)	10.12 (9.02~11.1)	14.31 (11.66~16.41)	24.44 (20.86~27.26)	1.36 (1.18~1.49)	1.19 (0.97~1.37)	1.28 (1.08~1.43)
Middle SDI	2.44 (2.07~2.86)	1.83 (1.34~2.49)	4.27 (3.5~5.17)	0.54 (0.46~0.63)	0.4 (0.3~0.53)	0.47 (0.39~0.57)	5.73 (5.11~6.56)	4.75 (4.03~5.46)	10.48 (9.43~11.74)	0.55 (0.49~0.63)	0.41 (0.35~0.47)	0.48 (0.43~0.53)
Low-middle SDI	1.89 (1.32~2.68)	1.23 (0.65~2.25)	3.12 (2.1~4.2)	0.75 (0.53~1.04)	0.55 (0.3~0.93)	0.65 (0.44~0.85)	4.53 (3.69~5.76)	3.63 (2.61~4.99)	8.17 (6.63~9.99)	0.8 (0.64~1)	0.6 (0.43~0.8)	0.7 (0.57~0.84)
Low SDI	0.93 (0.56~1.4)	0.58 (0.27~1.19)	1.5 (0.88~2.2)	0.87 (0.57~1.27)	0.66 (0.33~1.25)	0.77 (0.47~1.09)	1.99 (1.48~2.64)	1.48 (0.99~2.27)	3.46 (2.56~4.39)	0.88 (0.65~1.14)	0.71 (0.48~1.02)	0.8 (0.61~0.99)
World Bank Income Level												
World Bank High Income	17.17 (15.95~18.55)	23.15 (19.88~26.73)	40.33 (36.18~44.65)	3.63 (3.34~3.93)	2.82 (2.42~3.27)	3.19 (2.84~3.53)	37.59 (32.4~40.92)	57.87 (44.87~67.4)	95.46 (76.94~107.1)	3.58 (3.09~3.9)	3.08 (2.43~3.58)	3.33 (2.73~3.7)
World Bank Upper Middle Income	3.82 (3.39~4.3)	3.17 (2.63~3.84)	6.99 (6.13~7.92)	0.63 (0.56~0.7)	0.47 (0.39~0.55)	0.55 (0.48~0.62)	8.27 (7.44~9.26)	8.04 (6.95~9.14)	16.31 (14.61~18.15)	0.61 (0.54~0.68)	0.47 (0.41~0.54)	0.54 (0.48~0.6)
World Bank Lower Middle Income	2.93 (2.04~4.14)	2.05 (1.06~3.65)	4.98 (3.31~6.73)	0.67 (0.48~0.93)	0.49 (0.26~0.83)	0.58 (0.39~0.77)	7.1 (5.67~8.94)	5.83 (4.22~7.7)	12.92 (10.65~15.75)	0.72 (0.57~0.91)	0.57 (0.41~0.74)	0.65 (0.53~0.78)
World Bank Low Income	0.58 (0.37~0.87)	0.39 (0.22~0.77)	0.97 (0.62~1.41)	0.89 (0.6~1.29)	0.64 (0.38~1.16)	0.77 (0.51~1.09)	1.19 (0.88~1.6)	0.87 (0.61~1.32)	2.06 (1.57~2.71)	0.9 (0.66~1.19)	0.64 (0.46~0.91)	0.77 (0.6~0.97)
Region												
Andean Latin America	0.07 (0.05~0.09)	0.05 (0.03~0.07)	0.12 (0.09~0.15)	0.68 (0.52~0.87)	0.49 (0.33~0.64)	0.58 (0.45~0.71)	0.17 (0.13~0.21)	0.12 (0.1~0.15)	0.29 (0.24~0.35)	0.64 (0.5~0.81)	0.41 (0.33~0.52)	0.53 (0.43~0.64)
Australasia	0.38 (0.34~0.41)	0.39 (0.33~0.46)	0.77 (0.69~0.85)	4.32 (3.89~4.68)	2.87 (2.41~3.35)	3.48 (3.07~3.85)	0.9 (0.77~1.02)	0.96 (0.74~1.14)	1.87 (1.51~2.11)	3.82 (3.24~4.3)	2.68 (2.1~3.17)	3.18 (2.62~3.58)
Caribbean	0.17 (0.14~0.19)	0.09 (0.07~0.11)	0.25 (0.22~0.28)	1.37 (1.2~1.54)	0.67 (0.54~0.8)	1 (0.87~1.12)	0.31 (0.26~0.37)	0.2 (0.16~0.27)	0.52 (0.42~0.63)	1.32 (1.08~1.58)	0.72 (0.57~0.95)	1 (0.82~1.22)
Central Asia	0.04 (0.03~0.04)	0.03 (0.02~0.03)	0.06 (0.05~0.07)	0.21 (0.17~0.25)	0.09 (0.07~0.11)	0.14 (0.11~0.16)	0.11 (0.09~0.15)	0.09 (0.08~0.13)	0.21 (0.17~0.26)	0.41 (0.35~0.52)	0.27 (0.22~0.37)	0.33 (0.27~0.43)
Central Europe	0.51 (0.43~0.64)	0.4 (0.29~0.52)	0.9 (0.75~1.11)	0.89 (0.76~1.15)	0.49 (0.35~0.64)	0.66 (0.54~0.81)	2.01 (1.56~2.36)	2.66 (2.05~3.28)	4.68 (3.77~5.58)	2.35 (1.81~2.76)	1.83 (1.41~2.26)	2.08 (1.68~2.49)
Central Latin America	0.41 (0.37~0.44)	0.25 (0.21~0.31)	0.66 (0.6~0.73)	1 (0.9~1.1)	0.62 (0.51~0.75)	0.81 (0.74~0.9)	1.09 (0.87~1.35)	0.87 (0.7~1.14)	1.96 (1.61~2.43)	1.02 (0.82~1.27)	0.7 (0.56~0.92)	0.85 (0.7~1.06)
Central Sub-Saharan Africa	0.1 (0.06~0.18)	0.07 (0.04~0.14)	0.17 (0.1~0.26)	1.11 (0.74~1.86)	0.85 (0.48~1.56)	0.97 (0.63~1.42)	0.22 (0.15~0.35)	0.19 (0.13~0.29)	0.41 (0.29~0.58)	1.17 (0.85~1.72)	0.86 (0.58~1.29)	1.01 (0.74~1.36)
East Asia	0.95 (0.65~1.27)	0.62 (0.33~1.05)	1.57 (1.02~2.22)	0.23 (0.17~0.31)	0.15 (0.08~0.25)	0.19 (0.12~0.27)	1.95 (1.53~2.5)	1.28 (0.96~1.6)	3.23 (2.62~3.85)	0.24 (0.19~0.29)	0.13 (0.1~0.16)	0.17 (0.14~0.2)
Eastern Europe	0.28 (0.22~0.32)	0.28 (0.2~0.33)	0.56 (0.44~0.63)	0.33 (0.27~0.37)	0.16 (0.11~0.19)	0.21 (0.17~0.24)	0.75 (0.6~0.9)	0.89 (0.72~1.09)	1.64 (1.37~1.93)	0.61 (0.49~0.72)	0.38 (0.31~0.47)	0.48 (0.4~0.57)
Eastern Sub-Saharan Africa	0.33 (0.21~0.48)	0.24 (0.14~0.47)	0.57 (0.38~0.85)	1.01 (0.69~1.38)	0.85 (0.53~1.48)	0.94 (0.66~1.34)	0.66 (0.5~0.91)	0.53 (0.38~0.75)	1.2 (0.95~1.53)	1 (0.71~1.42)	0.83 (0.58~1.15)	0.92 (0.72~1.21)

(Continued)

10.3389/fcvm.2022.1003233

TABLE 3 (Continued)

	1990						2019					
	Death cases No*10^3 (95% UI)			ASDR/100,000 (95% UI)			Death cases No *10^3 (95% UI)			ASDR/100,000 (95% UI)		
	Male	Female	Both	Male	Female	Both	Male	Female	Both	Male	Female	Both
High-income Asia Pacific	1.79 (1.62∼2.03)	2.49 (2.02∼3.12)	4.28 (3.66∼5.07)	2.73 (2.44∼3.12)	2.41 (1.94∼3.02)	2.57 (2.15∼3.06)	4.01 (3.11∼4.61)	9.56 (6.01∼11.97)	13.57 (9.08∼16.51)	1.8 (1.4∼2.06)	2 (1.32∼2.45)	1.98 (1.4∼2.36)
High-income North America	5.88 (5.41∼6.33)	7.28 (6.13∼8.22)	13.16 (11.62∼14.39)	4.31 (3.96∼4.63)	3.01 (2.54∼3.4)	3.56 (3.14∼3.89)	11.57 (9.95∼12.98)	15.62 (12.29∼17.91)	27.19 (22.16∼30.24)	4.1 (3.53∼4.59)	3.3 (2.67∼3.77)	3.64 (3.02∼4.02)
North Africa and Middle East	0.9 (0.65∼1.2)	0.83 (0.51∼1.18)	1.73 (1.26∼2.18)	1.09 (0.79∼1.44)	1.14 (0.69∼1.59)	1.13 (0.82∼1.45)	2.01 (1.56∼2.41)	1.81 (1.4∼2.18)	3.82 (3.19∼4.44)	0.96 (0.75∼1.14)	0.97 (0.74∼1.17)	0.97 (0.81∼1.12)
Oceania	0.013 (0.008∼0.02)	0.005 (0.003∼0.009)	0.02 (0.01∼0.03)	1.17 (0.76∼1.77)	0.43 (0.24∼0.75)	0.79 (0.52∼1.12)	0.03 (0.02∼0.04)	0.012 (0.007∼0.02)	0.04 (0.03∼0.06)	1.07 (0.76∼1.54)	0.46 (0.3∼0.74)	0.75 (0.54∼1.04)
South Asia	1.87 (1.2∼2.87)	1.19 (0.48∼2.41)	3.06 (1.85∼4.37)	0.81 (0.53∼1.22)	0.68 (0.29∼1.24)	0.75 (0.47∼1.03)	4.73 (3.62∼6.47)	4.02 (2.65∼5.67)	8.75 (6.85∼11.05)	0.82 (0.62∼1.09)	0.7 (0.46∼0.96)	0.76 (0.6∼0.95)
Southeast Asia	0.37 (0.29∼0.53)	0.29 (0.21∼0.39)	0.66 (0.54∼0.86)	0.35 (0.27∼0.51)	0.25 (0.18∼0.33)	0.3 (0.24∼0.38)	0.93 (0.71∼1.31)	0.78 (0.6∼0.93)	1.7 (1.4∼2.13)	0.39 (0.3∼0.54)	0.28 (0.21∼0.33)	0.33 (0.27∼0.41)
Southern Latin America	0.59 (0.52∼0.67)	0.8 (0.68∼0.92)	1.39 (1.22∼1.56)	3.27 (2.9∼3.71)	3.39 (2.86∼3.91)	3.43 (3.01∼3.85)	1.15 (1.03∼1.26)	1.69 (1.41∼1.95)	2.84 (2.46∼3.16)	3.37 (2.99∼3.7)	3.13 (2.65∼3.59)	3.3 (2.85∼3.66)
Southern Sub-Saharan Africa	0.11 (0.09∼0.13)	0.11 (0.09∼0.14)	0.22 (0.19∼0.25)	0.98 (0.82∼1.18)	0.82 (0.68∼0.98)	0.9 (0.78∼1.04)	0.21 (0.18∼0.24)	0.22 (0.18∼0.25)	0.43 (0.37∼0.48)	1.18 (0.95∼1.34)	0.8 (0.66∼0.92)	0.96 (0.82∼1.07)
Tropical Latin America	0.89 (0.79∼0.95)	0.65 (0.52∼0.75)	1.53 (1.35∼1.66)	2.09 (1.86∼2.24)	1.53 (1.24∼1.72)	1.81 (1.59∼1.95)	1.76 (1.55∼1.98)	1.82 (1.52∼2.23)	3.58 (3.11∼4.14)	1.75 (1.53∼1.97)	1.38 (1.15∼1.69)	1.56 (1.34∼1.8)
Western Europe	8.56 (7.94∼9.24)	12.54 (10.81∼14.54)	21.1 (18.96∼23.33)	3.99 (3.67∼4.29)	3.21 (2.77∼3.72)	3.59 (3.21∼3.97)	18.95 (16.57∼20.69)	28.94 (22.91∼33.63)	47.89 (39.52∼53.66)	4.34 (3.79∼4.73)	3.75 (3.04∼4.32)	4.05 (3.4∼4.51)
Western Sub-Saharan Africa	0.34 (0.17∼0.54)	0.18 (0.08∼0.39)	0.51 (0.27∼0.81)	0.68 (0.35∼1.09)	0.47 (0.23∼0.99)	0.6 (0.33∼0.95)	0.64 (0.44∼0.92)	0.38 (0.24∼0.65)	1.02 (0.71∼1.42)	0.63 (0.44∼0.9)	0.48 (0.31∼0.76)	0.55 (0.39∼0.76)

CAVD, calcific aortic valve disease; ASDR, the age-standardized death rate; SDI, socio-demographic index.

10.3389/fcvm.2022.1003233

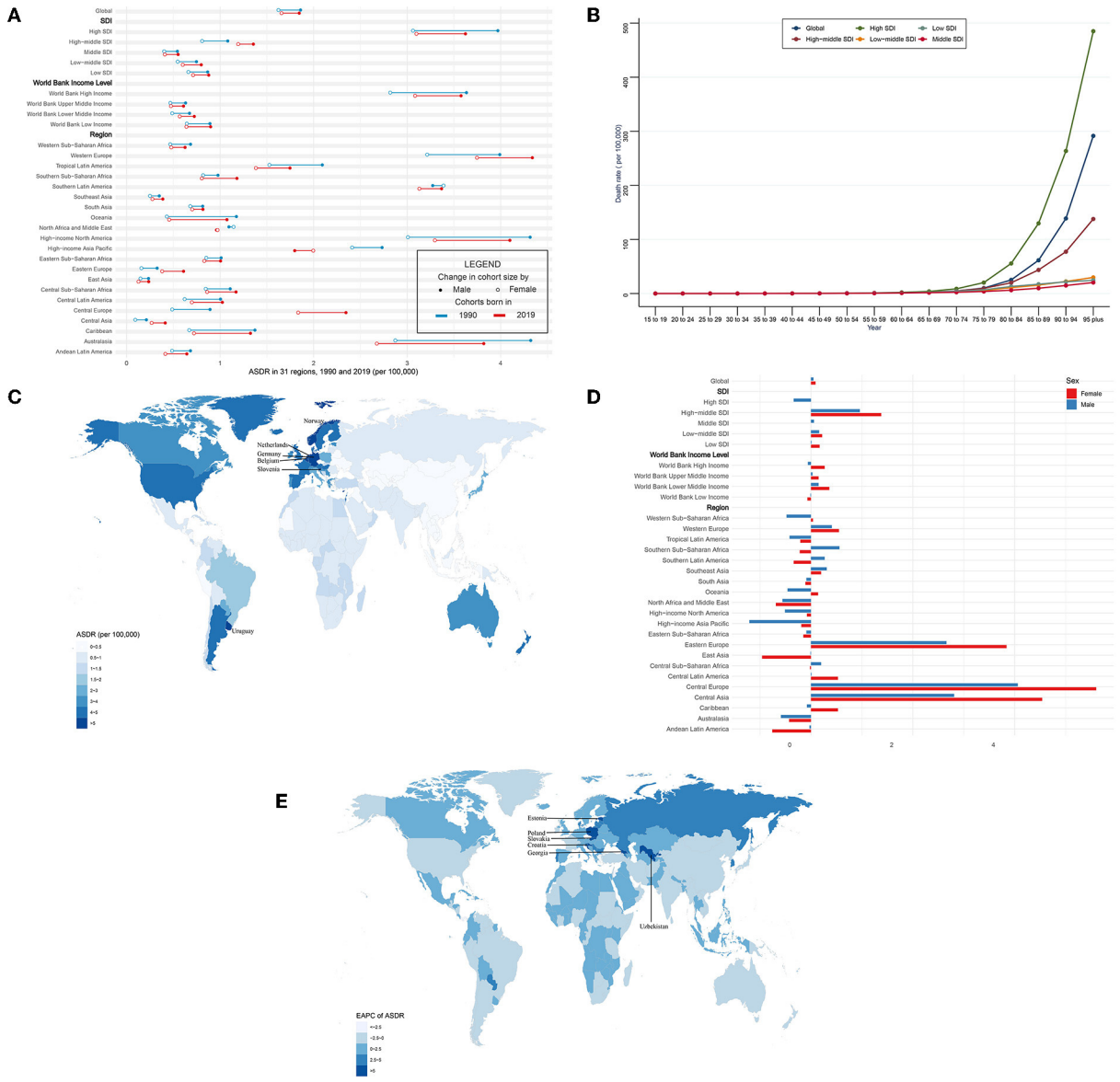

FIGURE 3
ASDR and its trend of CAVD. **(A)** ASDR in 31 regions from 1990 to 2019. **(B)** Death rate stratified by age in the globe and 5 SDI regions in 2019. **(C)** ASDR in 204 countries and territories in 2019. **(D)** EAPC of ASDR in 31 regions from 1990 to 2019. **(E)** EAPC of ASDR in 204 countries and territories from 1990 to 2019. CAVD, calcific aortic valve disease; ASDR, the age-standardized death rate; SDI, socio-demographic index; EAPC, estimated annual percentage change.

= −3.24, 95% CI −3.6∼−2.88), followed by Syrian (EAPC = −3.01, 95% CI −3.53∼−2.49) and Panama (EAPC = −2.99, 95% CI −3.44∼−2.53) (Figure 3E; Supplementary Table 2). It was indicated that the ASDR of CAVD was positively related to age, especially for those aged 80 years and over. And the fastest elevation of the ASDR was found among elderly patients in high SDI regions (Figure 3B).

Globally, CAVD-related death cases in female individuals were higher than those in male individuals (1990: 24,517 female and 28,780 male; 2019: 72,652 female and 54,175 male) (Table 3). But ASDR of CAVD in male individuals was higher than that in female individuals (1990: 1.86 per 100,000 in male and 1.62 in female individuals; 2019: 1.85 per 100,000 in male and 1.66 in female individuals) (Figure 3A, Table 3). And both sexes shared a quite low EAPC (0.05, 95% CI −0.06∼0.16 in male and 0.09, 95% CI −0.03∼0.21 in female individuals) (Figure 3D; Table 5). Subgroup analysis revealed that except for north Africa and the Middle East, high-income Asia Pacific in 2019, and southern Latin America in 1990, the CAVD-related death cases in female individuals were higher than those in male individuals (Table 3).

10.3389/fcvm.2022.1003233

TABLE 4 The DALYs of CAVD in 1990/2019.

	1990						2019					
	DALYs No *10^3 (95% UI)			ASDALYR/100,000 (95% UI)			DALYs No *10^3 (95% UI)			ASDALYR/100,000 (95% UI)		
	Male	Female	Both	Male	Female	Both	Male	Female	Both	Male	Female	Both
Global	533.66 (481.12~594.23)	442.23 (381.94~551.81)	975.89 (872.01~1109.79)	31.47 (28.7~34.63)	22.3 (19.27~27.31)	26.85 (24.07~30.31)	944.03 (864.57~1036.41)	893.72 (765.94~1032.79)	1837.75 (1637.02~2031.85)	27.4 (24.8~29.99)	20.48 (17.55~23.69)	23.9 (21.1~26.55)
SDI level												
High SDI	277.94 (259.85~300.65)	275.81 (241.47~320.12)	553.75 (508.56~609.84)	65.8 (61.39~71.14)	42.02 (36.76~48.87)	52.88 (48.59~58.27)	422.51 (380.72~457.52)	491.17 (404.32~565.07)	913.67 (778.95~1005.2)	49.45 (44.6~53.46)	36.76 (31.09~42.28)	42.88 (37.5~47)
High-middle SDI	101.8 (92.76~111.78)	76.25 (66.02~91.74)	178.05 (162.77~197.28)	21.96 (19.86~24.05)	13.14 (11.29~15.78)	17.25 (15.73~19.19)	200.7 (180.53~223.1)	194.95 (167.8~222.29)	395.65 (353.62~437.85)	23.75 (21.32~26.45)	16.88 (14.62~19.27)	20.21 (18.01~22.35)
Middle SDI	74.12 (62.61~87.44)	46.88 (34.06~66.91)	121 (98.91~146.12)	12.72 (10.78~14.89)	8.22 (6.01~11.42)	10.48 (8.62~12.68)	149.62 (132.77~171.97)	101.4 (86.96~116.54)	251.02 (227.01~281.66)	12.42 (11.02~14.3)	8.04 (6.87~9.23)	10.18 (9.21~11.4)
Low-middle SDI	52.18 (36.04~75.29)	28.92 (14.86~56.59)	81.11 (53.2~111.59)	15.98 (11.17~22.67)	9.84 (5.21~18.19)	12.97 (8.69~17.57)	113.93 (92.96~146.18)	73.3 (51.99~107.11)	187.23 (149.87~235.31)	16.69 (13.6~21.29)	10.54 (7.53~15.03)	13.56 (10.9~16.84)
Low SDI	27.27 (15.59~42.73)	14.12 (6.18~32.92)	41.39 (22.47~63.11)	20 (12.09~30.45)	12.05 (5.6~25.45)	16.14 (9.28~23.73)	56.66 (40.56~77.62)	32.42 (20.55~55.33)	89.08 (62.68~119.76)	19.28 (14.27~25.77)	12.27 (8.1~19.55)	15.8 (11.57~20.29)
World Bank Income Level												
World Bank High Income	321.94 (300.93~348.49)	312.1 (272.9~363.22)	634.04 (584.52~700.54)	61.79 (57.39~66.93)	39.16 (34.27~45.77)	49.58 (45.5~54.71)	511.77 (459.64~554.33)	598.84 (492.83~690.63)	1110.61 (949.42~1219.26)	50.31 (45.51~54.47)	37.37 (31.43~42.91)	43.65 (38.18~47.78)
World Bank Upper Middle Income	111.22 (97.79~125.66)	71.46 (58.47~92.05)	182.67 (159.1~211.25)	14.33 (12.7~16.1)	8.81 (7.28~11.08)	11.51 (10.08~13.17)	211.57 (190.72~237.53)	153.65 (135.97~174.46)	365.22 (333.42~407.17)	13.88 (12.46~15.56)	8.92 (7.89~10.11)	11.33 (10.34~12.61)
World Bank Lower Middle Income	82.7 (56.72~117.64)	48.72 (24.81~92.65)	131.42 (85.63~180.64)	14.76 (10.3~20.8)	9.17 (4.77~16.57)	11.99 (7.97~16.19)	184.94 (148.61~233.15)	121.24 (86.94~170.48)	306.18 (249.81~378.62)	15.43 (12.38~19.42)	10.11 (7.31~13.89)	12.74 (10.46~15.58)
World Bank Low Income	17.46 (10.32~26.88)	9.71 (4.89~22.31)	27.17 (15.88~41.61)	21.07 (13.23~31.79)	12.17 (6.65~24.55)	16.53 (10.36~24.3)	35.13 (24.73~48.74)	19.49 (12.91~33.59)	54.63 (38.98~75.56)	20.03 (14.65~27.02)	11.3 (7.79~17.93)	15.53 (11.55~20.75)
Region												
Andean Latin America	1.99 (1.52~2.61)	1.31 (0.85~1.86)	3.3 (2.47~4.28)	16.82 (12.88~22)	10.64 (6.98~14.46)	13.67 (10.36~17.42)	4.58 (3.59~5.73)	2.68 (2.12~3.37)	7.26 (5.88~8.87)	16.26 (12.83~20.32)	9.01 (7.13~11.27)	12.54 (10.21~15.28)
Australasia	6.84 (6.24~7.41)	5.31 (4.57~6.24)	12.15 (11.12~13.48)	68.98 (63.01~74.92)	38.66 (33.28~45.57)	52.52 (47.85~58.16)	12.6 (10.89~14.14)	11.37 (9.24~13.43)	23.97 (20.44~27.5)	54.42 (47.2~60.87)	35.92 (29.82~42.63)	44.54 (38.48~51.02)
Caribbean	4.36 (3.74~4.97)	1.95 (1.54~2.63)	6.31 (5.37~7.23)	32.07 (27.67~36.46)	13.73 (10.94~17.91)	22.61 (19.31~25.69)	7.35 (6.04~8.85)	3.98 (3.07~5.61)	11.32 (9.16~14.16)	30.35 (24.97~36.51)	14.62 (11.25~20.85)	22.09 (17.87~27.65)
Central Asia	1.11 (0.95~1.26)	0.64 (0.49~0.75)	1.76 (1.48~1.96)	5.2 (4.34~6.01)	2.23 (1.71~2.63)	3.48 (2.89~3.92)	3.41 (2.81~4.36)	2.13 (1.76~2.78)	5.54 (4.67~6.97)	9.99 (8.34~12.66)	5.37 (4.44~7.1)	7.45 (6.27~9.38)
Central Europe	12.88 (11.26~15.63)	8.12 (6.26~10.31)	20.99 (18.13~25.38)	20.47 (17.81~25.23)	9.77 (7.55~12.31)	14.59 (12.57~17.61)	41.63 (33.6~49.21)	42.47 (34.06~52)	84.11 (69.74~99.02)	47.43 (38.03~55.99)	31.61 (25.3~38.91)	39.15 (32.37~46.15)
Central Latin America	11.78 (10.63~12.65)	6.35 (5.18~7.77)	18.12 (16.45~20.01)	24.89 (22.56~26.86)	13.17 (10.89~15.99)	18.85 (17.19~20.94)	26.8 (21.59~33.45)	18.07 (14.49~23.94)	44.87 (36.84~55.56)	23.85 (19.28~29.74)	14.18 (11.37~18.77)	18.72 (15.4~23.13)
Central Sub-Saharan Africa	2.88 (1.57~5.32)	1.71 (0.86~3.97)	4.59 (2.59~7.53)	24.16 (14.68~42.41)	15.1 (8.1~31.22)	19.38 (11.77~30.04)	6.48 (4.05~10.65)	3.94 (2.6~6.74)	10.43 (6.84~15.6)	23.99 (16.3~36.81)	14.48 (9.81~23.15)	18.97 (13.23~26.91)
East Asia	29.92 (20.38~40.45)	17.06 (8.83~29.8)	46.99 (30.3~66.13)	5.94 (4.11~7.94)	3.5 (1.84~5.96)	4.71 (3.06~6.62)	55.07 (43.26~69.63)	31.74 (24.43~39.46)	86.82 (70.96~103.74)	5.76 (4.6~7.16)	3.07 (2.37~3.81)	4.36 (3.59~5.18)
Eastern Europe	8.32 (6.45~9.83)	5.9 (4.1~6.84)	14.22 (11.03~16.35)	8.42 (6.65~9.85)	3.4 (2.38~3.93)	5.25 (4.11~6.02)	29.01 (22.55~36.68)	17.11 (13.93~20.94)	46.12 (37.77~56.57)	23.15 (18.19~29.31)	8.09 (6.53~10.19)	14.17 (11.57~17.34)
Eastern Sub-Saharan Africa	9.82 (5.65~14.4)	5.86 (2.87~13.31)	15.69 (9.22~24.32)	22.59 (14.14~32.65)	15.05 (8.55~29.51)	18.86 (12.21~27.88)	18.82 (13.75~26.02)	11.15 (7.88~16.49)	29.97 (22.89~39.84)	20.54 (15.45~28.31)	13.36 (9.6~18.69)	16.91 (13.45~21.67)
High-income Asia Pacific	34.26 (31.85~38.06)	36.64 (31.16~45.45)	70.9 (63.43~81.93)	43.56 (39.89~48.49)	33.23 (28.12~41.23)	38.17 (33.96~44.37)	51.49 (43.83~58.02)	90.64 (64.56~109.85)	142.13 (109.6~165.94)	24.61 (21.03~27.68)	23.21 (17.78~27.46)	24.46 (19.89~28.22)
High-income North America	109.06 (102.39~116.75)	97.65 (84.74~110.92)	206.71 (189.98~224.97)	75.13 (70.26~80.38)	43.77 (38.39~49.86)	57.8 (53.37~62.81)	153.24 (137.21~166.81)	161.57 (134.8~183.81)	314.81 (274.62~346.35)	55.42 (49.7~60.13)	39.54 (33.4~45.19)	46.8 (41.53~51.25)

(Continued)

TABLE 4 (Continued)

	1990						2019					
	DALYs No *10^3 (95% UI)			ASDALYR/100,000 (95% UI)			DALYs No *10^3 (95% UI)			ASDALYR/100,000 (95% UI)		
	Male	Female	Both	Male	Female	Both	Male	Female	Both	Male	Female	Both
North Africa and Middle East	27.76 (20.25~37.09)	21.31 (13.35~32.5)	49.07 (36.29~61.47)	26.42 (19.41~35.22)	22.82 (14.04~33.61)	24.77 (18.02~31.02)	57.57 (43.05~70.16)	43.4 (34.34~54.03)	100.97 (84.2~119.65)	22.65 (17.4~27.32)	19.39 (15.36~23.64)	21.11 (17.59~24.72)
Oceania	0.41 (0.24~0.66)	0.14 (0.07~0.26)	0.54 (0.32~0.83)	22.99 (14.19~35.82)	8.29 (4.5~15.33)	15.64 (9.68~23.28)	0.92 (0.58~1.41)	0.35 (0.2~0.66)	1.27 (0.82~1.89)	22.02 (14.92~32.32)	9.08 (5.62~15.57)	15.58 (10.6~22.16)
South Asia	49.83 (30.99~78.1)	27.03 (10.29~59.44)	76.87 (44.62~111.6)	16.29 (10.43~25.03)	11.16 (4.47~22.5)	13.86 (8.35~19.67)	113.43 (85.7~161.11)	77.25 (48.78~115.63)	190.68 (144.06~248.6)	16.14 (12.32~22.5)	11.46 (7.4~16.6)	13.83 (10.63~17.66)
Southeast Asia	10.26 (8.05~14.83)	6.87 (4.97~9.84)	17.13 (14.08~23.37)	7.69 (6~11.16)	4.88 (3.57~6.67)	6.22 (5.14~8.24)	23.66 (18.26~34.39)	15.72 (12.12~18.98)	39.38 (32.23~50.17)	8.15 (6.31~11.67)	4.98 (3.86~5.97)	6.49 (5.36~8.18)
Southern Latin America	12.45 (11.1~14.1)	11.78 (9.98~13.52)	24.23 (21.71~27.03)	61.64 (55~69.69)	47.18 (40.21~53.84)	54.79 (48.95~61.1)	21.01 (19.06~22.94)	21.47 (18.69~24.43)	42.48 (38.29~46.44)	58.83 (53.32~64.23)	42.5 (37.24~48.25)	50.54 (45.69~55.27)
Southern Sub-Saharan Africa	3.21 (2.65~3.9)	2.55 (2.07~3.51)	5.76 (4.93~7.02)	21.62 (17.93~25.93)	14.68 (12.27~19.09)	17.96 (15.51~21.18)	5.95 (5~7.19)	3.79 (2.95~4.47)	9.74 (8.36~11.08)	23.98 (20.66~27.89)	12.16 (9.66~14.19)	17.24 (14.86~19.32)
Tropical Latin America	27.32 (24.46~29.6)	15.82 (12.48~19.36)	43.14 (38.39~47.88)	53.01 (47.46~56.75)	30.49 (24.41~36.23)	41.46 (36.63~45.36)	39.18 (35.4~44.29)	31.55 (27.03~39.01)	70.73 (63.57~80.92)	35.73 (32.12~40.23)	23.95 (20.52~29.57)	29.5 (26.5~33.74)
Western Europe	157.76 (146.96~170.87)	164.02 (143.33~191.92)	321.79 (294.95~357.15)	68.54 (63.73~74.1)	43.9 (38.46~51.7)	55.48 (50.82~61.36)	249.71 (224.03~270.26)	294.07 (245.2~337.05)	543.78 (471.46~598.09)	60.12 (54.05~65.02)	44.16 (37.6~50.43)	51.94 (45.69~56.95)
Western Sub-Saharan Africa	11.41 (5.83~18.35)	4.22 (1.76~10.77)	15.63 (8.04~24.98)	20.23 (10.4~32.37)	8.94 (4~21.12)	15.2 (8~23.99)	22.08 (15.16~32)	9.27 (5.4~17.95)	31.35 (21.26~45.26)	18.14 (12.51~26.24)	8.58 (5.37~15.16)	13.17 (9.11~18.49)

CAVD, calcific aortic valve disease; ASDALYR, the age-standardized disability-adjusted life years rate; SDI, socio-demographic index.

The variation tendencies of ASDR in both genders were identical in most regions except western Sub-Saharan Africa, Southern Sub-Saharan Africa, Southern Latin America, Oceania, Central Sub-Saharan Africa, and the Caribbean.

The DALY and its trend

Globally, the DALYs of CAVD increased by 88.3% from 975,894 in 1990 to 1,837,751 in 2019. On the contrary, the age-standardized DALY rate (ASDALYR) gradually declined from 26.8 per 100,000 to 1990 to 23.9 in 2019 (EAPC = −0.45, 95% CI −0.52∼−0.38) (Tables 4, 5). Subgroup analysis by socio-demographic factors showed that the high SDI regions had the highest DALY until 2019 (553,755 in 1990 and 913,672 in 2019), while the ASDALYR had the largest decrease (EAPC = −0.84, 95% CI −1.01∼−0.67) (Tables 4, 5). However, the ASDALYR in high-middle SDI regions had the fastest rise (from 17.3 per 100,000 in 1990 to 20.2 in 2019, EAPC = 0.51, 95% CI 0.36∼0.67). Among WBI levels, the situation was similar. Subgroup analysis by geographical regions demonstrated that high-income North America, Western Europe, and Southern Latin America were the top three regions with the highest ASDALYR (high-income North America: 57.8 per 100,000 in 1990 and 46.8 in 2019; Western Europe: 55.5 in 1990 and 51.9 in 2019; Southern Latin America: 54.8 in 1990 and 50.5 in 2019) (Table 4). Meanwhile, Central Europe had the most rapid increase of ASDALYR (EAPC = 4.02, 95% CI 3.68∼4.36), whereas high-income Asia Pacific showed the largest decline (EAPC = −1.32, 95% CI −1.74∼−0.9) (Table 5). Among 204 countries and territories, the highest ASDALYR was found in Cyprus (131.6 per 100,000) in 1990, followed by Bermuda (111.0 per 100,000), and it was in Cyprus (96.1 per 100,000) in 2019, followed by Slovenia (91.6 per 100,000) (Figure 4C; Supplementary Table 1). In the meantime, Poland showed the most rapid increase in ASDALYR during this period (EAPC = 7.77, 95% CI 6.57∼8.98), followed by Estonia (EAPC = 7.69, 95% CI 6.62∼8.77) (Figure 4E; Supplementary Table 2). In contrast, Syria showed the fastest decrease in ASDALYR (EAPC = −3.15, 95% CI −3.69∼−2.61). Moreover, the ASDALYR of CAVD was closely correlated to age globally and among five SDI regions. In detail, it slightly increased in patients under 75 years, while rapidly growing among patients older than 75 years. And the fastest elevation of the ASDALYR was in high SDI regions (Figure 4B).

Compared with female individuals, male individuals contributed more in ASDALYR until 2019 (male: 31.5 per 100,000 in 1990 and 27.4 in 2019; female: 22.3 per 100,000 in 1990 and 20.5 in 2019) globally (Figure 4A; Table 4). Subgroup analysis by SDI, WBI levels, and geographical regions all showed that male individuals had a higher burden of disability than female individuals. Nevertheless, male individuals showed a more pronounced downward trend than female individuals

TABLE 5 The temporal trends of ASIR, ASPR, ASDR, and ASDALYR from 1990 to 2019 of CAVD.

	EAPC of ASIR No. (95% CI)			EAPC of ASPR No. (95% CI)			EAPC of ASDR No. (95% CI)			EAPC of ASDALYR No. (95% CI)		
	Male	Female	Both	Male	Female	Both	Male	Female	Both	Male	Female	Both
Global	3.04 (2.87∼3.21)	3.06 (2.75∼3.38)	3.03 (2.8∼3.27)	3.67 (3.46∼3.88)	3.62 (3.31∼3.93)	3.65 (3.4∼3.91)	0.05 (−0.06∼0.16)	0.09 (−0.03∼0.21)	0.06 (−0.04∼0.15)	−0.5 (−0.61∼−0.39)	−0.37 (−0.44∼−0.3)	−0.45 (−0.52∼−0.38)
SDI level												
High SDI	2.71 (2.45∼2.98)	3.15 (2.81∼3.49)	2.93 (2.62∼3.23)	2.78 (2.54∼3.01)	3.26 (2.96∼3.57)	3.05 (2.78∼3.32)	−0.34 (−0.53∼−0.16)	0 (−0.1∼0.1)	−0.14 (−0.27∼−0.02)	−1.09 (−1.32∼−0.87)	−0.6 (−0.71∼−0.48)	−0.84 (−1.01∼−0.67)
High–middle SDI	4.94 (4.83∼5.04)	5.31 (4.98∼5.65)	5.1 (4.92∼5.27)	5.8 (5.63∼5.98)	6.49 (6.12∼6.87)	6.11 (5.87∼6.35)	0.96 (0.75∼1.17)	1.38 (1.06∼1.71)	1.17 (0.89∼1.45)	0.29 (0.17∼0.4)	0.79 (0.59∼0.99)	0.51 (0.36∼0.67)
Middle SDI	3.56 (3.14∼3.98)	4.57 (4.11∼5.03)	3.92 (3.5∼4.35)	7.65 (7.36∼7.95)	9.3 (8.95∼9.64)	8.19 (7.9∼8.49)	0.06 (−0.01∼0.13)	0 (−0.08∼0.08)	0.01 (−0.06∼0.08)	−0.12 (−0.19∼−0.04)	−0.2 (−0.28∼−0.11)	−0.17 (−0.24∼−0.1)
Low–middle SDI	0.75 (0.64∼0.87)	1.22 (1.04∼1.4)	0.83 (0.69∼0.97)	3.64 (3.46∼3.82)	4.94 (4.7∼5.18)	3.97 (3.76∼4.17)	0.16 (0.09∼0.24)	0.22 (0.13∼0.31)	0.16 (0.08∼0.24)	0.09 (0.04∼0.15)	0.13 (0.04∼0.23)	0.08 (0.01∼0.14)
Low SDI	0 (−0.04∼0.04)	0.49 (0.41∼0.56)	0.12 (0.07∼0.17)	1.47 (1.4∼1.54)	1.85 (1.78∼1.92)	1.51 (1.45∼1.57)	0.01 (−0.02∼0.05)	0.17 (0.09∼0.25)	0.07 (0.01∼0.12)	−0.19 (−0.23∼−0.15)	−0.03 (−0.13∼0.07)	−0.15 (−0.21∼−0.09)
World Bank Income Level												
World Bank High Income	3.03 (2.73∼3.32)	3.56 (3.18∼3.95)	3.28 (2.94∼3.63)	3.13 (2.84∼3.43)	3.73 (3.37∼4.08)	3.45 (3.13∼3.78)	−0.06 (−0.21∼0.08)	0.27 (0.17∼0.36)	0.12 (0.02∼0.22)	−0.81 (−0.98∼−0.64)	−0.31 (−0.4∼−0.22)	−0.56 (−0.68∼−0.44)
World Bank Upper Middle Income	5.14 (4.76∼5.51)	5.03 (4.73∼5.34)	5.1 (4.76∼5.44)	6.93 (6.65∼7.22)	7.5 (7.2∼7.79)	7.13 (6.86∼7.4)	0.03 (−0.04∼0.1)	0.15 (0.1∼0.2)	0.07 (0.01∼0.12)	−0.08 (−0.16∼0)	0.05 (−0.03∼0.12)	−0.04 (−0.11∼0.03)
World Bank Lower Middle Income	1.24 (1.05∼1.42)	1.47 (1.24∼1.7)	1.28 (1.08∼1.47)	3.42 (2.97∼3.86)	2.87 (2.37∼3.38)	3.24 (2.8∼3.69)	0.15 (0.08∼0.21)	0.36 (0.25∼0.46)	0.23 (0.15∼0.31)	0.07 (0.02∼0.12)	0.18 (0.09∼0.27)	0.1 (0.03∼0.16)
World Bank Low Income	0.06 (0.04∼0.08)	0.42 (0.38∼0.45)	0.17 (0.14∼0.21)	1.81 (1.72∼1.89)	2.3 (2.13∼2.48)	1.95 (1.83∼2.06)	−0.01 (−0.05∼0.03)	−0.07 (−0.14∼0)	−0.05 (−0.11∼0)	−0.24 (−0.3∼−0.19)	−0.35 (−0.46∼−0.24)	−0.29 (−0.37∼−0.21)
Region												
Andean Latin America	5.97 (5.43∼6.52)	3.72 (3.24∼4.19)	5.3 (4.78∼5.82)	9.3 (8.14∼10.48)	7.35 (6.26∼8.45)	8.76 (7.62∼9.91)	−0.03 (−0.14∼0.08)	−0.76 (−0.94∼−0.58)	−0.34 (−0.46∼−0.22)	−0.03 (−0.14∼0.07)	−0.82 (−1∼−0.65)	−0.35 (−0.47∼−0.23)
Australasia	7.65 (7.33∼7.96)	7.86 (7.69∼8.04)	7.72 (7.51∼7.94)	10.25 (9.63∼10.88)	10.22 (9.84∼10.6)	10.18 (9.7∼10.67)	−0.59 (−0.84∼−0.34)	−0.43 (−0.63∼−0.23)	−0.49 (−0.71∼−0.27)	−0.99 (−1.3∼−0.68)	−0.45 (−0.72∼−0.18)	−0.75 (−1.04∼−0.45)
Caribbean	3.87 (3.74∼3.99)	3.27 (3.1∼3.43)	3.75 (3.63∼3.87)	7.36 (7.01∼7.71)	6.94 (6.43∼7.45)	7.25 (6.88∼7.61)	−0.08 (−0.29∼0.13)	0.53 (0.33∼0.72)	0.12 (−0.09∼0.32)	−0.2 (−0.43∼0.04)	0.42 (0.26∼0.58)	−0.01 (−0.22∼0.19)
Central Asia	5.5 (5.12∼5.88)	4.43 (3.58∼5.28)	5.26 (4.72∼5.8)	7.59 (7.17∼8.02)	5.57 (4.58∼6.57)	6.92 (6.29∼7.55)	2.81 (2.54∼3.08)	4.54 (3.99∼5.09)	3.72 (3.32∼4.12)	2.64 (2.4∼2.88)	3.57 (3.19∼3.95)	3.08 (2.79∼3.36)
Central Europe	6.03 (5.8∼6.26)	6.87 (6.64∼7.09)	6.43 (6.21∼6.66)	6.47 (6.26∼6.69)	7.35 (7.14∼7.56)	6.92 (6.71∼7.12)	4.06 (3.7∼4.43)	5.6 (5.13∼6.08)	4.85 (4.43∼5.27)	3.41 (3.07∼3.74)	4.81 (4.44∼5.17)	4.02 (3.68∼4.36)
Central Latin America	3.49 (3.16∼3.81)	3.6 (3.19∼4.02)	3.5 (3.16∼3.83)	5.89 (5.39∼6.4)	6.97 (6.11∼7.83)	6.17 (5.57∼6.78)	0.01 (−0.25∼0.28)	0.53 (0.27∼0.78)	0.2 (−0.06∼0.46)	−0.22 (−0.49∼0.05)	0.34 (0.07∼0.6)	−0.04 (−0.31∼0.23)
Central Sub–Saharan Africa	0.01 (−0.07∼0.09)	0.26 (0.18∼0.35)	0.12 (0.02∼0.21)	1.17 (0.94∼1.4)	0.79 (0.64∼0.93)	1.06 (0.85∼1.27)	0.2 (0.14∼0.25)	−0.02 (−0.13∼0.09)	0.08 (0∼0.17)	−0.05 (−0.12∼0.02)	−0.25 (−0.36∼−0.14)	−0.13 (−0.22∼−0.04)

(Continued)

10.3389/fcvm.2022.1003233

TABLE 5 (Continued)

	EAPC of ASIR No. (95% CI)			EAPC of ASPR No. (95% CI)			EAPC of ASDR No. (95% CI)			EAPC of ASDALYR No. (95% CI)		
	Male	Female	Both	Male	Female	Both	Male	Female	Both	Male	Female	Both
East Asia	7.14 (6.4∼7.89)	7.96 (7.2∼8.72)	7.5 (6.75∼8.26)	11.67 (11.02∼12.32)	11.46 (10.83∼12.08)	11.5 (10.86∼12.13)	−0.01 (−0.29∼0.26)	−0.96 (−1.36∼−0.55)	−0.54 (−0.86∼−0.21)	−0.17 (−0.28∼−0.06)	−0.87 (−1.1∼−0.64)	−0.48 (−0.63∼−0.34)
Eastern Europe	7.55 (7.14∼7.95)	8.26 (7.68∼8.83)	7.75 (7.33∼8.16)	8.04 (7.62∼8.46)	9.05 (8.44∼9.68)	8.39 (7.97∼8.81)	2.66 (2.34∼2.99)	3.84 (3.44∼4.24)	3.46 (3.16∼3.77)	3.77 (3.46∼4.08)	3.59 (3.26∼3.93)	3.79 (3.5∼4.08)
Eastern Sub–Saharan Africa	0.03 (−0.07∼0.13)	−0.03 (−0.09∼0.04)	−0.02 (−0.1∼0.07)	1.72 (1.46∼1.98)	0.73 (0.65∼0.81)	1.39 (1.19∼1.6)	−0.09 (−0.14∼−0.03)	−0.15 (−0.31∼0.02)	−0.13 (−0.24∼−0.02)	−0.45 (−0.52∼−0.38)	−0.52 (−0.71∼−0.33)	−0.5 (−0.61∼−0.38)
High–income Asia Pacific	1.65 (1.45∼1.86)	1.51 (1.4∼1.62)	1.55 (1.43∼1.68)	2.11 (1.99∼2.23)	1.39 (1.26∼1.53)	1.71 (1.61∼1.81)	−1.21 (−1.65∼−0.78)	−0.19 (−0.62∼0.25)	−0.49 (−0.92∼−0.06)	−1.83 (−2.26∼−1.39)	−1 (−1.41∼−0.58)	−1.32 (−1.74∼−0.9)
High–income North America	1.34 (0.82∼1.85)	1.58 (1.01∼2.15)	1.43 (0.89∼1.98)	0.84 (0.3∼1.39)	1.15 (0.57∼1.74)	1.01 (0.45∼1.57)	−0.51 (−0.78∼−0.24)	−0.08 (−0.28∼0.12)	−0.28 (−0.49∼−0.07)	−1.43 (−1.78∼−1.09)	−0.83 (−1.05∼−0.61)	−1.15 (−1.42∼−0.88)
North Africa and Middle East	0.04 (−0.27∼0.35)	1.28 (1.09∼1.47)	0.42 (0.16∼0.68)	1.7 (1.29∼2.11)	4.19 (3.93∼4.45)	2.19 (1.84∼2.55)	−0.56 (−0.64∼−0.48)	−0.69 (−0.77∼−0.61)	−0.65 (−0.7∼−0.61)	−0.66 (−0.73∼−0.6)	−0.75 (−0.82∼−0.68)	−0.71 (−0.77∼−0.65)
Oceania	0.52 (−0.13∼1.17)	1.84 (1.51∼2.17)	0.9 (0.34∼1.45)	2.67 (1.29∼4.06)	5.48 (4.85∼6.13)	3.44 (2.28∼4.62)	−0.46 (−0.53∼−0.39)	0.14 (0.05∼0.24)	−0.28 (−0.36∼−0.2)	−0.28 (−0.35∼−0.22)	0.23 (0.15∼0.31)	−0.13 (−0.19∼−0.06)
South Asia	0.29 (0.26∼0.32)	0.86 (0.75∼0.97)	0.31 (0.26∼0.36)	1.48 (1.43∼1.53)	2.23 (2.11∼2.34)	1.52 (1.49∼1.55)	−0.09 (−0.17∼−0.01)	−0.11 (−0.24∼0.02)	−0.11 (−0.2∼−0.01)	−0.1 (−0.16∼−0.04)	−0.07 (−0.18∼0.03)	−0.12 (−0.19∼−0.05)
Southeast Asia	1.39 (1.15∼1.63)	1.99 (1.69∼2.28)	1.66 (1.39∼1.93)	5.82 (5.41∼6.22)	6.45 (6.04∼6.86)	6.09 (5.69∼6.5)	0.31 (0.22∼0.4)	0.2 (0.06∼0.34)	0.25 (0.13∼0.36)	0.15 (0.08∼0.21)	−0.06 (−0.16∼0.04)	0.06 (−0.02∼0.14)
Southern Latin America	4.77 (4.4∼5.14)	3.24 (2.84∼3.64)	3.96 (3.58∼4.35)	8.16 (7.46∼8.87)	6.67 (6.08∼7.26)	7.44 (6.81∼8.08)	0.27 (0.13∼0.41)	−0.34 (−0.43∼−0.24)	−0.11 (−0.21∼−0.01)	−0.13 (−0.28∼0.02)	−0.49 (−0.59∼−0.39)	−0.33 (−0.45∼−0.22)
Southern Sub–Saharan Africa	6.01 (4.87∼7.16)	−0.5 (−0.56∼−0.44)	5.08 (4.01∼6.15)	9.62 (8.13∼11.14)	−0.13 (−0.27∼0)	9.15 (7.62∼10.7)	0.56 (0.36∼0.76)	−0.22 (−0.38∼−0.07)	0.06 (−0.11∼0.23)	0.09 (−0.1∼0.28)	−0.88 (−1.04∼−0.72)	−0.41 (−0.58∼−0.24)
Tropical Latin America	0.71 (0.52∼0.9)	0.23 (0.12∼0.34)	0.48 (0.32∼0.64)	3.39 (3.11∼3.68)	3.28 (3.13∼3.43)	3.31 (3.08∼3.54)	−0.42 (−0.61∼−0.22)	−0.21 (−0.33∼−0.1)	−0.36 (−0.51∼−0.2)	−1.23 (−1.44∼−1.01)	−0.73 (−0.89∼−0.57)	−1.05 (−1.25∼−0.86)
Western Europe	5.65 (4.96∼6.34)	7.12 (6.12∼8.12)	6.35 (5.5∼7.2)	5.76 (5.03∼6.5)	7.4 (6.4∼8.41)	6.6 (5.72∼7.49)	0.41 (0.31∼0.5)	0.55 (0.47∼0.64)	0.47 (0.4∼0.54)	−0.51 (−0.61∼−0.4)	−0.08 (−0.15∼−0.01)	−0.31 (−0.38∼−0.24)
Western Sub–Saharan Africa	−0.06 (−0.11∼−0.01)	0.55 (0.51∼0.59)	−0.03 (−0.07∼0.01)	0.98 (0.83∼1.13)	1 (0.96∼1.03)	0.72 (0.58∼0.85)	−0.48 (−0.57∼−0.39)	0.04 (−0.01∼0.08)	−0.44 (−0.51∼−0.37)	−0.57 (−0.67∼−0.47)	−0.23 (−0.31∼−0.15)	−0.68 (−0.78∼−0.59)

ASIR, the age-standardized incidence rate; ASPR, the age-standardized prevalence rate; ASDR, the age-standardized death rate; ASDALYR, the age-standardized disability-adjusted life years rate; CAVD, calcific aortic valve disease; SDI, socio-demographic index.

10.3389/fcvm.2022.1003233

(EAPC of male individuals: −0.5, 95% CI −0.61∼−0.39; EAPC of female individuals: −0.37, 95% CI −0.44∼−0.3) (Figure 4D; Table 5).

Attributable risks

Three attributable risk factors of CAVD were available in GBD 2019, including lead exposure, high SBP, and a diet high in sodium.

First of all, lead exposure had a downtrend globally (EAPC = −0.36, 95% CI −0.5∼−0.23, $P < 0.001$) (Table 6). In detail, ASDR caused by lead exposure had the fastest reduction in high-income North America (EAPC = −1.45, 95% CI −1.65∼−1.25, $P < 0.001$), while it had a biggest rise in Central Europe (EAPC = 4.32, 95% CI 3.78∼4.86, $P < 0.001$). Taking sex into consideration, male individuals in high-income North America had the fastest reduction (EAPC = −0.36, 95% CI −0.5∼−0.23, $P < 0.001$), but female individuals in Central Europe showedthe most rapid increase (EAPC = 5.48, 95% CI 4.93∼6.04, $P <$

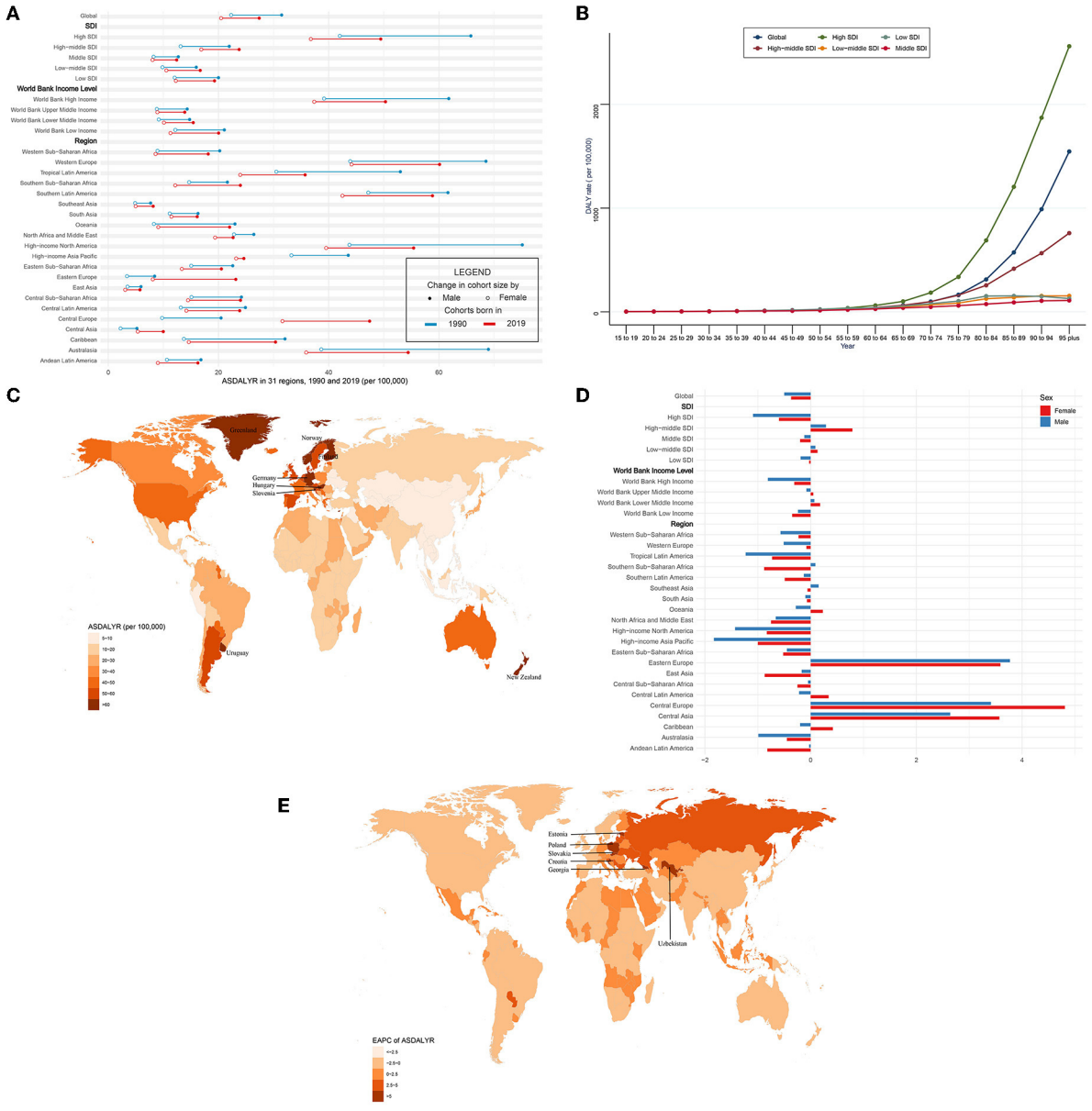

FIGURE 4
ASDALYR and its trend of CAVD. **(A)** ASDALYR in 31 regions from 1990 to 2019. **(B)** DALY rate stratified by age in the globe and 5 SDI regions in 2019. **(C)** ASDALYR in 204 countries and territories in 2019. **(D)** EAPC of ASDALYR in 31 regions from 1990 to 2019. **(E)** EAPC of ASDALYR in 204 countries and territories from 1990 to 2019. CAVD, calcific aortic valve disease; ASDALYR, the age-standardized disability-adjusted life years rate; SDI, socio-demographic index; EAPC, estimated annual percentage change.

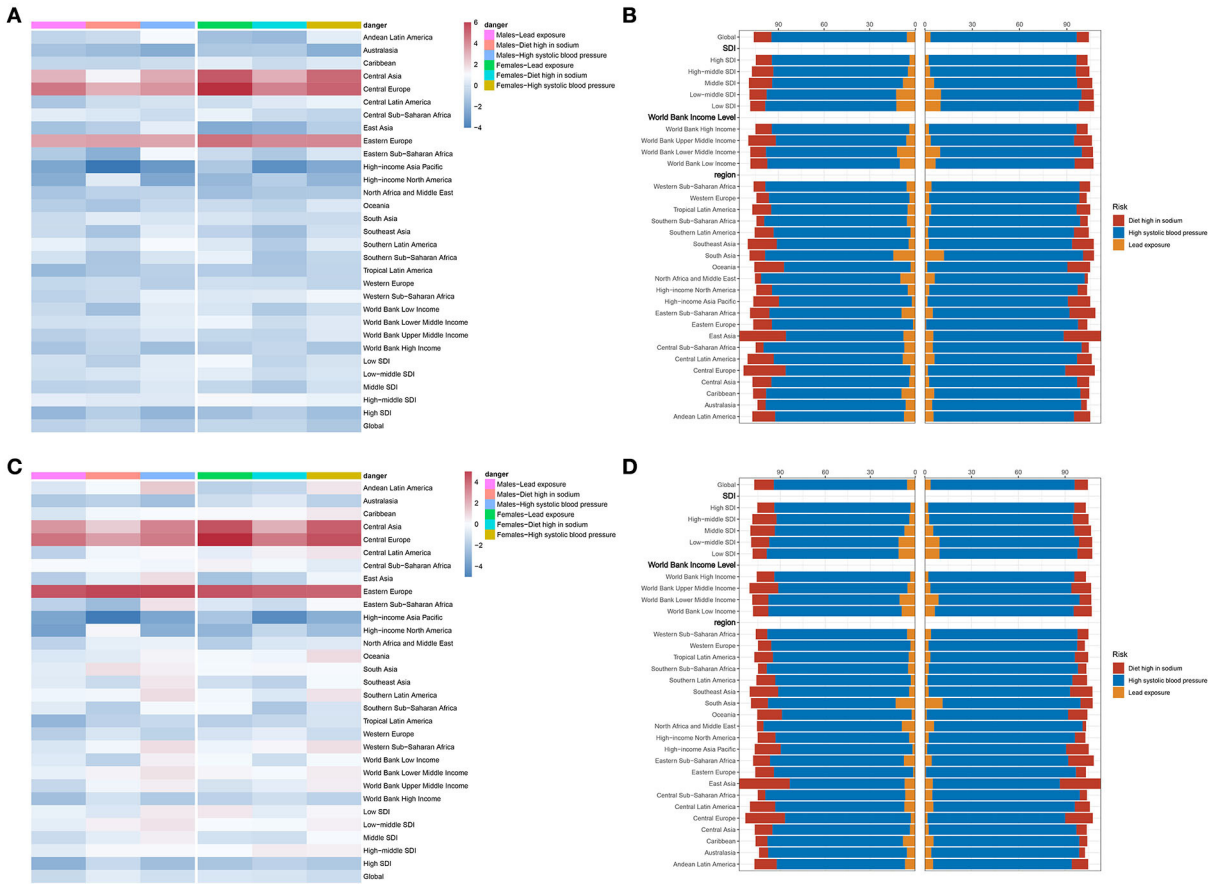

FIGURE 5
Attributable risks of CAVD. **(A)** EAPC and attributable risks of ASDR in 31 regions. **(B)** PAF of attributable risks of ASDR in 2019. **(C)** EAPC and attributable risks of ASDALYR in 31 regions. **(D)** PAF of attributable risks of ASDALYR in 2019. CAVD, calcific aortic valve disease; EAPC, estimated annual percentage change; ASDR, age-standardized death rate; PAF, population attributable fraction; ASDALYR, the age-standardized disability-adjusted life years rate.

0.001) (Figure 5A; Table 6). Second, ASDR from a diet high in sodium also showed a downtrend in the globe (EAPC = −0.17, 95% CI −0.27∼−0.07, $P = 0.001$), especially in high-income Asia Pacific (EAPC = −2.92, 95% CI −3.41∼−2.42, $P < 0.001$) (Table 6). However, Eastern Europe showed the most rapid increase with an EAPC of 3.42 (95% CI 3.04∼3.79, $P < 0.001$). As for sex stratification, male individuals in high-income Asia Pacific showed the fastest decrease (EAPC = −3.42, 95% CI −3.95∼−2.89, $P < 0.001$), whereas female individuals in Central Europe presented the fastest increase (EAPC = 3.69, 95% CI 3.4∼4, $P < 0.001$) (Figure 5A; Table 6). At last, high SBP, another attributable risk, also showed a downtrend around the world (EAPC = −0.68, 95% CI −0.77∼−0.59, $P < 0.001$), especially in high-income Asia Pacific (EAPC = −1.9, 95% CI −2.3∼−1.5, $P < 0.001$) (Table 6). Nevertheless, ASDR of CAVD resulting from high SBP in Central Europe appeared as the biggest rise (EAPC = 3.81, 95% CI 3.43∼4.19, $P < 0.001$). Meanwhile, males in high-income Asia Pacific had the sharpest decline (EAPC = −2.29, 95% CI −2.73∼−1.85, $P < 0.001$), while females in Central Europe presented the fastest increase (EAPC = 4.37, 95% CI 3.95∼4.8, $P < 0.001$) (Figure 5A; Table 6).

High SBP was considered the dominating contributor to ASRD (PAF = 89.08% in males, PAF = 92.76% in females) and ASDALY (PAF = 89% in males, PAF = 92.43% in females) globally (Figures 5B,D; Table 8). The details of PAF in different regions were listed in Table 8. Similar change trends and PAF were found in ASDALYR (Figure 5C; Tables 7, 8).

Relevant factors

The correlation of exposure factors with ASIR, ASPR, ASDR, and ASDALYR of CAVD were analyzed, which were stratified as social environment, natural conditions, and living habits (Figure 6).

TABLE 6 Attributable risks of ASDR in CAVD.

	Lead exposure			Diet high in sodium			High systolic blood pressure		
	Male	Female	Both	Male	Female	Both	Male	Female	Both
Global	−0.39 (−0.49∼−0.28)	−0.22 (−0.40∼−0.03)	−0.36 (−0.50∼−0.23)	−0.14 (−0.27∼−0.01)	−0.22 (−0.30∼−0.14)	−0.17 (−0.27∼−0.07)	−0.61 (−0.73∼−0.49)	−0.71 (−0.83∼−0.58)	−0.68 (−0.77∼−0.59)
SDI level									
High SDI	−1.27 (−1.42∼−1.12)	−0.99 (−1.15∼−0.82)	−1.15 (−1.29∼−1.02)	−0.53 (−0.76∼−0.30)	−0.51 (−0.68∼−0.34)	−0.46 (−0.67∼−0.26)	−1.33 (−1.58∼−1.09)	−1.05 (−1.20∼−0.90)	−1.17 (−1.34∼−0.99)
High–middle SDI	0.65 (0.33∼0.98)	1.14 (0.68∼1.61)	0.78 (0.40∼1.17)	0.48 (0.37∼0.59)	0.92 (0.75∼1.10)	0.66 (0.53∼0.78)	0.48 (0.24∼0.71)	0.76 (0.41∼1.10)	0.62 (0.32∼0.92)
Middle SDI	−0.40 (−0.48∼−0.33)	−0.22 (−0.28∼−0.15)	−0.39 (−0.46∼−0.32)	−0.33 (−0.43∼−0.23)	−0.75 (−0.88∼−0.62)	−0.50 (−0.60∼−0.41)	0.43 (0.37∼0.49)	0.19 (0.15∼0.23)	0.29 (0.25∼0.34)
Low–middle SDI	0.10 (0.02∼0.18)	0.59 (0.49∼0.69)	0.22 (0.14∼0.30)	0.34 (0.30∼0.39)	0.01 (−0.09∼0.11)	0.16 (0.10∼0.22)	0.58 (0.54∼0.63)	0.35 (0.28∼0.42)	0.46 (0.40∼0.51)
Low SDI	0.16 (0.08∼0.25)	0.94 (0.90∼0.98)	0.38 (0.33∼0.43)	−0.48 (−0.55∼−0.40)	−0.28 (−0.41∼−0.16)	−0.42 (−0.52∼−0.33)	0.56 (0.52∼0.60)	0.27 (0.25∼0.29)	0.41 (0.39∼0.44)
World Bank Income Level									
World Bank High Income	−0.84 (−0.97∼−0.71)	−0.54 (−0.73∼−0.34)	−0.72 (−0.86∼−0.58)	−0.26 (−0.45∼−0.06)	−0.19 (−0.33∼−0.06)	−0.18 (−0.35∼−0.02)	−1.03 (−1.21∼−0.85)	−0.79 (−0.93∼−0.66)	−0.90 (−1.03∼−0.76)
World Bank Upper Middle Income	−0.49 (−0.59∼−0.39)	−0.20 (−0.30∼−0.10)	−0.45 (−0.55∼−0.34)	−0.17 (−0.26∼−0.08)	−0.30 (−0.37∼−0.22)	−0.22 (−0.29∼−0.15)	0.38 (0.30∼0.45)	0.45 (0.37∼0.53)	0.39 (0.32∼0.47)
World Bank Lower Middle Income	0.18 (0.07∼0.29)	0.83 (0.72∼0.95)	0.39 (0.29∼0.50)	0.24 (0.20∼0.27)	0.06 (−0.01∼0.13)	0.14 (0.10∼0.19)	0.59 (0.55∼0.63)	0.48 (0.42∼0.55)	0.53 (0.48∼0.58)
World Bank Low Income	−0.13 (−0.21∼−0.05)	0.35 (0.30∼0.39)	−0.06 (−0.13∼0.00)	−1.00 (−1.07∼−0.93)	−0.65 (−0.80∼−0.50)	−0.88 (−0.99∼−0.77)	0.54 (0.52∼0.55)	0.09 (0.07∼0.11)	0.33 (0.31∼0.34)
Region									
Andean Latin America	−0.30 (−0.40∼−0.20)	−0.97 (−1.17∼−0.77)	−0.54 (−0.66∼−0.41)	−0.09 (−0.21∼0.02)	−1.18 (−1.39∼−0.97)	−0.46 (−0.59∼−0.33)	1.07 (0.83∼1.30)	0.60 (0.42∼0.79)	0.88 (0.67∼1.08)
Australasia	−0.88 (−1.08∼−0.68)	−0.72 (−0.90∼−0.54)	−0.79 (−0.97∼−0.61)	−1.11 (−1.34∼−0.87)	−0.65 (−0.84∼−0.45)	−0.89 (−1.11∼−0.67)	−1.64 (−1.97∼−1.30)	−1.52 (−1.80∼−1.25)	−1.59 (−1.89∼−1.30)
Caribbean	−0.23 (−0.32∼−0.15)	0.56 (0.43∼0.68)	−0.11 (−0.19∼−0.02)	−0.25 (−0.45∼−0.05)	−0.02 (−0.19∼0.14)	−0.24 (−0.43∼−0.04)	0.08 (−0.12∼0.28)	0.44 (0.28∼0.61)	0.18 (0.00∼0.37)
Central Asia	2.62 (2.34∼2.91)	4.58 (4.13∼5.04)	3.37 (3.04∼3.70)	1.23 (0.93∼1.53)	2.70 (2.05∼3.36)	1.85 (1.43∼2.28)	2.79 (2.49∼3.10)	4.22 (3.68∼4.76)	3.52 (3.11∼3.94)
Central Europe	3.92 (3.37∼4.47)	5.48 (4.93∼6.04)	4.32 (3.78∼4.86)	2.70 (2.49∼2.90)	3.69 (3.40∼4.00)	3.03 (2.80∼3.26)	3.27 (2.92∼3.61)	4.37 (3.95∼4.80)	3.81 (3.43∼4.19)
Central Latin America	−0.77 (−0.93∼−0.62)	0.09 (−0.03∼0.21)	−0.59 (−0.73∼−0.44)	0.06 (−0.28∼0.39)	0.48 (0.18∼0.79)	0.08 (−0.24∼0.41)	0.27 (0.04∼0.51)	0.76 (0.51∼1.00)	0.44 (0.20∼0.68)
Central Sub–Saharan Africa	0.56 (0.48∼0.63)	0.74 (0.70∼0.77)	0.53 (0.49∼0.56)	0.40 (0.36∼0.44)	0.02 (−0.07∼0.11)	0.19 (0.12∼0.25)	0.04 (0.00∼0.08)	−0.28 (−0.32∼−0.24)	−0.09 (−0.13∼−0.06)
East Asia	−0.93 (−1.18∼−0.68)	−1.69 (−1.97∼−1.41)	−1.31 (−1.57∼−1.06)	−0.52 (−0.62∼−0.41)	−1.42 (−1.64∼−1.19)	−0.87 (−1.00∼−0.73)	0.64 (0.37∼0.90)	−0.53 (−0.91∼−0.16)	0.05 (−0.25∼0.35)
Eastern Europe	2.91 (2.46∼3.35)	4.05 (3.70∼4.41)	3.48 (3.07∼3.89)	3.04 (2.63∼3.46)	3.51 (3.10∼3.91)	3.42 (3.04∼3.79)	2.91 (2.54∼3.28)	3.55 (3.15∼3.95)	3.42 (3.10∼3.74)
Eastern Sub–Saharan Africa	−0.64 (−0.72∼−0.55)	−0.07 (−0.17∼0.02)	−0.59 (−0.64∼−0.54)	−1.52 (−1.61∼−1.42)	−0.71 (−0.91∼−0.52)	−1.13 (−1.27∼−0.99)	0.92 (0.87∼0.96)	0.34 (0.21∼0.46)	0.63 (0.55∼0.70)
High–income Asia Pacific	−1.83 (−2.21∼−1.45)	−0.71 (−1.10∼−0.31)	−1.22 (−1.61∼−0.82)	−3.42 (−3.95∼−2.89)	−2.59 (−3.06∼−2.11)	−2.92 (−3.41∼−2.42)	−2.29 (−2.73∼−1.85)	−1.74 (−2.14∼−1.35)	−1.90 (−2.30∼−1.50)
High–income North America	−1.57 (−1.81∼−1.34)	−1.25 (−1.46∼−1.04)	−1.45 (−1.65∼−1.25)	0.51 (0.34∼0.68)	−0.50 (−0.72∼−0.27)	0.14 (−0.05∼0.33)	−1.80 (−2.16∼−1.44)	−1.33 (−1.65∼−1.02)	−1.55 (−1.83∼−1.27)
North Africa and Middle East	−0.82 (−0.97∼−0.67)	−1.04 (−1.17∼−0.91)	−0.92 (−1.05∼−0.78)	−0.41 (−0.48∼−0.34)	−0.72 (−0.79∼−0.65)	−0.52 (−0.57∼−0.46)	−0.32 (−0.41∼−0.23)	−0.67 (−0.80∼−0.55)	−0.54 (−0.63∼−0.44)
Oceania	−0.53 (−0.64∼−0.42)	−0.05 (−0.11∼0.01)	−0.46 (−0.54∼−0.38)	−0.83 (−0.94∼−0.72)	−0.37 (−0.50∼−0.24)	−0.70 (−0.81∼−0.58)	−0.15 (−0.22∼−0.09)	0.41 (0.31∼0.50)	0.04 (−0.03∼0.11)
South Asia	−0.01 (−0.15∼0.13)	0.33 (0.17∼0.49)	0.07 (−0.07∼0.22)	0.54 (0.46∼0.62)	−0.05 (−0.13∼0.03)	0.26 (0.19∼0.33)	0.32 (0.24∼0.40)	−0.04 (−0.15∼0.07)	0.15 (0.07∼0.24)
Southeast Asia	0.02 (−0.09∼0.13)	−0.35 (−0.48∼−0.22)	−0.16 (−0.28∼−0.04)	−0.84 (−0.95∼−0.72)	−1.02 (−1.18∼−0.86)	−0.94 (−1.07∼−0.80)	0.58 (0.53∼0.64)	0.17 (0.12∼0.23)	0.39 (0.34∼0.44)
Southern Latin America	0.72 (0.59∼0.85)	0.43 (0.30∼0.56)	0.51 (0.39∼0.63)	0.14 (−0.04∼0.31)	−0.62 (−0.72∼−0.52)	−0.28 (−0.40∼−0.16)	1.09 (0.98∼1.19)	0.54 (0.35∼0.72)	0.74 (0.61∼0.86)
Southern Sub–Saharan Africa	0.22 (−0.04∼0.47)	0.72 (0.53∼0.92)	0.14 (−0.07∼0.36)	−0.77 (−0.96∼−0.59)	−0.87 (−1.02∼−0.72)	−0.89 (−1.05∼−0.73)	0.33 (0.12∼0.54)	−0.22 (−0.40∼−0.04)	−0.02 (−0.21∼0.17)
Tropical Latin America	−1.20 (−1.32∼−1.08)	−0.58 (−0.64∼−0.52)	−1.05 (−1.13∼−0.96)	−0.75 (−0.91∼−0.59)	−0.77 (−0.87∼−0.68)	−0.83 (−0.96∼−0.69)	−0.44 (−0.60∼−0.29)	−0.30 (−0.35∼−0.24)	−0.41 (−0.52∼−0.30)
Western Europe	−0.20 (−0.37∼−0.03)	0.16 (−0.10∼0.41)	−0.06 (−0.26∼0.15)	0.04 (−0.13∼0.20)	0.12 (0.04∼0.20)	0.08 (−0.05∼0.20)	−0.52 (−0.64∼−0.39)	−0.31 (−0.41∼−0.21)	−0.41 (−0.51∼−0.31)
Western Sub–Saharan Africa	−0.41 (−0.57∼−0.25)	0.43 (0.34∼0.52)	−0.37 (−0.52∼−0.21)	−0.06 (−0.13∼0.00)	0.50 (0.44∼0.55)	−0.07 (−0.11∼−0.02)	0.72 (0.62∼0.83)	0.89 (0.82∼0.96)	0.59 (0.49∼0.69)

ASDR, the age-standardized death rate; CAVD, calcific aortic valve disease; SDI, socio-demographic index.

10.3389/fcvm.2022.1003233

TABLE 7 Attributable risks of ASDALYR in CAVD.

	Lead exposure			Diet high in sodium			High systolic blood pressure		
	Male	Female	Both	Male	Female	Both	Male	Female	Both
Global	−1.13 (−1.20∼−1.05)	−0.73 (−0.85∼−0.60)	−1.02 (−1.11∼−0.93)	−0.53 (−0.66∼−0.40)	−0.79 (−0.90∼−0.67)	−0.62 (−0.74∼−0.51)	−0.92 (−1.06∼−0.78)	−1.05 (−1.16∼−0.95)	−0.99 (−1.09∼−0.89)
SDI level									
High SDI	−2.45 (−2.61∼−2.28)	−1.83 (−1.97∼−1.69)	−2.23 (−2.37∼−2.09)	−1.15 (−1.41∼−0.90)	−1.37 (−1.60∼−1.15)	−1.18 (−1.42∼−0.93)	−2.01 (−2.31∼−1.70)	−1.69 (−1.90∼−1.48)	−1.84 (−2.09∼−1.59)
High–middle SDI	−0.56 (−0.81∼−0.31)	0.06 (−0.27∼0.40)	−0.41 (−0.68∼−0.13)	0.14 (0.08∼0.20)	0.40 (0.32∼0.48)	0.24 (0.19∼0.30)	0.11 (−0.04∼0.25)	0.32 (0.09∼0.55)	0.21 (0.02∼0.40)
Middle SDI	−1.07 (−1.15∼−1.00)	−0.87 (−0.95∼−0.80)	−1.07 (−1.14∼−0.99)	−0.48 (−0.59∼−0.38)	−0.96 (−1.12∼−0.81)	−0.66 (−0.77∼−0.56)	0.36 (0.29∼0.43)	0.09 (0.04∼0.14)	0.23 (0.17∼0.28)
Low–middle SDI	−0.46 (−0.55∼−0.37)	0.04 (−0.05∼0.13)	−0.36 (−0.45∼−0.28)	0.31 (0.25∼0.36)	−0.04 (−0.15∼0.07)	0.14 (0.07∼0.20)	0.57 (0.53∼0.61)	0.31 (0.23∼0.38)	0.44 (0.39∼0.48)
Low SDI	−0.37 (−0.46∼−0.28)	0.48 (0.45∼0.52)	−0.16 (−0.22∼−0.09)	−0.68 (−0.77∼−0.58)	−0.48 (−0.65∼−0.31)	−0.63 (−0.75∼−0.51)	0.44 (0.41∼0.47)	0.17 (0.14∼0.21)	0.32 (0.29∼0.34)
World Bank Income Level									
World Bank High Income	−1.99 (−2.10∼−1.87)	−1.38 (−1.55∼−1.21)	−1.78 (−1.90∼−1.66)	−0.85 (−1.05∼−0.64)	−0.98 (−1.16∼−0.80)	−0.84 (−1.04∼−0.65)	−1.66 (−1.88∼−1.43)	−1.40 (−1.57∼−1.22)	−1.52 (−1.70∼−1.33)
World Bank Upper Middle Income	−1.18 (−1.25∼−1.10)	−0.83 (−0.89∼−0.77)	−1.12 (−1.19∼−1.05)	−0.22 (−0.32∼−0.12)	−0.45 (−0.58∼−0.33)	−0.30 (−0.40∼−0.21)	0.35 (0.28∼0.42)	0.35 (0.31∼0.39)	0.34 (0.28∼0.39)
World Bank Lower Middle Income	−0.41 (−0.54∼−0.29)	0.19 (0.08∼0.30)	−0.25 (−0.37∼−0.14)	0.24 (0.20∼0.29)	−0.05 (−0.12∼0.03)	0.11 (0.07∼0.16)	0.60 (0.56∼0.65)	0.40 (0.35∼0.45)	0.50 (0.46∼0.54)
World Bank Low Income	−0.61 (−0.69∼−0.53)	−0.09 (−0.14∼−0.05)	−0.52 (−0.59∼−0.46)	−1.40 (−1.49∼−1.31)	−1.00 (−1.20∼−0.80)	−1.27 (−1.40∼−1.14)	0.33 (0.31∼0.35)	−0.11 (−0.16∼−0.07)	0.16 (0.13∼0.18)
Region									
Andean Latin America	−0.71 (−0.81∼−0.62)	−1.42 (−1.62∼−1.22)	−0.94 (−1.06∼−0.82)	−0.04 (−0.15∼0.08)	−1.19 (−1.40∼−0.98)	−0.39 (−0.52∼−0.26)	1.15 (0.90∼1.40)	0.52 (0.30∼0.74)	0.91 (0.68∼1.14)
Australasia	−1.70 (−1.93∼−1.48)	−1.01 (−1.20∼−0.82)	−1.47 (−1.68∼−1.25)	−1.43 (−1.72∼−1.13)	−0.64 (−0.89∼−0.39)	−1.18 (−1.46∼−0.89)	−1.97 (−2.36∼−1.58)	−1.43 (−1.79∼−1.07)	−1.75 (−2.13∼−1.38)
Caribbean	−0.78 (−0.88∼−0.68)	0.11 (0.01∼0.20)	−0.63 (−0.72∼−0.54)	−0.16 (−0.39∼0.07)	0.12 (−0.02∼0.27)	−0.13 (−0.33∼0.08)	0.06 (−0.16∼0.28)	0.46 (0.31∼0.61)	0.17 (−0.03∼0.36)
Central Asia	2.25 (1.97∼2.52)	3.71 (3.36∼4.06)	2.69 (2.41∼2.98)	1.07 (0.80∼1.35)	1.69 (1.17∼2.22)	1.31 (0.98∼1.65)	2.66 (2.37∼2.94)	3.45 (3.03∼3.88)	3.01 (2.68∼3.34)
Central Europe	3.00 (2.45∼3.54)	4.59 (4.13∼5.06)	3.34 (2.83∼3.85)	2.08 (1.93∼2.23)	2.87 (2.68∼3.06)	2.30 (2.15∼2.45)	2.82 (2.50∼3.13)	3.73 (3.41∼4.05)	3.20 (2.89∼3.52)
Central Latin America	−1.37 (−1.52∼−1.22)	−0.45 (−0.57∼−0.33)	−1.19 (−1.33∼−1.05)	−0.19 (−0.52∼0.13)	0.29 (−0.03∼0.61)	−0.16 (−0.48∼0.17)	0.11 (−0.14∼0.37)	0.54 (0.26∼0.81)	0.23 (−0.03∼0.49)
Central Sub–Saharan Africa	0.04 (−0.04∼0.11)	0.27 (0.23∼0.31)	0.07 (0.02∼0.11)	0.07 (0.01∼0.13)	−0.13 (−0.22∼−0.04)	−0.02 (−0.10∼0.06)	−0.18 (−0.22∼−0.14)	−0.52 (−0.57∼−0.47)	−0.29 (−0.33∼−0.25)
East Asia	−1.54 (−1.69∼−1.38)	−1.90 (−2.07∼−1.72)	−1.72 (−1.86∼−1.58)	−0.47 (−0.54∼−0.40)	−1.31 (−1.50∼−1.13)	−0.76 (−0.85∼−0.67)	0.69 (0.57∼0.81)	−0.23 (−0.45∼−0.02)	0.31 (0.17∼0.45)
Eastern Europe	3.65 (3.21∼4.09)	3.66 (3.35∼3.97)	3.70 (3.25∼4.14)	3.98 (3.58∼4.39)	3.38 (3.03∼3.73)	3.93 (3.55∼4.32)	3.96 (3.60∼4.32)	3.35 (3.00∼3.70)	3.83 (3.51∼4.14)
Eastern Sub–Saharan Africa	−1.37 (−1.46∼−1.28)	−0.68 (−0.80∼−0.57)	−1.30 (−1.37∼−1.23)	−2.11 (−2.24∼−1.98)	−1.08 (−1.31∼−0.85)	−1.66 (−1.84∼−1.48)	0.61 (0.56∼0.66)	0.11 (−0.04∼0.27)	0.39 (0.31∼0.48)
High–income Asia Pacific	−2.85 (−3.22∼−2.47)	−1.82 (−2.17∼−1.46)	−2.37 (−2.74∼−2.00)	−4.23 (−4.76∼−3.70)	−3.68 (−4.16∼−3.20)	−3.94 (−4.44∼−3.43)	−2.88 (−3.33∼−2.43)	−2.55 (−2.95∼−2.16)	−2.66 (−3.08∼−2.25)
High–income North America	−3.02 (−3.32∼−2.72)	−2.33 (−2.54∼−2.12)	−2.81 (−3.06∼−2.55)	0.17 (0.02∼0.32)	−1.23 (−1.51∼−0.95)	−0.29 (−0.49∼−0.09)	−2.56 (−3.05∼−2.08)	−2.06 (−2.44∼−1.69)	−2.32 (−2.71∼−1.94)
North Africa and Middle East	−1.35 (−1.51∼−1.19)	−1.50 (−1.66∼−1.34)	−1.40 (−1.56∼−1.25)	−0.42 (−0.47∼−0.37)	−0.73 (−0.82∼−0.64)	−0.50 (−0.56∼−0.45)	−0.34 (−0.40∼−0.29)	−0.62 (−0.74∼−0.50)	−0.48 (−0.56∼−0.40)
Oceania	−0.69 (−0.81∼−0.57)	−0.13 (−0.21∼−0.05)	−0.60 (−0.70∼−0.50)	−0.58 (−0.70∼−0.46)	−0.21 (−0.33∼−0.10)	−0.46 (−0.57∼−0.35)	0.21 (0.09∼0.33)	0.75 (0.62∼0.87)	0.39 (0.27∼0.50)
South Asia	−0.51 (−0.65∼−0.37)	−0.06 (−0.19∼0.07)	−0.42 (−0.54∼−0.29)	0.67 (0.57∼0.76)	0.14 (0.04∼0.23)	0.43 (0.35∼0.51)	0.33 (0.25∼0.42)	0.04 (−0.03∼0.12)	0.19 (0.13∼0.26)
Southeast Asia	−0.54 (−0.68∼−0.39)	−0.95 (−1.11∼−0.79)	−0.70 (−0.84∼−0.55)	−1.09 (−1.20∼−0.98)	−1.39 (−1.53∼−1.24)	−1.21 (−1.33∼−1.09)	0.50 (0.46∼0.53)	−0.07 (−0.11∼−0.04)	0.26 (0.24∼0.29)
Southern Latin America	−0.21 (−0.35∼−0.08)	−0.14 (−0.27∼0.00)	−0.26 (−0.39∼−0.13)	−0.19 (−0.39∼0.01)	−0.70 (−0.80∼−0.60)	−0.43 (−0.57∼−0.28)	0.73 (0.64∼0.83)	0.57 (0.38∼0.76)	0.62 (0.52∼0.72)
Southern Sub–Saharan Africa	−0.54 (−0.77∼−0.30)	−0.02 (−0.19∼0.14)	−0.62 (−0.82∼−0.41)	−1.50 (−1.71∼−1.30)	−1.74 (−1.91∼−1.57)	−1.65 (−1.83∼−1.46)	−0.13 (−0.33∼0.06)	−0.82 (−0.99∼−0.65)	−0.49 (−0.67∼−0.32)
Tropical Latin America	−2.32 (−2.44∼−2.21)	−1.47 (−1.53∼−1.41)	−2.12 (−2.21∼−2.02)	−1.38 (−1.56∼−1.20)	−1.21 (−1.34∼−1.08)	−1.39 (−1.55∼−1.22)	−1.15 (−1.32∼−0.98)	−0.80 (−0.89∼−0.71)	−1.04 (−1.18∼−0.90)
Western Europe	−1.52 (−1.68∼−1.36)	−0.81 (−1.06∼−0.55)	−1.27 (−1.46∼−1.08)	−0.75 (−0.95∼−0.55)	−0.45 (−0.55∼−0.34)	−0.63 (−0.79∼−0.46)	−1.36 (−1.52∼−1.20)	−1.05 (−1.18∼−0.91)	−1.21 (−1.35∼−1.07)
Western Sub–Saharan Africa	−0.75 (−0.91∼−0.58)	−0.28 (−0.36∼−0.20)	−0.91 (−1.08∼−0.74)	−0.18 (−0.26∼−0.10)	0.17 (0.10∼0.25)	−0.34 (−0.40∼−0.27)	0.70 (0.60∼0.80)	0.67 (0.61∼0.72)	0.45 (0.36∼0.55)

ASDALYR, the age-standardized disability-adjusted life years rate; CAVD, calcific aortic valve disease; SDI, socio-demographic index.

10.3389/fcvm.2022.1003233

TABLE 8 PAF of attributable risks of ASDR and ASDALYR to CAVD in 2019.

	ASDR (%)						ASDALYR (%)					
	Lead exposure		Diet high in sodium		High systolic blood pressure		Lead exposure		Diet high in sodium		High systolic blood pressure	
	Male	Female	Male	Female	Male	Female	Male	Female	Male	Female	Male	Female
Global	5.53	3.49	11.63	7.68	89.08	92.76	5.38	3.67	13.05	8.55	89.00	92.43
SDI level												
High SDI	3.78	2.34	10.54	7.03	90.59	93.75	3.13	2.09	11.41	7.40	90.89	93.80
High-middle SDI	4.88	3.18	14.07	8.56	88.51	92.55	3.95	2.77	16.16	10.06	88.61	92.24
Middle SDI	8.10	5.81	15.32	9.59	86.03	90.72	7.14	5.37	16.31	10.69	86.61	90.62
Low-middle SDI	12.61	10.14	11.26	7.75	85.19	89.13	11.10	9.37	12.02	8.42	86.36	89.58
Low SDI	12.48	9.88	9.89	9.65	86.22	87.66	11.08	9.33	9.42	9.54	88.04	88.58
World Bank Income Level												
World Bank High Income	3.97	2.52	10.74	7.04	90.45	93.63	3.29	2.24	11.79	7.49	90.75	93.67
World Bank Upper Middle Income	5.95	3.67	18.12	11.34	85.77	90.90	5.18	3.56	19.23	12.74	86.22	90.43
World Bank Lower Middle Income	12.00	9.61	10.26	7.06	86.28	89.95	10.45	8.79	10.77	7.56	87.58	90.50
World Bank Low Income	10.12	6.70	11.18	11.98	87.17	88.24	9.01	6.40	10.22	11.62	89.02	89.11
Region												
Andean Latin America	7.43	5.44	15.01	10.32	84.73	89.06	6.79	5.25	14.84	10.52	85.66	89.04
Australasia	6.33	4.55	5.43	3.54	92.09	94.54	5.47	4.12	6.08	3.71	92.70	94.91
Caribbean	9.09	5.86	8.51	5.62	89.06	92.73	8.14	5.56	8.00	5.14	90.48	93.56
Central Asia	4.05	2.69	12.47	7.63	90.56	93.85	3.46	2.47	11.83	6.65	91.83	94.79
Central Europe	3.24	1.85	27.67	18.73	82.06	87.15	2.93	1.75	26.44	17.68	84.00	88.35
Central Latin America	8.26	6.05	17.21	9.33	84.85	90.42	7.20	5.46	16.85	9.65	86.25	90.81
Central Sub-Saharan Africa	7.20	4.98	5.24	4.54	92.58	94.38	6.65	4.77	5.04	4.54	93.42	94.70
East Asia	7.82	5.32	30.72	23.72	77.28	82.65	7.04	5.10	33.79	26.36	76.74	81.56
Eastern Europe	1.51	0.77	12.28	5.87	92.78	96.34	1.33	0.71	12.49	6.44	92.97	96.25
Eastern Sub-Saharan Africa	9.04	4.98	12.73	16.46	86.91	86.67	7.55	4.42	11.25	16.37	89.39	87.63
High-income Asia Pacific	2.23	1.67	16.88	14.16	87.41	88.96	1.85	1.46	17.33	14.52	87.96	89.18
High-income North America	4.97	2.78	10.37	5.99	89.25	94.06	4.06	2.45	11.89	6.70	89.21	93.89
North Africa and Middle East	9.82	6.23	4.01	2.06	91.59	95.04	8.91	5.89	4.34	2.25	92.36	95.34
Oceania	3.07	1.52	19.48	14.40	83.29	88.83	2.36	1.21	16.46	12.39	86.64	90.72
South Asia	14.44	12.06	10.23	6.90	84.35	88.23	13.07	11.37	11.33	7.77	85.24	88.55
Southeast Asia	4.39	2.53	19.09	13.78	86.73	90.75	4.06	2.46	18.99	14.40	87.45	90.72
Southern Latin America	3.18	1.91	12.40	9.38	90.07	92.61	2.87	1.76	12.60	9.38	90.54	92.94
Southern Sub-Saharan Africa	5.46	2.64	5.12	4.84	93.88	95.77	4.71	2.50	5.84	5.38	94.38	95.83
Tropical Latin America	5.04	3.94	12.47	8.65	89.70	92.19	4.32	3.55	12.37	8.53	90.68	92.73
Western Europe	3.82	2.63	8.19	4.64	92.47	95.32	3.18	2.34	8.86	4.87	92.91	95.47
Western Sub-Saharan Africa	5.72	4.16	7.75	6.68	92.91	93.87	5.38	3.93	7.72	7.01	93.36	94.08

PAF, population attributable fraction; ASDR, age-standardized death rate; ASDALYR, the age-standardized disability-adjusted life years rate; CAVD, calcific aortic valve disease.

10.3389/fcvm.2022.1003233

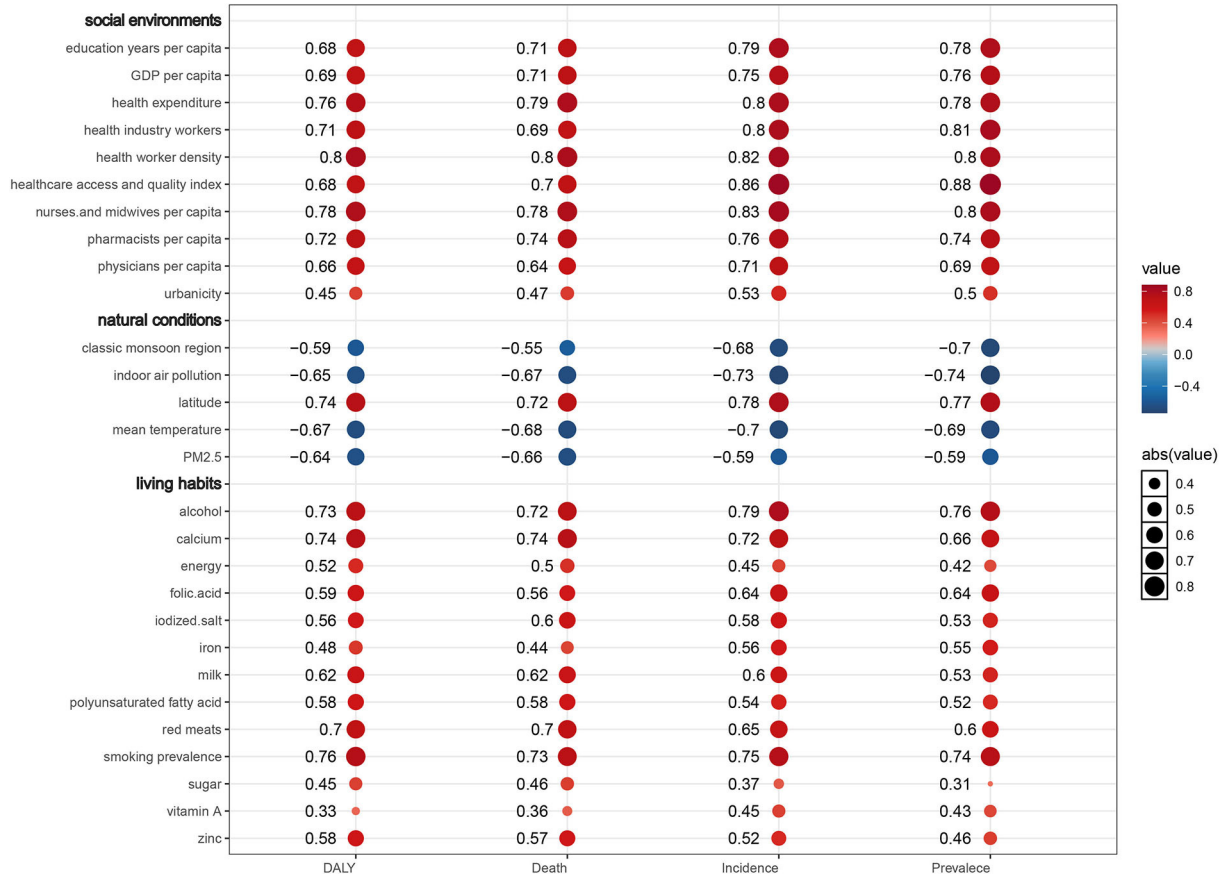

FIGURE 6
Covariates of CAVD. CAVD, calcific aortic valve disease.

Social environment and burden of CAVD

Health worker density ($R = 0.82$, $P < 0.001$), health industry workers ($R = 0.80$, $P < 0.001$), healthcare access and quality index ($R = 0.86$, $P < 0.001$), and nurses and midwives per capita ($R = 0.83$, $P < 0.001$) showed strong positive correlations to ASIR of CAVD. At the same time, education years per capita ($R = 0.79$, $P < 0.001$), Gross Domestic Product (GDP) per capita ($R = 0.75$, $P < 0.001$), health expenditure per capita ($R = 0.795$, $P < 0.001$), pharmacists per capita ($R = 0.76$, $P < 0.001$), physicians per capita ($R = 0.71$, $P < 0.001$), and urbanicity ($R = 0.53$, $P < 0.001$) showed moderately positive correlations toASIR. The relationships between social environment and ASPR, and ASDR as well as ASDALYR were analogous.

Natural conditions and burden of CAVD

As for natural environmental factors, classic monsoon region ($R = -0.68$, $P < 0.001$), indoor air pollution ($R = -0.73$, $P < 0.001$), mean temperature ($R = -0.7$, $P < 0.001$), and outdoor PM2.5 ($R = -0.59$, $P < 0.001$) were negatively correlated with ASIR of CAVD. However, latitude ($R = 0.73$, $P < 0.001$) had a moderately positive correlation. Similar results were found in the analysis of ASPR, ASDR, and ASDALYR.

Living habits and burden of CAVD

All living habit factors with significant correlations manifested positive correlations. However, these were moderately relevant factors not strong ones: alcohol ($R = 0.79$, $P < 0.001$), smoking prevalence ($R = 0.75$, $P < 0.001$), calcium ($R = 0.72$, $P < 0.001$), red meats ($R = 0.65$, $P < 0.001$), folic acid ($R = 0.64$, $P < 0.001$), milk ($R = 0.60$, $P < 0.001$), and so on. Consistent results were found in the relationships among ASPR, ASDR, ASDALYR, and these lifestyle-related factors.

Discussion

In this study, we comprehensively reported the recent global burden and trends from 1990 to 2019 according to the GBD 2019 study. Great regional differences were found in the disease distribution of CAVD. High SDI regions had the highest

burdens, especially in the elderly population, and still shoed an upwards trend. Although the ASIR and ASPR presented a global upwards trend, ASDR was relatively stable. Even ASDALYR gradually declined. Age was a powerful factor to develop CAVD and males were more likely to suffer from it. High SBP was a major attributable risk to CAVD. In addition, various covariates stratified as social environment, natural conditions, and living habits were found relative to the burden of CAVD.

Our results revealed that the epidemiological distributions of CAVD were markedly different around the world. High SDI regions had the highest burdens of CAVD including incidence, prevalence, deaths, and DALYs. Older age was a strong risk factor for calcific AS (1, 16). Interestingly, the highest age-standardized rates of these four statistical variables were still in high SDI regions. Several research elaborated on the significant associations between cardiovascular risk factors (such as smoking, high SBP, high body mass index, hyperlipemia, etc.) and CAVD (1, 17–20). Widely varied spatial distribution among the global population of these traditional cardiovascular risk factors might partly account for the differences in the geographical distribution of CAVD. In addition, high SDI countries such as the UK and the USA had more sound disease diagnosis and registry systems compared with other regions. Age was an extremely powerful factor in CAVD, no matter in incidence, prevalence, deaths, or DALYs. In this study, we found that CAVD-related deaths and DALYs surged among patients aged over 75 years. Once an estimate told that the hazard of AS increases by 75% for each decade increase in age (20). As life expectancy remains increasing, inevitably, the burden of AS is anticipated to surge (21). Globally, male individuals were more likely to suffer from CAVD than female individuals with higher prevalence cases, death cases, DALYs, and corresponding age-standardized rates (6). Moreover, female individuals tended to present more fibrotic remodeling and less calcification than male individuals (22). Meanwhile, female individuals showed a more advanced age of onset of the disease (21). Studies focused on sex-specific features implied that the progression, pathophysiology, and hemodynamic severity of aortic valve calcification varied in males and females (23–25). Therefore, in future, it is of great importance to consider sex-related difference in the clinical practice of diagnosis, treatment, and prognosis (23).

We found out that the ASIR and ASPR of CAVD displayed a pretty great uptrend from 1990 to 2019 globally. Despite that cardiac catheterization is the gold standard of diagnosis for CAVD, echocardiography examination, which provide wealthy and immediate information on cardiac structure and function, has been widely used in clinical diagnosis (26). With this convenient and relatively low-cost technique, more patients were screened especially in high-middle SDI and middle SDI regions. While the ASIR and ASPR in high SDI regions remained increasing, the growth rate had given way to high-middle SDI and middle SDI regions such as East Asia and Eastern Europe. Maybe medical services and public health were increasingly valued by the government in these regions. Taking China, for instance, transthoracic echocardiography was prevalently used in diagnosing and evaluating the severity of valvular heart disease (27). Thus, more cases were diagnosed and registered in these regions. However, the ASDR was relatively stable during the past 30 years, particularly in high SDI regions. And more encouragingly, globally, the ASDALYR of CAVD presented a gradual downward trend during this period, particularly in high SDI regions where the prevalence and ASPR were the highest in 2019 at the socio-demographic factor level (11), which sent a positive signal to control and ameliorate the confused and intractable disease. For the past few years, most individuals were diagnosed as asymptomatic patients, and it would take several years for the onset of symptoms during the regular follow-up. Transcatheter aortic valve replacement (TAVR), first performed on humans in 2002, turned out to be an epochmaking intervention for CAVD treatment recently, especially for those patients with advanced age and lack of surgery tolerance (28). In the 2020 ACC/AHA Guideline, TAVR was recommended in preference to surgery among patients over 80 years of age while surgical aortic valve replacement (SAVR) was first recommended among individuals aged younger than 65 years (26). Thus, since CAVD is highly correlated with age particularly among individuals over 70 years, emerging TAVR brought good news to these patients. In research, enrolling 246 consecutive AS patients who underwent TAVR, obvious hemodynamics improvement of the aortic valve and cardiac reverse remodeling were observed after a 3-year follow-up (29). Therefore, TAVR significantly improved the living qualities and reduced disabilities caused by CAVD, especially for patients with advanced ages.

We analyzed the three attributable risk factors (lead exposure, high SBP, and diet high in sodium) available in GBD 2019 of CAVD. We found out that high SBP remained the predominating attributable risk factor to CAVD, which is consistent with previous studies (20, 30, 31). The CANHEART Aortic Stenosis study, a large observational cohort study of 1.12 million individuals older than 65 years, using a population-based longitudinal approach revealed an independent and dose-response association between well-known cardiovascular risk factors such as hypertension, diabetes, as well as dyslipidemia and the risk of developing severe AS (20). Moreover, due to a higher prevalence in elder people and a higher HR, hypertension presented the highest attributed risk to AS. And these three risk factors combinedly accounted for approximately one-third (34.4%) of the attributable risk for AS (20). The PROGRESSA study indicated that high SBP had a significant relationship with faster progression of aortic valve calcification (AVC) (31). A novel finding was that high SBP could disturb the evaluation of the hemodynamic severity of AS and thus may cover up its progression (31). Systolic hypertension may increase the bending stress on the valve leaflets during

the ventricular ejection stage (31, 32). Meanwhile, it may cause faster and more abrupt closing of the aortic valve leading to the increase of tensile stress in early diastole (31, 33). All these mechanical stresses may damage endothelial cells of valve leaflets resulting in inflammatory activation and the infiltration of lipids (1, 17, 21, 31). Furthermore, a study consisting of 737 elder patients manifested that after adjustment for atherosclerosis-related risk factors, only ambulatory mean diastolic blood pressure (DBP) displayed a significant association with advanced AVC independently, which suggests that DBP may play a more important role in the early stage of CAVD than SBP (19). Fortunately, all these three attributable risks for CAVD displayed a downward trend in general, especially for high SBP. A systematic analysis from 90 countries showed that the increase in awareness, treatment, and control in high-income countries was substantial while it was less in low- and middle-income countries (34). Thus, ambulatory blood pressure monitoring and controlling, no matter whether SBP or DBP, could play a great important role in preventing CAVD.

Although the exact mechanism and pathophysiology of CAVD are still not clear, the existing research demonstrates that it is a series of the chronic progression of endothelium damage, lipid infiltration and oxidation, chronic inflammation, and finally fibrosis and biomineralization (1, 6, 17, 21, 35, 36). In this study, we found some relevant exposure factors related to the burden of CAVD, which may provide some ideas and orientations for prevention. Avoiding risk factors and reducing exposure are important for prevention. Our results revealed that alcohol, calcium, salt, milk, red meats, and smoking had a positive relationship with the burden of aortic aneurysm. In contrast, the classic monsoon region and temperature were negatively related to that. Alcohol consumption was positively associated with cardiovascular events and all-cause mortality presenting a curvilinear dose-response (37, 38). The influx of Ca^{2+} through CaV1.2 (an L-type voltage-gated Ca2+ channel) was proved to promote aortic valve calcification (39). A case-control study involving 132 individuals revealed that a small increase in calcium level would lead to a significant rise in the risk of AS (40, 41). And smoking, a conventional cardiovascular risk factor, was linked to CAVD (17, 42). Although there were no direct evidence to confirm the association between salt, temperature, and the development of CAVD, they might exert as intermediate variables. For example, salt was a risk factor for hypertension and high ambient temperature may serve as a protective factor (43–45). Therefore, avoiding smoking, lowering alcohol consumption, limiting calcium and salt intake, controlling blood pressure, and increasing the room temperature appropriately could be cost-effective measures to reduce the risk of developing AS and CAVD.

There are some limitations in this study. First, all of our analysis relied on the quality of the disease registry data. Inevitably, data on CAVD were sparse. Fortunately, several statistical approaches were adopted to reduce the influence. Second, GBD is a descriptive study that lacks causal argument. So, further analytical and experimental studies are needed to confirm these results. Third, potentially confounding factors may interfere with the calculation of correlation coefficients.

Conclusions

CAVD displays widely varied spatial distribution around the world and high SDI regions have the highest burdens. Although the ASIR and ASPR present an upward trend globally, ASDR is relatively stable. Even ASDALYR gradually declines. Age is a powerful factor to develop CAVD and male individuals are more likely to suffer from it. Blood pressure control, both SBP and DBP, should be paid high attention to. In addition, avoiding smoking, reducing alcohol consumption, limiting calcium and salt intake, and rising the room temperature appropriately might decrease the burden of CAVD. Our findings may aid in providing information on comprehensive prevention measures in response to the challenges of valvular heart disease.

Data availability statement

The original contributions presented in the study are included in the article/Supplementary material, further inquiries can be directed to the corresponding author.

Author contributions

JY and ZW designed the study, retrieved the data, analyzed the data, and performed the data visualization. JY, QB, SL, and ZY interpreted the results and wrote the manuscript. YY revised the manuscript. XX directed the study and checked and approved the manuscript. All authors consented to submit the manuscript.

Funding

XX was supported by the National Health Commission, Key Program of Science and Technology of Medical and Health of Zhejiang Province (WKJ-ZJ-2028).

Acknowledgments

We are grateful to the scholars, designers, and other contributors of the GBD 2019 study.

Conflict of interest

The authors declare that the research was conducted in the absence of any commercial or financial relationships that could be construed as a potential conflict of interest.

Publisher's note

All claims expressed in this article are solely those of the authors and do not necessarily represent those of their affiliated organizations, or those of the publisher, the editors and the reviewers. Any product that may be evaluated in this article, or claim that may be made by its manufacturer, is not guaranteed or endorsed by the publisher.

Supplementary material

The Supplementary Material for this article can be found online at: https://www.frontiersin.org/articles/10.3389/fcvm.2022.1003233/full#supplementary-material

References

1. Lindman BR, Clavel MA, Mathieu P, Iung B, Lancellotti P, Otto CM, et al. Calcific aortic stenosis. *Nat Rev Dis Primers.* (2016) 2:16006. doi: 10.1038/nrdp.2016.6

2. Yadgir S, Johnson CO, Aboyans V, Adebayo OM, Adedoyin RA, Afarideh M, et al. Global, regional, and national burden of calcific aortic valve and degenerative mitral valve diseases, 1990–2017. *Circulation.* (2020) 141:1670–80. doi: 10.1161/CIR.0000000000000848

3. Go AS, Mozaffarian D, Roger VL, Benjamin EJ, Berry JD, Borden WB, et al. Executive summary: heart disease and stroke statistics-−2013 update: a report from the American Heart Association. *Circulation.* (2013) 127:143–52.

4. Bartoli-Leonard F, Zimmer J, Aikawa E. Innate and adaptive immunity: the understudied driving force of heart valve disease. *Cardiovasc Res.* (2021) 117:2506–24. doi: 10.1093/cvr/cvab273

5. Zilla P, Yacoub M, Zühlke L, Beyersdorf F, Sliwa K, Khubulava G, et al. Global unmet needs in cardiac surgery. *Glob Heart.* (2018) 13:293–303. doi: 10.1016/j.gheart.2018.08.002

6. Alushi B, Curini L, Christopher MR, Grubitzch H, Landmesser U, Amedei A, et al. Calcific aortic valve disease-natural history and future therapeutic strategies. *Front Pharmacol.* (2020) 11:685. doi: 10.3389/fphar.2020.00685

7. Vos T, Lim SS, Abbafati C, Abbas KM, Abbasi M, Abbasifard M, et al. Global burden of 369 diseases and injuries in 204 countries and territories, 1990–2019: a systematic analysis for the Global Burden of Disease Study 2019. *Lancet.* (2020) 396:1204–22. doi: 10.1016/S0140-6736(20)30925-9

8. Murray CJ, Aravkin AY, Zheng P, Abbafati C, Abbas KM, Abbasi-Kangevari M, et al. Global burden of 87 risk factors in 204 countries and territories, 1990–2019: a systematic analysis for the Global Burden of Disease Study 2019. *Lancet.* (2020) 396:1223–49. doi: 10.1016/S0140-6736(20)30752-2

9. Ward JL, Kieling CC, Viner RM. Global, regional, and national mortality among young people aged 10-24 years, 1950-2019: a systematic analysis for the Global Burden of Disease Study 2019. *Lancet.* (2021) 398:1593–618. doi: 10.1016/S0140-6736(21)01546-4

10. de Martel C, Georges D, Bray F, Ferlay J, Clifford GM. Global burden of cancer attributable to infections in 2018: a worldwide incidence analysis. *Lancet Glob Health.* (2020) 8:e180–e90. doi: 10.1016/S2214-109X(19)30488-7

11. Gao T, Wang XC, Chen R, Ngo HH, Guo W. Disability adjusted life year (DALY): a useful tool for quantitative assessment of environmental pollution. *Sci Total Environ.* (2015) 511:268–87. doi: 10.1016/j.scitotenv.2014.11.048

12. Imamura F, O'Connor L, Ye Z, Mursu J, Hayashino Y, Bhupathiraju SN, et al. Consumption of sugar sweetened beverages, artificially sweetened beverages, and fruit juice and incidence of type 2 diabetes: systematic review, meta-analysis, and estimation of population attributable fraction. *BMJ.* (2015) 351:h3576. doi: 10.1136/bmj.h3576

13. Hong D, Lee S, Choi YJ, Moon S, Jang Y, Cho YM, et al. The age-standardized incidence, mortality, and case fatality rates of COVID-19 in 79 countries: a cross-sectional comparison and their correlations with associated factors. *Epidemiol Health.* (2021) 43:e2021061. doi: 10.4178/epih.e2021061

14. Fay MP, Tiwari RC, Feuer EJ, Zou Z. Estimating average annual percent change for disease rates without assuming constant change. *Biometrics.* (2006) 62:847–54. doi: 10.1111/j.1541-0420.2006.00528.x

15. Yi M, Li A, Zhou L, Chu Q, Song Y, Wu K. The global burden and attributable risk factor analysis of acute myeloid leukemia in 195 countries and territories from 1990 to 2017: estimates based on the global burden of disease study 2017. *J Hematol Oncol.* (2020) 13:72. doi: 10.1186/s13045-020-00908-z

16. Coffey S, Cox B, Williams MJ. The prevalence, incidence, progression, and risks of aortic valve sclerosis: a systematic review and meta-analysis. *J Am Coll Cardiol.* (2014) 63:2852–61. doi: 10.1016/j.jacc.2014.04.018

17. Cho KI, Sakuma I, Sohn IS, Jo SH, Koh KK. Inflammatory and metabolic mechanisms underlying the calcific aortic valve disease. *Atherosclerosis.* (2018) 277:60–5. doi: 10.1016/j.atherosclerosis.2018.08.029

18. Garg V. The role of lipoprotein(a) in calcific aortic valve disease: insights from a large-cohort genetic study. *JAMA Cardiol.* (2018) 3:24–5. doi: 10.1001/jamacardio.2017.4267

19. Iwata S, Russo C, Jin Z, Schwartz JE, Homma S, Elkind MS, et al. Higher ambulatory blood pressure is associated with aortic valve calcification in the elderly: a population-based study. *Hypertension.* (2013) 61:55–60. doi: 10.1161/HYPERTENSIONAHA.112.202697

20. Yan AT, Koh M, Chan KK, Guo H, Alter DA, Austin PC, et al. Association between cardiovascular risk factors and aortic stenosis: the CANHEART aortic stenosis study. *J Am Coll Cardiol.* (2017) 69:1523–32. doi: 10.1016/j.jacc.2017.01.025

21. Ferrari S, Pesce M. The complex interplay of inflammation, metabolism, epigenetics, and sex in calcific disease of the aortic valve. *Front Cardiovasc Med.* (2021) 8:791646. doi: 10.3389/fcvm.2021.791646

22. Voisine M, Hervault M, Shen M, Boilard AJ, Filion B, Rosa M, et al. Age, sex, and valve phenotype differences in fibro-calcific remodeling of calcified aortic valve. *J Am Heart Assoc.* (2020) 9:e015610. doi: 10.1161/JAHA.119.015610

23. Summerhill VI, Moschetta D, Orekhov AN, Poggio P, Myasoedova VA. Sex-specific features of calcific aortic valve disease. *Int J Mol Sci.* (2020) 21:5620. doi: 10.3390/ijms21165620

24. Parra-Izquierdo I, Castaños-Mollor I, López J, Gómez C, San Román JA, Sánchez Crespo M, et al. Lipopolysaccharide and interferon-γ team up to activate HIF-1α *via* STAT1 in normoxia and exhibit sex differences in human aortic valve interstitial cells. *Biochim Biophys Acta Mol Basis Dis.* (2019) 1865:2168–79. doi: 10.1016/j.bbadis.2019.04.014

25. Kararigas G, Dworatzek E, Petrov G, Summer H, Schulze TM, Baczko I, et al. Sex-dependent regulation of fibrosis and inflammation in human left ventricular remodelling under pressure overload. *Eur J Heart Fail.* (2014) 16:1160–7. doi: 10.1002/ejhf.171

26. Otto CM, Nishimura RA, Bonow RO, Carabello BA, Erwin JP, Gentile F, et al. 2020 ACC/AHA guideline for the management of patients with valvular heart disease: a report of the American college of cardiology/American heart association joint committee on clinical practice guidelines. *J Am Coll Cardiol.* (2021) 77:e25–197. doi: 10.1161/CIR.0000000000000923

27. Shu C, Chen S, Qin T, Fu Z, Sun T, Xie M, et al. Prevalence and correlates of valvular heart diseases in the elderly population in Hubei, China. *Sci Rep.* (2016) 6:27253. doi: 10.1038/srep27253

28. Kumar V, Sandhu GS, Harper CM, Ting HH, Rihal CS. Transcatheter aortic valve replacement programs: clinical outcomes and developments. *J Am Heart Assoc.* (2020) 9:e015921. doi: 10.1161/JAHA.120.015921

29. Zhou D, Yidilisi A, Fan J, Zhang Y, Dai H, Zhu G, et al. Three-year outcomes of transcatheter aortic valve implantation for bicuspid vs. tricuspid aortic stenosis. *EuroIntervention.* (2022) 18:193–202. doi: 10.4244/EIJ-D-21-00734

30. Aronow WS. Hypertension, aortic stenosis, and aortic regurgitation. *Ann Transl Med.* (2018) 6:43. doi: 10.21037/atm.2017.11.30

31. Tastet L, Capoulade R, Clavel MA, Larose E, Shen M, Dahou A, et al. Systolic hypertension and progression of aortic valve calcification in patients with aortic stenosis: results from the PROGRESSA study. *Eur Heart J Cardiovasc Imaging.* (2017) 18:70–8. doi: 10.1093/ehjci/jew013

32. Rieck AE, Cramariuc D, Boman K, Gohlke-Barwolf C, Staal EM, Lonnebakken MT, et al. Hypertension in aortic stenosis: implications for left ventricular structure and cardiovascular events. *Hypertension.* (2012) 60:90–7. doi: 10.1161/HYPERTENSIONAHA.112.194878

33. Arjunon S, Rathan S, Jo H, Yoganathan AP. Aortic valve: mechanical environment and mechanobiology. *Ann Biomed Eng.* (2013) 41:1331–46. doi: 10.1007/s10439-013-0785-7

34. Mills KT, Bundy JD, Kelly TN, Reed JE, Kearney PM, Reynolds K, et al. Global disparities of hypertension prevalence and control: a systematic analysis of population-based studies from 90 countries. *Circulation.* (2016) 134:441–50. doi: 10.1161/CIRCULATIONAHA.115.018912

35. Garcia-Rodriguez C, Parra-Izquierdo I, Castanos-Mollor I, Lopez J, San Roman JA, Sanchez Crespo M. Toll-like receptors, inflammation, and calcific aortic valve disease. *Front Physiol.* (2018) 9:201. doi: 10.3389/fphys.2018.00201

36. Kostyunin AE, Yuzhalin AE, Ovcharenko EA, Kutikhin AG. Development of calcific aortic valve disease: do we know enough for new clinical trials? *J Mol Cell Cardiol.* (2019) 132:189–209. doi: 10.1016/j.yjmcc.2019.05.016

37. Wood AM, Kaptoge S, Butterworth AS, Willeit P, Warnakula S, Bolton T, et al. Risk thresholds for alcohol consumption: combined analysis of individual-participant data for 599 912 current drinkers in 83 prospective studies. *Lancet.* (2018) 391:1513–23. doi: 10.1016/S0140-6736(18)30134-X

38. Holmes MV, Dale CE, Zuccolo L, Silverwood RJ, Guo Y, Ye Z, et al. Association between alcohol and cardiovascular disease: Mendelian randomisation analysis based on individual participant data. *BMJ.* (2014) 349:g4164. doi: 10.1136/bmj.g4164

39. Matsui M, Bouchareb R, Storto M, Hussain Y, Gregg A, Marx SO, et al. Increased Ca2+ influx through CaV1.2 drives aortic valve calcification. *JCI Insight.* (2022) 7:e155569. doi: 10.1172/jci.insight.155569

40. Wald DS, Bestwick JP. Association between serum calcium, serum phosphate and aortic stenosis with implications for prevention. *Eur J Prev Cardiol.* (2018) 25:551–6. doi: 10.1177/20474873187 56131

41. Wald DS, Bangash FA, Morris JK, Wald NJ. Mortality from aortic stenosis: prospective study of serum calcium and phosphate. *J Intern Med.* (2017) 281:407–11. doi: 10.1111/joim.12593

42. Myasoedova VA, Ravani AL, Frigerio B, Valerio V, Moschetta D, Songia P, et al. Novel pharmacological targets for calcific aortic valve disease: prevention and treatments. *Pharmacol Res.* (2018) 136:74–82. doi: 10.1016/j.phrs.2018. 08.020

43. Park S, Kario K, Chia YC, Turana Y, Chen CH, Buranakitjaroen P, et al. The influence of the ambient temperature on blood pressure and how it will affect the epidemiology of hypertension in Asia. *J Clin Hypertens.* (2020) 22:438–44. doi: 10.1111/jch.13762

44. Grillo A, Salvi L, Coruzzi P, Salvi P, Parati G. Sodium intake and hypertension. *Nutrients.* (2019) 11:1970. doi: 10.3390/nu11091970

45. He J, Huang JF Li C, Chen J, Lu X, Chen JC, et al. Sodium sensitivity, sodium resistance, and incidence of hypertension: a longitudinal follow-up study of dietary sodium intervention. *Hypertension.* (2021) 78:155–64. doi: 10.1161/HYPERTENSIONAHA.120.16758

Frontiers in
Cardiovascular Medicine

Innovations and improvements in cardiovascular treatment and practice

Focuses on research that challenges the status quo of cardiovascular care, or facilitates the translation of advances into new therapies and diagnostic tools.

Discover the latest Research Topics

See more →

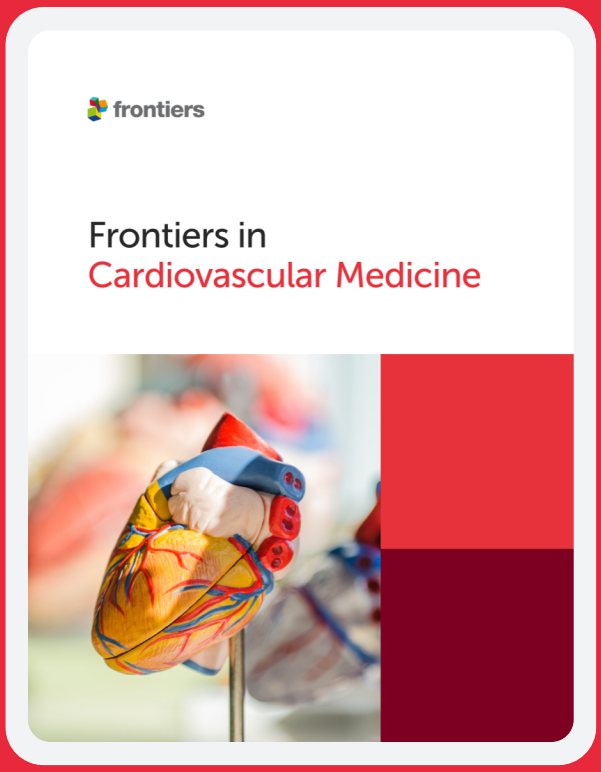

Frontiers

Avenue du Tribunal-Fédéral 34
1005 Lausanne, Switzerland
frontiersin.org

Contact us

+41 (0)21 510 17 00
frontiersin.org/about/contact